RL-TR-97-189
Final Technical Report
October 1997

PROCEEDINGS OF THE 1996 ANTENNA APPLICATIONS SYMPOSIUM

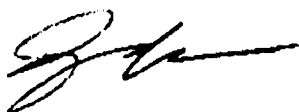University of Massachusetts

Daniel H. Schaubert, et al

19980422 118

Rome Laboratory
Air Force Materiel Command
Rome, New York

This report has been reviewed by the Rome Laboratory Public Affairs Office (PA) and is releasable to the National Technical Information Service (NTIS). At NTIS it will be releasable to the general public, including foreign nations.
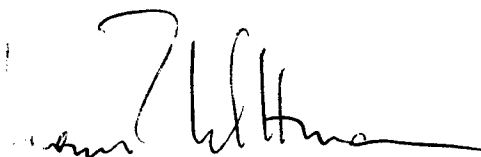
RL-TR-97-189 has been reviewed and is approved for publication.

APPROVED:

ZACHARY O. WHITE
Project Engineer

FOR THE DIRECTOR:

HORST R. WITTMANN, Director
Electromagnetics & Reliability Directorate

REPORT DOCUMENTATION PAGE

Form Approved
OMB No. 0704-0188

1. AGENCY USE ONLY *(Leave blank)*	2. REPORT DATE	3. REPORT TYPE AND DATES COVERED
	Oct 97	Final 18 - 20 Sep 96

4. TITLE AND SUBTITLE

PROCEEDINGS OF THE 1996 ANTENNA APPLICATIONS SYMPOSIUM

6. AUTHOR(S)

Daniel H. Schaubert, et al

5. FUNDING NUMBERS

C   - F30602-96-C-0262
PE - 62702F
PR - 4600
TA - 14
WU - P2

7. PERFORMING ORGANIZATION NAME(S) AND ADDRESS(ES)

University of Massachusetts
Department of Electrical & Computer Engineering
Amherst, MA 01003

8. PERFORMING ORGANIZATION REPORT NUMBER

9. SPONSORING/MONITORING AGENCY NAME(S) AND ADDRESS(ES)

Rome Laboratory/ERAA
31 Grenier St.
Hanscom AFB, MA 01731-3010

10. SPONSORING/MONITORING AGENCY REPORT NUMBER

RL-TR-97-189

11. SUPPLEMENTARY NOTES

Rome Laboratory Project Engineer: Zachary O. White, ERAA, 617-377-3191

12a. DISTRIBUTION AVAILABILITY STATEMENT

Approved for public release; distribution unlimited.

12b. DISTRIBUTION CODE

N/A

13. ABSTRACT *(Maximum 200 words)*

The Proceedings of the 1996 Antenna Applications Symposium is a collection of state-of-the-art papers relating to phased array antennas, multibeam antennas, satellite antennas, microstrip antennas, reflector antennas, HF, VHF, UHF and various other antennas.

14. SUBJECT TERMS

Antennas, Microstrip, Multibeam Antenna, Satellite Antennas, Reflector, Array Antennas, Broadband Antennas, HF, VHF, UHF

15. NUMBER OF PAGES

496

16. PRICE CODE

17. SECURITY CLASSIFICATION OF REPORT	18. SECURITY CLASSIFICATION OF THIS PAGE	19. SECURITY CLASSIFICATION OF ABSTRACT	20. LIMITATION OF ABSTRACT
UNCLASSIFIED	UNCLASSIFIED	UNCLASSIFIED	UL

Standard Form 298 (Rev. 2-89) (EG)
Prescribed by ANSI Std. 239.18
Designed using Perform Pro, WHS/DIOR, Oct 94

TABLE OF CONTENTS
FOR
1996 ANTENNA APPLICATIONS SYMPOSIUM

i

III. ARRAY ANTENNA SYSTEMS

IV. NUMERICAL ANALYSIS

V. ANTENNA TECHNOLOGY AND MEASUREMENT

I. PHOTONICS IN ANTENNA SYSTEMS

DIGITALLY RECONFIGURABLE ANTENNA

Kris W. Turk
California Microwave, Inc.
6022 Variel Avenue
Woodland Hills, CA 91367
Phone (818)712-4506 / FAX (818)712-4496

1. ABSTRACT

This paper describes a lightweight, high gain, digitally reconfigurable antenna that utilizes Synaptic antenna technology and Photistor™ device technology. We fabricated and tested a demonstration unit with switching junctions (Synapses) that change the type and size of the antenna in order to optimize its performance. The Synapses contain a number of optoelectronic switches (Photistors™) controlled by light from a laser source. Light energy is applied to the active area of a Photistor™ by an optical fiber causing it to become conductive. This activates a particular portion of the radiating structure. Removal of the optical energy from a Synapse deactivates that particular portion of the radiating structure. The Synapses are switched by a microprocessor located at the base of the antenna that receives digital frequency information from a receiver and reconfigures the antenna in near real-time to achieve the desired pattern and impedance match. Multiple Synapses are used to achieve a multi-octave bandwidth.

First, a brief history of this technology will be presented. Second, the system design, fabrication techniques, and test results will be discussed. Finally, future recommendations will be presented.

2. HISTORY

The need for a broadband (multiple octave) antenna has been apparent for many years. A Synaptic antenna tuned to a specific frequency is fairly narrowband; in order to appear broadband, the antenna reconfigures itself in near real time. Our original requirement was for a compact, lightweight, receive-only antenna that had 0 dBi gain at 20 MHz and +6 dBi gain at 2 GHz. The entire assembly had to take

1

up less than 0.5 ft^3 of space (stowed), weigh less than 4 lbs, and consume less than 200 mW of power. Our original proposal was for a reconfigurable monopole that would start as a short stub for operation at higher frequencies, and then "grow" in length to operate effectively at lower frequencies. The "growing" would be accomplished by Synaptic techniques. Our customer could not tolerate the ground radials needed for a monopole, so we proposed a center-fed dipole that could also change in length to optimize its performance. Our customer needed more gain than a standard dipole, so we proposed a collinear array of sleeved dipoles. The final design was the result of a number of trade-offs between the design constraints, budget constraints, performance requirements, and the current state of the art regarding Photistor^{TM} devices and laser diode sources. The specifications that were modified were frequency range (decreased to 100 MHz - 1 GHz), gain (decreased to 0 dBi across the band), and power consumption (increased to 1 W). The rest of the parameters were taken as goals of the development process.

3. SYSTEM DESIGN

The overall design of the Digitally Reconfigurable Antenna (DRA) consists of three subsystems: Radio Frequency (RF), Electro-Optic (EO), and Digital as shown in Figure 3-1. Figure 3-2 shows the layout of the DRA. It consists of a 10 foot radiating section containing four synapses, an 11 foot feed line containing an RG-142 coaxial cable and 12 optical fibers, a chassis/spool containing control circuitry and providing antenna storage, and interface cables for connecting RF, power, and control to a receiving system.

2
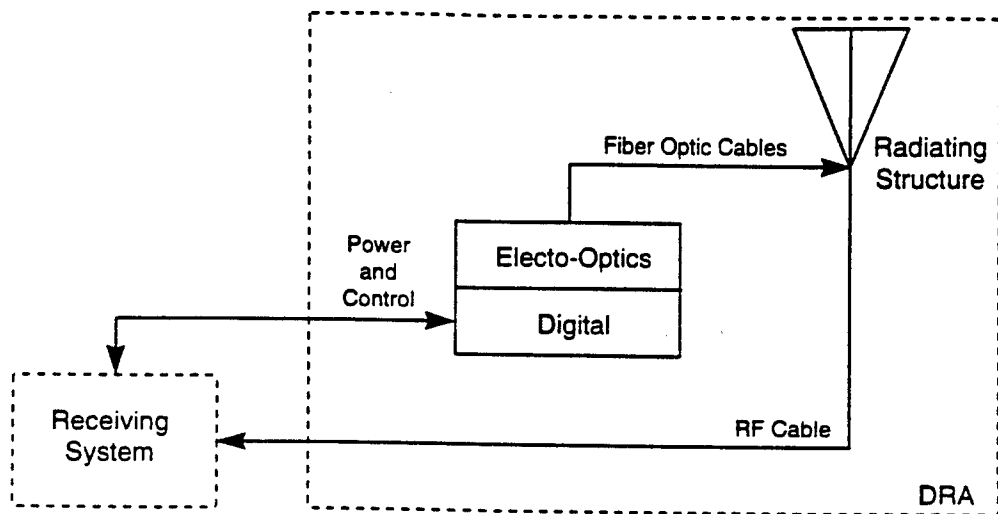
FIGURE 3-1. ANTENNA SYSTEM BLOCK DIAGRAM
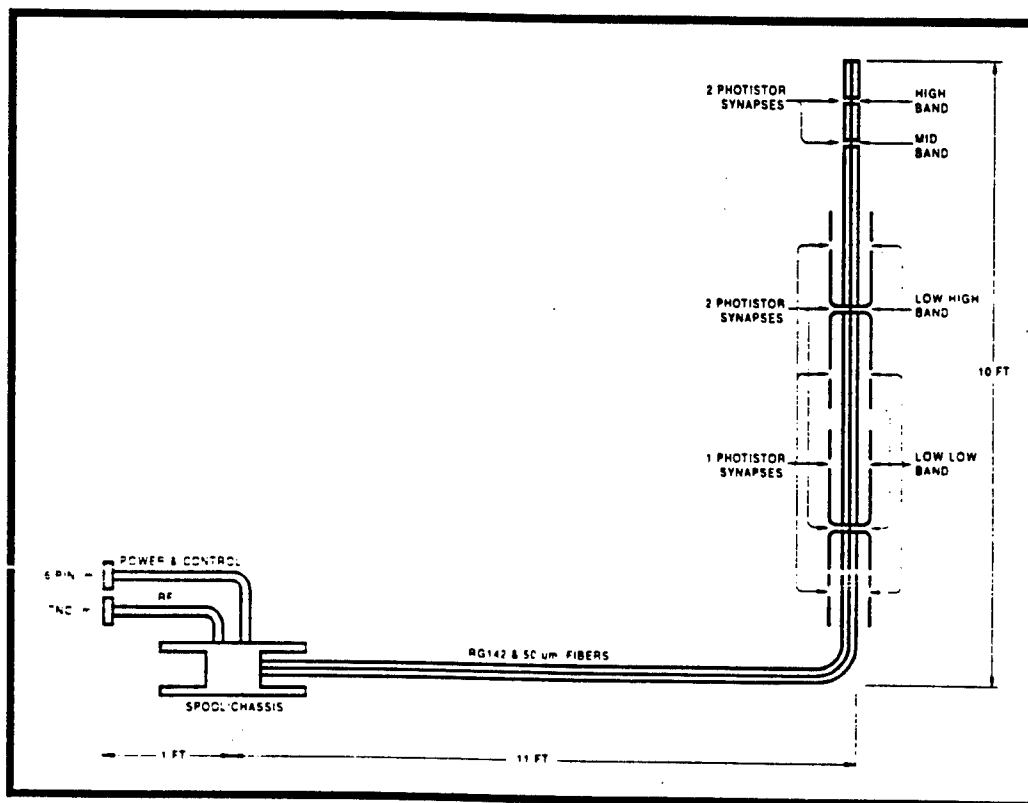
FIGURE 3-2. ANTENNA ASSEMBLY DIMENSIONS

3

3.1. RF Subsystem

The RF Subsystem consists of a coaxial cable that has four synapses; one for frequencies in the high band, one for frequencies in the mid band, and two for frequencies in the low band. The high band and mid band synapses are standard sleeved dipoles. The low band synapses are also sleeved dipoles, but they have been configured as a two element, collinear array. The sleeves in the low band array also have synapses in them. This further optimized the low band array into a low-low configuration and a low-high configuration. Figure 3.1-1 shows the layout of the various synapses, and their spacings, relative to the shorted end of the antenna (the top). The synapse on the right is the high band synapse, the next synapse is the mid band synapse, and the rest of the antenna is the low band array.
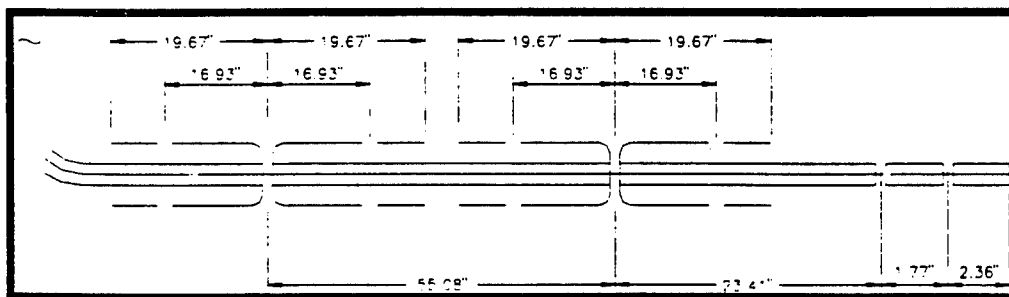
FIGURE 3.1-1. SLOT AND SLEEVE DESIGN

3.2. EO Subsystem

The EO subsystem consists of four lasers that branch out through optical splitters into 12 optical fibers. The fibers progress up the antenna and are attached to the Photistors™ that are bonded within the various synapses, thus forming the Synaptic junctions. The laser diodes operate at a wavelength of 820 nm and are pigtailed into optical fibers that have a 50 μm core size. The core size was chosen to match the size of the active area on the Photistor™, thereby maximizing the transfer of optical energy. Turning on a laser sends optical energy up the antenna to a synapse, causing the Photistors™ at that junction to become conductive,

4

essentially shorting out the synapse. Likewise, a laser that is turned off will cause a particular synapse to be open, and it will radiate. Figure 3.2-1 shows the different synapses, the number of Photistors™ within each one, which laser controls each synapse (L1, L2, L3 and L4), and which frequency band pertains to each synapse.
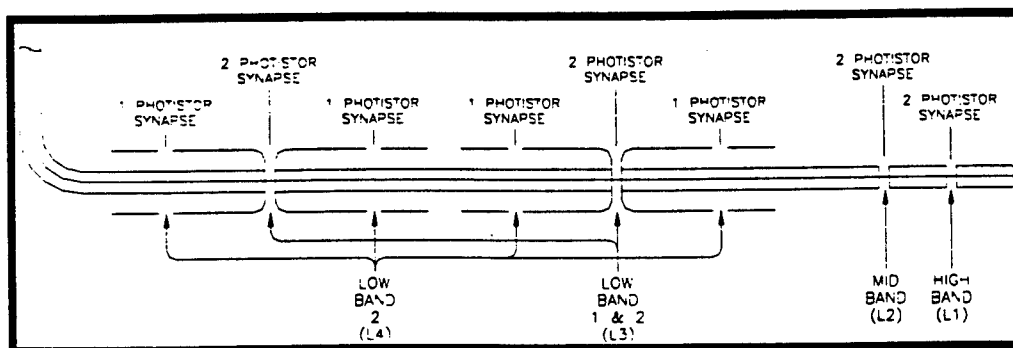
FIGURE 3.2-1. MULTI-BAND CONFIGURATIONS

3.3. Digital Subsystem

The digital subsystem consists of a microcontroller PC board that is responsible for handling the RS-232 interface, the power and control interface, and the control of the lasers. The microcontroller receives command words from the receiving system (via RS-232 at 19,200 bits per second) that instruct it to tune to specific frequencies. The microcontroller decodes the command words, finds the proper laser configurations in a lookup table, reconfigures the antenna by turning the appropriate lasers on or off, and sends back verification messages. The controller handles power conversion through a 24 volt to 5 volt DC-DC converter, and handles laser power control through two constant current totem poles (each totem pole powers two lasers). Figure 3.3-1 shows a block diagram of the DRA controller.
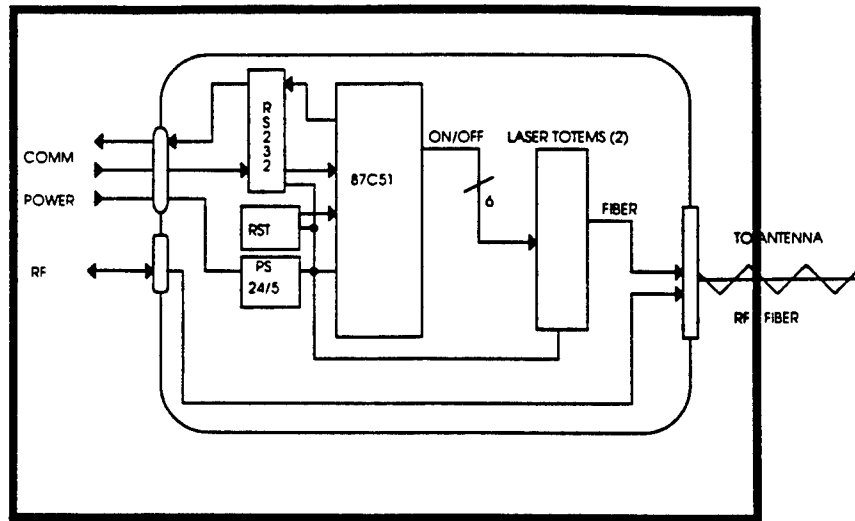
FIGURE 3.3-1. POWER AND CONTROL CIRCUIT

4. FABRICATION TECHNIQUES

4.1. Radiating Structure

The radiating structure was fabricated out of RG-142 coaxial cable. Gaps were cut in the shield and filled with epoxy to maintain spacing. The low band array Synaptic junctions were a special case due to the sleeves that were mentioned in section 3.1. Figure 4.1-1 shows a typical low band Synaptic junction. An additional, larger diameter shield was attached to the low band radiating structures to improve bandwidth. The larger shield was soldered to the smaller shield at the Synaptic junction, and a layer of neoprene foam was used to fill the space between them. The optical fibers were spiraled around the outside of the antenna to minimize optical loss and to facilitate storage. Figure 4.1-2 shows a cross section of the low band radiating structure. The antenna was covered with a weather resistant sleeve.
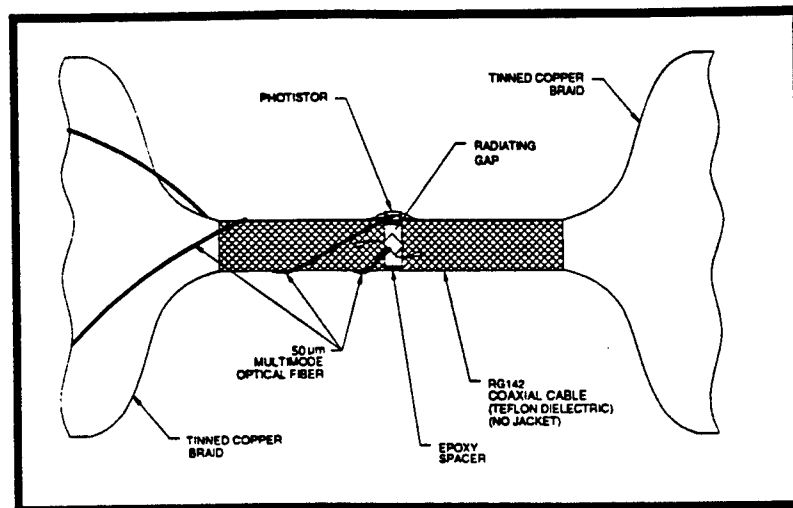
FIGURE 4.1-1. LOW-BAND SYNAPTIC JUNCTION
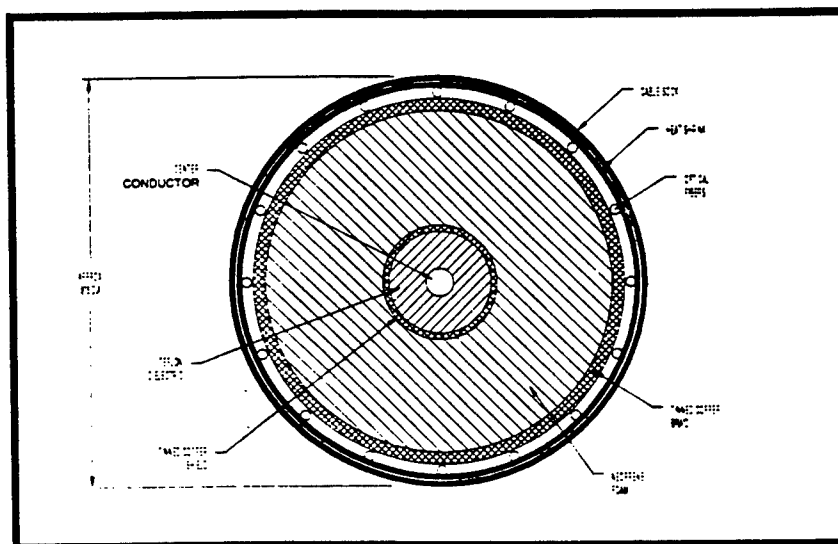
FIGURE 4.1-2. CROSS-SECTION OF LOW-BAND STRUCTURE

4.2. Photistor™ Switches

The Photistors™ (qty. 12) posed several fabrication challenges to become an integral part of a Synaptic junction. First, they had to be mechanically attached to the antenna and be able to survive deployment and storage. Second, they had to be electrically connected between the various radiating surfaces at each Synaptic

junction. Finally, they had to be optically connected to the laser sources via optical fiber. Figure 4.2-1 shows a plan view of a typical Photistor™ installation. Figure 4.2-2 shows a side view of a typical Photistor™ installation. Standard two-part epoxy was used to attach the Photistors™ (on their side) to the epoxy filled gap. Gold ribbon was used to attach the Photistor™ to the radiating surfaces using a parallel gap welder. The optical fiber was aligned with the center of the active area of the Photistor™ using an X-Y-Z positioner and a resistance feedback loop. Once the fiber was in position, it was attached to the Photistor™ using UV-cured optical epoxy. Finally, each Synaptic junction was encased in epoxy for rigidity, and covered with neoprene foam to maintain a uniform diameter.
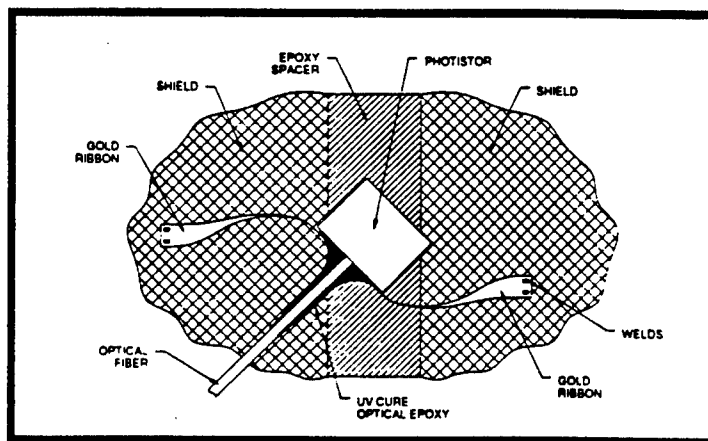
FIGURE 4.2-1. PHOTISTOR™ SWITCH INSTALLATION - TOP
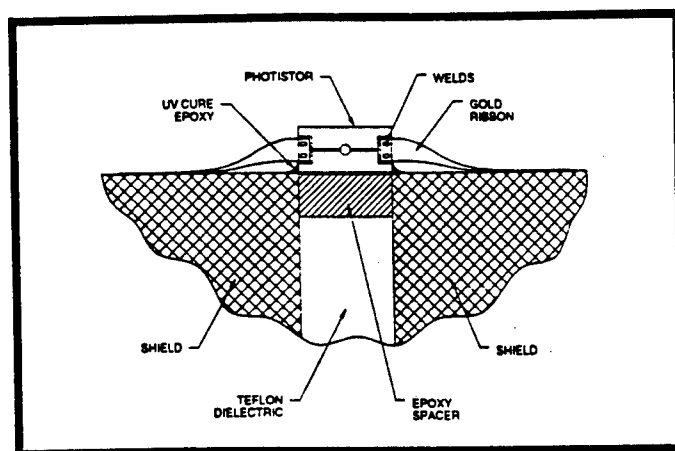
FIGURE 4.2-2. PHOTISTOR™ SWITCH INSTALLATION - SIDE

4.3. Electronics Chassis & Spool

The control electronics were housed inside the hub of a cable spool. This kept the antenna assembly compact and allowed for easy storage of the radiating structure. Figure 4.3-1 shows a plan view and a cross sectional view of the electronics chassis/spool. The electronics chassis consisted of four diode laser sources, eight 1x2 optical splitters, a manifold with 12 optical SMA connectors, the digital control PCB, the RF interface cable, and the power & control interface cable.
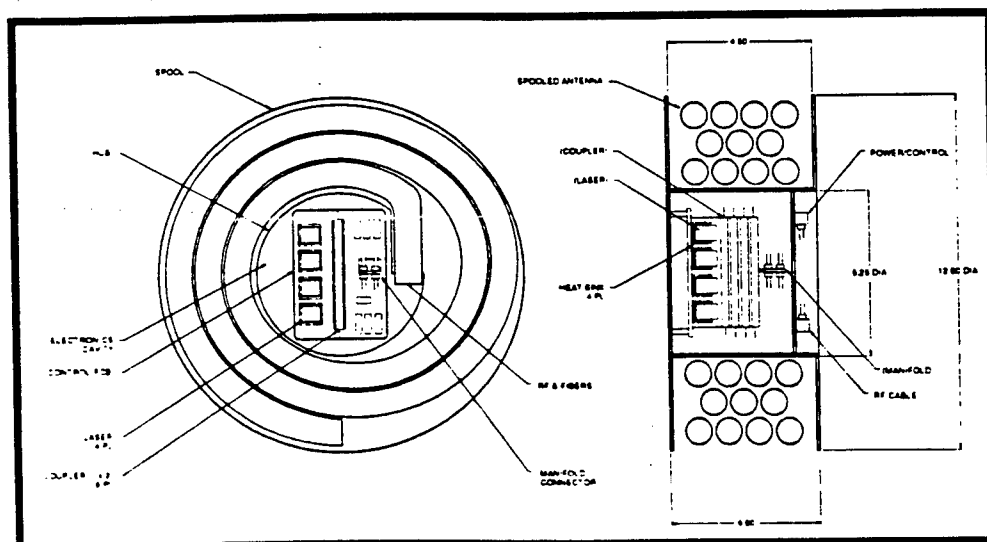
FIGURE 4.3-1. ANTENNA SPOOL AND ASSEMBLY.

9

5. TEST RESULTS

Initially, the DRA had a stringent set of performance criteria that needed to be met. Since this was a development program, the requirements and specifications that drove the design were considered goals, and a subsequent relaxation of the constraints was approved by the customer. Using the DRA Functional Test Procedure, the following areas were tested: RF Performance, Interface Requirements, Digital Performance, Physical Characteristics, and Power Consumption.

5.1. RF Performance

The original goal was for the antenna to have an operational frequency range of 20 MHz to 2 GHz, a Voltage Standing Wave Ratio (VSWR) of less than or equal to 2:1 across the operational frequency range, and peak gains ranging from 0 dBi at 20 MHz to +6 dBi at 2 GHz. Due to design constraints, the operational frequency range is 100 MHz to 1000 MHz. The DRA has a VSWR of less than or equal to 2:1 across most of the operational frequency range, but depending on the configuration chosen it does exceed 2:1 at a few select frequencies. The DRA has peak gains ranging from -7 dBi at 100 MHz to -10 dBi at 1 GHz. Again due to design constraints, the gain parameter was "optimized" into three specific frequency bands of interest. Therefore, peak gains of -5 dBi in the low band, -4 dBi in the mid band, and +2 dBi in the high band were achieved.

5.2. Interface Requirements

The original goal was for the antenna to have an RF interface consisting of a TNC male connector, a data interface consisting of an RS-232 running at 19,200 bits per second, and a power and control interface consisting of a 6-pin female connector (P/N LJTP02RE-09-35S). The DRA successfully achieved this goal.

10

5.3. Digital Performance

The original goal was for the antenna to have a tuning speed of less than 2 ms. The DRA successfully achieved this goal with a worst case tuning speed of 394 µs (≈0.4 ms). The antenna's tuning speed is defined as the period of time from the start of the receipt of a command word to when the impedance of the antenna reaches its proper value. This number was determined by connecting the antenna to a logic analyzer, applying a voltage source (with constant current) between the antenna's center conductor and shield, and measuring the time required for the voltage across the antenna to stabilize after changing configurations. Since changing configurations alters the impedance of the antenna, the voltage across the antenna will also change (since the current was held constant). The analyzer was triggered by the microcontroller's RS-232 receive line (Rx), which goes low at the start of a command word. Data were taken for all configuration changes that generated a time response. As expected, when lasers are turned on, the antenna exhibits a typical capacitive rise time, and when lasers are turned off, the antenna exhibits a very quick fall time.

5.4. Physical Characteristics

The original goal was for the antenna to have physical dimensions not to exceed 12" x 12" x 6", and a weight not to exceed 4 lbs. The DRA successfully achieved the physical dimensions goal, but weighed in at 5.1 lbs.

5.5. Power Consumption

The original goal was for the antenna to have an average power consumption of no more than 1 watt. The DRA successfully achieved this goal with an average power consumption of 725 mW. This number was calculated using actual measurements of current draw on the operating antenna, combined with a

11

statistical analysis of the duty cycles of the lasers and electronics during the various antenna configurations.

6. FUTURE DEVELOPMENT

The DRA represents the second generation of Synaptic Antennas. Future programs and additional funding would make the next generation of Synaptic Antennas possible. Continued development is necessary in a number of areas. The Photistors™ themselves need to be improved by two orders of magnitude. Instead of requiring 1 mW of optical energy to drive the "ON" resistance down to 10 Ω, the next generation would only need 100 μW of optical energy to drive the "ON" resistance down to 1 Ω. Requiring less optical energy would significantly lower the power consumption of the system, and if low power laser diodes could be used, would also significantly reduce the cost of the system. In addition, decreasing the size of the Photistors™ would enable many more devices to be used in a given application, thereby improving performance.

The laser diodes also need to be improved. Currently, they are only around 50% efficient with a relatively high threshold current value. For example, a typical laser diode takes 30 mA of electrical current to turn on (start lasing) and then delivers 1 mW of optical power out for every 2 mW of electrical power put in. As with smaller size, more efficient laser diodes with lower threshold currents would also enable many more devices to be used in a given application, thereby improving performance. In addition, advances in compact, laser diode arrays and optical fiber pigtailing techniques would also contribute to increased flexibility of design and improved performance.

IMPULSE PHOTOCONDUCTING ANTENNAS ACTIVATED BY PICOSECOND LASER PULSES

D. W. Liu, P. H. Carr, and D. F. Bliss

Rome Laboratory
Electromagnetics and Reliability Directorate (RL/ERAC)
Hanscom AFB, MA 01731-3010
617-377-3581 voice, 617-377-1074 FAX
dwliu@maxwell.rl.plh.af.mil

ABSTRACT

Reconfigurable microwave impulse antennas can be implemented optically. In this work, 50 - 100 picosecond laser pulses from a frequency-doubled, mode-locked, Q-switched YLF laser generate photoelectrons in dc-biased high resistivity semiconductor wafers. We have investigated InP:Fe, GaAs, and Low -Temperature grown GaAs (LTG - GaAs) for this application. The microwave radiation due to the dc-driven photocurrent is detected at the near field with an induction loop and at the far field by an impulse antenna. These signals are observed in real time with a Tektronix 11802 sampling oscilloscope. We have studied nonlinearities in the microwave radiation for optical fluence as high as $300\mu J/cm^2$. Nonlinearities at dc-bias fields as low as 12KV/cm were also observed. The relevant parameters involved for generating microwave pulses, such as photoconductivity, bias field strength, optical fluence, antenna element area, and experimental observations will be analyzed and discussed.

Since the output microwave pulse profile emulates the input optical signal, pulse-shaping can be implemented by modulating the optical beams. Multi-element phased array antennas can be established with multiple laser beams or with fiber optic feeds for individual elements. Because the $1.06\mu m$ excitation beam will be partially absorbed and partially transmitted through the semiconductor antenna element, 2-D and 3-D array are possible. We will also describe the results of a 3-D serial configuration as a proof of concept for this antenna.

13

HIGHLY PARALLEL OPTICAL DEVICE TO PRODUCE TRUE TIME DELAYS FOR PHASED ARRAY ANTENNAS

Betty Lise Anderson
Stuart A. Collins, Jr.
Charles A. Klein
Elizabeth A. Beecher
Stephen B. Brown
The Ohio State University Department of Electrical Engineering
205 Dreese Laboratory, 2015 Neil Avenue
Columbus, Ohio 43210

Abstract: In this paper we describe an optical unit that provides programmable true time delays (TTD's) for phased array antenna beam steering. The described system has several advantages over other TTD systems: a compact single optical unit can provide parallel control of over 169 array elements with six bit time delay resolution possible for each element. The time delays are produced by multiple reflections in a mirror cavity with continuous refocusing, while a single spatial light modulator selects between different optical paths for all the independent light beams. Moreover, the design is scaleable for pico- to nanosecond time delays. Amplitude control for beam shaping is be integrated into the device. The high degree of parallelism makes it ideally suited for multiple beam antennas. We describe the design and potential system configuration. We have built a proof-of-concept demonstration device and will present experimental data.

1. Introduction

Implementing true time delays (TTD's) for phased array antennas using photonics has received a great amount of interest lately with limited success [1]. Approaches to optical true time delay tend to fall into two categories: those using fibers [2-9] and those using long

free-space paths [10, 11]. One drawback of fiber approaches is the use of multiple optical switches, which tend to be expensive and lossy. Other fiber approaches broadcast the light over all possible paths at once, an approach that incurs enormous insertion losses. Wavelength division multiplexing schemes require complex tunable lasers. In the free-space systems, where there is no waveguiding of the light, beam diffraction necessitates physically large components. [10, 11] In addition, multiple optical switches, which are expensive and bulky, are used for switching the beams between sequential optical paths.

We propose here a system based on a completely new approach, using a simple optical cavity consisting of focusing mirrors to provide free-space optical paths of arbitrary length, and a spatial light modulator to select the paths. One TTD device can handle many independent light beams simultaneously, each corresponding to an individual antenna array element. This new optical TTD device a) reduces TTD system complexity by allowing compact, massively parallel control of multiple independent time delays, b) allows design flexibility for both long and short time delays, c) provides for amplitude control in receive pre-processing for nulling countermeasures, d) has the option of ruggedized solid block construction, e) has few physical components and does not require fiber couplers, and f) supports multiple beam antennas.

The basic device is designed to feed the individual antenna elements. One device provides the required independent time delays

15

and amplitude control for multiple antenna elements, to direct the beam in the transmit mode and in the receive mode to follow targets and null out interference. The device itself is controlled by input from the beamforming computer processor.

We begin in Section 2 by describing the White Cell, an optical cavity originally invented for spectroscopic applications, on which the TTD system is based. In that section we'll also describe some modifications to the White cell to adapt it to true-time delay applications. Even more performance and versatility can be realized by the dual White cell described in Section 3. Amplitude control for beam shaping and nulling is discussed in Section 4, and in Section 5 we describe how this true time delay unit will fit into a phased array antenna system. Our experimental results are given in Section 6. Section 7 discusses those factors that impact performance, such as dynamic range, resolution, and speed. A discussion and summary appear in Sections 8 and 9, respectively.

The material in this paper has been submitted in an Invention Disclosure, "Device for producing electronically/optically controlled incremental time delays," to the Ohio State University Office of Technology Transfer, disclosure #95ID45U.

2. Basic Design Concepts

The time delay cell uses a system of mirrors to bounce light back and forth inside two optical cavities sharing one common mirror. The

common mirror is a spatial light modulator, which controls the direction of any individual beam. Our design uses a separate light beam for each antenna element, and many beams circulate through the cell simultaneously. The beams are constantly refocused, thus avoiding the diffraction problems of other free-space systems.

This optical true time delay unit is based on the White Cell [12], a device originally designed for spectroscopic measurements requiring very long optical paths through a gaseous sample. We begin by explaining the operation of the original White cell, followed by a discussion of some modifications for the generation of variable true-time delays.

2.1 The Basic White Cell

The basic White cell is shown in Figure 1. It consists of three spherical mirrors, all of the same radius of curvature, shown in Figure 1(a). Mirror A is opposite Mirrors B and C, and separated from them by a distance equal to its radius of curvature. Its center of curvature lies on the optical axis, and falls between Mirror B and C. Mirrors B and C are aligned such that their centers of curvature land on Mirror A, each a distance δ from the optical axis, but on opposites sides of it as shown. Light leaving Mirror B is imaged onto Mirror C and vice versa.

In operation light enters the White Cell from a spot imaged onto a small, flat mirror called the input turning mirror, as shown in Figure 1 (b). This light beam has been prepared so that it expands to fill Mirror

17

B. Mirror B refocuses the beam to a point on Mirror A. If the beam enters the cell a distance $d1$ from B's center of curvature, it will be focused to a point the same distance d_1 on the opposite side of the center of curvature. From there, the beam is reflected by Mirror A,
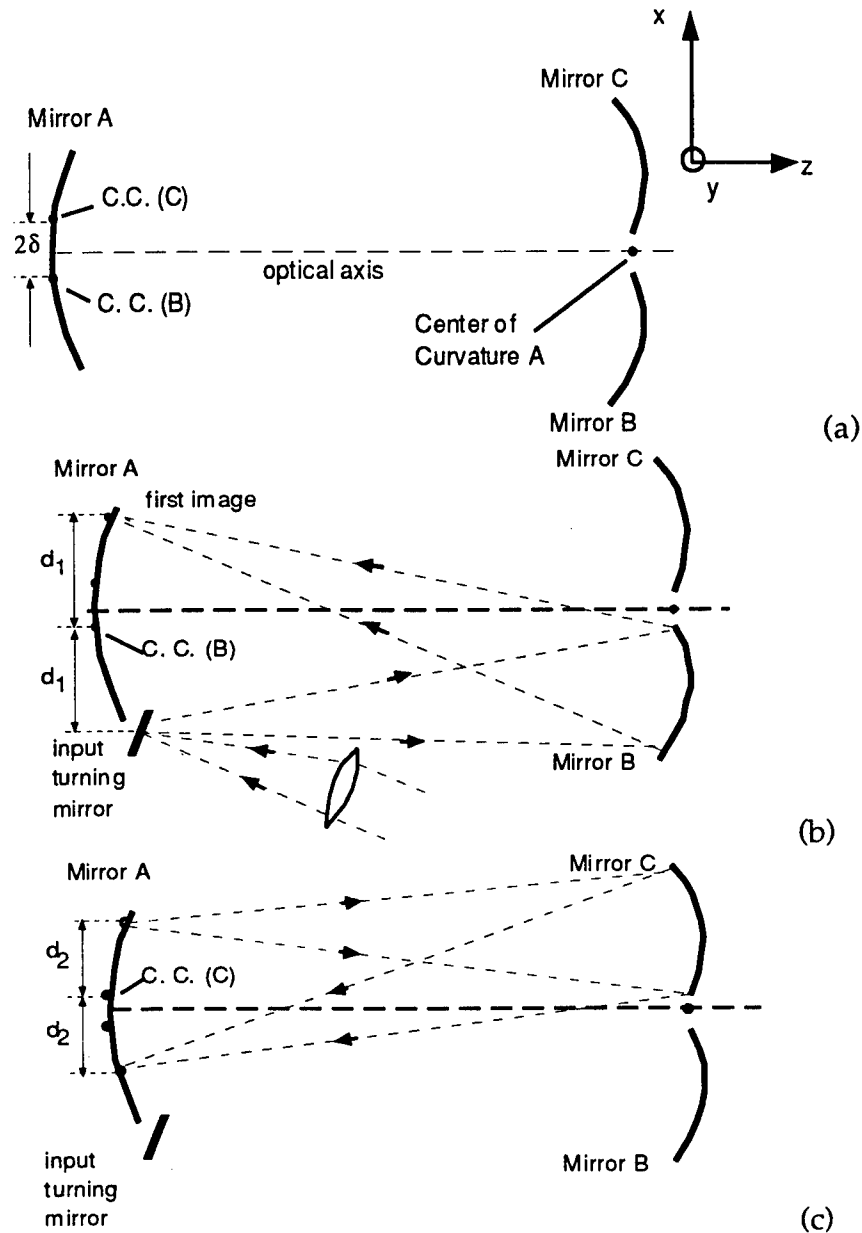
Figure 1. (a) The White cell; (b) path of first bounce; (c) second bounce.

expands again, and just fills Mirror C, as shown in Figure 1 (c). Since the point being imaged by C is located a distance d_2 from the center of curvature of Mirror C, C refocuses the light beam to a new spot d_2 away from C's center of curvature on the opposite side.

This process continues, with spots alternating from the top to the bottom of Mirror A, as shown in Figure 2 (a), which is drawn looking at Mirror A from the right in the previous figure. Note that the mirrors can be square sections of spherical mirrors, as shown in the figure. The centers of curvature of Mirrors B and C are indicated, and the spots are numbered in the sequence in which they appear. The optical axis is at the center of the figure, coinciding with spot number 8.

Figure 2 (a), however, shows a special case- the input beam is introduced on a line that contains the centers of curvature of Mirrors B and C. When the input beam is introduced *off* that line, say by an amount y_0, the spots alternate top and bottom *and* left to right, as shown in Figure 2(b). Consider a given beam as it propagates through the cell. The exact placement of each spot on Mirror A is determined by the following procedure illustrated in Figure 2 (c): from the *(j-1)*st spot, draw a line through the spot and the center of curvature of the next mirror the beam will strike (B or C). The *j*th spot will appear on this line, the same distance on the opposite side of the center of curvature as spot *(j-1)* was.

It is possible to use the entire area of Mirror A. Figure 2(d) shows Mirror A with a series of input spots introduced at the input

turning mirror at the bottom of the figure. The individual beams

maintain their independence, each tracing out a unique sequence of
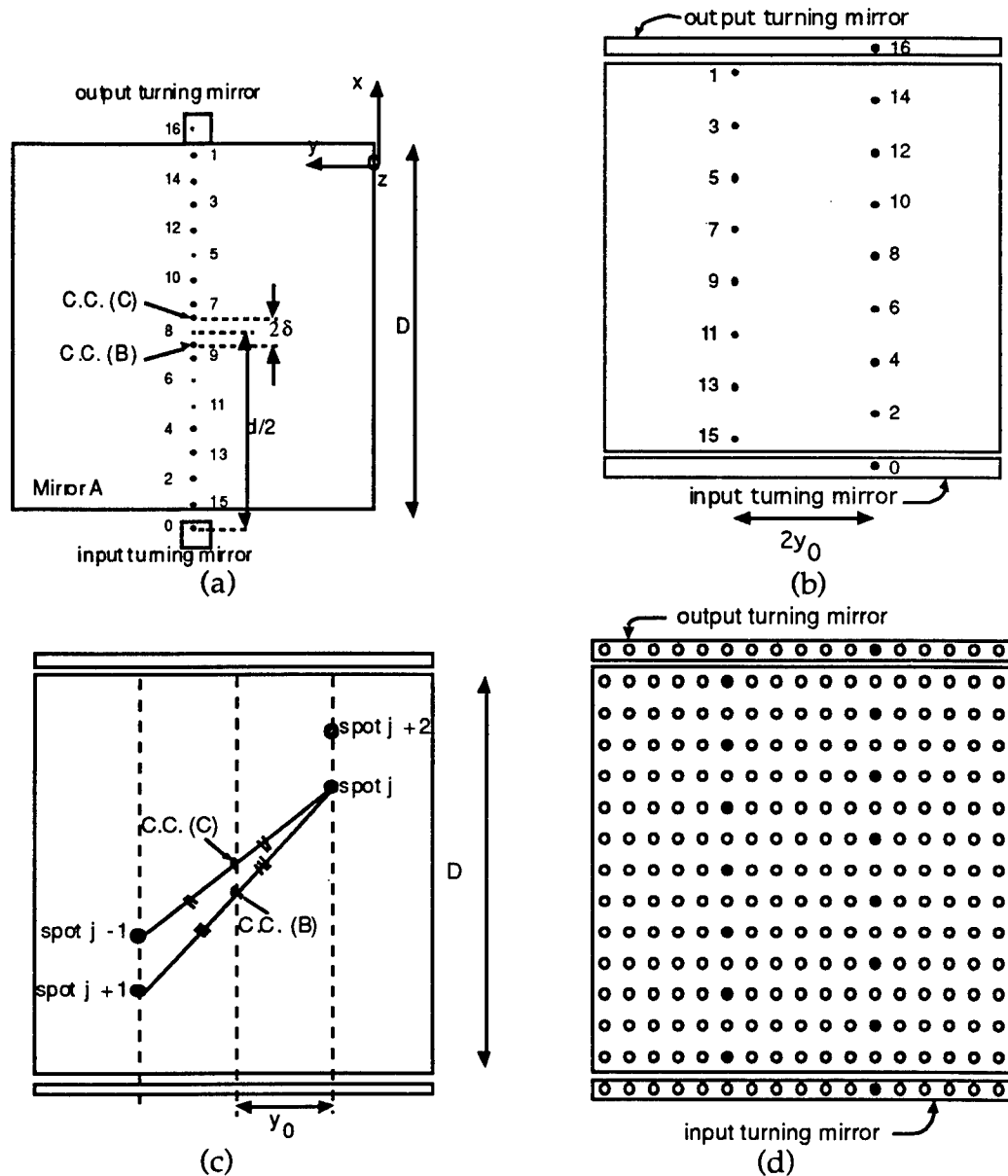
Figure 2. The mirror has been made square rather than round. (a)
Sequence of spots for an input beam in line with centers of curvature of
Mirrors B and C; (b) construction used to predict location of next spot; c)
the sequence of spots for an off-center beam; (d) an array of input beams,
with sequence of spots for one particular off-axis beam highlighted.

spots. No two beams ever strike the same point on Mirror A during the progression.

2.2. Modifications to the White Cell

We now make three modifications to the White cell to adapt it to true time delay applications. The modifications are shown in Figure 3. The first modification is to replace Mirror A with a flat mirror and a lens of focal length f, where f is equal to the radius of curvature of the original spherical mirror. In this case, the lens/mirror combination is optically equivalent to the mirror it replaces. Next, we replace the flat mirror with a spatial light modulator (SLM), which can be either electronically or optically addressed. We also require the input light to be polarized in the plane of the paper in Figure 3. The SLM reflects all light striking it, but is configured to rotate the direction of polarization of the beam at an addressed pixel. Finally, we add a polarizing beamsplitter. The beamsplitter reflects light polarized in the plane perpendicular to the paper but transmits light polarized parallel to the plane of the paper.

The modified White Cell shown in Figure 3 is the basic element of the true-time delay device. One way of implementing multiple time delays is to introduce a linear array of input beams into the cell via the input turning mirror. Each of these beams can be made to transit the cell a different number of times, by selecting the appropriate pixel of the spatial light modulator. The input beams are all polarized such that

21
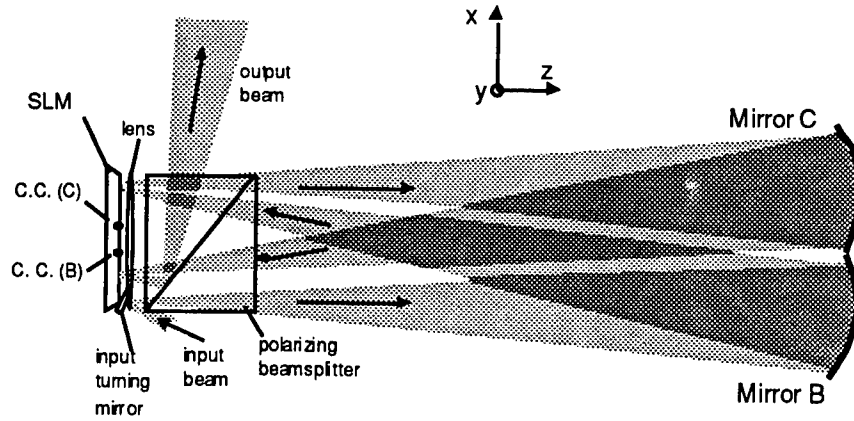
Figure 3. The modified White Cell. One beam is shown making two full transits of the cell, or twice the minimum path.

they pass through the beamsplitter unaffected. A particular beam is ejected after being reflected from some particular spot on the SLM by addressing that pixel to rotate the polarization of the beam, whereupon the beam is reflected by the beamsplitter and turned out of the cell. For example, the beam in Figure 3 is turned out after two passes through the cell.

With this approach we see that the time delays are in units of the transit time from Mirror A to the mirror opposite it and back, or

$$delay \ increment = \frac{2[R + (n-1)S]}{c}$$

(1)

where R is the distance between Mirror A and either Mirror B or C, n is the refractive index of the beamsplitter cube, and S is the length of the cube.

3. The Dual-Cell True-Time Delay Device

3.1 Even-Armed Dual White Cell

To complete the true-time delay photonic device a second pair of spherical mirrors (call them E and F) is added as shown in Figure 4, and a different beam ejection procedure is used. In this approach, the beams are allowed to make the complete number of transits; they bounce back and forth in the cell(s) until they strike the output turning mirror and are reflected out of the cell.

This cell is even-armed; that is, Mirrors E and F have the same focal lengths as each other, but different from B and C. Also, the lens next to the spatial light modulator is replaced by two different lenses, one for each White cell, on the output sides of the polarizing beamsplitter. These lenses are chosen to have appropriate focal lengths for the Mirrors B and C or Mirrors E and F. Now we have dual White cells, joined at the beamsplitter.

The two cells have different transit times because of the different separation distances of Mirrors E and F from the SLM compared to Mirrors B and C. In this configuration, each beam makes the same total number of transits before leaving the cell, but now the spatial light modulator is used to control how many of those transits are made to (B, C) and how many are made to (E, F). The minimum possible delay corresponds to a path having all the bounces through the shorter cell. The maximum delay results from making all passes through the longer cell. The smallest delay increment is the *difference* between the

23

path length in the shorter cell and the path length through the longer cell.

$$delay\ increment = \frac{2(R_{A,BC} - R_{A,EF})}{c}$$

(2)

The total delay is some integer multiple of that differential delay increment. For this reason, the device is very suitable for very small delays. By making the radii of Mirrors E and F nearly equal to the radii of B and C, the differential time delay can be made very small. Similarly, the delay difference can be quite large if the two cells are very different in length.
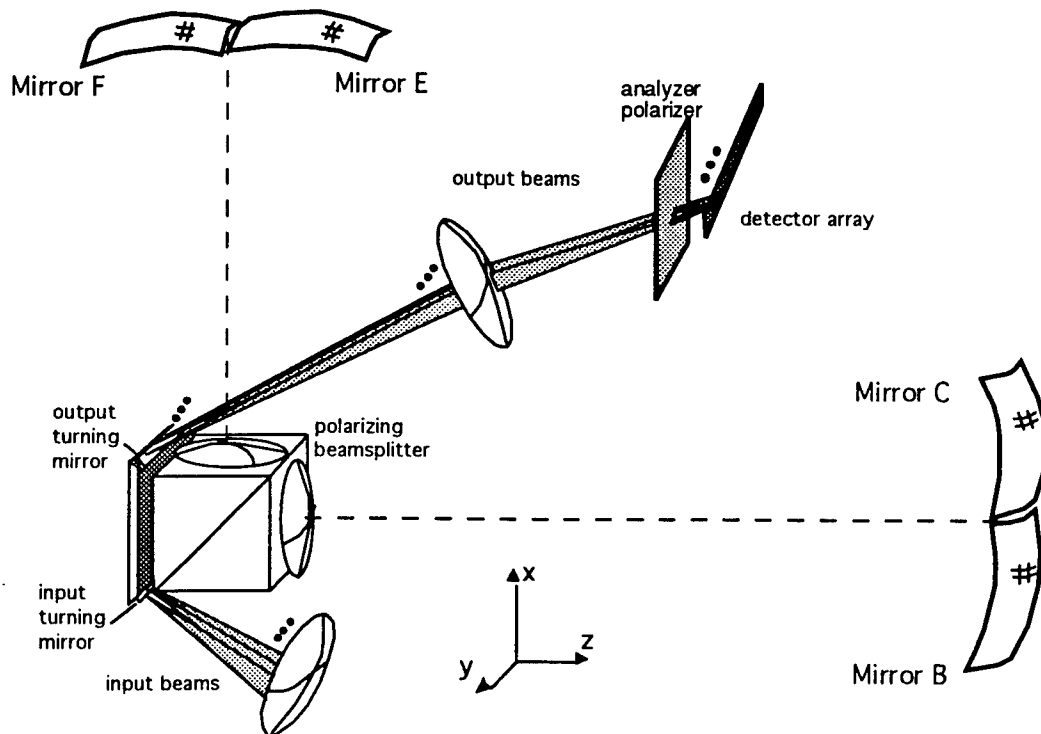
Figure 4. The complete true-time delay device.

3.2 The Uneven-Armed Dual White Cell

We can make a further improvement to the dual White cell. We remove the restriction that the two focusing mirrors in each White cell are identical. Figure 5 shows the case in which Mirrors B and C are the same, but Mirrors E and F have different focal lengths. Mirrors B and C could also be different from each other, but we will show later that there is no advantage to that.

Let m be the number of times each independent beam travels from the SLM to Mirror B, C, E or F and back to the SLM. From the input turning mirror, the geometry is such that all beams must go to Mirror B. From B the beams return to the SLM, completing the first transit, at which point their individual polarizations are either rotated or not. If the polarization of a particular beam is not rotated on the first bounce, it proceeds to Mirror C. If the polarization *is* rotated, the beam
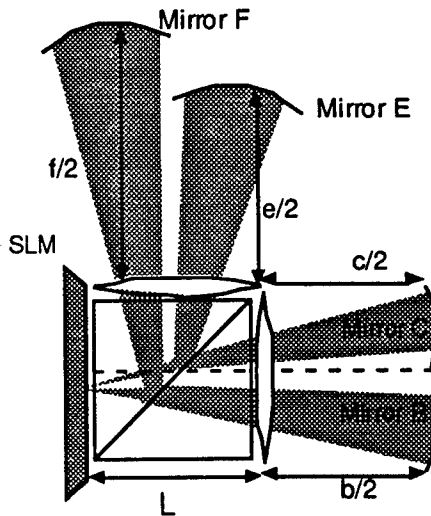
Figure 5. Asymmetrical dual White cell.
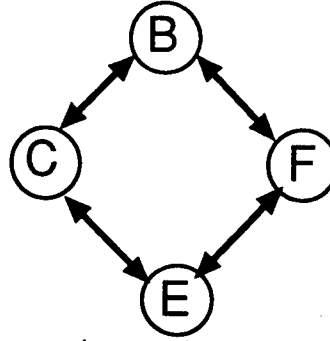
Figure 6. Transition diagram shows allowed progressions of the beams.

goes to Mirror F. After the second transit, each beam can go either to B or to E, based again on whether the corresponding pixel on the SLM is addressed.

A transition diagram is shown in Figure 6. We establish the rules of the progression to be a) every beam goes to Mirror B from the input turning mirror (first transit of the cell); b) a beam leaving B can go to either C or F but not E; c) other allowed transitions are shown in Figure 6, and d) the total number of transits m must be an even number, and the last bounce will be on the output turning mirror. For $m = 16$ transits, as shown for example in Figure 2(a), there are in fact 15 opportunities to change the polarization and therefore the path for this system.

The benefit of making the paths different is that a greater number of delays can be obtained for a given number of light beam bounces on the spatial light modulator. Call the path from the SLM to the focusing lenses near the beamsplitter L. Every path will have this length in common; i.e., no matter what path is chosen each beam will travel $2mL$ for m bounces. Since this distance is common to all delays,

we can neglect it, as we are interested only in differential delays. Next, let b be twice the distance between the lens and mirror B, so that a beam traveling to mirror B and back covers a distance of b. Let c be twice the distance from the lens to C, etc. If b is the shortest path, its length can also be subtracted from every pass since every beam will travel at least that far on each pass. Therefore we designate this reference distance as "0". Since we are taking c to be equal to b, it also contributes zero to the total differential delay.

Suppose the particular phased antenna array system design calls for a minimum true time delay increment between antenna elements of Δ. Then one can show that the ideal lengths of the arms result when path e requires a transit time Δ longer than paths b and c, and f has a transit time of $(m/2)\Delta$. For example, for a 16-transit system, the lengths of the four arms are, after common lengths are subtracted out: (b, c, e, f) = (0, 0, 1, 8)Δ.

The shortest delay possible results when a given beam bounces back and forth between Mirrors B and C for all m passes. Since b and c are both zero, the total differential delay is 0. To obtain a delay of 1Δ, the beam would be diverted to Mirror E $(e=1\Delta)$ one time, and bounce back and forth between B and C on all other bounces.

The maximum possible delay results when the beam passes from E to F and back as often as possible. This means $m/2$ trips to Mirror F and $\frac{m}{2}-1$ trips to Mirror E, since the first transit must go to Mirror B. The maximum delay is therefore

$$\text{maximum delay} = \left(\frac{m}{2}\right)\left(\frac{m}{2}\Delta\right) + \left(\frac{m}{2} - 1\right)(\Delta) = \left[\left(\frac{m}{2} + 1\right)\frac{m}{2} - 1\right]\Delta \tag{3}$$

We see that the maximum delay goes quadratically as the number of bounces. For 16 bounces, 72 different individual delays, from 0 to 71Δ, are possible. For 64 bounces, one can get 1,056 different delays. A straightforward algorithm exists to find the sequence required to produce any particular integer multiple of the delay Δ.

If amplitude control is implemented, the total number of delays is reduced slightly, as we will show in Section 4.

It may seem intuitive that even more delays would be possible if all four arms were different but that turns out not to be the case. Cases with four different arms either have no larger range of delays, or may not be able to generate every integer multiple of the basic delay increment Δ.

For example, suppose (b, c, e, f)= (0, 1, 2, 4)Δ were chosen instead of (0, 0, 1, 4)Δ for an eight-bounce system. Since the beam is required to go from b either c or e , the minimum delay is 4Δ. The maximum would be 22Δ, for a range of 18Δ. One cannot obtain, however, a delay of 5Δ. Other numbers are missing from the sequence as well. Using the (0, 0, 1, 2)Δ combination for 4 bounces, one has a range of 19Δ with every integer represented.

3.3. Construction Options

For a slightly different configuration, the optical path lengths in the two cells can also be made different by keeping the mirror radii all the same and varying the refractive index of the material between the beamsplitter and the mirror pairs.

The unit can be ruggedized by using a solid material instead of air as shown in Figure 7, whether the material is the same in both arms or different. There we see a possible solid block construction. The spherical mirror surfaces can be ground onto the ends of the glass or other optical material, and those surfaces can then be coated for enhanced reflectivity. Some change in material will be necessary to produce the lenses at the outputs of the beamsplitter. This solid construction is appealing because it is rugged and could be made comparatively temperature insensitive.
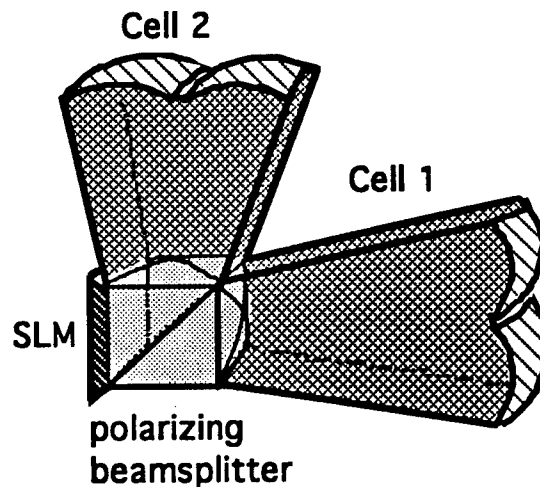
Figure 7. Solid block construction of the true time delay device.

4. Amplitude Control

For complete control of a radar beam, one wants, in addition to true-time delays, control of the amplitude of the signal sent by each antenna element, for purposes of beam shaping and nulling. Most photonic approaches to true-time delay have no amplitude control intrinsic to the design; it must be provided externally. In the modified White Cell approach, the amplitude control can be integrated directly into the true-time delay device by instructing the spatial light modulator to produce elliptical polarization of each beam just before it leaves the cell, and using an analyzing polarizer in front of the detectors.

This change to elliptical polarization is accomplished by applying the appropriate control signal to the pixels in the last column on the SLM, so that the last bounce is used for amplitude control rather than for timing. The analyzing polarizer will select the proper component to produce the desired amplitude.

When the last bounce is used for amplitude control, however, one can no longer choose between Mirror F and C on the final pass. If all beams end on C, then for 16 bounces, 64 different delays (0 through 63) are possible rather than 72. The maximum time delay for the general case using amplitude control is

30

$$\text{maximum delay} = \left(\frac{m}{2}\right)^2 \Delta$$

(4)

5. System Configuration

Figure 8 shows how the modified White Cell true-time delay device fits into a phased array antenna system. There is one beam through the cell for each antenna element; each beam is delayed independently. The device can be used in either transmit or receive mode.

In the transmit mode, shown in Figure 8(a), a separate polarized and RF-modulated light beam is introduced into the cell for each of N antenna elements. The m beams can be generated by N lasers, as shown in the figure, or by using a $1 \times N$ splitter and a single RF-modulated laser beam. The light source(s) can be of any single wavelength, and need not necessarily be lasers since the true time delay device will work for
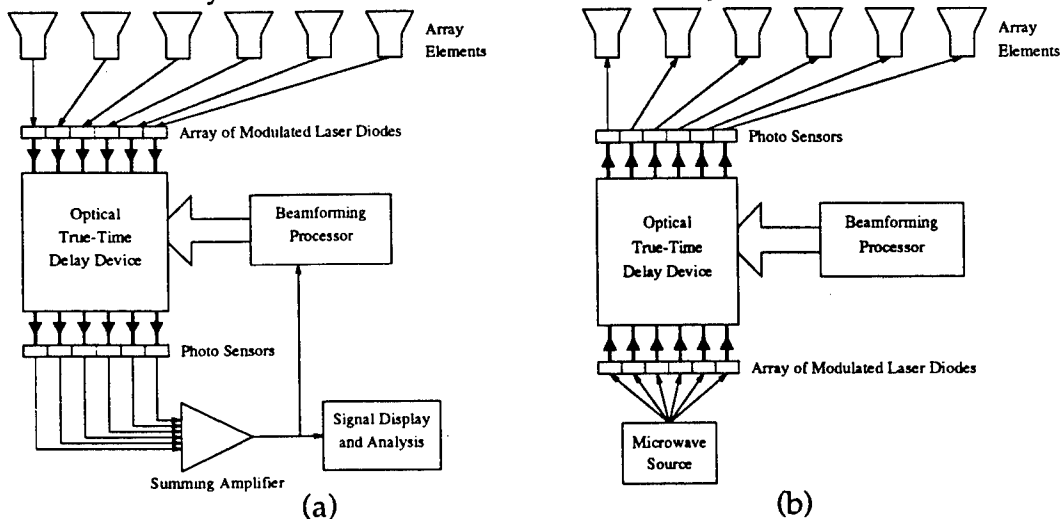
Figure 8. (a) Transmit system configuration; (b) receive system configuration.

incoherent as well as coherent light.

The N identical RF modulated pulsed light beams are introduced into the TTD device. The beams are given N individual time delays corresponding to the desired steering angle. Each independently time-delayed beam is detected by a photodetector that drives a transmit module (amplifier and antenna array element). The amplitude of the beam is individually adjusted for beam shaping.

Figure 8(b) shows the receive case, where N array element signals modulate N independent light beams. The beams are input into the TTD device, and are individually delayed to form the desired receive pattern. The amplitude control can be used for null steering during this receive pre-processing operation.

6. Experiment

We have built a modified White cell device and demonstrated controllable true time delays of a laser beam. The experimental apparatus, is shown in Figure 9(a). This implementation is the single White cell version of the TTD unit discussed in Section 2.2, in which the beam is ejected from the cell after a variable number of transits. Mirrors B and C are on the right, and the spatial light modulator is at the left, along with the beamsplitter and focusing lens.

The spatial light modulator is a Hughes Liquid Crystal Light Valve (LCLV) that is optically addressed using a collimated incandescent light source and a scanning slit. The White cell mirrors

have multiple dielectric coated front surfaces, optimized for a wavelength of λ=546 nm, and a radius of curvature of 500 mm. The lens to the right of the beamsplitter has a focal length of 400 mm. The lens is located 400 mm from the White cell mirrors, and 123 mm from the reflecting surface of the LCLV.

One element has been added to our apparatus, namely the auxiliary mirror shown just above the SLM. As previously discussed, the turning mirrors must be in the same plane as the reflecting surface of the LCLV, which is not physically possible with this light valve because that surface is buried behind a half-inch glass substrate. We therefore use an additional mirror called an auxiliary mirror located above the LCLV. The spots on the LCLV are imaged onto the auxiliary mirror and vice versa as shown in Figure 9(b). The polarizing beamsplitter is located in front of the LCLV and light is ejected from the system only after it bounces off the LCLV. For this reason, our demonstration cell was limited to delays that were multiples of two round trips through the cell.

The light beam being delayed was a green beam from a 3 mW Argon laser, λ =514 nm. It was pulsed using an external Pockel's effect optical gating device that produced ~250 ns pulses. A portion of the optical power was diverted for triggering, using a beamsplitter. The trigger detector was a Thor Labs DET1-S1 PIN detector followed by an HP 462A amplifier. The signal detector was a Newport Model 877 avalanche photodiode, used with an HP461A amplifier.

The digital oscilloscope compares the delayed beam to the trigger beam. Figure 10 shows an undelayed beam superimposed with three separately delayed beams. Each trace is an average of 60 pulses. The delays are, respectively, 0 ns, 7.2 ns, 14.0 ns, and 21.3 ns, respectively, giving an average delay difference of 7.1 ns. The measurement error is
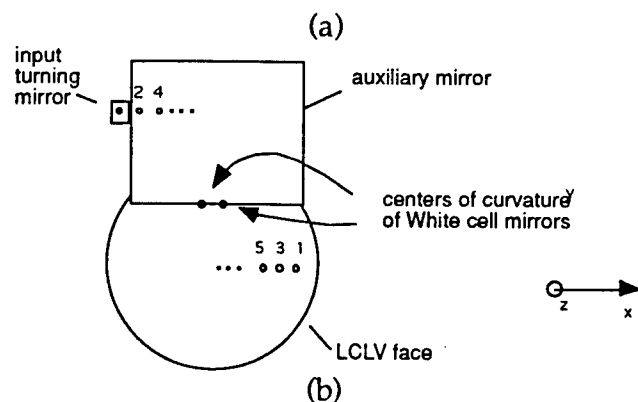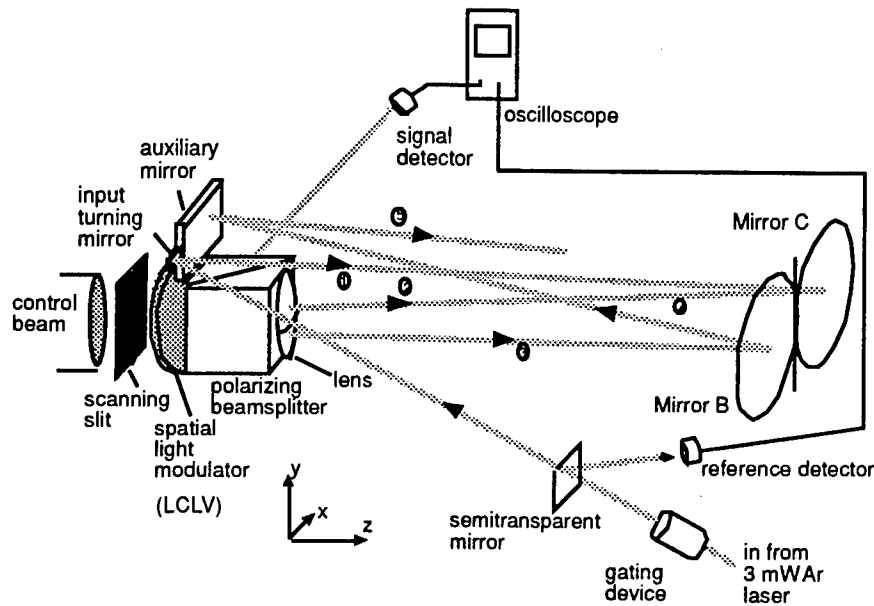
Figure 9. (a) Experimental apparatus; (b) front view of light valve and auxiliary mirror.

approximately ±1.2 ns, meaning our measured delay matches the predicted delay, based on physical measurements of the path of 6.8 ns. The lower trace is the trigger signal.

7. Performance

We next address the factors determining the number of delays obtainable, the delay resolution, number of beams supported, and switching speed.

First, the cumulative power losses due to imperfect reflection limit the total number of independent delays per beam. The greatest source of loss is expected to be at the polarizing beamsplitter, which is described by a transmission factor for p-polarized light and a reflection factor for s-polarized light. The losses, typically on the order of 0.03, will be experienced on each pass through the beamsplitter, that is, twice per cell transit. Properly coated mirrors and lenses will have losses on the order of 0.005 or better. For a single transit from the SLM to a mirror
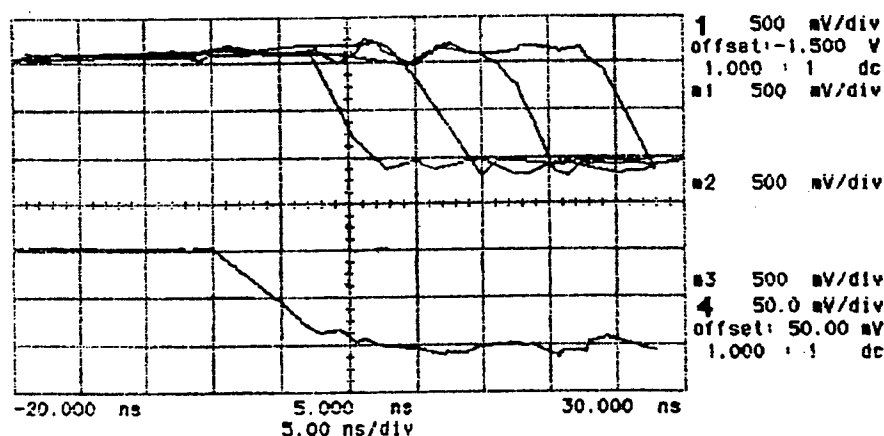
Figure 10. Experimental data: four successive delays of 0, 7.2, 14.0, and 21.3 ns.

and back, a given beam crosses the input and output faces of the beamsplitter and lens twice each, strikes a mirror once, crosses the input face of the SLM twice, and suffers some attenuation at the beamsplitting surface itself. The total loss in one transit will be about 11%. For 16 transits (72 delay increments), that results in a total transmission of 0.15, which is quite acceptable. There may be some additional loss due to scattering from the liquid crystal molecules in the spatial light modulator, as well. This has not been well characterized since loss is not an issue in typical SLM applications.

While the number of bounces is determined by the transmission losses, the number of independent beams is determined by the spatial light modulator size and resolution. Suppose the spot size is chosen to be 150 μm, a conservative value for which there is no interaction between light valve pixels. Then an area on the SLM of 9.6 mm × 2.4 mm on a side is sufficient to process 64 beams in parallel with 72 independent delays resulting from 16 bounces. Commercially available SLM's of 25.4 mm on a side can therefore be used in a single TTD device to process 169 independent light beams to drive 169 antenna elements. Alternatively, if a multiple beam antenna application is required, the 169 independent light beams could be used in a different fashion. If there were only 42 antenna elements, then 4 entirely different beams, each of which has full direction and shape control, could be produced.

The White cell is nicely suited to work with the light valve. First, it provides a compact array of spots, which fits conveniently onto the light valve. Second, the constant refocusing of the White cell maintains the array of small spots. The White cell and associated optics can be designed to provide spots that match the light valve pixel size.

The lengths of the delay increments are determined by the distance to the mirror pairs from the SLM, and the refractive indices of the material in the two cells. To get very long differential delays in the symmetrical device, on the order of nanoseconds, one would choose the differences between the White Cell arms to be large. For smaller delays, the various arms would be designed to be close in dimensions, or to use materials of different refractive indices. Delay increments smaller than 10 ps should be possible.

The time required to switch between beam steering directions is determined by the switching time of the spatial light modulator. There are various SLM technologies available [13], with different switching speeds. Response times of 50 µs have been measured for ferroelectric liquid crystals (FLC's) [14, 15], and response times as fast as 13 µs are predicted [16]. The FLC's have the low loss associated with liquid crystals, and can be made in arrays as large as 256 x 256. Contrast ratios of 70:1 are measured with greater values expected [17].

8. Discussion

The modified White cell approach has many advantages over other optical true-time delay designs. The primary advantage is compactness and robustness. The unit can be built as a solid block and be comparatively temperature insensitive and vibration immune. The physical size of the TTD device is determined by the number of beams, the delay increment, and the SLM resolution. The constant refocusing in the cells means that diffraction over long optical paths does not imply an increase in physical size of the unit as in other free-space schemes. Other advantages include flexibility in light source requirements, since there are no restrictions on source wavelength and the beam need not even be coherent, only polarized. The device is fully reciprocal in that it can be used equally well in receive or transmit mode. Finally, this is the only optical true-time delay approach reported to date that has integrated amplitude control for beam shaping and null steering. The design presented here can provide photonic true time delay for the high performance wideband phased array antennas of the future.

9. Summary

We have described a photonic true-time delay device that can, using commercially available components, produce 64 different delay times (six bit resolution) for 169 separate signals in parallel, with integrated amplitude control. The TTD device is based on the White

38

cell, an optical cavity designed to produce long optical paths in a compact device by using constant refocusing.

We modified the White cell first by replacing one mirror with a spatial light modulator that allows us to turn the beam out of the cell after a given number of passes. Then that device was modified further by adding a second White Cell of different length so that the SLM controlled how many transits a given beam made through each of the two different cells. This approach produces delays that are some multiple of the *path different* between the two cells.

The final modification was to make the two arms of one White cell different lengths as well; this allowed many more delays. to be implemented in a single device. We showed that for the even-armed devices, the number of possible delays was equal to the number of transits m multiplied by the basic delay increment Δ. For the uneven-armed device, that range expanded to greater than $m^2\Delta$.

Amplitude control is integrated into the TTD device by using the last bounce on the SLM for a partial polarization change rather than delay path switching. An analyzer polarizer at the detectors then passes the desired beam power. Using this technique the total number of independent delays is still $m^2\Delta$.

We have experimentally demonstrated, as proof-of concept, an electrically TTD unit that comprises one half of the proposed dual cell. We have shown three delays of 7.1 ns each; the delay increment is a

function of the choice of mirrors. In practice the delays could be from on the order of 10 picoseconds to many nanoseconds.

Acknowledgments

References

[1]   H. Zmuda and E. N. Toughlian, "Photonic Aspects of Modern Radar," in *The Artech House Optoelectronics Library*, B. Culshaw, A. Rogers, and H. Taylor, Eds. Norwood, MA: Artech House, 1994, pp. 550.

[2]   J. J. Lee, R. Y. Loo, S. Livingston, V. I. Jones, J. B. Lewis, H.-W. Yen, G. L. Tangonan, and M. Wechsberg, "Photonic Wideband Array Antennas," *IEEE Transactions on Antennas and Propagation*, vol. 45, pp. 966-982, 1995.

[3]   A. Goutzoulis, K. Davies, J. Zomp, P. Hyrcak, and A. Johnson, "Development and field demonstration of a hardware-compressive fiber-optic true-time-delay steering system for phased-array antennas," *Applied Optics*, vol. 33, pp. 8173-8185, 1994.

[4]   P. M. Freitag and S. M. Forrest, "A coherent optically controlled phased array antenna system," *IEEE Microwave and Guided Wave Letters*, vol. 3, pp. 293-295, 1993.

[5]   G. A. Ball, W. H. Glenn, and W. W. Morey, "Programmable fiber optic delay line," *IEEE Photonics Technology Letters*, vol. 6, pp. 741-743, 1994.

[6]   B. Kanack, M. Boysel, C. Goldsmith, C. Menni, G. Magel, and C. Takle, "Optical time delay network for phased arrays," , 1993.

[7]   D. D. Curtis and L. M. Sharpe, "True time delay using fiber optic delay lines," presented at International Symposium Antennas and Propagation, Dallas, TX, 1990.

[8]   R. D. Esman, M. Y. Frankel, J. L. Dexter, L. Goldberg, M. G. Parent, and D. Stilwell, "Two optical-control techniques for phased array: interferometric and dispersive-fiber true time delay," , 1993.

[9]   D. J. Page, "An introduction to the optical commutator," *IEEE Transactions on Antennas and Propagation*, vol. 44, pp. 652-658, 1996.

[10]   X. S. Yao and L. Maleki, "A novel 2-D programmable photonic time-delay device for millimeter-wave signal processing applications," *IEEE Photonics Technology Letters*, vol. 6, pp. 1463-1465, 1994.

[11]   N. A. Riza, "Transmit-receive time-delay beam-forming optical architecture for phased-array antennas," *Applied Optics*, vol. 30, pp. 4594-4595, 1991.

[12]   J. U. White, "Very long optical paths in air," *Journal of the Optical Society of America*, vol. 66, pp. 411-416, 1976.

[13]   U. Effron, "Spatial light modulator technology," . New York: Marcel Dekker, Inc., 1995.

[14]   N. Collings, J. Gourlay, D. G. Vaasl, H. J. White, C. Stace, and G. M. Proudley, "Measurements on ferroelectric liquid crystal spatial light modulators: contrast ratio and speed," *Applied Optics*, vol. 34, pp. 5928-5931, 1995.

[15]   M. G. Roe and K. L. Schehrer, "High-speed and high-contrast operation of ferroelectric liquid crystal optically addressed spatial light modulators," *Optical Engineering*, vol. 32, pp. 1662-1667, 1993.

[16]   A. Handschy, K. M. Johnson, G. Moddel, and L. A. Pagano-Stauffer, "Electro-optic applications of ferroelectric liquid crystal to optical computing," *Ferroelectrics*, vol. 85, pp. 279-289, 1988.

[17]   D. J. McKnight, K. M. Johnson, and R. A. Serati, "256 x 256 liquid-crystal-on-silicon spatial light modulator," *Applied Optics*, vol. 33, pp. 2775-2784, 1994.

OPTICALLY-CONTROLLED SERIALLY-FED PHASED ARRAY TRANSMITTER

Harold R. Fetterman, Yian Chang, Boris Tsap
Department of Electrical Engineering,
University of California at Los Angeles, CA 90095,
A. F. J. Levi, David A. Cohen,
Department of Electrical Engineering,
University of Southern California, Los Angeles, CA 90089-1111,
Irwin L. Newberg,
Hughes Aircraft Co.,
PO Box 92426, Los Angeles, CA 90009-2426

Abstract: We present a new optically controlled phased array system which has all the advantages of true time delay (TTD) yet only requires one tunable laser, one optical modulator and one fiber optic grating unit. A two-element serial-feed transmitter has been assembled to demonstrate the feasibility of this novel concept. The demonstration has shown TTD operation from 6 GHz through 12 GHz using both 10 ns and 1 ns pulses transmitted to five different directions. Also, NTSC video signals have been transmitted to illustrate the dynamic directional data communication potential of such a system.

1. Introduction

We present a new optically controlled system, suitable for phased array radar, microwave imaging, directional data communication and related applications. This system uses a serial-feed concept that represents a new departure, in these applications, that will yield a major simplification in both optical and microwave components. Unlike many of the systems[1]-[6] currently under investigation,

which use a parallel approach, our system with both phase and true time delays requires but a single tunable laser, modulator and time delay element[7].

In our design, the use of fiber optic techniques, such as long and low-loss delay lines, is intrinsic to the operation of the system. The approach presented is predicated upon using the pulsed nature of microwave radar systems in a similar manner to the clock system used in digital configurations. In this case precise timing control is used to distribute RF pulses with phase and time delay information to each element in an operating array. In addition to discussing the concepts of both transmit and receive modes, we also present an experimental two-element transmitter with five pointing directions exhibiting TTD operation from 6 GHz through 12 GHz.

2. Transmit Mode

The transmit function can be best described in terms of a timing unit and a distribution network as shown is Figure 1. The desired delays for a given RF beam direction are generated sequentially by the timing unit and then transformed into parallel signals to feed the antennas by the distribution network.

The timing portion uses an electrically tuned DBR laser which is amplitude modulated with the desired microwave pulses using an optical modulator. After the modulator the laser light is directed through an optical
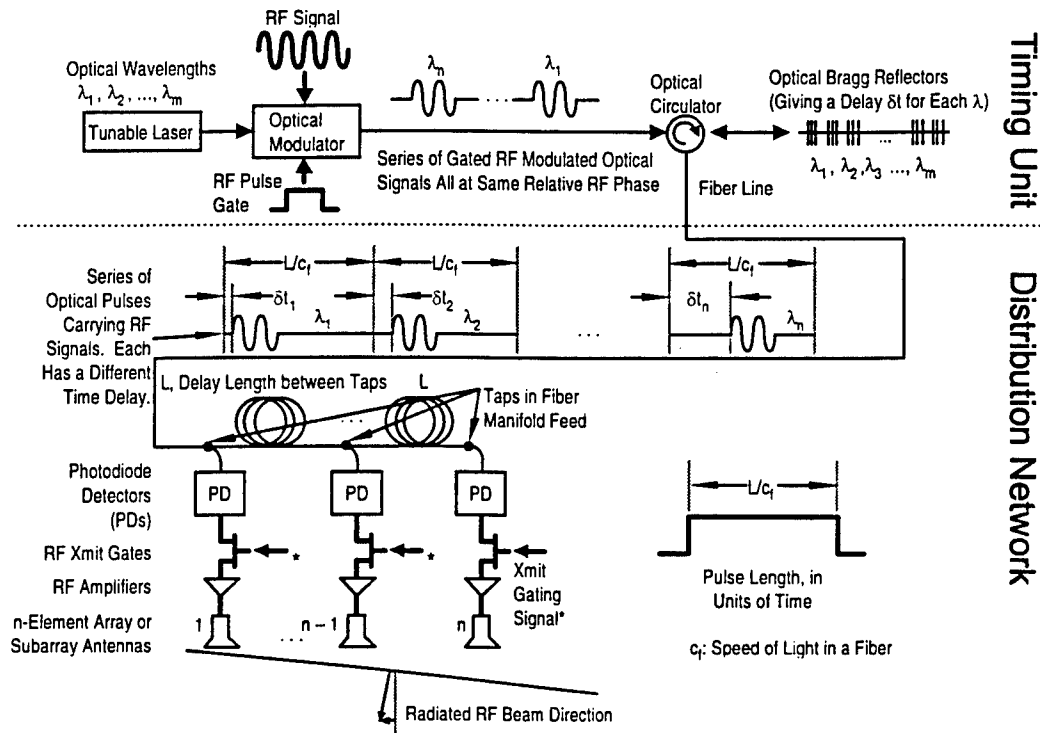
Figure 1. Basic transmit mode implementation for array of n elements.

circulator to a fiber optic grating. A typical laser light reflection spectrum from the grating is shown in Figure 2.

The grating reflects light back at different positions along the fiber depending upon the optical wavelength. Thus a wavelength-selective delay can be imposed onto each RF modulated optical pulse. In the basic system discussed here, each serially-fed optical pulse has a unique wavelength and therefore a unique time delay, relative to the RF pulse gate, which has been chosen to produce a given pointing direction. The number of pulses in the fully loaded tapped delay line corresponds to the number of radiating elements in the array or
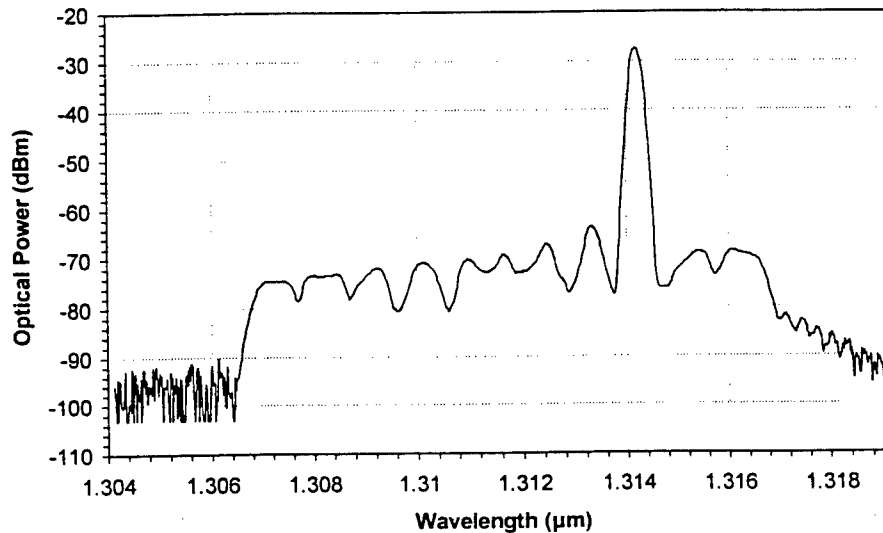
Figure 2. Typical reflection spectrum of laser light from the fiber grating. It also shows the spontaneous emission background level resulting from reflection of the other reflectors.

subarray. Specifically, the first pulse is intended for the nth element and the nth pulse is intended for the first element. The RF amplitude and phase of each element can be controlled independently, therefore multi-beam patterns can be formed using the same hardware configuration.

Returned light from the third port of the circulator enters the distribution network formed by the tapped delay line. It is important to note that this delay line is used to transform serial signals into parallel ones, and does not generate the delays for beam steering. Once the series of optical pulses arrive at the correct delay line taps for each antenna element, the microwave modulation is obtained using photodetectors. The microwave signals from these detectors are

simultaneously gated on with microwave switches (Xmit gates) when the tapped delay line is fully loaded. Each element's microwave pulse has the correct time delay set by the fiber grating to form a radiating beam in the desired direction. After the signal is radiated the switches are turned off and the line is reloaded. The number of radiating directions is limited only by the number of available laser wavelengths and Bragg reflectors. Although our initial efforts use a two-wavelength laser system and a fiber grating with discrete wavelength selectivity, the system will ultimately use a continuously tunable DBR laser with a continuously chirped grating to provide continuous scanning.

3. Receive Mode

In the basic receive mode the time delays are generated in a manner similar to that in the transmit mode, except there is no gating because a receiver has to "listen" continuously. As shown in Figure 3, a simplified receive system utilizes the same timing unit and tapped delay line configuration as in the transmit mode. The tapped delay line in Figure 3 will be loaded with λ_1, λ_2, ..., λ_{2n} pulses carrying LO signals that are phase shifted by ϕ, 2ϕ, ..., $2n\phi$ to the mixers. The other mixer inputs are the antenna received RF signals. At the beginning of receiving, the λ_1 pulse supplies the nth mixer and the λ_n pulse supplies the first mixer. After L/c_f in time, the λ_2 pulse will reach the nth mixer and become its LO signal carrier. At
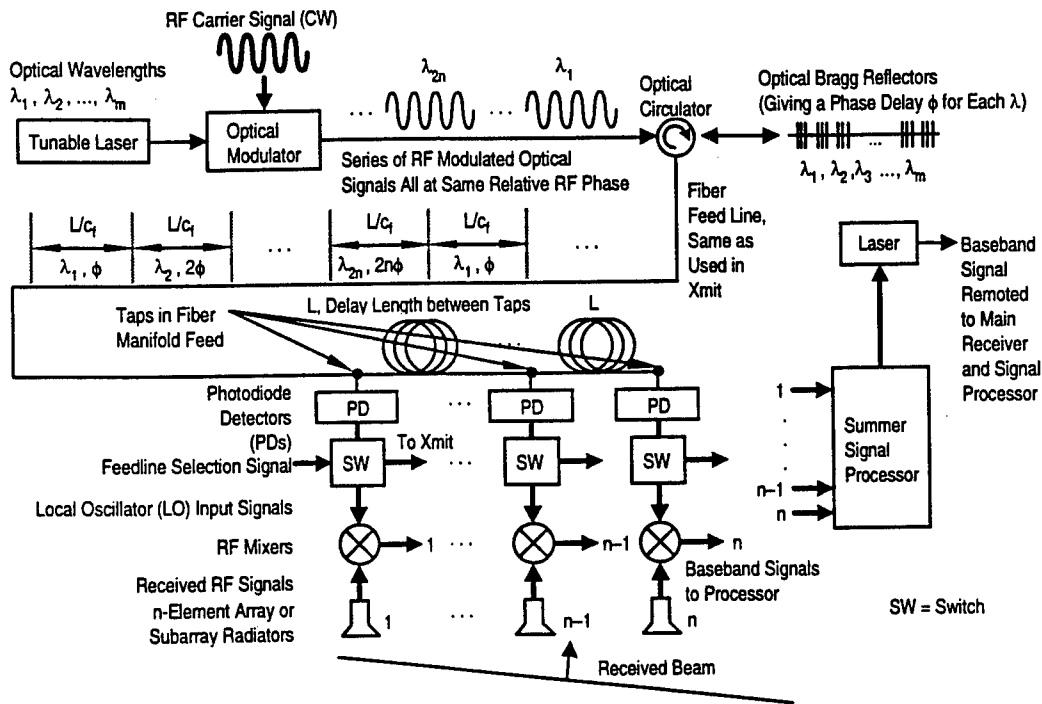
Figure 3. Basic received mode implementation for array of n elements.

the same time, the λ_{n+1} pulse will be supplying the first mixer. Note that the receiver is still "listening" to the same direction after such wavelength progression because only the relative phases between mixers (differential phase ϕ) are important. This wavelength progression continues until the λ_{2n} pulse arrives the first mixer

In order to resume receive operation, a second tapped delay line (not shown in Figure 3 for simplicity) with an extra nL delay length will be switched to feed the nth mixer with λ_1 and the first mixer with λ_n. The first tapped delay line will be reloaded during this period and it will be switched to when the second line

47

is exhausted. The conjugate differential phase (ϕ) of that in transmit (-ϕ) has to be used because the mixers generate a difference frequency and subtract the phases of the two input signals. This phase requirement can be achieved by using the fiber grating in reverse direction or by using the transmit wavelengths in reverse order. This mixing technique provides the desired wideband squint-free operation but has some limitations on short pulse and large array applications. The IF (baseband) signals from the mixers are then added coherently in a simple summer signal processor to form the received antenna beam signal. A low frequency laser, also shown in Figure 3, can then be used to transmit the baseband signal information to a remote area for full array signal processing.

4. Demonstration

To establish the viability of this serial approach, we have built a two-element transmitter with five optical wavelengths thus giving us five pointing directions. One external cavity tunable laser (wavelength = λ_t) and one fixed wavelength laser (wavelength = λ_f) were used in conjunction with two optical modulators to generate the wavelengths needed. By pulse gating and RF modulating the CW λ_t and λ_f signals alternately, a fast tunable laser switching between two wavelengths (λ_t and λ_f) was simulated. The repetition rate of wavelength switching was 25 MHz, which corresponds to the tapped fiber delay length L$\approx$4m. The five values

of λ_t were from 1307.50 nm through 1311.50 nm, separated by 1 nm. λ_f was set at 1309.50nm. These wavelengths were selected based on the fiber grating used such that the relative time delays between the λ_t pulses and the λ_f pulse were -40 ps, -20 ps, 0 ps, 20 ps, and 40 ps.

The time delayed RF signals feeding the two-element antenna array were monitored on a digital sampling oscilloscope's (DSO's) channel 1 and 2 (CH1 & 2). By correctly gating the RF signals coming out from the photodetectors, CH1 received the λ_t pulse (variable delay) and CH2 received the λ_f pulse (delay reference). Two pulse widths have been tested: 10 ns and 1 ns. The 10 ns pulses offer a flat middle portion suitable for time delay measurements using the DSO with best-fit sine functions. By monitoring the CH1 of the DSO, Figure 4 shows three of the five time delays we can generate at 10 GHz. The time delays measured from the two channels of the DSO agree with the above mentioned designed grating delays at RF frequencies from 6 GHz through 12 GHz. The 1 ns pulses, with a 10 GHz center frequency, contain frequency components from 8 GHz through 12 GHz and are suitable for demonstrating the wide instantaneous bandwidth of the system. Figure 5 shows 10 GHz 1 ns pulses with two of the five possible time delays.

Because this demonstration transmitter only has two elements, its radiating beam width is very broad (~60°). In order to demonstrate squint-free operation
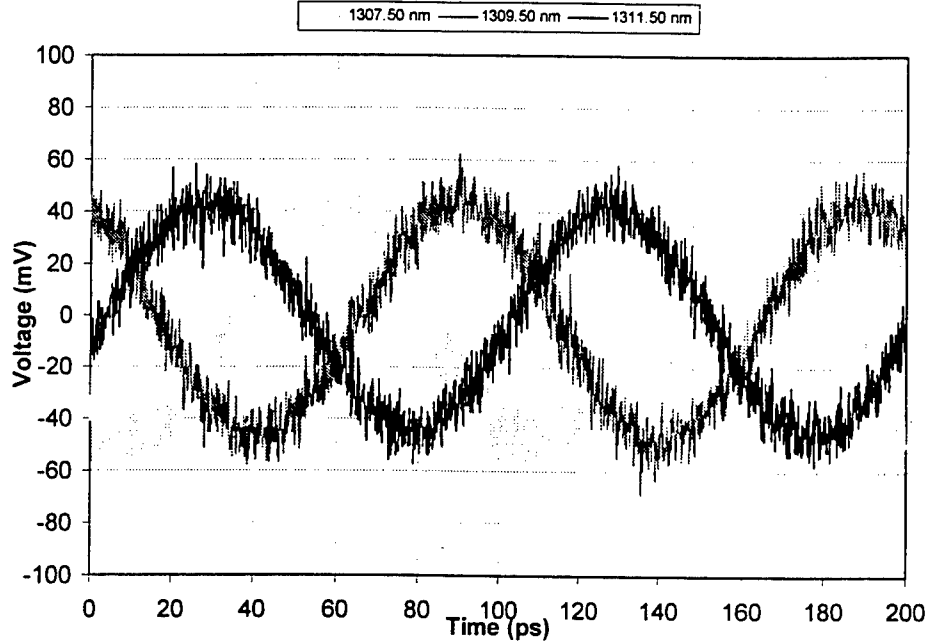
Figure 4. The middle portions of the 10 GHz 10 ns pulses carried by three different wavelengths. These waveforms were recorded from the CH1 of the DSO, the CH2 waveform (not shown) was in phase with the 1309.50 nm one due to the same path length. This shows that -40 ps, 0 ps, and 40 ps TTDs, with respect to the CH2 signal, have been generated.

with better resolution, radiation node was used instead of antinode. The two

optical modulators were biased at different modulation slopes to provide an extra

π phase shift between the two elements.

The radiation node direction was measured by moving the receiving horn

around with the same distance from the two-element array until the received

signal was minimized. Using an antenna separation 2.54 cm, the theoretical node

directions are -28°, -14°, 0°, 14°, and 28°. Figure 6 shows the measured node

direction vs. RF frequency at different optical wavelengths with 10 ns pulses. It
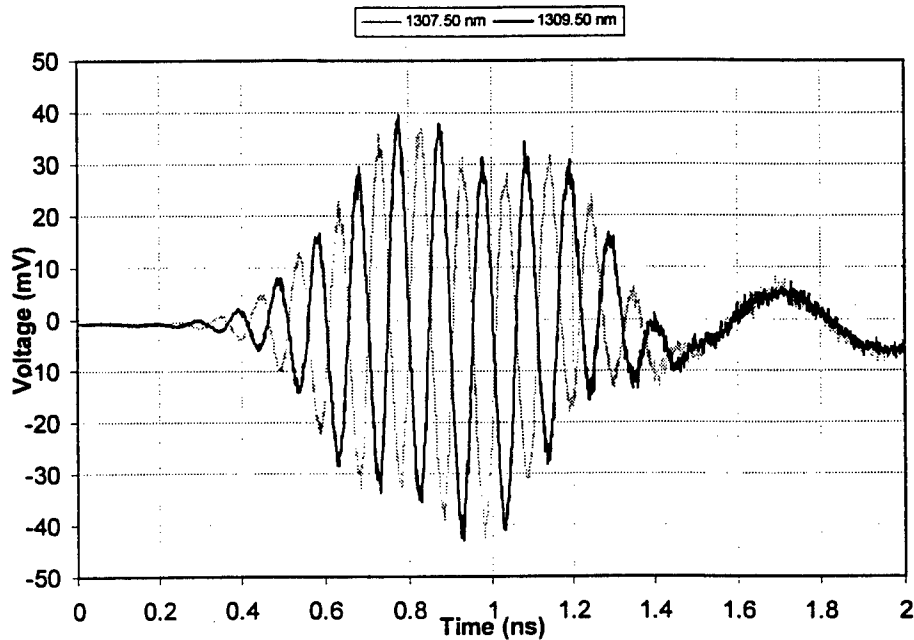
Figure 5. 10 GHz 1 ns pulses carried by 1307.50 nm and 1309.50 nm optical carriers monitored on the CH1 of the DSO. The 1307.50 nm pulse leads the 1309.50 nm pulse by 40 ps.

illustrates squint-free operation with some fluctuations. This is mainly caused by the fact that only two elements were used in this transmitter, resulting a large uncertainty in minimizing the received signal. By using more antenna elements, direct measurements on the antinode directions will provide a good resolution with fluctuations minimized.

To demonstrate the wide instantaneous bandwidth of the transmitter, the 10 GHz, 1 ns pulses were radiated and again the radiation node directions were measured. These node directions are the same as those in Figure 6. The spectra of the received signals at a node are shown in Figure 7. The black curve was

◇ 1307.50 nm □ 1308.50 nm △ 1309.50 nm ○ 1310.50 nm ✕ 1311.50 nm
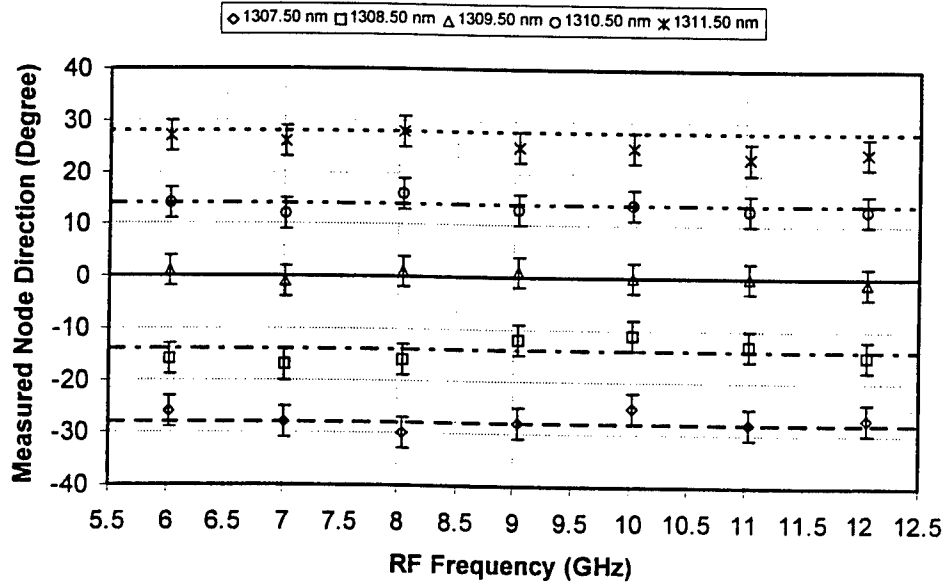
Figure 6. Measured node direction vs. RF frequency at different λ_ts with λ_f fixed. The straight lines show the theoretical values. This shows the TTD nature of our system.

obtained when both antennas were radiating. Because of the extra π phase shift introduced by biasing the optical modulators, the signals from the two antennas interfered destructively resulting a low power level from 8 GHz through 12 GHz.

To further demonstrate the two antenna signals cancel out, one antenna was disconnected from the system and the spectrum of the other antenna was measured. The result is shown with the gray curve in Figure 7. By comparing the two curves in Figure 7, it is clear that destructive interference occurred from 8.5 GHz through 11.5 GHz when both antennas were radiating. This demonstrates the wide instantaneous bandwidth of the transmitter.
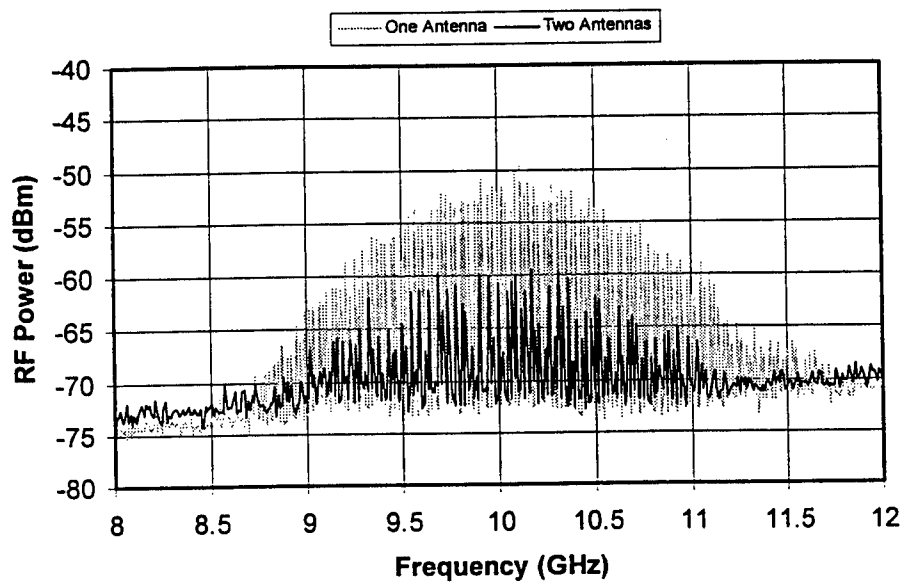
Figure 7. The spectra of the detected 1 ns pulses centered at 10 GHz. The receiving horn was located at the node (-28°). The gray curve is the signal from only one antenna. The black curve shows that the signals from the two antennas cancel each other as expected for a node. This exhibits the wide instantaneous bandwidth of the transmitter.

In order to demonstrate the potential of using such a transmitter for dynamic directional data communications, NTSC baseband video signals were transmitted to two switchable pointing directions. A microwave modulator was added after the XMIT gate for each element. The RF pulses with steering time delays were used as the LO signals of the mixers. The video signals were sent to the IF ports of the mixers. Therefore the time delayed RF pulses were AM modulated with the video signals in the mixers. The modulated pulses were then

53
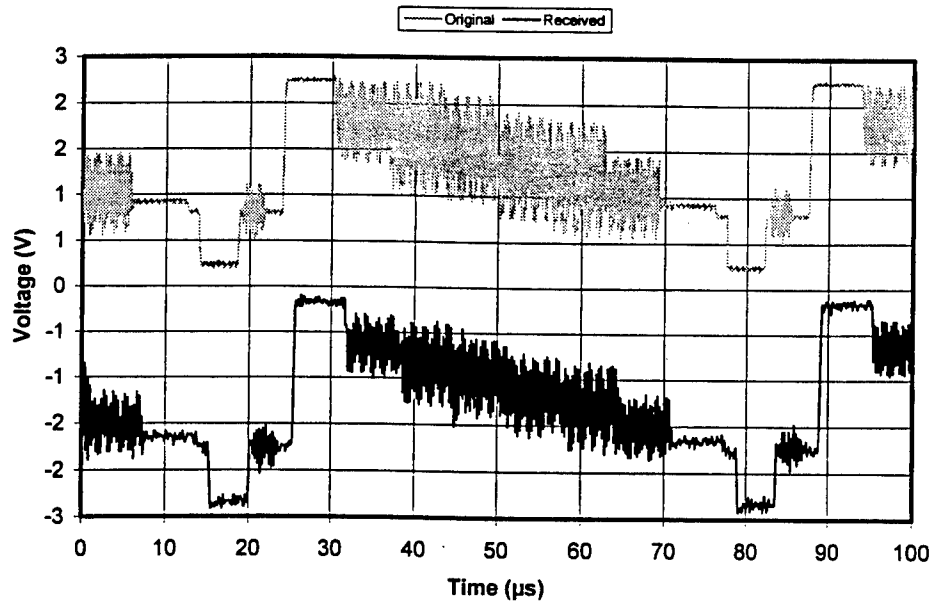
Figure 8. The original and received NTSC baseband colorbar video signals. There are slight differences when shown on an oscilloscope. But there is no perceivable degradation when viewed on a TV screen. The time delay in the received signal is due to propagation.

sent to the antennas and radiated to the desired direction. For better resolution and higher distinguish ratio, again radiation nodes were used.

On the receiver side, the detected signal was mixed with an LO signal to generate an IF signal at TV's channel 2 frequency. This channel 2 signal was then sent to a TV set for demodulation and displaying. The recorded received baseband video signal is shown in Figure 8 together with the original signal. Although there are slight differences between these two signals when shown on an oscilloscope, there is no perceivable degradation when displayed on a TV. When

the radiation node was switched toward the receiving horn, the received RF signal was lowered by 30 dB and only noise was displayed on the TV screen. Even though we have chosen NTSC analog video signals for this demonstration, digital signals can also be directionally transmitted in a similar manner.

5. Conclusion

A new serially-fed true time delay system has been presented and the basic concept has been experimentally verified. It uses only one tunable laser, one optical modulator and one delay element to achieve beam steering. The system is quite versatile and can be used to control both one and two dimensional arrays. Furthermore, a natural extension can be used both for the receive mode and for passive imaging. Essentially, by using the natural timing of our pulsed radar we are able to greatly simplify and to increase the flexibility of optically controlled systems.

The two-element, five-delay transmit system we have presented is a relatively basic unit which demonstrates the concept of a serial-feed. It is possible to greatly enhance this system in several areas and to extend it to multiple frequencies and beams. As an example of the power of this concept for communications, we have also demonstrated its use in directional TV satellite type transmission. Finally, this system represents a major departure from

traditional parallel connected configurations. Because of its simplicity, we foresee its implementation in many new related application areas.

6. Acknowledgment

7. References

[1]   D. Dolfi, P. Joffre, J. Antoine, J.-P. Huignard, et al., "Photonics for phased array radars," *Proceedings of the SPIE - The International Society for Optical Engineering*, vol. 2560, pp. 158-165, 1995.

[2]   H. R. Fetterman, Y. Chang, D. C. Scott, S. R. Forrest, et al., "Optically controlled phased array radar receiver using SLM switched real time delays," *IEEE Microwave and Guided Wave Lett.*, vol. 5, no. 11, pp. 414-416, 1995.

[3]   L. Xu, R. Taylor and S. R. Forrest, "True time-delay phased-array antenna feed system based on optical heterodyne techniques," *IEEE Photon. Technol. Lett.*, vol. 8, no. 1, pp. 160-162, 1996.

[4]   R. D. Esman, M. Y. Frankel, J. L. Dexter, L. Goldberg, et al., "Fiber-optic prism true time-delay antenna feed," *IEEE Photon. Technol. Lett.*, vol. 5, no. 11, pp. 1347-1349, 1993.

[5]   L. J. Lembo, T. Holcomb, M. Wickham, P. Wisseman and J. C. Brock, "Low-loss fiber optic time-delay element for phased-array antennas," *Proceedings of the SPIE - The International Society for Optical Engineering*, vol. 2155, pp. 13-23, 1994.

[6]   A. Molony, C. Edge and I. Bennion, "Fibre grating time delay element for phased array antennas," *Elect. Lett.*, vol. 31, no. 17, pp. 1485-1486, 1995.

[7]   G. A. Ball, W. H. Glenn and W. W. Morey, "Programmable fiber optic delay line," *IEEE Photon. Technol. Lett.*, vol. 6, no. 6, pp. 741-743, 1994.

TWO-DIMENSIONAL MULTIWAVELENGTH OPTICALLY CONTROLLED PHASED ARRAY ANTENNAS

Ming C. Wu and Dennis T. K. Tong

UCLA, Electrical Engineering Department

66-147 Engineering IV, 405 Hilgard Ave.

Los Angeles, CA 90095-1594

1. Abstract

A novel two-dimensional multiwavelength optically controlled phased array (MWOCPAA) is demonstrated. The architecture employs a multiwavelength laser source to dramatically reduce the system complexity. A programmable dispersion matrix, implemented by Bragg fiber gratings, is cascaded with switched optical delay lines for beaming steering in both elevation and azimuthal plane. Relative time delays of a prototype 4×2 MWOCPAA with 2-bit × 2-bit resolution are experimentally measured. The results agree well with the theoretical prediction.

2. Introduction

Considerable effort has been focused on optically controlled phased array antenna (OCPAA) because of its attractive features such as broad bandwidth, compact size, light weight, low loss, EM interference immunity, remoting capability, and more importantly, wide instantaneous bandwidth and squint-free beam forming. Practical deployment of OCPAA depends upon the overall system

complexity, reliability and cost. One solution to these problems is by exploiting the wavelength domain of lightwave [1-7]. In particular, we have previously demonstrated a multiwavelength optically controlled phased array antenna (MWOCPAA) in which a programmable dispersion matrix (PDM) is employed in conjunction with a multiwavelength laser source to generate all the required time delays for beam steering. The PDM can be implemented by dispersive fibers or Bragg grating fibers. Dispersive fiber approach requires precise alignment of wavelength, and long fiber are necessary for long time delays. Moreover, the dispersion-generated time delays is accompanied by dispersion-induced signal distortion. In this paper, we proposed and experimentally demonstrate the use of Bragg fiber grating in the PDM to ease the problems. We will also show the extension of the multiwavelength scheme to two-dimensional (2-D) phased array antenna system by cascading the PDM with switched optical delay lines (SODL). Experimental results of a 2-D MWOCPAA prototype with 4×2 elements will be presented.

3. PDM Using Bragg Fiber Grating

Figure 1 shows the schematic diagram of the 1-D MWOCPAA system. It comprises (1) a multiwavelength laser source to provide an array of optical wavelengths $\{\lambda_1, \lambda_2, ..., \lambda_p\}$, (2) an electro-optic modulator (EOM) to modulate the

microwave signal onto the optical wavelengths, (3) the PDM to control the relative time delays among the optical wavelengths and (4) a wavelength-division-multiplexed (WDM) demultiplexer to establish a "optical wavelength-to-array element" mapping. The number of optical wavelengths is equal to the number of array element. Potential candidates for the multiwavelength laser source include monolithically integrated multiwavelength distributed feedback lasers [8] and, as will be demonstrated in this paper, monolithic mode-locked semiconductor lasers. The details of the PDM is shown in Fig. 2. The PDM with n-bit resolution in general consists of n dispersive elements, which is realized by Bragg fiber gratings in this demonstration, and n + 1 2 × 2 optical switches. The fiber gratings implemented in the PDM can be treated as "taylorable-dispersion" elements. By fabricating a series of grating reflector along the an optical fiber with each grating matched to a different wavelength of the multiwavelength source (i.e. G_i reflects λ_i), relative time delays are generated among different optical wavelengths because different wavelengths are reflected at different position. Bragg fiber gratings are uniformly spaced on the optical fiber at each stage of the PDM. The grating spacing in successive PDM stage increases exponentially so that the relative time delays between adjacent optical wavelengths exhibited at each stage of the PDM increases exponentially, i.e. τ_1, $2 \cdot \tau_1$, $2^2 \cdot \tau_1$,..., $2^{n-1} \cdot \tau_1$. Here, τ_1 is the relative time delay in the first stage of the PDM:

$$\tau_1 = \frac{2 \cdot \Delta L_1 \cdot n}{c} \qquad (1)$$

where ΔL_1 is the grating spacing in the first stage, n is the refractive index of the fiber, and c is the velocity of light in free space. Optical circulators are inserted between each stage to routed the lightwave. By programming the 2×2 optical switches, the total relative time delays of the PDM, τ_{PDM}, is

$$\tau_{PDM} = \sum_{i=1}^{n} 2^{i-1} \cdot \tau_1 \cdot S_i \qquad (2)$$

where $S_i = 0$ or 1 is the state of the i-th optical switch. Eqn. (2) indicates that τ_{PDM} can vary from 0 to $(2^n - 1) \cdot \tau_1$ in increments of τ_1. At the receiver, a WDM demultiplexer directs λ_i to the i-th element of the array, giving rise to a linear time shifts of $\{0, \tau_{PDM}, 2 \cdot \tau_{PDM}, ..., (m-1) \cdot \tau_{PDM}\}$ across the array elements. The steering angle θ is

$$\theta = \sin^{-1}\left(\frac{c \cdot \tau_{PDM}}{\Lambda}\right) \qquad (2)$$

for all RF frequencies, where Λ is the distance between array elements.

4. 2-D MWOCPAA Using Cascaded PDM and SODL

For 2-D MWOCPAA system, cascaded PDMs similar to those proposed in [3, 5] can be adopted. Alternatively, we shall demonstrate a 2-D MWOCPAA

system without the undesirable optical/electrical/optical conversion by cascading the PDM with the switched optical delay lines (SODL) [1, 5]. The wavelength-independent SODL's are cascaded with the wavelength-dependent PDM to provide the scanning in the second dimension. Figure 3 displays the schematic diagram of a p × q 2-D MWOCPAA with n-bit × m-bit resolution. This architecture allows all-optical true time delay process. The 1 × q optical coupler placed after the PDM is employed to split the lightwave into q columns of the phased array. Each column of the array is attached with a SODL (except the first one) to introduce time delays among the columns. The details of SODL is well-known and can be found in [1]. Figure 4 shows a typical SODL with m bits resolution. It is worthwhile to mention that the SODLs associated with each column are different because the time increments in successive SODL has to increase appropriately to preserve the linear time delays across the azimuthal plane during the beam steering operation. Fully processed optical wavelengths are then demultiplexed and routed to assigned array elements of each column to maintain the same "optical wavelength-to-array as in the 1-D array.

Each elements in the 2-D phased array can then be characterized by two values of time delay: $\{\tau_{elev}, \tau_{az}\}$. The time delay in the elevation plane, τ_{elev}, is controlled by the PDM and is *wavelength-dependent* while the time delay in the elevation plane, τ_{az}, is controlled by the SODL and is *wavelength-independent*.

Elements in the same column have the same values of τ_{az}, and similarly, τ_{elev} is the same for elements in the same rows.

/

5. Experiment

To demonstrate the feasibility of the 2-D MWOCPAA, a 4×2 experimental prototype with 2-bit×2-bit scanning resolution is constructed. An 80 GHz monolithic colliding-pulse mode-locked (CPM) semiconductor is used as the multiwavelength laser source [9]. The CPM laser is passively mode-locked at 1548.09 nm with a mode spacing of 0.62 nm. The reduced mode partition noise in the mode-locked laser makes it a suitable multiwavelength source for this application [10]. A 2-bit resolution PDM is employed for elevation beam control. Four gratings are implemented at both stage of the PDM to reflect the optical wavelength at 1546.85, 1547.47, 1548.09 and 1548.71 nm from the CPM laser. The grating spacing in the first and the second stage of the PDM are 1 cm and 2 cm respectively. All the gratings used in the setup have a reflectivity of 85 % and a FWHM reflection-band of 0.15 nm. The lightwave is then splitted by a 1×2 optical coupler. A SODL with 2-bit resolution is connected to one branch of the optical coupler for azimuthal plane beam control. The length of the delay lines in this first and the second stages of the SODL are 1 cm and 2 cm, respectively.

The RF signal is applied to all wavelengths through an EOM with 5 GHz bandwidth. A tunable fiber Fabry-Perot filter with 10 GHz bandwidth is placed after the SODL to select different wavelength channels for time delay measurement. The selected channel is converted back into electrical signal by a high speed photodetector. The time delay is measured by an HP 8510 microwave network analyzer.

6. Results

Figure 5 shows the measured relative time delay in the elevation plane as a function of optical wavelength. These are the *wavelength-dependent* time delays created by the PDM in each column of the array. The time delays are measured relative to that at λ = 1546.85 nm. Using either grating or both simultaneously, the measured time delays between adjacent wavelength obtained from these measurements are 98.38, 201.30 and 292.59 ps, compared to the theoretical values of 97.33, 194.67 and 292 ps, respectively. These small differences are due to deviations in grating positions and mismatches between optical wavelengths and grating pitches.

Figure 6 shows the measured time delay among the optical wavelengths in the second column of the array. These time delays are measured relative to λ = 1546.85 nm in the first column of the array. The relative time delay among the

optical wavelengths in the each column are generated by PDM in which the optical wavelengths is routed through the first fiber grating only. However, by routing the lightwave through either delay lines of the SODL or both simultaneously, the extra time delay between the two column of the array shifts the lines upward. The measured time delays are 44.44, 98.33 and 150 ps, compared to the theoretical value 48.67, 97.33 and 146 ps, respectively. These small differences are due to deviation in lengths of the fiber delay lines at both stages of the SODL.

7. Discussion

A remarkable feature of the 2-D MWOCPAA scheme is the reduction of optical and RF splitting loss. The only optical splitting loss is contributed by the $1 \times q$ optical coupler, which is used to distribute the lightwave to various column of the array. Moreover, simultaneous modulation of all the optical wavelength by a single modulator eliminates RF splitting loss.

The array size can be scaled up by increasing the number of optical channels or by wavelength re-use. Multiwavelength distributed feedback laser array chip with 18 equally-spaced channels has been reported [8] and even larger arrays are possible. Wavelength re-use in conjunction with multiple PDM/SODL can be employed to further multiply the array size. High speed beam forming is

possible by using EO switch that has a typical switching time of less than 1 ns at the expense of higher PDM and SODL optical insertion loss. Since the resolution of the scanning beam angle depends on the number of stages in the PDM and the SODL, the required hardware increases only logarithmically with the resolution.

8. Conclusion

In conclusion, we have demonstrated 2-D MWOCPAA system. Cascaded SODL and PDM results in a hardware compressive architecture. The elevation and azimuthal beam angle are controlled by wavelength-dependent time delay created from PDM and wavelength-independent time delay created from SODL respectively. Moreover, when compared to the PDM comprises dispersive fiber, the use of fiber grating in PDM as taylorable dispersive element significantly reduces the system size and eliminates the dispersion-induced signal distortion. An experimentally prototype 4×2 MWOCPAA with 2-bit×2-bit resolution demonstrates the feasibility of this approach.

9. Acknowledgment

10. References

[1] A. Goutzoulis and K. Davies, "All-optical hardware compressive wavelength-multiplexed fiber optic architecture for true time delay steering of 2-D phased array antennas," *Proc. SPIE*, 1992, vol. 1703, pp. 604 - 614.

[2] R. Soref, "Optical dispersion technique for time-delay beam steering," *Appl. Opt.*, 1992, vol. 31, pp. 7395-7397.

[3] R. D. Esman, M. Y. Frankel, J. L. Dexter, L. Goldberg, M. G. Parent, D. Stilwell, and D. G. Cooper, "Fiber-optic prism true time-delay antenna feed," *IEEE Photon. Technol. Lett.*, 1993, vol. 5, pp. 1347-1349.

[4] P. M. Freitag and S. R. Forrest "A coherent optically controlled phased array antenna system," *IEEE Microwave and Guided Wave Lett.*, 1993, vol. 3, pp. 293 -295.

[5] L. J. Lembo, T. Holcomb, M. Wickham, P. Wisseman, and J. C. Brock, "Low-loss fiber optic time-delay element for phased-array antennas," *Proc. SPIE*, 1994, vol. 2155, pp.13-23.

[6] H. R. Fetterman, Y. Chang, A. A. Levi, D. Cohen, and I. L. Newberg, "Serially fed optically controlled phased arrays," SPIE Annual Meeting 1996, Paper 2844-33, August 7-8, 1996, Denver, Colorado, USA.

[7] D. T. K. Tong and M. C. Wu, "A novel multiwavelength optically controlled phased array antenna with a programmable dispersion matrix," *IEEE Photon. Technol. Lett.*, 1996, vol. 8, pp. 812-814.

[8] C. E. Zah, F. J. Favire, B. Pathak, R. Bhat, C. Caneau, P. S. Lin, A. S. Gozdz, N. C. Andreadakis, M. A. Koza, and T. P. Lee, " Monolithic integration of multiwavelength compressive-strained multiquantum-well distributed-feedback laser array with star coupler and optical amplifier." *Electron. Lett.*, vol. 28, pp. 2361 - 2362, 1992.

[9] Y. K. Chen and M. C. Wu, "Monolithic colliding-pulse mode-locked quantum-well lasers," *IEEE J. Quantum Electron.*, vol. 28, pp. 2176-2185,1992.

[10] P. T. Ho, "Phase and amplitude fluctuations in a mode-locked laser, *IEEE J. Quantum Electron.*, 1985, vol. 21, pp. 1806-1813.
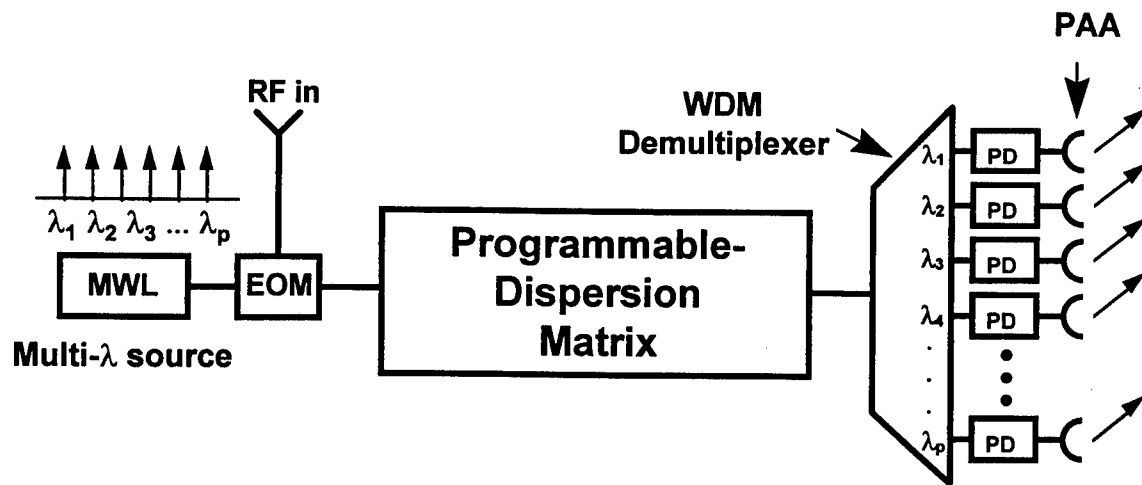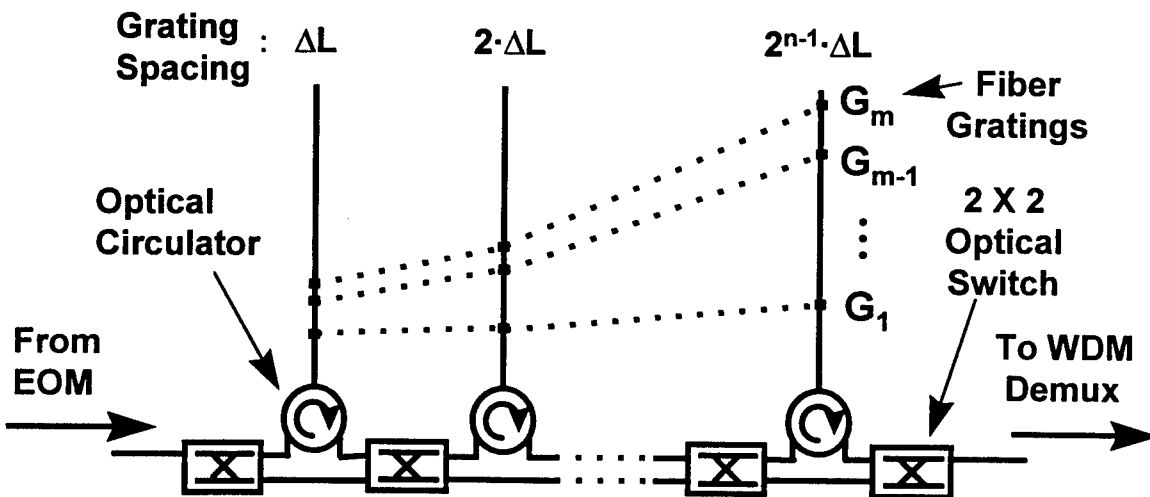
Fig. 1 Schematic diagram of 1-D MWOCPAA using a PDM

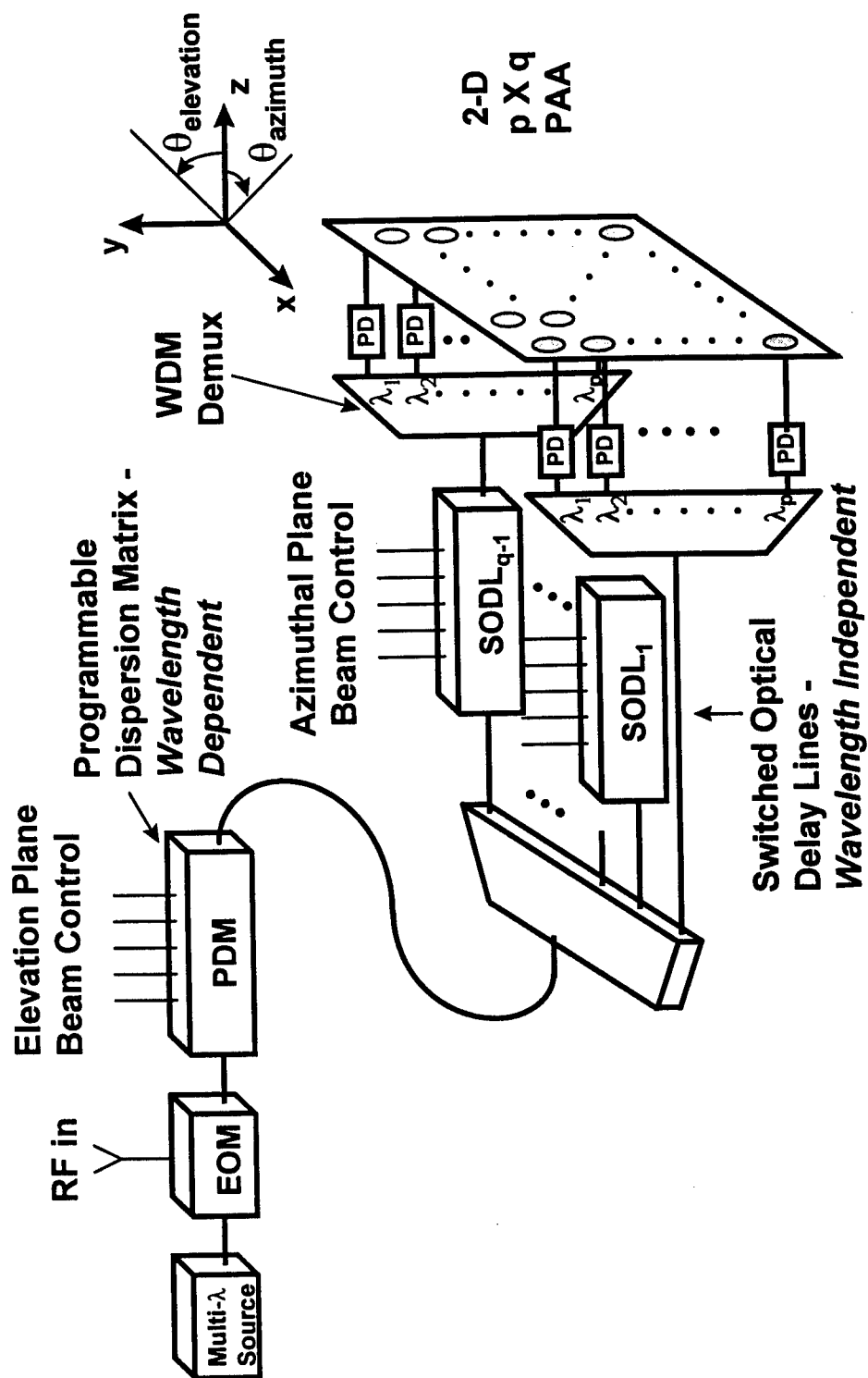
Fig. 2 A n-bit resolution Bragg fiber grating PDM
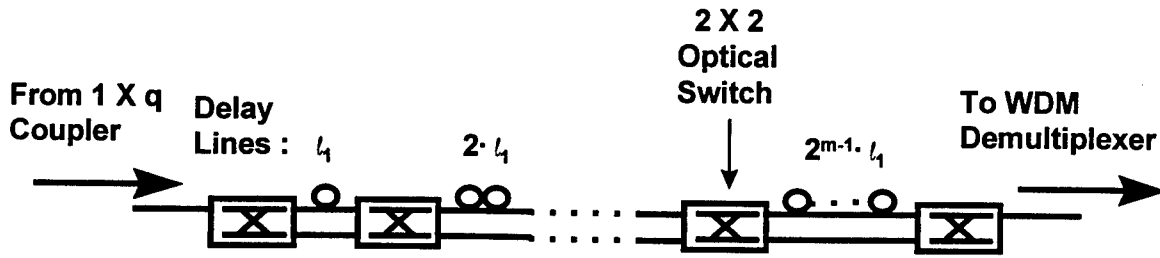
68

Fig. 3 Schematic diagram of a p X q 2-D MWOCPAA

Fig 4. A m-bit resolution switched optical delay lines (SODL).
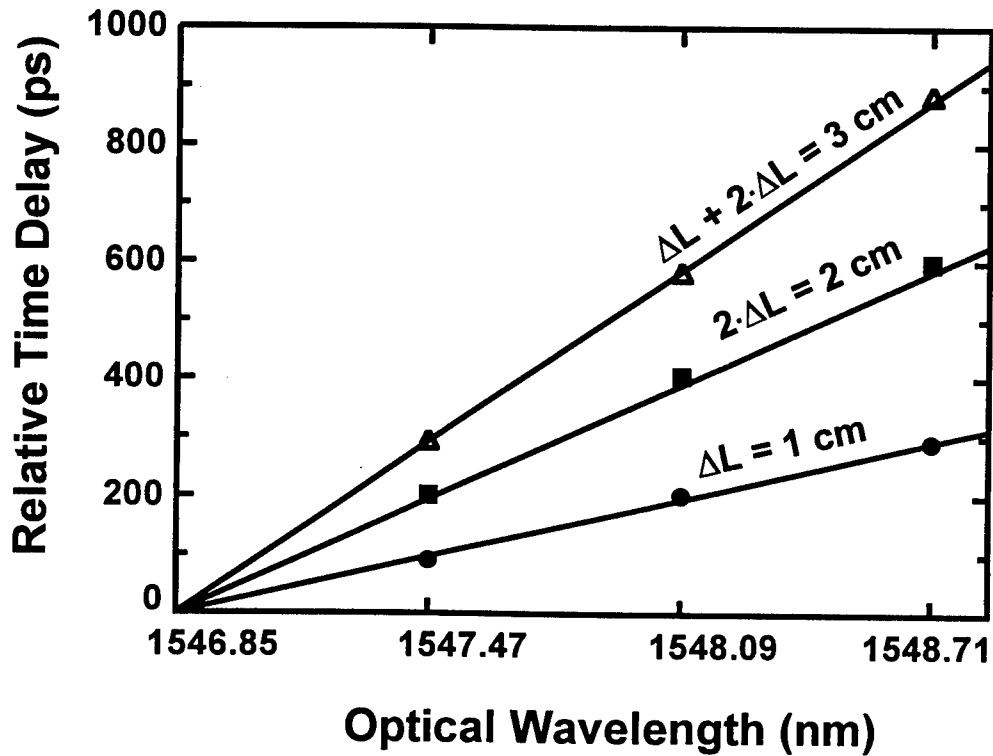
Fig. 5 Relative time delay in elevation plane at various optical wavelengths generated by either fiber grating or both simultaneously. The lines are the theoretical prediction and the markers are the measured data.

Fig. 6 Measured relative time delay between two columns of the array
generated by SODL. These time delays are measured relative to
λ = 1546.85 nm in the first column. The relative time delay among
the wavelengths in the same column are maintained by the first fiber
grating the PDM during these measurement. The dotted line indicates
zero time delay between the two columns.

A COMPACT VERSION OF AN OPTICALLY SCANNING MMW ANTENNA: FEEDER DESIGN
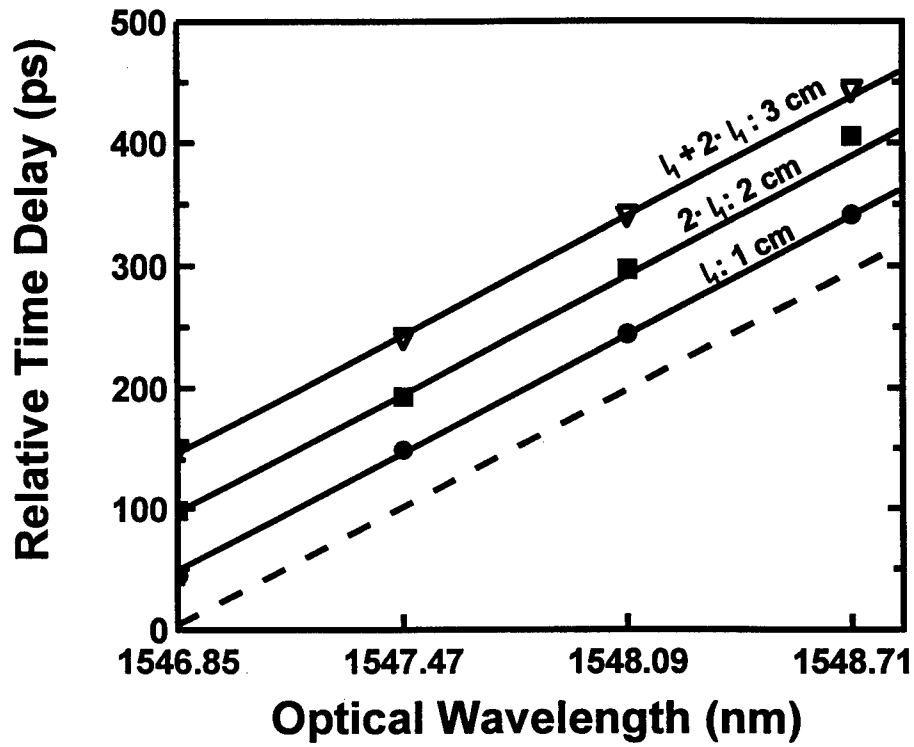
Vladimir A. Manasson, Lev S. Sadovnik, Kalin Spariosu

WaveBand Corporation

375 Van Ness Ave., Suite 1105

Torrance, CA 90501

Abstract: A new design of a scanning MMW antenna controlled by light is proposed. The design constitutes further development of an antenna the demonstration of which has been reported previously. The operation of the antenna is distinct from the photonically controlled phased arrays, and its principal component is a photo-induced plasma grating generated in a silicon plate. This development will result in a new rigid and compact design along with a substantial decrease in the required pumping power. A basic component of the new architecture, the feeder, has been designed, fabricated and tested. A simple model describing the radiation going out of the feeder has been developed and verified experimentally.

1. Introduction

Phased-array antennas offer an attractive alternative to mechanically scanning devices. Their advantages include compactness, higher scanning speed, and high flexibility in beamforming and beamshaping. Even more promising are recently developed photonically scanning antennas which utilize fiber-optic links to transmit the control signals to phase-shifters. A phase-shifter is the principal element for both types of phased arrays: the electronically scanned and the one based on photonics links. Unfortunately the phase shifter still roses a challenging problem at MMW frequencies. A typical antenna array should have a large number of elementary radiators, each with individual controls and thus with an individual

phase shifter. The cost associated with such a large number of required phase shifters prevents the use of phased arrays in most cases. In our earlier papers [1,2] we demonstrated a new approach to photonically controlled MMW antennas. The new antenna is more of an optically controlled distributed "smart" aperture than an array of individually controlled radiators. This approach permits to dramatically simplify the antenna controls resulting in lower cost. The first working models of our antenna required significant optical power for the control. In this paper we present a new design of the antenna which is expected to result in light power requirements decreased at least 5-6 times. The new design is more compact and more sturdy.

2. Operating Principles

The central component of the new antenna is a photo-induced plasma-grating (PIPG). It is implemented by way of a semiconductor slab illuminated through a spatial light modulator (SLM). For SLM one can use a liquid-crystal display (LCD). Signal processing for the electronic control of LCDs is highly developed, versatile, and cost effective. These advantages apply directly to our new beamforming technology.

The semiconductor slab illuminated through an LCD contains an electron-hole plasma distribution in a pattern that follows the LCD pattern. The plasma changes locally the dielectric constant of the semiconductor material and therefore interacts with the millimeter waves (MMW) passing the semiconductor slab. If the LCD pattern is a periodical structure with opaque and transparent strips then the photo-

induced plasma creates a diffraction grating for the MMWs. It has been shown [1,2] that the PIPG effectively diffracts a MMW beam in directions determined by the optical grating theory.

The schematic diagram of the PIPG antenna is shown in Figure 1.
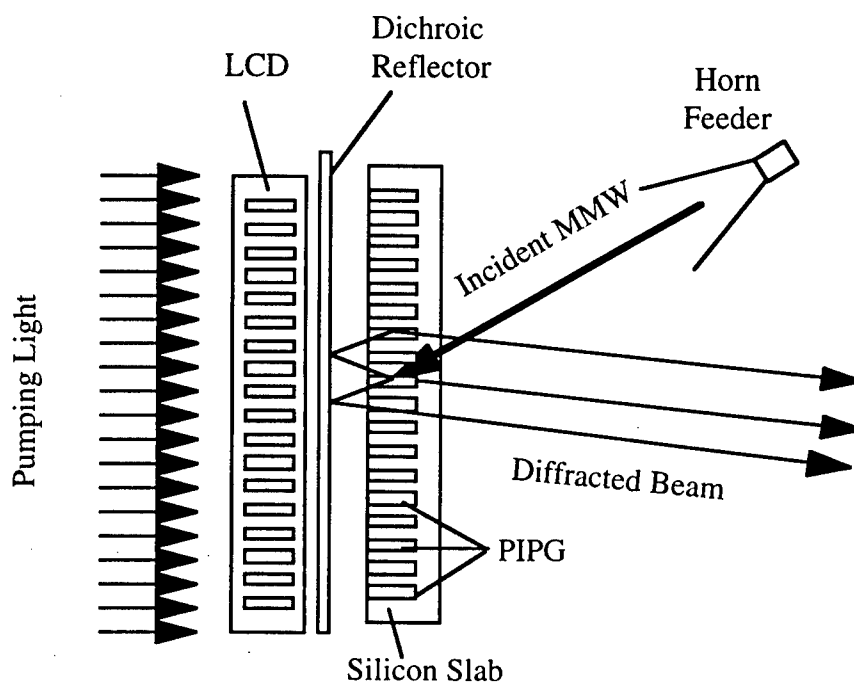
Figure 1. Schematic diagram of an optically-controlled MMW antenna.

In our design the MMW beam and the pumping light impinge upon the semiconductor slab from opposite directions. The incident MMW beam coming from the horn feeder experiences multiple diffraction and reflection from a dichroic reflector. The dichroic reflector is made of an Indium-Tin Oxide film and it efficiently reflects MMWs while being almost totally transparent to the pumping

light. Varying the grating period causes angular scanning of the output radiation. The particular geometry of Fig. 1 provides a single output beam within a 30 degree scanning range.

The antenna shown in Figure 1 can provide two-dimensional scanning. Obviously, an extension into the second dimension requires illuminating a semiconductor slab of a large area. There are, however, many applications where only one-dimensional scanning is needed. This realization prompted a new antenna design which operates at a much lower pumping power. From the new antenna we expect a higher efficiency, compactness, greatly improved heat dissipation, and pumping power economy.

3. New Antenna Design

The new antenna architecture differs from our previous design in that it uses a dielectric (Teflon) plate as the MMW guiding medium. Thus, we confined the MMW propagation from the free space to a 2-D dielectric slab waveguide. The main goal is to minimize the region of MMW-plasma interaction, limiting it to the narrow strip, and therefore to significantly lower the size of the illuminated area and thus the required pumping power.

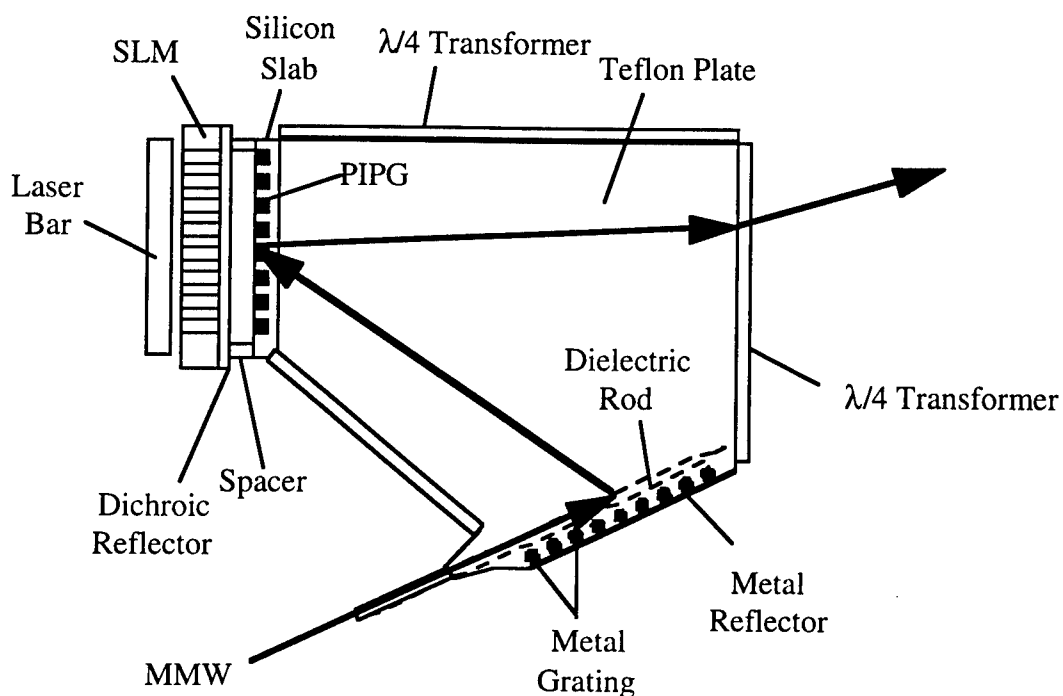The schematic design of the new antenna is shown in Figure 2.

Figure 2. Schematic diagram of a light-controlled monolithic scanning MMW antenna.

The antenna consists of a Teflon plate, a silicon plate carrying the PIPG, a pumping semiconductor laser bar, an SLM, a feeder, and a quarter-length transformer. The Teflon plate is a beamforming propagation medium. The feeder is based on the principle of a leaky-wave antenna. It consists of a dielectric (quartz) rod imbedded in the Teflon plate and loaded with a metal grating that launches the MMW toward the silicon plate. The interaction of the MMW beam with PIPG results in an outcoming beam which experiences refraction at the Teflon-plate/air interface. To prevent back reflection from the interface we use a quarter-wavelength transformer which is part of the Teflon plate but has a reduced thickness.

4. The Feeder

The feeder is an important part of any antenna. A leaky-wave antenna loaded with a metal grating is attractive because it is compact and very flexible in terms of beamforming. The main direction of the launched beam is determined by the grating period. The desired beamshape can be achieved by varying the distance between the quartz rod and the metal wires (grating) and by varying the grating period.

To computer-simulate the direction of propagation of the beam generated by the feeder we used formulas derived for the grating-loaded leaky-wave antennas operating in free space [3] but with the free space wave vector k_0 replaced by the effective propagation constant within the Teflon slab β_{eff}. To verify the validity of such simplification we compared our calculations with experiments.

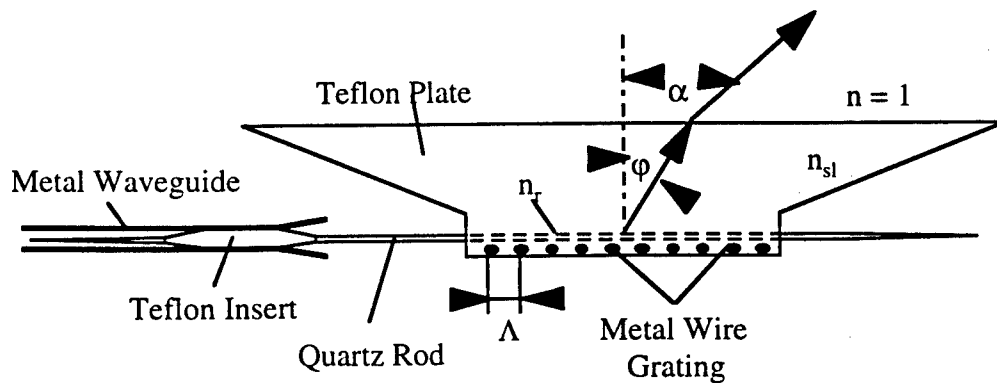The leaky-wave feeder design is schematically shown in Figure 3.

Figure 3. Leaky-wave grating-loaded feeder.

In the following calculations we define k_0 as the free space wave vector; β_{sl} and β_r as the effective propagation constants for the Teflon slab and for the quartz rod imbedded in the Teflon slab respectively; $n_{sl} = \beta_{sl}/k_0$ and $n_r = \beta_r/k_0$ as the effective refractive indexes for the slab and the rod respectively; λ as the free space wavelength for the MMW, Λ as the grating spacing, t as the slab thickness, and d as the rod diameter.

All calculations have been performed for the fundamental modes.

Teflon slab. Assuming TE_0 mode propagating in the Teflon slab we find the effective refracting index n_{sl} form the equation [4]:

$$W = U \tan U, \qquad (1)$$

where $W = \pi t (n_{sl}^2 - 1)^{1/2}/(2\lambda)$ and $U = \pi t (\varepsilon_{Teflon} - n_{sl}^2)^{1/2}/(2\lambda)$.

Quartz rod. The fundamental mode is HE_{11}. We find the effective index n_r from the equation [4]:

$$\{[UJ_1(U)]^{-1}(d/dU)[J_1(U)] + [WK_1(W)]^{-1}(d/dW)[K_1(W)]\} \times$$
$$\{[UJ_1(U)]^{-1}(d/dU)[J_1(U)] + (n_{sl}^2/\varepsilon_{quartz})[WK_1(W)]^{-1}(d/dW)[K_1(W)]\} =$$
$$(n_r^2/\varepsilon_{quartz})(V/UW)^4, \qquad (2)$$

where $V = \pi d (\varepsilon_{quartz} - n_{sl}^2)^{1/2}/(2\lambda)$, $W = \pi d (n_r^2 - n_{sl}^2)^{1/2}/(2\lambda)$,

and $U = \pi d(\varepsilon_{quartz} - n_r^2)^{1/2}/(2\lambda)$; J_1 is a Bessel function of the first kind, and K_1 is the modified Bessel function of the second kind.

For the beam radiating in free space from a leaky waveguide loaded with metal grating the radiation angle is [3]:

$$\varphi = \arcsin(\beta/k_0 - \lambda/\Lambda),\qquad (3)$$

where β is the propagation constant within the waveguide. We modify this expression by substituting of β_r for β, and β_{sl} for k_0:

$$\varphi = \arcsin(\beta_r / \beta_{sl} - \lambda/\Lambda),\qquad (3a)$$

or
$$\varphi = \arcsin(n_r / n_{sl} - \lambda/\Lambda).\qquad (3b)$$

At the Teflon/air interface the outgoing beam experiences refraction. To determine the direction of propagation in free space we used the Snell's law formula, substituting n_{sl} for the refractive index of Teflon:

$$\alpha = \arcsin(n_{sl}\sin\varphi).\qquad (4)$$

In our experiment the parameters were as follows: t = 2.44 mm, d = 1.0 mm, $\Lambda = 1.92$ mm, $\varepsilon_{quartz} = 3.78$, $\varepsilon_{Teflon} = 2.08$, frequency f = 90 GHz and 94.3 GHz.

Using these parameters we calculated the following results. At the frequency of f = 90 GHz: n_{sl} = 1.361, n_r =1.401, φ = -14.3 deg., and α = - 19.4 deg. At the frequency of f = 94.3 GHz: n_{sl} = 1.367, n_r = 1.417, φ = - 10.1 deg., and α = -13.8 deg .

The measured far field radiation patterns are shown in Figures 4 and 5 for f = 90 GHz and 94.3 GHz, respectively. One can see that the directions of the main lobes are in good agreement with the calculations made with our simple model.
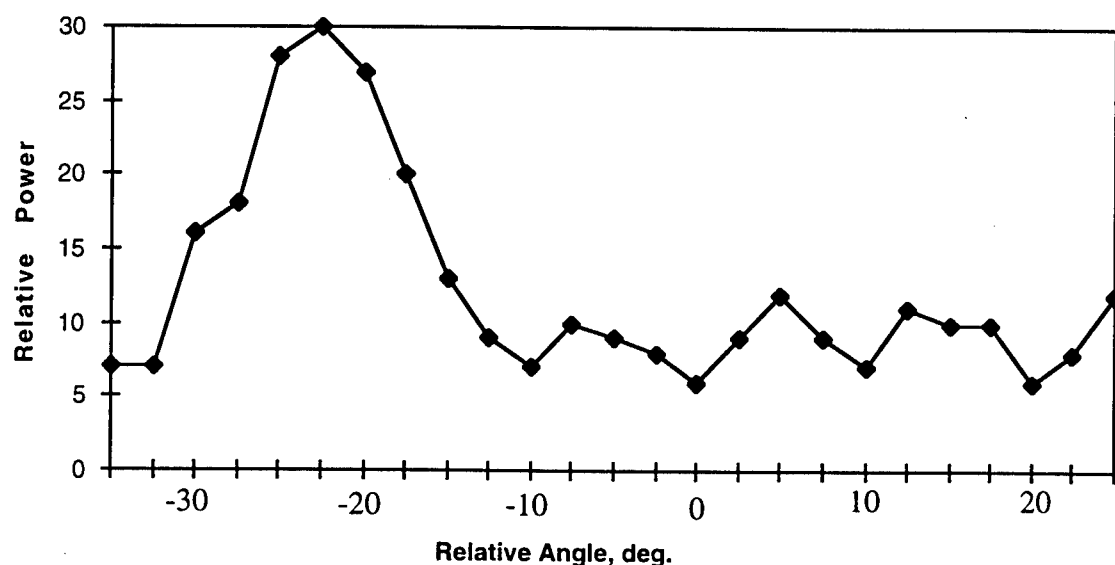

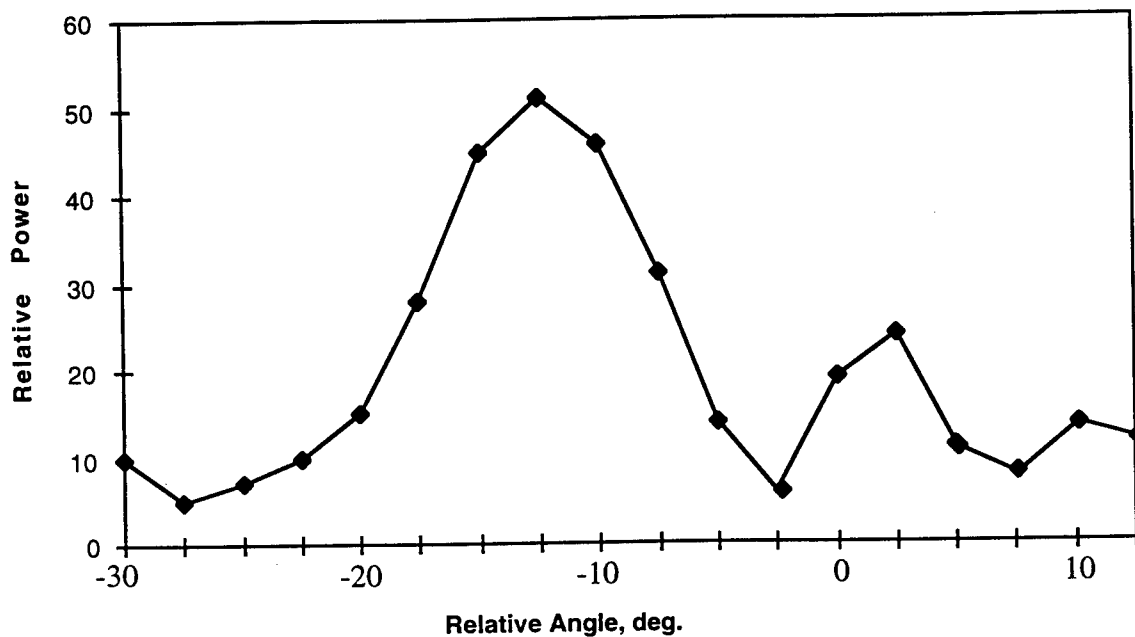Figure 4. Far-field pattern measured at a frequency of 90 GHz.

Figure 5. Far-field pattern measured at a frequency of 94.3 GHz.

5. Conclusion

We performed a preliminary design of a new scanning MMW antenna controlled by light. In comparison with our previous antenna model the new one is a sturdy, compact device with expected higher efficiency and lower power consumption. A new feeder for the antenna was designed, fabricated and tested. A simple theoretical model based on effective refractive indexes was proposed to describe the radiation pattern of the feeder. Calculations based on this model yield results that are in a in a good agreement with experimental data. The next step will be to fabricate the whole antenna and test its parameters.

6. Acknowledgments

7. References

[1]   V. A. Manasson, L. S. Sadovnik, A. Moussessian, D. B. Rutledge, "Millimeter Wave Diffraction by a Photo-Induced Plasma-Grating", *IEEE Trans. Microwave   Theory Tech.*, vol. MTT-43, pp. 2288-2290, 1995.

[2]   V. A. Manasson, L. S. Sadovnik, P. I. Shnitser, R. Mino, J. S. Kruger, "Millimeter-Wave Optically Scanning Antenna Based on Photoinduced Plasma Grating", *Opt. Eng.* vol. 35(2), pp. 357-361, 1996.

[3]   F. Schwering and A. A. Oliner, "Millimeter-Wave Antennas", *in Antenna Handbook*, Y. T. Lo and S. W. Lee ed., vol. III, Chapt. 17, New York: Van   Nostrand Reinhold, 1993.

[4]   A. W. Snyder and J. D. Love, *Optical Waveguide Theory*, Chapman and Hall,   1983.

mm-WAVE DIELECTRIC SCANNING ARRAY TRANSMITTER

FOR

WIRELESS APPLICATIONS

Randall E. Lehmann, Nai-Hsiang Sun* and Jerome K. Butler*

Texas Instruments, Inc.
*Southern Methodist University
13532 North Central Expressway, M/S 245
Dallas, TX 75243

ABSTRACT

Wireless applications are in need of low-cost, high performance components to meet ever-increasing bandwidths and higher frequencies. An integrated mm-wave MMIC dielectric grating transmitter has been developed that provides beam scanning capability as the frequency of the source is changed.

A gallium arsenide (GaAs) monolithic millimeter-wave integrated circuit (MMIC) varactor-controlled oscillator (VCO) provides a highly linear tunable source at Q-band. Epitaxially grown 0.25-μm MESFETS are employed in the VCO MMIC to achieve a fundamental frequency source and three stages of buffer amplification to achieve >10 dBm output power and prevent frequency pulling.

A dielectric corrugated diffraction grating antenna has been designed that demonstrates 15 degrees/GHz scan capability with a 5-degree beamwidth at 38.5 GHz. Low-loss alumina ceramic is used as the dielectric for this demonstration, but for low-cost commercial applications, this design could easily be implemented in a soft-substrate material or molded into a specific shape to conform to an existing structure. Most notably, this could be done on the bumper side panels of automobiles thus not to interfere with the primary concern of most auto designers—the body style and lines of contour.

This integrated transmitter, which operates in the 38.5-GHz PCS frequency range, could easily be multiplied up to 77 GHz to provide a low-cost, compact transmitter solution for auto radar applications.

1. Introduction

1.1 Statement of the Problem

A need exists for high-performance, low-cost electronically scanning array radars for military and commercial applications. Many solid-state phased-array radars are now being fielded using microwave frequencies primarily for military air-to-ground terrain mapping, air-to-air combat missions, and ground-to-air surveillance applications. [1-3] To enhance the spatial resolution for other applications, such as missile guidance, smart munitions, and automotive radar, shorter wavelengths are required. For communication systems, where wide bandwidth and potentially covert data links are desired, millimeter-wave (mm-wave) systems provide excellent solutions.

The problem being addressed by this research is to develop an advanced mm-wave active scanning array transmitter using a dielectric grating antenna. Bragg diffraction gratings have been studied extensively, especially at optical wavelengths. [4-9] Previous researchers have demonstrated mm-wave grating antennas that require metal waveguide interfaces to inject the electromagnetic signal into the dielectric. [10,11] Another technique employs slotline feeds, which requires access to the backside of the dielectric for the coupling structures. [12] Specifically for this research, the intent is to show theoretical and experimental results of an integrated mm-wave active scanning array transmitter.

1.2 Approach

As frequency is increased to achieve the shorter wavelengths required for these mm-wave systems, producing large amounts of power becomes more difficult. Standard device and circuit technology employed at microwave frequencies cannot

84

always be used successively at mm-wave frequencies. As an example, a standard 0.5-μm gate-length metal semiconductor field effect transistor (MESFET), which currently is an excellent device to produce several watts of rf power at X-band frequencies (7 to 12 GHz), has a maximum frequency of operation of about 20 GHz. To achieve reasonable device gain and output power at Q-band (33 to 50 GHz), the device gate length must be shorter and appropriate device and material changes made. For this research a 0.25-μm gate length, epitaxially grown MESFET is being used to enhance mm-wave performance.

A corrugated dielectric waveguide has been developed for Q-band frequency operation, based on earlier diffraction grating research performed at Southern Methodist University, [4,10] and serves as the foundation for development of an integrated scanning array transmitter employing active components. The dielectric grating antenna has been simulated by a multiple layer slab waveguide model that can be solved by the wave equation and matching boundary conditions between dielectric layers. The difference between a periodic and a uniform slab waveguide is that the periodic waveguide has a permittivity that varies periodically along the propagation direction. Various numerical methods have been used to analyze these structures.[13] To be compatible with available monolithic microwave integrated circuit (MMIC) components and typical thin-film networks (TFNs), the dielectric waveguide grating antenna has been fabricated using polished alumina ceramic. A Q-band MMIC varactor controlled oscillator (VCO), developed at Texas Instruments, has been integrated with this dielectric grating antenna to demonstrate a fully integrated solution.

Shown in block diagram form in Figure 1, the integrated mm-wave transmitter consists of a MMIC VCO electromagnetically coupled to corrugated dielectric

waveguide radiating elements. The radiated signals from each perturbation of the dielectric waveguide are spatially combined to achieve a beam capable of being scanned as the frequency of the VCO is changed.
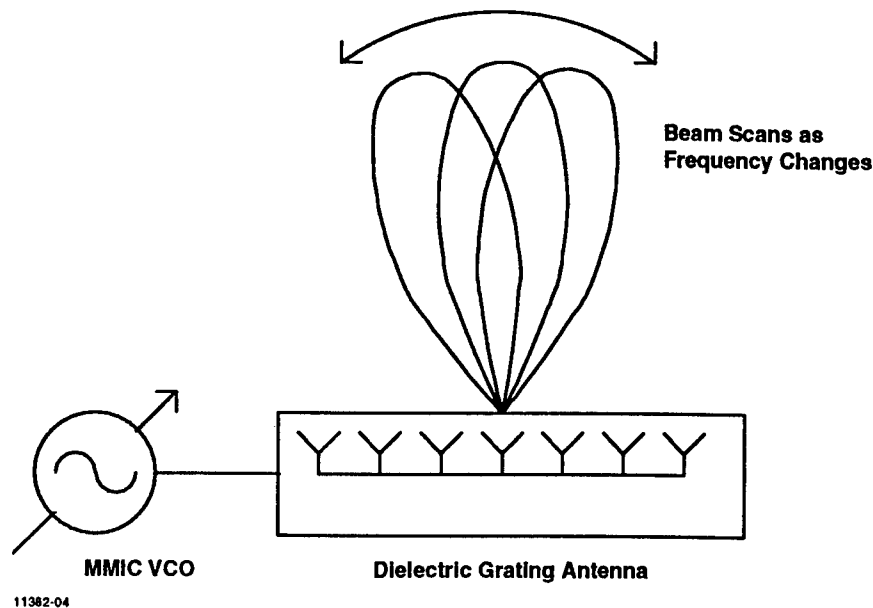

Figure 1. Millimeter-wave integrated transmitter features electrical scan capability

The principle of this integrated scanning array antenna can be applied to transmitters and receivers, using hybrid, monolithic and photonic technologies. This single integrated transmitter can be replicated m × n times to achieve a high power two-dimensional electronically scanned array (ESA). The power from each individual transmitter (or unit cell) is spatially combined to produce a large amount of radiated power from the array. A significant advantage of this approach is that each unit cell produces low rf output power with low dc power dissipation. MMIC chip size is kept small, resulting in lower chip cost and easier integration. Because of the distributed nature of the array (Figure 2), thermal heating due to the active device dc power dissipation is spread evenly across the array. A future advanced

antenna might consist of many grating antennas fabricated on a soft substrate or a single wafer of GaAs- or InP-based semiconductor, which would feature both mm-wave and optoelectronic components to achieve a high performance optically controlled (or quasi-optical) scanning array.
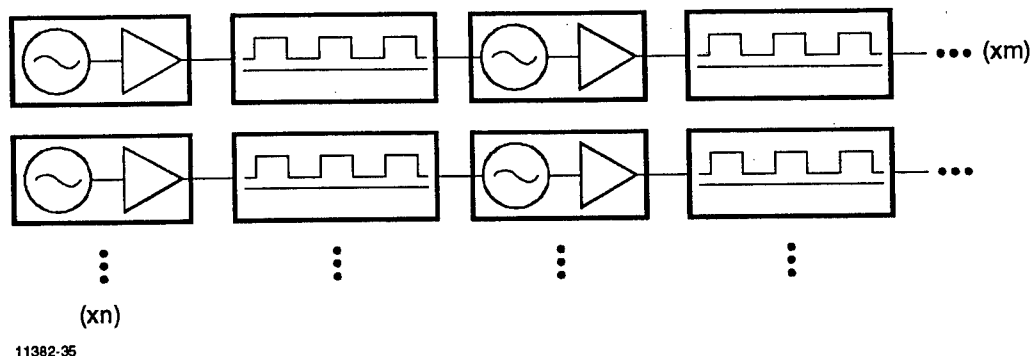

11382-35

Figure 2. Multiple sources can be frequency locked to produce large amounts of radiated power from an array

2. Dielectric Bragg Diffraction Grating

2.1 Diffraction Theory

Dielectric waveguides are employed in many applications, ranging from mm-wave frequencies up through optical wavelengths. [14-20] Compared to conventional metal waveguides, dielectric waveguides offer significant advantages for transmission of rf energy because of their flexibility and light weight. At mm-wave frequencies, dielectric waveguides provide a lower loss transmission medium than conventional metallic conductors, such as microstrip or stripline. For this research, rectangular dielectric waveguide is the medium of choice for electromagnetic propagation in the grating antenna.

Diffraction gratings are commonly employed in the design of semiconductor distributed feedback lasers, electro-optic modulators and optical directional couplers. Bragg's law for diffraction is also applied in the investigation of atomic structure of crystalline materials. These principles have been applied to mm-wave and submillimeter-wave components for use as radiating antennas, often referred to as leaky-wave antennas. [6,15,23-25]

When periodic structures are employed, which for the case of antennas may be multiple wires, slots or perturbations, the plane wave incident upon the periodic grating diffracts into various directions described as the diffraction orders (or space harmonics) for the grating. As shown in Figure 3, the diffracted waves propagate in directions in which phase constants along the grating match on the two sides (or multiples of 2π phase differences between grating elements). The scattered waves will combine to produce maximum intensity if the differences from adjacent perturbations are an integral number of wavelengths (Bragg's Law):

$$2 \Lambda \sin \theta = n \lambda \qquad n = 0,1,2,... \qquad (1)$$

where Λ is the period of the perturbations, θ is the angle of incidence of the electromagnetic wave, λ is the incident wavelength, and the dielectric constant of the medium is assumed to be 1.

A simple uniform cross-section dielectric slab waveguide would represent a slow-wave structure, but when corrugations are introduced, a fast complex wave is produced that radiates power. The bulk of the guided energy, however, remains waveguide is an example of a periodic traveling-wave structure. When the period
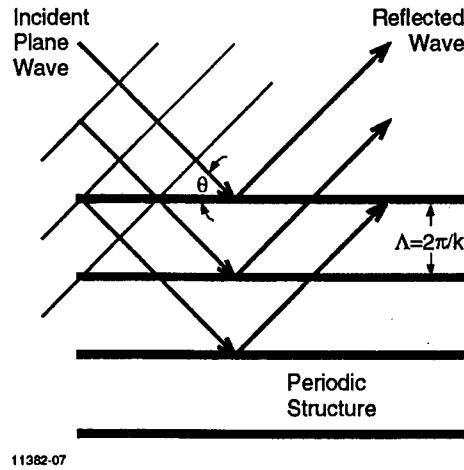
Figure 3. A periodic grating causes diffraction scattering of a plane wave

of the corrugations meets the proper conditions for mode-coupling resonance, radiation occurs at an angle between backfire and endfire, and a stopband is formed. This stopband is evident by a significant increase in input standing wave ratio (SWR), and often a change in the radiation properties of the grating antenna across this frequency range. [11]

Periodic traveling-wave structures are often analyzed with the aid of Floquet's theorem. [4] In general terms, Floquet's theorem states that a time-harmonic electromagnetic field ψ (x,y,z) of a normal mode guided along an axially periodic structure can be described as

$$\varphi(x, y, z + d) = e^{jk_o d}\varphi(x, y, z) \tag{2}$$

The Floquet wave number, k_o, which is generally complex, is referred to as the fundamental propagation constant. Bloch also investigated periodic structures in

89

crystals, arriving at a similar conclusion for the case of Schrodinger's equation. [11]

To analyze the characteristics of periodic structures, the k versus β diagram is used as a graphical representation of the dispersion relation

$$\beta^2 - \varepsilon_r k_o^2 = 0 \tag{3}$$

For a transverse electromagnetic (TEM) line filled with lossless isotropic dielectric (permittivity ε_r), forward-traveling and backward-traveling waves can be represented by two straight lines with slopes $\pm\varepsilon_r^{-1/2}$ passing through the origin (Figure 4).
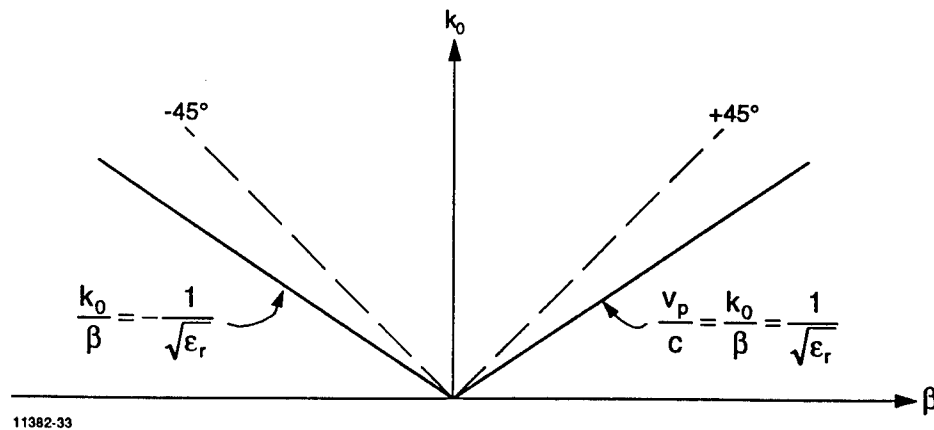

Figure 4. k-β diagram illustrates the dispersion relation for a dielectric-loaded, uniform TEM line

When a TEM line is loaded with a periodic structure the dispersion relation contains an infinite set of spatial harmonic solutions in addition to the basic TEM solutions. The dispersion relation for this axially periodic structure is a functional relation between k_{zo} and k_o in the form of a transcendental equation

$$D(k_{zo}, k_o) = 0 \qquad (4)$$

Solutions of the form

$$k_{zo} = k_{zo}(k_o) \qquad (5)$$

represent the fundamental propagation constants of the modes of the traveling-wave structure. [11] All spatial harmonic wave numbers must also simultaneously be solutions to the transcendental equation.

For a periodic grating on a dielectric substrate the dispersion characteristics can be studied by use of the mode-coupling principle. The k-β diagram can be obtained by examining the dispersion curves of the two interacting modes of the unloaded structures. Shown qualitatively in Figure 5, the Brillouin diagram illustrates the interaction observed as a result of the coupling of the substrate to the periodic structure. The uncoupled modes are the straight lines associated with each of the space harmonics. The curved lines represent the mode-coupling effects for
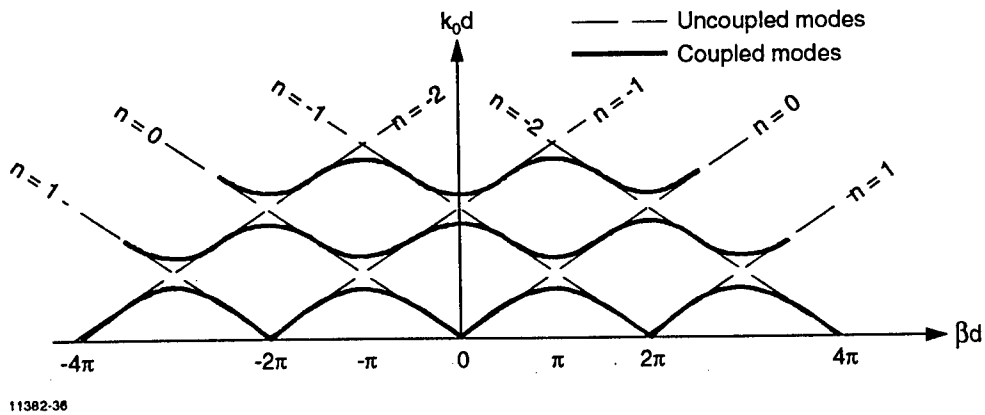

11382-36

Figure 5. Brillouin diagram shows the effect of mode coupling between the substrate and a periodic grating

91

contradirectional coupling where the forward and reflected waves are present. When the group velocities are equal and of opposite sign, a stop band appears. The precise shapes of the dispersion curves depend on the type and degree of loading of the periodic structure. [11]

In a periodic traveling-wave structure, the forward-traveling and backward-traveling waves can be qualitatively described as in Figure 6. Radiation occurs in the fast-wave region (FWR) bounded by the ±45-degree lines. Radiated beams would be formed in the end-fire region of the leaky wave antenna in the 0- to 45-degree angular space while beams formed in the back-fire direction (toward the source) would be found in negative angle space (referenced to 0 degree at broadside to the antenna).
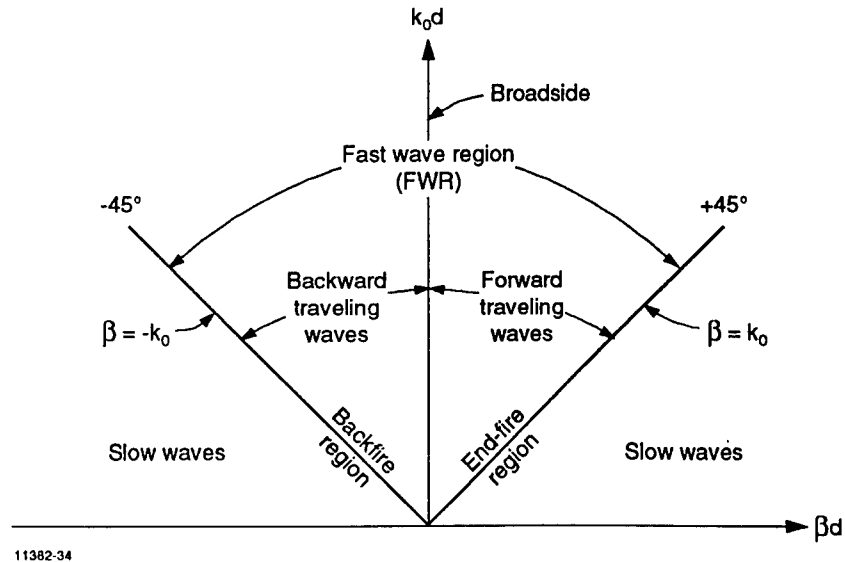

11382-34

Figure 6. The k-β diagram describes the location of backward- and forward-traveling waves radiated from a grating structure

For a periodic traveling-wave antenna with N periods, the radiation pattern can be written as [11]

$$|f(\theta)|^2 = \frac{1}{N^2}\left(\frac{\sin(N\varphi/2)}{\sin(\varphi/2)}\right)^2 \tag{6}$$

where

$$\varphi = k_o \Lambda \sin\theta - \beta\Lambda \tag{7}$$

and Λ is the corrugation period and θ is the observation angle measured from broadside.

Modes in periodic waveguide structures can be analyzed using the Floquet-Bloch theory applied to multiple layer dielectric structures, as shown in Figure 7. A transfer matrix method allows solutions to be obtained by matching the boundary conditions at each of the dielectric interfaces. The field in the periodic waveguide can be expressed in terms of the Floquet-Bloch functions, [13]

$$\Psi(x,z) = \sum_{n=-\infty}^{\infty} \Psi(x)e^{-\gamma_n z} \tag{8}$$

where

$$\gamma = \alpha + j\beta \tag{9}$$

(α and β are the attenuation and propagation constants, respectively.) Each term in Eq. 8 is referred to as a space harmonic, with the $n=0$ spatial harmonic usually being dominant.
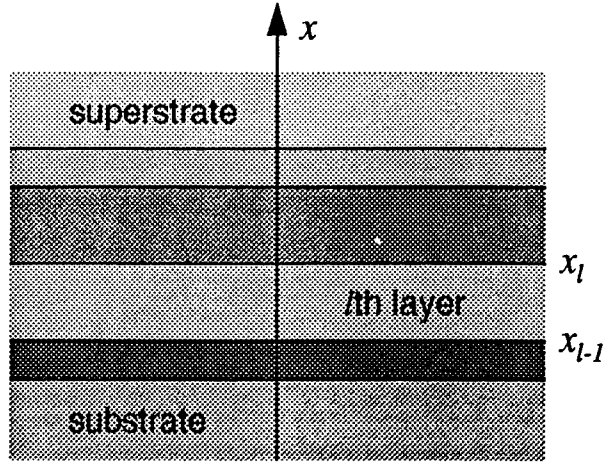
11378-7

Figure 7. Multilayer dielectric structure is analyzed using the Floquet-Bloch theory

2.2 Computation of Modal Propagation Constants

Design of the corrugated grating antenna for leaky wave operation at the frequency of interest requires computation of the eigenvalue solutions to the wave equation. Using MODEIG II (© Southern Methodist University), a program that numerically solves the wave equation for multiple dielectric-layer structures, the effective dielectric constant, ε_{eff}, can be found for the desired TM mode in an (assumed) infinitely wide waveguide. This ε_{eff} is then used to accurately calculate the grating period of the structure. Figure 8 illustrates the representative cross section of the simulated structure. The dielectric constant of the alumina ceramic base (slab waveguide) is 9.8. The effective dielectric constant of the grating structure, assuming a 50-percent duty cycle and square corrugations, is computed as the volume average permittivity:

$$\varepsilon_{avg} = (\varepsilon_1 d_1 + \varepsilon_2 d_2) / d \qquad (10)$$
$$= 1 + (\varepsilon_r - 1) / 2 \qquad \text{for } \varepsilon_1 = 1, \varepsilon_2 = \varepsilon_r, d = d_1 + d_2$$
$$= 5.4$$

where ε_1, d_1, are the permittivity and width of the grooves (air), and ε_2, d_2 are the permittivity and width of the teeth.
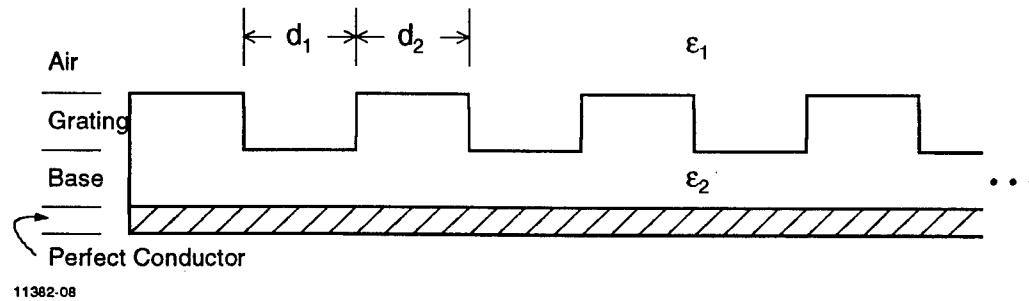

11382-08

Figure 8. A simulated dielectric grating structure is used to compute modal coefficients

3. Grating Antenna Design

3.1 Design

A corrugated dielectric grating antenna has been selected for use in this research. This structure is easy to build, requires no thin-film metallization, and is small in size. Radiation from the grating antenna is affected primarily by the perturbation of the dielectric (teeth) and the propagation constant within the base layer. The radiation loss due to the perturbations causes the incident wave to decay exponentially as it travels down the length of the grating. As discussed in the previous section, the base thickness and tooth height must be chosen to achieve an acceptable percentage of energy within the base layer so that the energy can be spread across the full length of the grating. If the energy is not well confined to the base, the majority of the radiation will occur within the first few teeth of the grating, resulting in a small effective radiating aperture.

95

The antenna is designed to have a center frequency at 38.5 GHz to enable it to be driven by a GaAs MMIC VCO, which operates in this frequency range. The main concern of the antenna design is to achieve radiation from the structure at or near the second Bragg condition. The grating period of the corrugated structure is determined from the TM eigenmode solutions discussed in section 2. Corrugations were assumed to be rectangular with a 50-percent duty cycle.

The first and second Bragg resonances, shown in Figures 9 and 10, occur at $\beta\Lambda=\pi$ and $\beta\Lambda=2\pi$, respectively. Referring to the Brillouin diagram of Figure 5, the magnitudes of the $n = -1$ and $n = 0$ modes are equal at $|\beta\Lambda|=\pi$.

$$|\beta_{-1}\Lambda| = |\beta_o\Lambda| = \pi \tag{11}$$

$$\mathrm{Re}\,(k_{x-1}) \approx \mathrm{Re}\,(k_{xo}) \tag{12}$$

As discussed in section 2 the n-1 spatial harmonic is the backward-traveling wave and the $n = 0$ is the forward-traveling wave. The backward-traveling wave can be viewed as a reflected wave of the $n = 0$ spatial harmonic.
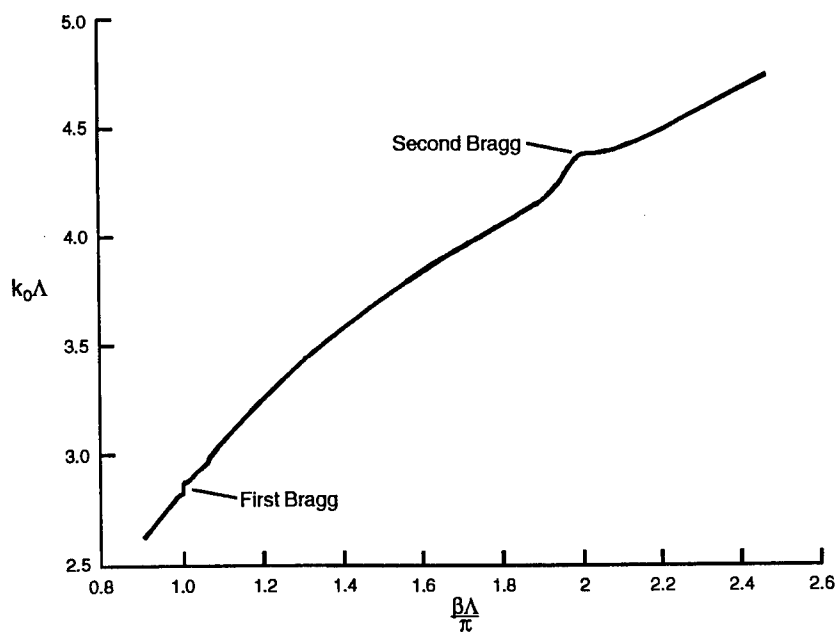
Figure 9. Dispersion diagram illustrates the first and second Bragg resonances
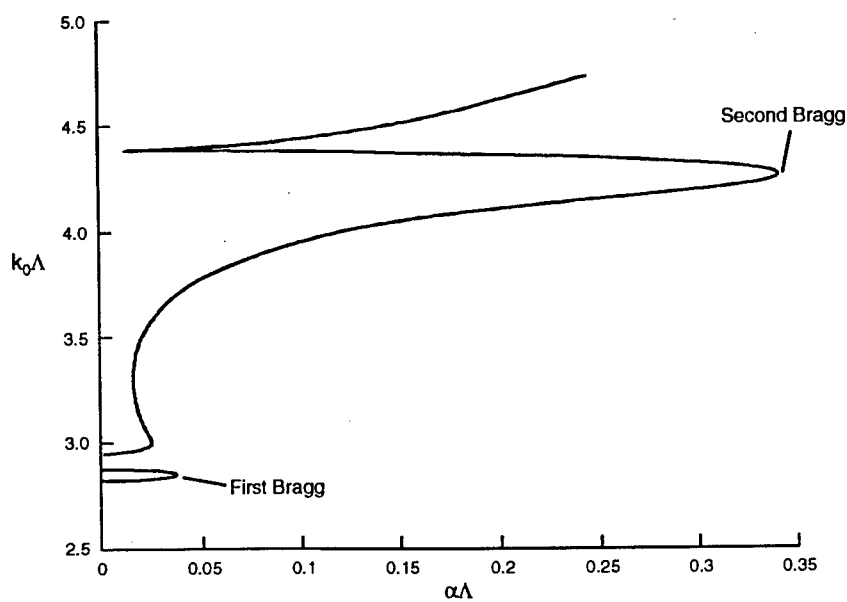
11382-02

Figure 10. Attenuation diagram illustrates the first and second Bragg resonances

11382-03

97

At the second Bragg resonance, $\beta\Lambda=2\pi$ and

$$\left|\beta_{-2}\Lambda\right| \approx \left|\beta_o\Lambda\right| \approx 2\pi \qquad (13)$$

A significant increase in the attenuation coefficient is caused by the strong reflection of the incident wave, creating a high standing wave ratio (SWR) stop band. The forward and backward spatial harmonics result in the group velocity $d\omega/d\beta = 0$, meaning that the energy is not transferred through the dielectric waveguide and no energy is radiated. [13]

For the grating period computed above, $k_o\Lambda=4.175$, which falls in the region just slightly below the second Bragg resonance on both plots. This would imply that the main beam would be found close to broadside, but in the direction of the source terminal (back-fire direction).

Dielectric material for the corrugated antenna was chosen to be alumina ceramic, with a relative permittivity, ε_r, of 9.8. A wide variety of dielectrics, such as soft substrates, could be used in this application, especially if cost were a driving issue. Implementation in a soft substrate medium would also permit a degree of flexibility for conformal applications.

The dimensions of the Q-band grating antenna (Figure 11) are summarized in Table 1. The grating is constructed with very accurately sawed ceramic pieces (tolerances $< \pm0.05$ mm) that are epoxied onto a base ceramic with the prescribed grating period. Greater placement accuracy could be obtained with sawing or
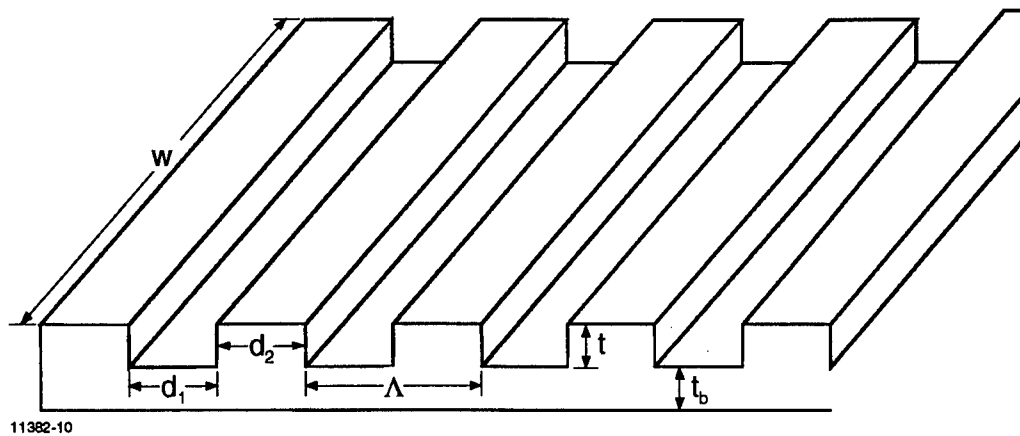
Figure 11. A grating antenna with rectangular corrugations is used as the transmitting antenna.

11382-10

TABLE 1. Q-BAND GRATING ANTENNA DIMENSIONS

Frequency (GHz)	Period (Λ) (mm)	Base Thickness (t_b) (mm)	Tooth Height (t) (mm)	Grating Width (w) (mm)
38.5	5.18	0.381	0.381	15.2

etching a single piece of ceramic to obtain the grating structure, but for this proof-of-concept demonstration, this manual method of assembly proved adequate.

3.2 Simulation

Based on the ideal periodic structure discussed in section 2, a simple mathematical simulation of the grating antenna can be calculated from Eq. 6. For an ideal 9-period corrugated grating antenna operating at 39 GHz with 0.381-mm tooth height and a 50-percent duty cycle, the mathematical model exhibits a radiated main beam near broadside, as shown in Figure 12. Calculated sidelobe levels are below 10 dB. The 3-dB beamwidth is 5.5 degrees.
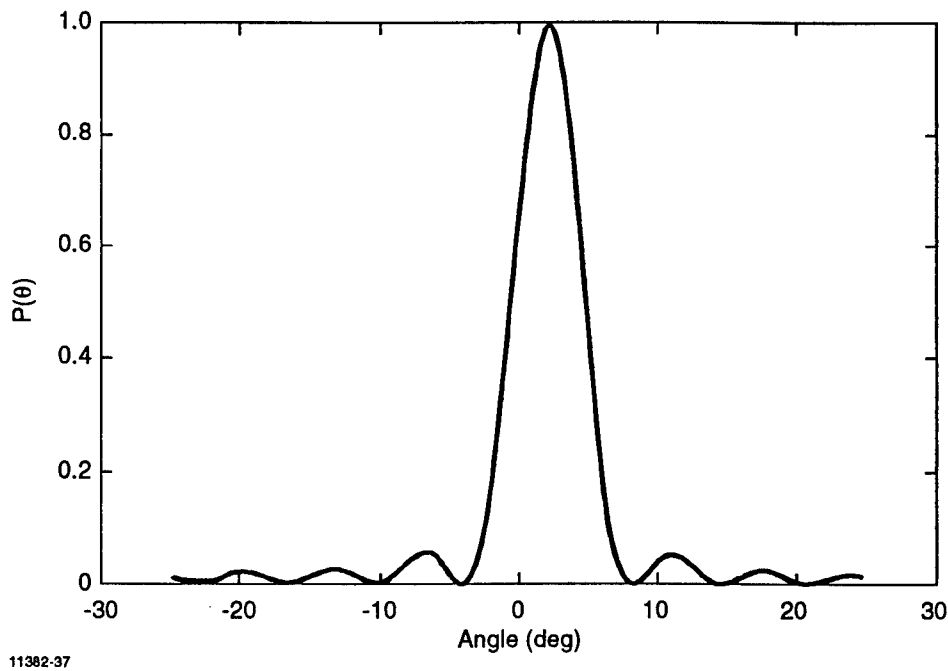
**Figure 12. Calculated radiation pattern for a 9-period grating antenna
shows a 5.5 degree 3-dB beamwidth**

3.3 Experimental Performance

Measurements were made on the corrugated dielectric antenna (Figure 13), by using it as a transmitter and measuring the radiated energy with a standard horn antenna. A 2.4-mm precision coaxial connector launch provided the interface from a mm-wave signal generator to a 50-ohm microstrip transmission line (Figure 14). The microstrip line, fabricated on 0.381-mm-thick alumina ceramic, served as the TM mode interface to the grating antenna.
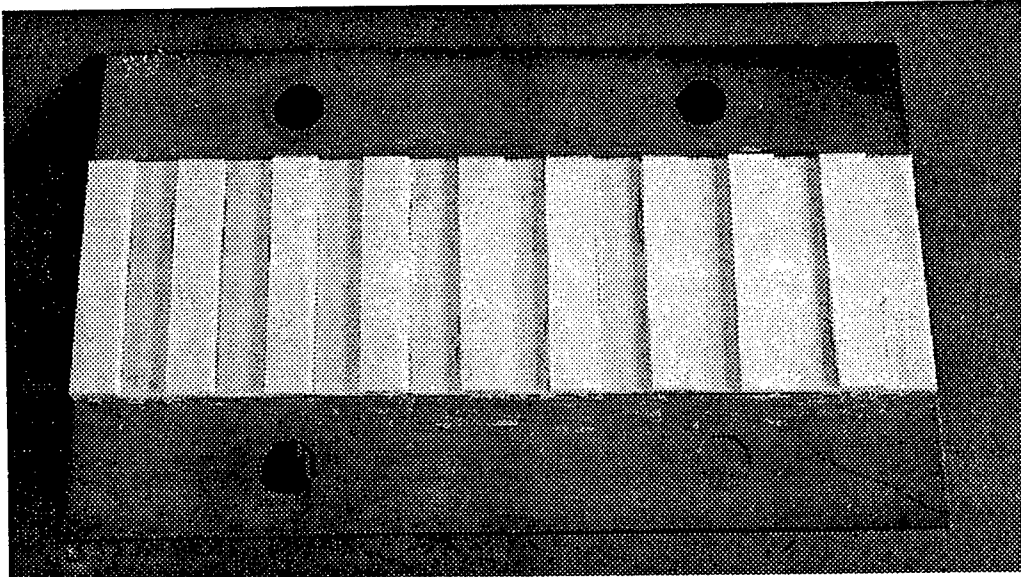
11382-13

Figure 13. Q-band corrugated dielectric grating antenna uses polished alumina ceramic mounted on a metal carrier
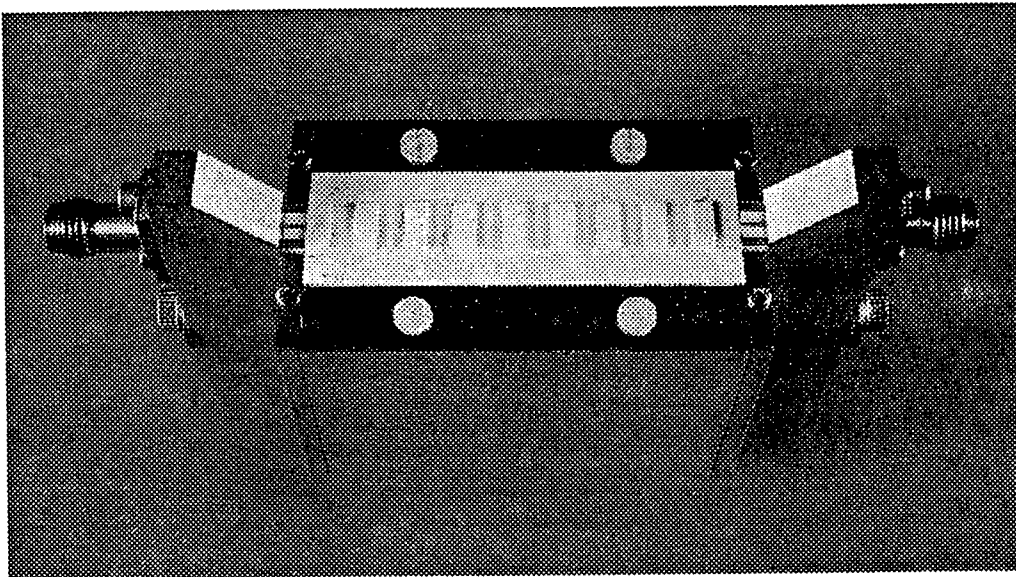
11382-14

Figure 14. Grating antenna test fixture employs 2.4-mm precision coaxial connectors

The antenna designed with a 5.2-mm grating period demonstrates a main beam radiation pattern, which is in the back-fire direction from broadside, as expected, because the calculations indicated that it was slightly below the second Bragg resonance. To account for the finite grating width, the grating period was increased to 5.6 mm to move the main beam to broadside at 39 GHz. Figure 15 shows the measured radiation pattern in the θ plane, with φ kept constant, as the frequency is swept. Cross-polarization energy is approximately 20 dB down. With a grating period of 5.6 mm and a tooth width of 15.2 mm, the second Bragg main lobe occurs at nearly broadside at a frequency of 39 GHz. The 3-dB beamwidth is approximately 5 degrees, which correlates well with the mathematical simulation described in Section 3.2 (predicted beamwidth is 5.5 degrees). Angular scan versus frequency is about 15 degrees/GHz. This scan rate of approximately 30 degrees for a 10-percent frequency variation is typical for grating structures of this type. [19]
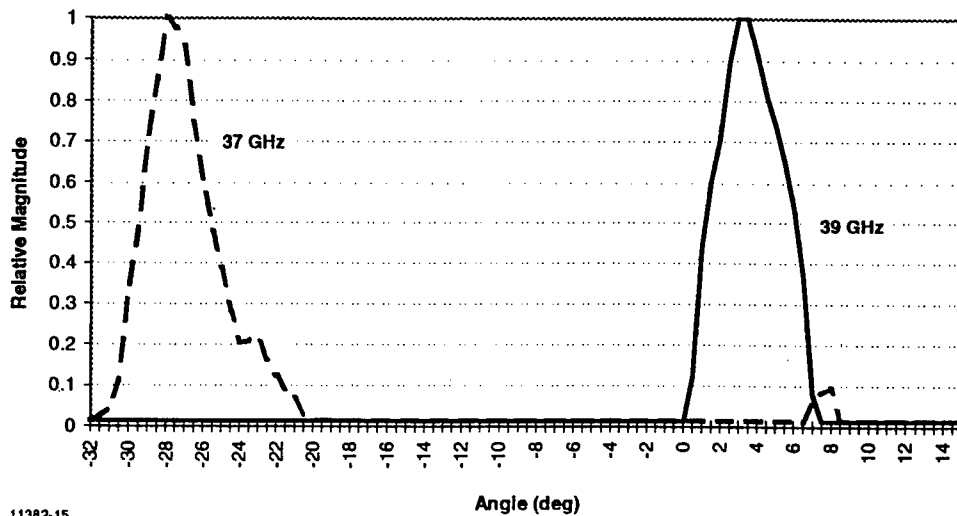

Figure 15. Q-band grating antenna provides 5-degree beamwidth and 15-degree/GHz scan capability

102

4. Millimeter-Wave MMIC VCO/Buffer Amplifier

4.1 Description

The monolithic varactor-controlled oscillator/buffer amplifier is a gallium arsenide (GaAs) integrated circuit designed and fabricated at Texas Instruments to provide highly linear tuning capability at mm-wave frequencies using standard metal semiconductor field effect transistor (MESFET) technology. [24] Shown in Figure 16, the chip is 2.0×4.4 mm in size, fabricated on a 100-µm thick substrate.
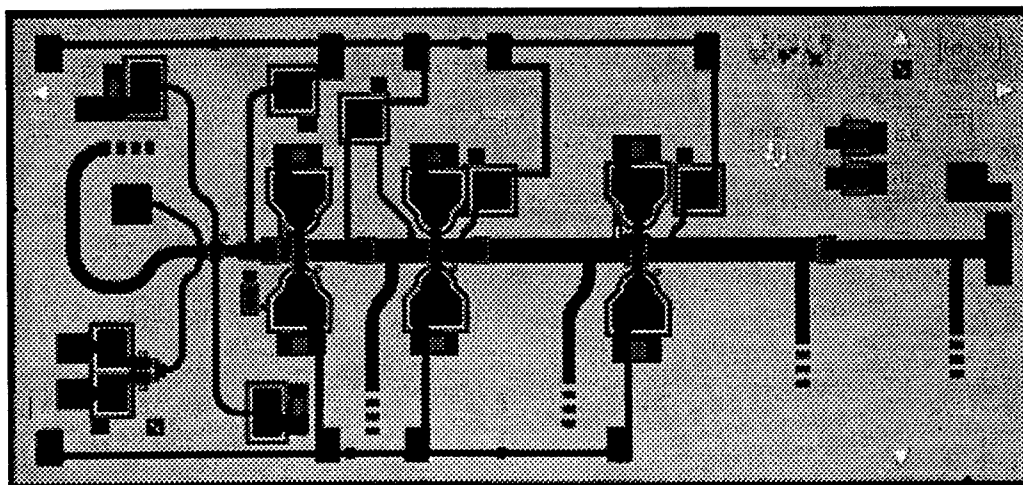
11382-19 (3266-24)

Figure 16. GaAs MMIC varactor-controlled oscillator/buffer amplifier features linear frequency tuning in a small, easy-to-integrate chip

The oscillator employs a transistor in a common-gate configuration to achieve a fundamental frequency oscillator at approximately 40 GHz. A GaAs Shottky diode varactor fabricated on the MMIC provides frequency tuning capability. Three stages of amplification on the chip buffers the oscillator from load variations, provides power gain, and flattens the output power across the tuning band. A simplified circuit schematic is shown in Figure 17.
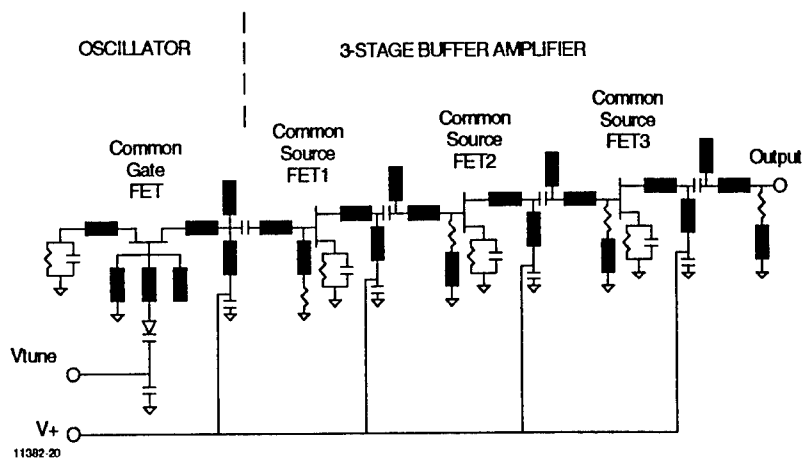
Figure 17. MMIC VCO/buffer amplifier circuit schematic illustrates the integrated
GaAs varactor/FET oscillator and three stages of FET amplification

4.2 Experimental Performance

The MMIC VCO operates in a self-biased mode from a 5-volt bias voltage connected to the drain terminals of the MESFETs. Tuning of the varactor is accomplished with a separate 0- to 5-volt bias line connected to the varactor diode on the chip. Typical drain current for the entire chip is 150 mA at room temperature. Total dc power consumption is 750 mW.

The MMIC chip is mounted on a 0.381-mm-thick alumina ceramic using conductive epoxy. Shown in Figure 18, the MMIC VCO/buffer amplifier assembly has the required dc bias connection lines, bypass capacitors and 50-ohm microstrip transmission line mounted on a metal block. This assembly is easily tested independently of the grating antenna.

Measured frequency and power performance of the MMIC VCO assembly at room temperature is summarized in Figure 19. Tuning bandwidth for a 0- to 5-volt tuning range is approximately 300 MHz with an output power of >10 dBm (10 mW).
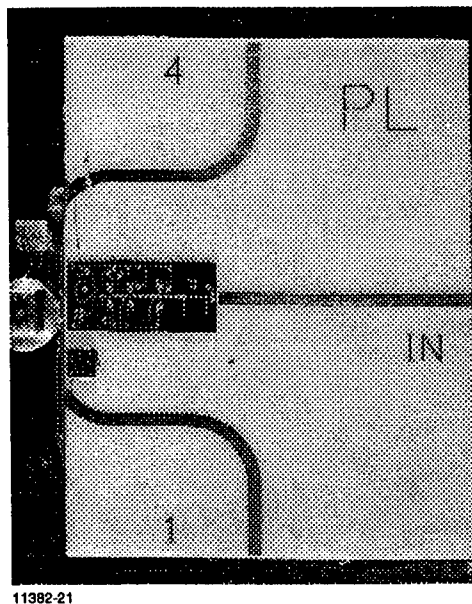
104

Figure 18. The MMIC VCO/buffer amplifier, mounted on a ceramic thin-film network, provides an integrated assembly which easily interfaces with the grating antenna
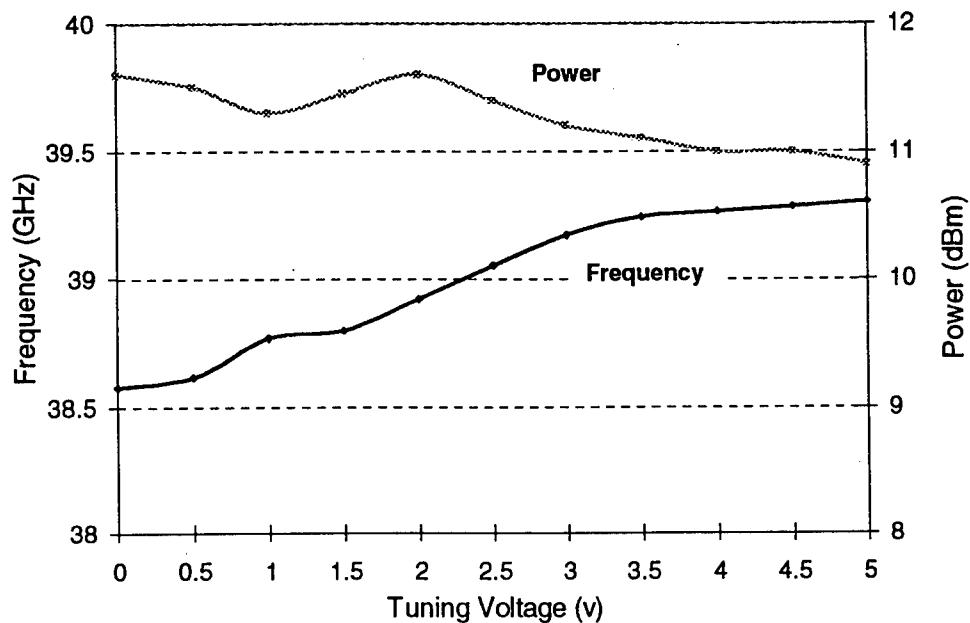

11382-23

Figure 19. MMIC VCO/buffer amplifier provides frequency tuning with greater than 10-mW output power in Q-band
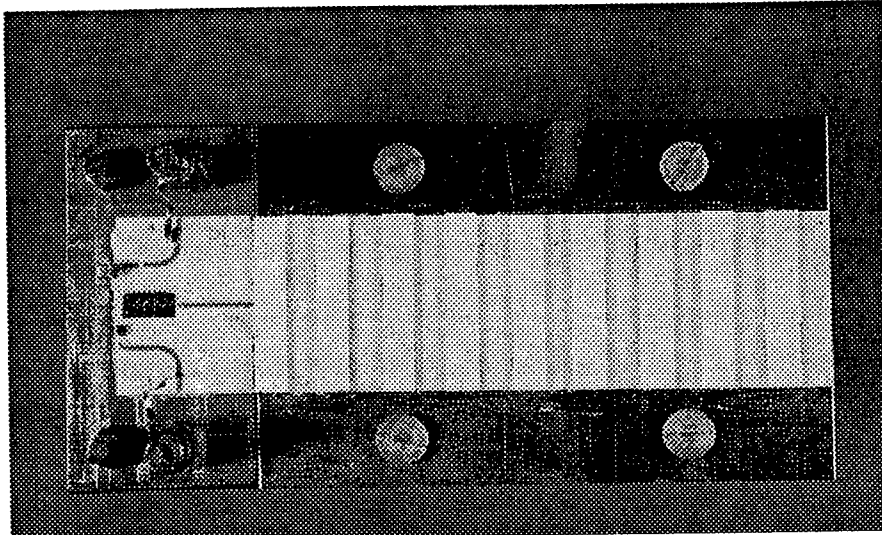
5. Integrated MMIC Scanning Array Transmitter

5.1 Description

An integrated mm-wave scanning array transmitter has been demonstrated using a GaAs MMIC and a dielectric corrugated grating antenna. Operating at Q-band, the integrated transmitter provides signal source generation, amplification, and frequency tuning capability. Because of the periodic nature of the dielectric grating, the change in frequency of the VCO translates into electronic scan capability from the grating antenna.

Figure 20 shows the $5.1 \times 2.5 \times 0.14$ cm integrated assembly. The VCO/buffer amplifier assembly is mounted on a brass block for ease of rf testing, and bias posts are used to inject the dc bias voltages. The grating antenna is mounted on a metal carrier plate that can be easily be attached to a test block for integration with the VCO assembly. Size of this assembly could easily be reduced for specific system insertions.

During the course of rf testing, distorted antenna patterns were observed when the VCO/buffer amplifier assembly was not properly shielded. A metal cover, lined with rf absorbing material was made to help isolate the sensitive receiving antenna in the test area from the extraneous radiation emanating solely from the MMIC chip. Shown in Figure 21, the metal structure attached to the test block with screws and covered only above the VCO/Buffer Amplifier Assembly.

11382-25

Figure 20. GaAs MMIC, TM mode planar launch and dielectric grating antenna are assembled to achieve a fully integrated scanning array transmitter
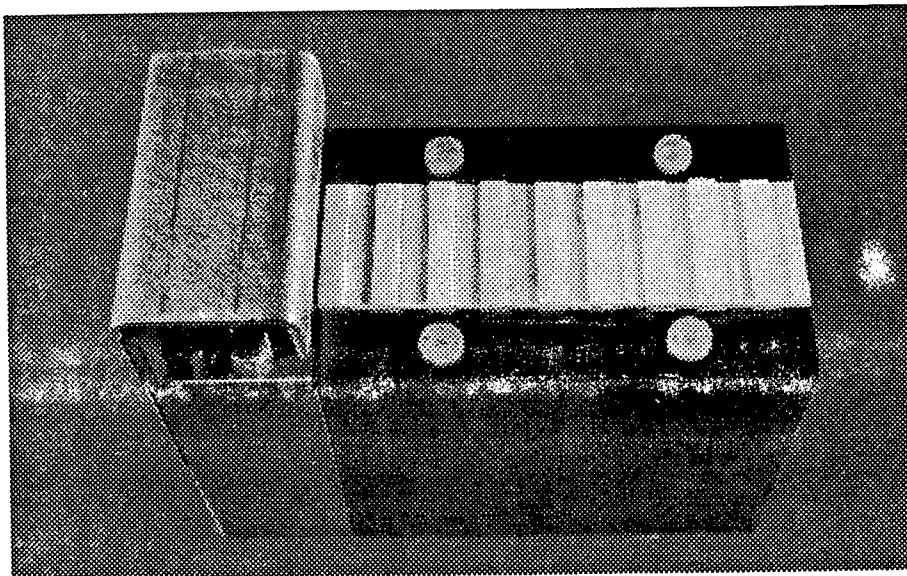
11382-26

Figure 21. A metal cover, lined with RF absorbing material, reduces extraneous radiation from the MMIC chip

5.2 Experimental Performance

Radiation patterns were measured using a Q-band standard pyramidal horn antenna connected to a Hewlett Packard power meter. The power sensor (detector) was directly connected to the receiving antenna WR22 waveguide flange and both were securely mounted to a platform. The receiving antenna remained fixed in the far field, while the integrated transmitter was moved in 1-degree increments to obtain the antenna patterns. Anechoic material was placed around the entire test area to minimize undesirable reflections.

Measured frequency scan performance in the θ-plane of the integrated transmitter is shown in Figure 22. As described earlier, the 3-dB beamwidth of the radiated main beam is 5 degrees with an angular scan capability of 15 degrees/GHz. For the
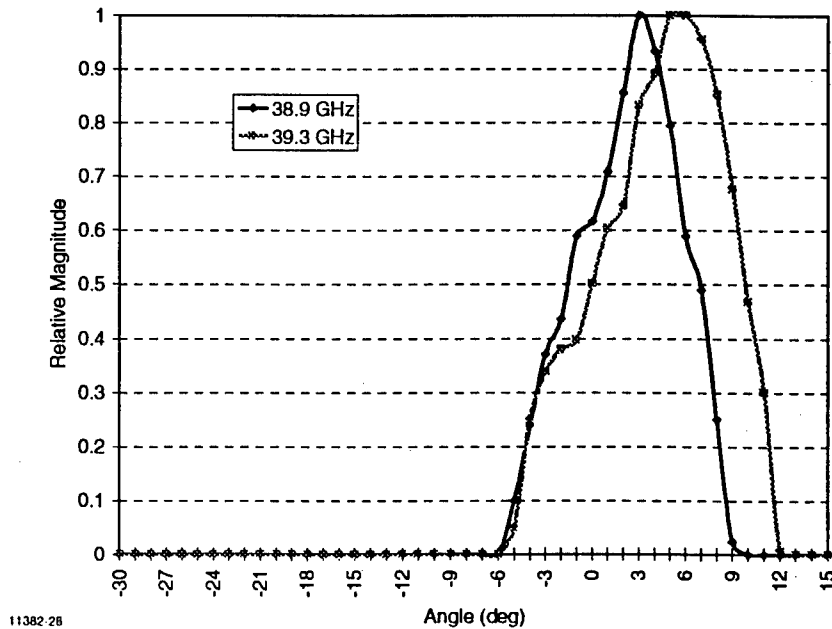
Figure 22. Integrated transmitter demonstrates 15-degree/GHz scan performance in the θ-plane

300 MHz of tuning range that the MMIC VCO covers, total angular scan coverage is 1.2 degrees. This scan coverage could easily be extended by employing a wider bandwidth tunable oscillator. Beamwidth is determined by the number of corrugations of the scanning array. Wider or narrower beamwidths could be achieved by making the number of periods of the grating antenna less or greater, respectively.

6. Conclusions

A fully integrated Q-band GaAs MMIC scanning array transmitter that provides signal generation, frequency tuning and frequency scan capability has been demonstrated. A periodic traveling-wave structure has been analyzed and implemented as a dielectric corrugated grating antenna operating near the second Bragg resonance. A planar microstrip interface has been implemented to launch the desired TM mode into the Bragg diffraction grating. By matching the field patterns of the TM mode at the interface, a fully integrated millimeter-wave grating antenna transmitter has been developed. Frequency scan capability of the grating is 15 degrees/GHz, with a 5-degree beamwidth. This integrated transmitter technology has wide ranging applicability as a single element or in multielement arrays for mm-wave military and commercial radars, sensors, and communication links. [25-27]

REFERENCES

[1]   D. K. Barton, "A half century of radar," *IEEE Trans. Microwave Theory Tech.*, vol. MTT-32, no. 9, pp. 1161-1170, Sept. 1984.

[2]   W. R. Wisseman, L. C. Witkowski, G. E. Brehm, R. P. Coats, D. D. Heston, R. D. Hudgens, R. E. Lehmann, H. M. Macksey and H. Q. Tserng, "X-band GaAs single-chip T/R radar module," *Microwave Journal*, vol. 30, no. 9, pp. 167-173, Sept. 1987.

[3]   R. E. Lehmann, D. C. Zimmermann, G. E. Brehm, D. T. Bryant, J. E. Chapman, D. M. Drury, D. D. Heston, J. B. LaGrange, F. L. Opp, C. L. Orr, T. A. Pankaskie, R. D. Ragle, S. Sanzgiri and R. E. Williams, *Advanced Solid-State Radar Module,* Final Report for the Air Force Wright Aeronautical Laboratories, Report no. AFWAL-TR-86-1135, Feb. 1987.

[4]   G. Hadjicostas, J. K. Butler, G. A. Evans, N. W. Carlson and R. Amantea, "A numerical investigation of wave interactions in dielectric waveguides with periodic surface corrugations," *IEEE J. Quantum Electron.,* vol. QE-26, no. 5, May 1990.

[5]   C. Elachi and C. Yeh, "Periodic structures in integrated optics," *J. Applied Physics,* vol. 44, pp. 3146-3152, July 1973.

[6]   W. S. C. Chang, "Periodic structures and their applications in integrated optics," *IEEE Trans. Microwave Theory Tech.,* vol. MTT-21, pp. 775-785, 1974.

[7]   H. Kressel and J. K. Butler, *Semiconductor lasers and heterojunction LEDs,* Academic Press, 1977.

[8]   A. Yariv, "Coupled-mode theory for guided-wave optics," *IEEE J. Quantum Electron.,* vol. QE-9, pp. 919-933, Sept. 1973.

[9]   D. Marcuse, *Theory of Dielectric Optical Waveguides,* Academic Press, New York, 1991.

[10]   C. Yeh, *Theoretical and Experimental Investigation of Slab Waveguides with Periodical Grating Layer,* PhD Dissertation, Southern Methodist University, Dallas, 1992.

[11]   A. Hessel, "General characteristics of traveling-wave antennas," *Antenna Theory, Part 2,* R.E. Collin and F. J. Zucker, eds., McGraw-Hill, New York, 1969.

[12]   S. Kawasaki and T. Itoh, "A layered negative resistance amplifier and oscillator using a FET and a slot antenna," *IEEE MTT-S Microwave Symposium Dig.,* 1991, pp. 1261-1264.

[13]   J. Liu, *A Numerical Investigation of Periodic Waveguides,* PhD Dissertation, Southern Methodist University, Dallas, 1995.

[14]   J. K. Butler, W. E. Ferguson, G. A. Evans, P. J. Stabile and A. Rosen, "A boundary element technique applied to the analysis of waveguides with periodic surface corrugations," *IEEE J. Quantum Electron.,* vol. QE-28, no. 7, pp. 1701-1709, July 1992.

[15] F. Schwering and S. T. Peng, "Design of dielectric grating antennas for millimeter wave applications," *IEEE Trans. Microwave Theory Tech.*, vol. MTT-31, pp. 199-209, Feb. 1983.

[16] T. Itoh, "Application of Gratings in a Dielectric Waveguide for Leaky-Wave Antennas and Band-Reject Filters," *IEEE Trans. Microwave Theory Tech.*, vol. MTT-25, no. 12, Dec. 1977.

[17] A. Rosen, R. Amantea, P. J. Stabile, A. E. Fathy, D. B. Gilbert, D. W. Bechtle, W. M. Janton, F. J. McGinty, J. K. Butler and G. A. Evans, "Investigation of active antenna arrays at 60 GHz," *IEEE Trans. Microwave Theory Tech.*, vol. MTT-43, no. 9, pp. 2117-2125, 1995.

[18] V. A. Manasson, L. S. Sadovnik, A. Moussessian and D. B. Rutledge, "Millimeter-wave diffraction by a photo-induced plasma grating," *IEEE Trans. Microwave Theory Tech.*, vol. MTT-43, no. 9, pp. 2288-2290, 1995.

[19] R. J. Mailloux, F. K. Schwering, A. A. Oliner and J. W. Mink, "Antennas III: array, millimeter-wave, and integrated antennas," Ch. 12, *Handbook of Microwave and Optical Components, Vol. 1*, K. Chang, ed., John Wiley & Sons, New York, 1989.

[20] E. A. J. Marcatili, "Dielectric rectangular waveguide and directional coupler for integrated optics," *Bell Syst. Tech. J.*, vol. 48, pp. 2071-2102, Sept. 1969.

[21] R. C. Johnson, ed., *Antenna Engineering Handbook*, McGraw-Hill, New York, 1993.

[22] M. Guglielmi and A. A. Oliner, "A practical theory of image guide leaky wave antennas loaded by periodic metal strips," *Proc. 17th European Microwave Conference*, Rome, Sept. 7-11, 1987, pp. 549-554.

[23] T. Tamir, "Leaky wave antennas," *Antenna Theory, Part 2*, R.E. Collin and F.J. Zucker, eds., McGraw-Hill, New York, 1969.

[24] R. E. Williams, *Gallium Arsenide Processing Techniques*, Artech House, Dedham, MA, 1984.

[25] D. Hughes, "Aerospace electronics may guide smart cars," *Aviation Week & Space Technology*, Nov. 8, 1993.

[26] R. Schneiderman, "Intelligent-vehicle market moves into the fast lane," *Microwaves & RF*, June 1993.

[27] R. K. Jurgen, "Smart cars and highways go global," *IEEE Spectrum*, May 1991.

111

LOW COST ELECTRONICALLY SCANNED
MILLIMETER WAVE ANTENNA

Ekkehart O. Rausch[*] and Andrew F. Peterson[**]
Georgia Institute of Technology
Georgia Tech Research Institute
Atlanta, Georgia

Abstract: Low cost, compact, electronically scanned antennas are needed for commercial as well as military applications. This antenna was realized by constructing a Ka-band millimeter wave Rotman lens. Various lens designs were generated and input into a mathematical model. The core of the model is an integral equation formulation that relates the various field components in the waveguide apertures. The scattering matrices output by the model were processed to provide beam patterns and insertion loss. The beam patterns, in turn, were evaluated to determine the sidelobe levels. Maximum sidelobe levels of the order of $\leq$ -30 dB and a one way insertion loss $\leq$ 3 dB were predicted with this modeling process. The optimized millimeter wave lens design was fabricated and tested by measuring the 53 port scattering matrix associated with the lens. The measured scattering matrix was processed in a similar manner as the computed matrix. All beam patterns were weighted with a Taylor function. A maximum sidelobe level $\leq$ -30 dB was obtained. The measured insertion loss ranged between 1 and 2 dB depending on the particular beam port that was excited.

1. Introduction

Millimeter Wave (MMW) components are compact and well suited for integration into missile seeker heads, smart munitions, automobile collision avoidance systems, and synthetic vision systems. In these applications, low cost, rapid inertialess scanning of the antenna is desirable. Most MMW antennas that operate at frequencies equal to or greater than 35 GHz use either a mechanical scanning

---

[*] Senior Research Scientist at the Georgia Tech Research Institute
[**] Associate Professor in the Electrical Engineering Department at Georgia Tech

approach or phase shifters for electronic steering. Phase shifters that operate at MMW frequencies are costly and introduce considerable RF losses. Mechanically steered antennas are relatively low in cost, but are slow in response, sensitive to shock and vibration, and have moving parts that are subject to wear and failure. Thus, low cost, high reliability, and electronic scanning are generally incompatible unless the design is based on a MMW Rotman lens. This Rotman lens consists of a parallel plate region with waveguide ports distributed around the periphery of the plates. Beam-forming or focal ports are located on one side of the plates. These ports are fed by a switch array. The array ports are on the opposite side, each connected to an antenna element. Energy, input into a specific focal port, will emerge from the antenna elements and produce a beam along a particular direction. Switching the input from focal port to focal port will steer the beam electronically in one dimension as shown in Figure 1. This concept may be extended to two dimensions by modifying the Rotman lens equations and generating 2-dimensional surfaces for the focal and array contours.
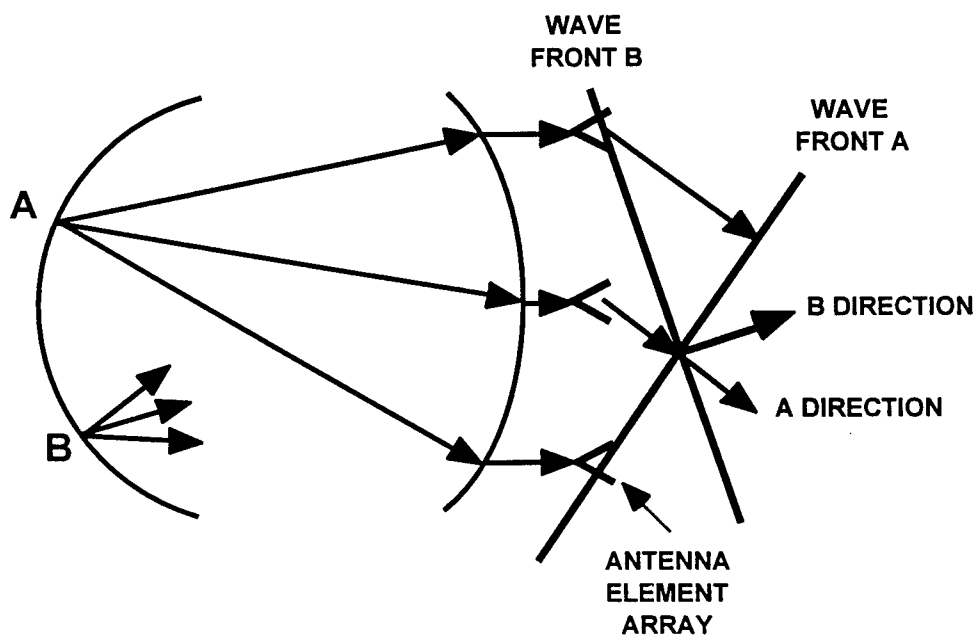

Figure 1. Principle of Operation of Rotman Lens

However, the main objective of this project was to demonstrate proof-of-concept. Therefore, the design was restricted to one-dimensional scanning. Currently, the lens is manufactured in aluminum. However, the possibility exists to implement both the lens and the switch array in plastic.

A typical MMW lens design operating between 33 and 37 GHz is shown in Figure 2. The design was generated with the aid of a mathematical model. Both the model and the lens design guidelines are discussed in the following sections.
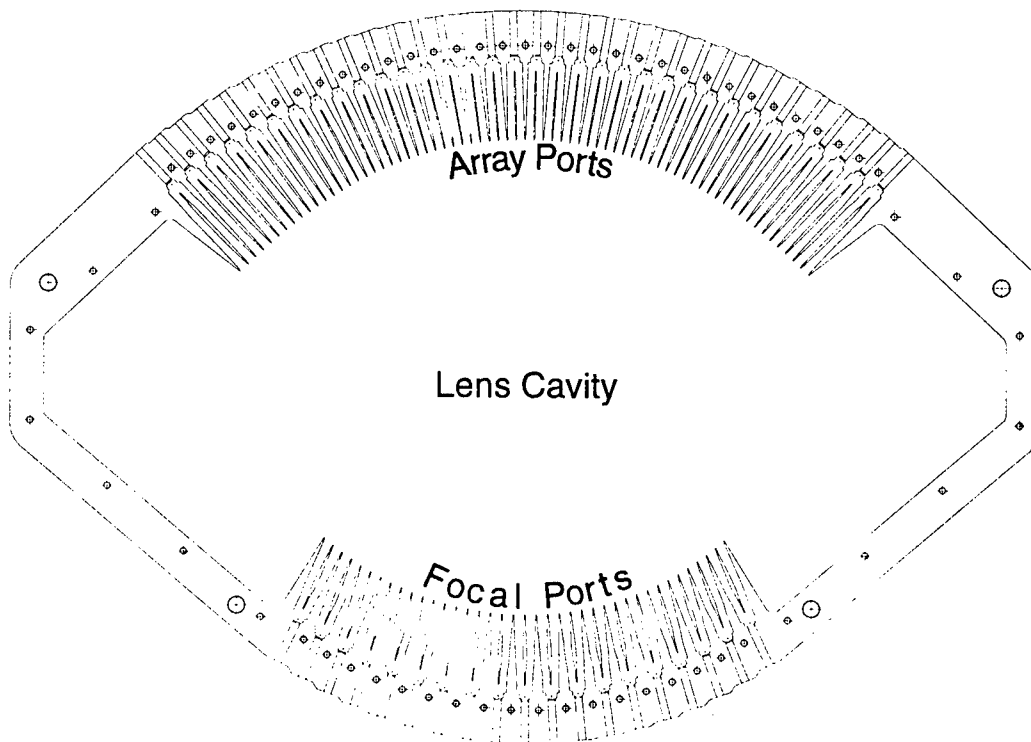

Figure 2. Ka-band Rotman lens design

2. Lens Analysis Model

The rectangular waveguide feed lines, shown in Figure 2, are used to route the signals between input and output ports through the lens cavity. The waveguides are generally tapered along their transverse dimension to provide an improved

impedance match at the apertures, which are located along the lens cavity boundary. A mathematical description of the N-port device can be obtained in terms of a scattering matrix (S-matrix), which relates the complex-valued amplitudes of input and output signals at a single frequency. For a given waveguide mode input at the n-th port, the amount of output waveguide mode produced in the m-th port can be determined from the S-matrix. The S-matrix, in turn, may be processed further to obtain lens performance parameters such as beam sidelobe levels and insertion loss.

To compute the S-matrix, the contributions from each mode in each waveguide aperture around the lens must be combined into an integral equation. The integral equation is essentially equivalent to Maxwell's equations and is used to rigorously incorporate all electromagnetic effects, such as mutual coupling, associated with the lens interactions. The discrete form of the integral equation can be rewritten in matrix form, producing a generalized scattering matrix. The generalized S-matrix contains information about the primary (dominant) waveguide modes, as well as higher-order waveguide modes and is defined as follows:

$$
\begin{bmatrix} b_1 \\ b_2 \\ \vdots \\ b_{NM} \end{bmatrix} = \begin{bmatrix} S_{11} & S_{12} & \cdots & S_{1,NM} \\ S_{21} & S_{22} & & \vdots \\ \vdots & & \ddots & \vdots \\ S_{NM,1} & \cdots & \ddots & S_{NM,NM} \end{bmatrix} \begin{bmatrix} a_1 \\ a_2 \\ \vdots \\ a_{NM} \end{bmatrix}
\tag{1}
$$

The parameters $\{a_{nm}\}$ denote the complex-valued coefficients associated with the m-th mode and n-th port propagating toward the lens interior while the set $\{b_{nm}\}$ denotes the coefficients propagating away from the lens interior. The diagonal elements of the matrix provide information about the energy reflected at each port for a particular mode. Off-diagonal elements yield information about the energy transferred between ports.

Each element of the generalized S-matrix above may be determined by using an integral equation that constrains the waveguide aperture fields around the lens periphery. The integral equation imposes the consistency condition that the total

magnetic field in aperture p must be the same as the superposition of the radiated magnetic fields produced there by the various modes of all other waveguide apertures (including aperture p).

In a practical lens configuration, the higher-order modes excited in the apertures of the various ports do not propagate beyond the tapered transition to a single-mode waveguide. Thus, these modes carry no net energy away from the lens, and can be eliminated from the generalized S-matrix by a procedure that accounts for their presence. In the process, the generalized scattering matrix of order NM is reduced to an ordinary N by N scattering matrix, where N is the total number of ports. Furthermore, the reference planes associated with the resulting S-matrix can be shifted to other desired locations along the waveguides to compare the computed values with experimental data.

3. Lens Design

A typical lens design is initiated by solving the Rotman equations [1]. The output contains the x, y coordinates for the positions of the array and focal ports. The input parameters for the lens are the number of array elements (34), number of beams (19), element spacing (0.59λ), maximum operating frequency (37 GHz), maximum scan angle (22.2°), and focal length ($15\lambda_g$). The numbers in parentheses are the optimized parameters selected for the MMW lens. λ is the wavelength in air and λ_g is the guided wavelength within the lens. The Rotman lens design has three perfect foci located at 0° and the maximum scan angles. In between these angles the foci are not perfect which means that the path lengths from a particular focal port to the emerging wavefront are not equal. The focal length was selected so that the design path length errors were minimized with respect to phase to a value $\leq 2.0^{\circ}$.

Unfortunately, the Rotman equations do not provide any information about the waveguide type and orientation or the configuration of the sidewall that joins the focal to the array contour. These entities are crucial to lens performance, because they will affect the sidelobes of the antenna beam patterns. In general, the sidewall is lined with dummy ports or an absorber to attenuate spill-over energy.

A small amount of energy, however, is not absorbed, but reflected from the sidewall, and interferes with the direct beam as shown in Figure 3.
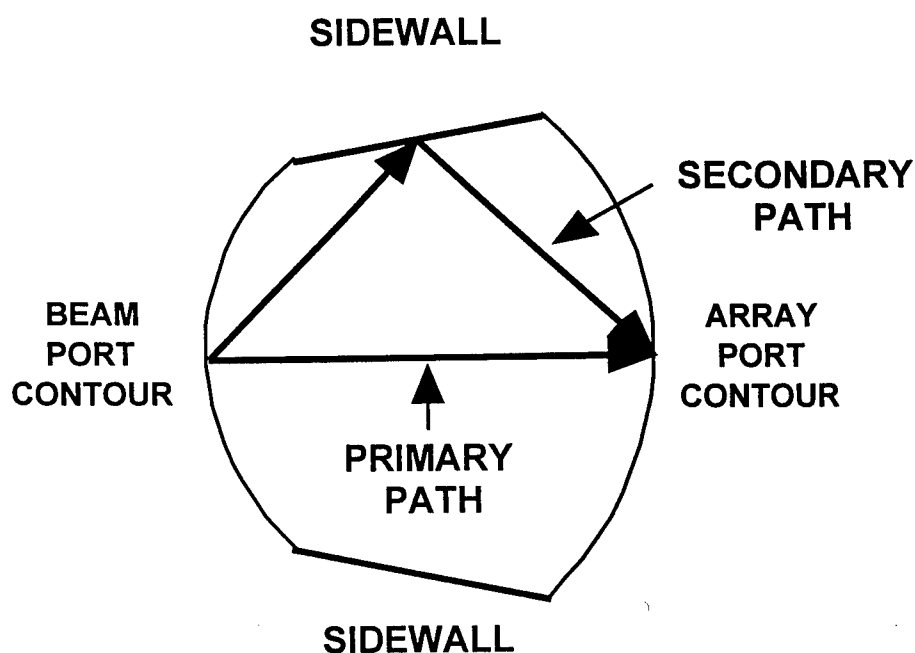
SIDEWALL

SIDEWALL

Figure 3. Interference of reflected and direct energy due to straight sidewall

The large path difference between the direct and reflected ray leads to rapidly oscillating amplitude and phase ripples along the array ports that yield large far-out sidelobes as indicated by the theoretical beam patterns shown in Figure 4. These beam patterns were computed with our lens model. The large sidelobes in Figure 4 can be eliminated if the sidewall configuration is redesigned as shown in Figure 5. The computed beam patterns corresponding to Figure 5 are displayed in Figure 6. Sidelobe reduction is possible because the triangular design redirects and confines the multipath energy within the triangular sidewall region.
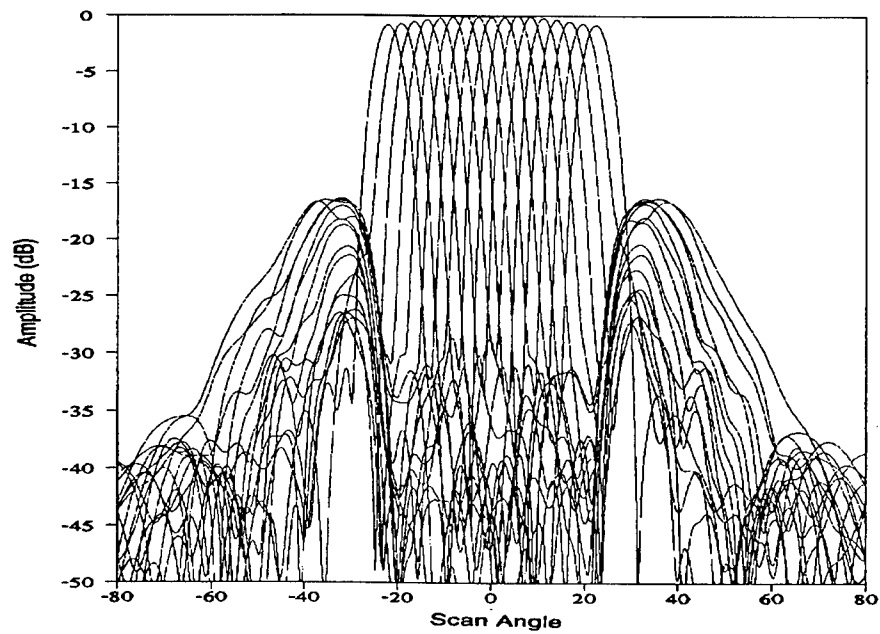
Figure 4. Computed MMW lens beam patterns of straight sidewall design

Figure 5. Proper sidewall design
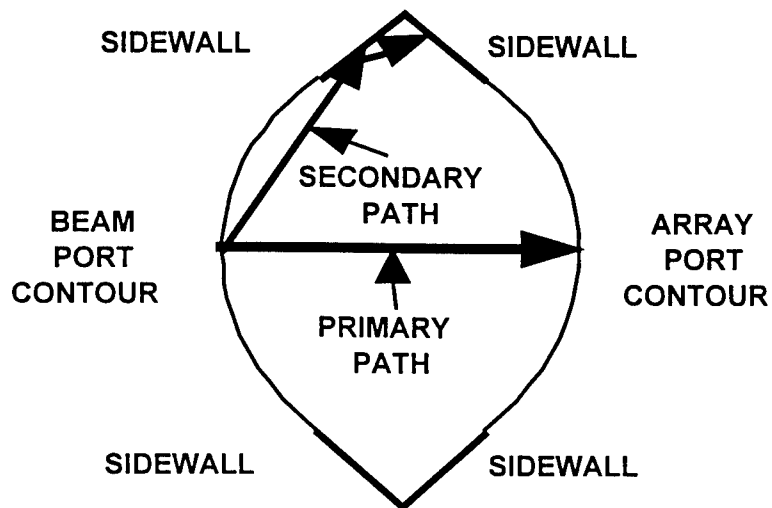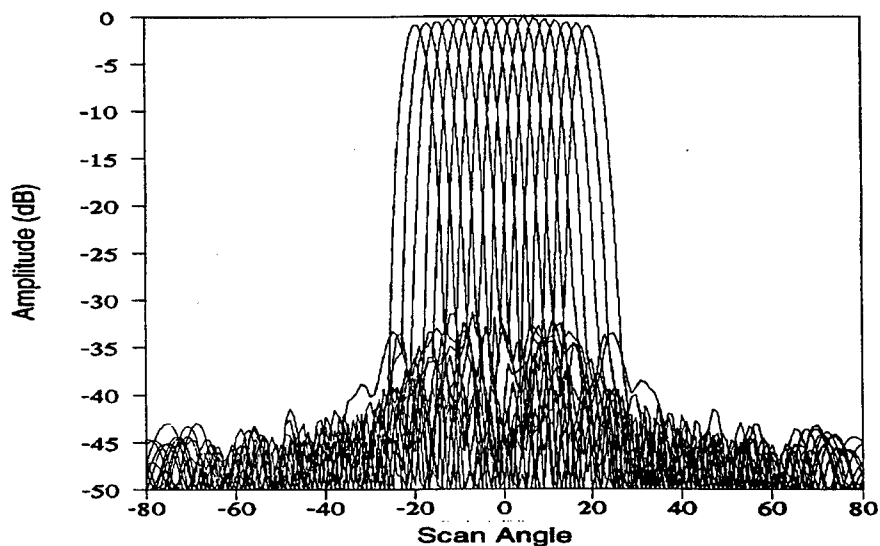
Figure 6. Computed MMW lens beam patterns of triangular sidewall design

For the MMW lens the dummy ports were replaced by an absorber selected on the basis of low reflection coefficients. Figure 7 shows the measured reflection coefficients as a function of frequency for carbon impregnated foam designated as
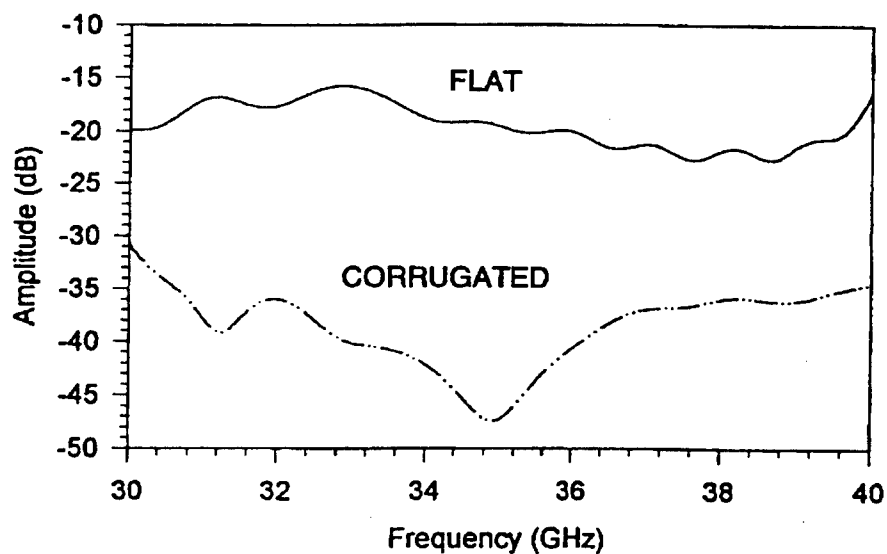

Figure 7. Reflection coefficients for a flat and corrugated MMW absorber

AEMI-20 and manufactured by Advanced Electromagnetics, Inc. in Santee, Ca. Both the incident and reflection angle was $0°$. The upper curve was produced by a flat absorber surface. Lower reflection coefficients, i.e., $\leq$ -35 dB, between 33 and 37 GHz were measured for a corrugated (or egg-crate) surface. Even lower coefficients (< 40 dB) were observed when the angle between the incident and reflected rays was greater than $0°$. For this reason, the corrugated surface was incorporated into this design.

The sidelobes between the maximum scan angles (i.e., close-in sidelobes) are primarily affected by the array and beam port design, not the sidewall. In general, the feed waveguides expand toward the lens cavity to provide a better impedance match between the waveguides and the lens interior, similar to a horn transition. However, the point of maximum expansion at the waveguide lens cavity interface must be restricted to less than $\lambda_g/2$ where λ_g is the guided wavelength, otherwise received electromagnetic energy will be transferred into higher order modes within the taper. The higher order modes cannot propagate through the waveguides, but will be reflected back into the lens interior, because the waveguides only support the fundamental TE_{10} mode. The reflected energy will interfere with energy from the primary path. The small difference between the primary and reflected paths will cause slowly varying phase and amplitude ripples along the array ports. These ripples, in-turn, will result in high close-in sidelobes.

A lens design with port widths greater than λ_g was input into the model. The resultant beam patterns are shown in Figure 8, where sidelobes in excess of -15 dB are observed. This problem was solved by splitting each port into two and by combining the two split ports with a magic tee whose difference port was terminated with a load. Beam patterns resulting from this design, which included a triangular sidewall. are as shown in Figure 6.
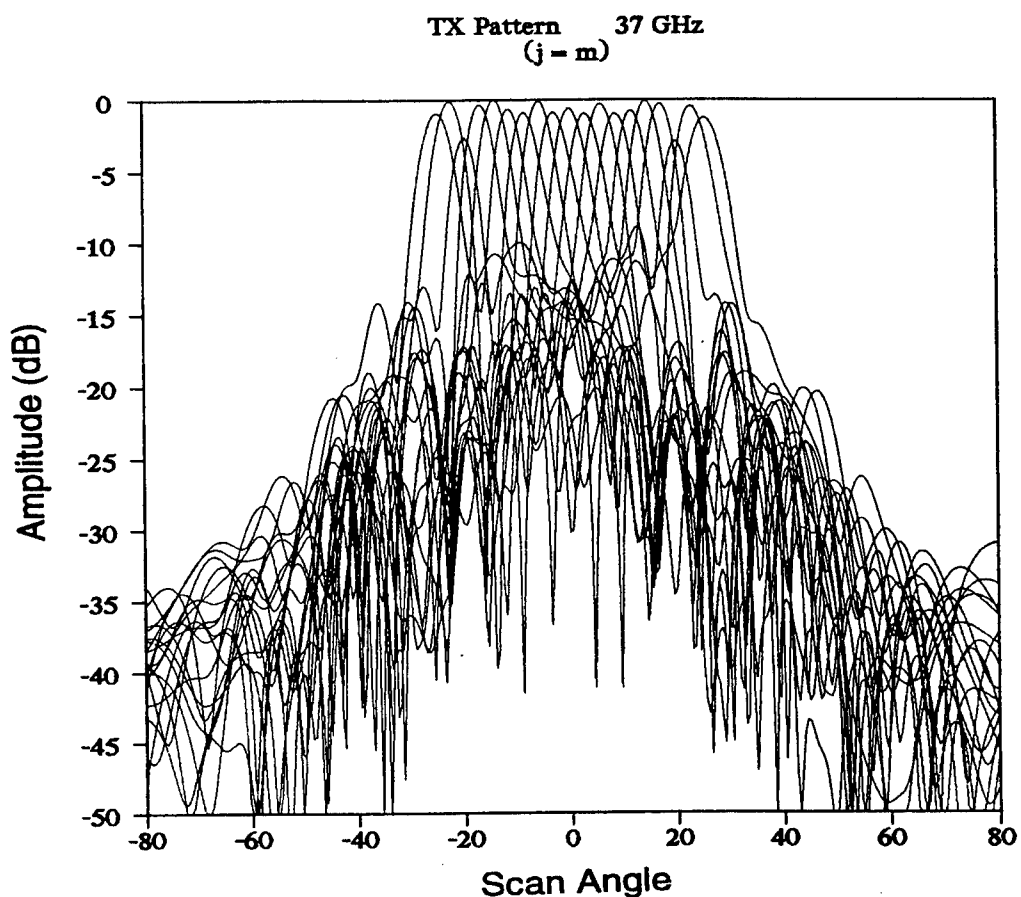
120

TX Pattern   37 GHz
(j = m)

Figure 8. Computed MMW lens beam patterns. Port widths greater than $\lambda_g/2$.

4. Lens Fabrication

The coordinates output by the Rotman lens software were combined with the WR22 coupler to generate a full computer aided design (CAD) of the Rotman lens. Overall tolerance specifications were $\pm$ 0.0005". Computer numerically controlled milling machines were used to rough out the lens interior, followed by an electrical discharge machining (EDM) process to fabricate the intricate structures of the 53 couplers. The lens cavity was polished to an approximate surface roughness of 3 micrometers. The lens was made in two halves with the cut at the mid section of the waveguide a-dimension to minimize radiation coupling between adjacent waveguides. Each half was 1" thick to provide a rigid
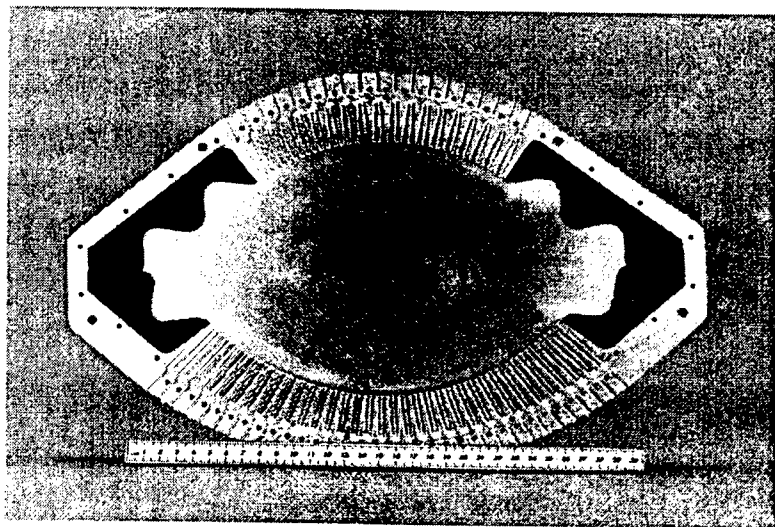
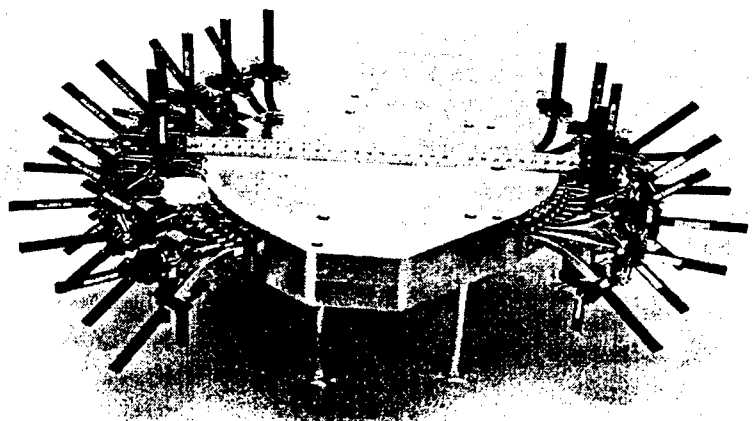Figure 9. Photograph of MMW lens interior

Figure 10. Assembled MMW lens

cavity structure. The material was aluminum to shorten the fabrication time. The absorber was cut along a line that connected a set of peaks and valleys along the main axis of the corrugated pattern. The slice was 0.224" thick and was trimmed with scissors to conform to the interior sidewall configuration of the lens. A photograph of the bottom half of the lens is shown in Figure 9. The complete lens, ready for network analyzer measurements, is shown in Figure 10. The exterior waveguide loads were secured with standard paper clips to minimize port to port measurement time.

5. Measurements

The scatttering parameter matrix for the 53-port Rotman lens was measured with an HP 8510B network analyzer, an HP 8340B synthesized sweeper and an HP 8516A test set. The HP 8510B processor was connected to a 80486 personal computer via an IEEE 488 interface card. The computer read the S_{11}, S_{12}, S_{21} and S_{22} at 51 frequencies between the 30 to 40 GHz band and stored the data on the hard disk.

The S-matrix was processed further to determine the beam patterns and insertion loss of the lens. The beam patterns were determined with Equation 2,

$$P_{K\theta} = 20 \log \left| \sum_{\ell} W_{\ell} S_{K\ell} e^{-j\phi_{K\ell}(\theta)} \right| \qquad (2)$$

where K denotes a specific beam port. The term $\sum_{\ell} W_{\ell} S_{K\ell} e^{-j\phi_{K\ell}}$ represents the vectorial sum of all S-parameters from the Kth beam port to all ℓ array ports. $\phi_{K\ell}(\theta)$ is the phase that must be added to the ℓth array port to determine the power radiated in a particular direction θ due to the excitation of the K beam port. $\phi_{K\ell}(\theta)$ is given by

$$\phi_{K\ell} = (2\pi d_{\ell} \sin \theta) / \lambda \qquad (3)$$

where d_ℓ is the distance from the center of the antenna array to the ℓth antenna element. In this case,

$$d_\ell = \pm (0.5 + \ell)\, 0.59\lambda, \quad \text{where } \ell = 0,1,...., M \tag{4}$$

and M = 15. The w_ℓ are the components of a Taylor weighting function to suppress the sidelobes. In this case, the Taylor function was configured to yield -40 dB sidelobes for an ideal beam pattern. The resultant output is a series of plots as a function of the scan angle θ. Each plot corresponds to the excitation of one beam port. Beam patterns computed in this manner at 32.8 GHz and 36.8 GHz using the measured S-matrix components of the MMW lens are shown in Figures 11 and 12. Each pattern contains the main lobes, that are associated with the various beam ports, plus the superposition of all sidelobes from all K beam patterns. A visual inspection shows a maximum sidelobe level of $\leq$30 dB.
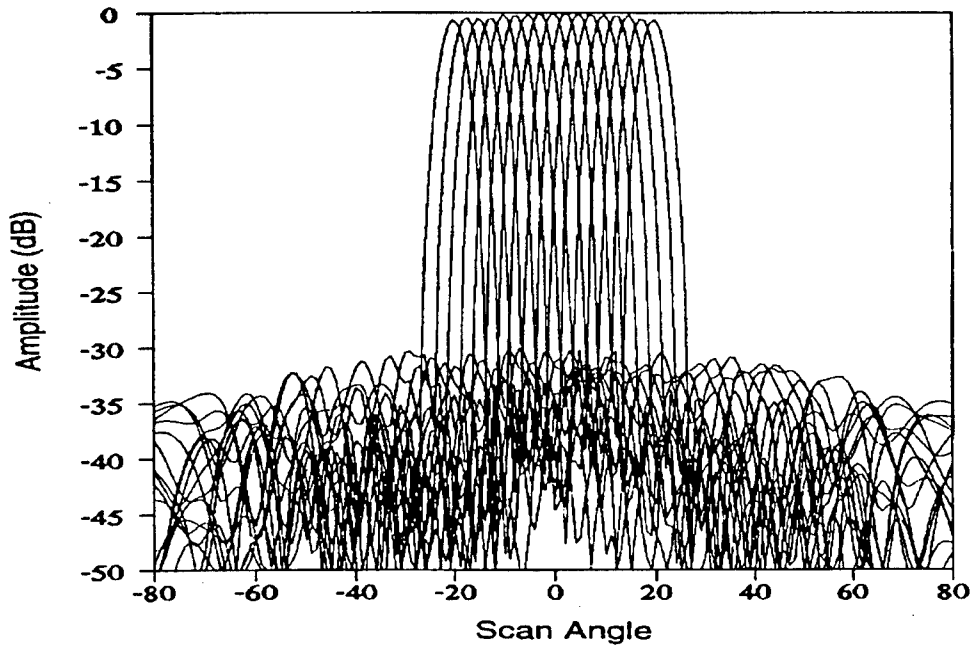
Figure 11. Measured beam patterns for the MMW lens at 32.8 GHz
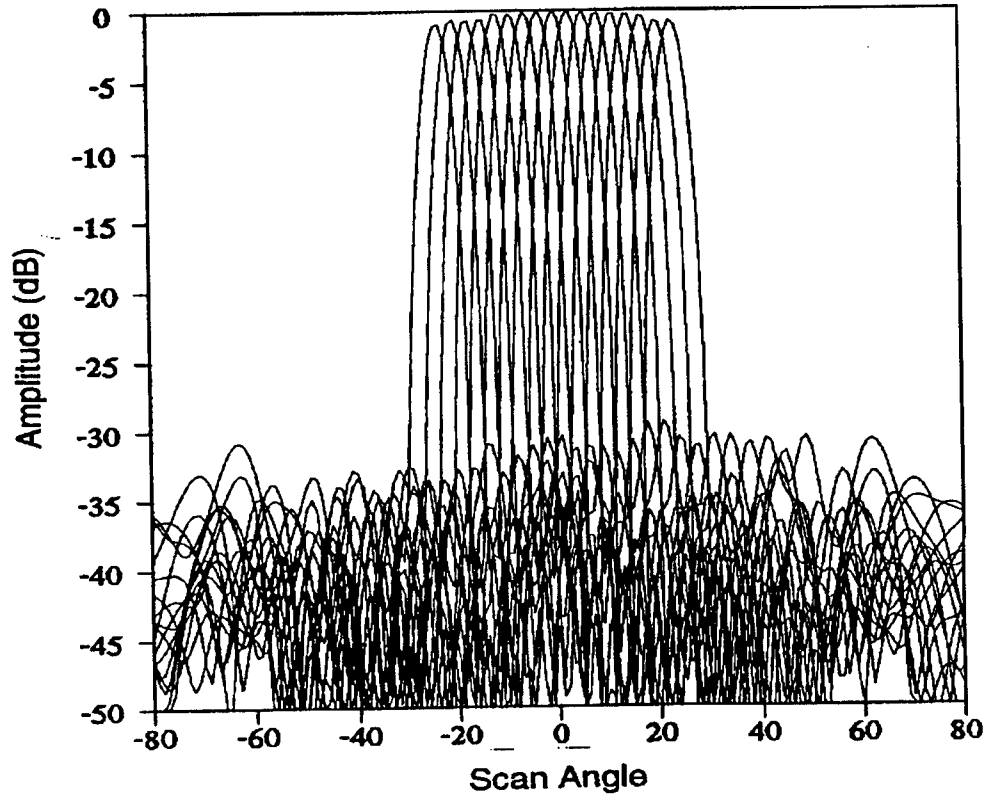
Figure 12. Measured beam patterns for the MMW lens at 36.8 GHz

The insertion loss, also derived from the S-parameters, is given by Equation 5.

$$L_K = -10\log \sum_{\ell} |S_{K\ell}|^2 \tag{5}$$

$|S_{K\ell}|^2$ represents the power at the ℓth array port due to the Kth beam port.

The insertion loss at 32.8 and 36.8 GHz for all K beam ports are shown in Figures 13 and 14, respectively. The losses range between 1 and 2 dB. Losses increase at the outer beam ports (higher scan angles) because these ports may not be pointing directly toward the center of the lens array contour giving slightly higher losses. This hypothesis, however, has not yet been confirmed.

125

Figure 13. Measured insertion loss for the MMW lens at 32.8 GHz
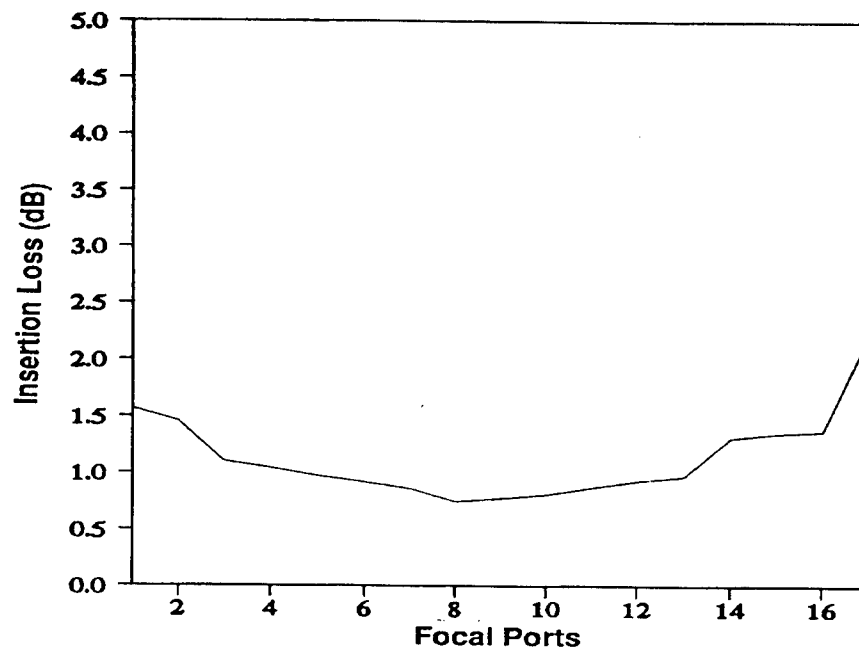
Figure 14. Measured insertion loss for the MMW lens at 36.8 GHz

126

6. Conclusions

A Rotman lens was developed that operates in the millimeter wave Ka-band region between 33 and 37 GHz. The design was supported by a model that can predict the sidelobe level and insertion loss of the millimeter wav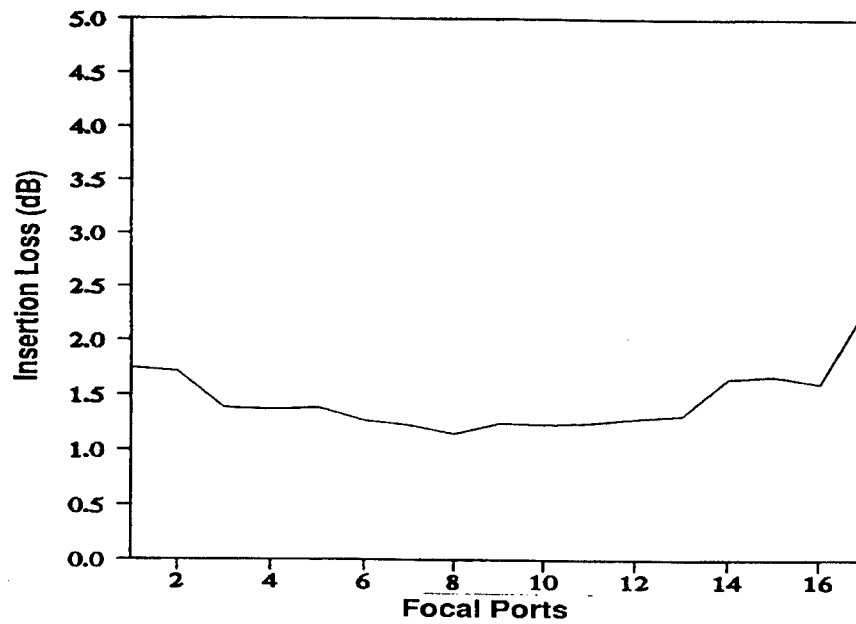e Rotman lens. The model utilizes mathematical expressions for the various electro-magnetic "modes" in rectangular waveguides. Contributions from each mode in each waveguide aperture are combined in an integral equation that incorporates all electromagnetic effects associated with interactions inside the lens cavity. The computed performance parameters were validated with measurements that provided -30 dB maximum sidelobe levels and ≤ 2 dB insertion loss.

A disadvantage of the present design is the E-plane folded hybrid power combiner that requires long fabrication times and the use of loads. Nevertheless, the present design offers excellent performance that could be utilized in an operational system.

7. References

[1]. W. Rotman and R.F. Turner, "Wide Angle Lens for Line Source Applications," IEEE Trans. Ant. Propagat., vol. AP-11, pp. 623-632, November 1963.

8. Acknowledgements

LOW-COST MICROWAVE AND MM-WAVE INTEGRATED PHASED ARRAYS WITH FERRITE CONTROL

Ernst F. Zaitsev
Yuri P. Yavon
George A. Yufit
Michael R. Beltran
Jacob S. Khodorkovsky

BELTRAN, INC.
1133 East 35 Street
Brooklyn, NY 11210

Abstract

An important problem of modern microwave technique is the realization of affordable planar and simply controlled electrically scanning antennas, especially for millimeter waves. In this paper we will discuss the development of a new class of antennas, an integrated phased array antenna (IPHAR). It consists of two anisotropic electrically controlled layers, and a plane of dielectric rods. For specific antenna applications, the new design possesses the capability of multibeam and adaptive pattern nulling operation and may be successfully applied in mobile radiocommunications.

Short microwaves and millimeterwaves are of great interest today because they are at a midpoint between microwaves and light waves and have the advantages of both. For example, long and short mm-waves (3, 8, mm) have propagation transparent windows just as do microwaves but they are not scattered in fog and dust, which compares with the infrared waves. At the same time, mm-waves have a very large information capacity and have small sizes of waveguiding units just like light waves.

But the solution of this problem on the basis of traditional phased arrays with discrete elements meets with serious difficulties due to small sizes of the controlled elements (phase shifters, radiators and power dividers), which are needed to satisfy the $\lambda/2$ distance between the radiating elements for broad angle scanning. The price of phased arrays is extremely high ($500-$1000 per element) and is not acceptable for a wide spectrum of applications.

Some alternative ways were proposed particularly antennas of traveling wave type with ferrite control.

The main component of this new antenna is a ferrite-dielectric waveguide, along which radiating discontinuities such as dipoles or slots are placed periodically. The scanning takes place due to phase velocity changes of the waveguide mode when ferrite elements become magnetized.

128

Different waveguide structures and antennas, based on this structure, have been investigated [1-13]:

- Circular and square ferrite waveguide with longitudinal magnetization and radiating dipoles, placed under/above the waveguide [1], [2], slots or other radiating discontinuities [3]-[5].
- Metal rectangular waveguide with ferrite-dielectric filling, transverse magnetization and radiating slot [6, 7].
- Open three-layer, ferrite-dielectric waveguide of one toroid or dual-toroid types with transverse magnetization and different positions or radiators on the waveguide surface [8-13].

The last variant is of the greatest interest. The important advantages of such antennas are planar integrated design, low cost, simple control with low control power and the ability to operate at millimeter-wave frequencies.

1. Antenna Design and Operation

The theoretical and experimental research described in this paper has been mainly devoted to the antenna shown in Figures 1 and 2. The antenna (Figure 1) consists of two ferrite layers, 1 and 2, and plane dielectric rods, 3, equidistantly placed between ferrite layers (ferrite-dielectric-ferrite – FDF– structure). The rods are made of material with a large value of dielectric constant, ε_3. Ferrite and dielectric antenna elements form a system of parallel, three-layer, open waveguides negligibly coupled with each other due to $\varepsilon_3 \gg 1$. The structure period is about 0.5λ, where λ is the free-space wavelength. Along each waveguide on the external surface of ferrite layer (1) the metal dipoles are disposed with the period $d \cong 0.5\lambda$. The external surface of the layer, 2, is covered by the metal screen, 5. The antenna is arranged on the dielectric plate, 6. Elements 1, 2, 3, and 6, are bonded together. Control wires, 7, are placed between dielectric rods, 3, and in the grooves of the external surface of the plate, 6. Control current magnetizes the ferrite layers, 1 and 2, in opposite directions axially. A continuous magnetic circuit is formed by layers, 1 and 2, and additional ferrite elements, 8, bonded to these layers.

Variations of the magnetization level of the ferrite layers, 1 and 2, change the phase velocity of the waveguide mode, leading to the scanning of the gain maximum in the H-plane.

The excitation of all waveguides may be realized by a flared E-field horn, but the best type of feed is the series power divider; for example, standard

waveguide, 9, with coupling holes, 10, as shown in Figure 1. The divider has a small cross section and, by proper choice of coupling coefficients, it is possible to realize any desirable aperture amplitude distribution in the transverse direction.

The E-plane scanning is provided by phase shifters, 12, 13, placed between the power divider and radiating aperture. Each phase shifter, which measures 15 to 20 mm in length, is a part of the three-layer waveguide structure, 1, 2, and 3, but individually controlled. For that purpose a pair of additional II-ferrite elements, 12 and 13, with control wire, 14, has been used to make the magnetic circuit continuous. The electric current in wires, 7, does not disturb phase shifters. Thus, E-plane scanning is accomplished as usual in phased arrays.

This design needs "N+1" control currents, where N is the number of rows of dipoles which form N line-source antennas. The design with two control currents is shown in Figure 2.

The antenna is excited by the set of rectangular waveguides, 7, which are coupled with an electrically controlled distribution unit through coupling slots or dipoles, 8. Distribution unit is similar to the line-source antenna, mentioned above, and has its own control wire, 9. For the purpose of phase, correction metal or dielectric slabs may be placed into the channel waveguides, 7.

The H-plane electrical scanning in antennas takes place because of changing phase velocity of the wave in FDF-waveguide due to the magnetization of ferrite elements, 1,3, with the current flowing in 6. The E-plane electrical scanning in the planar antenna is realized by magnetization of power divider unit, due to current flowing in wires, 9. Thus, 2D-scanning with the help of two control currents is possible.

1.1.   Beam Location, Scanning Sector. Let all radiating dipoles be disposed equidistantly along the FDF-waveguide with period d. Assume also that only the fundamental wave mode can propagate in waveguide, its phase propagation constant in the x-axis direction is β_+. All dipole fields will be synphase at the angle θ with respect to the yz-plane:

$$kd \sin \theta = \beta_+ d - n \cdot 2\pi \qquad (1)$$

where $k = \omega/c = 2\pi/\lambda$, n is an integer.

Let v_+ be a waveguide mode phase velocity, $q = \beta_+ /k = c/v_+$ — the relative wave moderation coefficient. We can derive the beam location equation, dividing (1) by kd:

$$\sin \theta = q_+ - n\lambda / d \qquad (2)$$

A ferrite elements magnetization in the FDF-waveguide leads to a q_+ variation from 3.5 to .2. The λ/q ratio is usually about 2. Hence $n=2$ in equation (2).

As follows from (2) a scanning sector width is defined by a wave moderation coefficient range variation:

$$\sin \theta_{max} - \sin \theta_{min} = q_{+max} - q_{+min} \qquad (3)$$

This is the reason for maximizing the controlled q variance by choosing the optimum configuration and sizes of the FDF-waveguide.

Formula (2) describes the case when the antenna operates as transmitting one, and a signal source is acting at the left port of the waveguide (Figure 1). When the same antenna operates as a receiving one, its beam location is given by

$$\sin \theta = q_- - n\lambda / d \qquad (4)$$

Since the FDF waveguide is nonreciprocal the forward and back traveling waves moderations q_+ and q_- differ from each other. Therefore the beam locations for receiving and transmitting operations are also different.

Nevertheless, there is no need for special receiving antenna research, because we may use the generalized reciprocity principle [14]. In accordance with this principal all characteristics of any receiving antenna are identical to the same antenna characteristics at the transmitting operation, if the medium dielectric and magnetic permeability tensors have been transposed, i.e.,

$$\varepsilon'_{ij} = \varepsilon_{ji}, \mu'_{ij} = \mu_{ji} , i,j = x,y,z \qquad (5)$$

This means for the antenna ferrite elements that the constant magnetization sign has been changed to opposite.

1.2. The Influence of Reflected Waves, and Parasitic Waveguide Mode Influence.

The reflected waves from radiating elements in conventional (reciprocal) traveling wave antennas are always summarizing in the same phase when the antenna beam is directed along the normal one. This produces a great reflection from the antenna input and a pattern diagram distortion, since the back wave forms its own radiation field in addition to the field excited by main wave. The result is an increasing of the grating lobes and main beam doubling.

In our case a synphase reflection summation occurs in the other condition due to nonreciprocity ($q_+ \neq q_-$), namely:

$$\beta_+ d + \beta_- d = m\ 2\pi \quad \text{or} \quad q_+ + q_- = m\ \lambda/d,$$

where m is an integer. Usually the q_+ and q_- values are in the same interval when ferrites are magnetized, and

$$q_+ + q_- \cong 2q_0 = \text{const},$$

where q_0 is a moderation coefficient, when ferrite magnetization is absent. Therefore, if the d/λ ratio is chosen in such a way that $2q_0\ d/\lambda \neq m$ (differs from an integer), then a synphase reflection summation is eliminated from the scanning sector. Such a d/λ choice means that the antenna beam must not be directed along the normal when ferrite is not magnetized. In this case the whole scanning sector is displaced just asymmetrically with respect to the normal.

Note that another d/λ ratio choice is possible, which (in accordance with (2)) provides the beam location almost at one side from the normal. In this case we replace the antenna input (output) to the opposite waveguide port, then the scanning sector will also be on the other side from the normal. Thus, we can make the total scanning sector two times greater by switching the antenna input between two waveguide ports.

When waveguide sizes are optimal for the maximum moderation value q range, 3 to higher order modes can be propagating additionally besides the fundamental waveguide mode. The waveguide input matching transformer must eliminate these parasitic modes' excitation. But in any case they will be exciting by the dipole currents. However, since dipole coupling with the waveguide is quite weak, the amplitude all the parasitic modes will be small with respect to the main

mode amplitude. Because the higher order modes have other moderation values their synphase summation usually does not take place both in forward and backward directions. Hence the total amplitude of any parasitic mode remains small in comparison with the fundamental one, which leads to negligible diagram distortion.

1.3. Angle-frequency dependence for beam location. We can obtain, after taking the derivative of (1) with respect to frequency,

$$\frac{1}{c}\sin\theta + \frac{\omega}{c}\cos\theta \cdot \frac{d\theta}{d\omega} = \frac{d\beta}{d\omega} = \frac{1}{v_g}$$

where v_g is the main waveguide mode group velocity ($\beta = .\beta_+$ or β_-).
Denoting $q_g = c/v_g$ as the group moderation coefficient we have

$$d\theta = \left(\frac{q_g}{\cos\theta} - tg\theta \right) \frac{d\omega}{\omega} \tag{6}$$

At $\theta = 0$:

$$d\theta|_{\theta=0} = q_g \frac{d\omega}{\omega}$$

The q_g value is somewhat greater than the phase velocity moderation and q_g is about 5 for a three-layer FDF waveguide. If $\Delta\omega/\omega = 1\%$, then the beam removal will be $\Delta\theta \cong 0.05$ rad $\cong 2.9$ deg.

The worst case corresponds to maximum scanning angle in the direction to the antenna input (output). If $\theta = -30$ deg. and $\Delta\omega/\omega = 1\%$, then we shall have $\Delta\theta \cong 0.063$ rad $\cong 3.6$ deg.

The angle-frequency dependence can limit frequency spectrum of a signal having too wide band width. If a signal itself has a narrow band width, then antenna can operate at 3-5% frequency range, but angle-frequency dependence must be taken into account in operating program of the beam control electron system.

Note that conventional phased antenna arrays with parallel phased channels also have the angle-frequency dependence, which is described by following expression

$$d\theta = -tg\theta \frac{d\omega}{\omega}$$

For $\Delta\omega/\omega$ = 1% this formula gives $|\Delta\theta|$ = 0.33 deg. at θ = 30 deg. It is essentially less with respect to IPHAR.

The situation is better when signals with frequency modulation are used. In these cases the signals can have the wide frequency width because angle-frequency correction can be used in IPHAR.

1.4.   Pattern Diagrams for Different Amplitude Distributions, Gain and Efficiency. In the antenna under consideration power is supplied to radiating elements through FDF waveguide segments of various lengths and some power dissipates in these waveguide segments. Hence is it clear that efficiency and other antenna characteristics essentially depend on amplitude distribution (AD). It is sufficient to carry out comparative studies of different AD's for the case when the beam is directed at a 90 degree angle to the antenna plane, i.e., field is synphase over aperture.

Let us use the model of continuously excited linear antenna, replacing a system of discrete radiators with a relative amplitude distribution $f(n)$, n = 1,...,M by a radiating source continuous along the x-axis with length $L=Md$. Such a source field distribution function $f(x)$, $0 \le x \le L$, is the skirting function for discrete distribution $f(n)$. It is known from the antenna arrays theory that a continuous model is applicable and gives good results, if the number of radiators is large (in practice $\ge$ 10), and the side diffraction maxima are absent in the pattern diagram. From a mathematical point of view it means that radiator field summarizing is approximately replaced by integration.

In single mode approximation the main mode power $P(x)$ is transmitted through the waveguide cross-section. Part of this power is radiated at segment dx:

$$dP_r = p(x)P(x)dx$$

134

and the same amount of power is absorbed

$$dQ = 2\alpha P(x)dx$$

where α – the main mode decrement, $p(x)$– the radiation coefficient per unit length. Hence we derive

$$\frac{dP}{dx} = -[p(x) + 2\alpha]P \qquad (7)$$

Its solution for boundary condition $P(0)=1$ and the given $p(x)$ is

$$P(x) = \exp[-2\alpha x - \int_0^x p(\xi)d\xi], \ 0 \le x \le L \qquad (8)$$

The amplitude distribution is described by means of function

$$f(x) = \sqrt{p(x)P(x)} \qquad (9)$$

The antenna pattern diagram (without taking radiator directivity into account) is equal to

$$\Phi(u) = \int_0^L f(x)e^{jkx\sin\theta}dx = \int_0^L f(x)e^{jux/L}dx \qquad (10)$$

where
$$u = \frac{2\pi L}{\lambda}\sin\theta$$

Let us consider some cases.

All dipoles are identical: $p(x) = 2\alpha_r = $ const. Then, denoting $\alpha_s = \alpha + \alpha_r$ – total decrement, we have

$$P(x) = e^{-2\alpha_s x}, \ f(x) = \sqrt{2\alpha_r}\, e^{-\alpha_s x} \qquad (11)$$

AD decreases exponentially. The relative AD decay at the antenna ending is equal to $\beta = e^{\alpha_s L}$.

The pattern diagram can be found by substituting (11) in (10):

$$\Phi(u) = L\frac{1 - be^{ju}}{-\ln b - ju} \qquad (12)$$

The normalized pattern diagrams are shown in Figure 3. The exponential AD decay leads to "blur" pattern diagram zeros, side lobes level (SLL) increases

and beam width enlargement. The pattern diagram for $b=1$ meets the uniform AD. If $b=1$ then SLL increases to -12 dB, the beam width changes slightly. If $b=0.2$, then the beam width increase is equal to 15% (at -the 3dB level), SLL=-11dB. If $b<0.1$ then the pattern diagram become one with a single lobe.

Thus, if b>0.2 then the exponential AD ranks only moderately below the uniform AD. Note that aperture efficiency remains rather high until b decreases to 0.1.

The length L must be chosen to find the width of the pattern diagram and we have only radiating losses $\alpha_n L$ to optimize antenna characteristics (the losses αL in FDF structure are given).

An important antenna parameter is the gain factor. Let us consider factor g which we shall call the relative gain factor because it is equal to the ratio of gain factor of a given array to the maximum gain factor of the same array when AD is uniform and losses are absent. The inverse ratio g^{-1} can be called gain loss. We have

$$g = \frac{2\alpha_r(1-b)^2}{(\alpha_r + \alpha)^2 L} \qquad (13)$$

The absolute gain factor is in direct proportion with L

$$G = \gamma g L / \lambda \qquad (14)$$

where the coefficient γ depends on array radiating element directivity in the transverse (relative to x-axis) plane. For example, the isotropic element has $\gamma = 2$.

Let us rewrite (13), denoting $a = \alpha L$ as the total waveguide's own attenuation (with no dipoles), $A=\alpha_s L$ – the total attenuation with dipoles:

$$g = 2\frac{A-a}{A^2}(1-e^{-A})^2 \qquad (13a)$$

We derive from condition $\partial g/\partial A = 0$ the optimal value A_{opt} as a function of a. The calculated function) $A_{opt}(a)$ is shown in Figure 4 and the graph of g_{max} vs a at optimal A is in Figure 5 (solid line marked by A). For convenience, a and A factors are given in dB.

136

It is seen, for example, that if $a=0$, then the optimal coupling with dipoles is such that $A_{opt} = -11$ dB ($b \approx 0.3$, only 8% power is lost in the ending load), total gain losses are about 0.9dB. If $a = 6$dB, then $A_{opt} = 19$dB, gain losses are at the rate of 3 dB; about half of this amount is due to power dissipation in the waveguide and load, and the other half to a decrease in aperture efficiency because of AD ending decay.

An analysis of expression (13a) shows that the α_r factor deviation from the optimal 30- 40% value (especially increasing) causes a small gain variation.

Case of uniform AD. Function $p(x)$ is to be such as to satisfy the equation

$$f^2(x) = p(x)P(x) = C = \text{const.}$$

The equation for $P(x)$ is

$$\frac{dP}{dx} + 2\alpha P = -C$$

Let us add to the boundary condition $P(0) = 1$ the condition $P(L)=0$, which means that power does not reach to the ending load. The solution is

$$p(x) = \frac{2\alpha}{e^{2\alpha(L-x)} - 1} \tag{15}$$

In this case g is given by

$$g = \frac{2\alpha}{e^{2\alpha} - 1} \tag{16}$$

The dependence g vs a is represented in Figure 5 (dashed line B). A comparison with curve A shows that if losses are small ($a<3$dB), then the uniform AD is beneficial, because there are no losses in the ending load and aperture efficiency is 1. But even with moderate losses ($a>7$dB) the exponential AD may be of advantage, because the initial waveguide segment absorbs too much and radiates too little if the AD is uniform.

Let us now consider now the following problem: α and L are given, and it is necessary to find the dipole coupling function $p(x)$ which provides maximum gain:

$$G = \frac{\gamma}{\lambda}\left(\int_o^L f(x)dx\right)^2 \tag{17}$$

137

where $f(x)$ is expressed by $P(x)$ and the desired function $p(x)$ through (9). Let us introduce an auxiliary function

$$\varphi(x) = \tfrac{1}{2}\int_0^x p(\xi)d\xi, \quad \varphi(0) = 0$$

Then

$$p(x) = 2\varphi'(x), \quad f(x) = \sqrt{2\varphi'(x)}\, e^{-\alpha x} e^{-\varphi(x)}$$

We now meet a classical problem of the calculus of variations: to find the function $\varphi(x)$ which furnishes the extreme of the functional

$$\int_0^L F(x,\varphi.\varphi')dx$$

where in our case, in accordance with (17)

$$F - e^{-\alpha x} e^{-\varphi} \sqrt{\varphi'} \tag{18}$$

The desired function satisfies the Euler equation

$$\frac{\partial F}{\partial \varphi} - \frac{d}{dx}\frac{\partial F}{\partial \varphi'} = 0$$

Substituting into it (18), we derive the differentiation equation of the second order

$$\frac{\varphi''}{2\varphi'} - \varphi' + \alpha = 0 \tag{19}$$

and the first boundary condition $\varphi(0) = 0$ (it leads automatically to $P(0) = 1$), the second boundary condition is $P(L) = 0$.

Finally, we can find as a result the desired optimal coupling function $p(x)$ and the power transmitted through the waveguide

$$P_{opt}(x) = \frac{2\alpha}{1 - e^{2\alpha(x-L)}}, \quad P(x) = e^{-2\alpha x}\frac{e^{2\alpha(x-L)} - 1}{e^{2\alpha x} - 1} \tag{20}$$

The maximum gain, when function $f(x)$ is optimal, is equal to

$$G_{max} = \frac{\gamma}{2\alpha\lambda}\ (1 - e^{-2\alpha L}) = \frac{\gamma L}{\lambda}g$$

where

$$g = \frac{1 - e^{-2a}}{2a}, \quad a = \alpha L \tag{21}$$

The curve (21) is shown in Figure 5 (dashed and dotted line C).

Comparing curves A, B, C in Figure 5, we see, that with $a<5$ dB, to accept the uniform AD, and $a>5$ dB – exponential with $p(x)$=const, then the loss in gain in comparison with case C is less than 0.5 dB.

Because the first case is the simplest and very convenient, it can always be recommended , including the case when $a>5$dB (optimal A factor should be chosen with the help of Figure 28), if there is no elevated requirements to the pattern diagram. The gain loss in comparison with maximum available will be less than 0.9 dB.

If a very low side lobe level is needed, then decreasing both sides of the antenna amplitude distribution may be used. To achieve this it is enough to short down the dipoles nearest to input. Calculations show that by this means SLL can be diminished to - 16–17 dB, but losses will increase up to 1.5–2 dB.

Another way to diminish SLL is to form a four-times-larger phased array possessing amplitude distribution symmetrically falling from the center and having a gap with one wavelength between the modules. This case corresponds to -23 dB SLL.

2. Analysis of Three-Layer FDF Waveguiding System

The electrodynamic analysis of the antenna is necessary for a proper understanding of wave phenomena in the system and to find its main properties in order to:

- choose the optimum configuration and sizes of the waveguide structure cross section which provides the maximum phase efficiency, minimum losses and parasitic interactions and optimum coupling with dipoles;
- evaluate the additional losses and pattern distortions due to parasitic mode excitation;
- define the influence of the waveguide structure on dipole radiation characteristics and evaluate the patterns and antenna gain changes when the ferrite layers are magnetized;

- estimate fabrication tolerances of the antenna elements.

The basis for the solution of the last three problems was developed in [15]. If the propagating modes in a nonreciprocal FDF structure are known, the method [15] makes it possible to calculate the currents in the dipoles (simplified equivalent of these currents is the function f(x) in the previous section) and, hence, the pattern diagram for different magnetizations.

In this section we will consider some questions related to the first problem: how to calculate the modes in a waveguiding FDF structure, estimate controllable phase shift and find the main mode which excites the radiating elements with the most effectiveness.

2.1. Electrodynamic Properties of Ferrite as Electrically Controlled Microwave Medium.

A weak static magnetic field H_0 is commonly used in electrically controlled phase shifting ferrite designs: this field is much less than its resonance value at a given frequency, but it is great enough to achieve "technical" saturation M_{max} of ferrite material. This regime is advantageous because of low power losses in ferrite (the resonance frequency is far away for operating frequency) and low control.

This operating regime's relative magnetic permeability tensor with field H_0 directed along the Y-axis can be written as

$$\hat{\mu} = \begin{bmatrix} \mu & 0 & -j\kappa \\ 0 & \mu & 0 \\ j\kappa & 0 & \mu \end{bmatrix} \tag{22}$$

where μ is the demagnetized ferrite's magnetic permeability, and κ is proportional to the average static magnetization M_0 (taking into account its sign). We can write, neglecting losses:

$$\kappa = \frac{\omega_M}{\omega}$$

where ω – operating frequency, $\omega_M = \gamma M_0$, γ – gyromagnetic ratio.,

In reality tensor $\hat{\mu}$ diagonal elements differ slightly from each other and from the μ of demagnetized ferrite. But these differences are small and can be neglected with no influence on the accuracy of the analysis. Usually $0.85 < \mu <$

0.95 and varies slightly when ferrite is magnetizing. The μ value can be determined accurately by experimental measurement.

The μ and κ values in (22) are complex because of power losses. There are no appropriate analytical formulas for imaginary parts of μ and κ in case of a weak magnetized field H_0, when the domain structure is not destroyed. Hence they have to be measured.

Usually at first the theoretical analysis of a lossless waveguide is developed and then the waveguide propagation constant is corrected, taking losses into account.

When choosing a ferrite material it is necessary to keep in mind that losses increase at low frequencies due to so called "natural" ferromagnetic resonance.

These frequencies are close to the γM_s value, where M_s is the saturation magnetization. Hence the M_s value of the material should satisfy the inequality $2\gamma M_s < \omega$ at the given operating frequency ω. Magnetization corresponding to "technical" saturation M_{max} (in case of a weak H_0 field) is slightly less than M_s. Because the range of M_0 is limited: $-M_{max} \leq M_0 \leq M_{max}$, the operating range of κ is also limited: $-0.4 \leq \kappa \leq 0.4$.

2.2. Multimode Analysis of FDF Waveguide (Phase Velocities and Losses of Operating and Parasitic Modes). A deep understanding of the electromagnetic process in an FDF-waveguide is required for the optimization of the electrical parameters of IPHAR. The study of this process constitutes a so called "internal problem", the solution of which, using a combination of an analytical method of lines, Galerkin's numerical method and "coupled waves" method, resulted in the determination of the optimal cross-section sizes of the 1D- and 2D- structures.

The models of waveguiding FDF-structure for integrated scanning antennas [34] are shown in Figure 6 (a,b,c). The FDF-waveguide is a planar 3-layer (ferrite-dielectric-ferrite) structure having a metal shield at its side and current carrying metal strips (wires) for control of magnetization rate which are disposed between ferrite layers. The FDF-waveguide is excited by an electric field parallel to the layers.

The existence of a dielectric pivot with high dielectric permeability in the middle of the FDF-structure provides the essential phase velocity decrease of operating in a quasi-LE_{11} mode and effective control of waveguide characteristics by ferrite magnetization. The magnetization of the ferrite layers leads also to a variation of the field configuration of other modes of electromagnetic wave propagating in the FDF-waveguide. Difficulty in the modes analysis of the FDF-structure is caused by the nonhomogeneity of its cross-section along two dimensions and by the gyrotropy of some areas of the structure.

We consider below only FDF structure (C) in Figure 6, which is the simplest model of waveguiding structure for scanning traveling wave antenna with ferrite control. An electrodynamic analysis of the model (modes system, their field structure, definition of propagation constants of waveguide modes, their dependence vs geometrical dimensions, electrical and magnetic parameters of the structure, magnetization of its ferrite elements) allows us to determine all the main laws of wave processes that affect the IPHAR operation. Note that relative dielectric permeability is 13–15 for ferrite and 40 for the central dielectric layer.

The mode analysis of this model was made by mean of the equivalent lines method. It allows one to obtain complete information about all propagating and nonpropagating eigenwaves. At the same time it is necessary to remember that this model of real multimode structure is more valid to describe only low order propagating modes, one of which is the operating one, the others parasitic. All these modes can be excited at the FDF structure input, or by means of their field interaction with waveguide radiating nonhomogeneities. Taking into account the symmetry of FDF structure excitation and symmetry of radiating elements' disposition, it is enough to study only "even" propagating modes, which fields have an even dependence of the structure of the E_y, H_x, H_z components with respect to the y coordinate.

Figures 7 and 8 show the curves of moderation factor m of "even" modes vs the D dimension for two FDF-structures having electrical and magnetic shields in the cross-sections $y = + D/2$ and $y = -D/2$. The thicknesses of the ferrite and dielectric layers (along x)are close to optimal from the viewpoint of good control for the mode whose field does not depend on y. The wave length for calculating

was accepted as equal to 8 mm, the thicknesses of the ferrite and dielectric slabs were 0.7 and 0.3 mm, respectively. Magnetizations of ferrite slabs with shield and with dipoles are equal to $+s$ and $-3s/4$, respectively.

The solid lines curves coincide with the hybrid H_{pqe} and H_{pqm} modes, created by the LE and H-modes, when s = 0. Other curves (dashed lines) coincide with hybrid E_{pqm} and E_{pqe} modes, created by LM and E-waves when s = 0. The last index (m, e) characterizes the shield type at $y = +D/2$ and $y = -D/2$, the middle one – the half wave number over the y coordinate. The first index means the number of the mode in the order of moderation factor reduction and coincides with a special configuration of field component H_z (E_z) vs z.

Note that: 1) there is an essential difference in the behavior of the E- and H-modes when ferrite is magnetized; 2) both FDF- structures are multimode with a strong dielectric effect of the main H-mode, for example, when D = 3.5mm; 3) moderation factors of lower H and E-modes in structures with a magnetic shield are closely allied near one of the saturation states ($+s>0$).

Analysis shows that the effect of the distributed coupling of modes (in particular, because of low E- and H mode degradation by the moderation factor) in an FDF-structure can essentially affect IPHAR operation capability. In practice the appearance of these effects depends on the FDF-structure parameters. Specifically, such degradation of the low E- and H-modes in a model structure with the above-mentioned thicknesses of ferrite and dielectric layers takes place when $+s$ is about 0.3, which means a deep saturation state.

Curves of power flux distribution over the FDF-structure cross-section for some modes are represented in Figures 9 and 10. Note that field components and power distributions are essentially affected by ferrite layers magnetization. In spite of this, E_y of operating mode H_{11m} is always maximal in the middle of the FDF-structure, that is, beneficial for effective mode excitation in the structure input for any s value.

It is evident that the possibility of appropriate phase velocity (moderation factor) control for operating mode H_{11m} by means of an s variation is very important. The level of "control ability" significantly depends on the relationship of the ferrite and dielectric layer thicknesses. Also, the important characteristics of

every waveguide mode in the IPHAR structure are electric field orientation in the place of disposition of radiating elements (dipoles), and this field's constancy during the control process. The analysis shows that field characteristics of the operating mode depend on the thicknesses of the ferrite and dielectric slabs. Therefore, to choose FDF- structure operating parameters for IPHAR means to seek compromises between the various requirements.

Note that the operating mode power flux divides almost equally between the three layers of the structure; and causes an approximately equal "responsibility" for the dielectric and magnetic losses in the material of each layer for the total absorption of the main mode. The contributions of the layers to the losses change very little when the ferrite is magnetized. At the same time, absorption losses vary essentially because of degradation of the main and parasitic modes. These losses can be called "excessive" losses of mode transformation.

The absorption losses evaluation of various modes in the FDF structure was made by means of known "disturbance" formulas. As an example, the relationship between standard losses (losses per length unit) for two typical structures at a 35 GHz frequency band are shown in Figure 11a,b. Total losses, which are the sum of losses in metallization (Σ), dielectric losses (d) and magnetic losses (m) in ferrite are less than $\alpha[dB/\lambda]=0.5$. At the same time an evaluation of "excessive" losses (by the "coupled waves" method) gives $\alpha[dB/\lambda]>1$.

The main conclusions related to this section are: maximum wave propagation of main waveguide mode is provided by the optimal width of the dielectric; phase efficiency increases when the width of ferrite layers becomes twice the width of the rod; further increase of ferrite width does not affect phase efficiency. However, the field value on the external surface of the ferrite strongly depends on the ferrite width; thus, by changing the ferrite width one can get desirable coupling between waveguide and dipole. The presence of the metal layer on the opposite external surface of the ferrite element has a negligible effect on the main mode propagation constant and does not increase the attenuation of the main waveguide mode.

In the three layer ferrite-dielectric-ferrite structure with optimal cross section, about one-third part of the electromagnetic wave power is concentrated in

each layer. The external medium transfers only one-tenth of the power. Full remagnetization of the ferrite elements according to the hysteresis loop corresponds to q variations from 3.3 to 4.2, which is in good agreement with experimental data. The calculated attenuation coefficient also agrees closely with the experimental one and equals about 0.4 dB/λ for λ equal to 8 mm.

In the optimal sized waveguide three or four higher order modes can propagate in addition to the fundamental mode. The wave propagations of these modes are less than that of the fundamental mode and the electric field has no rapid decrease in the transverse direction.

Methods which take into account the distributed coupling between the nearest waveguides have also been developed. The main wave coupling is rather weak and may be ignored. The high order mode coupling is rather strong because the field concentration near the dielectric rod is less than for the fundamental mode, but the amplitudes of these higher modes are very small and may be ignored.

3.   Experimental Results

The experimental results are considered below for two IPHAR designs: line source antenna (LSA) and planar antenna with N+1 currents.

The design of the 8-mm LSA consists of the FDF-waveguide with a shield and a dipole array spread over the ferrite slabs that are glued to the dielectric slab, the width of which is less than that of the ferrite slab. The upper slab has the dipole array on its outer surface. The lower slab is metallized at its lower surface and has two lugs at its upper surface edges. The height of these lugs is equal to the thickness of the dielectric slab; the lugs are used as magnetic shorts. The controlling wires are placed between the lug and the dielectric slab. Both FDF-waveguide ports have two matching transformers.

The FDF-waveguide is fabricated of a dielectric slab (0.30x3.40x90 mm) and of ferrite slabs (0.70x9.00x90.0 mm). The number of dipoles is 21. They are placed over a range of 84 mm at 4.2 mm periods. The dipole size is 2x0.5 mm .

The magnetic circuit cross-section is 0.7x90=63 mm . The controlling winding has 16 turns of wire (8 at each dielectric slab side) 0.25 mm in diameter.

The measured VSWR is less than 1.3 in the 33.0 - 36.0 GHz band, less than 2.0 in the 30 - 38 GHz band. The matching does not change, practically, while scanning.

The FDF-waveguide overall attenuation is about 4.5 dB (when the dipoles are absent). There are the additional "radiation" losses when the dipoles are placed on the FDF-waveguide, these losses are extreme in the 34 - 35.5 GHz frequency band (the overall attenuation is 7 dB at 35 GHz).

The pattern diagrams were measured at 35 GHz. If the controlling current varies from -0.5 to +0.5 A, then the antenna beam moves from -30 to +10 deg. (0 deg. direction is the perpendicular to the antenna plane). The gain change while scanning is 1.5 dB, its maximum value is 14 dB (in the middle of the scanning sector).

The measured pattern diagrams in the H-plane and in the E-plane are shown in Figure 12. The side lobe level is less than -10 dB.

The design of the planar antenna contains 22 x 25 = 550 radiating elements and has the parameters given in Table I. In the three-layer ferrite-dielectric-ferrite waveguide, losses are 0.3-0.4 dB/cm, but the efficiency of the antenna is about 3 dB and is comparable with traditional cm-wave phased arrays made of discrete elements with ferrite phase shifters. The radiation pattern of this antenna for different beam locations is shown in Figure 13.

Integrated phased arrays with ferrite control present a new class of antennas with specific features. They have:
- planar low-profile design (antenna is less than a wavelength in a free space);
- control (antenna has the ability to be driven only by only two currents during 2D scanning);
- low-cost in series and mass production.

IPHAR may be designed and fabricated in microwave and millimeterwave frequency ranges (X,Ku,K,Ka,V,W-bands). Due to its integrated design, the assumed cost of the antenna in mass fabrication is many times less than the cost of traditional phased array with discrete element design, which cost $500-$1,000 USD per element, and ten times less as compared to phased arrays with module design, which cost $200-$300 USD per element.

TABLE I	
DESIGN PARAMETERS OF AN 8-MM 550 DIPOLE ANTENNA	
Wavelength range	8 mm
Number of radiating elements	550
Gain	25 dB
Beamwidth	4*5 deg.
Sidelobes	-13 dB (H-plane, -20 dB (E-plane) It is possible to decrease beamwidth to 1-2 deg. and SL to -20 dB
Scanning sector	20*40 deg.
Loss	3-4 dB
VSWR input	less than 1.5
Radiating power	pulse 10 kW, mean 20 W
Energy of one beam switching	4-5 mJ
Beam switching time	4 microsec.
Control circuit consuming power at fixed beam position	8-12 W

The arrays with a planar multilayer design can be fabricated using high tech MMIC-PCB technology. This is another reason for its low cost in mass production and is the reason why IPHAR has a good future of broad civil and military applications.

4. References

[1] E.F. Zaitsev and A.N. Fedotov, *Traveling Wave Antenna*, Russian patent 1072154, July 16, 1982.

[2] E.F. Zaitsev and A.N. Fedotov, "Traveling Wave Scanning Array with Ferrite Control," *Radiotechnica I Electronica*, vol. 33, pp. 661-666, March 3, 1988.

[3] E.F. Zaitsev, Yu. P. Yavon, Yu. A. Komarov and A.N. Fedotov, *Traveling Wave Antenna*, S.U. Patent 1596416, June 6, 1987.

[4] J. Ajoka and J. Strahan, *Perforated Waveguide Element of Phase with Ferrite Filling*, Int. Patent N. 85/0272-1.

[5] S.H. Wong et al., "Series Ferrite Scan (SFS) – a Low Cost Phased Array Technique," *AP-S Int. Symp.*, pp. 68-71, 1977.

[6] R.A. Stern, et al., *Scanning Phased Array*, U.S. Patent 4785304, November 20, 1986.

[7] E.F. Zaitsev and Yu. P. Yavon, "Parameters of Radiating Slot in Nonreciprocal Waveguide," *Radiotechnica I Electronica*, vol. 28, pp. 669-675, April 4, 1983.

[8] E.F. Zaitsev et al., "MM-wave Electrically Scanning Array Based on Gyrotropic Structure with Ferrite Control, *Proc. XXIII General Assembly of the International Union of Radio Science (URSI)*, Prague, Czechoslovakia, pp. 400, August 1990.

[9] E.F. Zaitsev et al., "MM-wave Electrically Scanning Antenna on Planar Gyrotropic Structure with Ferrite Control," *Proc. 20th European Microwave Conf.*, Budapest, Hungary, pp. 1501-1504, September 1990.

[10] E.F. Zaitsev, Yu. P. Yavon, Yu. A. Komarov, "MM-wave Integrated Phased Arrays with Ferrite Control," *Symposium Digest of International Microwave Symposium 1991 IEEE MTT-S*, Boston, Massachusetts, USA, 1991.

[11] E.F. Zaitsev et al., *Electrically Scanning Antenna*, Russian Patent 1596413, February 2, 1987.

[12] E.F. Zaitsev et al., *Scanning Antenna with Ferrite Control*, SU Patent 1370690, December 12, 1985.

[13] E.F. Zaitsev and Yu P. Yavon, "Some CIS Trends in Array Antenna Research," *Workshop on Active Antennas*, ESTEC-Noordwijk, The Netherlands, pp. 11-12, June 1992.

[14] E.F. Zaitsev, V.N. Diky and I. Babenko, "Calculation of Nonreciprocal Receiving Antenna Characteristics," *Radiotechnica I Electronica*, vol. 25, pp. 639-640, March 3, 1980.

[15] E.F. Zaitsev et al., "MM-wave Integrated Phased Arrays with Ferrite Control," *IEEE Transactions on Antennas and Propagation*, vol. 42, No. 3, pp. 304-310, March 1993.

148
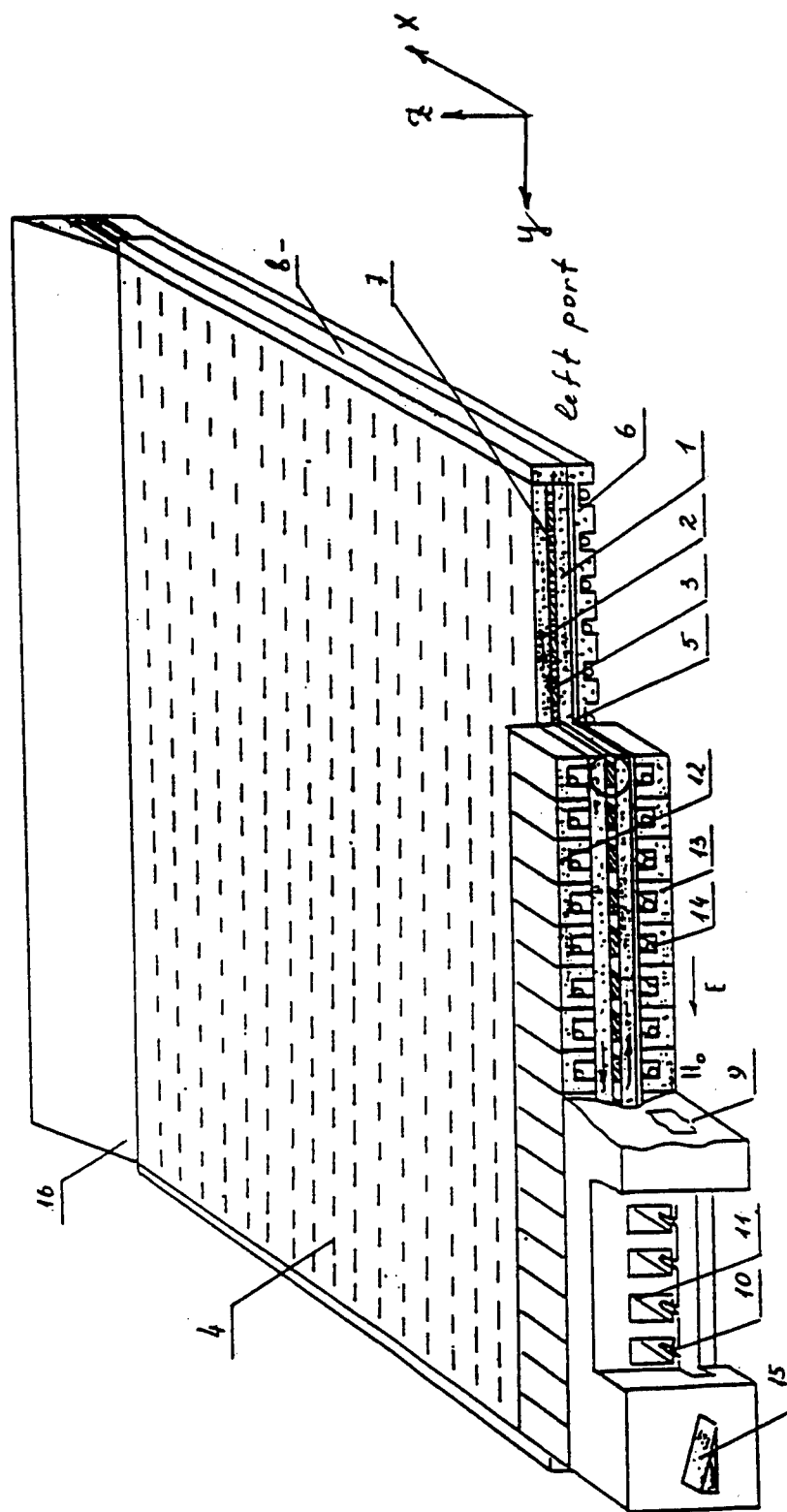
Figure 1. Plane traveling wave phased array.
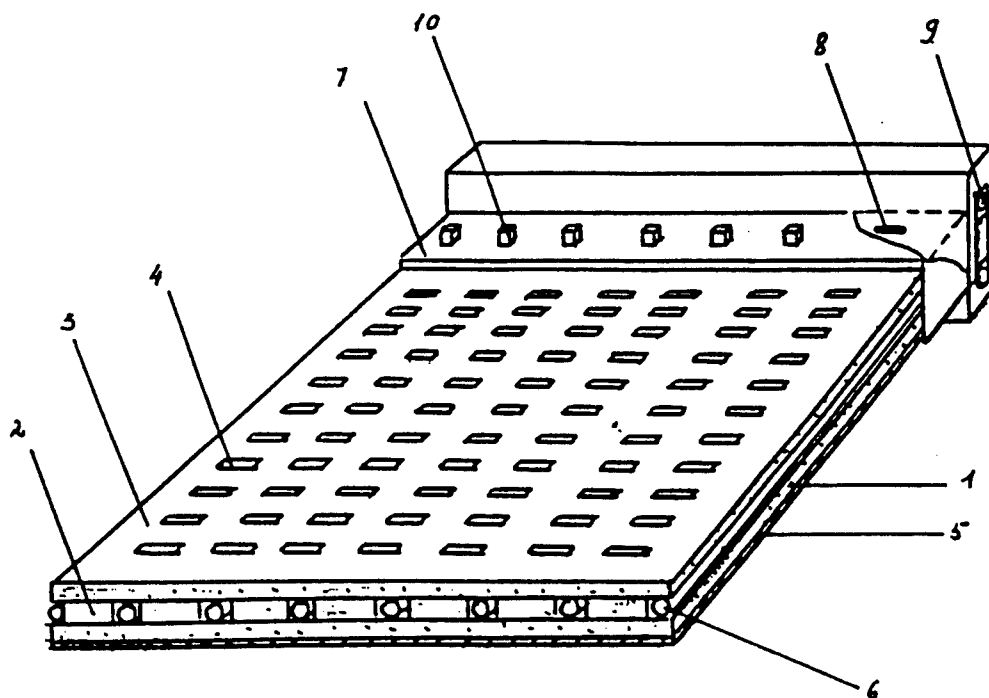
Figure 2. Planar phased array (2D-scanning by 2C).
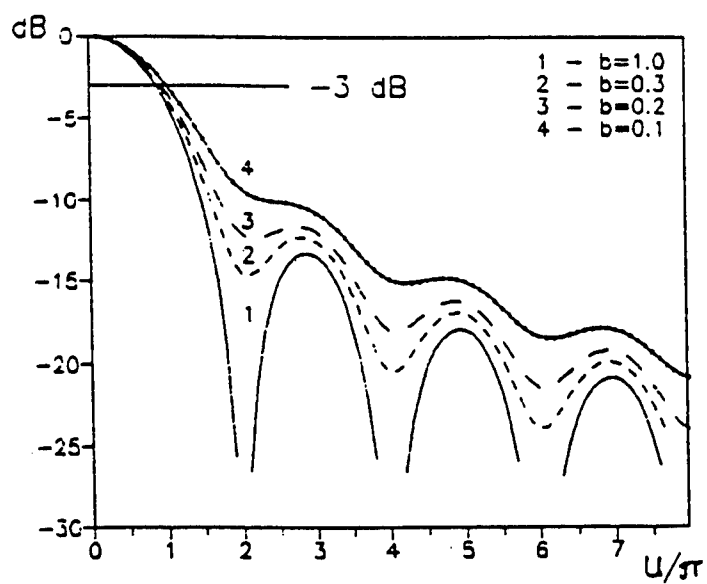
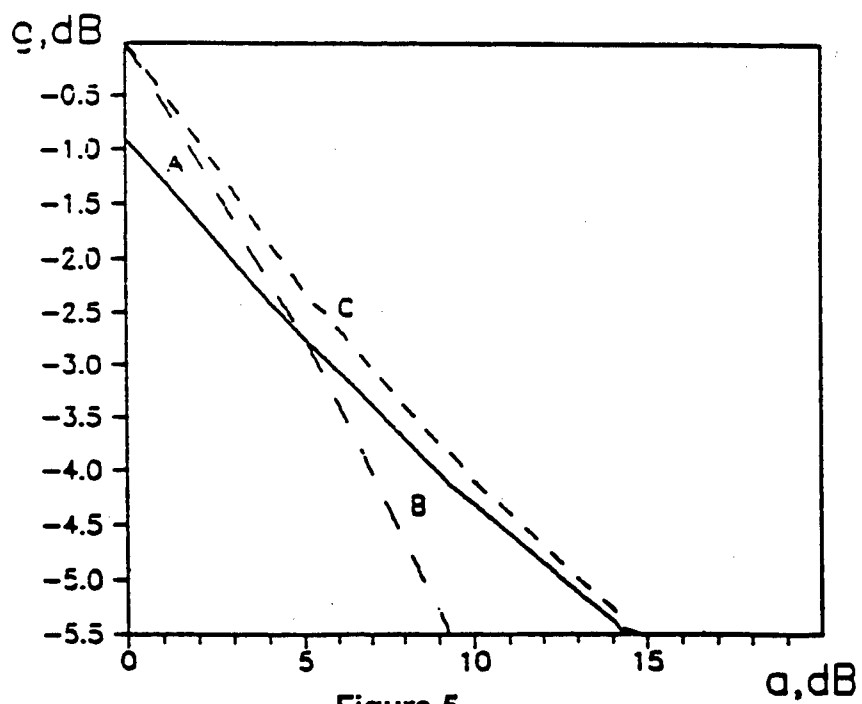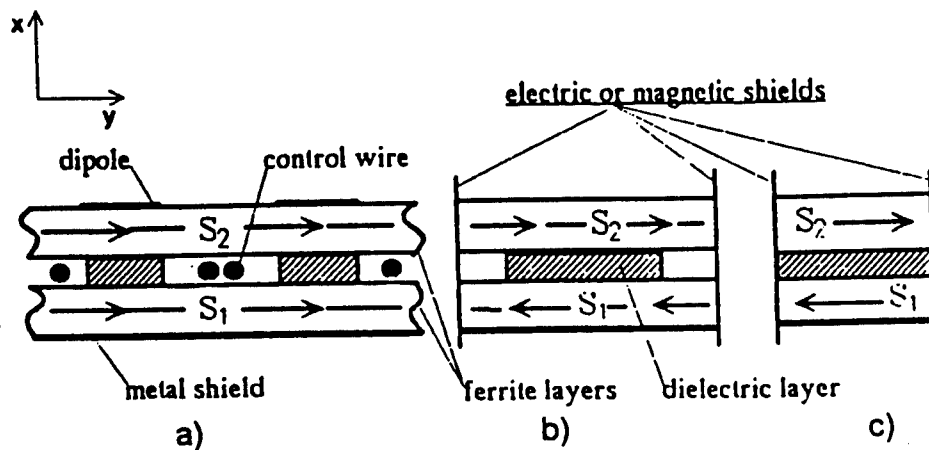

Figure 3.
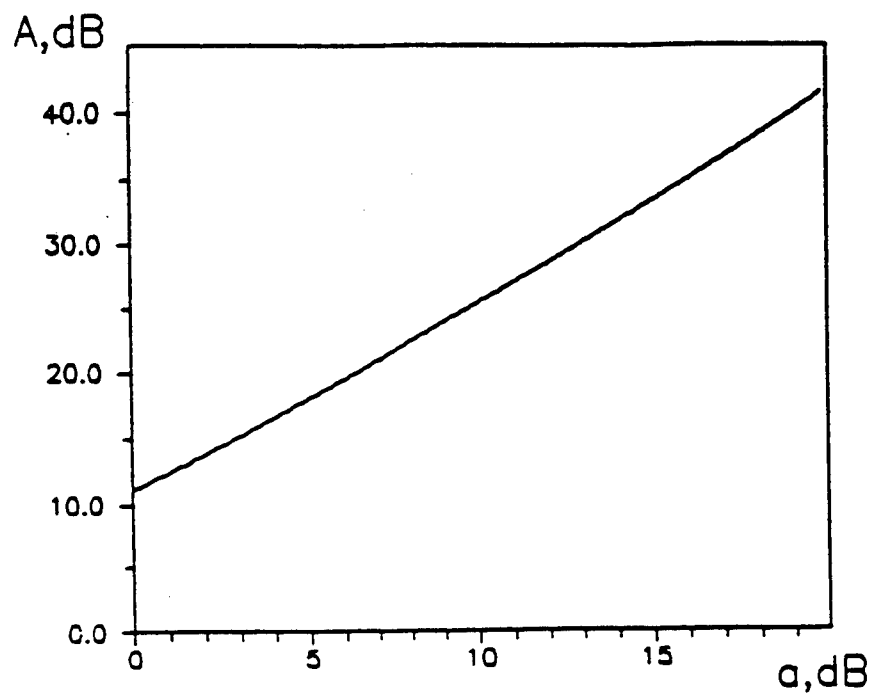
Figure 4.

Figure 5.
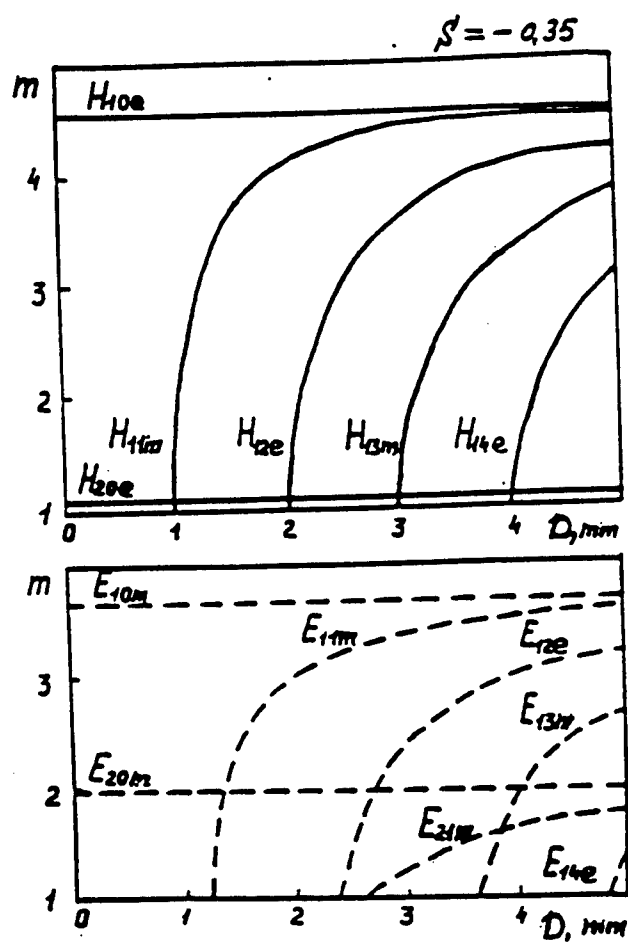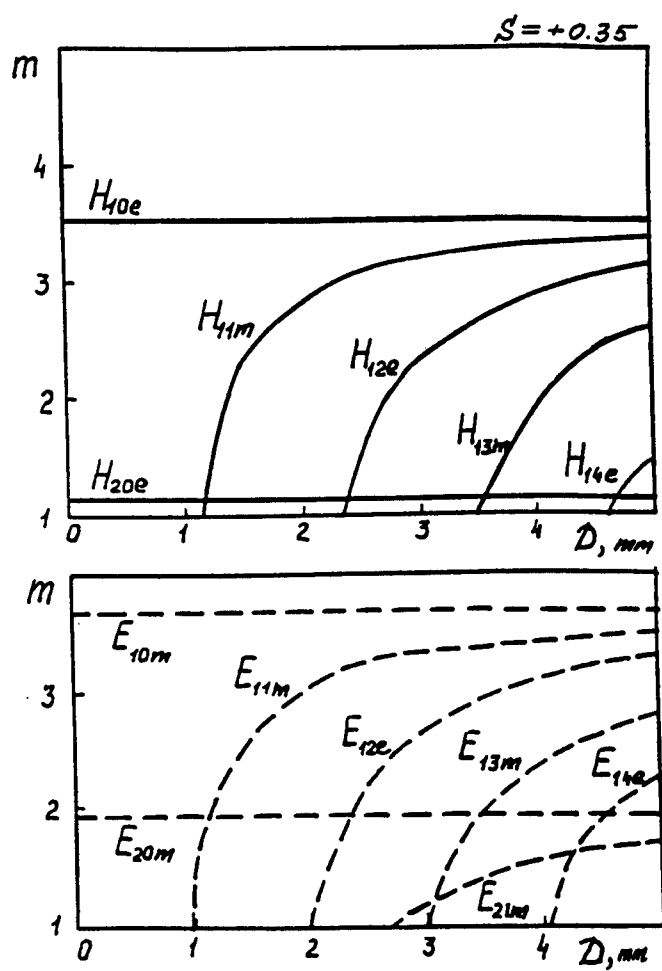
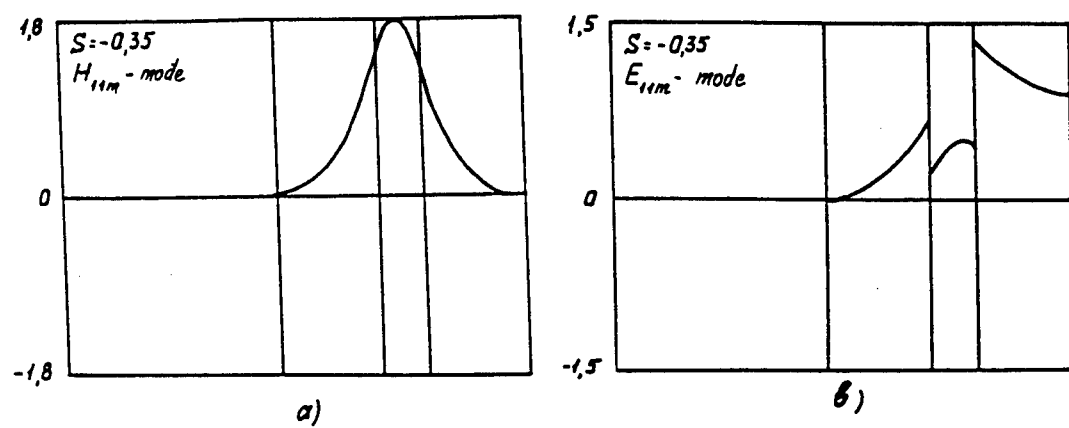Figure 6. Cross section of FDF structures.
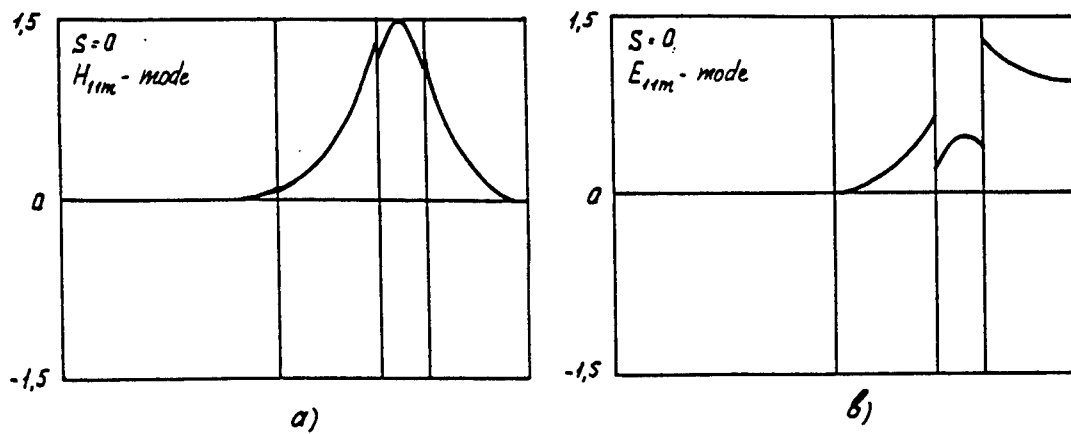

Figure 7.

Figure 8.
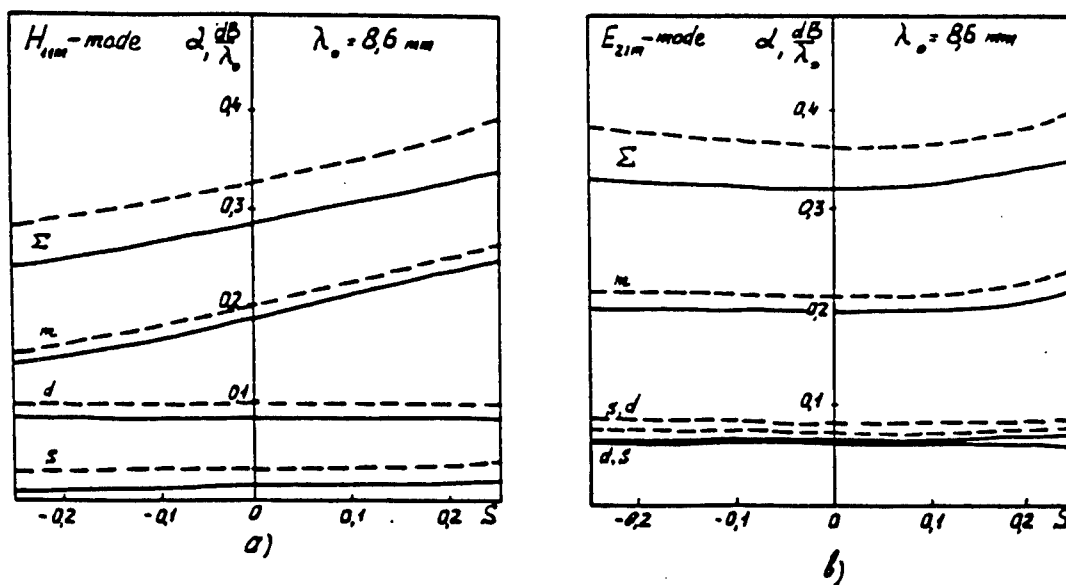

a)

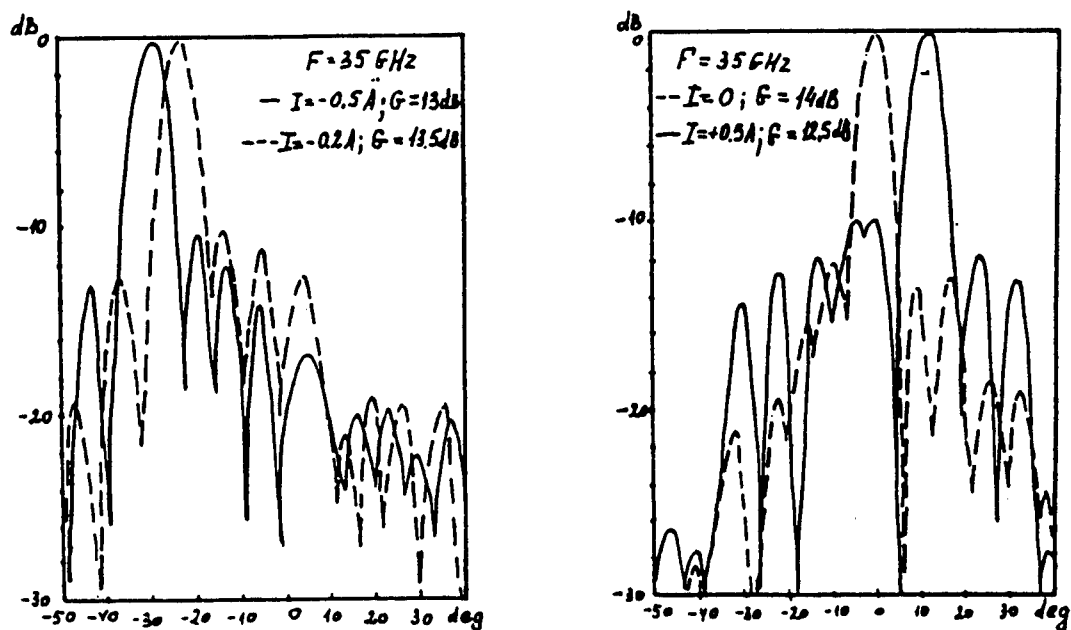б)

Figure 9.
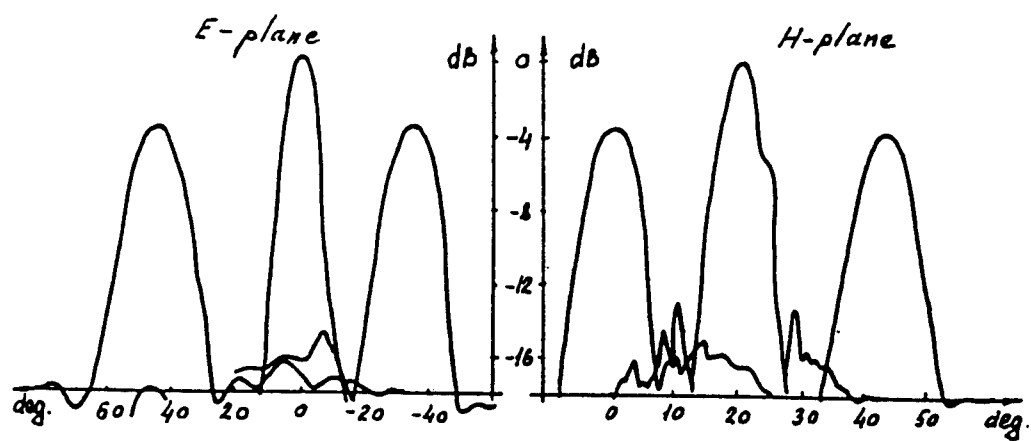
Figure 10.

Figure 11.

154

Figure 12.

Figure 13.

INTEGRATION OF TAPERED SLOT ANTENNAS ON MMIC SUBSTRATES THROUGH DIELECTRIC MICROMACHINING

Thomas J. Ellis and Gabriel M. Rebeiz
Radiation Laboratory
University of Michigan
Ann Arbor, MI 48109

Abstract - A new type of dielectric substrate has been developed that can significantly improve the performance of tapered slot antennas and for the first time allow them to be integrated successfully onto the thick, high dielectric constant substrates used for commercial MMIC designs. The new substrate consists of a standard dielectric material that has been micromachined with a uniform, periodic series of holes. The effect of the micromachining is to artificially lower the dielectric constant of the substrate and to suppress the excitation and propagation of surface waves within the material. These two effects result in a 167% improvement in directivity and a 70% improvement in efficiency of a $4\lambda_0$ long TSA on a $0.14\lambda_d$ thick, $\varepsilon_r = 10.5$ dielectric substrate at 10 GHz. The micromachining can be achieved using standard via-hole processes resulting in low production costs. This technology can be scaled geometrically allowing for low frequency prototyping to be done inexpensively and later scaled up for high frequency applications such as imaging, radar, and power combining systems.

1. Introduction

The tapered slot antenna (TSA) was first introduced by Gibson *et al.* [1] in 1979. It consisted of a length of slotline printed on a dielectric substrate which flared outward along its length resulting in end-fire radiation (Figure 1). The TSA has many desirable properties which make it a popular choice for the design engineer. When properly designed it can have high directivity (10 - 20 dB) and efficiency (80% - 90%), with the E-plane and H-plane patterns being nearly symmetric in spite of the antenna being much thinner than it is wide. The fact that

it is a planar antenna makes it simple and inexpensive to fabricate and integrate monolithically with receivers and other systems, as well as form into 1 and 2 dimensional arrays. The limiting factor for using the TSA is the relative thickness of the dielectric substrate which they are fabricated on. An "effective" thickness has been previously defined to be

$$t_{\text{eff}} = t(\sqrt{\varepsilon_r} - 1)$$

which takes into account both the physical thickness and the relative dielectric constant of the substrate. Yngvesson *et al.*[2] have experimentally determined the range of normalized effective thickness for proper operation to be approximately

$$0.005 \leq \frac{t_{\text{eff}}}{\lambda_0} \leq 0.03$$

depending on the overall length of the antenna (the range given is for a TSA from about $4\lambda_0$ to $6\lambda_0$). If the antenna is made on a material that is thinner the main beam broadens and directivity is lost. Conversely, if the antenna is made on a thicker substrate surface waves develop which cause two different problems with the antennas performance. First, there is a reduction in efficiency associated with energy being coupling away from the desired radiated signal and into substrate modes. Second, when the surface waves that are excited reach the edges of the substrate they radiate. This undesired radiation can significantly interfere with the antenna, especially on boresight, and cause deep nulls in the resulting patterns. The

157

combination of the lower efficiency and poor patterns make the TSA an unacceptable option on the thick, high dielectric substrates that are used for monolithic circuits.

2. Micromachined Dielectrics

The dielectric substrate developed was bulk micromachined with a periodic series of via holes throughout the entire substrate (Figure 2). The process had two effects on the original dielectric material. The first is a lowering of the "effective" dielectric constant associated with the removal of material in the form of via holes. Several different geometrical placements were explored with their arrangements being shown in Figure 3. By defining a unit cell for each different arrangement simple volume calculations can be done to predict the dielectric constant of the micromachined structure. The "artificial" dielectric constant that results can be calculated using simple dielectric mixing models. A simple volumetric model was used and shown in Figure 4. Several experiments involving transmission lines and resonators were performed to verify the predicted values with the measured values being within 10 % of the predicted values for all cases. It is also interesting to note that a large range of dielectric constants can be synthesized through the control of hole diameter and spacing. This concept of synthesizing an "artificial" dielectric constant has many applications both in and outside of planar antenna design.

The second effect that the micromachining has on the dielectric is to disrupt the formation and propagation of substrate modes (surface waves). When the TSA is fabricated on an electrically thick substrate, the slotline fields excite substrates modes that propagate within the dielectric. These unwanted fields are disruptive to the TSA operation as explained previously. To gain a better, although admittedly simplified understanding of the process of the surface wave disruption, a variation of the classic "grounded dielectric slab" problem was analyzed. If you approximate the micromachined substrate as a two dimensional grounded dielectric slab with a series of grooves etched into it (see Figure 5) the approximation is reasonably good if the holes are arranged so the surface wave effectively "sees" the same hole-gap structure in whatever direction it propagates. When the problem is solved the original boundary conditions remain with the addition of the continuity requirements in the propagation direction. The added boundary conditions are satisfied when

$$\underbrace{k_{z1}w}_{air\_gap} \geq \underbrace{k_0w}_{free\_space} \sqrt{\varepsilon_r - 1}$$

with $k_{z1}w$ being the phase shift across the air gaps and k_0w being the phase shift across an equal physical distance in free space. For the surface wave to propagate the holes must be small enough to get an "average" propagation constant throughout the material dominated by the remaining dielectric material. While this

159

averaging is occurring the surface waves are "pulled" across the gaps by the fields in the remaining dielectric material. At some point the holes become too large for this to occur and, since a surface wave cannot propagate unguided through free space, propagation is stopped.

To support the above analysis, a simple experiment involving FEM analysis was constructed. Two dielectrically loaded waveguide were designed and analyzed from 1 to 12 GHz (see figure 6). The first was a reference X-band guide ($0.5\lambda_o$ long at 10 GHz) loaded with a uniform dielectric material with $\varepsilon_r = 10.5$. This was used to represent the surface waves in standard dielectric material. A waveguide structure was chosen because the TE_{10} mode is representative of the surface waves and numerically simple to solve. A second waveguide was constructed the same physical dimensions but with holes placed in the same orientation to the waveguide mode E-field as the surface wave would experience on the micromachined substrate. The resulting insertion loss for both simulations are displayed. The effect of the lower artificial dielectric constant can be seen in the shift of the lower frequency cutoff in the micromachined response. Also note that until a certain high frequency is reached both waveguides allow propagation with very low loss. The micromachined guide, however, shows the disruption the holes have on propagation above a certain "cutoff" frequency in agreement with the previous analytical example.

3. Experimental Results

Several different TSAs were constructed, each having the same physical dimensions (see Figure 7) but with different hole orientations. The dielectric material used for all of the antennas was Duroid with a thickness of 50 mils (1270 μm) and a dielectric constant $\varepsilon_r = 10.5$. All of the antenna patterns were measured at the center design frequency of 10 GHz. The input impedance for the TSA is well behaved and approximately equal to the slotline feed impedance. Initial results agreed well with predicted impedance values so rigorous measurements were not taken.

As stated previously, the grounded dielectric slab problem is a simplified model for the actual micromachined dielectric. For the example to hold true the alignment of the holes must be made to closely resemble the periodic structure defined in the example (Figure 5). This suggests that the orientation of the holes controls the degree to which the surface waves are suppressed. This can be seen in the measured antenna patterns (Figure 8). For the same artificial dielectric constant ($\varepsilon_{eff} \approx 5$) the patterns change significantly as the hole geometry is varied. Since the greatest effect to the patterns from the surface waves occurs in the end-fire direction, optimum performance is achieved by aligning the holes for maximum suppression in that direction (the "hexagonal" geometry). The directivity for each

antenna was calculated using both co-pol and cross-pol measurements taken over a full 2π rotation. The results listed in Table 1 show that the improvement in performance is directly related to the hole placement (all of the antennas have approximately the same "artificial" dielectric constant).

Gain measurements were taken from 8.5 GHz to 12 GHz for three of the antennas. The results of the measurements are displayed in Figure 9. It is also important to note that the improvement is across a large bandwidth, indicating that the surface wave suppression is not a narrow-band resonant effect. The micromachined dielectric effectively utilizes the inherent wide-band performance of the TSA. With the gain and directivity measurements, the efficiency of the different antennas was computed (Table 2). As the material is changed from its reference (with no micromachining) to the "hexagonal" geometry the efficiency jumps dramatically approaching that of a TSA on thin, low ε_r Duroid, which was used as a reference goal for optimum performance.

Most of the initial fabrication and measurements for this research was done at 10 GHz. This simplified fabrication and testing and reduced any tolerance issues. The improvements due to micromachining are not, however, restricted to the lower frequencies. All of the different antenna designs were scaled geometrically to 30 GHz and their patterns measured (Figure 10). The same improvements are seen as the hole geometry is varied, with a direct comparison between the two

frequencies shown in Figure 11. The small difference in the patterns is attributed to a different measurement techniques, coaxial probing for the 10 GHz and diode detection at 30 GHz, and a small difference in scaling (the substrate was scaled by 70% while the frequency was scaled by 67%). It is clear from the comparison that this technique can be scaled consistently in frequency and there are no foreseeable problems with scaling to 60GHz or 94 GHz for high frequency Silicon or GaAs integrated circuits.

4. Conclusion

A new technique involving simple bulk micromachining has been presented that will allow, for the first time, the successful operation of tapered slot antennas on thick, high dielectric constant materials. Proper antenna operation is achieved through the combination of an artificially lowered dielectric constant and through surface wave suppression. The micromachining can be achieved using standard via-hole technology common to current MMIC fabrication processes which will allow for the improvements with little additional fabrication costs. The improvements gained through proper geometry design on the thick, high ε_r substrates allow the TSA to approach the performance of one designed on thin low ε_r material. The technique has also been shown to be scaleable in frequency, allowing for simple and inexpensive low frequency prototyping to be done for very

high frequency designs. The current work presented is currently being scaled to higher frequencies for radar, imaging and power combining applications.

5. Acknowledgments

REFERENCES

[1]   P.J.Gibson , "The Vilvaldi Aerial," *Proc. 9th European Microwave Conference*, 1979, pp.101-105

[2]   K.S.Yngvesson *et al.* , "Endfire Tapered Slot Antennas on Dielectric Substrates," *IEEE Trans. Antennas & Prop.*, vol.33, pp1392-1400, Dec 1985
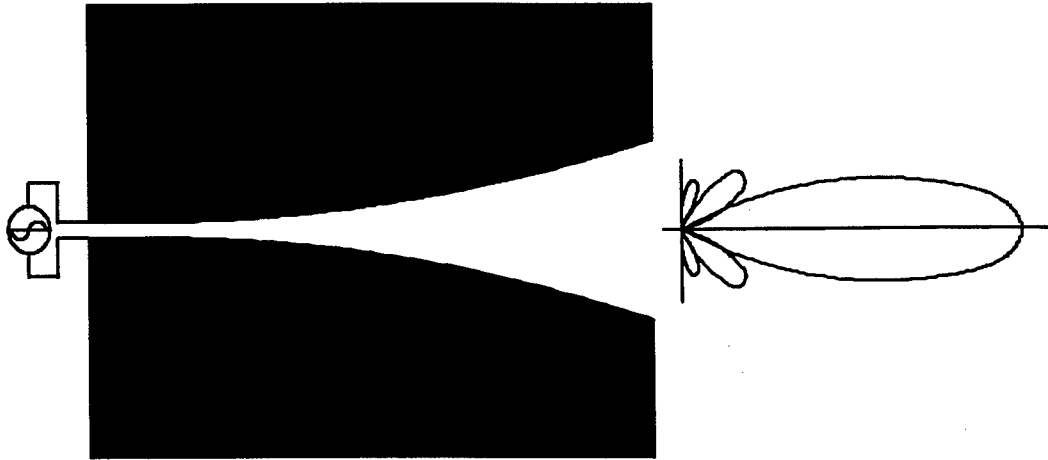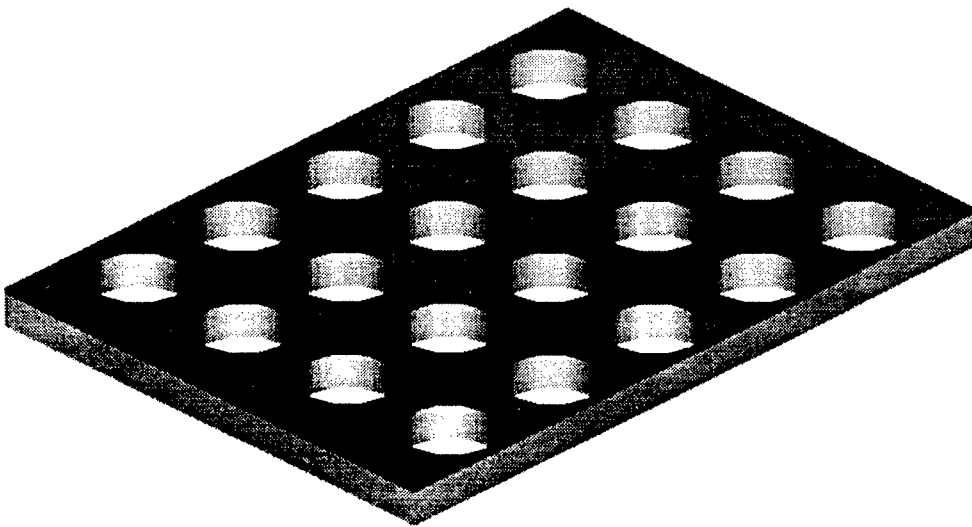
Figure 1. The "Vivaldi" tapered slot antenna.

Figure 2. The micromachined dielectric substrate.
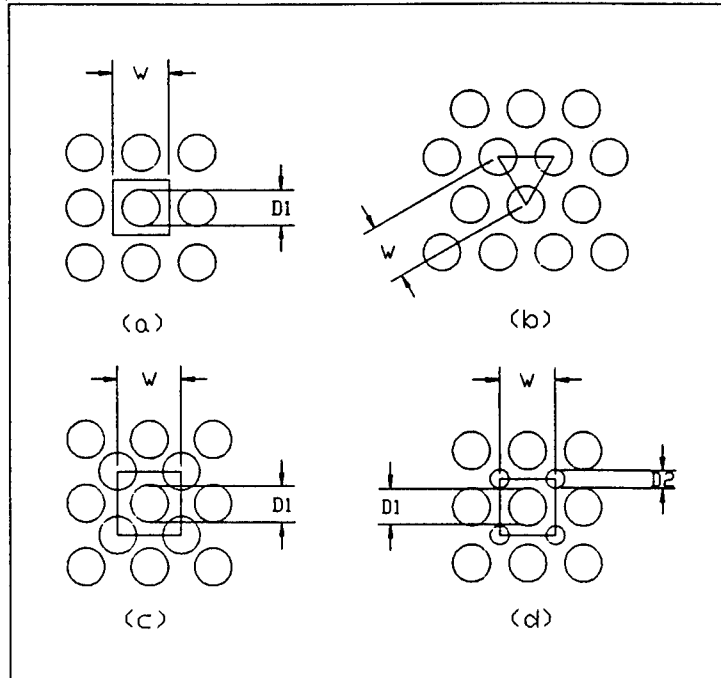
Figure 3. Unit cell definitions used to calculate the "effective" dielectric constant of the micromachined dielectric substrates. (a) Rectangular (b) Triangular (c) Hexagonal (d) Interlaced
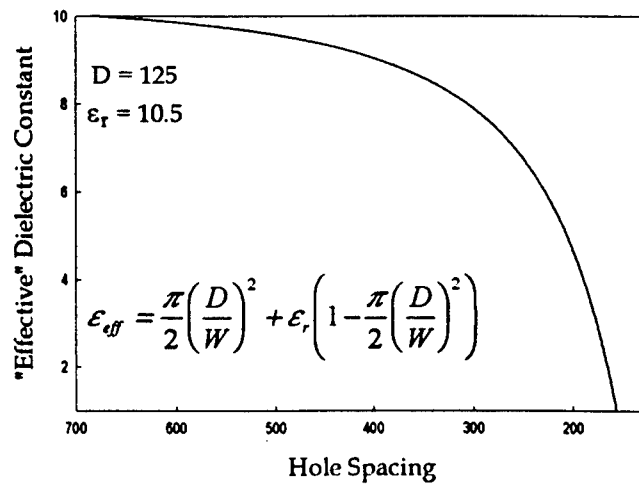
Figure 4. Artificial dielectric constant calculated using a simple mixing model for the "Hexagonal" geometry.
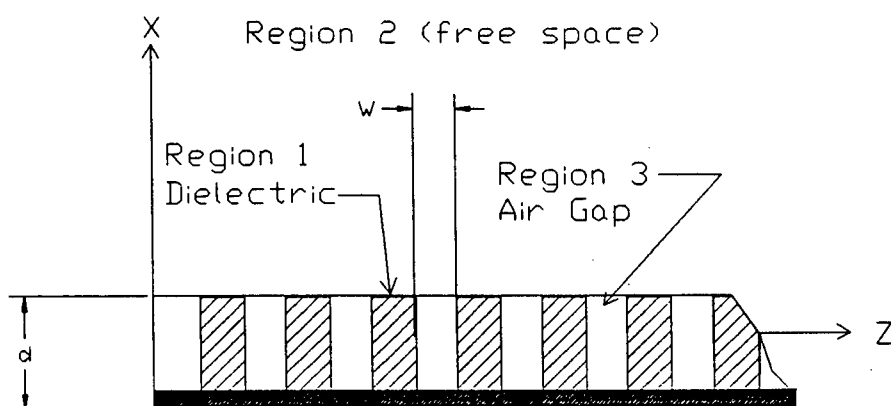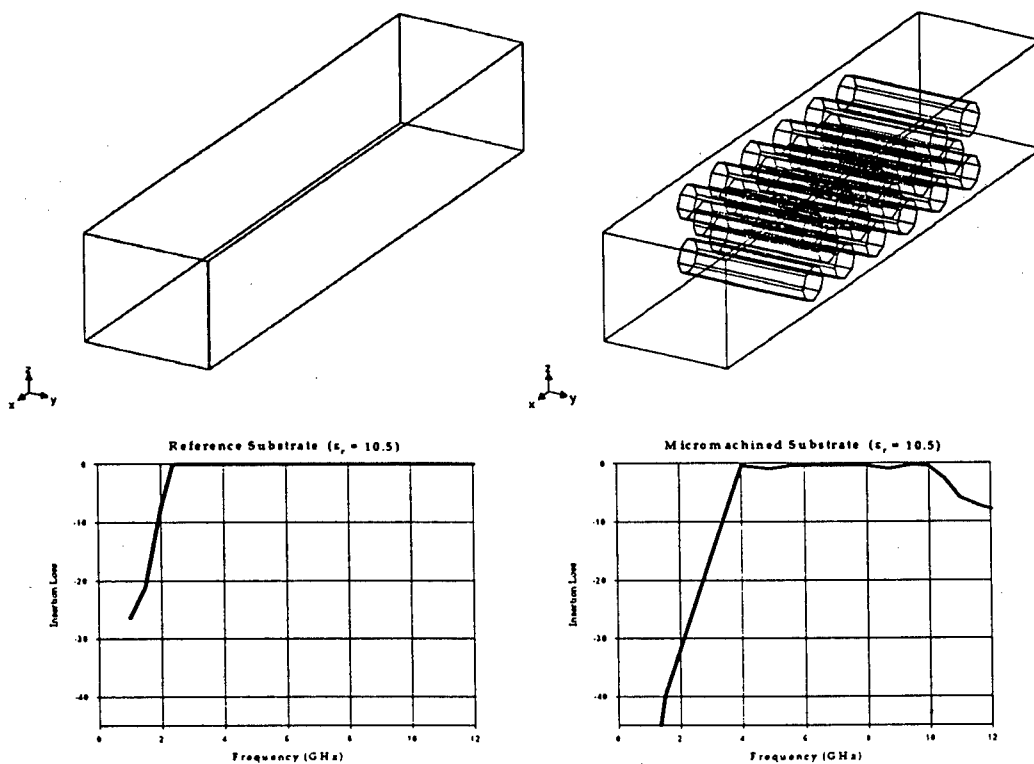
Figure 5. The periodic grounded dielectric slab geometry.

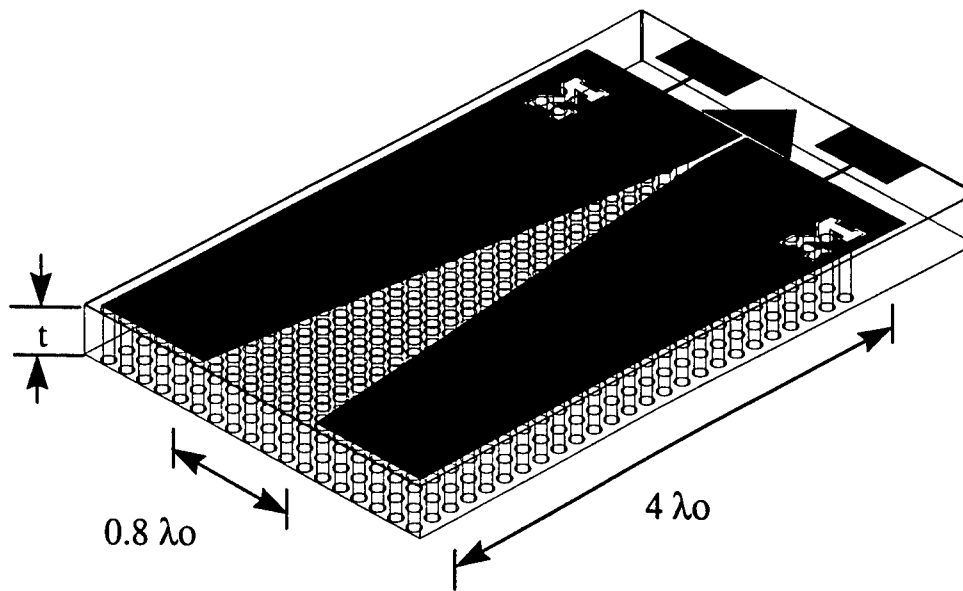Figure 6. FEM simulation displaying the effects of micromachining on TE$_{10}$ mode waveguide propagation.

Figure 7. The micromachined tapered slot antenna.

	Thin Reference	Thick $\varepsilon_r=10.5$ Reference	Rectangular Spacing	Triangular Spacing	Hexagonal Spacing
t_{eff}/λ_0	0.015	0.095	0.058	0.05	0.049
Directivity	13	4	6	8	11

Table 1. Design parameter and directivity for the tapered slot antennas.

	Thin Reference	Thick $\varepsilon_r=10.5$ Reference	Rectangular Spacing	Triangular Spacing	Hexagonal Spacing
Efficiency	85 %	50 %	------		80 %

Table 2. Micromachined tapered slot antenna efficiency based on absolute power measurements.
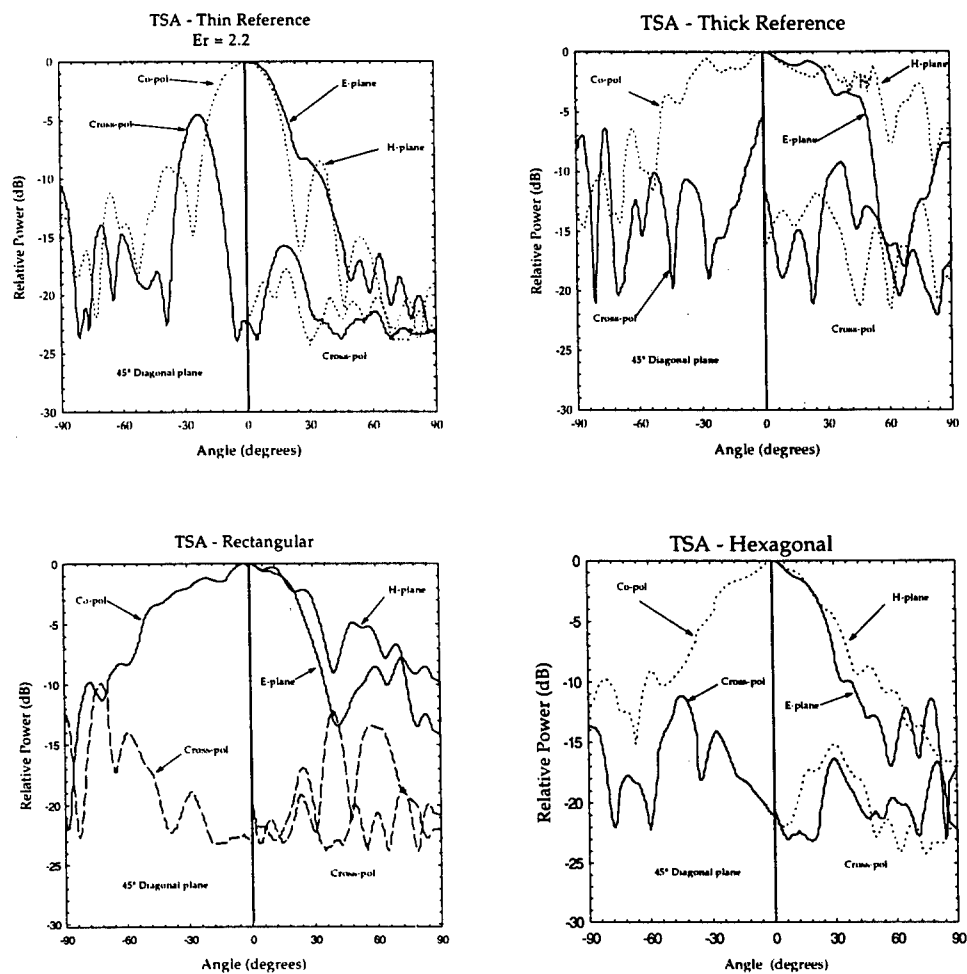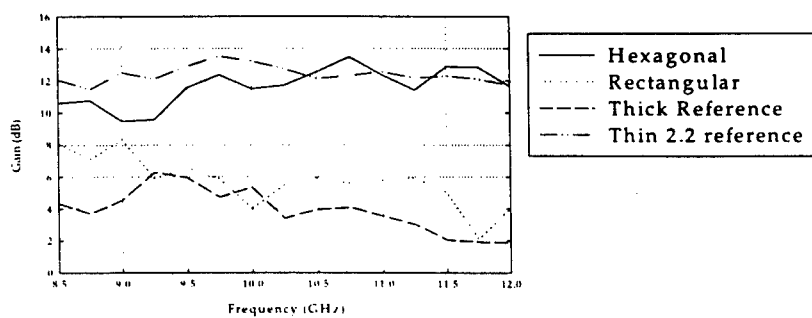
Figure 8. TSA patterns at 10 GHz.

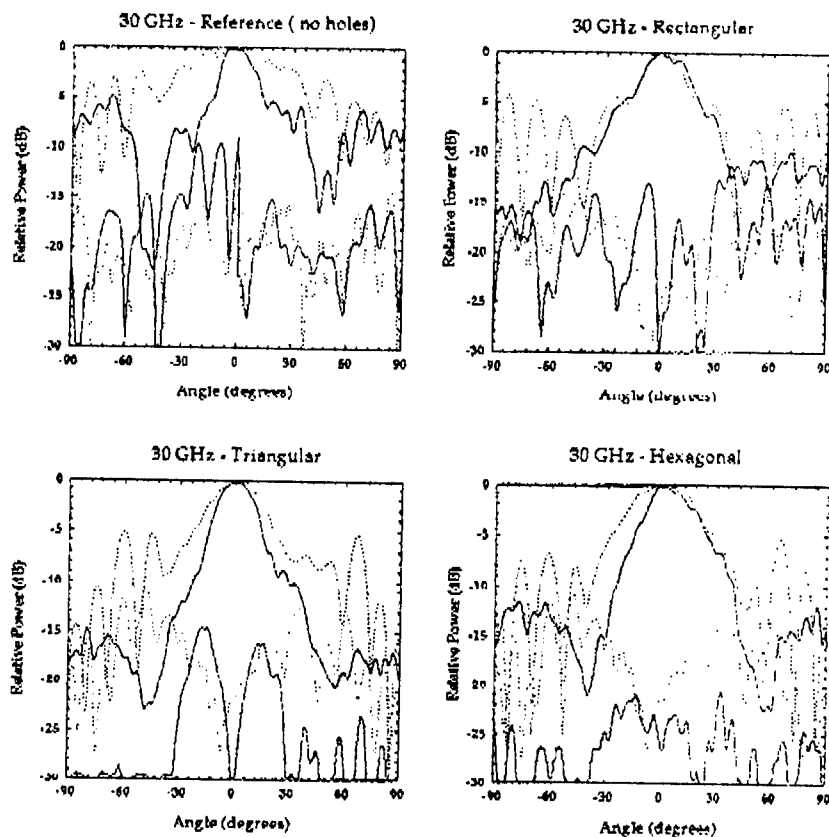Figure 9. Measured gain data for the tapered slot antennas.

Figure 10. Measured antenna patterns for TSAs scaled to 30 GHz (—— E-plane ●●●●● H-plane).
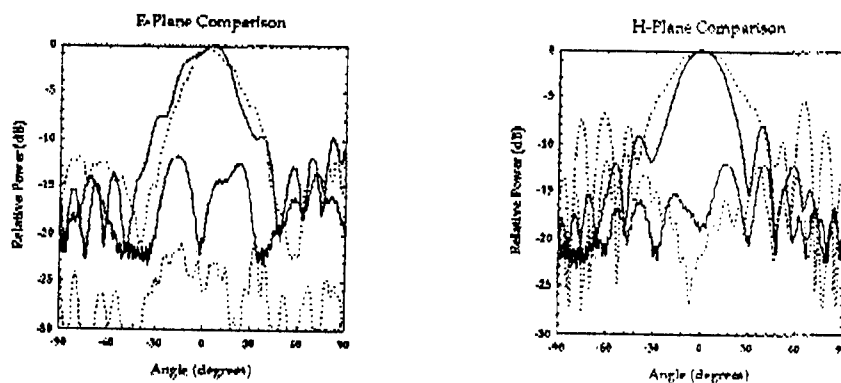

Figure 11. Comparison of patterns for TSA scaled from 10GHz and 30 GHz (—— E-plane ●●●●● H-plane).

III. ARRAY ANTENNA SYSTEMS

Micromachined Packaging For Circuit and Antenna Applications

Linda P. B. Katehi

Department of Electrical Engineering and Computer Science
The Radiation Laboratory-
The University of Michigan,
Ann Arbor, MI 48109
USA

1.0 ABSTRACT

High frequency applications impose very strict requirements on circuit performance including low loss, low dispersion and negligible parasitics. Presented herein is a micromachining approach that offers flexibility to the design of circuits and antennas by allowing for on-wafer packaging and locally reduced substrate thickness to achieve excellent electrical performance. The fabrication of these circuits is based on conventional Si/GaAs/InP fabrication techniques and, as such, they preserve their monolithic character while at the same time allow for high density and three-dimensional integration.

2.0 INTRODUCTION

Micromachined high-frequency circuits with integrated packaging offer light weight and controllable parasitics, which makes them appropriate for hand-held communication systems and miniature intelligent millimeter-wave sensors where system requirements impose strict limits on electrical performance. Recent advances in semiconductor processing techniques allow for integration in all of the directions of the three-dimensional space. The capability to incorporate one more dimension, and a few more parameters, in the circuit design, leads to revolutionary shapes and integration schemes. These circuit topologies have reduced ohmic loss and are of free parasitic radiation or parasitic cavity resonances without loosing their monolithic character. Integration capabilities are thereby extended and performance is optimized. The evolution of micromachined circuits and antennas for operation in microwave and millimeter-wave frequencies is still in its infancy. However, presented here is a description of recent accomplishments in this area, with emphasis on the effort performed at the University of Michigan. There are two techniques which have shown promise for use, and which extensively use micro-

machining to realize novel circuits. The first utilizes dielectric membranes to support transmission line and antenna configurations [1]-[2] and emphasizes optimization of circuit performance. The second technique introduces new concepts in packaging such as adaptive or conformal packaging and, in addition to improvement in performance, it emphasizes size/volume/cost reduction [3]. The merits of each approach, in relation to electrical performance, fabrication, and compatibility, will be presented, and the impact of the newborn technologies to the state of the art will be discussed. In the following sections a variety of micromachining approaches will be described as they apply to both monolithic circuits and antennas.

3.0 DIELECTRIC MEMBRANE SUPPORTED CIRCUITS

The successful development of a membrane-supported transmission line, called microshield, was presented for the first time in the 1991 MTT-S International Microwave Symposium [1]. The microshield is only one of the possible membrane-supported geometries shown in Figure 1. All of these geometries are evolutions of conventional planar lines with one major difference: the substrate material underneath the lines has been removed and a membrane is utilized to support the conductors. Figure 1a shows a finite ground coplanar waveguide line, where the material between the conducting planes has been removed to reduce loss and dispersion. Furthermore, the line is shielded to eliminate parasitic radiation. The second of the micromachined geometries, Figure 1b, is the microshield line, very similar in shape with the conventional coplanar waveguide. This line has zero dispersion, limited parasitic radiation and the capability to suppress the excitation of the unwanted slot-line mode due to the presence of the folded ground which operates as a continuous air bridge. Figure 1c shows a membrane stripline which is characterized by zero dielectric loss, zero dispersion, zero parasitic radiation
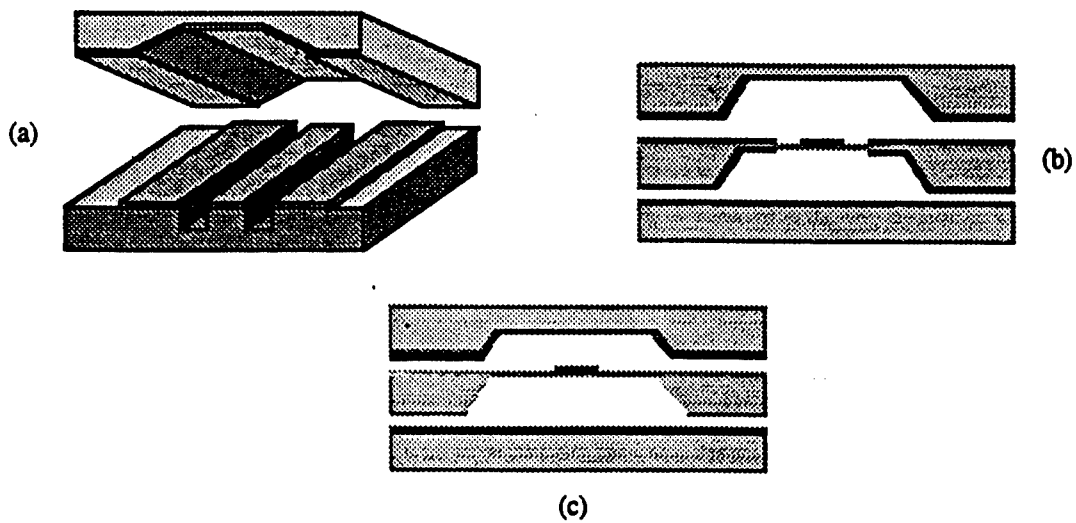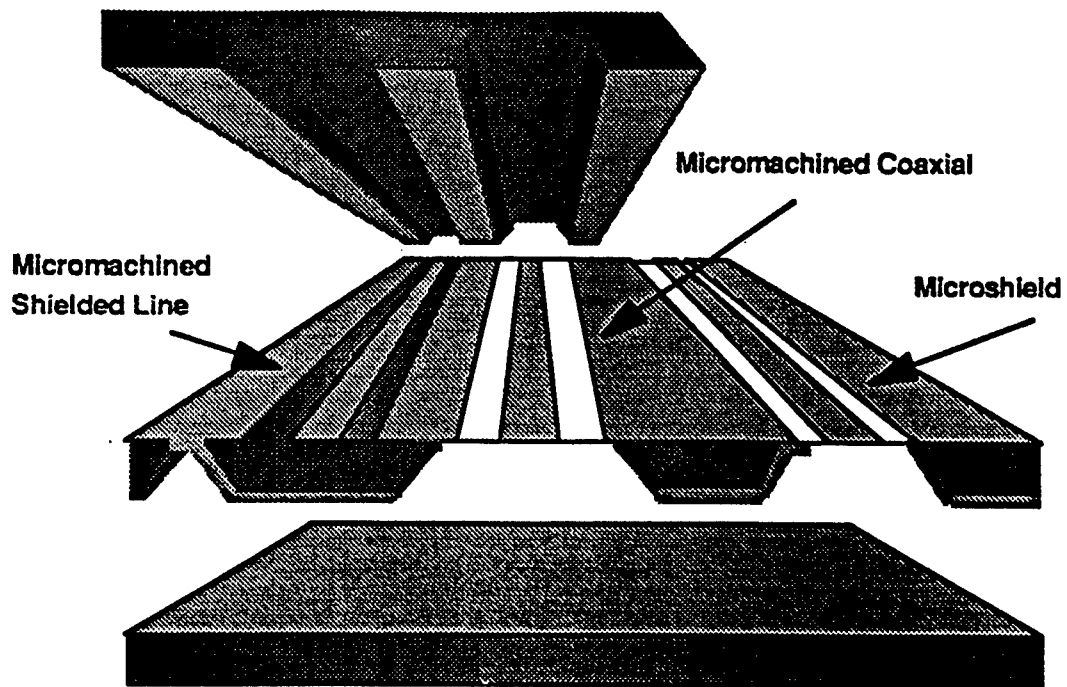
Figure 1: Micromachined Transmission Lines. (a) Packaged Finite Ground Coplanar Waveguide, (b) Microshield, (c) Packaged Membrane Microstrip

while maintaining compatibility to planar monolithic geometries. This propagating structure is completely shielded and can provide passive circuit components with optimum performance. The membrane line as a transmission medium has created the basis of a new technology for circuit and antenna applications in the millimeter and sub-millimeter-wave regions. The success of membrane-supported circuits relies on the development of thin-film dielectric membranes or diaphragms with good electrical and mechanical properties. These thin-film layers are grown on Si or GaAs wafers, and are used to support the planar conducting strip lines. In view of the previously mentioned performance objectives, the thin films must have low losses at microwave and millimeter-wave frequencies, as well as compatibility with semiconducting and conducting materials. Furthermore, mechanical considerations include reduced sensitivity to applied pressure and temperature variations, along with increased membrane or diaphragm sizes.

Transmission lines and circuits printed on dielectric membranes have demonstrated zero dispersion, very low loss and very small parasitics. The presented results confirm the capability of these circuits to provide excellent performance in millimeter-wave frequencies. In the following, many of the presented measurements have been performed in the Ka and W bands. In all cases, measurements were made on a vector network analyzer (HP8510) and a Thru-Reflect-Line (TRL) calibration technique was employed to de-embed the measurements to the reference planes of the circuits.

3.1 Effective Dielectric Constant

During Ka and W-band measurements, data were taken that allowed the extraction of the effective relative dielectric constant ($\varepsilon_{r,eff}$) of the microshield line from 10–40 GHz to 75-100 GHz [5]. The measured values of $\varepsilon_{r,eff}$ show a very minor influence of the membrane on the propagation characteristics of the microshield line. The membrane is a 1.5 micron thick tri-layer composite of $SiO_2/Si_3N_4/SiO_2$ with thicknesses of 7000Å/3000Å/4000Å. The dielectric constant of the oxide is 3.9 and of the nitride is 7.5. The presence of the dielectrics results in a value of 1.08, as shown in Figure 2, for $\varepsilon_{r,eff}$, instead of the unity value that would be expected if the signal were propagating entirely in air. Also, very low dispersion is indicated, since the measured $\varepsilon_{r,eff}$ remains very nearly constant vs. frequency. This fact means the absence of substrate moding i.e. single-mode TEM wave propagation over a very wide bandwidth.

3.2 Attenuation in Micromachined Lines

The attenuation in membrane micromachined lines is

due to conductor losses only, if the lines are shielded, and it may be augmented by radiation losses if the lines are operating in an open environment. In the following two sections we will briefly describe how each type of loss varies with frequency and ways to reduce or eliminate it.
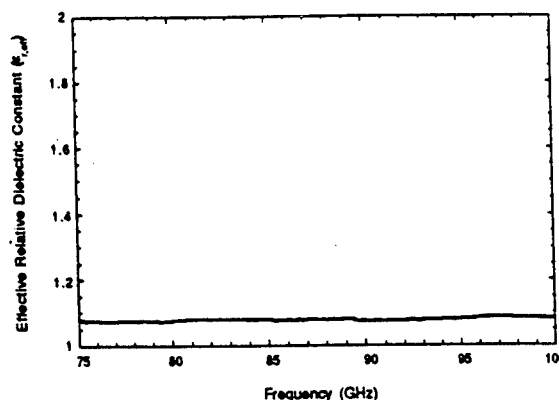

Figure 2: Measured Effective Constant for a Microshield Line.

- *Ohmic Losses*

Conductor loss in membrane lines critically depends on the operating frequency, size of the circuit and aspect ratio. For a microshield line where the line geometry simulates a coplanar waveguide, the aspect ratio (s+2w)/s (see Figure 1) plays a very important role. Specifically, lines where the inner conductor is very narrow and the slots are also narrow, will have a much higher conductor loss from lines of the same characteristic impedance but with wider inner conductor and wider apertures. Furthermore, lines of higher impedance tend to exhibit lower conductor loss. For all the above reasons the measured loss of a microshield line has been found to be much lower than the loss of a coplanar waveguide of the same aspect ratio. On wafer and electro-optic sampling measurements performed at Michigan has demonstrated the low loss characteristics of the microshield line. Measured loss shows that the microshield attenuation constant in dBs/mm is three times lower than that of the conventional coplanar waveguide for frequencies up to 40 GHz. These measurements have shown that losses in these membranes lines remain extremely low as we cross 100GHz and move toward 1000GHz operating frequencies, (see Figure 3).This is due to the fact that the membrane line has only conductor loss contrary to the conventional CPW which suffers from dielectric and radiation loss in addition to ohmic loss. Furthermore, the conductor loss in dB per guided wavelength varies as the inverse of the square root of the frequency. As a result, circuits which

173

are scaled so that their electric lengths remain the same will have lower conductor loss in W band from the loss they would exhibit in Ka band. Based on the above observations, we have been able to design microshield lines for operation in W band with very low losses. Specifically, low-pass and band-pass filters in W band have exhibited losses with less than 1 dB insertion loss. Similar observations apply to the membrane microstrip.

• *Radiation Losses*

Radiation losses have a different frequency and geometry dependence. The membrane microshield geometry has exhibited tremendously low radiation to the point where we do not even consider it. Band-pass filters at 250 GHz have demonstrated a loss less than 1 dB [7]. For the membrane microstrip the situation changes. W-band band-pass coupled resonator filters have exhibited high radiation loss. However, this loss can be suppressed through the use of Si micromachined packages. Measured W-band self-packaged band-pass filters with 16% bandwidth have exhibited less than 0.6 dB loss throughout the pass-band. The presence of radiation loss becomes apparent as the operating frequency increases beyond the point where the first high-order mode is excited on the line. In conventional lines printed on glass ($\varepsilon_r=4.5$) or GaAs ($\varepsilon_r=12.7$), the higher order modes are triggered at frequencies as low as 80 GHz. As soon as the first higher order mode is excited, the substrate triggers higher order substrate modes which are strongly coupled to the line propagating mode resulting in power leakage. From that point on, the line loss is mostly attributed to radiation, while ohmic and dielectric loss play a secondary role.
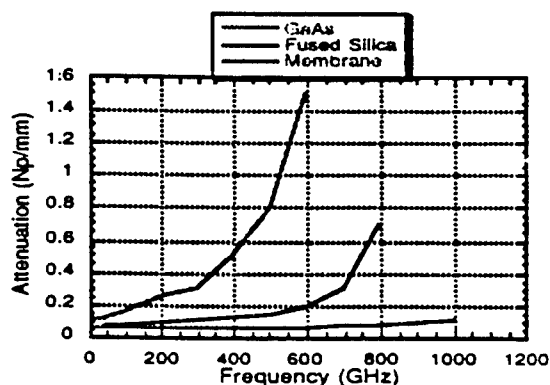

Figure 3: Electro-optic Sampling Results for Coplanar Waveguide Lines Printed on GaAs, Fused Si and GaAs.

This well understood fact has been observed experimentally through electro-optic sampling measurements [6]. Figure 3, shows the measured loss factor for three coplanar waveguide lines printed on GaAs, Fused Silica and Si Membrane indicating excessive losses in GaAs for frequencies exceeding 300 GHz. Fused silica behaves well up to 500 GHz but its performance breaks down at around 700GHz. The micromachined coplanar waveguide exhibits minimal loss for frequencies as high as 1THz reflecting the excellent performance of the line.

ON-WAFER PACKAGED COMPONENTS

Silicon micromachining can offer what conventional means have not been able to provide; packages which conform to the circuit geometry, require much less space, and provide superior mechanical, thermal, and electrical performance. Recently, at the University of Michigan, Si micromachining was used to develop self-packaged circuit components which have demonstrated superior electrical performance when compared to conventionally developed components. These micromachined components are of microstrip or coplanar waveguide (CPW) type and they are surrounded by an air-filled cavity in the upper region and a substrate-filled cavity in the lower region. Both cavities are integrated monolithically with the circuits to provide completely shielded geometries which are appropriate for a broad range of applications including high density interconnect networks and vertical transitions. The use of on-wafer packaging can lead to elimination of unwanted parasitic mechanisms such as parasitic coupling and parasitic radiation.

As discussed earlier, Si micromachining allows for an on-wafer packaging without affecting the integration capability. To illustrate the effect of a micromachined conformal package in the reduction of cross-talk, a back-to-back right angle bend is designed in an open as well as packaged configuration (Figure 4). The conventional microstrip environment is referred to as "open" while the shielded one is referred to as "packaged".

In this work, the circuits and upper cavities are developed on high and low resistivity silicon substrates, respectively, with a thickness of 500 μm. In the packaged circuits the wafer has been thinned locally under the transmission line to 320 μm to provide better propagating conditions (quasi-TEM propagation). Both open and packaged circuits incorporate 50 ohm lines. In the packaged configuration, the bottom wafer supports the planar circuits and lower cavity of the package while the top wafer has the upper cavities (Figure 4).

Ground pads have been incorporated on the same plane as the conducting lines for bonding between the upper and lower cavities. These planes are located 380 μm away from the conducting line to ensure a microstrip mode of propagation.
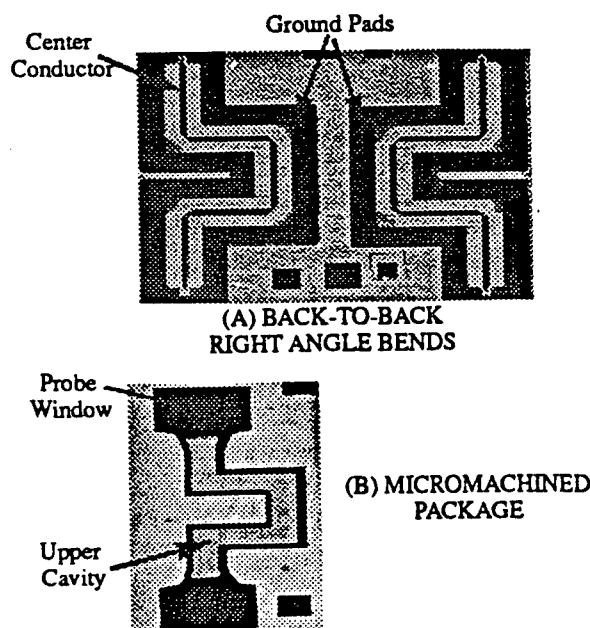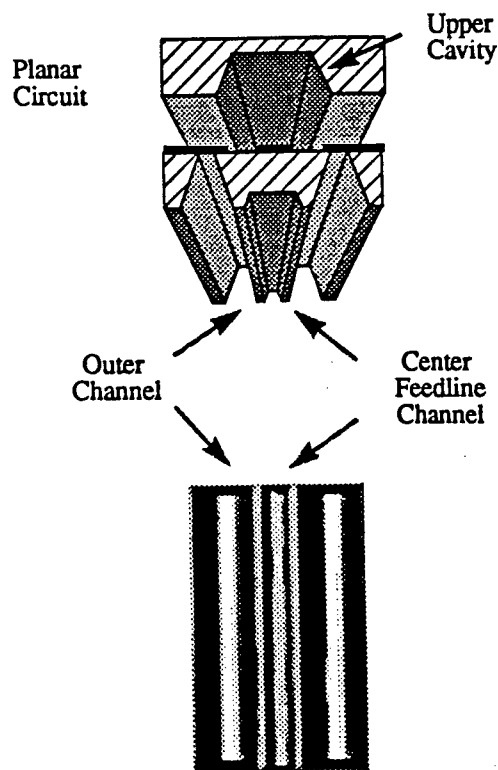
Figure 4: On Wafer Packaged Microstrip Bends

(a) Cross-Section of Micromachined Package

(b) Photograph of Bottom of Lower Cavity Wafer

Figure 5: (a) Illustration of the Package Cross Section with Localized Substrate Region for the Conducting Line. (b) Photograph of the Lower Side of the Package

For the back-to-back right angle bend, the conformal package is developed using the techniques described in [3]. There are two distinct fabrication issues addressed in this work. First, reduction of wafer thickness under the conducting lines and second, the realization of convex corners around the bends in the upper and lower cavity regions. To locally reduce the thickness of the wafer from 500 to 320 μm and provide the necessary DC contact areas, a two step etch procedure was employed. Initially the outer channels of the lower package were removed while the center feedline channel is protected with silicon dioxide. Next, the oxide masking layer is removed and the wafer is etched an additional 170 μm to locally reduce the center regions to 320 microns (See Figure 5). Convex corner undercutting is compensated by including centered squares at the edge of each convex corner [4]. The compensation squares are approximately 1.4 times the desired etch depth. Such a correction has been incorporated in the designs for the upper and lower wafers.

Measured data are discussed regarding coupling of the planar bend geometries. The coupling of the planar bend geometry to nearby elements is characterized with on-wafer probing. A Short-Open-Load-Thru calibration method is employed using 150 μm pitch Picoprobes from GGB Industries with an 8510C Network Analyzer and Alessi Probe station. Cross-coupling effects are determined by measuring the input of the bend structure and the output

of a neighboring element adjacent to the bend geometry. environments is compared in Figure 6. In the lower frequency range the difference in the insertion loss is due to ohmic losses in the cavities of the packaged bend. In Figure 6, the open structure has coupling as high as -20 dB in the 5 to 30 GHz range. Similar measurements have been performed on the packaged structure. The results demonstrate coupling less than -45 dB which is very close to the coupling between the two probes when left out of contact in air.

To illustrate this packaging approach in an antenna application, a package surrounding the feeding line of a microstrip patch antenna has been incorporated in the design (See Figure 7). In this circuit, only the substrate under the feeding line has been thinned to ensure clean propagation of a dominate microstrip mode. The substrate under the
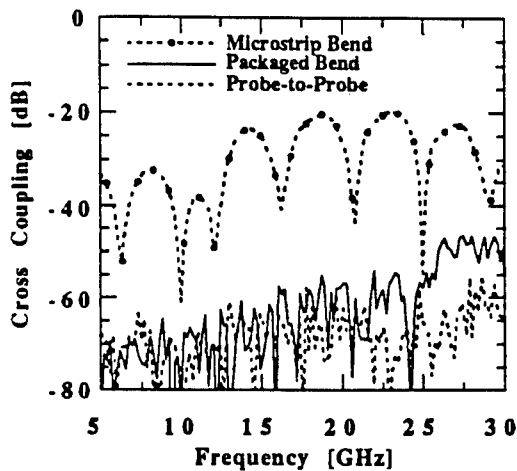
Figure 6: Coupling Between two Open and two Packaged Bended Lines as Compared to the Coupling Between two Probes Left Open.

antenna has been left at its original thickness but dielectric material has been removed locally to provide higher antenna efficiency. In Figure 8, the performance of the open and packaged design is shown which illustrates that the package provides the appropriate shielding while maintaining the desired strength of the patch resonance. As observed from the measurements, the bandwidth of the packaged antenna is higher than the bandwidth of the open antenna by 110% (VSWR ≤ 1.8). This increase indicates higher antenna efficiency and is attributed to the fact that the propagation characteristics (β, Z_0) in the package feed-line are less sensitive to the frequency due to the improved TEM propagation on the line and the effective dielectric constant under the antenna is substantially reduced due to the removed material. Therefore, the resulting package can be easily extended to array applications where feedline radiation can be eliminated.

4.0 MICROMACHINED COMPONENTS

The performance advantages of membrane supported transmission lines can be clearly demonstrated by observing the characteristics of various distributed circuits which are common to planar microwave circuitry and MMICs. The broadband TEM propagation afforded by membrane supported transmission lines permits a significant increase in performance levels for typical planar circuits such as filters, stubs, and power dividers. As an example of a micro-

machined component let us consider a low-pass filter with cut-off frequency at 22GHz. This filter is made as a combination of distributed components, *stubs*, and lumped elements, *MIM capacitors*, carefully placed on the stubs in between the coupling lines (see Figure 9). The filter is printed on a thin Si membrane and is excited from two probe pads located on the silicon substrate. This filter represents a new approach to component design where distributed and lumped elements are combined appropriately to improve electrical performance. In this particular filter, the resonating stubs have been utilized to provide the low-pass character, while the capacitors have been placed to compensate for inductive parasitics, reduce the required size and also suppress the parasitic pass bands which normally occur at $2f_c, 3f_c$ etc. Pictures of the front and back of this membrane filter revealing the location of the capacitors and the Si cavities are shown in Figures 9a and 9b. Furthermore, theoretical and experimental results for this filter are shown in Figure 9c and indicate excellent agreement. These results confirm the very low loss characteristics of the lines and demonstrate the capability of effectively suppressing the parasitic pass-bands to below -40 dB at frequencies as high as $5f_c$ [7].

5.0 CONCLUSIONS

A new micromachined technology suitable for three-dimensional planar circuit configurations has been presented. At higher frequencies, problems associated with the substrates make conventional approaches unfeasible, and membrane supported circuit components offer the only planar alternative to costly waveguide-based approaches. Micromachined transmission lines and circuits have been shown to perform very well in frequency bands all the way up to W-band (110 GHz). Circuits commonly used in CPW implementations are shown to have superior performance when realized with membrane supported transmission lines like the microshield line. The microshield line has a relative effective dielectric constant of 1.07 through 100 GHz and, as a result, it exhibits zero dispersion and zero substrate loss. The micromachined CPW has the lowest attenuation yet demonstrated for planar transmission lines. Filters and resonant stubs have been measured up to 250 GHz and have demonstrated an unparalleled electrical performance. Micromachining has also opened the doors to techniques for fabricating circuits that were previously restricted by cumbersome machining processes. Interdigitated filters were thought to be limited to very low frequencies where they could be manufactured using mechanical techniques, but membrane technology has allowed them to become high performance alternatives at 30 GHz. Membrane milli-

meter-wave microstrip inductors have been developed and fabricated on a high-resistivity silicon substrates using micro-machining techniques with resonant frequencies in the submillimeter-wave region. Last but not least, on-wafer packaging can eliminate parasitic coupling and radiation by component-specific electromagnetic shielding without disturbing the monolithic character of the circuit

6.0 ACKNOWLEDGEMENTS

REFERENCES

1. N.I. Dib, W.P. Harokopus, L.P.B. Katehi, C.C. Ling and G.M. Rebeiz, "A Study of a Novel Planar Transmission Line," presented at the *1991 IEEE MTT-S International Symposium*, Boston, MA, June 1991.

2. T.M. Weller, G.M. Rebeiz and L.P.B. Katehi, "Experimental Results on Microshield Transmission Line Circuits," presented at the *1993 International Symposium of the IEEE Microwave Theory and Techniques* Society, Atlanta, Georgia, June 1993.

3. C. Y. Chi and G. M. Rebeiz, "Planar microwave and millimeter- wave lumped elements and coupled-line filters using micro-machining techniques," *IEEE Trans. Microwave Theory Tech.*, December, 1994.

4. R. F. Drayton, T. M. Weller, and L. P. Katehi, "Development of Miniaturized Circuits for High-Frequency Applications using Micromachining Techniques," International Journal of Microcircuits and Electronic Packaging, Third Quarter, 1995.

5. S.V. Robertson, L.P.B. Katehi, and G.M. Rebeiz, "W-Band Microshield Low-Pass Filters," in *1994 IEEE MTT-S Digest*, pp. 625-628.

6. H.-J. Cheng, J. F. Whitaker, T. M. Weller and L. P. B. Katehi, "Terahertz-Bandwidth Characteristics of Coplanar Transmission Lines on Low Permittivity Substrates," IEEE Transactions on Microwave Theory and Techniques, Vol. 42, No. 12, December 1994, pp. 2399-2406.

7. T.M. Weller, L.P.B. Katehi and G.M. Rebeiz, "A 250 GHz Microshield Band Pass Filter," IEEE Microwave and Guided Wave Letters, Vol. 5, No. 5, pp. 153-156.
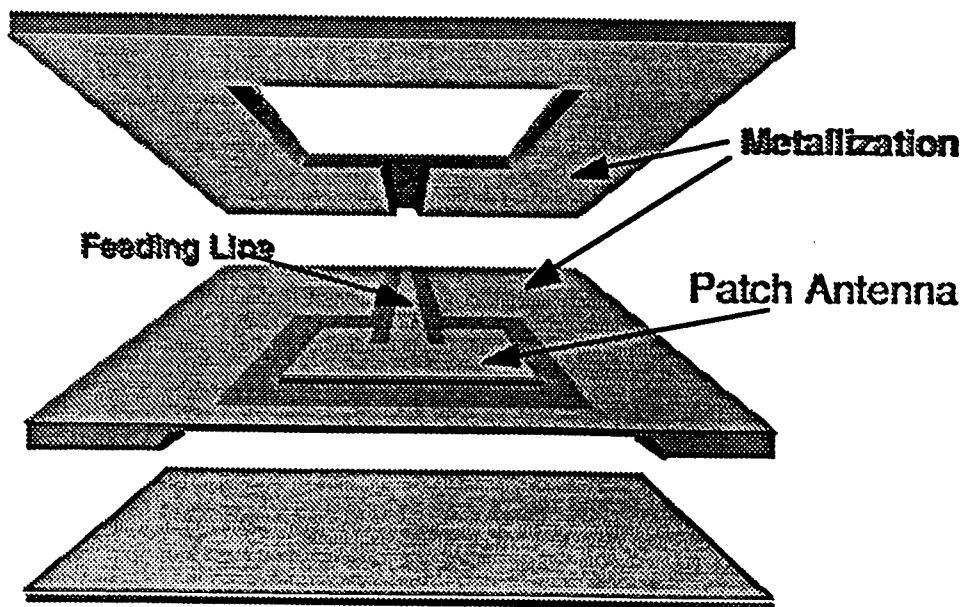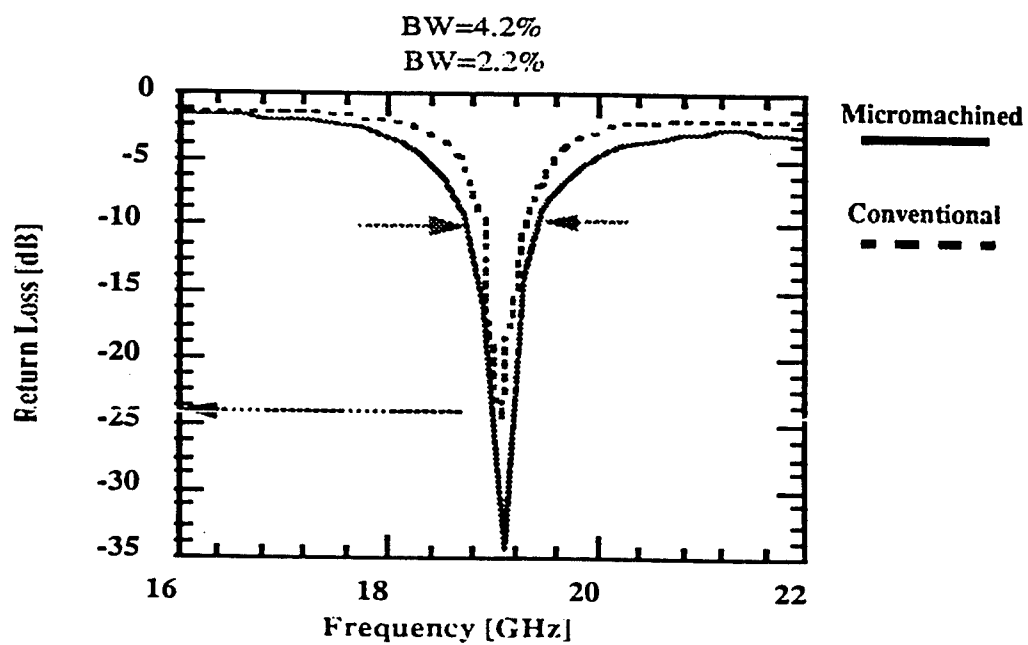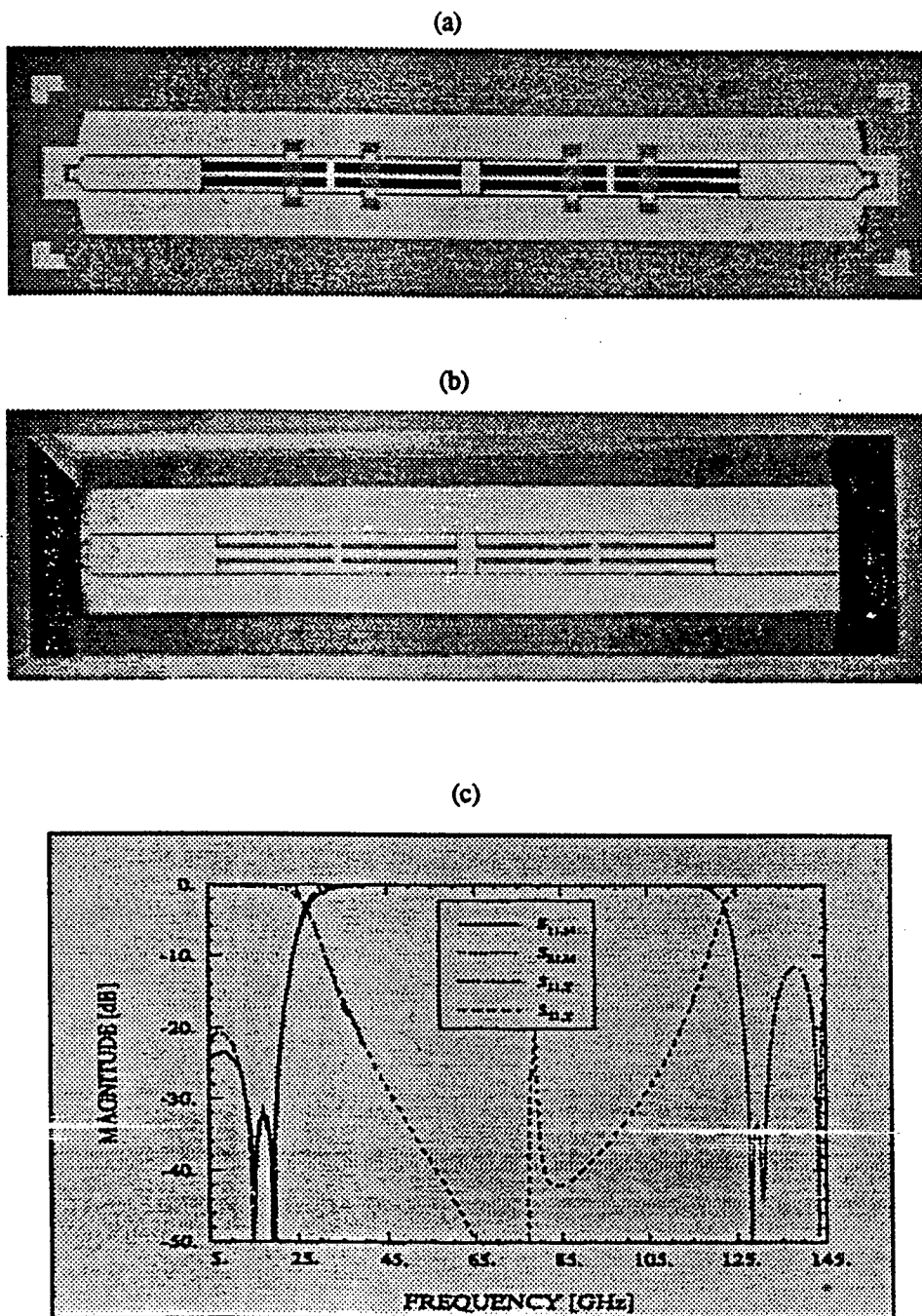
Figure 7: Micromachined Antenna

Figure 8: Input Match

(a)

(b)

(c)

Figure 8: Micromachined membrane Low-Pass Filter: (a) Front View, (b) Back View, (c) Theoretical and Experimental Results

A LOW-COST PHASED ARRAY ANTENNA PACKAGING TECHNOLOGY

T.E. Noll, K. Jayaraj, Brian Farrell
Foster-Miller, Inc.
195 Bear Hill Road
Waltham, MA 02154

Thomas Perkins, Dennis Glynn
Dedicated Electronics, Inc.

Abstract: This paper describes a generic low cost phased array antenna packaging technology that uses a highly impermeable liquid crystal polymer (LCP) substrates in multichip module substrate with aperture coupled patch antennas.

Our technology offers a cost effective approach for fabricating phased array transmitter and receiver modules. The approach has a number of advantages over other conventional approaches, including:

1) Low thermal impedance achieved by attaching devices directly to a CTE matched, high conductivity heat sink.

2) Efficient, easy to fabricate slot coupled RF feeds combined with a high density flex circuit based interconnection.

3) Excellent electrical performance up to 40 GHz due to the low dielectric constant (2.6 at 1 GHz), and low loss tangent of the LCP.

4) High sensitivity low noise performance with LNAs directly connected to antenna elements.

5) Low-cost MCM-L processing methods.

This packaging technology is very flexible and compatible with a wide variety of chip and package assembly techniques such as wire bonding and perimeter/ball grid array SMT and is especially suited for direct chip attachment using flip chip bonding methods.

The paper describes preliminary results on a patch antenna fabricated from the LCP substrate, showing 6 dB gain in the Ku band application area, and on the low cost MCM-1 processing methods used. This technique will enable efficient, large area flat antenna structures to be fabricated with this innovative MCM based module approach.

1. Introduction

The volume of information required to be relayed between space platforms, and earthbound fixed/mobile/airborne radio terminals is increasing at exponential rates. For example the Global Broadcast Service (GBS) employs high capacity, high power satellites to provide an unprecedented, high speed flow of crucial information to military commanders. Information likely to be transmitted via GBS includes air tasking order updates, battle damage assessment reports, targeting information, maps and weather information, and entertainment (via the Direct Broadcast Service). Current goals involve increasing data rates of 10 Kbps to 25 Mbps. The technology discussed in this paper will reduce manufacturing costs of GBS arrays, while providing higher density packages with excellent performance. Prominent features of this innovative technology include reduced size and weight, efficient thermal management and reliable performance.

This paper will discuss a low cost, ultra-thin, conformal active phased array receiver module for radar and communication links that Foster-Miller, Inc. is developing. The active assembly would be fabricated using Foster-Miller's innovative Liquid Crystal Polymer (LCP) dielectric substrates [1,2] and incorporate microwave monolithic circuits (MMIC) and DC power/logic chips integrated with inverted stripline patch antennas [3-8]. The design frequency for the array will be 19.2 to 21.2 GHz for satellite downlink applications and can be designed for a range of applications from low frequency to 40 GHz, in other words from Iridium to future high data rate satellite communications. The design is particularly applicable to airborne GBS terminals where size, weight, thin

profile, scanning capability and thermal management are critical to compliant operational fulfillment.

The specifications listed in Table 1 is for a typical GBS Receive terminal. Building on our prior development at Foster-Miller of LCP based microwave packaging and a demonstration of a patch antenna built with this innovative materials we will design fabricate and test a functional antenna element while specifically addressing processes that will be required to produce these receivers for both military and commercial markets.

Foster-Miller has successfully demonstrated the following results which will be confirmed in this proposed effort by building and testing a patch antenna receiver module:

- That aperture coupled circular patch antennas work very efficiently (>6 dB gain at Ku band) with liquid crystal polymer dielectrics, replacing more expensive quartz or foamed dielectric materials.

Table 1.   Typical GBS Receive terminal specifications

Parameter	Specification	Design Goal
Frequency band	20.2 to 21.2 Ghz	19.2 to 21.2
Polarization	Left hand circular	Switchable to RHCP desired to be compatible with MILSTAR
Data rate	23.6 Mbps	
Figure of Merit (G/T)	-15.4 dB/deg K	As close as possible
Scan angle	±70 deg	

- That these antennas and MCM packages can be easily fabricated with low cost conventional printed circuit board processing.

- That our proposed multilayer microwave packaging can effectively manage the flow of heat out of the power amplifier devices into an integral heat sink and from there out to the system cooling.

- That an operational array could be designed with our proposed technology that would enable tight antenna element spacing while providing low cost assembly because of innovations such as the slot aperture coupled vias for RF signals, blind vias and flex circuit techniques for routing digital and control circuits.

- That significant savings can be achieved by utilizing MMIC flip chip attachment with conductive polymers and by replacing hand soldered discrete components with integral resistors fabricated onto the LCP circuits.

- That this overall package will have significant reliability because of the improved assembly methods, thermal management and the low CTE of the LCP and heat sink.

2. Foster-Miller's Proposed Package Architecture

LCP substrates exhibit the key characteristics for microwave packaging. Our proposed approach in Figure 1 is presented as a cross section showing the arrangement of devices and interconnect. Most of the digital and DC control is not shown for clarity. This view is actually of several sections combined into one. The interconnects we are using are as follows:

Figure 1. Foster-Miller's proposed approach for multilayer microwave packaging

- Two point orthogonal feed incorporating a Lange coupler to achieve circular polarization (not shown for clarity in Figure 1).

- The pads and solder or conductive polymer bumps for DC are shown but actually would be at the edge of the chip (into and out of the slice).

- One layer of the LCP is extended to a flex circuit that goes through the heat sink to bring DC I/O in. This is a key innovation of our approach, exploiting mechanical properties of the LCP films which are similar to polyimide films used in flex circuits and providing for a higher density packaging.

- A typical laser drilled v-shaped via is shown connecting the flex DC/control circuitry to other circuits not shown in this view. From the top of the via the

184

circuit runs perpendicular to this view and routs over to the chip connections.

- The slot coupled vertical interconnect for bringing the microwave RF signal into the phase shifter and mixer chip is a second key innovation of this program.

- The coaxial input (not to scale) is shown as it would bring the exciter power into the power splitter circuitry. This input is similar to that shown in Figure 2.

The thermal management would mainly be achieved using thermal vias underneath the low noise amplifier chip that allow the heat to flow directly to the heat sink through the LCP layers as shown in Figure 2. The thermal interface between layers uses either solder or conductive polymer bumps to effectively transmit the heat.
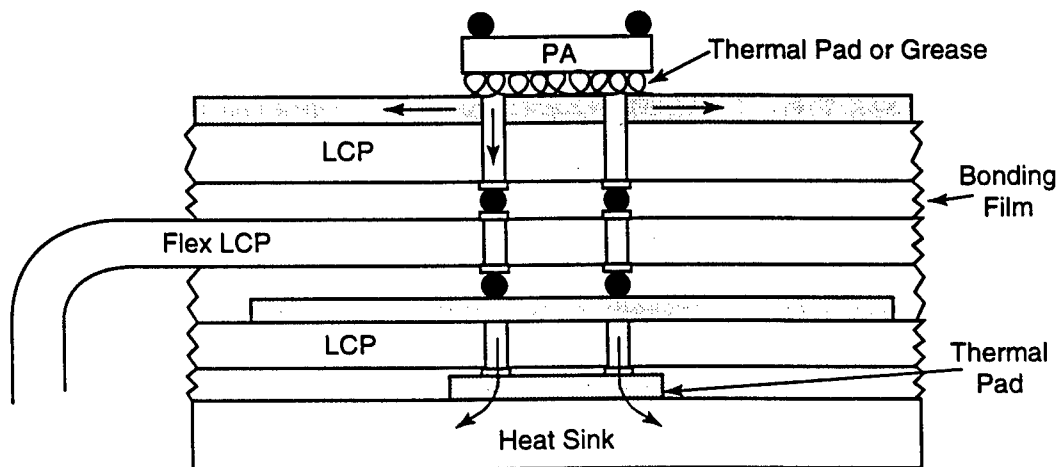
*Arrows Show Heat Flow   325-P-96374-7

Figure 2.   Use of thermal vias to manage heat in transmit module

A cutaway view of our approach (Figure 3) shows the orientation of the devices and circuitry more clearly. While every interconnect cannot be represented in this view because of our flip chip (connecting bumps up) approach, these views do show how a complex package can be assembled with a set of simple, and therefore low cost, techniques.

3. Fabrication and Assembly Process

The basis for this low cost approach is the combination of our innovations with conventional processing as shown in the process sequence in Figure 4. The LCP circuits can be fabricated as double side flex circuits or MCM-Ls with vias
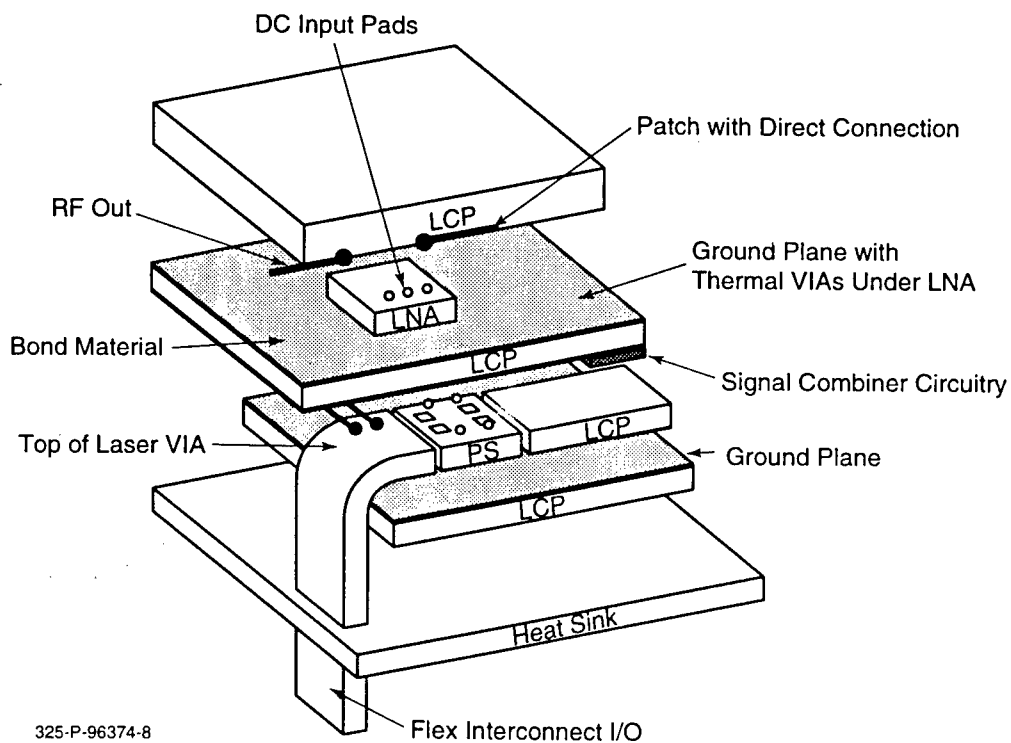
Figure 3. Cutaway of MCM showing chip and interconnect locations in module

186

```
┌─────────────────────┐
│ Fabricate Double Sided │
│    LCP Substrates      │
└─────────────────────┘
           │
           ▼
┌─────────────────────┐
│   Laminate Patch      │
│     Substrate         │
└─────────────────────┘
           │
           ▼
┌─────────────────────┐        ┌──────────────┐
│    Attach MMIC        │───────▶│  Continuity  │
│  Chips (PA & PS)      │        │     Test     │
└─────────────────────┘        └──────────────┘
           │
           ▼
┌─────────────────────┐
│  Bond Double Sided    │
│     Substrates        │
│      Together         │
└─────────────────────┘
           │
           ▼
┌─────────────────────┐        ┌──────────────┐
│  Attach Driver Logic  │───────▶│  Continuity  │
│    MMIC Chip          │        │     Test     │
└─────────────────────┘        └──────────────┘
           │
           ▼
┌─────────────────────┐
│  Bond to Heat Sink,   │
│ Inserting Flex Through │
│   Slot in Heat Sink   │
└─────────────────────┘
           │
           ▼
┌─────────────────────┐
│      Attach           │
│   Coaxial Feed        │
└─────────────────────┘
           │
           ▼
┌─────────────────────┐
│   Functional Test     │          298-P-95687-5
└─────────────────────┘
```
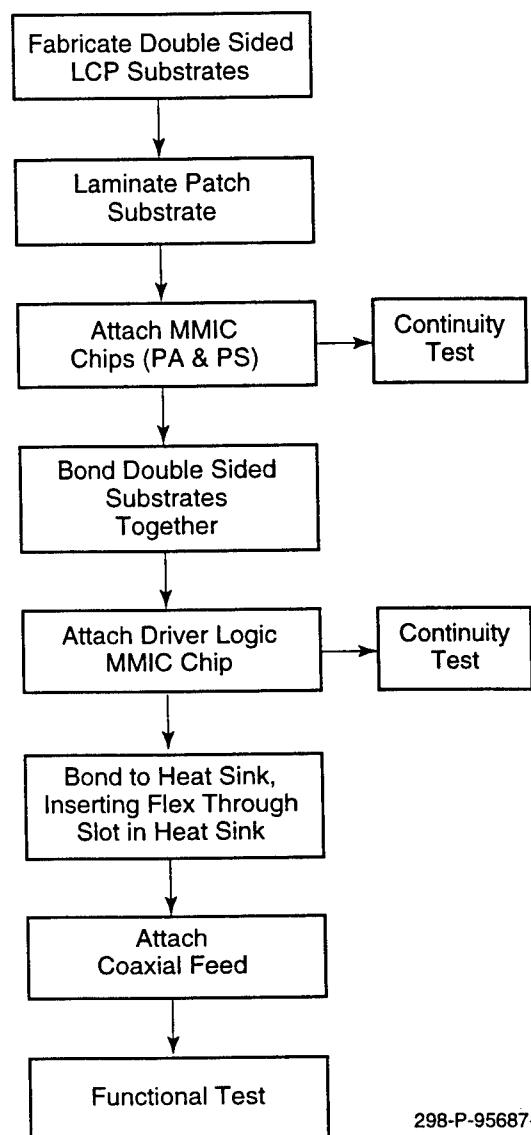
Figure 4.   Array module assembly sequence

formed using laser drilling and standard through hole plating techniques. The ICs

as shown in Figure 1 are then flip chip attached using solder or conductive

polymers. At this point these circuits can be tested to ensure completed circuits

are good. The layers of LCP, flex circuitry, and the heat sink are then bonded

together in one of several ways. For conventional MCMs and printed circuit

boards we have laminated the layers with additional LCP films but this process is done at too high a temperature for many devices and for the solder used to attach them. Two types of low temperature bonding materials are also possible:

- A thermoplastic fluoropolymer adhesive with excellent low loss characteristics commonly used to bond Teflon circuit boards together (available from several companies).

- A thermoset resin filled Teflon bond sheet (Speedboard M from W.L. Gore and Associates).

These materials would maintain the electrical performance because they are very thin and perform as well as the LCP at high frequencies. The CTE and mechanical properties would also not be affected since the stronger LCP would control these unreinforced materials in the overall package.

We have fabricated an aperture slot coupled radiating patch antenna using the liquid crystal polymer substrates and successfully tested the unit at Dedicated Electronics facility. Figure 5 shows a view of the antenna with the LCP package assembled in a metal frame with a coax connector for the RF feed. This part does not have active circuits but did demonstrate the effectiveness of the LCP with aperture coupling.

Figure 6 shows the VSWR response we obtained from the testing for the optimal configuration. This result confirmed our prediction that LCP material would be an excellent medium for phased array antenna modules.
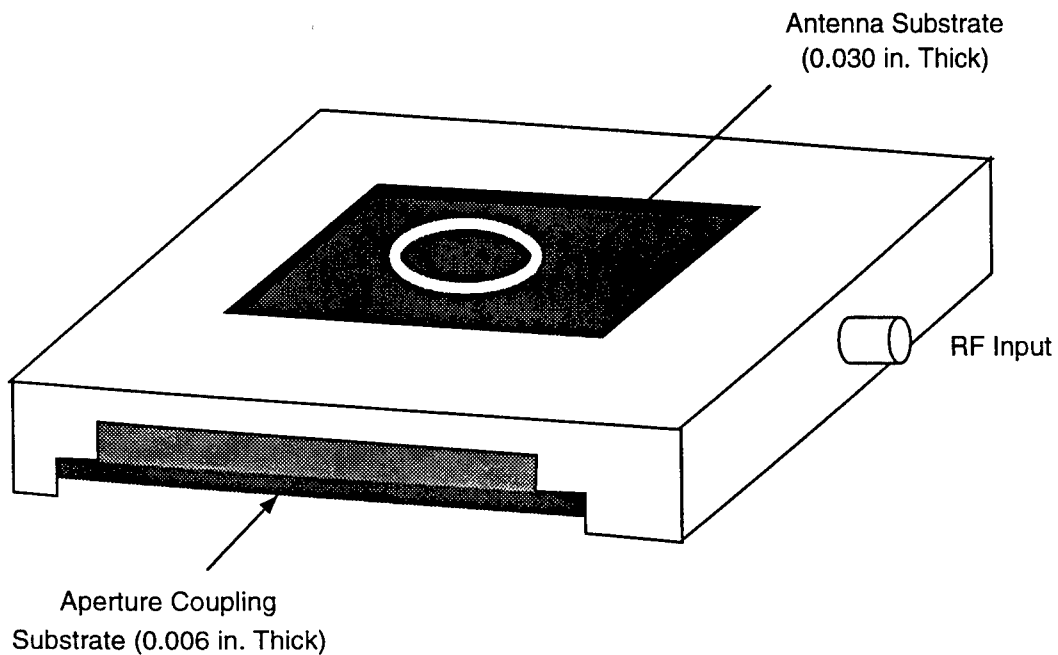
353-OH-4342-2

Figure 5.   Cavity-enclosed aperture coupled circular patch antenna
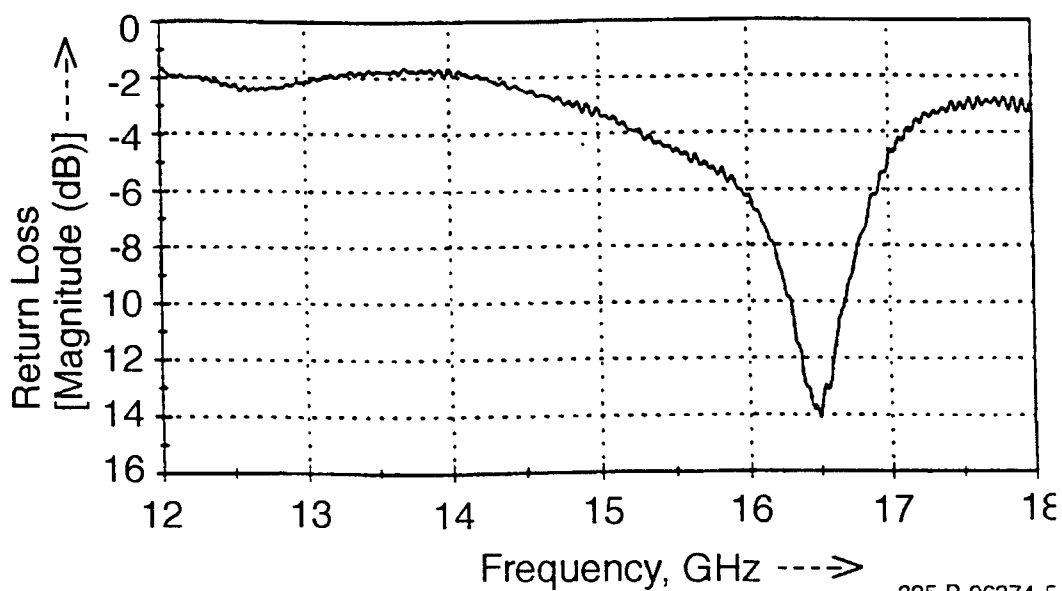
325-P-96374-5

Figure 6.   Measured return loss on 6 dB gain patch antenna on LCP substrate

189

4. Liquid Crystal Polymer Dielectrics

The key to the Foster-Miller approach to electronic packages is the performance characteristics of the liquid crystal polymers.

Thermotropic (i.e., melt processed) liquid crystal polymers (LCPs) are well-suited for advanced electronic packaging applications because they possess a low dielectric constant (2.6 at GHz), can be processed into thin films, and can support an exceptionally small I/O pitch (2 mil). Thermotropic LCPs also have high operating temperature (250°C), low moisture absorption (<0.02 percent), excellent barrier properties for hermeticity, high resistance to chemicals and solvents, tailorable coefficient of thermal expansion and can readily withstand solder reflow process conditions.

Structurally the high degree of molecular order of LCP molecules allows this material to attain a very tight packing density similar to a log jam in a river. LCPs derive their outstanding properties from this tightly packed rigid-rod formation which at a macroscopic level results in a structure that is self-reinforced. This tight molecular packing when combined with the LCPs extremely low gas solubility provides a structure with excellent gas barrier properties, potentially making the package hermetic.

Foster-Miller's LCP biaxial sheet/film extrusion process eliminates the problems associated with other processing methods and provides a high degree of control for tailoring properties such as CTE, tensile strength and modulus. The LCP

material is capable of supporting very high density pitches because of its surface flatness and uniformity, and its tolerance of higher temperature processing. The low cost substrate process is the same whether it is a 3 layer construction for routing a pad array or a 4 to 8 layer board that performs interconnection and power distribution.

In addition to the excellent mechanical properties the LCP materials show significant promise for use in microwave packages, from VHF to millimeter wave. Packages fabricated with both microstrip and conductor backed coplanar waveguides as shown in Figure 7 confirm that the LCP dielectric with thin metallization works satisfactorily, as it did in the patch antenna discussed above.

The effectiveness of the LCP dielectrics for near hermetic packaging is due to the low moisture and oxygen permeability, especially with films extruded with Foster-Miller's unique biaxial orienting dies. The ICs are enclosed in a package of LCP layers and metal sealing them from environmental effects. Although unoriented films exhibit good barrier properties, biaxially oriented films show orders of magnitude lower values. Foster-Miller pioneered the development of a unique process to biaxially orient Vectra and other LCP materials.

Properties of Foster-Miller's biaxially oriented LCP compared to other barrier films are illustrated in Figure 8. These LCPs have unique physical properties:

- The in-plane coefficient of thermal expansion (CTE) can be optimized using a Foster-Miller proprietary extrusion process which imparts selected biaxial orientation.

191
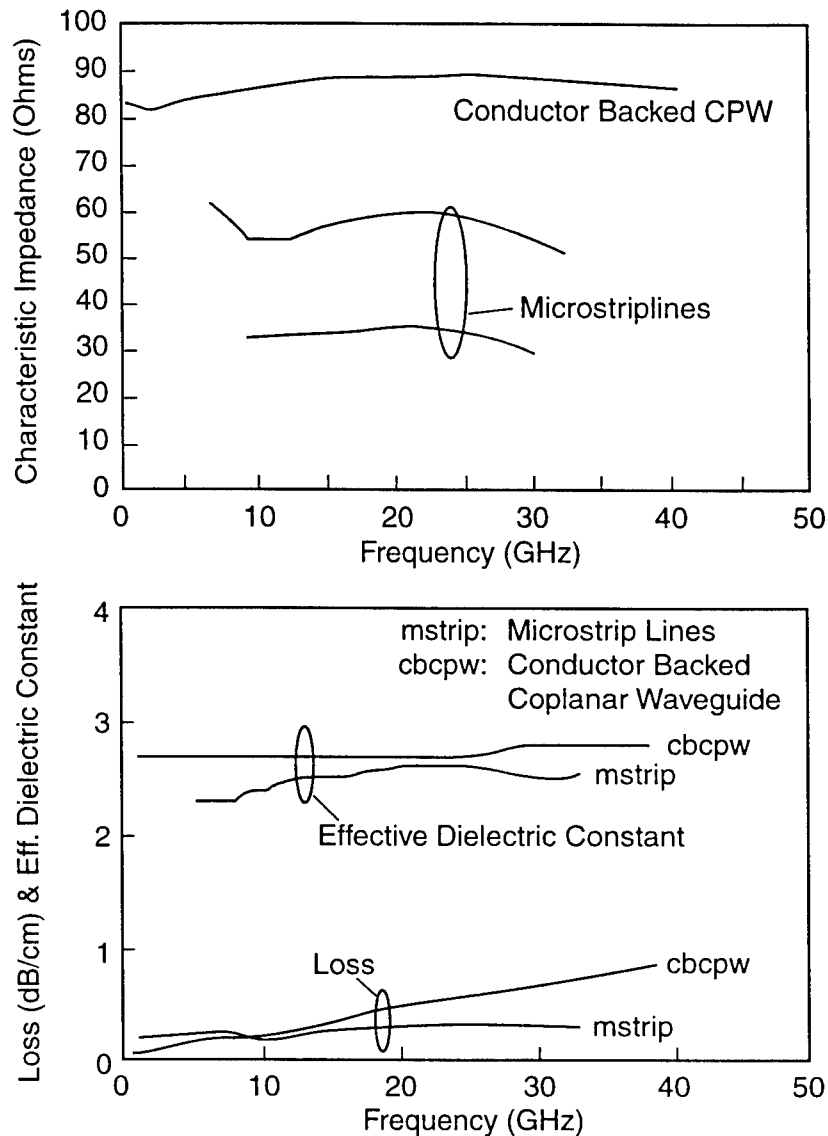
353-OH-4342-1

Figure 7. Measured characteristics of microstrip and coplanar waveguides on LCP

- LCPs are strong, tough engineering plastics which can support large modules without cracking or breaking.

- LCPs are suited for PWBs and MCMs - dielectric constant <3, tan d <0.005, no moisture absorption, and can be made into films of various thickness.

- The temperature capability is over 240°C.

192

325-P-96395-5
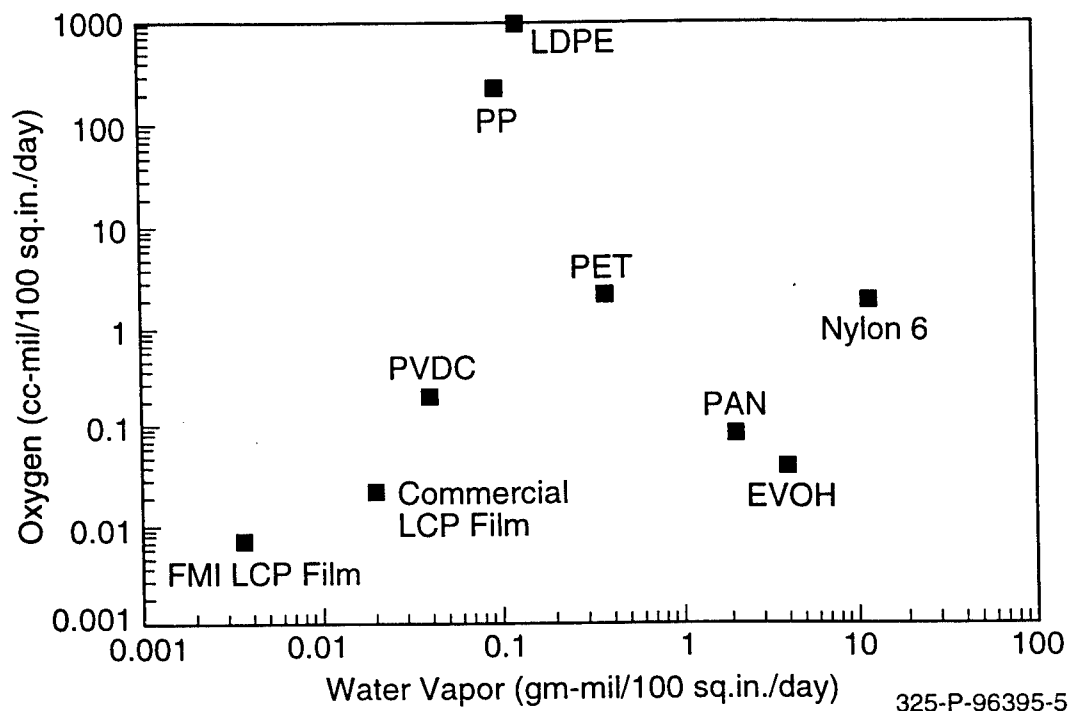
Figure 8. **Oxygen and water vapor permeability of various barrier films**

- LCPs are a thermoplastic and can be sealed with the application of temperature and pressure or ultrasonically.

- LCPs are highly impermeable to water, ions and other gases.

5. Polymer Packaged Based Antenna Development

The overall objective of this work is to develop a low cost, low profile, lightweight integrated MMIC based thin active receiver front end array for microwave systems using multilayer liquid crystal polymer multichip modules as a packaging medium. Our technique features several innovations. These include:

- High sensitivity, low noise figure to meet G/T with LNAs directly connected to antenna elements.

193

- Multiple layer substrate liquid crystal polymer suitable for low noise PHEMT amplifier, phase shifter, and mixer MMIC chip interconnections and patch antenna arrays.

- Slot coupled vertical transmission line interconnects eliminating the need for hard-wired vertical interconnects having 50 ohms impedance. This improves efficiency because VSWR is consistent and tedious assembly labor operations are eliminated. Electrical performance is repeatable since only controlled dimensional properties affect it.

- Flip chip bumped MMIC and silicon chip insertion can be employed, further eliminating the need for hundreds of wire bonds. This technique also will result in lower VSWR for microwave interconnections since reactive inductance of wirebonds is eliminated.

- Inverted stripline circular patch construction will permit all active electronics requiring moisture seals to be embedded within the confines of the LCP peripherally sealed to promote hermeticity.

- Electromagnetically coupled parasitic elements will provide increased gain or bandwidth as needed. These eleme ` are placed on the outside surface of the antenna face.

- Thermal management is achieved by use of thermal vias and heat sink pedestals. Transistor junction temperatures are held to less than 150°C in spite of assumed ambient/heat sink temperatures of 125°C.

- High reliability (high MTBF) is achieved by eliminating wire bonds through bumping chips, good heat transfer, even distribution of heat dissipating devices throughout the module, and use of prescreened, reliable chips.

- Grating lobes are minimized. 3-D layered construction permits close (1/2 wavelength) spacing of antenna elements.

- Processes for integral capacitors and resistors with LCP substrates will be developed and used in demonstration vehicles.

Electronically steered phased array antennas have numerous applications in both military and commercial applications. Specifically identified military applications that we are targeting this technology demonstration for include the MILSATCOM program as well as MILSTAR, and DSCS, along with the previously mentioned Global Broadcast Service and Direct Broadcast Service.

Promising commercial applications include worldwide telephone networks using satellites, land-based voice and data communications, direct broadcast satellites, unmanned vehicles, tracking and location devices, commercial aviation, security surveillance, navigation, collision avoidance and meteorology.

6. Summary of Research Results to Date

During the last year we successfully demonstrated the following:

- That aperture coupled circular patch antennas work extremely efficiently with liquid crystal polymer dielectrics, replacing more expensive quartz or foamed dielectric materials.

- That these antennas and MCM packages can be easily fabricated with low cost conventional printed circuit board processing.

- That our proposed multilayer microwave packaging can effectively manage the flow of heat out of the power amplifiers devices into an integral heat sink and from there out to the system cooling.

- That a linear or rectangular array could be designed with our proposed technology that would enable 1/2 density while providing low cost assembly because of innovations such as the slot aperture coupled vias for RF signals, blind vias and flex circuit techniques for routing digital and control circuits,

- That significant savings can be achieved by utilizing flip chip attachment with conductive polymers and by replacing hand soldered discrete components with integral resistors fabricated onto the LCP circuits.

- That this overall package will have significant reliability because of the assembly methods, the management of heat, and the low CTE of the LCP and heat sink.

7. References

[1] K. Jayaraj, T. E. Noll and D. R. Singh, "A Low Cost Multichip Packaging Technology for Monolithic Microwave Integrated Circuits," *IEEE Transactions on Antennas and Propagation*, Vol. 43, No. 9, September 1995.

[2] K. Jayaraj, Thomas E. Noll, and Donald Singh, "RF Characterization of a Low Cost Multichip Packaging Technology for Monolithic Microwave and Millimeter Wave Integrated Circuits," *ISSSE*, October, 1995.

[3] J.A. Navarro , et al, "A 29.3 GHz Cavity Enclosed Aperture-Coupled Circular-Patch Antenna for Microwave Circuit Integration," *IEEE Microwave and Guided Wave Letters*, Vol 1, No 7, July 1991.

[4] David M. Pozar, "A Practical Guide to Microstrip Antenna Design," Presentation at Hanscom AFB, May 1994.

[5] I. J. Bahl, P. Bhartia, *Microstrip Antennas*, Artech House.

[6] E. Levine et al, "A Study of Microstrip Array Antenna with the Feed Network," *IEEE Transactions on Antennas and Propogation*, Vol. AP 37, pp 426-434, April 1989.

[7] Glam-Minh Luong and Kai Chang, "Analysis and Development of a Broadband Interconnect for Microstrip Lines," *Microwave and Optical Technology Letters,* Vol. 5, No. 8 July 1992.

[8] Chien-Hsun Ho, Lu Fan, and Kai Chang, "Slot-Coupled Double-Sided Microstrip Interconnects and Couplers," *1993 IEEE MTT-S Digest,* pp. 1321-1324.

A Flexible, Multifunction Communications Antenna

T. R. Holzheimer

Raytheon E-Systems

Greenville Division

Greenville, Texas   75403

Abstract:

    Certain applications are constrained in available
surface area for the location of multiple antennas. A task
was undertaken in order to combine several communication
antenna functions into one single aperture and install the
resultant antenna on a given surface. A flexible (pliant)
and multifunction communications antenna was developed,
fabricated and tested for potential installation on a
multitude of different shaped surfaces. The antenna was
required to have a minimum of 3 inches of flexure across the
corner to corner diagonals. The height of the antenna was
designed to be less than 3.75 inches. The maximum size of
the antenna is 19 inches by 19 inches square. The
performance degradation of the antenna was to be minimized
with flexure and still provide the necessary communications
links. The antenna provides communications capability in
the UHF and VHF bands with L-Band receive capability for L1
and L2 GPS. The VHF portion of the antenna was capable of
handling 50 Watts of CW power while the UHF portion was
capable of handling 200 Watts of CW power. The UHF portion
of the antenna was designed to have both a high angle and a
low angle mode of operation. The four RF ports of this
antenna were designed for simultaneous operation. A
secondary issue was the development and testing of an
installation method allowing for a nondestructive removal of
the antenna. Several design modifications had to be
implemented in order to reduce mutual coupling between the
various communication functions. All modes were successful
except for low angle UHF and results are presented
illustrating the achieved performance of this flexible
multifunction antenna.

1.0 Introduction:

A large number of antennas exist on structures with one antenna for each function and frequency band of interest. Locations to install multiple antennas can quickly disappear as a result of lack of available surface area. Typical solutions are to combine antennas and/or delete antennas and frequency bands from the available surface area.[1] However, a major installation problem still exists which is mating the antenna(s) to the arbitrarily shaped available surface. The solution requires a pliant antenna that combines multiple antennas and frequency bands into one aperture.

Dealing with multiple communication antennas easily illustrates the additional problem of multiple separate antennas. Lack of available surface area to install additional antennas and the potential for coupling of one transmitter to another become serious problems. The classic solution is to increase the spacing between the antennas in order to minimize this coupling. The lack of available surface area quickly becomes the limiting factor in how many antennas can be placed on a particular structure. The standard requirements such as field-of-view must still be met. Multifunction antennas are a solution, but without some modifications to the antenna, they are usually designed to match a particular surface. An antenna that is capable of being installed on a multiple of surfaces is desired and is best handled by a pliant antenna design.

This has been investigated by several different groups with varying degrees of success. Each antenna has its limitations such as surfaces it can be installed on and still survive as well as how many antennas are combined in the aperture. An array antenna has been built that can be taped to a minimally bent set of flat surfaces and then

rolled up into a tube when not in use.[2] Another antenna is built to look like a cushion which is laid on an available surface, but has only a maximum of two functions combined into a single aperture.[3] These antennas do not attempt to combine multiple communication functions into a single aperture.

The focus of this study was to develop a pliant antenna that could be installed on a group of arbitrary surfaces with three functions combined in a single aperture. The functions that were combined in this aperture design are VHF, UHF and GPS. The VHF and UHF are both transmit and receive while GPS is receive only. The priority on GPS was for the L2 frequency, but both L1 and L2 were considered.

2.0 Antenna Requirements:

A pliant, multifunction communications antenna was designed for implementation on several different shaped surfaces. The antenna had to have a minimum of three inches of flexure from corner to corner along the fore to aft line of the antenna. See figure 1 for a drawing of the antenna defining the localized directions. The maximum dimensions that the antenna is allowed are 3.75 inches in height and 19 inches square. Communications capability was required in the UHF and VHF frequency bands. The requirements are summarized in Table I.

VHF Element

GPS
Element

UHF Element

FORE

PORT

STARBOARD

CONNECTOR BLOCK

AFT
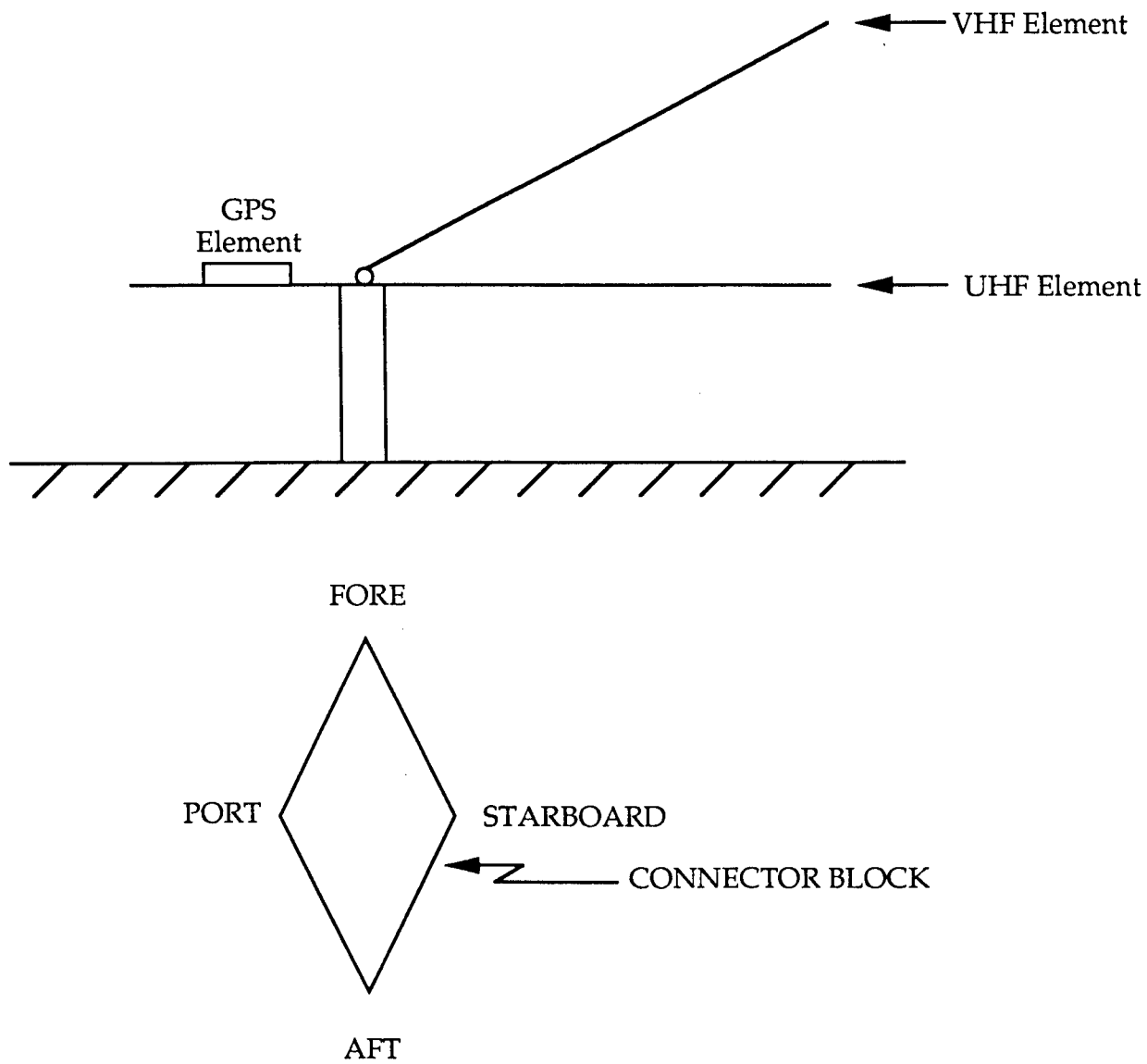
Figure 1.   Multifunction Communication Antenna Drawing
With Directions.

Table I. Multifunction Communication Antenna Requirements

Frequency Bands:
    VHF - 118 to 136 or 136 to 174 MHz with (118 to 174 MHz desired)
    UHF - 240 to 320 MHz
    GPS - L1 and L2

Polarization:
    VHF - Vertical
    UHF High Angle (mode 0) - RHCP
    UHF Low Angle (mode 1) - Vertical
    GPS - RHCP

Azimuthal Coverage:
    360 degrees

Elevation Coverage:
    VHF - Standard Monopole Coverage
    UHF High Angle - Upper Hemisphere
    UHF Low Angle - Monopole Coverage

Gain :
    VHF - 0 dBli
    UHF High Angle - +3.5 dBic
    UHF Low Angle - + 3 dBli
    GPS - + 3 dBic

VSWR:
    VHF - 2.0:1 with 2.5:1 maximum
    UHF - 2.0:1 with 2.5:1 maximum
    GPS - 2.0:1 maximum

Power Handling:
    VHF - 50 Watts CW
    UHF - 200 Watts CW
    GPS - Receive Only

Weight:
    25 Pounds or Less

Size:
    19 Inches Square, 3.75 Inches in Height

An additional mechanical requirement to withstand pressure was imposed of 2.0 psi (4.0 psi utlimate) on the edges and 10 psi (20 psi ultimate) on the top surface.

Lastly, the antenna had to be easily attached and removed without the addition of any holes to the surface it was to be attached to. This requirement imposed the greatest design and construction effort. Ultimately, the antenna had to be mounted via an insulating layer. An antenna mount incorporating an insulating layer solved the problem.

3.0 The Multifunction Antenna Solution:

The antenna that met the above requirements is pictured in figures 2 thru 4. The antenna is pliant with the required 3 inches of flexure from Fore to Aft. The antenna weighed 20 pounds and exceeds the requirement by a 5 pound reduction. The antenna met the size constraints and all power handling required for each frequency band. The full VHF frequency band was met with one whip antenna appropriately slanted for wind handling. The only capability that requires additional work was the low angle or mode 1 gain for the UHF frequency band.

The antenna is layout is shown in figure 1. The UHF antenna was a four point fed, air loaded, microstrip patch antenna.[4] The GPS antenna was a dual stacked microstrip patch antenna. The VHF antenna was the classic whip design. Figure 5 shows the network used in the UHF portion of the antenna. The four feed points provide dual linear polarized outputs and when correctly summed both senses of circular polarization become available. In this case only right hand circular polarization was desired as illustrated by the loading of the other port. Each pair of opposite side feed points are summed thru a 180 degree hybrid for linear polarization. The two linear polarization's, which are 90
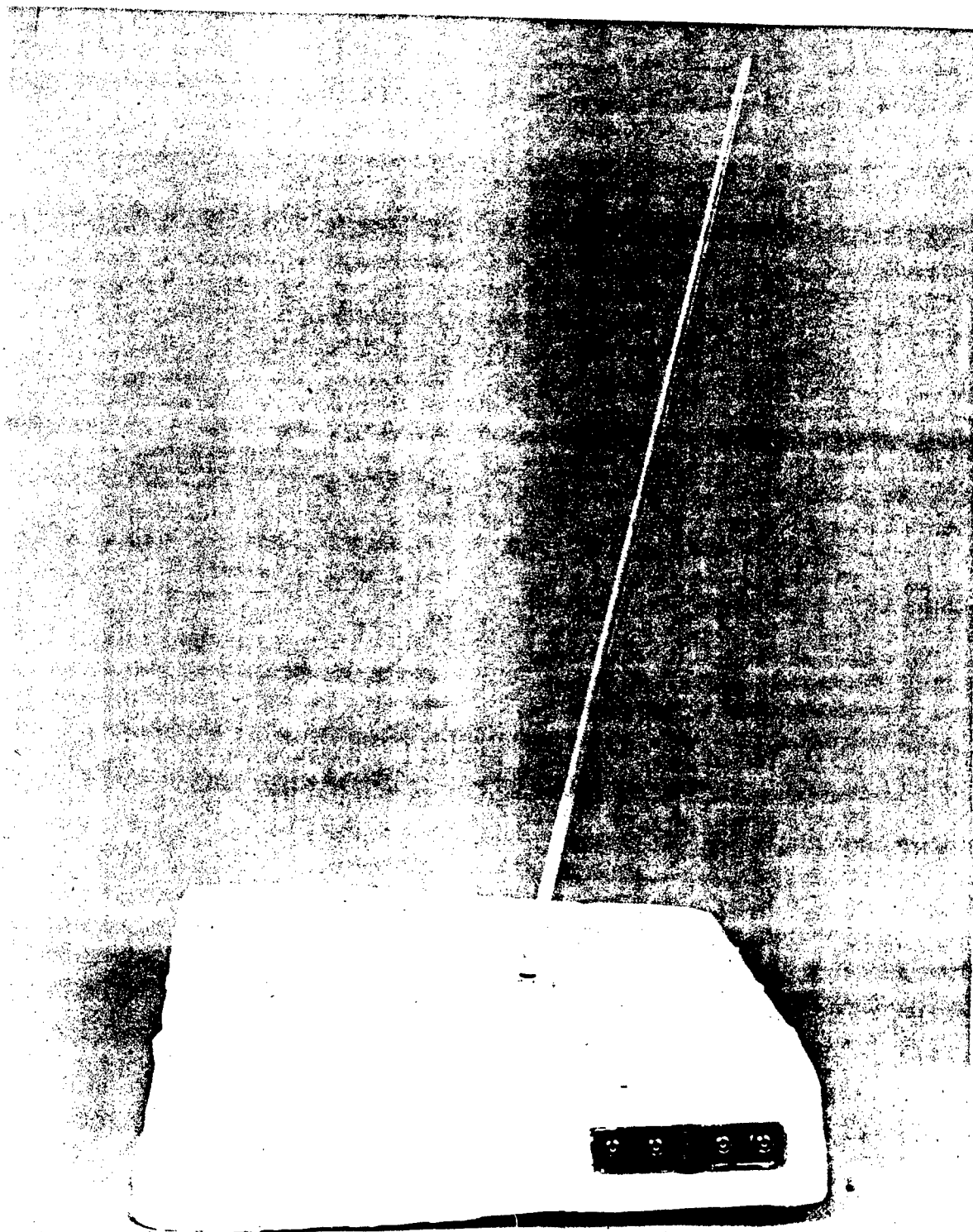
Figure 2. Multifunction Communication Antenna Side View.
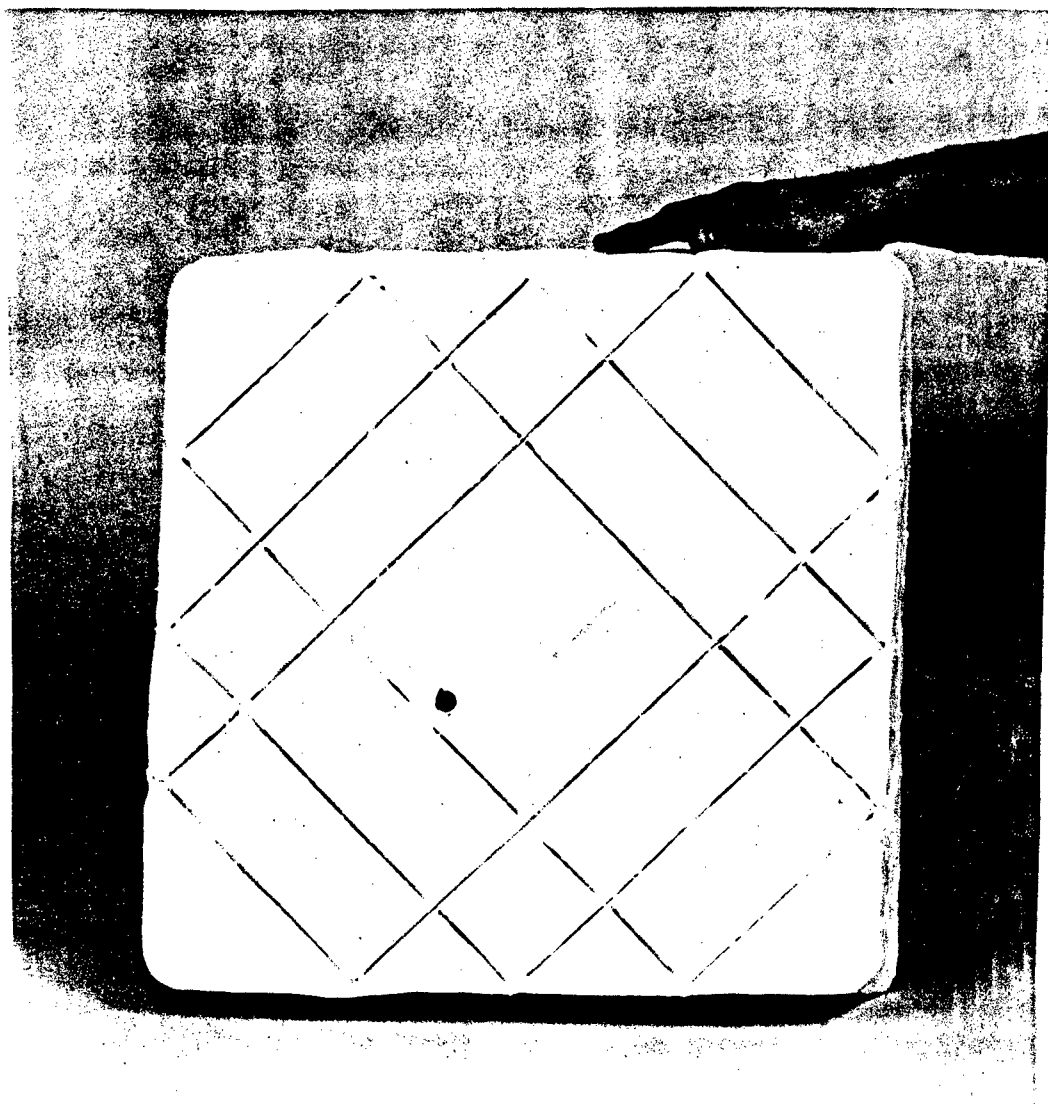
Figure 3. Multifunction Communication Antenna Top View
Without Whip Antenna.
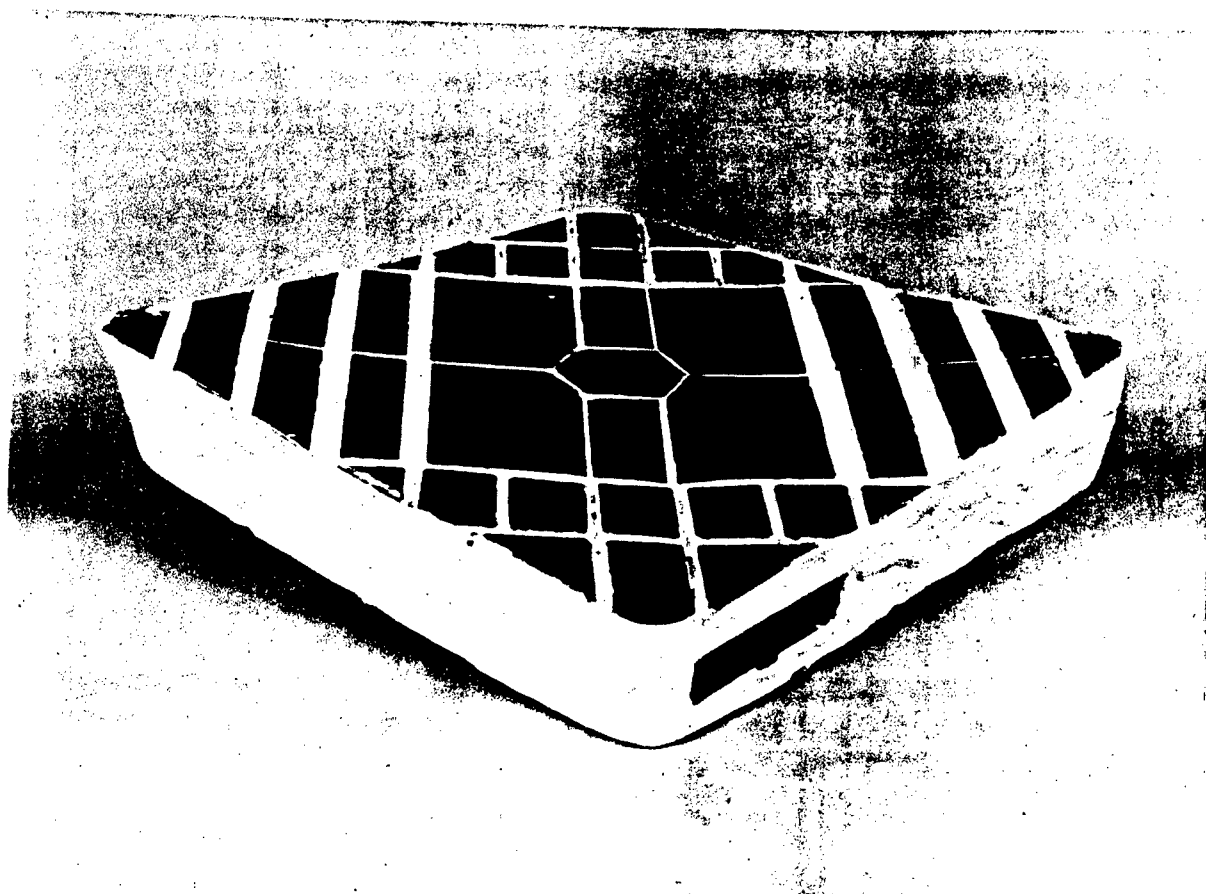
Figure 4. Multifunction Communication Antenna Back View.
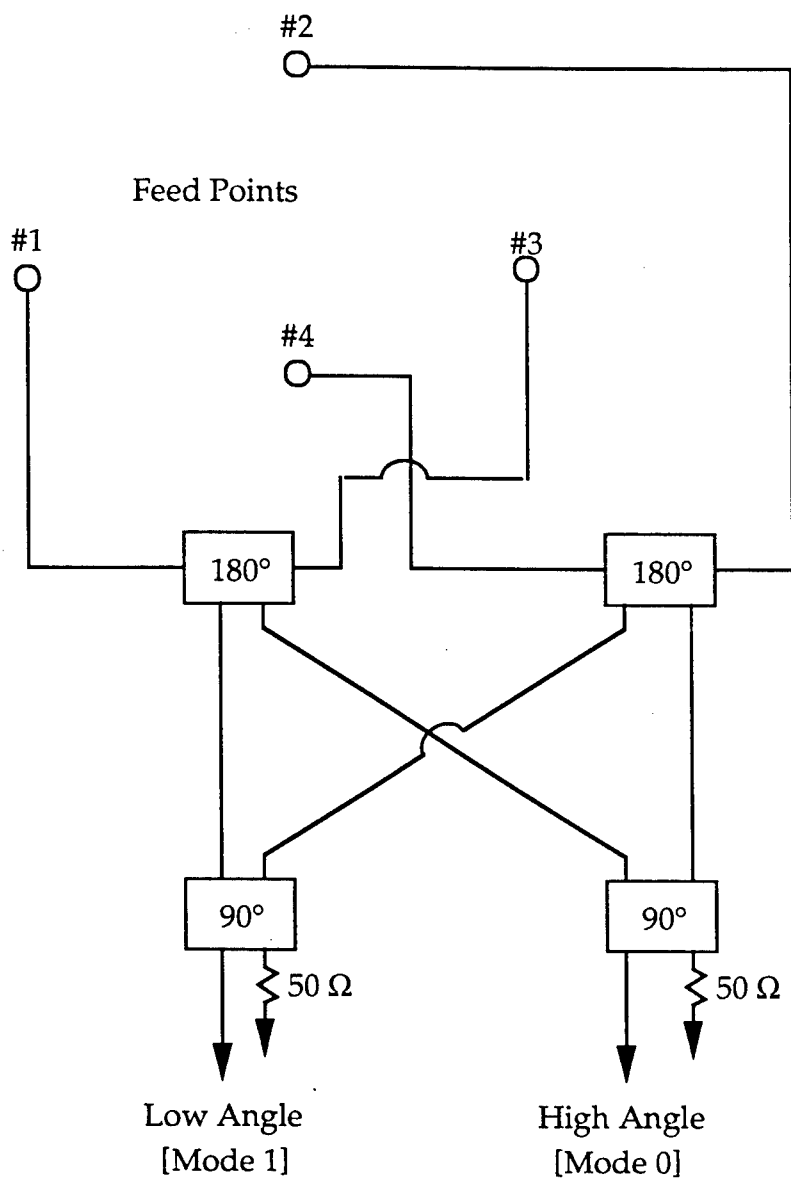
Figure 5. UHF Feed Network Diagram For The Multifunction Communication Antenna.

degrees apart, are then summed in a 90 degree hybrid in order to provide circular polarization. The other two outputs of the 180 degree hybrids are summed in another 90 degree hybrid which results in the low angle or mode 1 of the UHF portion.

The antenna center is at a zero field point and is thus grounded via a metallic cylinder. Figure 6 shows the internals of the antenna prior to the addition of the feeds, cables and microstrip patch. The cylinder is also shown in figure 6. The VHF antenna is fed from the top of the cylinder with a standard matching network into a whip antenna. The whip antenna was slanted back 30 degrees from zenith. The matched antenna met the desired full frequency band of operation from 118 to 174 MHz.

The GPS antenna mounts off to the side of the VHF whip and on top of the UHF antenna. There was a slight amount of tuning needed to bring the L1 frequency VSWR into specification compliance which was high due to the covering attached to the whole outside of the antenna. Test results along with problems encountered are described and discussed in the next section.

4.0 Design Problems and Resolutions:

Two antenna functions interacted with each other while the third function remained unaffected. The antenna function that was unaffected by the other two designs was the GPS antenna. This occurred because a filter was designed to be inline with the GPS antenna feed and is housed inside the cylinder supporting the VHF whip antenna. The frequency separation of almost two octaves also helped minimize any potential interactions due to the other functions. The functions that interacted were the UHF and the VHF functions.
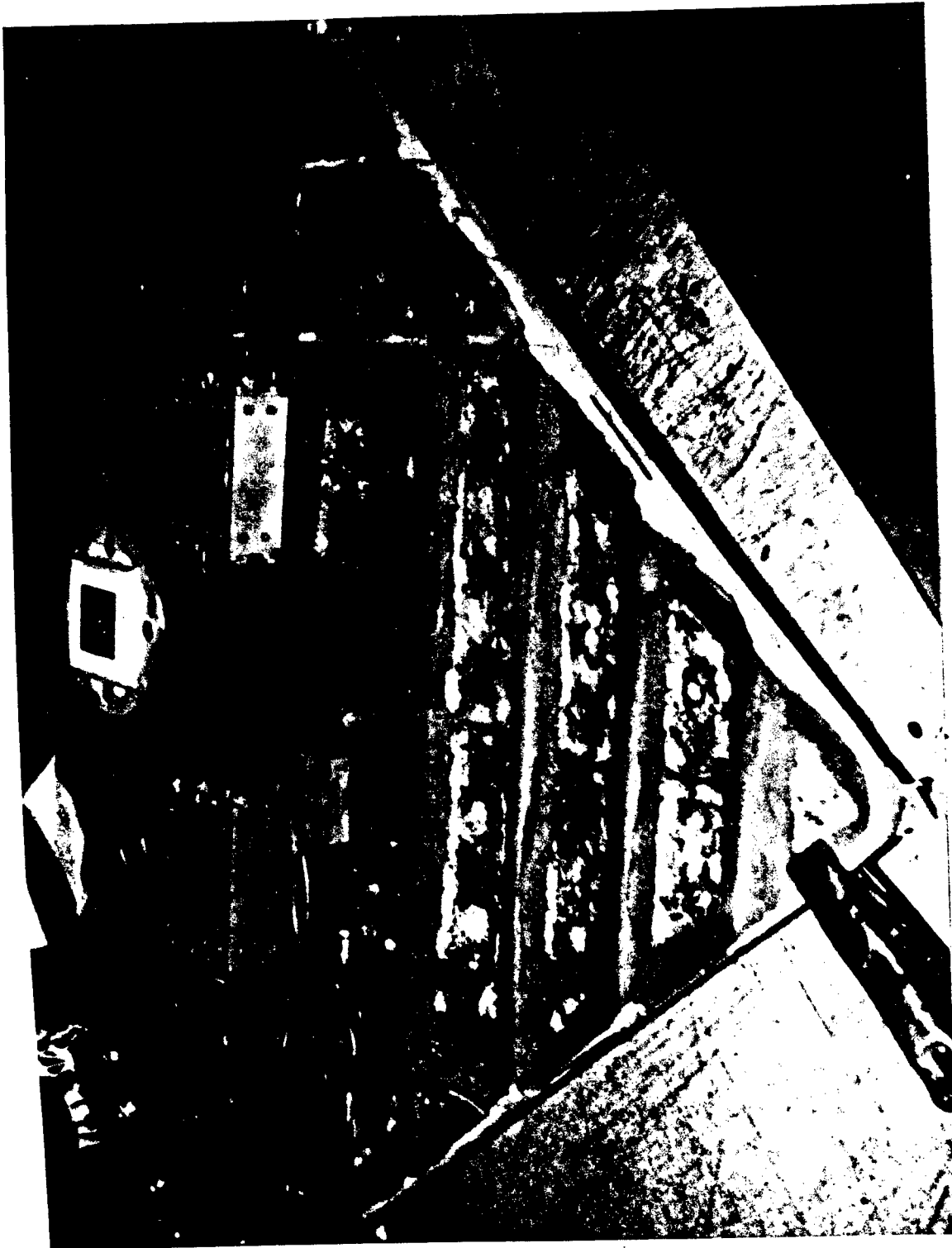
Figure 6.   Internals Prior To Full Assembly of The
                    Multifunction Communication Antenna.

The VHF antenna interacted with the UHF antenna due to the close proximity of the VHF whip mounted on the UHF patch and the fact that there was only 66 MHz of frequency separating the high end of the VHF band from the low end of the UHF portion of its frequency band. This caused a very high VSWR to appear at the VHF antenna output. This VSWR was reduced to less than 2.5:1 by the addition of an inductance and small amount of attenuation via a length of coiled transmission line located inside the metallic cylinder of the antenna. The 2.5:1 maximum VSWR is essential due to transceiver protection circuitry.

The UHF portion of the antenna experienced the greatest problems. The matching of the feed points changed as the antenna is given curvature from the flat condition. This was fixed by designing the feed points in such a way so that the impedances measured on each feed were close to identical in shape on the Smith Chart. Figure 7, shows the before impedance plots prior to addition of matching transmission lines. The transmission lines were connected at the ground plane in order to ensure good grounding of the outer transmission line shield and to provide for physical hard mounting points.

The UHF portion of the antenna was also the most affected by attachment to the appropriate surface to which it was installed. The antenna was installed in all cases via an insulating layer. This provided the means for removal of the antenna without affecting the surface it was attached to and without destroying the antenna. Figures 8 and 9 illustrate the problem encountered when the antenna is loosened from the ground plane by removal of the insulating layer. Figure 8 is with the insulating layer in place, and figure 9 shows the effect when the insulating layer is not intact. Both figures are of gain and when the insulating layer disappears the gain also drops off dramatically as

Feed 1

Feed 2

Feed 3

Feed 4
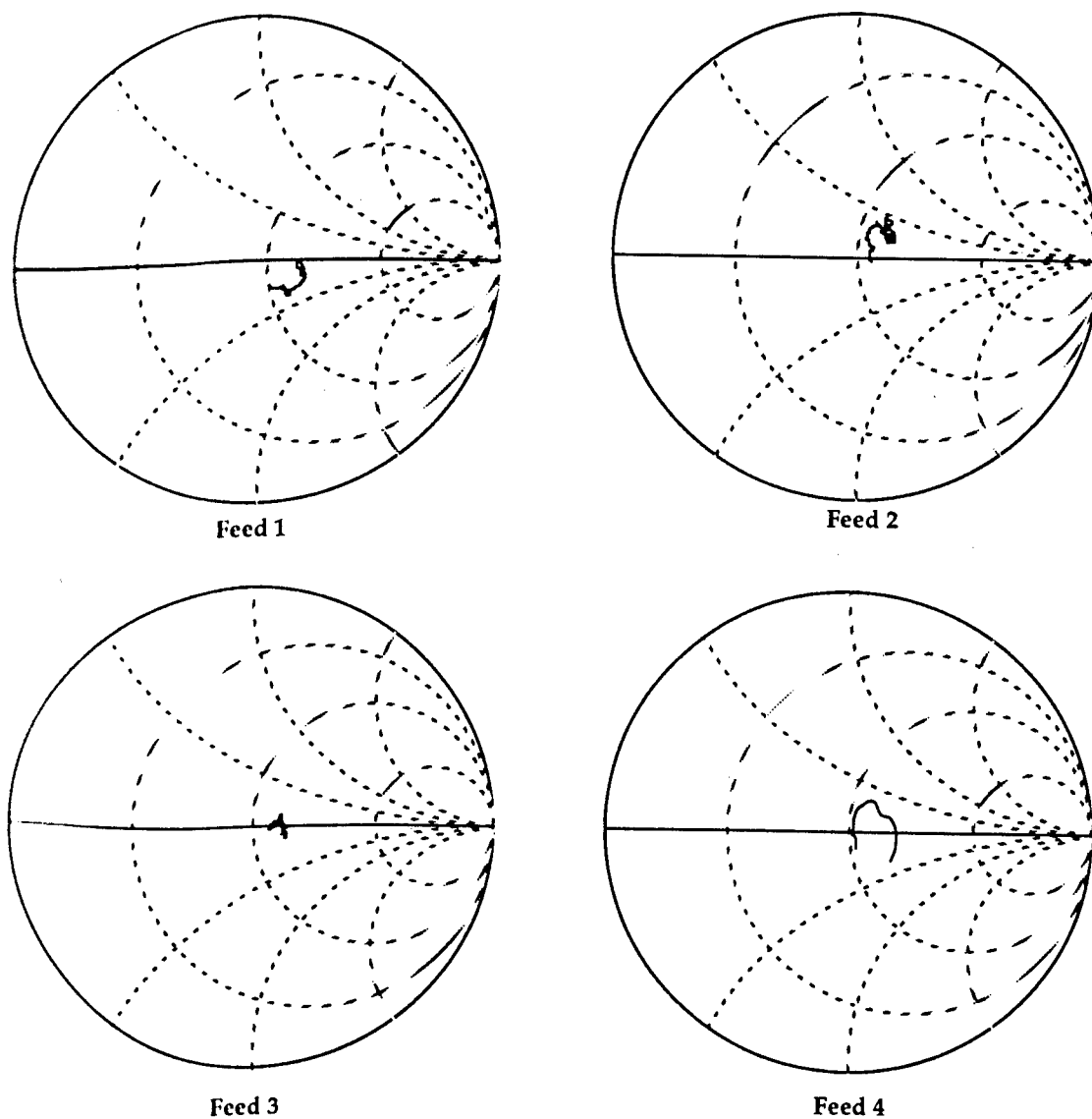
Figure 7   Impedance Plots of the Four Feed Points for the
UHF microstrip Patch Antenna Portion.
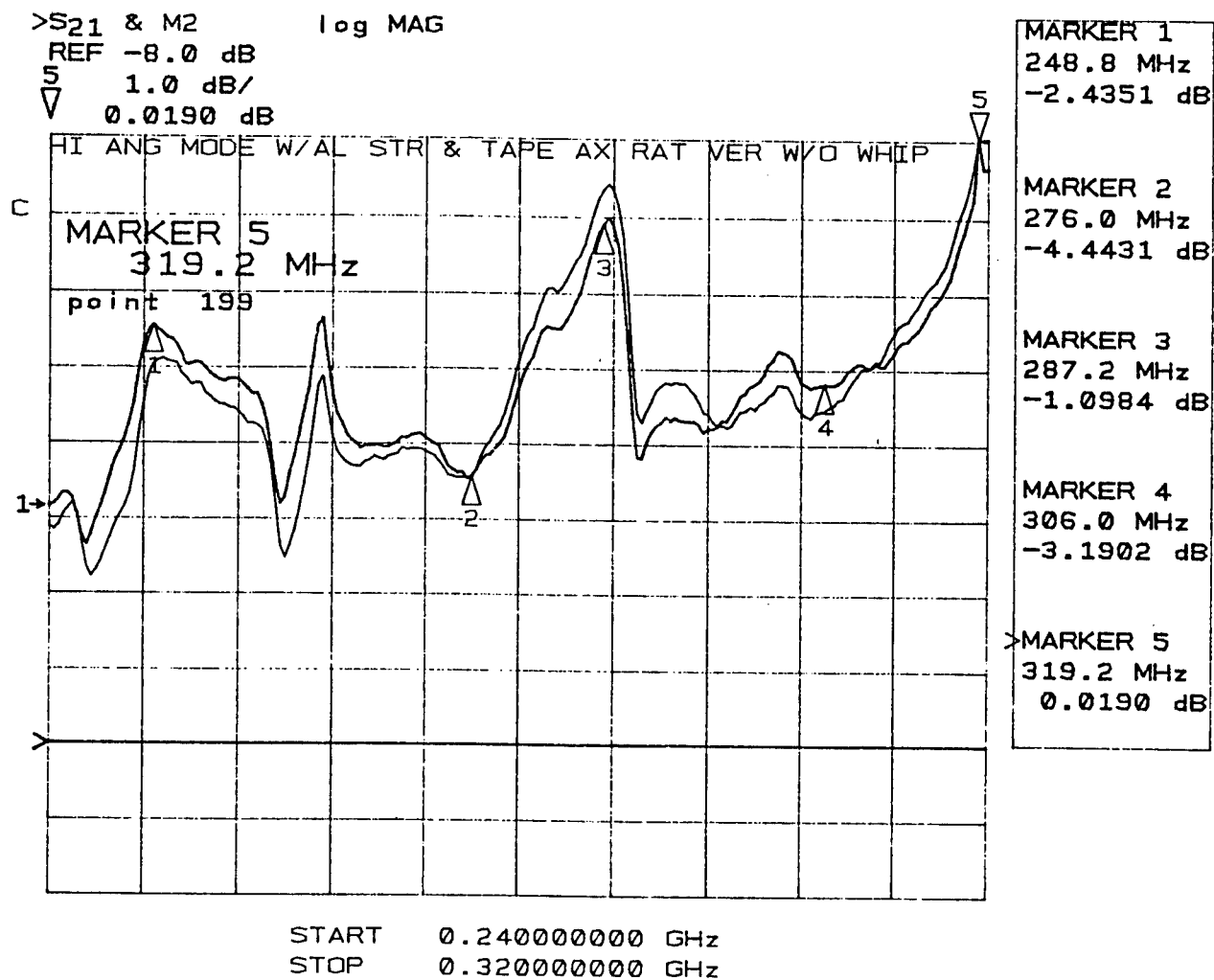
Figure 8   UHF Portion High Angle (Mode 0) gain versus
Frequency correctly Installed.
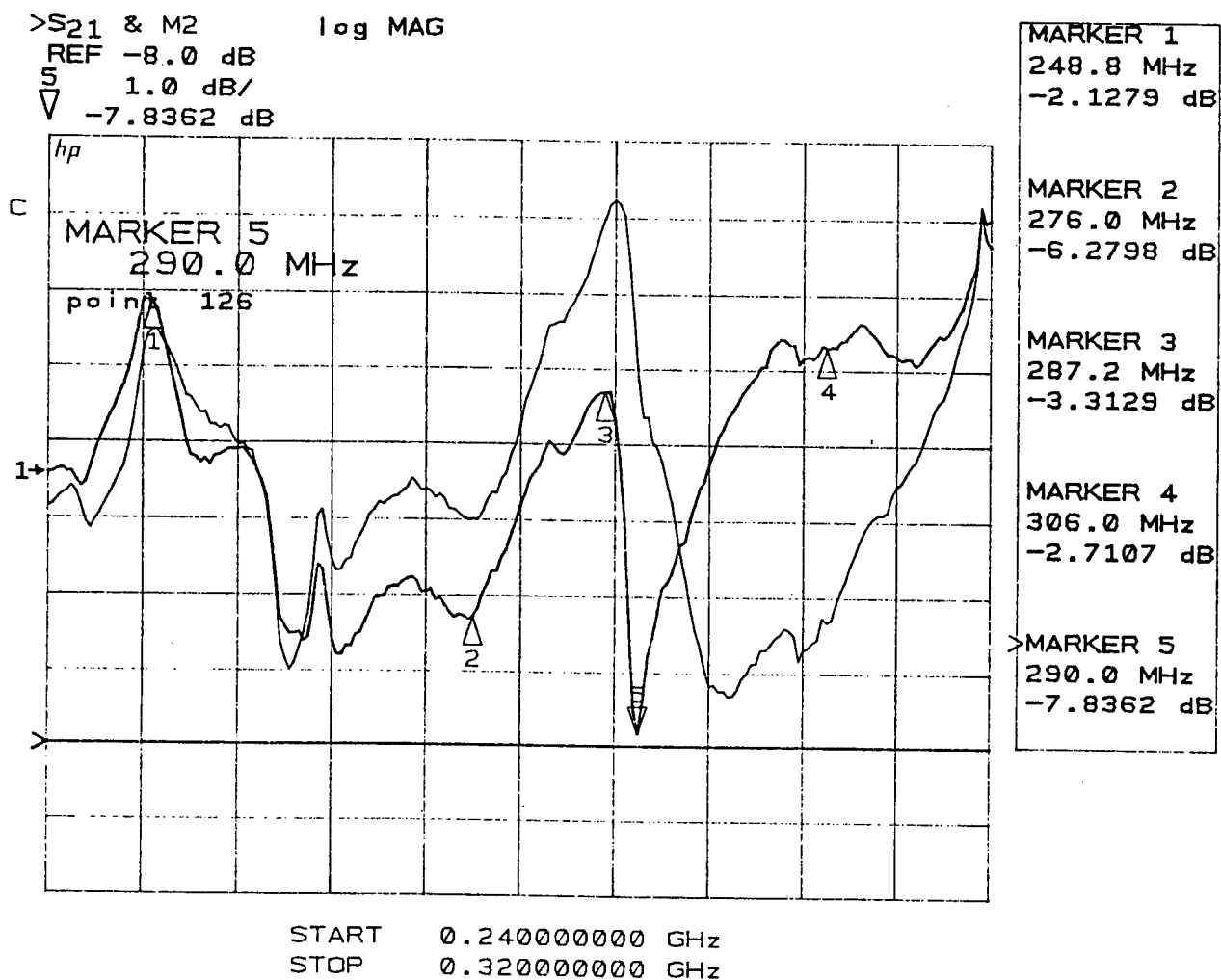
Figure 9. UHF Portion High Angle (Mode 0) Gain Versus
Frequency incorrectly Installed.

213

shown in figure 9. The antenna is matched in the configuration where the insulating layer is intact. This illustrates that the antenna is highly installation dependent as expected.

Based on the results shown in figures 8 and 9 a proprietary method was developed for installation and removal of the multifunction communication antenna. This installation method used an insulating material which could be easily removed. The test results shown in the following figures used the proprietary installation.

5.0 Multifunction Antenna Measurements:

Measurements of VSWR were made on all four ports of the multifunction antenna. They are shown in figures 10 thru 13. The GPS VSWR curve of figure 10 meets the specification for L2 and with slight tuning will meet those for L1. Due to available field test time, tuning of L1 was postponed. The VHF function, see figure 11, exhibited a worst case VSWR of 2.4:1 which is still below the required 2.5:1. The UHF high angle mode had a worst case VSWR of 1.5:1 as shown in figure 12. Part of the VSWR is low due to masking by the hybrids involved in the network of figure 5. The low angle mode exhibited the worst VSWR, as shown in figure 13, of 3.4:1.

Radiation patterns were made of the UHF high angle mode and are shown in figures 14 and 15. The radiation patterns, in figure 14, show a slight skewing at the high end of the frequency band of approximately 10 degrees. After remeasuring the high end it was discovered that the pattern shown was outside of the desired operating frequency band. The single frequency UHF function patterns shown in figure 15 show excellent balance in the 3 dB beamwidth and in gain.
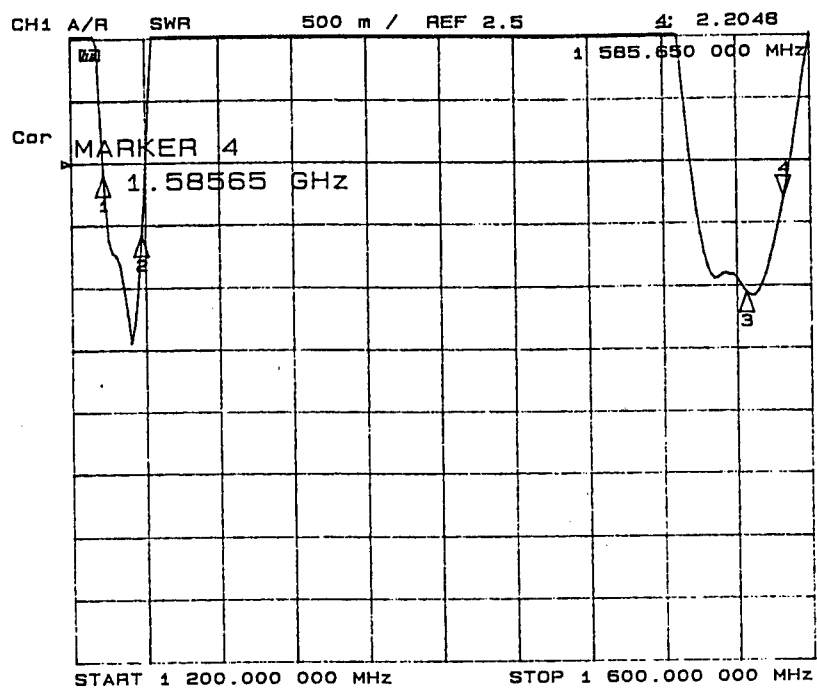
Figure 10.   GPS Function VSWR versus Frequency.
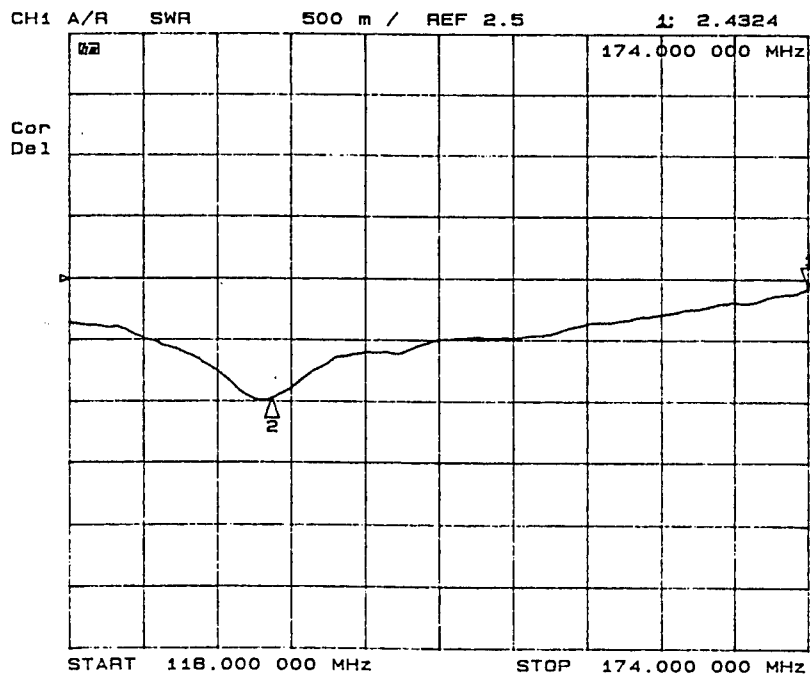
Figure 11.   VHF Function VSWR versus Frequency.

215
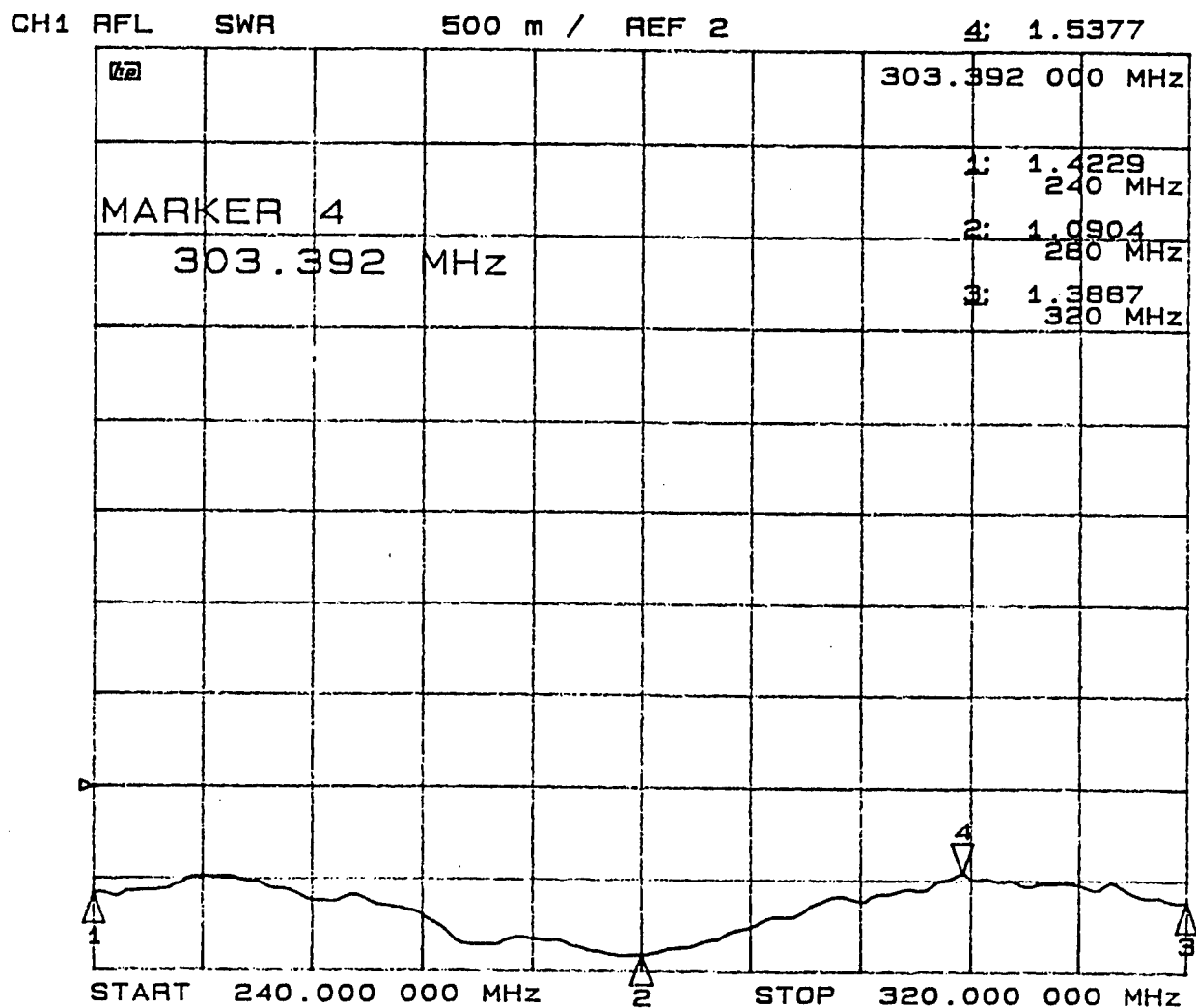
Figure 12. UHF Function High Angle (Mode 0) VSWR Versus
Frequency.
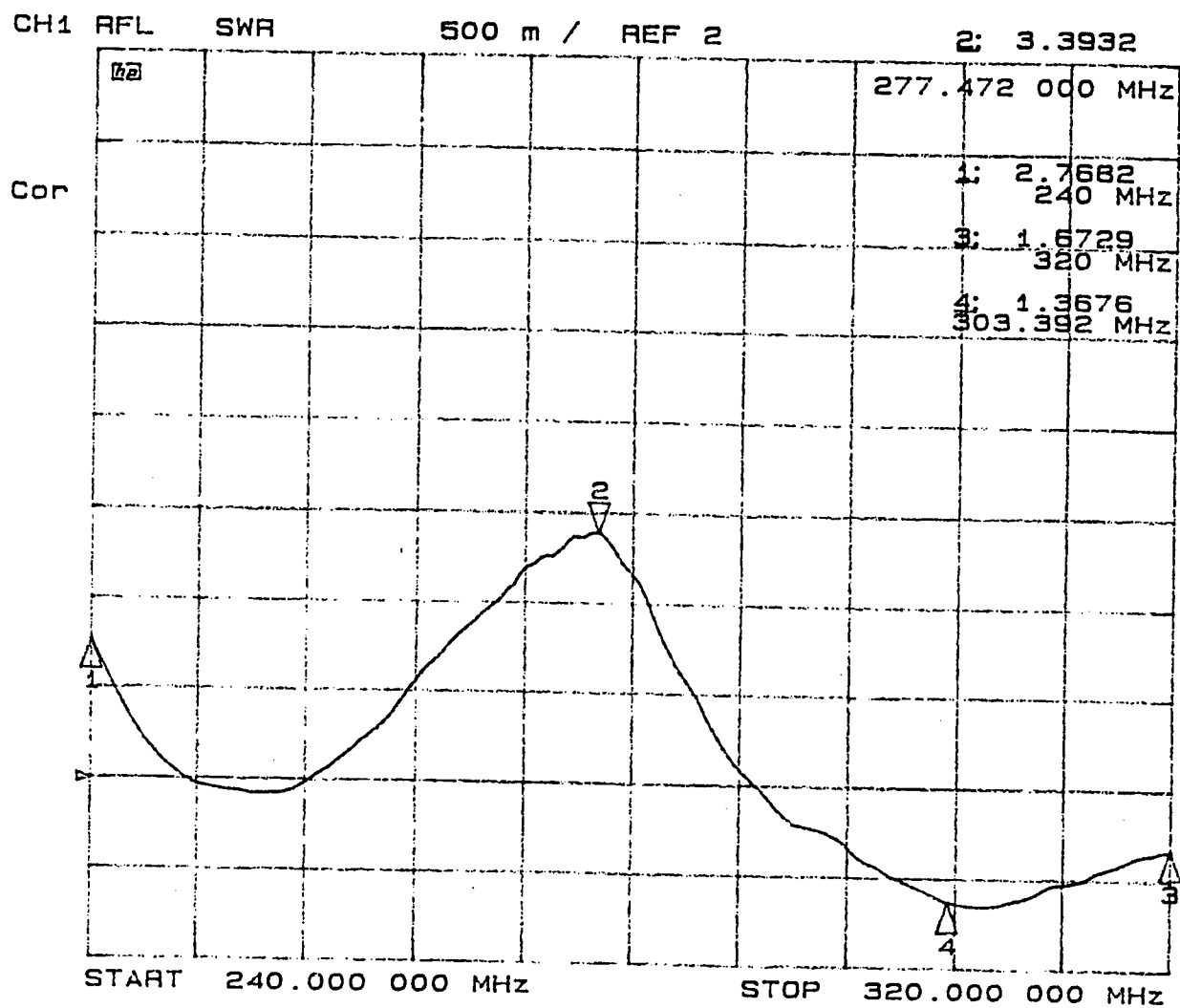
Figure 13. UHF Function Low Angle (Mode 1) VSWR Versus
Frequency.
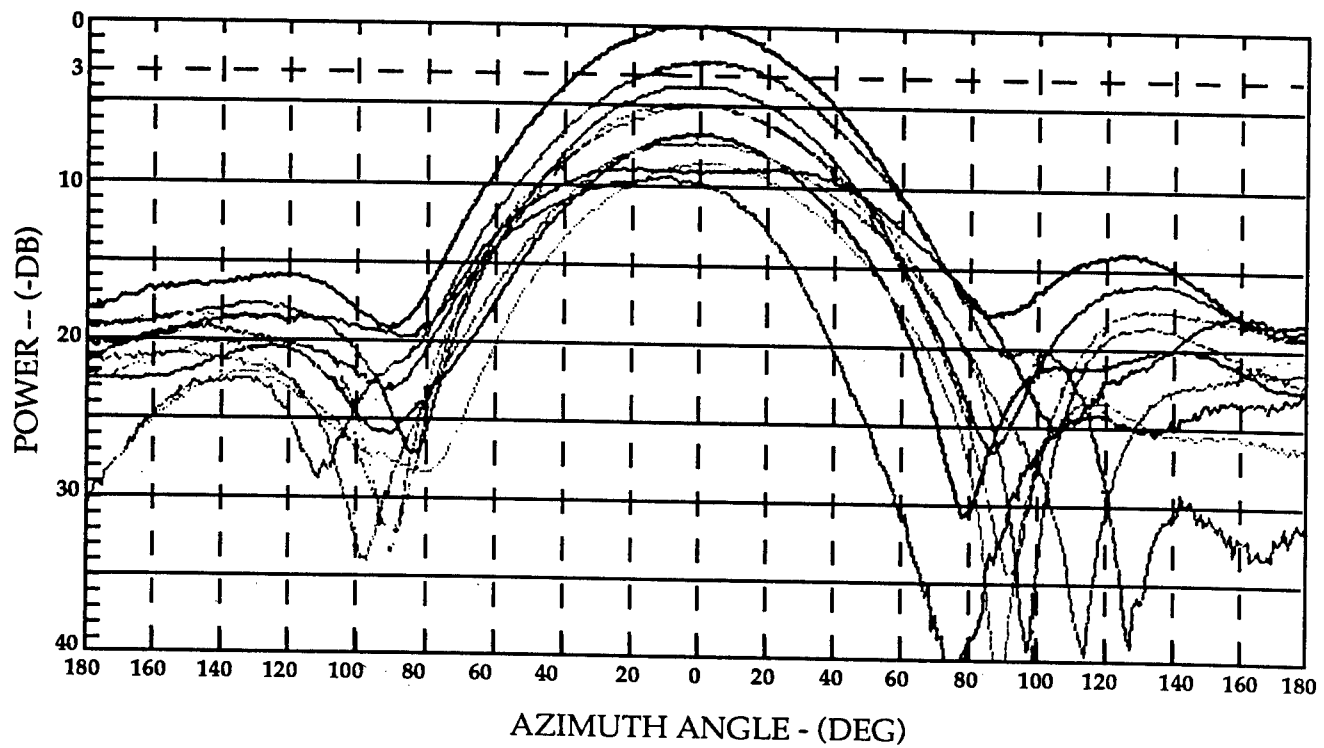
Figure 14. UHF Function High Angle (Mode 0) Radiation
Patterns Across the Frequency Band.

218

27 Mar 1995
.248 GHz

27 Mar 1995
.304 GHz
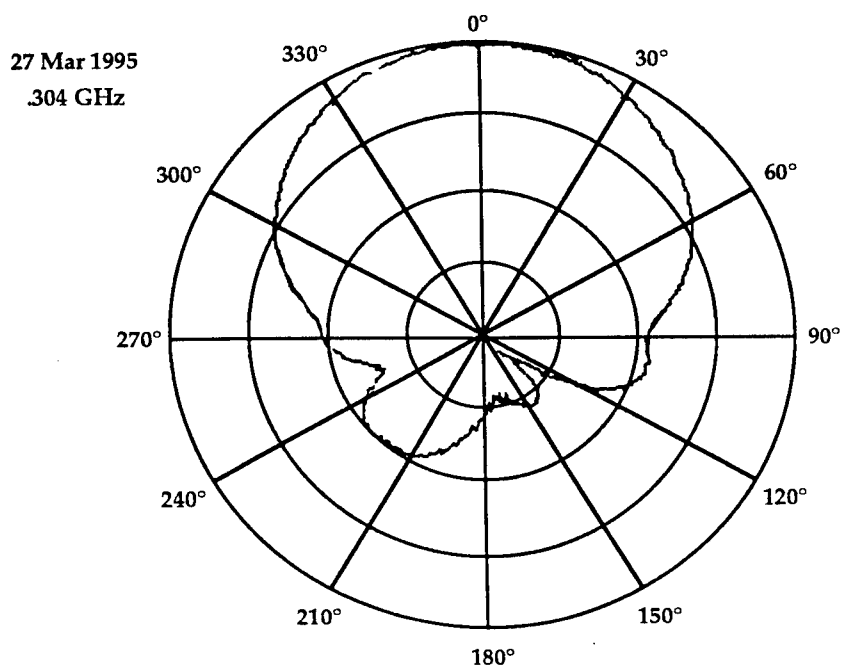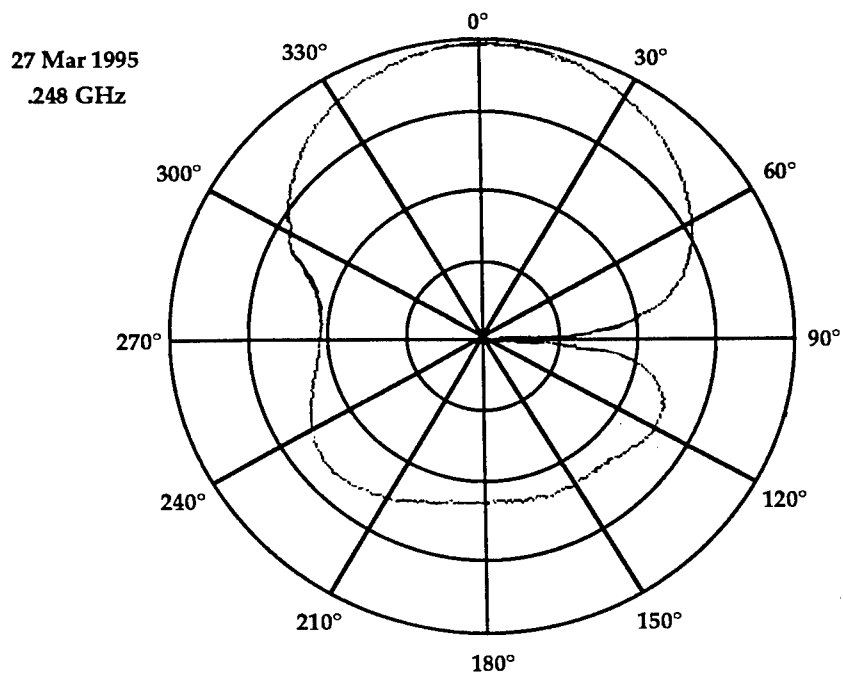
Figure 15. UHF Function High Angle (Mode 0) Radiation
Patterns at Frequency = 248 and 302 MHz.

The gain of the UHF function high angle mode met the +3.5 dBic gain requirement. This was determined by measuring the antenna with a linear source and then measuring the axial ratio. These values were then put through the equations summarized in succinct form in the appendix of this paper.[5], [6]

The UHF low angle mode failed to meet the specified requirements, never the less it exhibited excellent radiation patterns as shown in figures 16 thru 18. Figure 16 is a pattern in the fore to aft direction while figure 17 is in the port to starboard direction. Figure 18 is an azimuthal radiation pattern. The patterns were best in expected shape at the low end of the band, but deviated as the frequency rose to the high end of the frequency band. Part of the deviation is attributed to an antenna installation problem detected after the tests were performed.

A typical radiation pattern of the VHF function is shown in figure 19. The pattern is as expected matching a typical monopole shape with a gain of +5 dBli at 136 MHz.

A typical radiation pattern of the GPS function is shown in figure 20. The pattern is as expected matching a typical radiation pattern shape with a gain of +3.0 dBic at 1227 MHz.

6.0 Summary:

The multifunction antenna described above met the requirements of table I except for the low angle mode gain. The GPS function requires some slight tuning of L1, but it met the minimum requirements and was not pursued at this time. Flexibility was obtained and a proprietary method of installation and removal was successfully implemented.
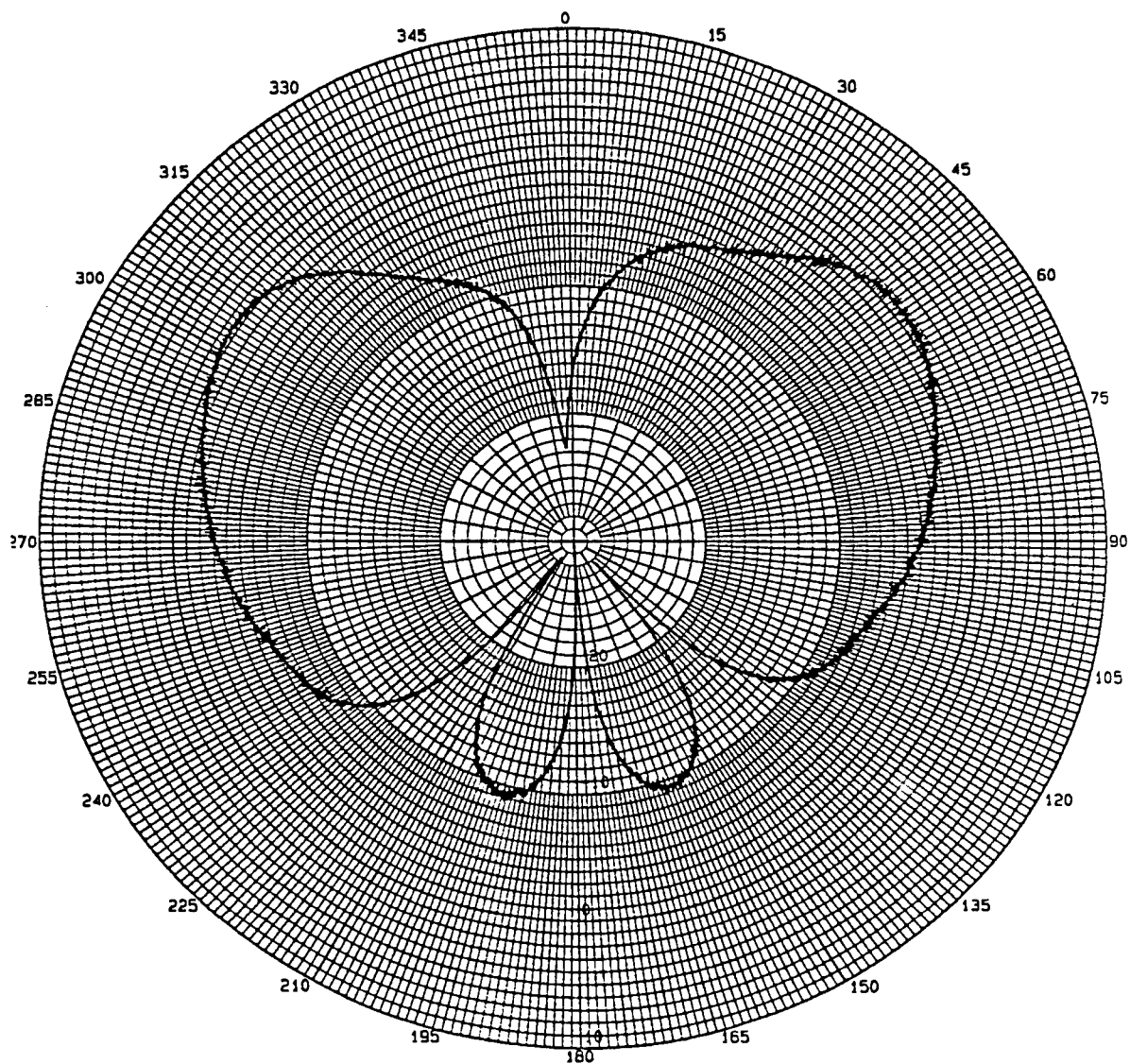
Figure 16. UHF Function Low Angle (Mode 1) Radiation
Pattern (fore to aft) at Frequency = 240 MHz.

221
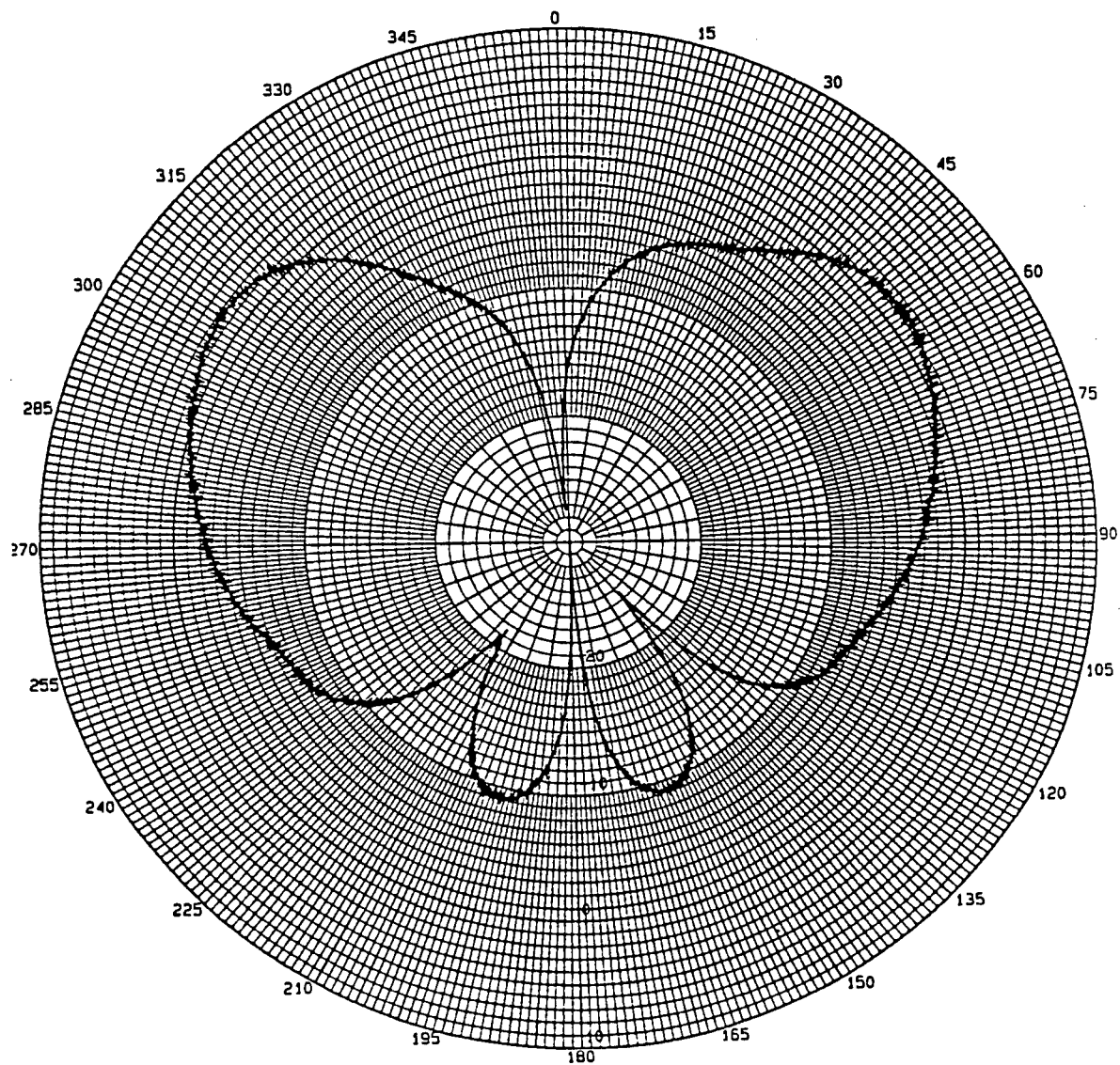
Figure 17. UHF Function Low Angle (Mode 1) Radiation
            Pattern (port to starboard) at 240 MHz.
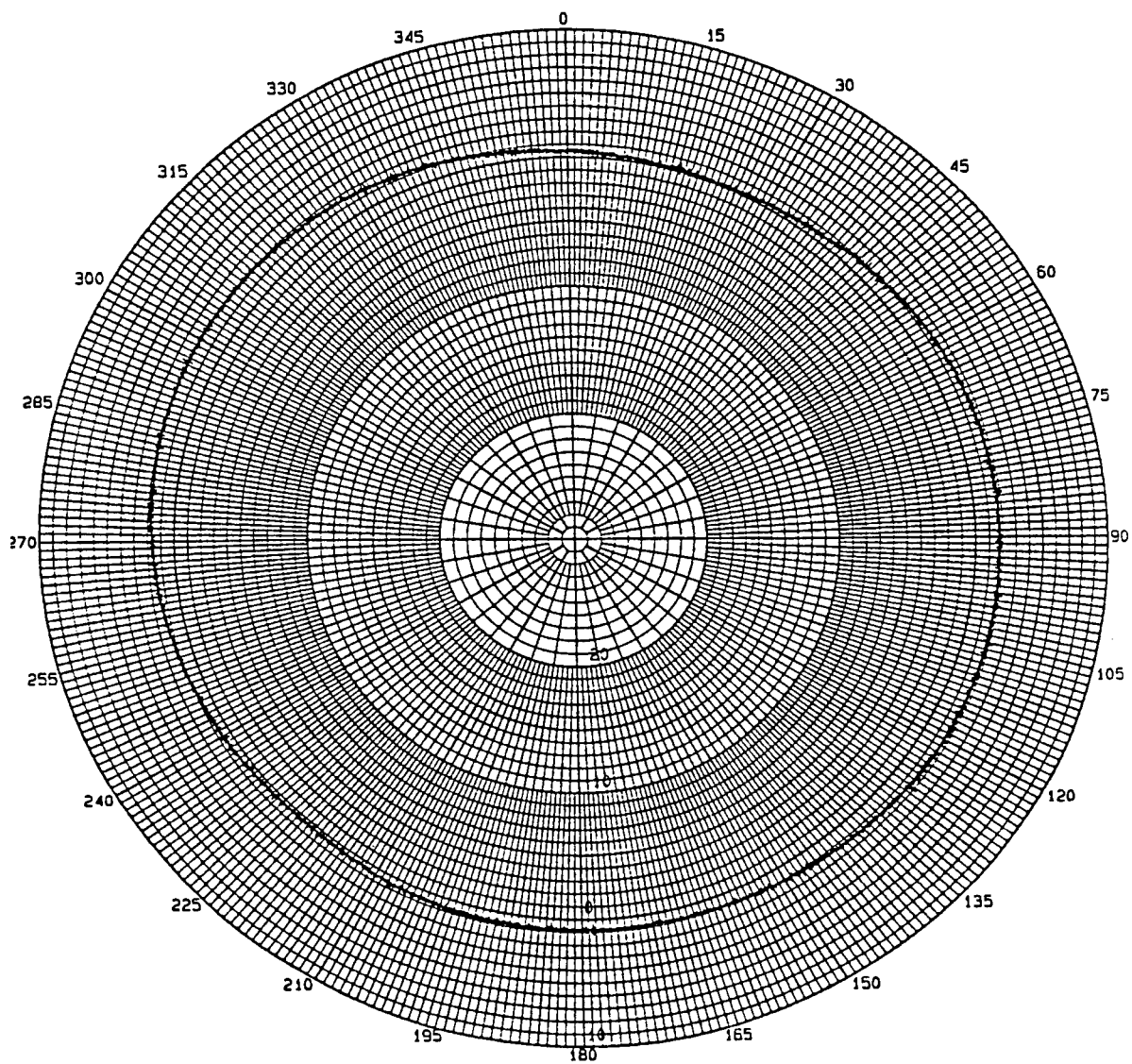
Figure 18.   UHF Function Low Angle (Mode 1) Azimuthal
Radiation Pattern at 240 MHz.
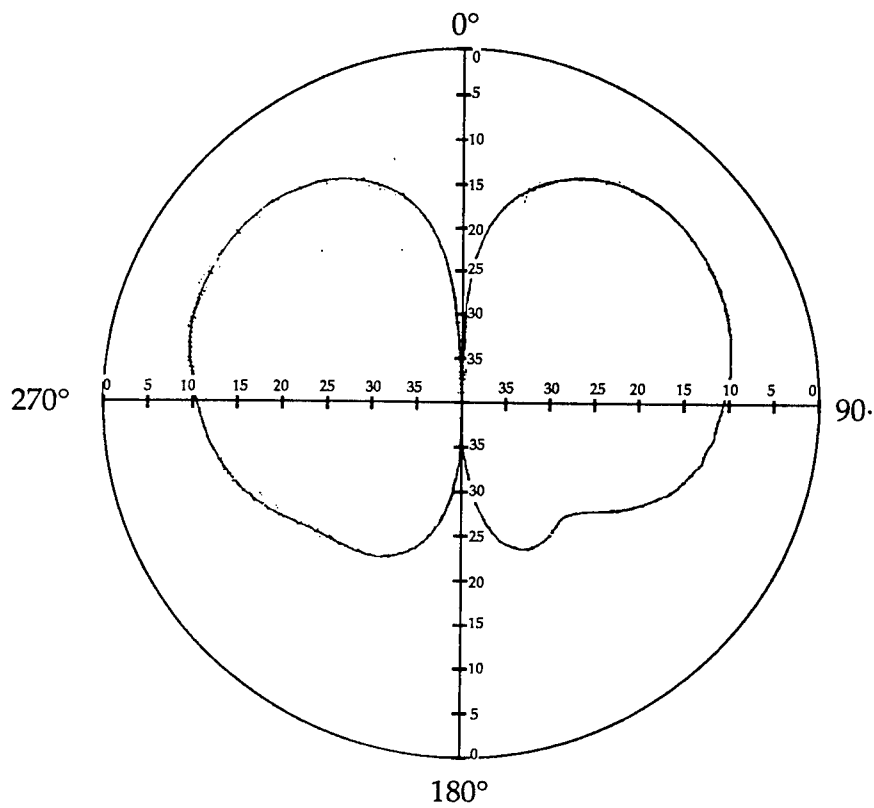
Figure 19.   VHF Function Radiation Pattern at Frequency =
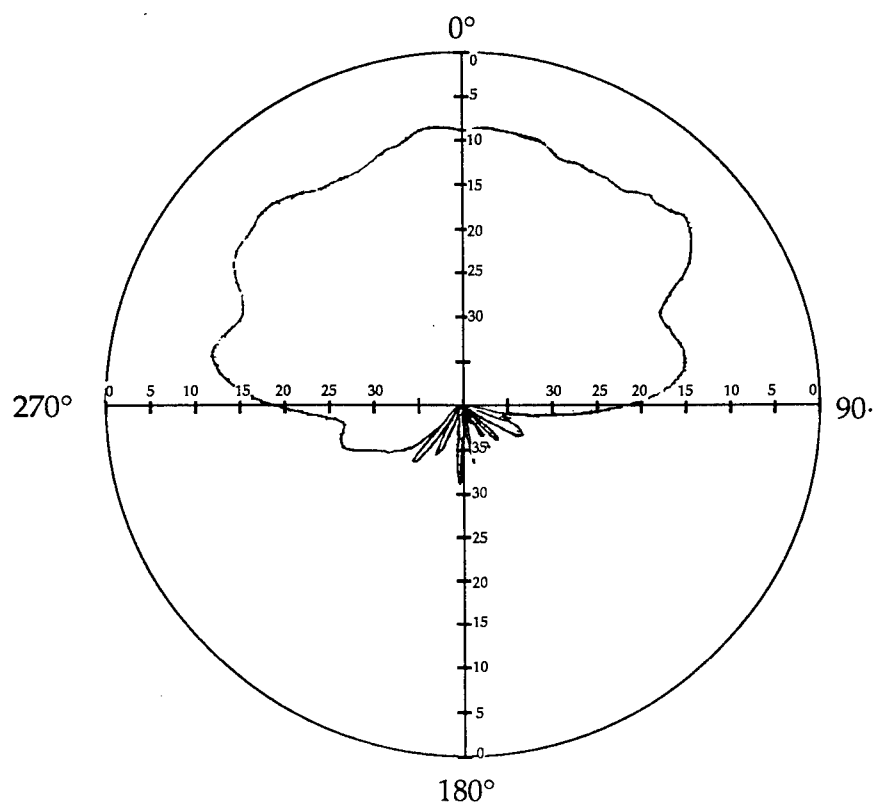136 MHz and Peak Gain = +5 dBli.

Figure 20. GPS Function Radiation Pattern at Frequency =
1227.6 MHz with Peak Gain = +3 dBic.

Future work includes correcting the low angle problem and obtaining a decrease in overall multifunction antenna height. The antenna pictured in figures 2 thru 4 has been field tested and is in continued field testing which has proven successful in all categories described.

7.0 Acknowledgements:

The author is grateful to the efforts of Vincent Marotti, Chris Matier and John Consenza of Dorne and Margolin who made this all possible.

8.0 References:

[1] Lo, Y. T. and Lee, S. W., Antenna Handbook: Theory, Applications, and Design, Van Nostrand Reinhold Company, New York, 1988.

[2] Ed Joy, "Doing Away With Satellite Dishes: Flat "Window Curtain" Antenna Offers Alternative For TV, Phone & Other Signals," Research News, Press Release, Georgia Institute of Technology, 4 March, 1994.

[3] Ball Aerospace And Communications Group, Telecommunication Products Division, UHF Satcom Antenna Data Sheet for AN0624A.

[4] D. H. Schaubert, F. G. Farrar, A. Sindoris and S. T. Hayes, "Microstrip Antennas with Frequency Agility and Polarization Diversity," IEEE Trans. AP, Vol. AP-29, No. 1, January, 1981, pp 118-123.

[5] P. J. Sroka, "Nomograph Saves Time In Converting Antenna Gain," Microwaves, March, 1974, pp 54-55.

[6]   E. Kramer, "Determine Polarization Loss The Easy Way,"
        Microwaves, July, 1975, pp 54-55.

Appendix:

A summary of the equations for the calculation of circular
gain from references [5] and [6] is shown below.

$$GCF = 20 \, Log\{1/\sqrt{2}(1 + 1/\, 10^{\wedge}AR/20)\}$$

GCF = Gain Correction Factor
AR = Axial Ratio

where the gain is then calculated as follows:

Gain (circular) = Gain (linear) + GCF

and

Gain (Linear) = Gain (standard) +

                        ΔGain (Standard - Unit Under Test)

227

EFFECTS OF LARGE HOLES IN A DUAL-POLARIZED
SERIES-FED MICROSTRIP PATCH ARRAY

Patrick Westfeldt, Jr.
Travis Newton
Darwin Glaze
Ball Aerospace and Communications Group
Broomfield, CO 80038

ABSTRACT

Edge-fed microstrip patch antennas can support series feeds in both directions because of the mode purity for excitations along the patch axis. The resulting square array of m by m patches consists of m series-fed rows (or columns) with m elements in each row (or column). Both polarizations exist at the same time in the aperture, providing m E-plane rows in the x-direction and m E-plane rows in the y-direction. Ball Aerospace has built lightweight panels of this type for many years, for use in a variety of military and commercial applications.

This paper records a brief design history of a successful attempt to provide large holes in the middle of each patch antenna in the array, for the purpose of inserting additional sensors from the back of the panel. The initial approach involved short-circuiting the holes between patch and ground plane metallization, to minimize the coupling effect between antenna and sensors. Although intuitively logical, this approach completely destroyed the performance of the antenna because of coupling between the cross-polarized rows and columns. The successful, if not optimum, design involved removing the short circuit from patch to ground, while choking the back radiation with an external cut-off waveguide.

1.   Introduction

Figure 1 illustrates the typical dual-polarized panel configuration addressed in this paper. The panels are 6x6 element arrays, fabricated in a lightweight honeycomb construction approximately 3 feet on a side, with linear dual polarization series feeds. There are 12 connectors, corresponding to ports for each of 6 E-plane rows in the X-direction and 6 E-plane rows in the Y-direction. The unique feature of the configuration is the simultaneous implementation of series E-plane feeds in the X- and Y-direction, a condition made possible by the polarization purity of microstrip patches fed on the centerline of the resonant dimension.
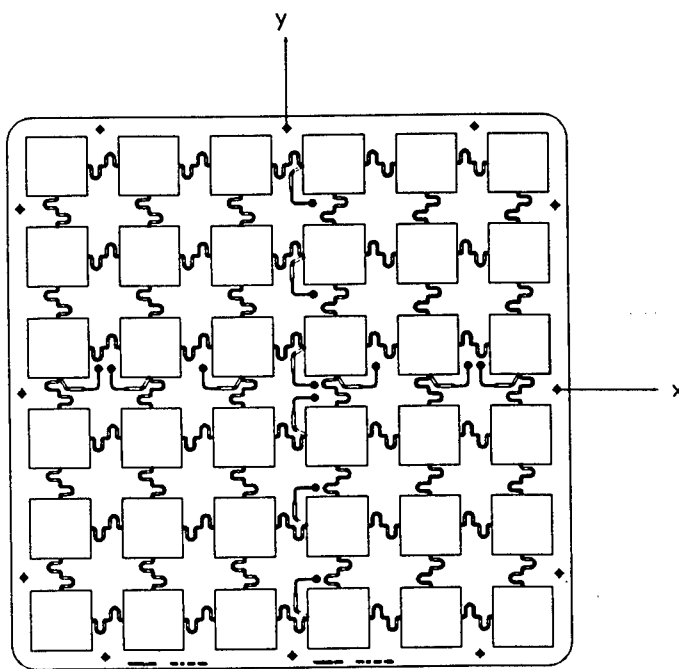
Figure 1.   Dual-Polarized Microstrip Patch Array (6 x 6)

Figure 2 is a typical E-plane pattern for one of the rows (or columns) of the 6x6

panel, with gain on the order of 13.0 dBil. In practice, panels are combined in

various arrangements, and fed with higher level corporate power combiners.

Electronic steering may also be implemented in the H-planes of the X- and Y-

directions.
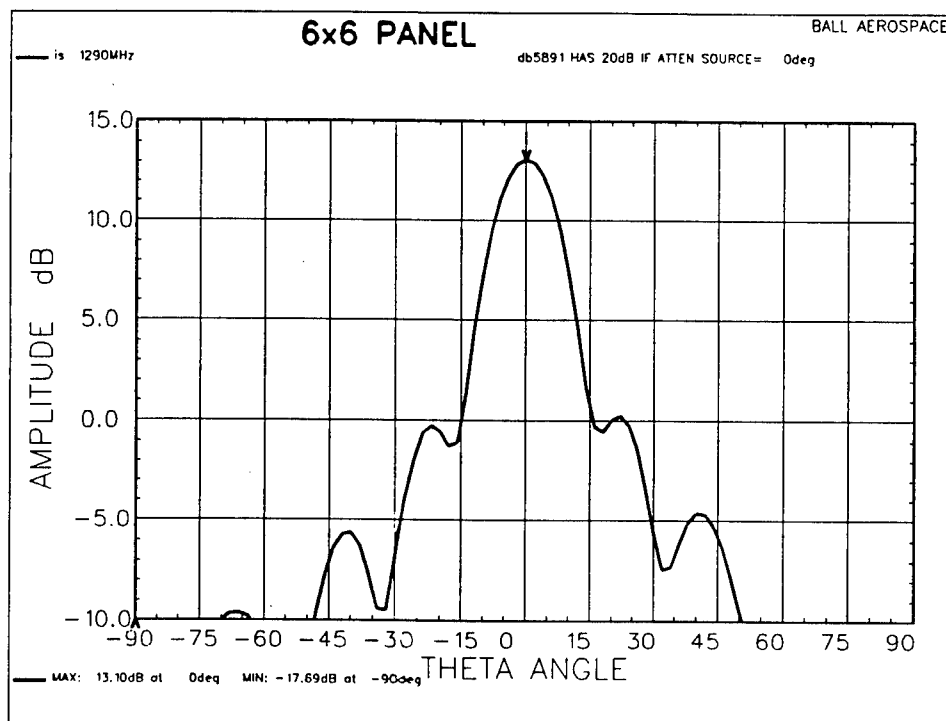
Figure 2.   Typical E-Plane Pattern of a Single Row in a 6x6 Panel

2. Special Requirement and Initial Design

Ball Aerospace was asked to produce a special design for this type of panel, in which large holes were to be drilled in the center of each microstrip patch radiator to accommodate an auxiliary array of non-metallic sensors. The basic form factor was to remain the same as other designs, and the hole diameters were to be about 1.375 inches, as shown in the layout of **Figure 3.**
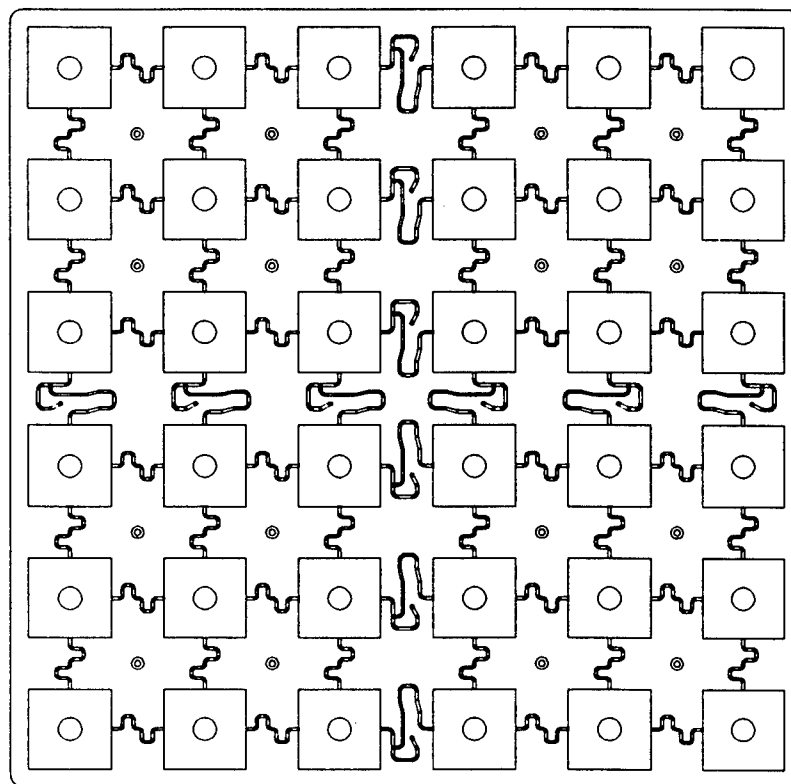
Figure 3.   Panel Layout with Large Holes Centered in each Microstrip Patch

Because the center of a microstrip patch is a point of maximum current and minimum voltage, the initial design approach was the establishment of short circuit hole walls between the patch and ground plane metallizations. This seemed intuitively logical, because coupling between the non-metallic sensors and the patch radiators could also be minimized. As shown in **Figure 4**, brass inserts were fabricated, soldered and laminated into the antenna panels.

Brass Shorting Tube
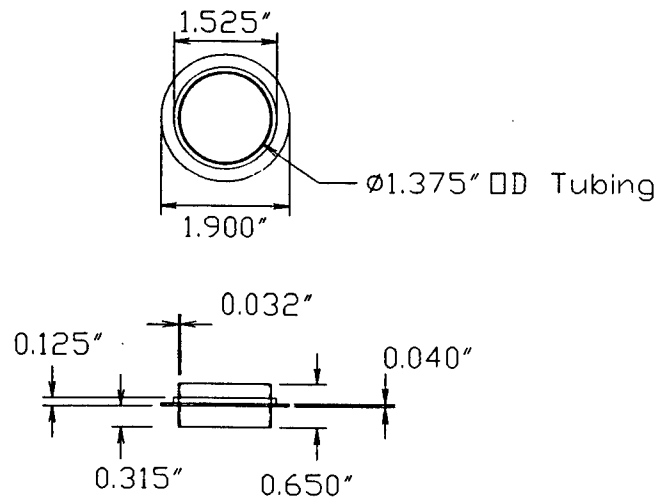
Figure 4.   Brass Insert for Installation in 6x6 Panels

The patch resonant dimensions, series feed lengths and input matching were optimized for a single 1 by 6 array, assuming that the cross-coupling effects would be minimal. The E-plane pattern for a single 1x6 is shown in **Figure 5** below.

| Isolated 6-element Row | HOLY SINGLE ROW | BALL AEROSPACE |
| Brass Shorting Inserts | | |
| ── is 924MHz A-CHAN GAIN PHI= 0deg ABSOLUTE AMPLITUDE db6551 HAS 20dB IF ATTEN SOURCE= 0deg |
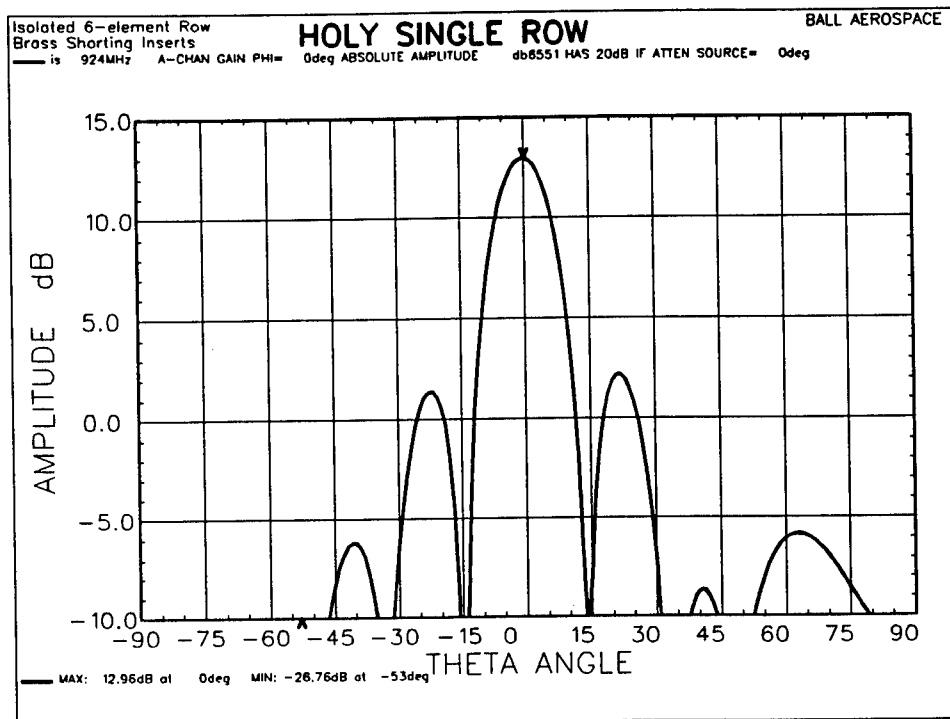
Figure 5. E-Plane Pattern for Isolated 1x6 Array with Brass Inserts

3. Full Array Design

From the isolated 1x6 results, the design for the full array was completed, and a full 6x6 panel (EMU #1) was built and tested, with unfortunate results. The E-

233

Plane pattern for EMU #1 is shown in **Figure 6**, with a severely spoiled main beam.
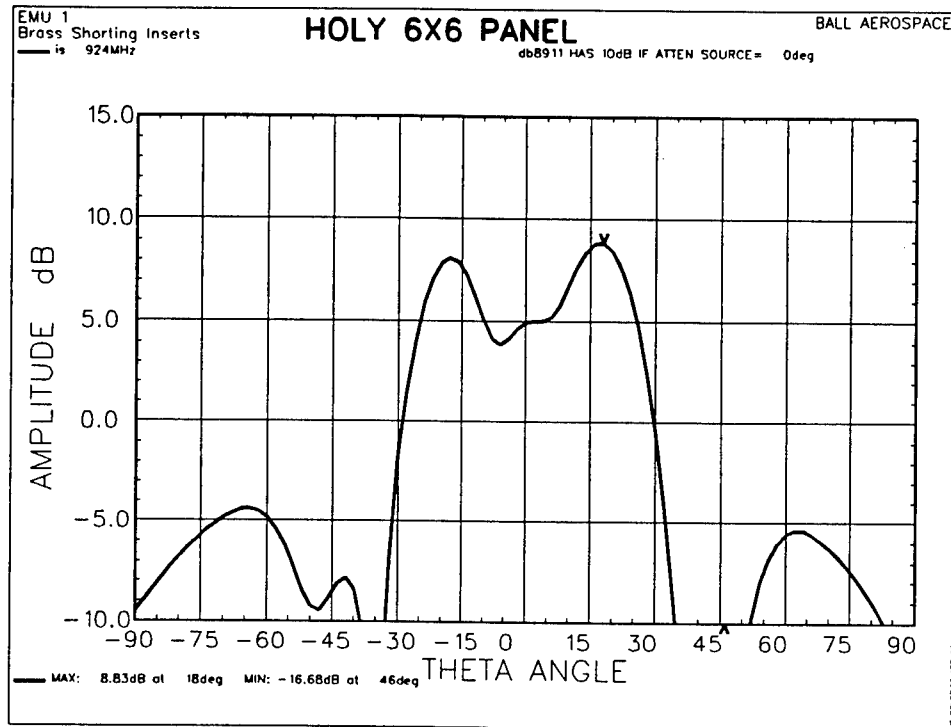
Figure 6.　　Single Row E-Plane Pattern in 6x6 EMU #1 (Brass Inserts)

Pattern synthesis was carried out to establish the excitation which could have resulted in the measured pattern of **Figure 6**. Of course, significant phase and amplitude errors were deduced, compared to the excitation of the isolated 1x6. It finally became clear that the large short-circuit hole in the middle of each patch permitted the excitation of a "monopole" mode of the patch, which coupled to the

cross-polarized feed lines. With some chagrin, we also realized that we had

previously designed and produced low profile monopole antennas at Ball with

structures analagous to the patches with brass inserts. The full antenna was

redesigned, this time with open holes (environmentally protected) in the center of

each patch. As shown in the pattern of **Figure 7**, this technique restored the

typical array performance. In fact, it turned out that pattern perturbations from the

auxiliary sensor array were minimal.
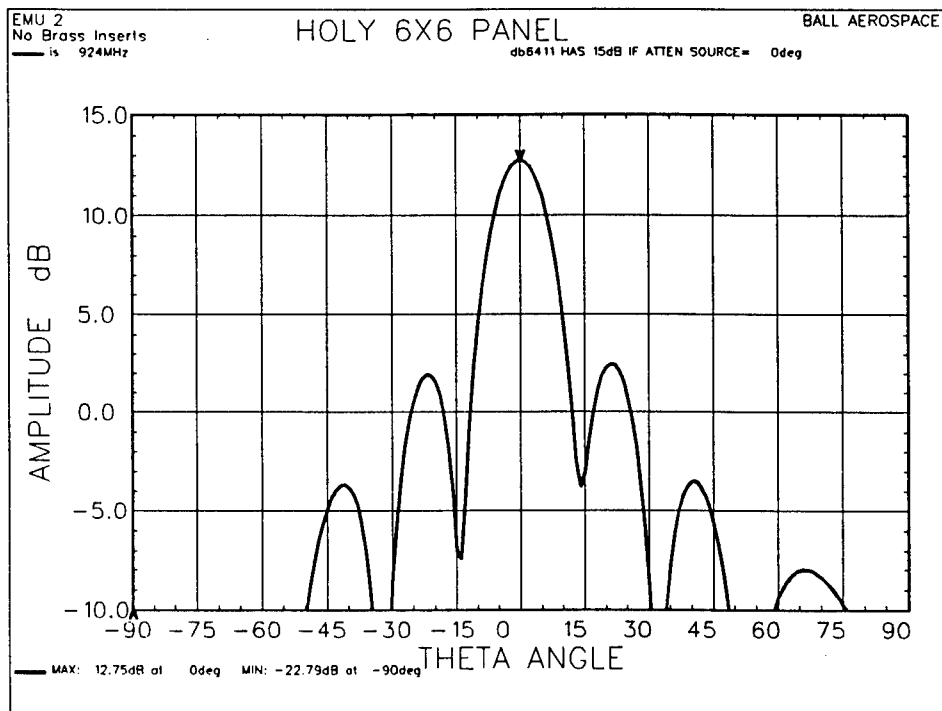
Figure 7. Single Row E-Plane Pattern in EMU #2 (No Brass Inserts)

There was also a low order concern that radiation from the holes backwards would affect system operation. Although this concern was shown to be unfounded for the application at hand, the effect was addressed by the installation of cut-off circular waveguide chokes soldered to the panel ground plane. This modification reduced the back radiation an additional 15 dB, resulting in a level about -35dB below the main lobe

4. Conclusion

This paper presented a short chronology of an interesting antenna design modification problem. It was shown that a proven design for a dual-polarized microstrip patch array was successfully altered by the addition of rather large holes in the center of each patch.

MODELING AND MEASUREMENTS OF SINUOUS ANTENNAS

J. M. Bowen and P. E. Mayes
Center for Computational Electromagnetics
University of Illinois
Urbana, IL 61801

P. G. Ingerson
Antenna Systems Laboratory
TRW Space and Defense
Redondo Beach, CA 90278

Abstract - The logarithmic spiral antenna has many favorable qualities such as wideband performance, circular polarization, and low profile. The sinuous antenna, which is related to the logarithmic spiral antenna, shares these qualities and is also sensitive to orthogonal senses of polarization. However, for certain design parameters half-power beamwidth variations were noted both in numerical modeling and in experimental measurements of a sinuous antenna. The frequency-independent performance of a multi-arm logarithmic spiral can be inferred from its continuously self-scaling and self-complementary structure. The sinuous antenna is not continuously self-scaling, so frequency-independent performance is not guaranteed. In fact, the sinuous antenna may be self-scaling only for a discrete set of scale factors, i.e. when the geometry is log-periodic. However, the sinuous antenna allows for design parameters which do not produce log-periodic geometry. It is such a set of parameters that yields an antenna with a minimum of variation in beamwidth across a log-period in frequency.

This paper will describe numerical modeling of sinuous antennas with different design parameters. The minimal beamwidth variations will be illustrated for a certain design that is not log-periodic. The paper will also describe some experimental measurements on sinuous antenna reflector feeds.

1. Introduction

The first part of this paper concerns the numerical modeling of several types of multi-arm, self-complementary spiral antennas. The logarithmic spiral antenna has long filled the need for a low-profile, wideband, circularly polarized antenna and has found use in direction finding, electronic countermeasure, and communication applications. Since the logarithmic spiral antenna is continuously

self-scaling, frequency independent performance is expected in the absence of truncation effects. The sinuous spiral antenna [1] and the folded spiral antenna share the same properties as the logarithmic spiral antenna, but they are sensitive to orthogonal polarizations as well. Even though the sinuous and folded spiral antennas are geometrically related to the logarithmic spiral antenna, they are quasi log-periodic structures, so frequency independent performance is not guaranteed even in the absence of truncation effects. The term quasi log-periodic refers to the fact that for certain design parameters, the sinuous spiral and folded spiral antennas are log-periodic, but for other design parameters they are not. It was noticed both experimentally [2] and numerically [3] that frequency independent performance was not achieved for a log-periodic folded spiral antenna. This paper will show that frequency independent performance can be achieved by a folded spiral antenna that is not log-periodic. This paper will also outline the differences between a folded spiral antenna and a sinuous spiral antenna.

The second part of this paper concerns the use of sinuous spiral antennas as feeds for reflector antennas. Data will be shown on the measured half-power beamwidth (HPBW) of a sinuous spiral feed and the calculated aperture efficiency of a reflector system using this feed.

2. Modeling Methodology

The numerical modeling of the antennas was carried out using the Finite Element Radiation Model (FERM) software package developed at MIT Lincoln Laboratory [4]. This code was primarily written to analyze scattering from a perfect-electric conductor (PEC) in free space, although the ability to model

antennas and finite conductivity is included as well. Despite the name, the FERM code is a surface patch, Method of Moment (MoM) code that uses the Rao-Wilton-Glisson (RWG) current basis function [5] and Galerkin testing. The FERM code includes a rudimentary mesh generator which can be used to create a mesh of the scattering object using flat, triangular patches. Once the MoM problem is solved and the coefficients of the basis functions are known, the surface current on the scatterer can be calculated. At this point observables such as the far field patterns, input impedance, and half-power beamwidths can be calculated.

3. Spiral Geometry

The centerline of a logarithmic spiral antenna arm can be generated from a simple formula

$$r = r_0 \cdot e^{a\phi},\tag{1}$$

where r_0 is the minimum radius, a is the expansion rate, and (r,ϕ) are the usual cylindrical coordinates. Once the centerline is known, the outer and inner edges of the arm can be generated by rotating the centerline by $+\delta/2$ and $-\delta/2$ respectively. For a self-complementary antenna, $\delta = \pi/N$, where N is the number of arms. This can be seen in Figure 1 which shows a single turn of a logarithmic spiral arm. The figure shows that the outer (forward) and inner (backward) edges are simply rotated versions of the centerline. The single turn shown in Figure 1 can be considered to be a cell of the entire spiral arm, since the rest of the arm can be created by scaling the single turn by $r_0 e^{a2\pi n}$, where m is a

set of integers. The logarithmic spiral can also be considered to be continuously self-scaling since any scaling factor can be written as $r_0 e^{a\mu}$, which is tantamount to a rotation of the original curve. To create an antenna out of the spiral arm, the inner end of the spiral arm is truncated with a feed region at some minimum radius, and the outer end is truncated at some maximum radius. The minimum and maximum radii depend upon the frequency range over which the antenna will operate. Finally, the single spiral arm can then be successively copied and rotated $N-1$ times by 2δ each time to create a multi-arm antenna. A typical mesh for a four-arm, logarithmic spiral antenna is shown in Figure 2.

The folded spiral antenna is directly related to the logarithmic spiral antenna and can be generated from a "parent" logarithmic spiral antenna. Figure 3 shows how the folded spiral arm centerline can be generated from the logarithmic spiral arm centerline simply by folding the centerline back into an angular range which is less than 2π. The centerline of the folded spiral arm can still be generated from Equation 1, however, in this case the ϕ variable is interpreted as an "arc angle" which runs over the same range as in the parent logarithmic spiral arm rather than the cylindrical coordinate. As shown in Figure 3, the azimuthal variation of the arm is limited by the parameters α_p. The outer and inner edges of the arm can be generated by rotating the centerline by $+\delta/2$ and $-\delta/2$ respectively. As in the case of the logarithmic spiral arm, the portion of the folded spiral arm shown in Figure 3 can be considered a cell of the entire spiral arm. For α_p's all equal, the rest of the spiral arm can be created by scaling this cell with appropriate factors, which implies a log-periodic structure. However, in contrast to the logarithmic spiral arm, the folded spiral arm is not continuously self-scaling, i.e., an arbitrary

scaling is not equivalent to a rotation. The α_p variables introduce extra design parameters in addition to those available with the logarithmic spiral arm, but if the α_p's are allowed to vary from cell to cell, the folded spiral arm is no longer log-periodic. In the same manner as for the logarithmic spiral, a folded spiral antenna can be created from the folded spiral arm, and a typical mesh for an entire folded spiral antenna is shown in Figure 4.

The sinuous spiral antenna looks similar to the folded spiral antenna, but according to its patent [1] the centerline of a sinuous spiral arm is given by

$$\phi = (-1)^p \alpha_p \sin\left[\pi \frac{\ln(r/R_p)}{\ln(R_p/R_{p+1})} \right] \tag{2}$$

where α_p, the cell angle, and R_p, the cell radius are defined in Figure 5. A cell scaling factor can also be defined as $\tau_p = R_p/R_{p+1}$. As previously, once the centerline is created the outer and inner edges can be generated by rotating the centerline by $\pm \delta/2$. For constant α_p and τ_p, the cell shown in Figure 5 can be scaled by a discrete set of scale factors to create the rest of the sinuous spiral arm, which again implies a log-periodic structure, but not a continuously self-scaling structure. In addition to the α_p variables, another set of design parameters, the τ_p variables, is associated with the sinuous spiral. As in the case of the folded spiral arm, if the α_p and τ_p variables are allowed to vary from cell to cell, the sinuous spiral arm is no longer log-periodic. A typical sinuous spiral antenna mesh is shown in Figure 6.

It should be noted that a set of τ_p's could also be defined for the folded spiral arm, and in this case the folded and sinuous spiral arms would have the same degrees of freedom in their design. There is not great deal of difference between folded and sinuous spiral arms designed with the same parameters as shown in Figure 7. The folded spiral arm has sharper tips and thicker arcs between the tips than the sinuous spiral arm, and it will be seen later that antennas using the same parameters will give similar performance.

4. Modeling Results

The results of modeling the various spiral antennas include monitoring the input impedance and HPBW of the antenna as a function of frequency. To limit the computation time required, only a portion of the full spiral antenna was modeled over a frequency range covering at least one log-period. The structure of the antenna was made large enough to avoid truncation effects over this frequency range, and the performance of the entire antenna is assumed to be the same over other log-periods of frequency.

For comparison purposes the HPBW and input impedance of logarithmic spiral antenna is shown in Figures 8a and 8b. Figure 8a shows the E_θ and E_ϕ HPBWs for a cut in the $\phi=45°$ plane. As can be seen, the HPBW variations are smooth and do not exceed 10° over the whole band. Figure 8b shows the input impedance over the band and the analytic value expected for a four-fold symmetric antenna. The input impedance of an infinite, planar, four-fold symmetric antenna can be calculated analytically [6] as 133Ω. Because opposite spiral arms in this case were fed with a single voltage generator, the analytic value has to be doubled

242

to 266Ω. The difference between the calculated value and the analytic value for the real part of the input impedance does not exceed 10% over the band, and as with the HPBW, the variation in input impedance are smooth. Differences between the calculated value and the analytic value can be attributed to the fact that the modeled antenna is not of infinite extent.

Figures 9a and 9b show HPBW and input impedance data for a folded spiral with constant parameters over the cells. Figure 9a shows the HPBW for the right hand sense of excitation in the $\phi=45°$ plane, and Figure 9b shows the input impedance. Even though the antenna structure is log-periodic, it is obvious that it does not have frequency independent performance. There are abrupt variations in the HPBW of up to 30°, and the input impedance shows resonant-like behavior at the same frequencies where the abrupt variation in the HPBW occurs. In contrast to the logarithmic spiral antenna shown in Figure 2, the folded spiral antenna shown in Figure 4 is excited with four voltage generators, one for each arm. The voltage generators are located at the junction between the wagon wheel at the center of the antenna and the triangular fins. This was done to make the feed region as self-complementary as possible. Thus, in this case the analytic value of the input impedance is 133Ω.

Figures 10a and 10b show the HPBW and input impedance for sinuous spiral with variable parameters over the cells, and the improvement in frequency independent performance is obvious. The HPBW variations are smooth and do not exceed 10° over the band. The input impedance displays a smooth, sinusoidal variation over the band. To show that the improvement is due to the variable parameters rather than the sinuous geometry, a folded spiral with the same

parameters was modeled. Figures 11a and 11b show the HPBW and input impedance for a folded spiral with variable parameters over the cells. Again the improvement in frequency independent performance is obvious and of the same character as the sinuous antenna.

5. Reflector Measurements

A variable parameter sinuous spiral antenna based on the one modeled above was built and measured as a feed to a reflector antenna system. Important differences between the feed antenna and the one that was modeled were that the feed antenna was a cavity backed conical spiral antenna whereas the modeled one was a planar one in free space. The modeled spiral parameters were used as a starting point for the design of the feed antenna, which is pictured in Figure 12. The HPBW of the feed alone was measured, and the data is shown in Figure 13. This data does not look nearly as good as the calculated data primarily due to the presence of the cavity. To determine its efficacy as a feed antenna, the measured patterns were used as input to calculate the aperture efficiency of the reflector system as a function of frequency and feed displacement along the z-axis. This calculated data is shown in Figure 14, and for a displacement of z=-3", the aperture efficiency stays constant over frequency. This location corresponds to placing the apex of the conical spiral at the focal point of the reflector.

6. Conclusion

This paper has shown that in order for folded and sinuous spiral antennas to achieve frequency independent performance, their structure must be non log-periodic. The antennas can be made non log-periodic by using a design which

allows the α_p and τ_p parameters to vary from cell to cell. Even though the variable parameter design analyzed in this paper show a great improvement over the constant parameter design, it is far from certain that the variable parameter design is optimum. This paper has also shown that there is little difference between the folded spiral geometry and the sinuous spiral geometry. As long as each antenna is designed with the same parameters, their performance will be very similar. This paper has also presented some data on using the cavity-backed, conical, sinuous spiral antenna as a feed to a reflector system.

7. Acknowledgments

8. References

[1]   R. H. DuHamel, Inventor, "Dual polarized sinuous antenna," U. S. Patent 4,658,262, April 14, 1987.

[2]   P. G. Ingerson, P. M. Ingerson, and D. C. Senior, "Comparison of sinuous and MAW spiral antennas for wideband, dual polarized multi-arm applications," Proceedings of the Antenna Application Symposium, Urbana, Illinois, Sept. 1991.

[3]   J. M. Bowen and P. E. Mayes, "Investigation of anomalous beamwidth variation in the sinuous spiral antenna," IEEE Antennas & Propagation Society International Symposium Digest, Vol. 2, pp. 1306-1309, June 1994.

[4] S. Lee, D. A. Shnidman, and F. A. Lichauco, "Numerical modeling of RCS and antenna problems," Technical Report 785, Lincoln Laboratory-- Massachusetts Institute of Technology, Lexington, MA, Dec. 1987.

[5] S. M. Rao, D. R. Wilton, and A. W. Glisson, "Electromagnetic scattering by surfaces of arbitrary shape," IEEE Trans. Antennas & Propagation, Vol., AP-30, pp. 409-418, May 1982.

[6] G. A. Deschamps, "Impedance properties of complementary multiterminal planar structures," IRE Trans. Antennas & Propagation, Vol. AP-7, pp. S371-378, Dec., 1959.
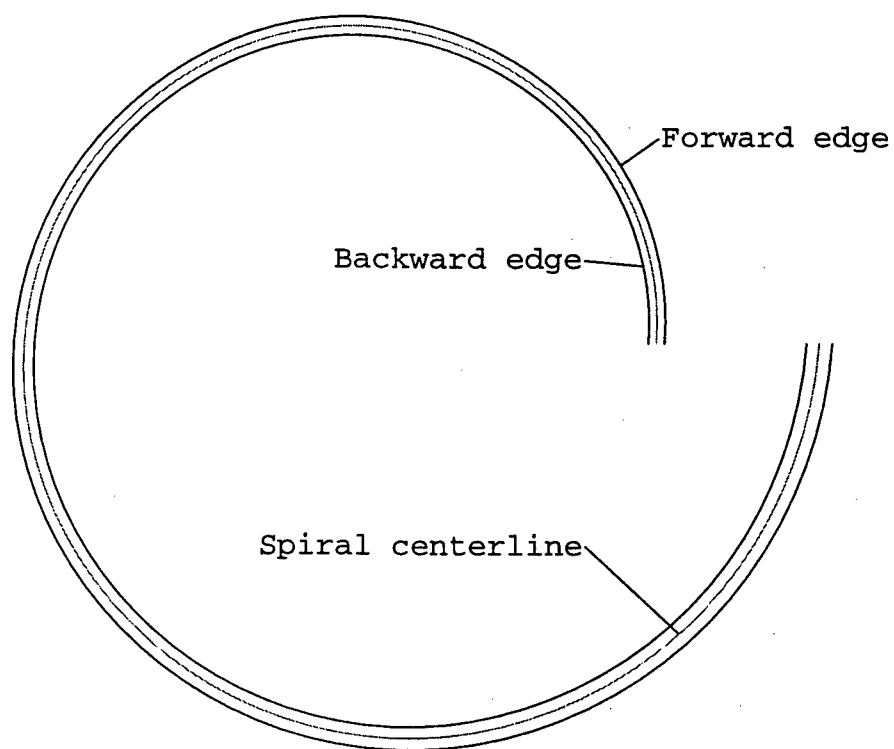
Figure 1. Single cell of a logarithmic spiral arm. The centerline is defined by Equation 1, and the forward and backward edges may be generated from the centerline by a rotation of $\pm\delta/2$.
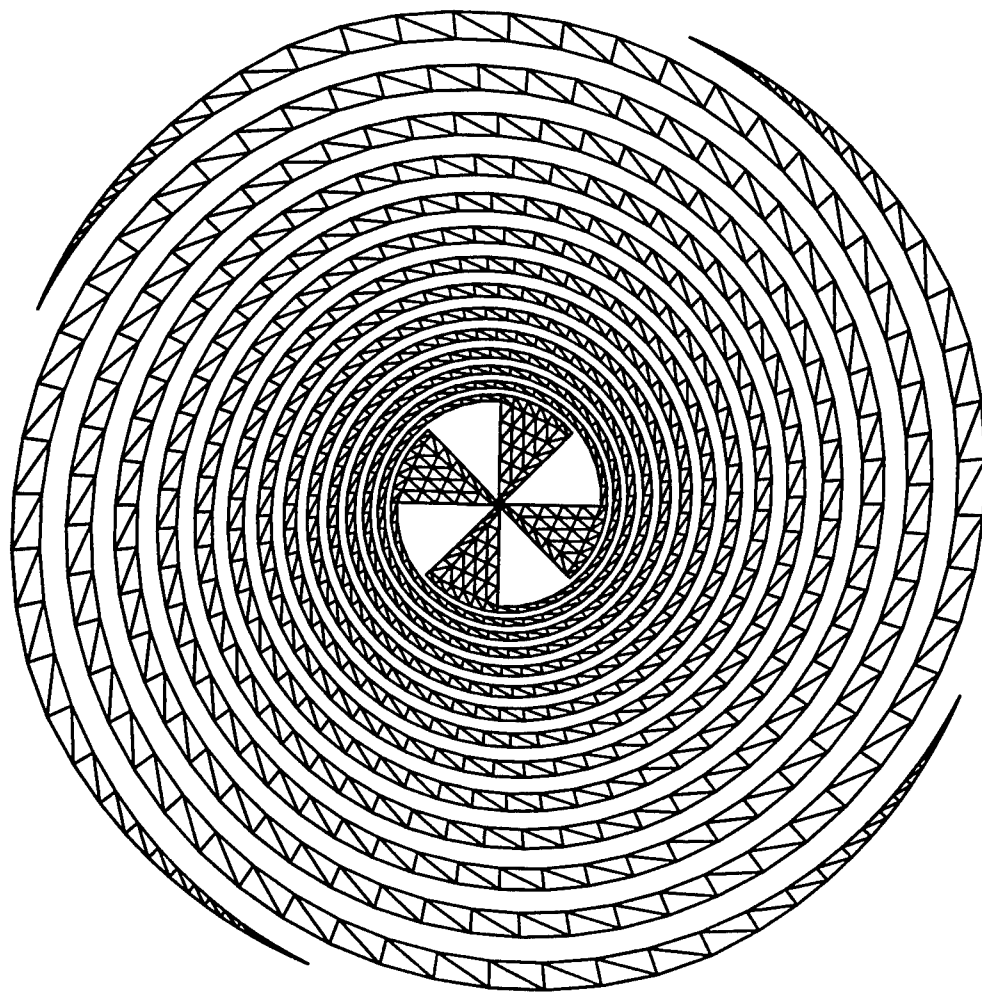
Figure 2. Typical mesh of a four-arm, logarithmic spiral antenna.
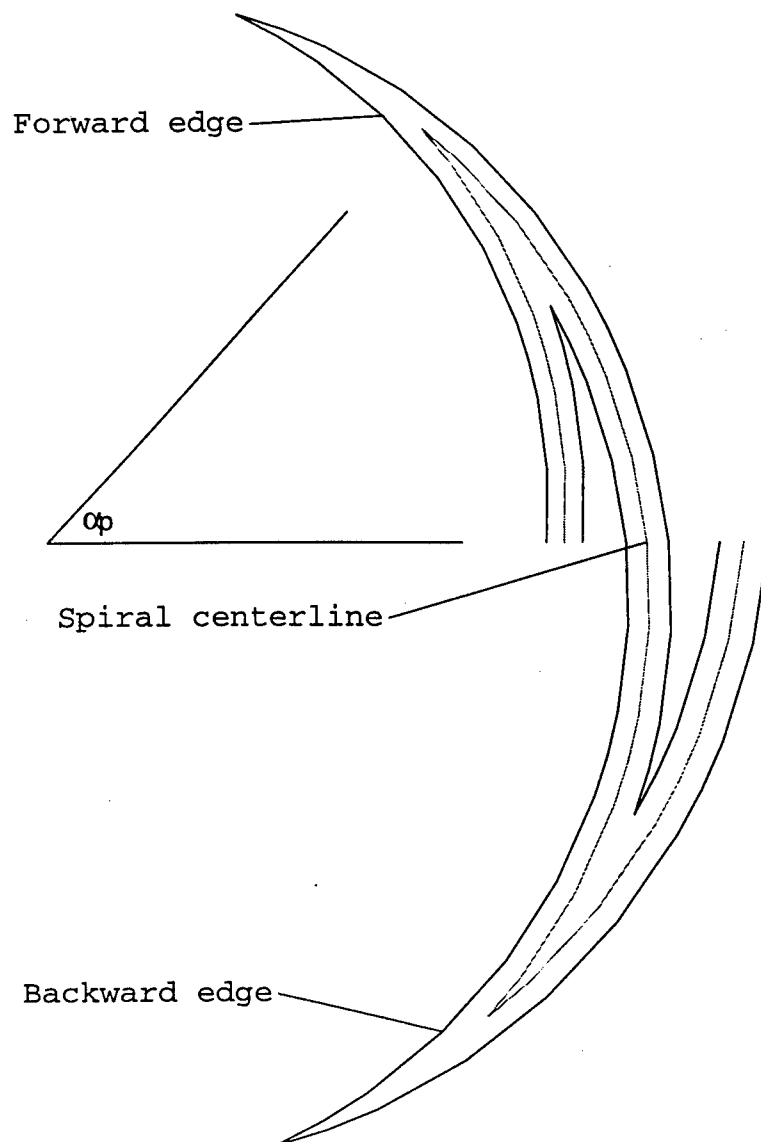
Figure 3. Single cell of a folded spiral antenna. The cell is generated from a "parent" logarithmic spiral with the centerline folded into an azimuthal range defined by the α_p parameters.
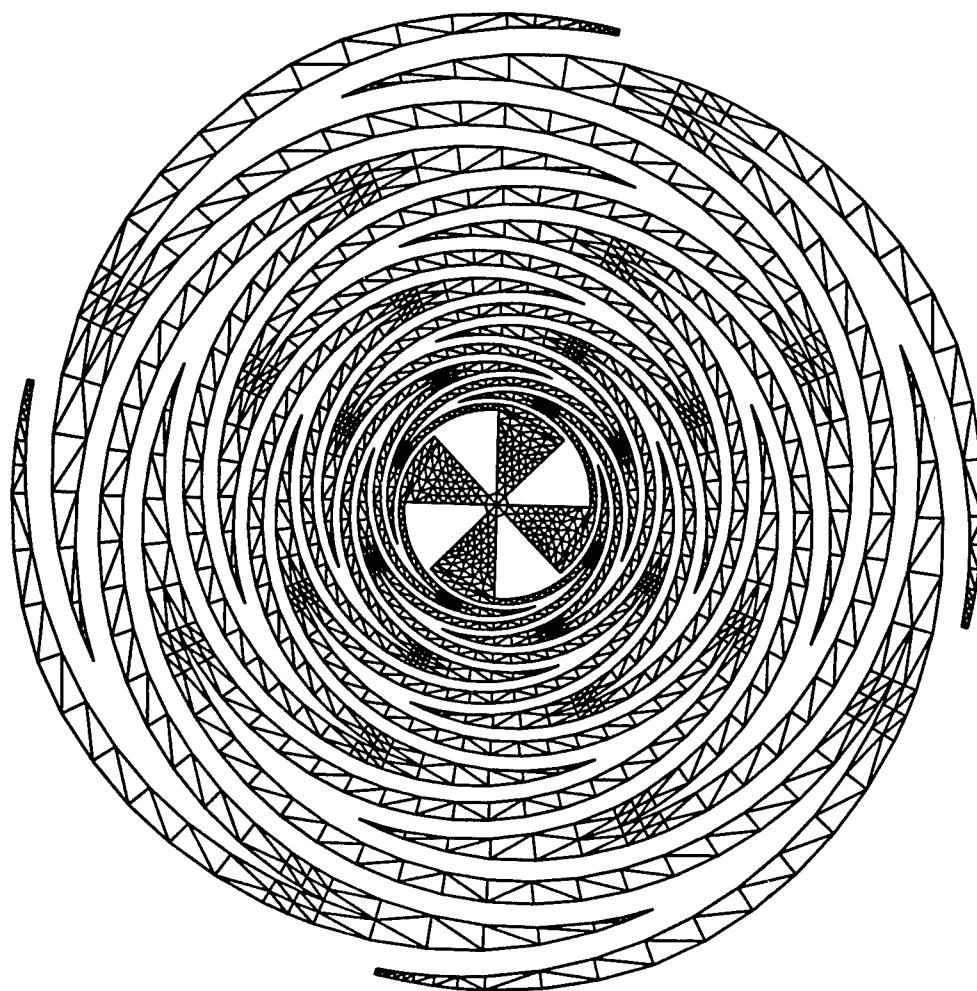
Figure 4.   Typical mesh of a four-arm, folded spiral antenna.
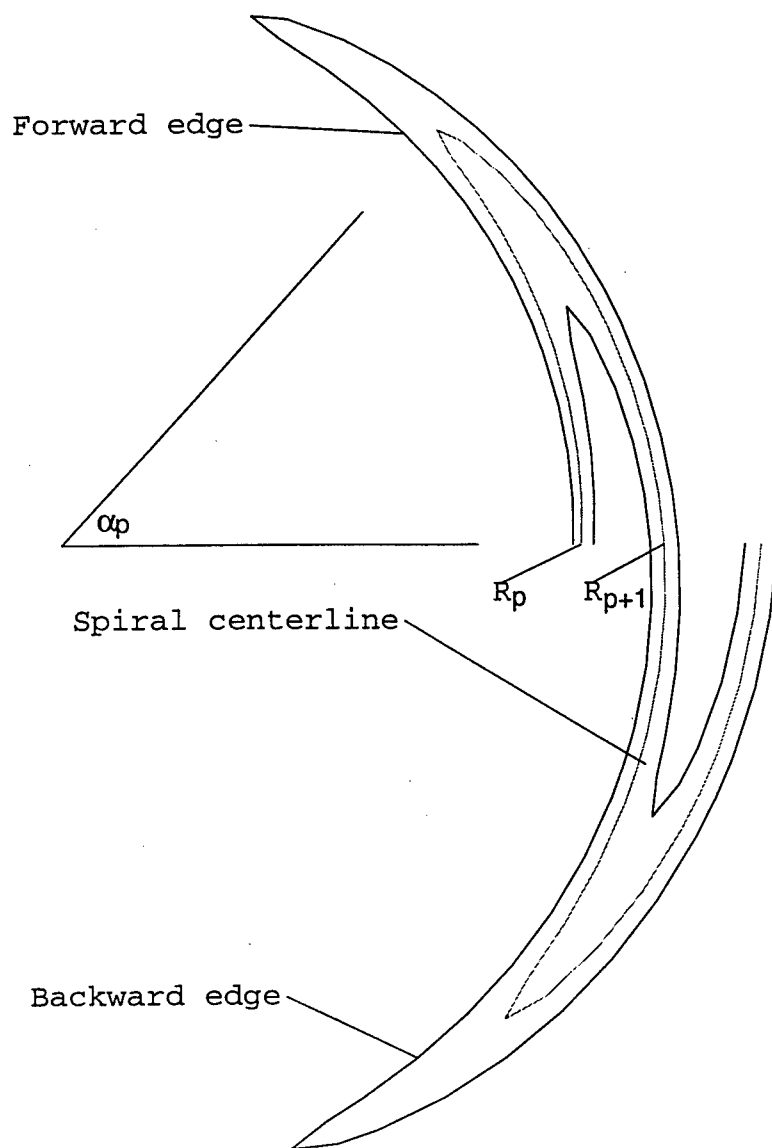
Figure 5. Single cell of sinuous spiral antenna. The centerline is defined by Equation 2, and the forward and backward edges may be generated from the centerline by a rotation of $\pm \delta / 2$.

251
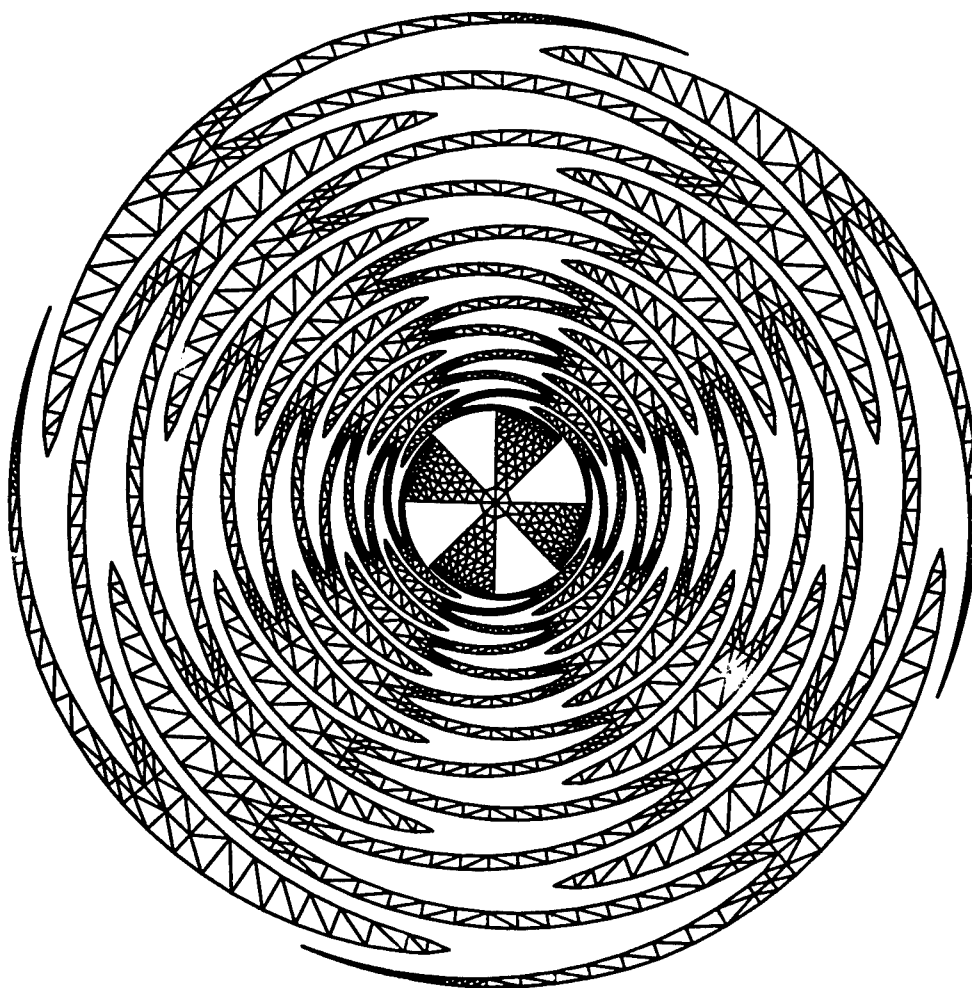
Figure 6.   Typical mesh of a four-arm, sinuous spiral antenna.
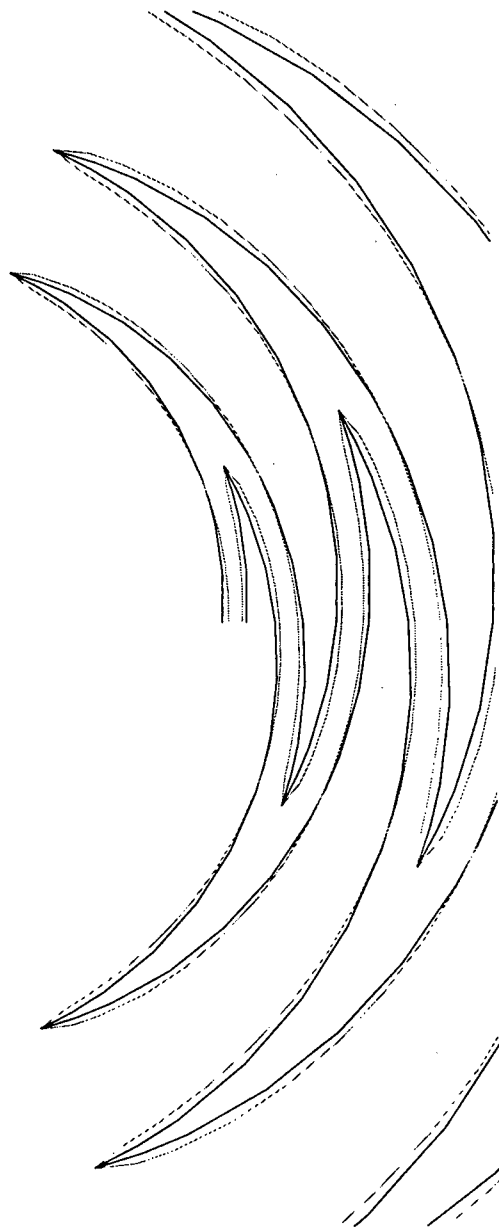
Figure 7.   Comparison of the folded (solid) and sinuous (shaded) geometries. The folded geometry has sharper tips and thicker arcs between the tips than the sinuous geometry.

253
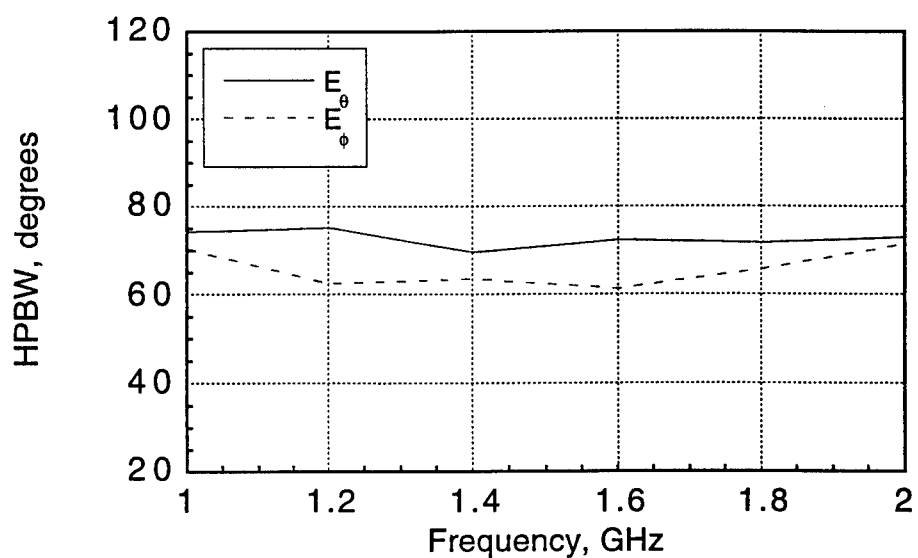
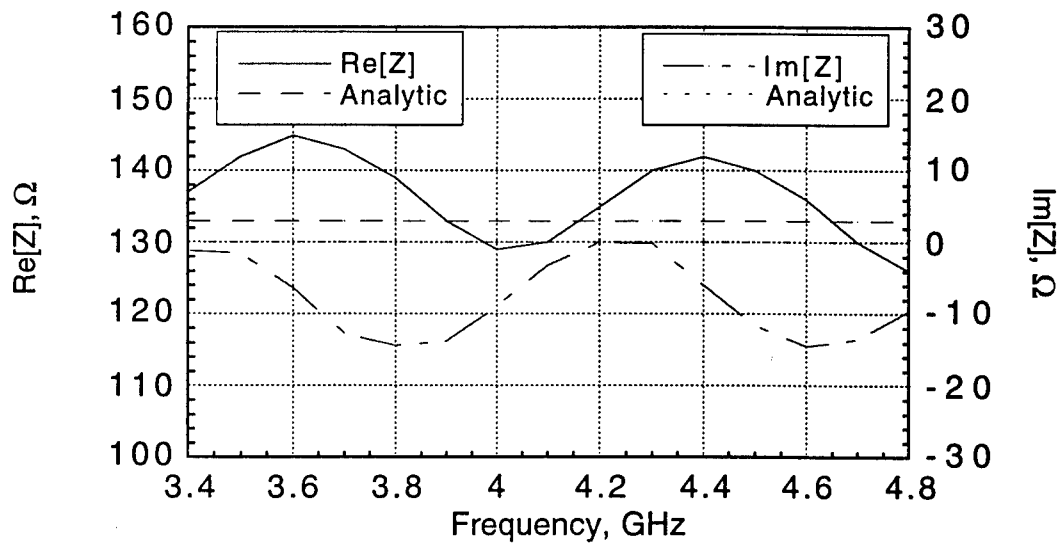Figure 8a.   HPBW for the logarithmic spiral antenna in the $\phi=45°$ plane.
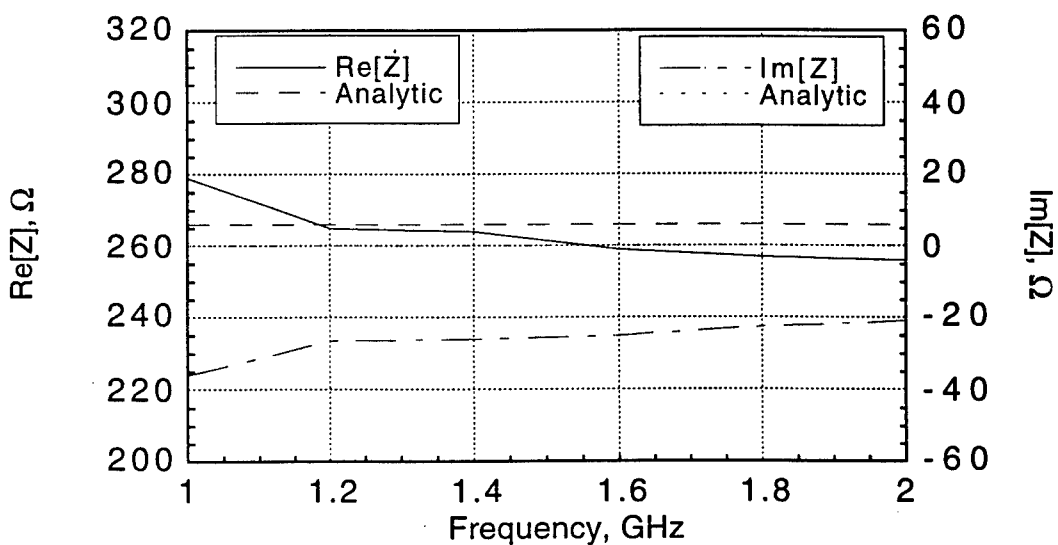
Figure 8b.   Input impedance for the logarithmic spiral antenna. The analytic value
in this case is $266+j0\Omega$.
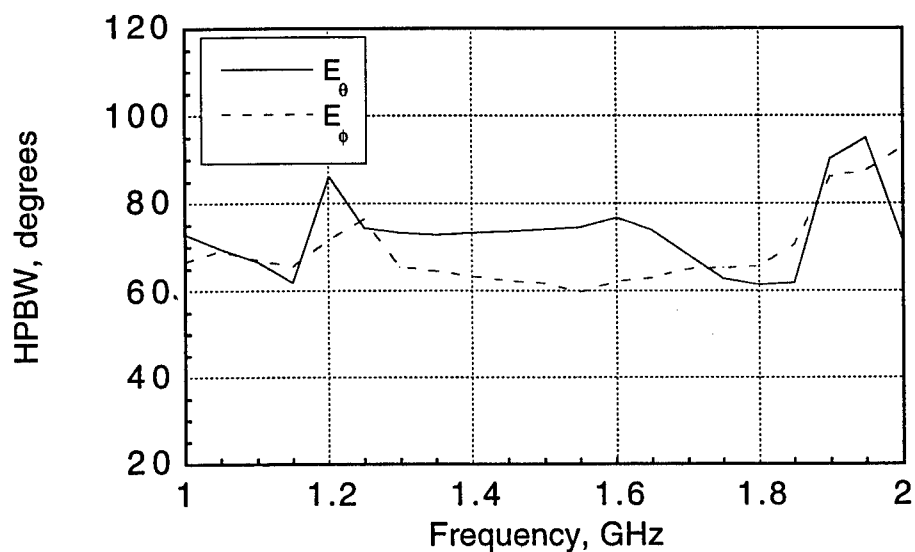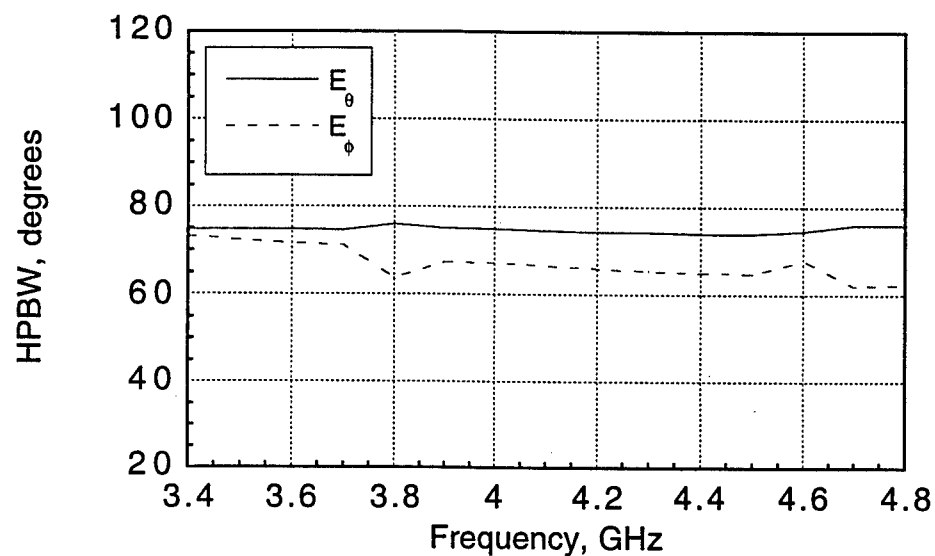
Figure 9a. HPBW for the constant parameter folded spiral antenna in the φ=45°
plane for right hand excitation.
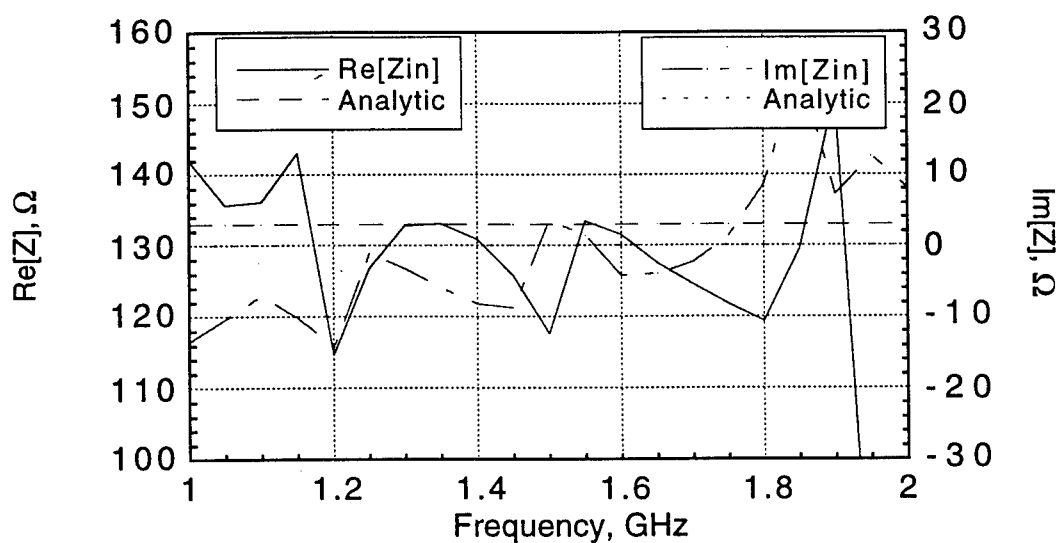
Figure 9b. Input impedance for the constant parameter folded spiral antenna. The
analytic value in this case is 133+j0Ω.
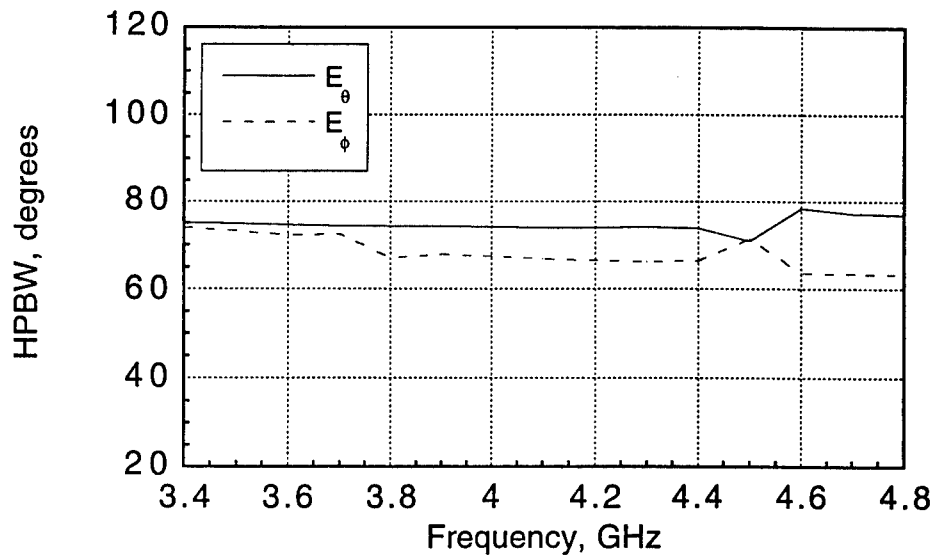
Figure 10a.   HPBW for the variable parameter sinuous spiral antenna in the $\phi=45°$ plane for right hand excitation.
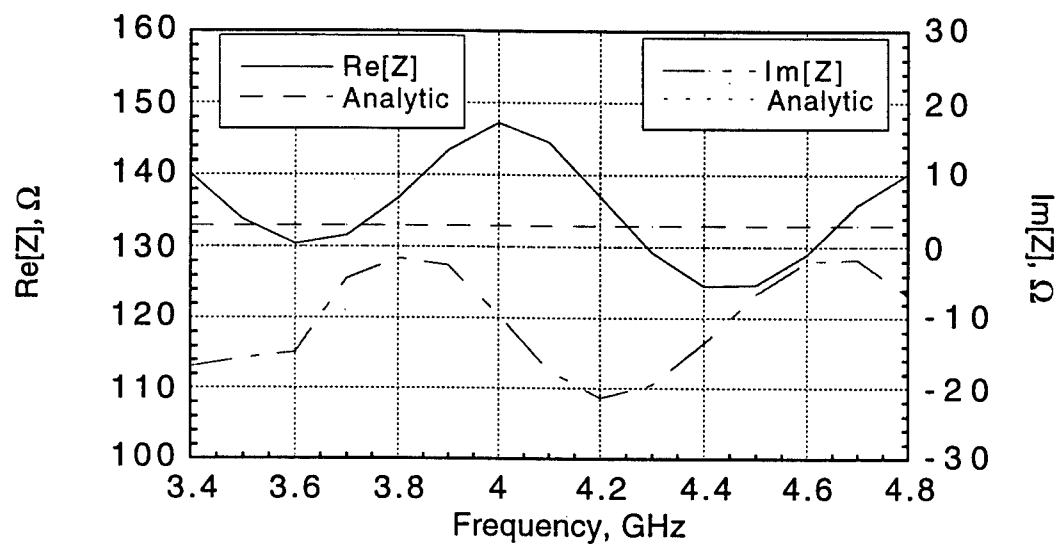

Figure 10b.   Input impedance for the variable parameter sinuous spiral antenna. The analytic value in this case is $133+j0\Omega$.
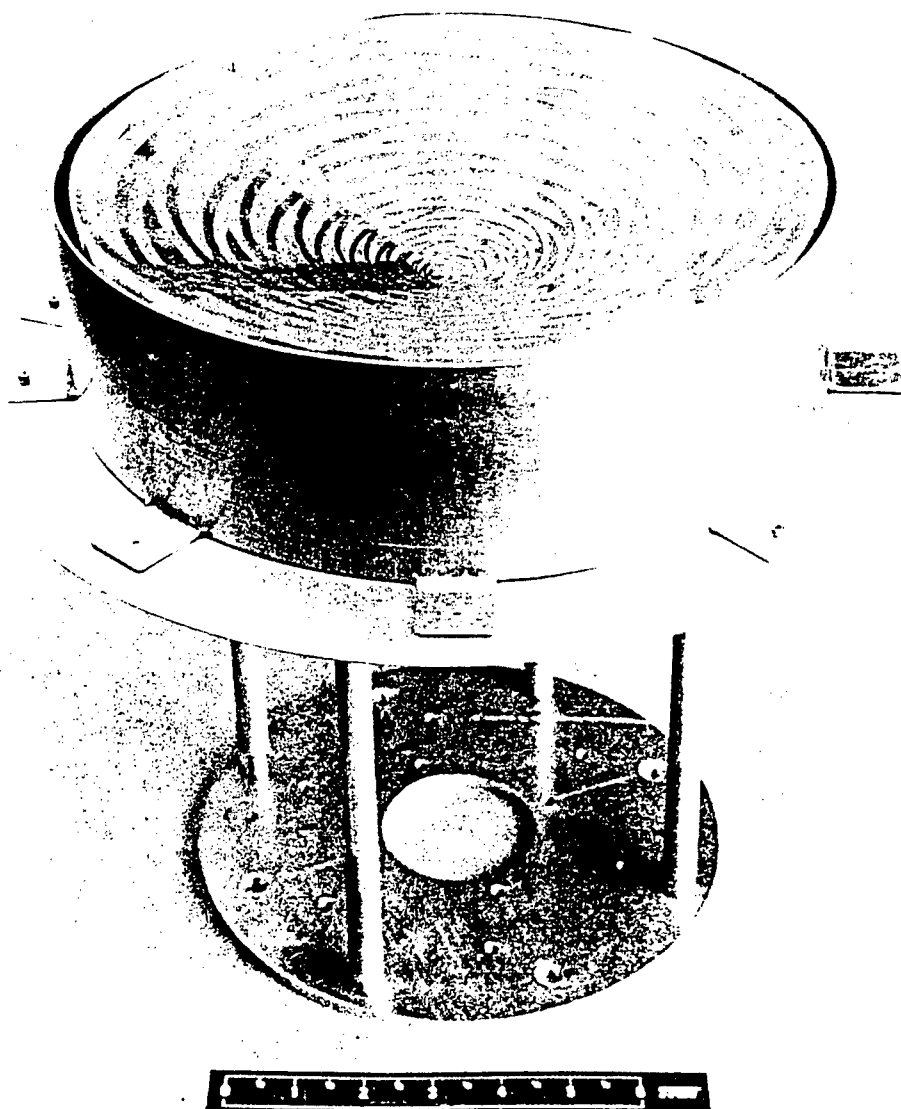
256

Figure 11a.   HPBW for the variable parameter folded spiral antenna, in the $\phi=45°$ plane for right hand excitation.

Figure 11b.   Input impedance for the variable parameter folded spiral antenna. The analytic value in this case is $133+j0\Omega$.

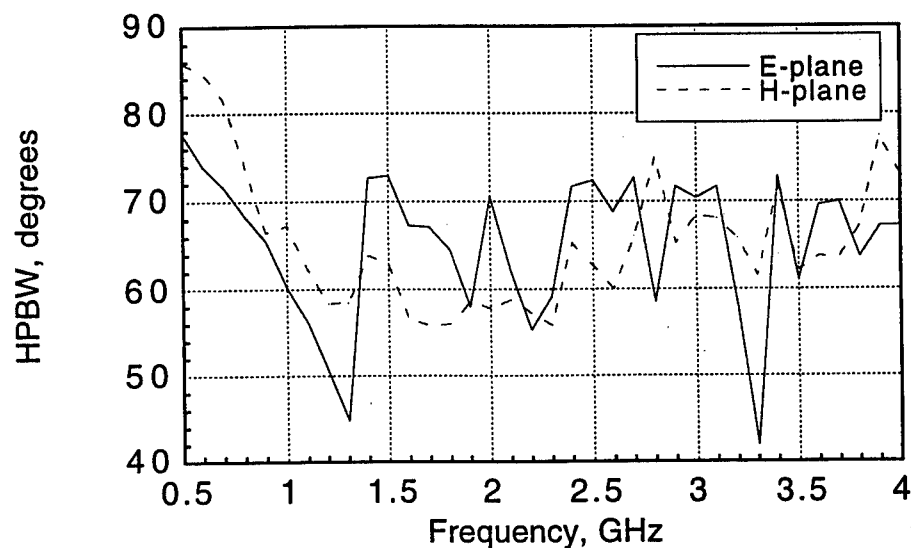Figure 12.   Cavity-backed, conical, sinuous spiral feed antenna.

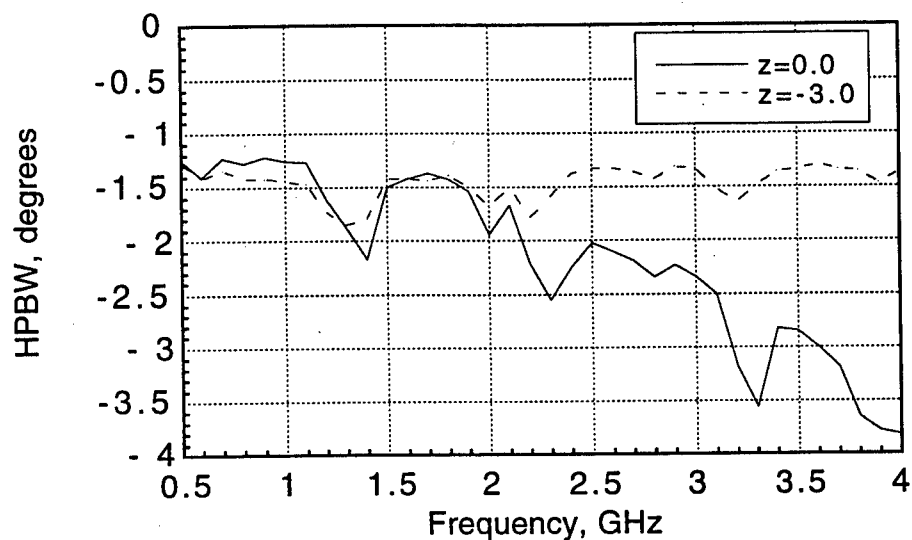Figure 13. Measured HPBW of the feed antenna pictured in Figure 12.

Figure 14. Calculated aperture efficiency of the reflector system using the measured patterns of the feed antenna. The two curves are for two locations of the feed antenna along the z-axis of the reflector. For the z=-3 location, the aperture efficiency is nearly constant, implying that this location puts the phase center of the feed antenna at the focal point of the reflector.

SCATTERING FROM A CYLINDRICALLY CONFORMAL SLOTTED-WAVEGUIDE ARRAY ANTENNA

Guoxin Fan and Jian-Ming Jin

Electromagnetics Laboratory

Department of Electrical and Computer Engineering

University of Illinois at Urbana-Champaign

Urbana, Illinois 61801-2991

1. Introduction

Slotted-waveguide array antennas are widely used on modern airborne radars. However, conventional planar slotted-waveguide antennas have a significant contribution to the overall radar cross section (RCS) of the host vehicle. Reduction of the antenna's RCS is one of important aspects for the stealth technology. The RCS of a slotted-waveguide antenna consists of two parts: one comes from the surface of the antenna and the other from the slots. As is well known, the RCS of a flat plate is generally higher than that of a smooth curved surface. Therefore, it is possible to reduce the RCS by replacing a planar slot array with a curved slot array.

Because of a large number of slots and the mutual coupling between slots and between slots and waveguide, the analysis of scattering from a slotted waveguide array is very difficult. As a result, only planar slot antennas have been considered in the past [1–2]. Recently, Fan [3] presented the theory of analysis and design of cylindrically-conformal slotted-waveguide array antenna with a curved waveguide as the main guide and sectoral guides as the branch guides. In this paper we analyze its scattering properties, and to simplify the analysis, we neglect the coupling between the main guide and the branch guides.

2. Theory

Consider a slotted waveguide array on a cylindrical surface whose radius is ρ_3, as depicted in Fig. 1. The cross section of each guide is an annular sector with inner radius ρ_1, outer radius ρ_2, and subtended angle ϕ_0, and the thickness of curved walls of guides is $t = \rho_3 - \rho_2$. Each waveguide is terminated at $z = z_1$ and z_2 with an arbitrary load. All radiating slots are longitudinal slots cut in the outer wall of the guides.

For the ith slot, its inter and outer apertures, S_i^I and S_i^{II}, divide the space into three regions, the waveguide region (region a), the region outside the cylinder (region b) and the slot region (region c), respectively, as shown Fig. 2. By invoking the equivalence principle and enforcing the continuity of the tangential magnetic fields across S_i^I and S_i^{II}, we can obtain integral equations satisfied by the equivalent magnetic currents, $\mathbf{M}_i^I$ and $\mathbf{M}_i^{II}$, as

$$\sum_j \mathbf{H}_{\tau i}^a(\mathbf{M}_j^I) + \mathbf{H}_{\tau i}^c(\mathbf{M}_i^I) - \mathbf{H}_{\tau i}^c(\mathbf{M}_i^{II}) = 0 \qquad \mathbf{r} \in S_i^I \qquad (1)$$

$$\sum_j \mathbf{H}_{\tau i}^b(\mathbf{M}_j^{II}) + \mathbf{H}_{\tau i}^c(\mathbf{M}_i^{II}) - \mathbf{H}_{\tau i}^c(\mathbf{M}_i^I) = -\mathbf{H}_{\tau i}^{pri} \qquad \mathbf{r} \in S_i^{II} \qquad (2)$$

To seek a numerical solution of (1) and (2), we first expand each equivalent magnetic current using the global sinusoidal basis functions

$$\mathbf{M}_j^\alpha = \hat{z} M_j^\alpha = \hat{z} \sum_{q=1}^{N_j^\alpha} V_{qj}^\alpha \sin \alpha_{qj} \xi \qquad \mathbf{r} \in S_j^\alpha \qquad \alpha = I, II \qquad (3)$$

where $\alpha_{qj} = q\pi/l_j$, and l_j is the slot length of the jth slot. Application of Galerkin's procedure yields

$$\begin{bmatrix} \left[Y_{pq}^{ij}(a) + Y_{pq}^{ij}(c, S_i^I; S_j^I) \right] & \left[-Y_{pq}^{ij}(c, S_i^I; S_j^{II}) \right] \\ \left[-Y_{pq}^{ij}(c, S_i^{II}; S_j^I) \right] & \left[Y_{pq}^{ij}(a) + Y_{pq}^{ij}(c, S_i^{II}; S_j^{II}) \right] \end{bmatrix} \left\{ \begin{bmatrix} V_{qj}^I \\ V_{qj}^{II} \end{bmatrix} \right\} = \left\{ \begin{bmatrix} 0 \\ I_{pi} \end{bmatrix} \right\} \qquad (4)$$

The admittance matrix elements due to the internal coupling in the waveguide are given by

$$Y_{pq}^{ij}(a) = \iint\limits_{S_i^I} \iint\limits_{S_j^I} G_{zz}^a(\mathbf{r}, \mathbf{r}') \sin\alpha_{pi}\xi \, \sin\alpha_{qj}\xi' \, dS \, dS' \tag{5}$$

where G_{zz}^a is the $\hat{z}\hat{z}$ component of the magnetic-source magnetic-field dyadic Green's function for a sectoral waveguide,

$$G_{zz}^a = \frac{k^2}{j\omega\mu} \sum_{m=0}^{\infty} B(m,n) \cos\nu\varphi \, \cos\nu\varphi' \frac{1}{jh_{mn}} \Big\{ -2jh_{mn}\delta(z-z')$$

$$+ (\lambda_{mn}^2/\triangle_{mn}) \Big[e^{-jh_{mn}|z-z'|} - R_{mn}^< e^{j2h_{mn}z_1} e^{-jh_{mn}(z+z')}$$

$$- R_{mn}^> e^{-j2h_{mn}z_2} e^{jh_{mn}(z+z')} + R_{mn}^< R_{mn}^> e^{-jh_{mn}(z_2-z_1)} e^{jh_{mn}|z-z'|} \Big] \Big\} \tag{6}$$

where

$$B(m,n) = \frac{1}{1+\delta_{0m}} \frac{1}{k^2} \frac{[B_\nu(\lambda_{mn}\rho_2)]^2}{N_{\lambda_{mn}}\phi_0} \tag{7}$$

$$B_\nu(\lambda_{mn}\rho) = J_\nu'(\lambda_{mn}\rho_1)Y_\nu(\lambda_{mn}\rho) - Y_\nu'(\lambda_{mn}\rho_1)J_\nu(\lambda_{mn}\rho) \tag{8}$$

$$N_{\lambda_{mn}} = \int_{\rho_1}^{\rho_2} \rho\Big[B_\nu(\lambda_{mn}\rho)\Big]^2 d\rho = \frac{1}{2\lambda_{mn}^2}\Big\{(\lambda_{mn}^2\rho^2 - \nu^2)\Big[B_\nu(\lambda_{mn}\rho)\Big]^2\Big\}_{\rho_1}^{\rho_2} \tag{9}$$

$$\triangle_{mn} = 1 - R_{mn}^< R_{mn}^> e^{-jh_{mn}(z_2-z_1)} \tag{10}$$

In the above, $\nu = m\pi/\phi_0$, $h_{mn} = \sqrt{k^2 - \lambda_{mn}^2}$, λ_{mn} are the roots of $B_\nu(\lambda_{mn}\rho_2) = 0$, and $R_{mn}^<$ and $R_{mn}^>$ are the mode reflection coefficients for mode (m,n) at $z = z_1$ and $z = z_2$, respectively. The integrals in (6) can be evaluated analytically. For self-admittance elements, the summation of slowly converging series can be accelerated using the Kummer transform.

The admittance matrix elements due to the external coupling of the cylinder are given by

$$Y_{pq}^{ij}(b) = \iint\limits_{S_i^{II}} \iint\limits_{S_j^{II}} G_{zz}^b(\mathbf{r}, \mathbf{r}') \sin\alpha_{pi}\xi \, \sin\alpha_{qj}\xi' \, dS \, dS' \tag{11}$$

262

where G_{zz}^b is the $\hat{z}\hat{z}$ component of the magnetic-source magnetic-field dyadic Green's function for a conducting cylinder. For large cylinders, there are two complemental asymptotic solutions. One is given by Boersma and Lee [4]:

$$G_{zz}^b \sim G_0(t)\left\{ v\left(\beta\right)\left[\cos^2\tilde{\theta} + \tilde{q}\left(1 - \tilde{q}\right)\left(2 - 3\cos^2\tilde{\theta}\right)\right]\right.$$

$$\left. - \tilde{q}\beta v'\left(\beta\right)\left[\frac{11}{12}\cos^2\tilde{\theta} + \tilde{q}\left(\frac{11}{6} + \frac{2}{3}\tan^2\tilde{\theta} - \frac{187}{64}\cos^2\tilde{\theta}\right)\right]\right\} \tag{12}$$

and the other is given by Bird [5]:

$$G_{zz}^b \sim G_0(t)\left\{ v\left(\beta\right)\left[\cos^2\tilde{\theta} + \tilde{q}\left(1 - \tilde{q}\right)\left(2 - 3\cos^2\tilde{\theta}\right)\right] - \tilde{q}\left[v\left(\beta\right)\left(\frac{31}{72}\sin^2\tilde{\theta} - \frac{5}{24}\right)\right.\right.$$

$$\left.\left. + v_1\left(\beta\right)\left(\frac{11}{60} - \frac{17}{36}\sin^2\tilde{\theta}\right) + v_2\left(\beta\right)\left(\frac{1}{24}\sin^2\tilde{\theta} + \frac{1}{40}\right) + \frac{j\beta}{5}v_0^{(1)}\left(\beta\right)\right]\right\} \tag{13}$$

where β, $\tilde{q}$ and $\tilde{\theta}$ are parameters, and v, v_1, v_2 and $v_0^{(1)}$ are the surface Fock functions, all are defined in [4] and [5]. Among (11) and (12), the latter is suited for the calculation of the mutual admittance between two distant slots whose centers have the same z-coordinate, whereas the former can be used for the calculation of self-admittance and mutual admittance in all other cases. For mutual admittance, the quadruple integrals can be reduced to a single integral by using midpoint integration and average slot-length approximation. For self-admittance, G_{zz}^b can be written as the sum of the Green's function for the infinite conducting plane and a perturbation term due to the curvature of the cylinder. The corresponding quadruple integrals can be reduced two double regular integrals though a change of variables and transformation of coordinates.

The admittance matrix elements due to the mutual coupling of the slot-cavity of sectoral cross-section, $Y_{pq}^{ij}(c, S_i^\alpha; S_j^{\alpha'})$ $(\alpha, \alpha' = I, II)$, can be expressed exactly in terms of the Bessel and modified Bessel functions of the first and second kinds with orders zero and one.

For a plane wave of arbitrary polarization and incident angle, whose electric field is given by

$$\hat{e}^{inc} = (\hat{\theta}^{inc}\cos\psi + \hat{\phi}^{inc}\sin\psi)e^{-jk[\rho\sin\theta^{inc}\cos(\phi-\phi^{inc})+z\cos\theta^{inc}]} \tag{14}$$

where ψ is the polarization angle and $(\theta^{inc}, \phi^{inc})$ denote the incident angles, the exciting vector can be written as

$$I_{pi} = j2Y_0\frac{\sin\psi}{\pi k}\frac{(2w/\rho_3)(p\pi/l_i)}{(k\cos\theta^{inc^2} - (p\pi/l_i)^2}\left[1 - (-1)^p e^{jkl_i\cos\theta^{inc}}\right]$$

$$\cdot e^{jk(z_{0i}-l_i/2)\cos\theta^{inc}}\sum_{n=0}^{\infty}\frac{\epsilon_n j^n\cos\left[n(\phi_{0i} - \phi^{inc})\right]}{H_n^{(2)'}(k\rho_3\sin\theta^{inc})}\text{Sam}(nw/\rho_3) \tag{15}$$

where z_{0i} and ϕ_{0i} are the coordinates of the center of the ith slot, $\text{Sam}(x)$ is a sampling function.

Once the magnetic currents on the slot apertures are obtained, we can calculate the scattered fields and RCS of the slot array.

3. Numerical Example

A computer program is developed based on the formulation described above. An 8×8 slot array is analyzed. The slotted-guides are identical with $\rho_1 = 31.096$ cm, $\rho_2 - \rho_1 = 1.016$ cm, $t = 0.08$ cm, $\phi_0 = 0.0699587$ rad and the average thickness of the side walls $\triangle = 0.3$ cm. All slots have the same length $l = 1.6$ cm, width $2w = 0.16$ cm, and offset $\delta = 0.15$ cm. The frequency of the incident wave is $f = 9.1$ GHz.

To demonstrate the effect of the curvature of the host cylinder on the RCS of a conformal slot array, Figs. 3 show the RCS for $\rho_1 = \infty$, $\rho_1 = 500$ cm, $\rho_1 = 200$ cm, $\rho_1 = 100$ cm, and $\rho_1 = 50$ cm in E-plane. As can be seen, the cylinder's curvature has a significant effect on the patterns and values of the RCS in the E-plane. When ρ_1 becomes large, the RCS approaches that for a planar array.

When ρ_1 decreases, the grating lobes begin to disappear and the maximum RCS decreases.

Fig. 4 shows the frequency responses of a 8×8 array ($\rho_1 = 100$ cm) with matched and shorted terminals, respectively. It is very interesting to note that the RCS of the slot array is almost identical no matter the waveguides are matched or shorted when the frequency is not close to the working frequency. At the working frequency, the RCS is substantially different. This implies that when the frequency of the incident wave is not close to the working frequency of the slot array, the energy entering the waveguides is very trivial and the main contribution to the RCS is the wave scattered by the slots directly.

References

[1] L. Josefsson, "Slot coupling and scattering," *1990 IEEE Antennas Propagat. Int. Symp.*, pp. 942-945, Dallas, June 1990.

[2] J. Chen and J.-M. Jin, "Electromagnetic scattering from slot antennas on waveguides with arbitrary terminations," *Microwave Opt. Tech. Lett.*, vol. 10, no. 5, pp. 286-291, Dec. 1995.

[3] G. Fan, "Cylindrically conformal slotted-waveguide array antenna," Ph.D. thesis, Tsinghua University, Beijing, China, Apr. 1995.

[4] J. Boersma and S. W. Lee, "Surface field due to a magnetic dipole on a cylinder: Asymptotic expansions of exact solution," Univ. of Illinois at Urbana-Champaign, Electromagnetics Lab., Rep. 78-17, 1978.

[5] T. S. Bird, "Accurate asymptotic solution for the surface field due to aperture in a conducting cylinder," *IEEE Trans. Antennas Propagat.*, vol. 33, no. 10, pp. 1108-1117, Oct. 1985.
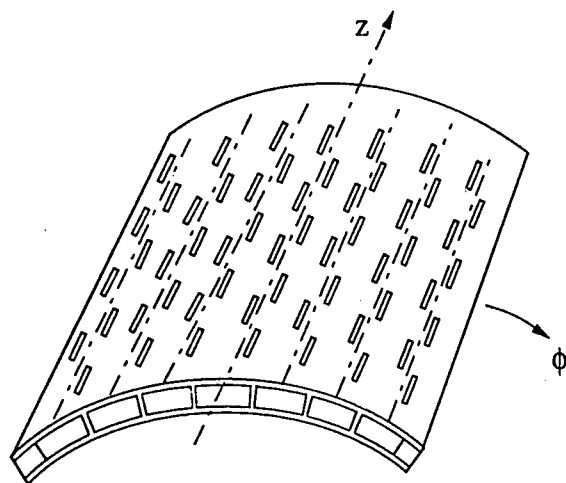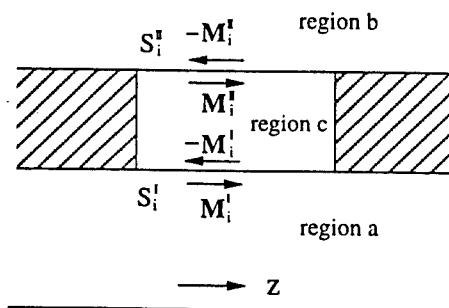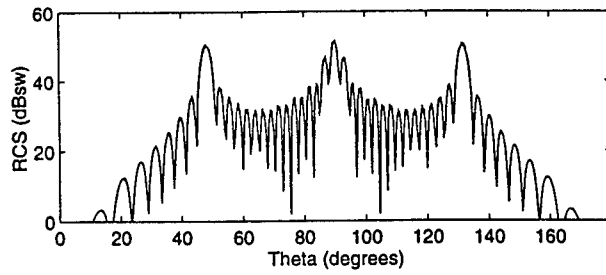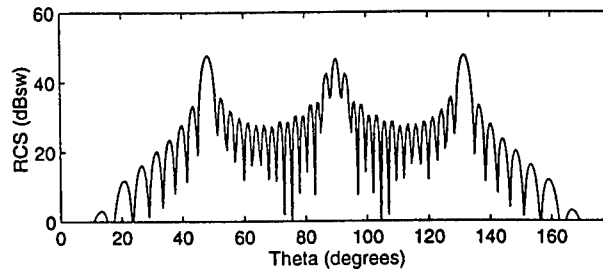
Figure 1: Conformal slotted-waveguide array.
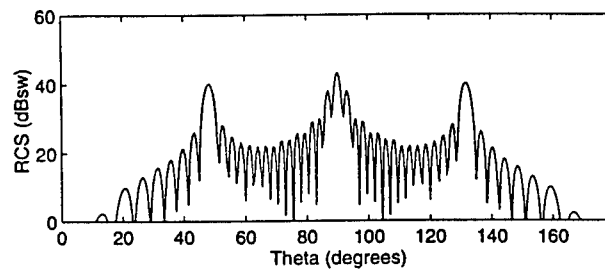

Figure 2: Division of three regions and surface magnetic currents.
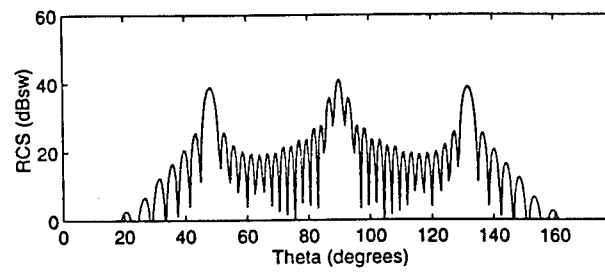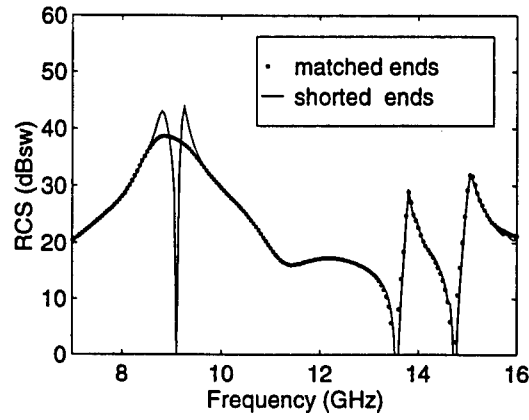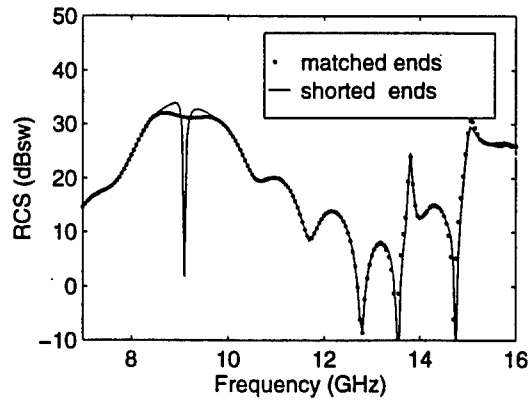
(a)

(b)

(c)

(d)

Figure 3: The effect of the cylinder's curvature on the RCS in the H-plane for a 16×16 slot array with matched terminals at $f = 9.1$ GHz. (a)—·— planar, —— $\rho_1 = 500$ cm, (b) $\rho_1 = 200$ cm, (c) $\rho_1 = 100$ cm, (d) $\rho_1 = 50$ cm.

(a)

(b)

Figure 4: RCS of a 8 × 8 conformal slot array ($\rho_1 = 50$ cm) as a function of frequency. (a) $\theta^{inc} = 90^0$, $\varphi^{inc} = 0^0$; (b) $\theta^{inc} = 90^0$, $\varphi^{inc} = 45^0$.

Time-Domain Pulse System for Inverse Scattering and Imaging

FU-CHIARNG CHEN AND WENG CHO CHEW

ELECTROMAGNETICS LABORATORY
CENTER FOR COMPUTATIONAL ELECTROMAGNETICS
DEPARTMENT OF ELECTRICAL AND COMPUTER ENGINEERING
UNIVERSITY OF ILLINOIS
URBANA, IL 61801

Abstract: In this paper, a time-domain pulse radar system is used for inverse scattering and imaging. An ultra-wideband time-domain pulse system has been developed at the University of Illinois for nondestructive evaluation and microwave imaging purposes.

1. Introduction

The ultra-wideband time-domain pulse radar system has drawn a lot of attention recently. The ultra-wideband signal provides much more information for target sensing and imaging as compared to the more conventional narrow-band CW radar system. Recently, a time-domain pulse radar system has been developed at the University of Illinois for nondestructive evaluation (NDE) and inverse scattering and imaging purposes [1,2,3]. The collected time-domain measurement data are processed with nonlinear iterative inverse scattering imaging algorithms such as the distorted Born iterative method (DBIM) [4,5] and the local shape function (LSF) method [6,7,8] developed at the University of Illinois.

2. Time-Domain Pulse System

The ultra-wideband time-domain pulse radar system consists of a 20 GHz digital sampling oscilloscope, an ultra-wideband Vivaldi antenna array, two microwave switches, two ultra-wideband amplifiers and a 10 GHz monocycle pulse source [1,3]. The automated pulse system control program combines the GPIB control card and

digital switch control card using the C programming language. The one-dimensional ultra-wideband Vivaldi antenna array consists of 5 transmitters and 6 receivers. The dimensions of the Vivaldi antenna [9] are shown in Figure 1. The antenna patterns of the Vivaldi antenna at different frequencies are shown in Figure 2 to 5. Figure 2 shows the pattern at 2 GHz and Figure 3 shows the pattern at 3 GHz. From these two figures, we can see that the antenna has a higher directivity at a higher frequency because the beamwidth decreases when the frequency increases. Figure 4 shows the co-polarization (E_x) and cross-polarization (E_y) patterns at 2 GHz. In Figure 5, the co-polarization and cross-polarization patterns at 3 GHz are shown. From these two figures, we can see that the co-polarization and cross-polarization have a good polarization isolation, which is higher than 20 dB. The full array's 30 measurement data sets from 5 transmitting antennas and 6 receiving antennas have been collected successfully using the digital switch control card to switch the two microwave switches attached to the Vivaldi antenna array.

3. Inverse Scattering and Imaging

Two iterative nonlinear inverse scattering imaging algorithms, the Distorted Born Iterative Method (DBIM) [4,5] and the Local Shape Function (LSF) [6,7,8] method, have been applied successfully to process the measurement data to reconstruct the images of the test targets. Figures 6-8 show the reconstructed results of different test targets. Figure 6 shows the reconstructed image of a metallic cylinder using the LSF method. The front curvature of the cylinder facing the Vivaldi antenna array is clearly observed. Figure 7 shows the reconstructed image of a PVC pipe using DBIM permittivity reconstruction. Figure 8 shows the reconstructed image of two metallic cylinder rods using the LSF method. From these images we have shown that the pulse system can detect and reconstruct the metallic and dielectric targets in air. The pulse system can also detect a metallic target located in

the concrete block [3].

4. Conclusions

We have shown the feasibility of the time-domain pulse system as an inverse scattering and imaging system by combining the pulse system hardware and inverse scattering imaging algorithms successfully.

5. References

[1] F.-C. Chen and W. C. Chew, "Time-Domain Ultra-Wideband Radar System For Nondestructive Evaluation", *URSI Radio Science Meeting Digest*, Baltimore, Maryland, July 21-27, 1996.

[2] F.-C. Chen, W. C. Chew, and W. H. Weedon, "Inverse Scattering Imaging Using Time-Domain Ultra-Wideband Radar", *URSI Radio Science Meeting Digest*, Baltimore, Maryland, July 21-27, 1996.

[3] F.-C. Chen and W. C. Chew, "An Impulse Radar Nondestructive Evaluation System", *Twenty-third Annual Review of Progress in Quantitative Nondestructive Evaluation*, Brunswick, Maine, July 28-Aug. 2, 1996.

[4] W. C. Chew, *Waves and Fields in Inhomogeneous Media*. New York: Van Nostrand, 1990.

[5] W. C. Chew and Y. M. Wang, "Reconstruction of two-dimensional permittivity distribution using the distorted Born iterative method,", *IEEE Trans. Medical Imag.*, vol. 9, no. 2, pp. 218-225, 1990.

[6] W. C. Chew and G. P. Otto,"Microwave imaging of multiple metallic cylinders using shape functions," *Micro. Guided Wave Lett.*, vol. 2, no. 7, pp. 284-286, 1992.

[7] G. P. Otto and W. C. Chew,"Microwave inverse scattering-Local shape function (LSF) imaging for improved resolution of strong scatters,", *IEEE Trans.*

Microwave Theory Tech., Vol. MTT-42 No. 1, pp. 137-141, July 1994.

[8] W. H. Weedon and W. C. Chew,"A local shape function (LSF) method for time-domain inverse scattering,", *IEEE Antennas and Propagation Society International Symposium Digest*, Ann Arbor, MI, June 28-July 2, 1993.

[9] K. M. Frantz,"An investigation of the Vivaldi flared radiator." M.S. thesis, University of Illinois at Urbana-Champaign, 1992.
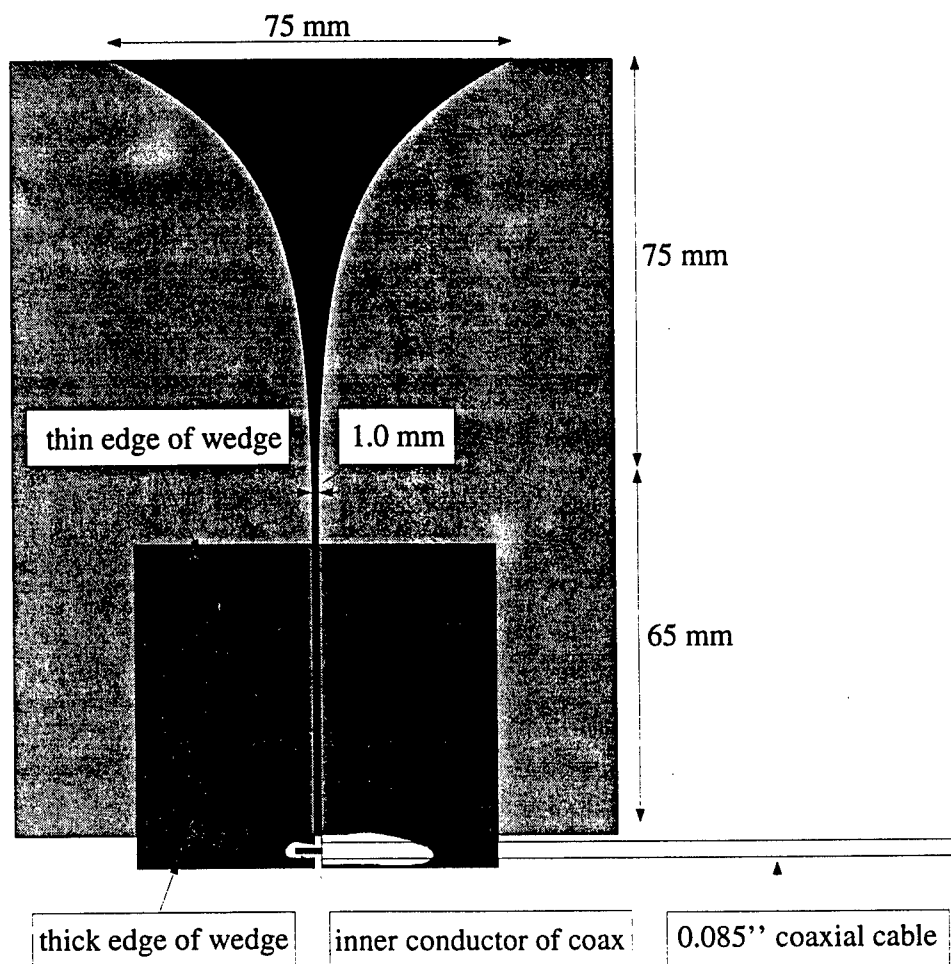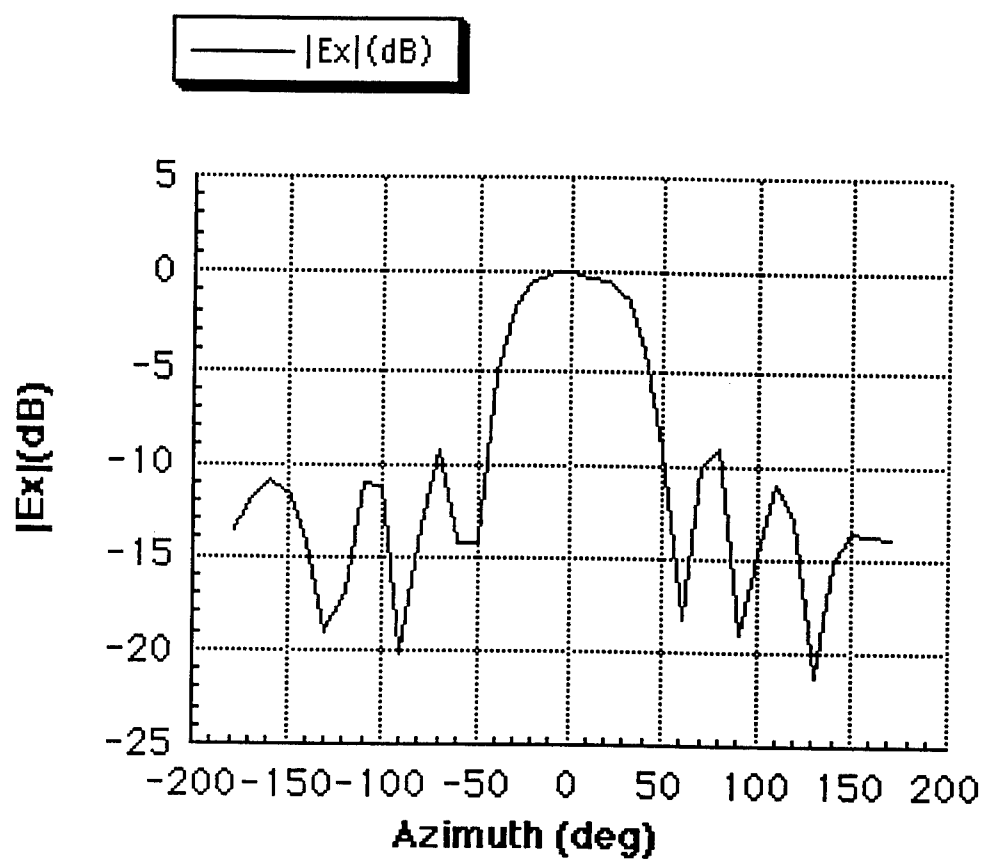
Fig. 1. The dimensions of the Vivaldi antenna.

75 mm

75 mm

65 mm

thin edge of wedge 1.0 mm

thick edge of wedge inner conductor of coax 0.085'' coaxial cable

Fig. 2. The antenna pattern of the Vivaldi antenna at f=2GHz.

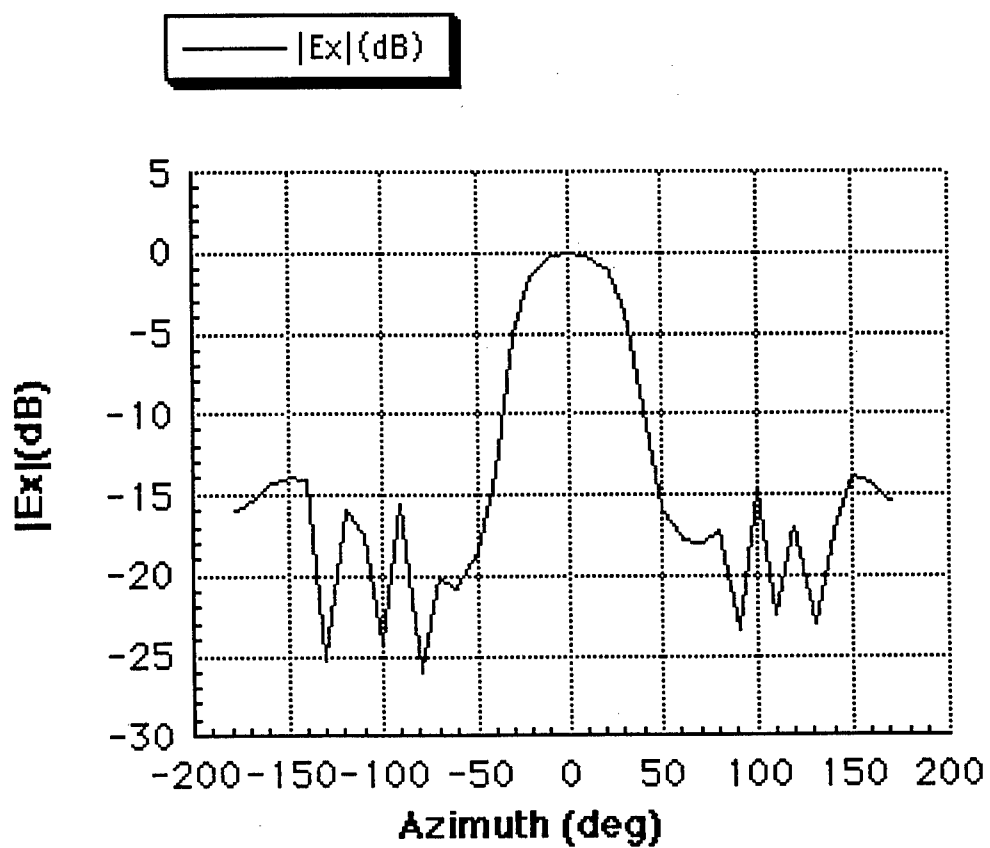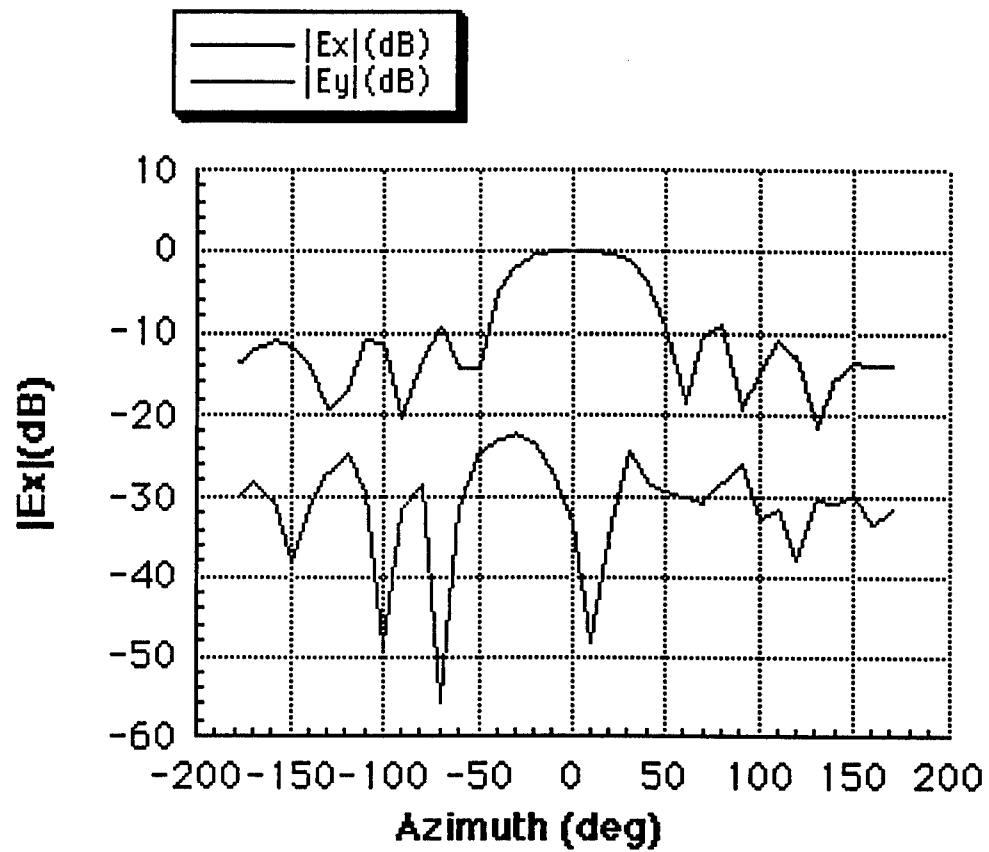**Fig. 3.** The antenna pattern of the Vivaldi antenna at f=3GHz.

Fig. 4. The Co-polarization and cross-polarization patterns at f=2GHz.

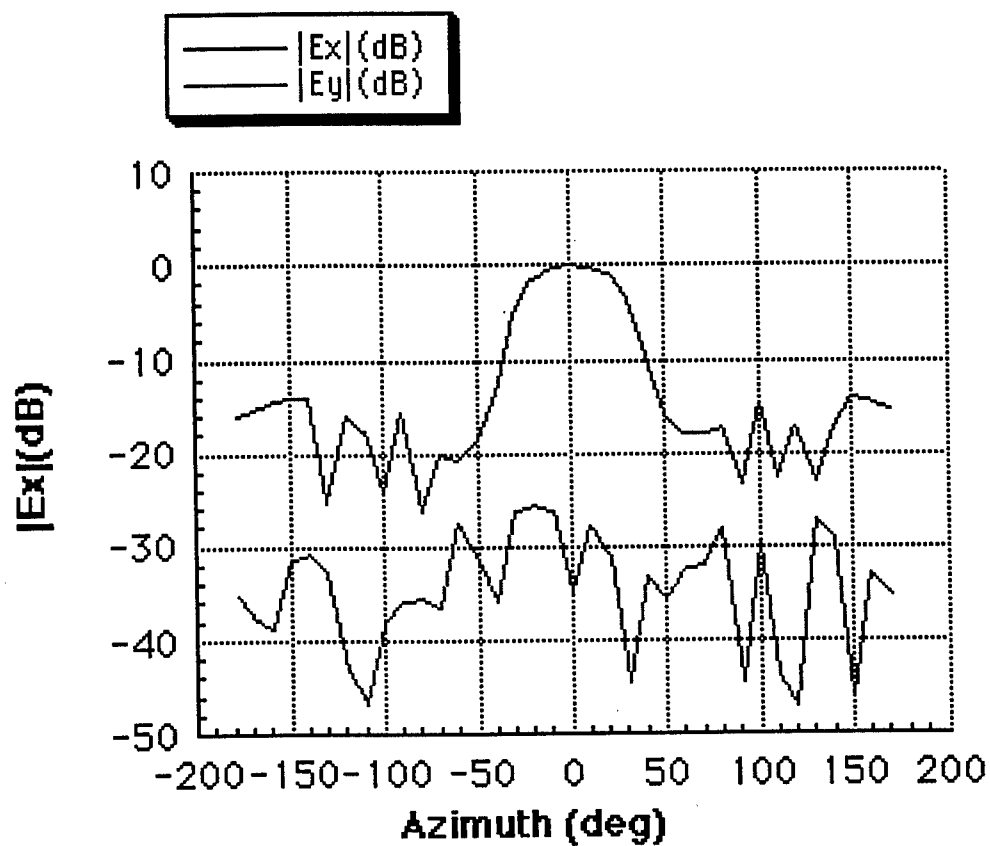**Fig. 5.** The Co-polarization and cross-polarization patterns at f=3GHz.

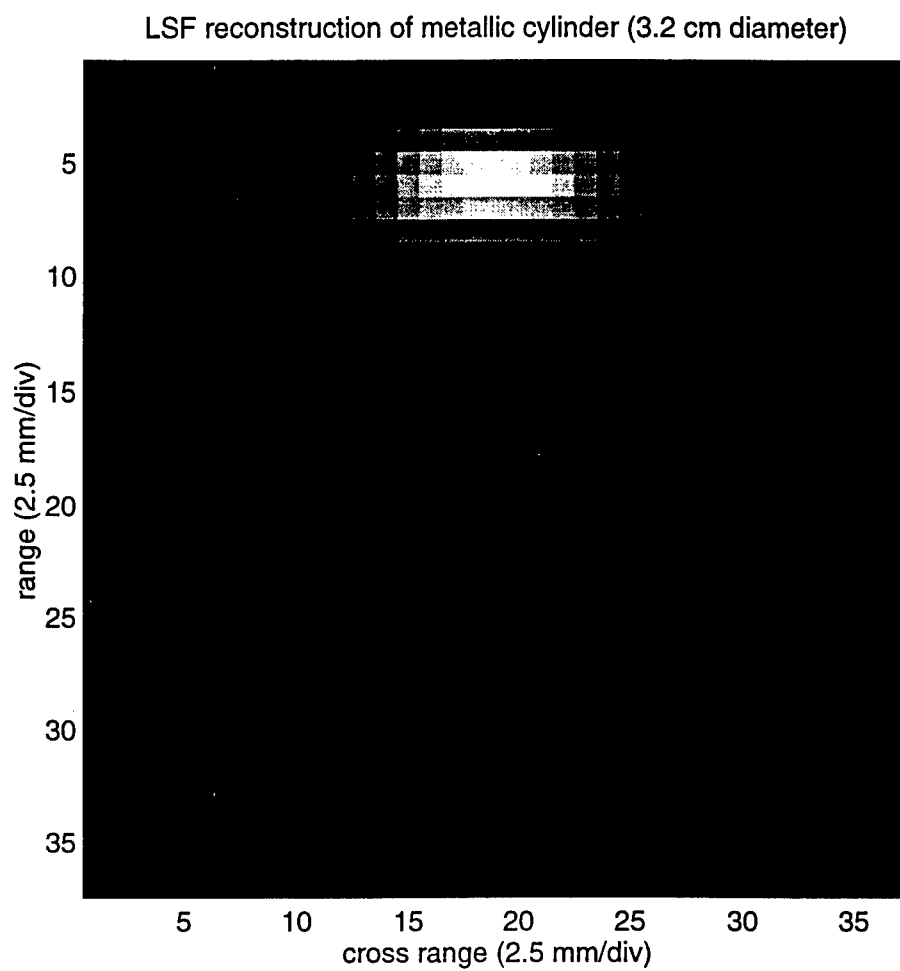LSF reconstruction of metallic cylinder (3.2 cm diameter)

Fig. 6. The reconstructed image of the metallic cylinder.

DBIM reconstruction of PVC pipe (diameter 4.8cm)
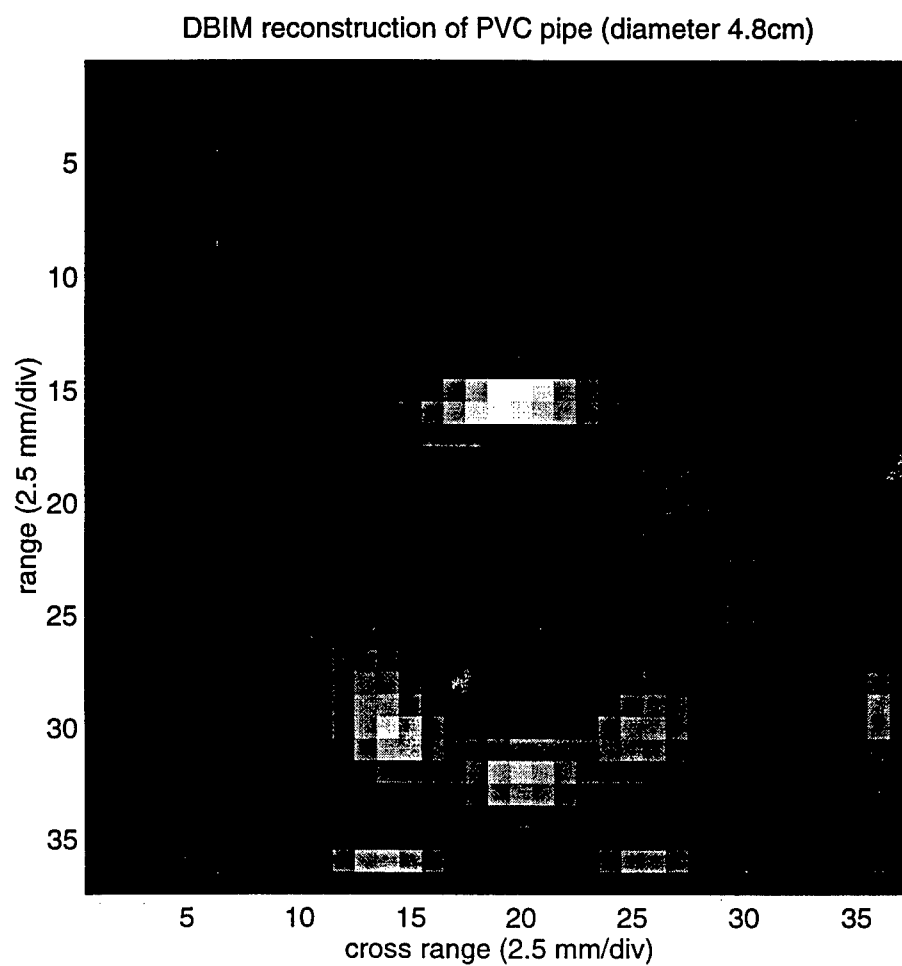
Fig. 7. The reconstructed image of a plastic pipe.

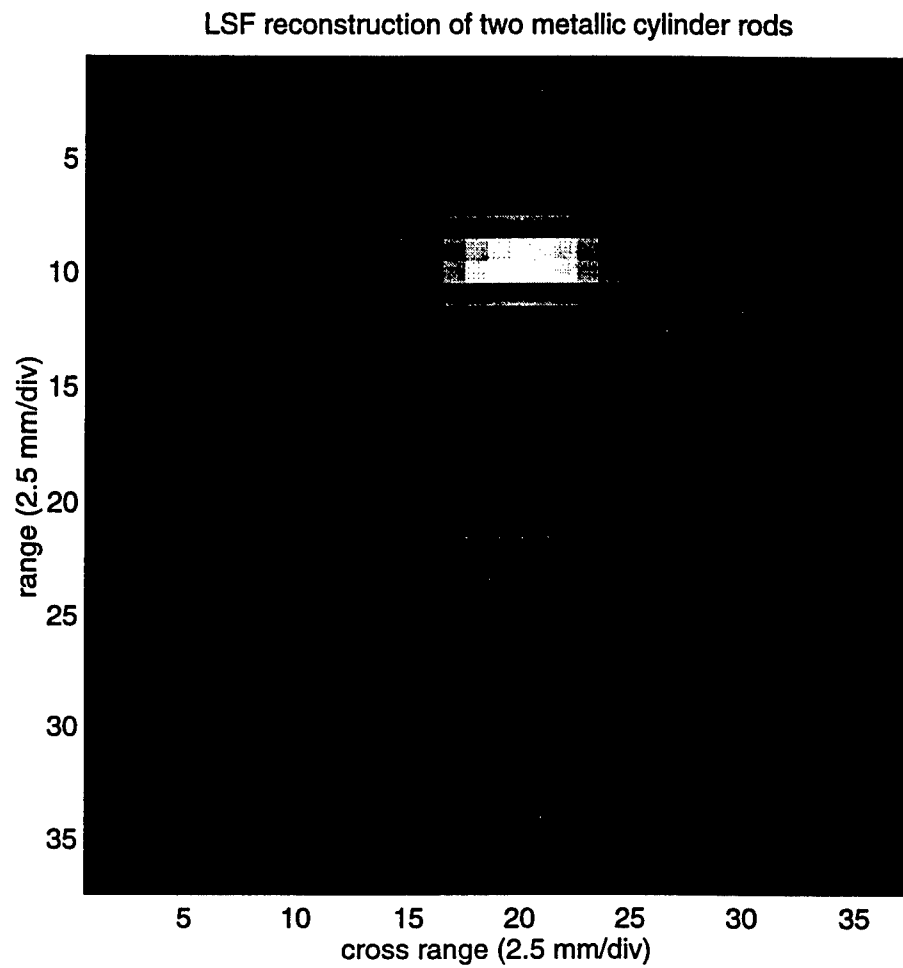LSF reconstruction of two metallic cylinder rods

Fig. 8. The reconstructed image of two metallic cylinder rods.

NUMERICAL ANALYSIS OF DIVERSITY ANTENNA SYSTEMS FOR HAND-HELD COMMUNICATION DEVICES

Karen Marie Coperich
University of Illinois
Urbana, IL

Abstract

The formidable task of antenna operation within a multipath environment is often combated by utilizing multiple diversity antennas with independent spatial distributions and polarizations. The benefit of additional antennas is measured by the correlation between the diversity channels. With the aid of a simplified multipath model, the correlation can be directly related to real physical parameters of the antenna system. Specifically, the correlation coefficient is related to the far field pattern of the radiating antenna system. The Finite Difference Time Domain (FDTD) and Method of Moments (MOM) numerical methods can model the diversity antennas mounted upon a portable hand-set and generate the far field pattern. Analysis of various antennas configurations will illustrate the affect on diversity system performance in a multipath environment.

Section I: Introduction

Mobile and personal communication devices operate in surroundings which not only rely upon the multipath environment but are also plagued by it. Classically, free-space line-of-sight communication links are governed by the Friis transmission formula. However, when obstacles and/or motion are present in the vicinity of either the transmit or receive antennas, a multipath environment is created. The signal received in such a region corresponds to multiple incident waves that have been spatially and temporally separated from the original source due to scattering from obstacles. Each individual path may vary in distance and losses. Since a line-of-sight path may not necessarily be present, receiving antennas are generally broad-beamed in order to "accept" incident waves that have been reflected in numerous directions. Relying on scattering is absolutely necessary when there is no direct line of sight between the transmitter and receiver. However, this same phenomenon also causes destructive summation of the fields, called fading, in

unpredictable locations. "The prediction of the exact field in a particular spot is an intractable electromagnetics problem because the boundary conditions are generally too numerous and some are transitory [1]."

Diversity Antennas versus Array Antennas

An array antenna consists of fixed antennas spaced by some distance (often $\lambda/2$). They are generally combined at RF after passing through preset phase shifters and transmission lines that were designed for the desired phase relationship, see Figure 1(a). On the other hand, a space-diversity scheme, as depicted in Figures 1(b) and (c), in most instances has multiple RF front ends and weights that are continuously adjusted for coherent combining, typically at IF or baseband [2, 3]. As a result, directional antenna arrays can reduce fading but can not increase the received signal level unlike diversity schemes which can accomplish both. Diversity reception increases the average signal-to-noise ratio (SNR) but only by a few decibels. This could just as easily be accomplished by increasing the source power. The salient feature of diversity reception is the capability to reduce the variance of the signal envelope. This effect can not be achieved by increasing the transmitted power [4].

Types of Diversity Antennas

Typical means of diversity implementation that influence antenna designs include frequency, polarization, and spatial distributization. A frequency diversity scheme uses a set of narrowband antennas each of which can be thought of as a bandpass filter centered at a different frequency for each diversity channel.
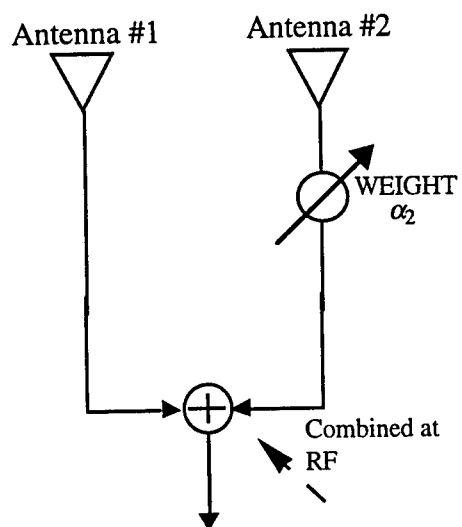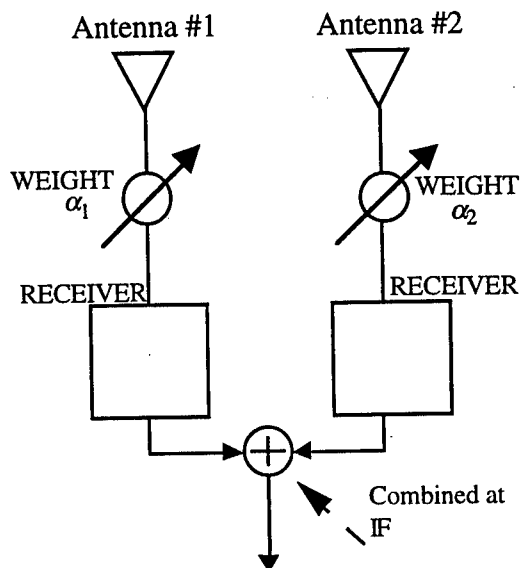
282

Figure 1(a) Array antenna [2].

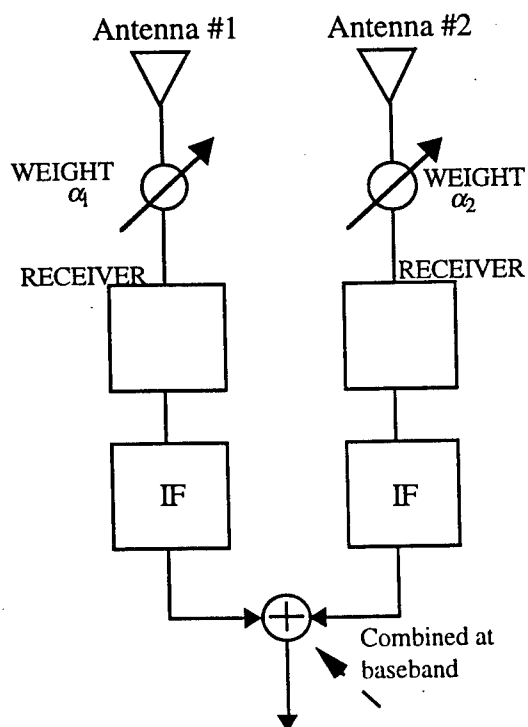**Figure 1(b)** Diversity antenna [2].

Figure 1(c) Diversity antenna [2].

Interchannel correlation is dependent on the frequency bandwidth of the antennas. Disadvantages of this system include a larger frequency allocation and a separate transmitter/receiver system for each frequency used. On the other hand, polarization diversity does not necessarily complicate the transmitter/receiver circuitry. However, the power received by each individual orientation is one-half (or -3 dB) that of a linear antenna under the same conditions. Orthogonal polarizations are chosen for best results and to allow placement of the antennas in close proximity. This feature is useful when the physical dimensions of the system are limited. Spatial diversity takes advantage of the fact that the signal path from the source to two different locations is different. Therefore, it is hoped that if one antenna is located in a fading null that the other diversity elements are not also experiencing destructive interference. There is no additional frequency bandwidth needed for such an architecture. Limitations are mainly in the allowable system dimensions.

After an antenna has converted a free-space wave to a guided wave, the signal can be combined with the output of other antennas in numerous ways (see Figures 2(a)-(d)). Various signal processing techniques such as selection, switched, maximal ratio, and equal-gain combining are used. This method of diversity implementation can be incorporated alternatively or concurrently with the antenna diversity techniques previously mentioned.
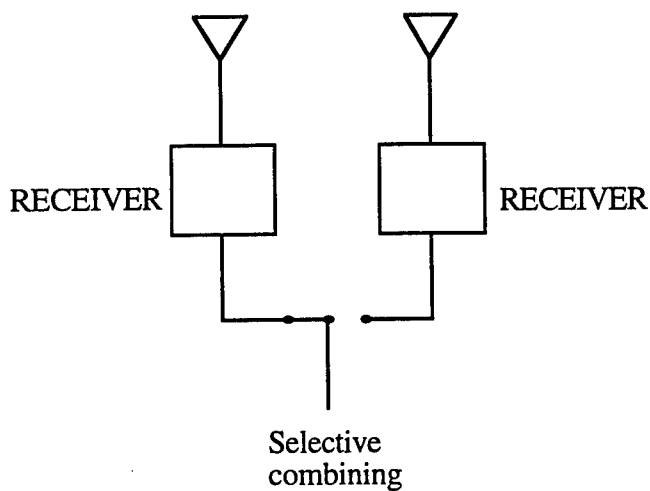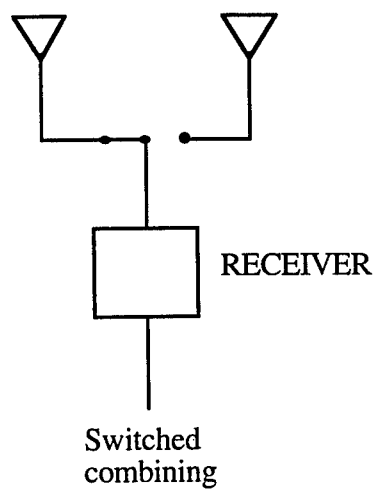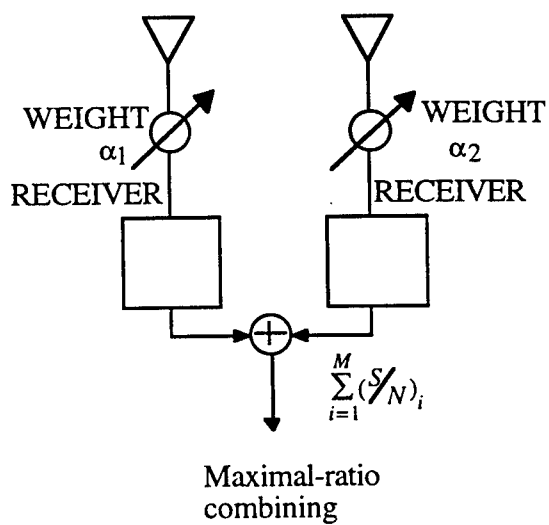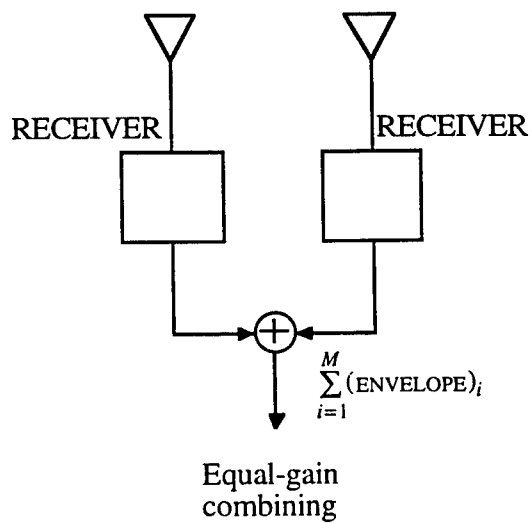
Figure 2 Diversity combination methods [2]. **(a)**
Selective combining. **(b)** Switched combining. **(c)**
Maximal-ratio combining. **(d)** Equal-gain
combining.

Figure 2 Continued.

Uncorrelated Channels

With the ultimate goal of creating two uncorrelated channels, it is useful to quantify the similarity between received signals of the diversity channels in terms of physical parameters. Low correlation is desired in order to compensate for lost information caused by noise and fading. The signal correlation coefficient, ρ_s, is related to the envelope correlation coefficient, ρ_e, of two narrowband signals in the following manner: $\rho_e = |\rho_s|^2$ [3]. If the following six assumptions are made, ρ_s can be written directly in terms of the far-field radiation patterns of the diversity antennas as shown in Equations (1).

1. The fading signal envelope is Rayleigh distributed.
2. Orthogonal polarizations are uncorrelated.
3. Each individual polarization is spatially uncorrelated.
4. Either polarization (q or f) is equally likely.
5. The field arrives in the horizontal (q = p /2) plane only.
6. The time-averaged power density per steradian is
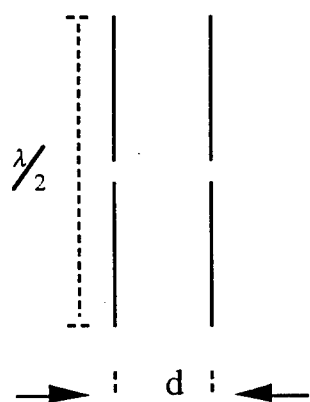constant in the horizontal plane

$$\rho_s = \frac{\int_0^{2\pi} E_{12}(\phi)d\phi}{\sqrt{\left(\int_0^{2\pi} E_{11}(\phi)d\phi\right)\left(\int_0^{2\pi} E_{22}(\phi)d\phi\right)}} \qquad (1a)$$

$$E_{mn}(\phi) = E_{\theta_m}\left(\frac{\pi}{2},\phi\right)E_{\theta_n}{}^*\left(\frac{\pi}{2},\phi\right) + E_{\phi_m}\left(\frac{\pi}{2},\phi\right)E_{\phi_n}{}^*\left(\frac{\pi}{2},\phi\right) \qquad (1b)$$

$E_{\theta,\phi_{n,m}}$ denotes the far-field pattern of a specific component and specific radiating antenna while all other antennas are terminated. Three different terminations were used in this work for the passive antenna. The antenna which was not electrically driven, was either open circuited, not present, or loaded by a 50 Ω lumped load.

The diversity signal combination techniques presented earlier determine the load termination of the diversity antennas. The correlation for a selective or switched combining technique (see Figure 2) requires that $\vec{E}_1$ and $\vec{E}_2$ in Equation (1) to be computed while the second antenna is open circuited. However, for the techniques such as maximal ratio and equal gain combining, which mix signals from both elements, a matched load is used to create a parasitic element.

To illustrate, the correlation between a pair of dipole antennas, as shown in Figure 3, is derived in Equations (2). Due to the circular symmetry of a dipole's far-field radiation pattern in the azimuth plane, Equation (2a) reduces to a function of only the separation distance, d. The power pattern of a single dipole is represented by P, and S is the power density per steradian, both of which are constant in the azimuth plane.

$$\overline{\rho}_s = \int_{MCS} E_1(\Omega) \cdot E_2^*(\Omega) S(\Omega) d\Omega \qquad (2a)$$

$$\overline{\rho}_s = \iint P_\theta(\theta)\, e^{j\vec{k}\cdot\vec{d}} S(\theta,\phi) d\theta d\phi \qquad (2b)$$

$$\overline{\rho}_s = \int_0^{2\pi} e^{jkd\cos\phi} d\phi \qquad (2c)$$

$$\rho_s = J_o(kd) \qquad (2d)$$

Figure 3 Dipoles for diversity reception.

Since the pair of dipole antennas is circularly symmetric, the correlation coefficient is purely real. From Figure 4, observe that as kd becomes larger the correlation decreases. In fact for kd $\geq$ 2.0, ρ_e<0.2. This result is not only intuitively satisfying but justifies the common rule of thumb that array elements placed $\lambda/2$ away are independent.
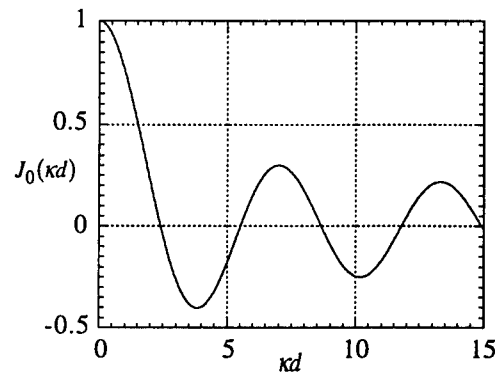

Figure 4 Bessel function of the 1st kind of the zeroth order.

Personal Communication Devices

Small hand-held devices are a particularly challenging problem due to the physical size limitation and proximity to the head. To date, numerical methods such as the Method of Moments (MoM) and Finite Difference Time Domain (FDTD) schemes have been used to provide information such as radiation patterns and input impedance for such complex geometries. Numerical diversity analysis is another potential application. At the frequency band allocated for such devices, approximately 900 MHz, $\lambda/2$ antenna element separation is not possible for portable devices. Therefore, if the antennas can not be physically separated enough

to achieve spatial independence, their antenna radiation patterns can not be omnidirectional in a diversity scheme. By selecting diversity antennas that minimize the numerator in Equation (1), spatial diversity can be implemented even in physically restrictive scenarios.

Section II: FDTD Analysis
Planar Inverted-F Antenna (PIFA)

The practical example studied included two diversity antennas positioned on a hand-held receiver. The diversity antennas selected were planar inverted-F antennas (PIFAs), chosen primarily for their thin profiles. This is an alternative to the commonly mounted $\lambda/4$ monopole. Even at 900 MHz, a $\lambda/4$ monopole, of approximately 3.3 inches, is still physically a bit cumbersome in conjunction with its transmitter/receiver unit. Additionally, the phone unit is not a good approximation for a ground plane; this effect on the radiation pattern will be shown.

The PIFA antenna is very similar to a $\lambda/4$ microstrip patch antenna. However, its physical dimensions are reduced by replacing the shorting wall with only a shorting pin as shown below in Figure 5. The patches are often supported by a dielectric substrate though none was used for the results in this work.
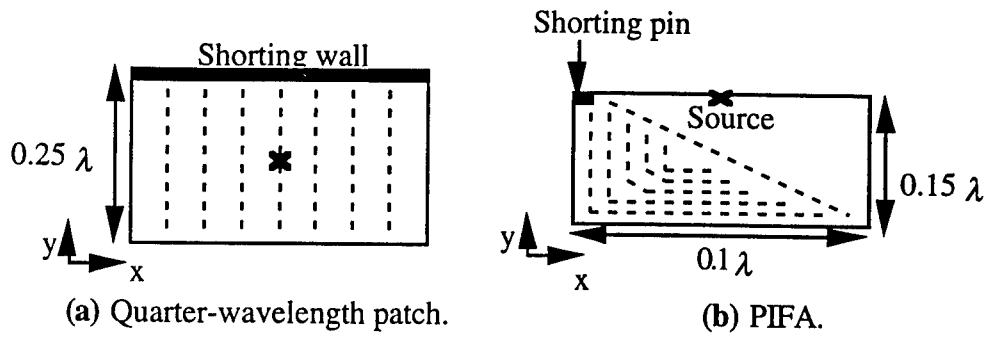
(a) Quarter-wavelength patch.

(b) PIFA.

Figure 5   Antenna patches

When the PIFA at a height 0.04 λ above a 1λ X 1λ ground plane was modeled using the FDTD code [5]. The geometry occupies a 40 X 40 X 50 = 80,000 cell volume of uniform grid spacing $\Delta x = \Delta y = \lambda /40$ and $\Delta z = \lambda /100$. Absorbing boundary conditions (ABCs) terminated all five sides of the volume except for the PEC ground plane beneath the patch. For comparison, the PIFA radiation pattern in the top half plane is shown along with the far-field radiation patterns of a $\lambda/4$ patch. Though the PIFA pattern is slightly distorted, the reduced aperture size is beneficial. As indicated in Figure 5, the current distribution upon the quarter-wavelength patch is almost strictly in the y-direction. Thus, the E_θ component of the yz cut is noticeably larger in Figure 6(a). The symmetry is excellent, due to image theory, and the main beam is quite broad.

The PIFA pattern in Figure 6(b) displays similarities relative to the original shorted $\lambda/4$ patch. The first observation is the asymmetry, due to the replacement of the shorting wall with a small conducting pin. E_θ continues to dominate; but, the large lobe in the quadrant of $-90 < \theta < 0$ is due to the fringing effects that are more dominant at the bottom edge of the patch.
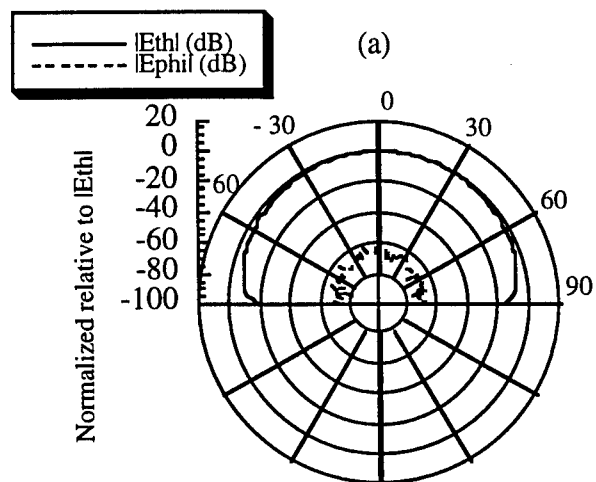
Figure 6 **(a)** Far-field pattern of quarter-wavelength patch antenna over ground plane (yz plane). **(b)** Far-field pattern of PIFA patch over ground plane (yz plane).
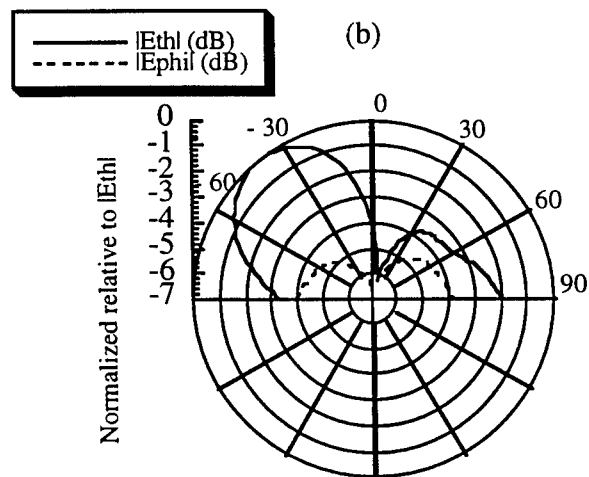

Figure 6   Continued.

291

Performance Of Antennas With Handset

Operation of the PIFA antenna over a large ground plane, relative to the antenna dimensions, is only a preliminary step. A model for the telephone handset must next be included. The full geometry (see Figure 7) now includes a second identical PIFA for diversity and occupies a 74 X 97 X 96 = 689,088 cell volume using a non-uniform mesh. The gap feed shown in Figure 7 was replaced by a coaxial feed terminated by a first-order Mur boundary condition at the z=0 plane so that reflections are dissipated. The far-field pattern in the yz plane is shown in Figure 8 in which both PIFA antennas are excited. Comparison of the yz plane with those in Figure 6 indicates the effect of the finite dimensional conductive box and the superposition of the individual PIFA radiation patterns.
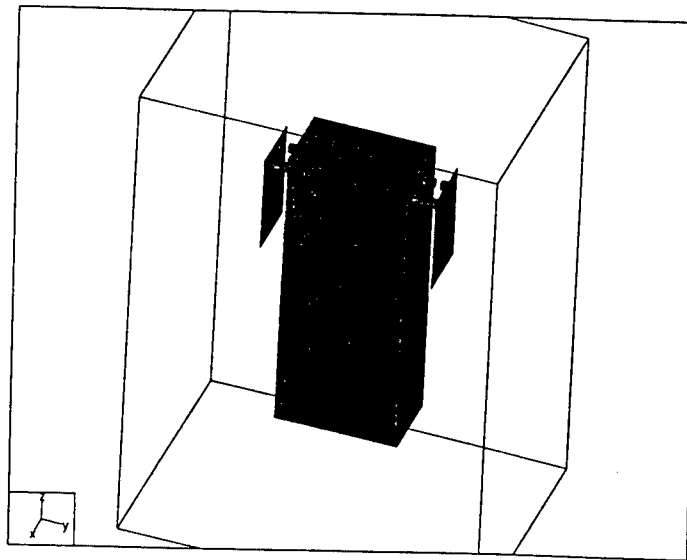
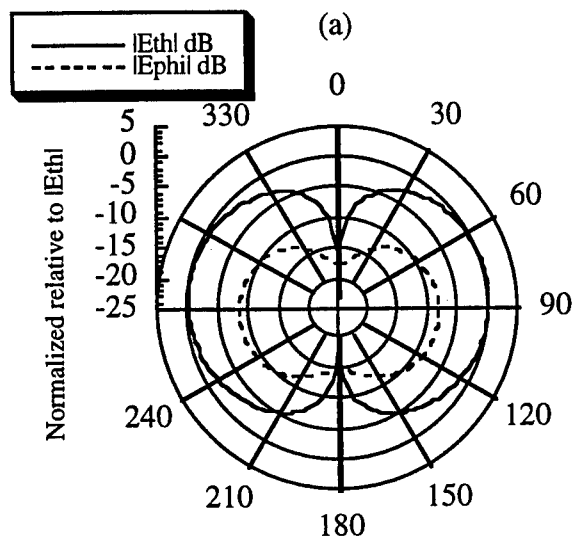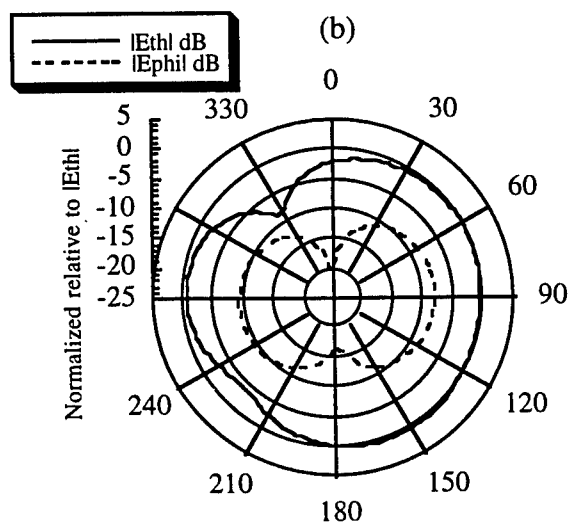

Figure 7 FDTD handset model.

Figure 8 (a) Far-field pattern of two PIFAs upon conductive box (yz plane). **(b)** Far-field pattern of single PIFA upon conductive box (yz plane).

When computing the correlation coefficient using Equation (1), the individual diversity element patterns are needed. With the left PIFA removed, the

results of exciting only the right PIFA can be see in Figure 8b. The fact that the back lobe is smaller for -90< θ <0 facilitates independence once the second PIFA is also mounted. The correlation coefficient results in Table 1 dramatically vary depending on the load type. Depending on the publication, the envelope correlation coefficient, $\rho_e = |\rho_s|^2$, for structures similar to Figure 7 have been reported in the range from 0.01606 to 0.8 [6] and [7]. Therefore, direct comparison with established results is difficult. Due to FDTD modeling difficulties such as thin wires and matched termination of the coaxial feed, the results for an open and nonexistent PIFA load types seem the most plausible.

Table 1 Correlation between two PIFAs on a conductive box (using FDTD).

Load Type	ρ_s^2
Open	0.0568
50 Ω	0.6769
Short Circuit	0.9114
Diversity antenna not present	0.2120

In order to show the effect of the radiation pattern on the correlation coefficient, another example will be presented. A λ/4 monopole mounted on top of the handset will replace the PIFA mounted on the left side of the handset. The monopole's coordinates are symmetrical with respect to the handset's x-direction dimensions and are 0.02λ away from the left side of the box. The far-field pattern of the monopole in Figure 9 was generated in the presence of only the handset unit;

no other antennas were mounted. The diversity performance results are expected to improve because of the dissimilarity between the individual PIFA and monopole patterns.
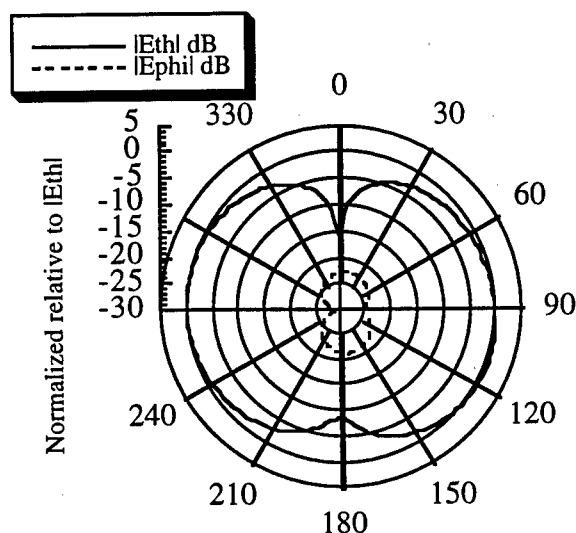
Figure 9 Far-field pattern of monopole upon conductive box (yz plane).

As with the two PIFA configuration, the envelope correlation is severely dependent on the load type. Reported results for monopole/PIFA geometry configuration range from 0.26 to 0.7 [8] and [7], using the MoM and FDTD methods respectively. Unfortunately, the results in Table 2 do not satisfy the physically intuitive prediction. One possible explanation is the construction of the monopole; a gap feed was used rather than coaxial line.

Table 2 Correlation between PIFA and monopole upon a conductive box (using FDTD).

Load Type	PIFA(#1) and Monopole (#2) ρ_s^2
Open	0.9436
Short Circuit	0.2146
Diversity antenna not present	0.7167

As mentioned earlier, FDTD modeling of fine features is difficult and often inaccurate. A case in which this becomes apparent is diversity analysis of two parallel dipoles as shown in Figure 3. The closed-form expression for $\rho_s = J_o(kd)$ heavily relies on the symmetry of the problem. When modeling a thin wire, one has two choices: create a fine mesh or use a subcell wire; both techniques possess their own difficulties. A one-cell width dipole can only approximate a cylindrical wire due to its square cross-sectional area. The $1/\rho$ dependence of the normal E-field and circumferential H-field will be altered. Locating the phase center of the geometry is possible by conveniently choosing the total volume size. However, this is not the case for a subcell wire which is asymmetrically located at one edge of the Yee cell. Additionally, the update equations are forced to assume $1/r$ dependence; this assumption is only valid for a wire radius much less than a wavelength is size.

FDTD simulations of the dipole pair failed to match the predictions of Equation (2) using both of the wire modeling techniques. This is a severe limitation

of the applicability of FDTD for diversity analysis. These wire modeling techniques have generally been sufficient for other computations such as input impedance [9].

Section III: MoM Analysis

Diversity Performance

The NEC handset model (Figure 10) is nearly a clone of the FDTD model. Excitation within the MoM framework is accomplished by impressing a voltage source upon one of the feed wire subsections, effectively acting as a gap source. The far-field patterns of a single monopole and dual excitation of the pair of PIFAs in Figure 10 are found in Figures 11(a) and 11(b), respectively.

Using Equation (1), the azimuth cut of the far-field patterns yields the correlation coefficient results in Table 3. Unlike the FDTD results, the envelope correlation coefficient is roughly the same order of magnitude independent of load type; this is a more realistic result.
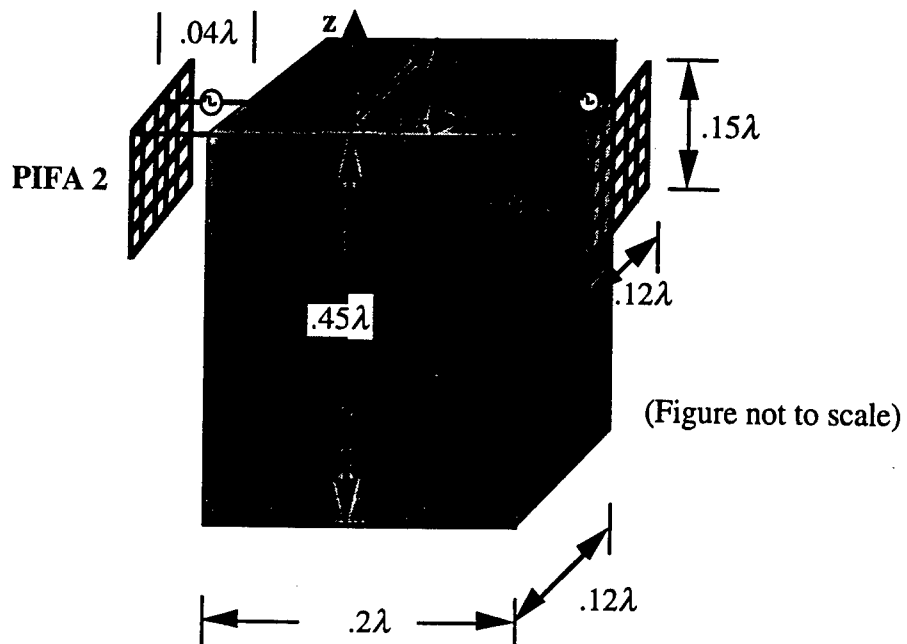
Figure 10   Schematic of NEC handset model

Table 3 Correlation between two PIFAs on a conductive box (using MoM).

Load Type	ρ_s^2
Open	0.3361
50 Ω	0.3248
Short Circuit	0.3255
Diversity antenna not present	0.3470

Figure 11(a) Far-field pattern of single PIFA upon conductive box (xz plane). **(b)** Far-field pattern of two PIFAs upon conductive box (xz plane). **(c)** Far-field pattern of monopole upon conductive box (xz plane).

As before, PIFA #2 will be replaced with alternative antennas such as a monopole and a normal mode helix. The correlation between PIFA #1 and each of these antennas (see Table 4) is expected to be smaller simply because of their beam shape as seen in Figure 11(c) and 11(b) where 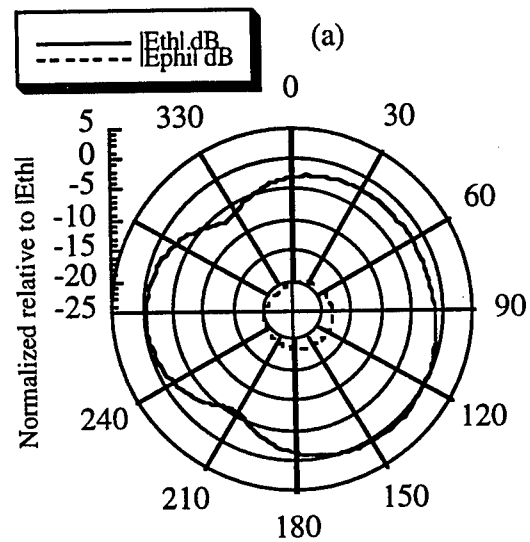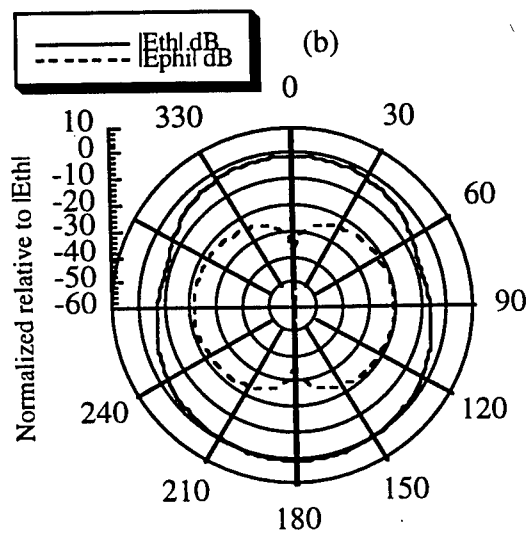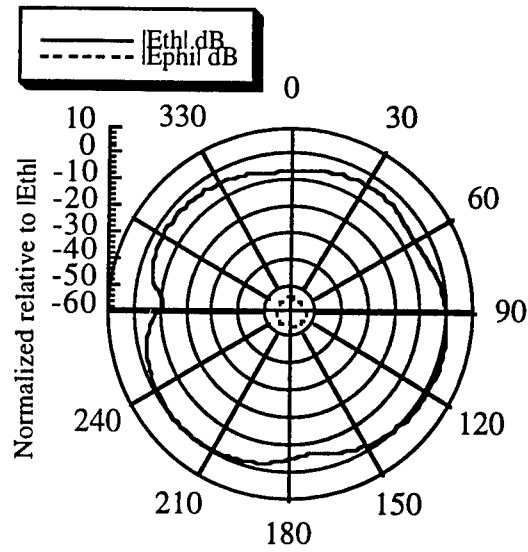each antenna was in the presence of the handset but not a second diversity antenna. The correlation results, when using a monopole, appear to coincide with the results by Ogawa, $\rho_e = |\rho_s|^2 = 0.26$ [8]. The use of a helix antenna for diversity reception did not improve over the two PIFA diversity results. A normal mode helix possesses a $\sin\theta$ distribution (see Figure 4.4(a)) just like a linear dipole antenna, but it is elliptically polarized. It is different from the endfire helix for this reason as well as its size. An endfire antenna has a diameter of at least $\lambda/2$ while the normal mode antenna must have a total wire length $<< 1$. The normal mode helix shown in Figure 12 was created out of straight wire segments in order to lend itself to FDTD simulations in cartesian coordinates.

However, FDTD modeling of this helix was not performed due to the inaccurate wire modeling experienced with the PIFA, monopole, and dipole. The physical dimensions of a typical hand-held receiver are not large enough in comparison with the end-fire helix at 850 MHz.

$$h=0.0227\ \lambda$$
$$s=0.0567\ \lambda$$

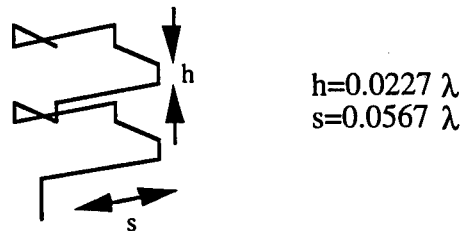**Figure 12** NEC model of normal mode wire helix.

For the data in Table 4, the dipole centers are separated by 0.11 and have a 1 mm radius. Each azimuth field pattern was found with the second diversity element absent. As expected, the two vertical dipoles yield the correct value according to Equation (2d).

$$\rho_s = J_o(kd) = J_o(\left(\frac{2\pi}{\lambda}\right)\cdot(0.1\lambda)\ ) = J_o(0.6283) = 0.9036$$

Table 4 Correlation between PIFA and monopole on a conductive box

(using MoM).

Load Type	PIFA(#1) and Monopole (#2) ρ_s^2	PIFA (#1) and Helix (#2) ρ_s^2
Open	0.2523	0.3149
50 Ω	0.2788	0.4583
Short Circuit	0.2888	0.4616
Diversity antenna not present	0.2892	0.4604

In fact, when two normal mode helices were arranged in a similar manner, the result was nearly the same: $\rho_s = 0.9037 - j0.002$, which is due to the uniform pattern in the azimuth plane, though the helix is elliptically polarized. The results presented in Table 4.3 enforce the symmetry concepts by noting that ρ_{12} and ρ_{21} are conjugates of each other. Clearly, the dipoles that are cross-polarized are uncorrelated as expected. Unlike the FDTD method, analysis of wire structures is rudimentary in the MoM regime.

Conclusions

The contributions of this work consist of a clear comparison between two numerical analysis methods for diversity system performance computations. The

loading of the second diversity element drastically effects ρ_e when using FDTD method but not the MoM. The two methods only yield agreeing results if the geometry can be modeled equally as well in both schemes. While the FDTD method limits the inclusion of small or thin features, its ability to include dielectrics in its model is unique. Also, the time signature allows tremendous flexibility in signal excitation and monitoring. The MoM code produces equivalent results when the geometry is representable. The MoM's main benefit is that it has no discretization errors occur due to approximations of the true dimensions of a geometry's features.

As modeling techniques are improved so will the applicability of the numerical methods. Advanced FDTD schemes that utilize contour surfaces, extrapolation techniques, and compact absorbing boundary conditions will facilitate more precise and efficient modeling and generation of performance characteristics.

The FDTD method also appears to lend itself to the inclusion of time-varying parameters such as noise sources or tone jammers. The possibility of complete electromagnetic modeling combined with a synthesized communication environment would be a valuable analysis tool.

References

[1] K. Siwiak, *Radiowave Propagation and Antennas for Personal Communications*. New York: Artech House, 1995.

[2] W. Lee, *Mobile Communications Design Fundamentals*. New York: Wiley, 1993.

[3] W. Jakes, *Microwave Mobile Communications*. New York: IEEE Press, 1974.

[4] J. D. Parsons and J. G. Gardiner, *Mobile Communication Systems*. New York: Halsted Press, 1989.

[5] W. D. Becker and V. T. Betz, "TAP: Time-domain analysis program for solving Maxwell's equations: ver. 3.25," Electromagnetics Communications Laboratory, University of Illinois at Urbana-Champaign, 1992.

[6] M. Jensen and Y. Rahmat-Samii, "FDTD analysis of PIFA diversity antennas on a hand-held transreceiver unit," *1993 IEEE AP-S International Symposium Digest*, Ann Arbor, MI, June 27-July 2, 1993, pp. 814-817.

[7] M. Jensen and Y. Rahmat-Samii, "Performance analysis of antennas for hand-held transreceivers using FDTD," *IEEE Transactions on Antennas and Propagation*, vol. 42, no. 8, pp. 1106-1113, August 1994.

[8] K. Ogawa and T. Uwano, "A Diversity Antenna for Very Small 800 MHz Band Portable Telephones," *IEEE Transactions on Antennas and Propagation*, vol. 42, no. 9, pp. 1342-1345, September 1994.

[9] R. Luebbers and K. Kunz, *The Finite Difference Time Domain Method for Electromagnetics*. Ann Arbor: CRC Press, 1993.

USING FDTD AND PML TO ANALYZE COMPLICATED MICROSTRIP STRUCTURES

S. Y. Chen and W. C. Chew

Center for Computational Electromagnetics
Department of Electrical and Computer Engineering
University of Illinois
Urbana, IL 61801

Abstract: In this paper, finite-difference time-domain method (FDTD) is used to analyze some complex microstrip structures. Perfectly matched layer (PML) is applied to build absorbing boundary conditions (ABCs). Results and comparisons with other authors' results are included.

1. Introduction

Since the initial work of K.S.Yee [1], the FDTD method has been widely used in the field computation. This method is attractive because it exchanges the complexity of problems with labor by the computer and it is conceptually easy to perform. The main problem of FDTD is the implementation of the absorbing boundary conditions. The most frequently used ABCs are Mur's first and second order ABCs [2]. The absorption effect of Mur's ABCs depends on the frequency and incident angle, and hence cannot provide perfect absorption.

Recently, a new kind of ABC named perfectly matched layers (PML) has been proposed by Berenger, which can provide very good absorption for all frequencies and incident angles [3]. Chew and Weedon recently use modified Maxwell's equations with stretched coordinates to derive PML [4]. By using this concept, one can easily extend PML to more complicated structures. Based on this explanation, a computer code has been developed to analyze complicated microstrip structures.

2. Modified Maxwell's Equations and PML

For a general medium, we define the modified Maxwell's equations in frequency

305

domain as

$$\nabla_e \times \mathbf{E} = i\omega\mu\mathbf{H}, \tag{1}$$

$$\nabla_h \times \mathbf{H} = -i\omega\epsilon\mathbf{E}, \tag{2}$$

$$\nabla_h \cdot \epsilon\mathbf{E} = \rho, \tag{3}$$

$$\nabla_e \cdot \mu\mathbf{H} = 0, \tag{4}$$

where

$$\nabla_e = \hat{x}\frac{1}{e_x}\frac{\partial}{\partial x} + \hat{y}\frac{1}{e_y}\frac{\partial}{\partial y} + \hat{z}\frac{1}{e_z}\frac{\partial}{\partial z}, \tag{5}$$

$$\nabla_h = \hat{x}\frac{1}{h_x}\frac{\partial}{\partial x} + \hat{y}\frac{1}{h_y}\frac{\partial}{\partial y} + \hat{z}\frac{1}{h_z}\frac{\partial}{\partial z}. \tag{6}$$

The plane wave solution to (1)-(4) can be written as

$$\mathbf{E} = \mathbf{E}_0 e^{i\mathbf{k}\cdot\mathbf{r}}, \tag{7}$$

$$\mathbf{H} = \mathbf{H}_0 e^{i\mathbf{k}\cdot\mathbf{r}}, \tag{8}$$

where

$$\mathbf{k} = \hat{x}k_x + \hat{y}k_y + \hat{z}k_z. \tag{9}$$

Substituting (7) and (8) into (1) and (2), combining (4), we obtain the dispersion relation

$$k^2 = \omega^2\mu\epsilon = \frac{1}{e_x h_x}k_x^2 + \frac{1}{e_y h_y}k_y^2 + \frac{1}{e_z h_z}k_z^2. \tag{10}$$

Note that Equation (10) satisfies a 3D ellipsoid equation, and hence we can rewrite it as

$$k_x = k\sqrt{e_x h_x}\sin\theta\cos\phi, \tag{11}$$

$$k_y = k\sqrt{e_y h_y}\sin\theta\sin\phi, \tag{12}$$

$$k_z = k\sqrt{e_z h_z}\cos\theta. \tag{13}$$

Note that when e_i, h_i, $i = x, y, z$ are complex, the wave will be attenuated as it propagates along the i direction so that this medium can be used as an absorber. We use following parameters to characterize this kind of medium

$$(\mu, \epsilon, e_x, e_y, e_z, h_x, h_y, h_z).$$

A special case is a vacuum and the parameters can be written as

$$(\mu_0, \epsilon_0, 1, 1, 1, 1, 1, 1).$$

Under the matching condition that $e_x = h_x$, $e_y = h_y$, and $e_z = h_z$, the wave impedance is given by

$$\eta = \frac{|\mathbf{E}|}{|\mathbf{H}|} = \sqrt{\frac{\mu}{\epsilon}}. \tag{14}$$

Now we consider the wave behavior at the interface of two matched media. The parameters of these two media are shown in Fig. 1. We assume that a plane wave is obliquely incident on the interface. Furthermore, the arbitrarily polarized wave can be decomposed into TE^z and TM^z modes. By matching the tangential components of E field and H field at the interface, we obtain the reflection and transmission coefficients as follows:

$$R^{TE} = \frac{k_{1z}e_{2z}\mu_2 - k_{2z}e_{1z}\mu_1}{k_{1z}e_{2z}\mu_2 + k_{2z}e_{1z}\mu_1}, \tag{15}$$

$$T^{TE} = \frac{2k_{1z}e_{2z}\mu_2}{k_{1z}e_{2z}\mu_2 + k_{2z}e_{1z}\mu_1}, \tag{16}$$

$$R^{TM} = \frac{k_{1z}h_{2z}\epsilon_2 - k_{2z}h_{1z}\epsilon_1}{k_{1z}h_{2z}\epsilon_2 + k_{2z}h_{1z}\epsilon_1}, \tag{17}$$

$$T^{TM} = \frac{2k_{1z}h_{2z}\epsilon_2}{k_{1z}h_{2z}\epsilon_2 + k_{2z}h_{1z}\epsilon_1}. \tag{18}$$

To satisfy the phase matching condition, $k_{1x} = k_{2x}$ and $k_{1y} = k_{2y}$, we choose

$$\theta_1 = \theta_2, \phi_1 = \phi_2, \tag{19}$$

$$\mu_1 = \mu_2, \epsilon_1 = \epsilon_2, \tag{20}$$

$$e_{1x} = e_{2x} = h_{1x} = h_{2x}, \tag{21}$$

$$e_{1y} = e_{2y} = h_{1y} = h_{2y}, \tag{22}$$

and we can show that both $R^{TE} = 0$ and $R^{TM} = 0$ for all incident angles and all frequencies. In order to absorb the wave in region 2, we choose the parameters of mediun 2 as

$$(\mu_1, \epsilon_1, 1, 1, s_2, 1, 1, s_2),$$

where s_2 is a complex number. In this case, we can rewrite (11)-(13) as

$$k_{1x} = k_{2x} = k \sin\theta \cos\phi, \tag{23}$$

$$k_{1y} = k_{2y} = k \sin\theta \sin\phi, \tag{24}$$

$$k_{1z} = k \cos\theta, \tag{25}$$

$$k_{2z} = s_2 k \cos\theta, \tag{26}$$

where $k = \omega\sqrt{\mu_1\epsilon_1}$. If $s_2 = s_2' + is_2''$, the wave will attenuate in the z direction. The same procedure can be applied to build ABCs in the x and y directions.

For a general matched medium, we let $s_x = 1 + i\sigma_x/\omega\epsilon$, $s_y = 1 + i\sigma_y/\omega\epsilon$, $s_z = 1 + i\sigma_z/\omega\epsilon$, $-i\omega = \partial/\partial t$ and rewrite curl equation (1) in the time domain as

$$\mu\frac{\partial \mathbf{H}_{sx}}{\partial t} + \frac{\sigma_x \mu}{\epsilon}\mathbf{H}_{sx} = -\frac{\partial}{\partial x}\hat{x} \times \mathbf{E}, \tag{27}$$

$$\mu\frac{\partial \mathbf{H}_{sy}}{\partial t} + \frac{\sigma_y \mu}{\epsilon}\mathbf{H}_{sy} = -\frac{\partial}{\partial y}\hat{y} \times \mathbf{E}, \tag{28}$$

$$\mu\frac{\partial \mathbf{H}_{sz}}{\partial t} + \frac{\sigma_z \mu}{\epsilon}\mathbf{H}_{sz} = -\frac{\partial}{\partial z}\hat{z} \times \mathbf{E}, \tag{29}$$

where $\mathbf{H} = \mathbf{H}_{sx} + \mathbf{H}_{sy} + \mathbf{H}_{sz}$. Similarly, we can write (2) as

$$\epsilon\frac{\partial \mathbf{E}_{sx}}{\partial t} + \sigma_x\mathbf{E}_{sx} = \frac{\partial}{\partial x}\hat{x} \times \mathbf{H}, \tag{30}$$

$$\epsilon\frac{\partial \mathbf{E}_{sy}}{\partial t} + \sigma_y\mathbf{E}_{sy} = \frac{\partial}{\partial y}\hat{y} \times \mathbf{H}, \tag{31}$$

$$\epsilon\frac{\partial \mathbf{E}_{sz}}{\partial t} + \sigma_z\mathbf{E}_{sz} = \frac{\partial}{\partial z}\hat{z} \times \mathbf{H}, \tag{32}$$

where $\mathbf{E} = \mathbf{E}_{sx} + \mathbf{E}_{sy} + \mathbf{E}_{sz}$. Note that $\mathbf{E}_{si}$, $\mathbf{H}_{si}$, $i = x, y, z$ are two-component vectors. The equations (27)-(32) contain 12 scalar equations, and we can use the Yee-scheme

to discretize them. We now let $\mathbf{H}_{sx} = \hat{y}H_{sxy} + \hat{z}H_{sxz}$, $\mathbf{E} = \hat{x}E_x + \hat{y}E_y + \hat{z}E_z$, and substitute them into (27). By equating the z component, we have

$$\mu \frac{\partial H_{sxz}}{\partial t} + \frac{\sigma_x \mu H_{sxz}}{\epsilon} = -\frac{\partial}{\partial x}E_y. \tag{33}$$

By using the formula in [5], we obtain

$$H_{sxz}^n(i,j,k) = \alpha_m H_{sxz}^{n-1}(i,j,k) - \beta_m \left\{ \frac{E_y^{n-1}(i+1,j,k) - E_y^{n-1}(i,j,k)}{\triangle x} \right\}, \tag{34}$$

where

$$\beta_m = \left(\frac{\mu}{\triangle t} + \frac{\sigma_x}{2} \right)^{-1}, \tag{35}$$

$$\alpha_m = \left(\frac{\mu}{\triangle t} - \frac{\sigma_x}{2} \right) / \left(\frac{\mu}{\triangle t} + \frac{\sigma_x}{2} \right). \tag{36}$$

Applying the same procedure, we can obtain 12 difference equations.

3. Treatment of Source and Boundary Conditions

A parallel magnetic current sheet is used to excite the field, and the current is Gaussian in time. It can be described as

$$\nabla \times \mathbf{E} = -\mu \frac{\partial \mathbf{H}}{\partial t} - \mathbf{M}. \tag{37}$$

To excite a Gaussian pulse without distortion, a magnetic current should be imposed according to its actual spatial distribution, but unfortunately, it is an unknown. To solve this problem, we first launch a wave by specifying E_x uniformly and $E_y = 0$ underneath the metal strip as shown in Fig. 2. After the wave travels a certain distance, it will be 'purified'. Then we collect the E field data on the $x - y$ plane at the end of the strip. The equivalence magnetic source can be calculated as

$$\mathbf{M} = -2\hat{z} \times \mathbf{E}. \tag{38}$$

We use this source to launch the wave and obtain Gaussian pulse in two directions almost without distortion. The backward going one is absorbed by PML. This kind of excitation can reduce the mesh dimension and hence save the CPU time.

The structures considered in this paper have a substrate with a metal strip. The strip is assumed to be a PEC with zero thickness and the tangential components of E field are set to be zero. For calculating the tangential E components at the interface of the air and dielectric, average permittivities $(\epsilon_0 + \epsilon_1)/2$ is used [6]. PEC is used to terminate the PML, because the fields are nearly zero at the end of PML.

4. Numerical Results

A. Microstrip Branch Line Coupler

We first studied a microstrip branch line coupler, which can be used to divide power equally between port 3 and port 4 with a 90 degree phase difference. The parameters used in the simulation are shown in Fig. 3. The space steps and time step are chosen to be $\triangle x = 0.265\,mm$, $\triangle y = 0.406\,mm$, $\triangle z = 0.406\,mm$, $\triangle t = 0.441\,ps$, and the simulation size is $26\triangle x \times 76\triangle y \times 117\triangle z$. In all numerical computations, 11 cells of PML are used to build absorbing boundary in each direction. The Gaussian function is

$$f(t) = e^{-(t-t_0)^2/T^2},$$

where the Gaussian half-width is $T = 15\,ps$ and the delay time t_0 is set to be $3T$.

To allow the response at all four ports to become nearly zero, 4,000 time steps are performed. The computation time is about 4 hours on a DEC Alpha workstation. By using FFT, we obtain the amplitude of scattering parameters and phase difference between port 3 and port 4 as shown in Fig. 4 and Fig. 5, which show good agreement with the results given in [7]. At the working frequency, $|S_{31}|$ and $|S_{41}|$ are both approximate -3dB as we have expected, and the phase difference between port 3 and port 4 is nearly 90^0.

B. Microstrip Antenna

The structure of microstrip antenna analyzed is shown in Fig. 6. The space steps and time step are chosen to be $\triangle x = 0.53\,mm$, $\triangle y = 0.75\,mm$, $\triangle z = 0.7534\,mm$,

$\Delta t = 1$ ps, and the simulation size is $26\triangle x \times 154\triangle y \times 137\triangle z$. The Gaussian half-width is $T = 34$ ps and the delay time t_0 is set to be $3T$. Because of its resonant property, 8,000 time steps are used to perform the simulation. The result of return loss $|S_{11}|$ is shown in Fig. 7. In addition, we can use the following formula to obtain input impedance Z_{in} from S_{11},

$$Z_{in} = Z_0 \frac{1 + S_{11}e^{j2kL}}{1 - S_{11}e^{j2kL}}, \tag{39}$$

where k is the wave number and L is the distance from reference plane to the edge of antenna. $\epsilon_{eff} = 2.2$ is used to calculate the wave number, and Z_0 is assumed to be 50Ω. The results are shown in Fig. 8.

One of the methods to expand the bandwidth of microstrip antenna is to use a rectangular ring antenna [8] and the structure of a ring antenna studied is shown in Fig. 9. Applying the same procedure, we calculate the return loss $|S_{11}|$, input impedance Z_{in} and VSWR of these two antennas. The results are shown in Fig. 10, Fig. 11, and Fig. 12, from which we can see that the bandwidth is expanded as we have expected.

5. Conclusions

PML is successfully used to build ABCs for the FDTD analysis of complicated structures. Compared with other ABCs, FDTD implement of PML is more straight-forward, and hence provides a flexible tool to deal with complicated microstrip structures.

Modified Maxwell's equations are used to explain the property of PML and to analyze the wave propagating in PML. By using this concept, we can see the general behavior of wave and easily extend PML into more complicated cases.

By properly choosing $\sigma_i, i = x, y, z$, we can control the attenuation in three directions and build a good absorber. Theoretically, σ_i can be chosen as large as

possible to reduce the mesh dimension, but sharp variation of σ_i will cause numerical reflection, because PML does not exist in a discretized space [9].

6. References

[1] K. S. Yee, "Numerical Solution of Initial Boundary Value Problems Involving Maxwell's Equations in Isotropic Media", *IEEE Trans. Antennas Propagat.*, vol. AP-14, pp. 302-307, May 1966.

[2] G. Mur, "Absorbing Boundary Conditions for the Finite-Difference Approximation of the Time-Domain Electromagnetic Field Equations", *IEEE Trans. Electromagn. Compat.*, vol. EC-23, pp. 377-382, Nov. 1981.

[3] J. P. Berenger, "A Perfectly Matched Layer for the Absorption of Electromagnetic Waves", *J. Computational Physics*, vol. 144, pp. 185-200, Oct. 1994.

[4] W. C. Chew, W. H. Weedon, "A 3D Perfectly Matched Medium From Modified Maxwell's Equations with Stretched Coordinates", *Micro. Opt. Tech. Lett.*, vol. 7, no. 13, pp. 599-604, September 1994.

[5] R. W. Ziolkowski, N. K. Madsen, And R. C. Carpenter, "Three—Dimensional Computer Modeling of Electromagnetic Field: A Global Lookback Lattice Truncation Scheme", *J. Computational Physics*, vol. 50, pp. 360-408, 1983.

[6] X. Zhang and K. K. Mei, "Time Domain Finite Difference Approach to the Calculation of the Frequency Dependent Characteristics of Microstrip Discontinuities", *IEEE Trans. Microwave Theory Tech.*, vol. 36, pp. 1775-1787, December 1988.

[7] D. M. Sheen, S. M. Ali, M. D. Abouzahra, and J. A. Kong, "Application of the Three-Dimensional Finite-Difference Time-Domain Method to the Analysis of Planar Microstrip Circuits", *IEEE Trans. Microwave Theory Tech.*, vol. MTT-38, no. 7, pp. 849-857, July 1990.

[8] V. Palanisamy, R. Garg, "Rectangular Ring and H-Shaped Microstrip Antennas-Alternatives to Rectangular Patch Antenna", *Electronics Letters*, vol. 21, no. 19, pp. 874-876, September 1985.

[9] W. C. Chew, J. M. Jin, "Perfectly Matched Layers in the Discretized Space: An Analysis and Optimization", *Electromagnetics*, vol. 16, no. 4, pp. 325-340, July 1996.
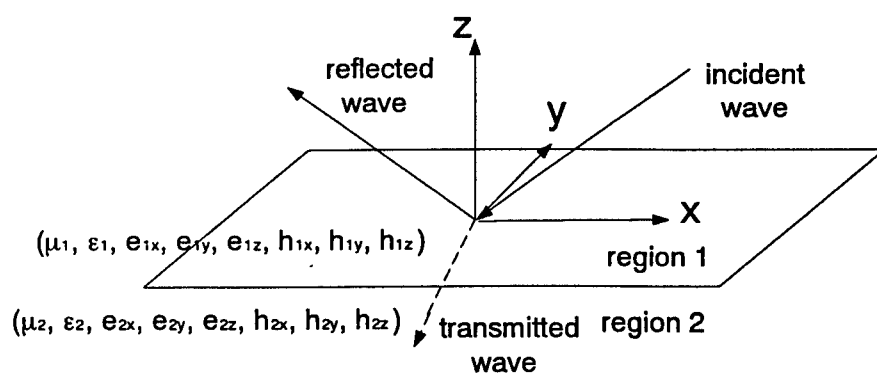
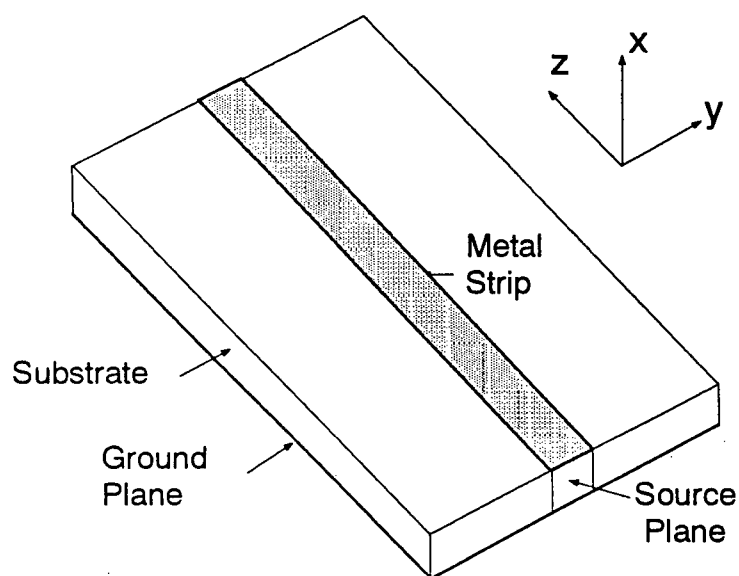**Fig. 1.** Plane wave with arbitrary polarization incident on the interface of two PML.
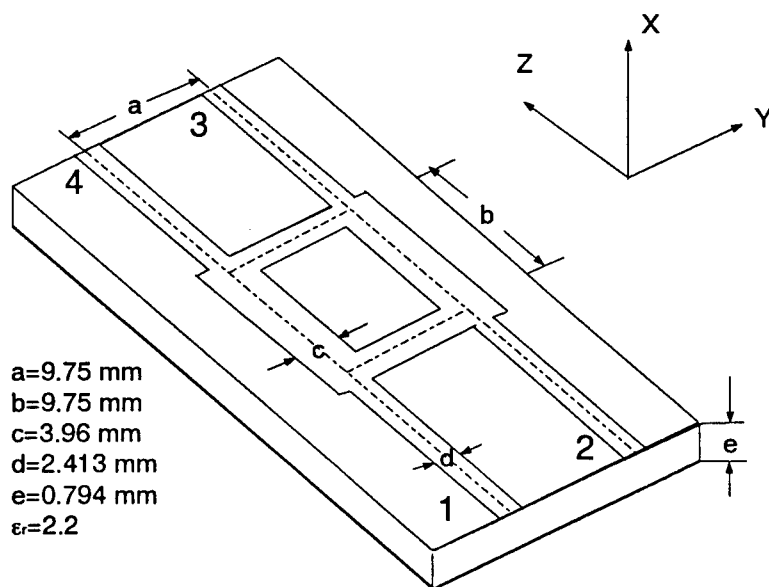

Fig. 2. Microstrip Excitation.

a=9.75 mm
b=9.75 mm
c=3.96 mm
d=2.413 mm
e=0.794 mm
ε_r=2.2

Fig. 3. Branch line coupler.

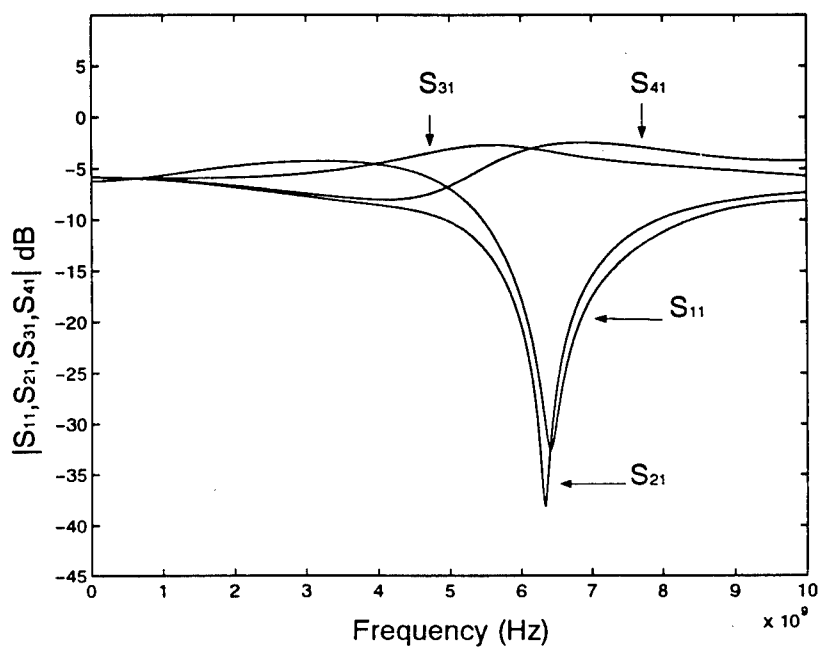**Fig. 4.** Amplitude of scattering parameters of the branch line coupler.

314
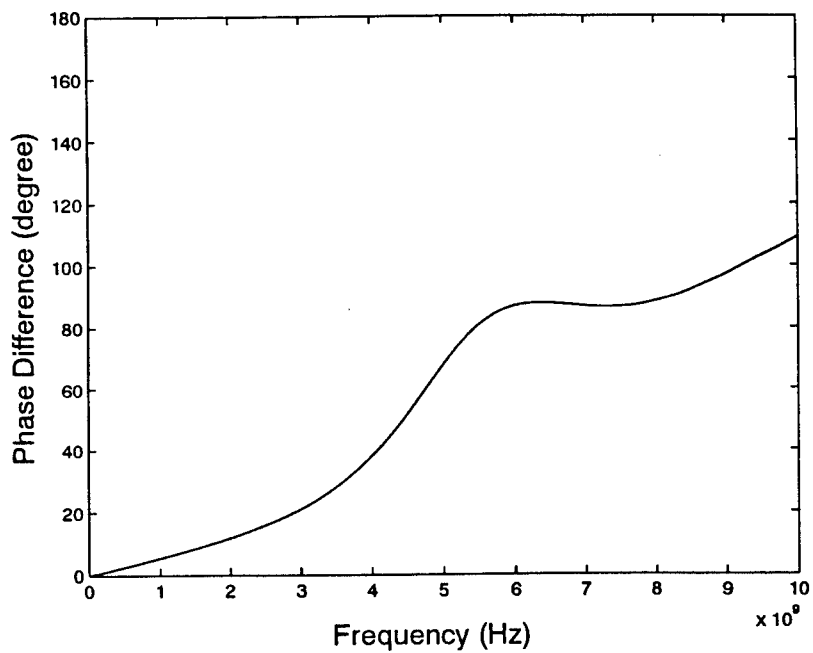
Fig. 5. Phase difference of port 3 relative to port 4.

a=83.6 mm
b=55 mm
c=39.5 mm
d=4.5 mm
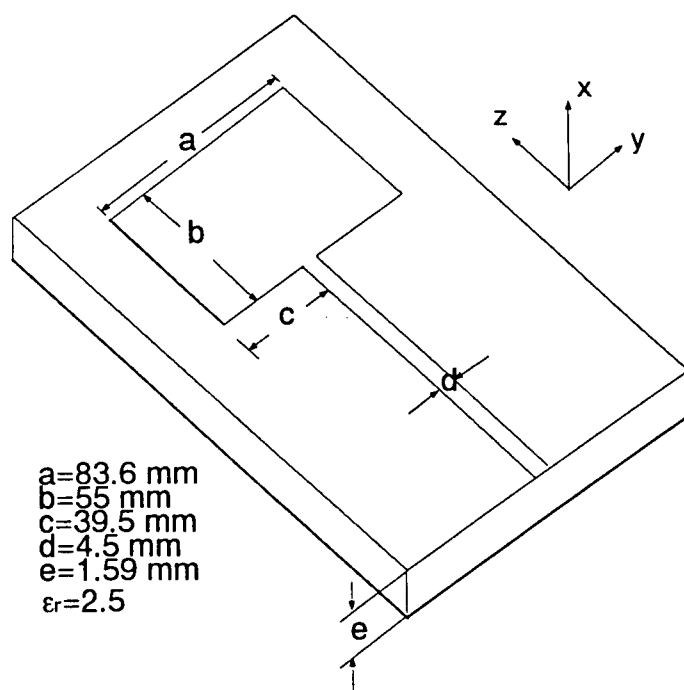e=1.59 mm
ε_r=2.5

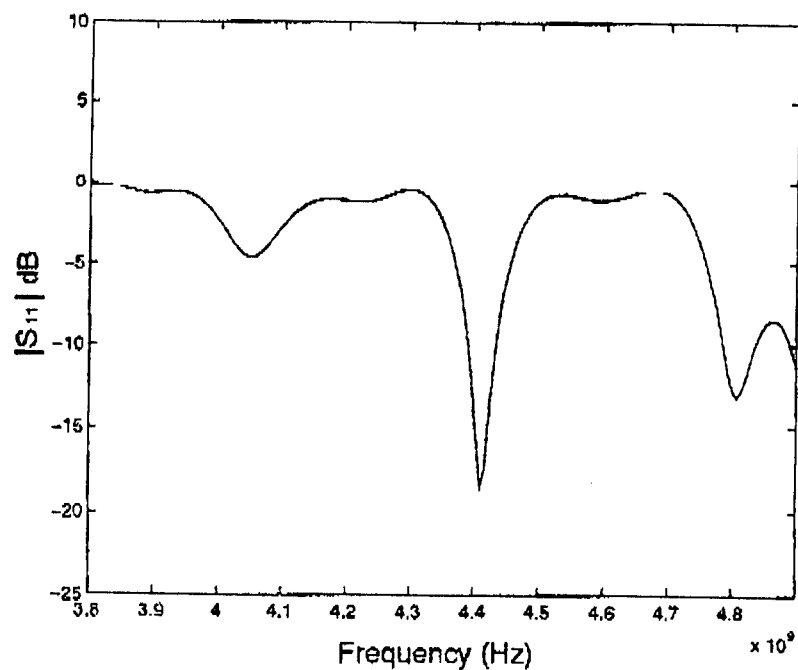**Fig. 6.** Line-feed rectangular patch.

Fig. 7. Return loss of the rectangular patch.
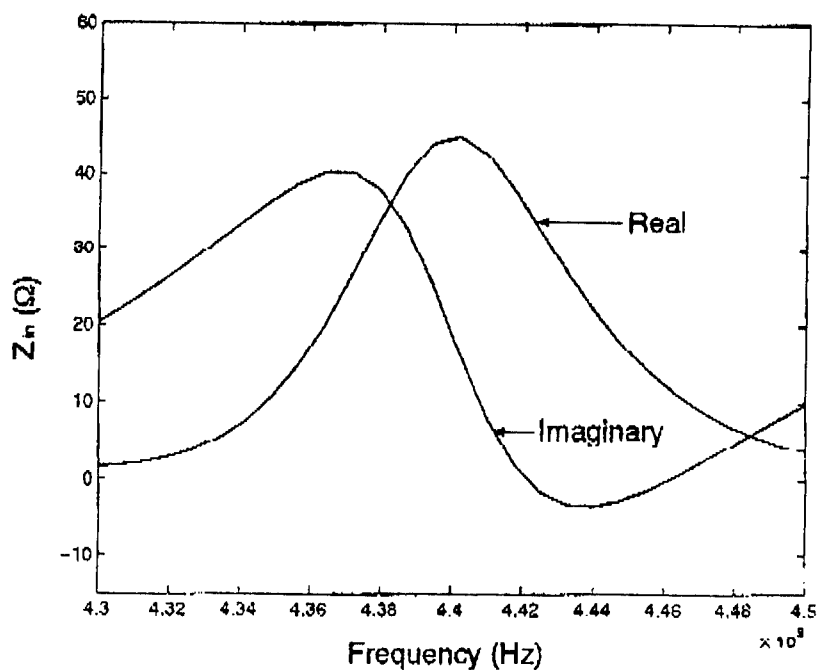
Fig. 8. Input impedance of the rectangular patch near the operating frequency.

316
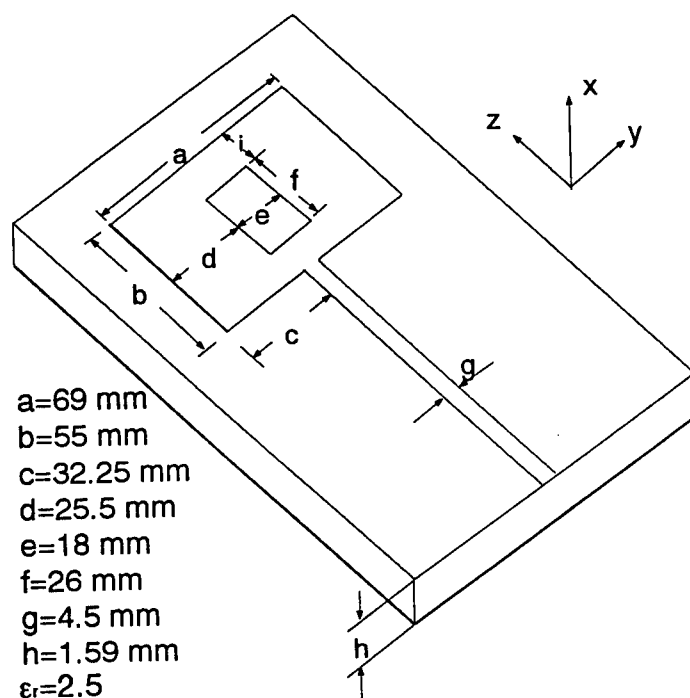
Fig. 9. Line-feed rectangular ring.

a=69 mm
b=55 mm
c=32.25 mm
d=25.5 mm
e=18 mm
f=26 mm
g=4.5 mm
h=1.59 mm
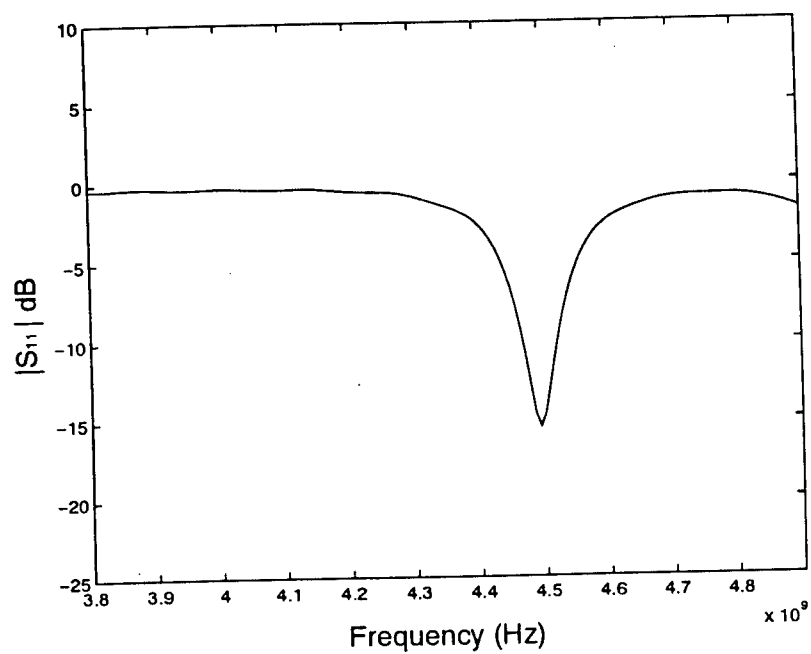ε_r=2.5

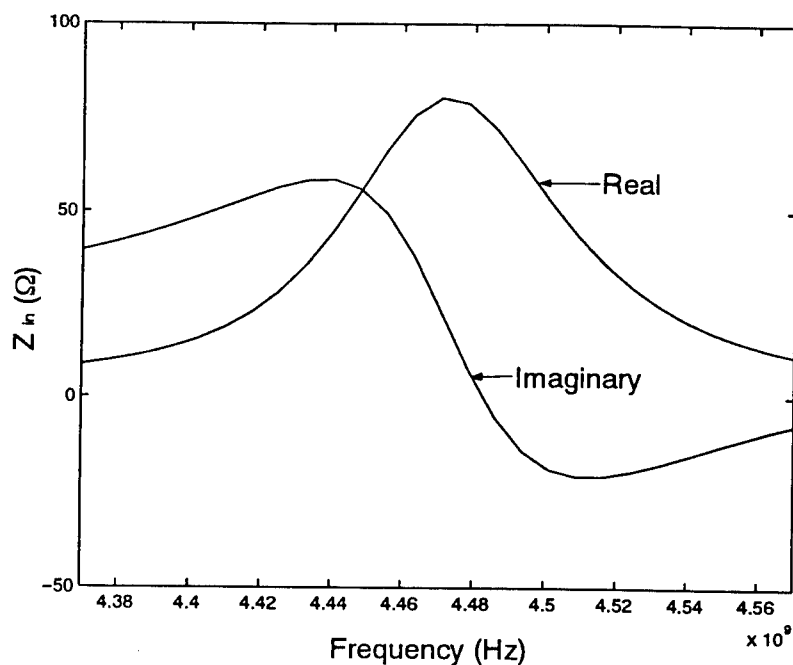**Fig. 10.** Return loss of the rectangular ring.

317

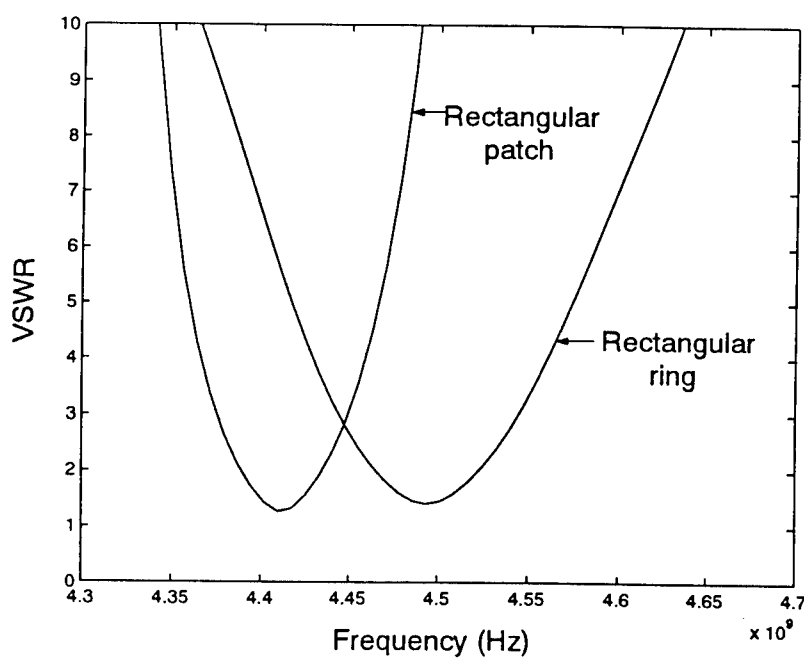**Fig. 11.** Input impedance of the rectangular ring near the operating frequency.

Fig. 12. VSWR near the operating frequency.

HYBRID FEM/SBR METHOD TO COMPUTE THE RADIATION PATTERN FROM A MICROSTRIP PATCH ANTENNA IN A COMPLEX GEOMETRY

A. D. Greenwood, S. S. Ni, J. M. Jin, and S. W. Lee
Center for Computational Electromagnetics
Department of Electrical and Computer Engineering
University of Illinois at Urbana-Champaign
Urbana, Illinois 61801-2991

Abstract: A previously introduced technique to compute the scattering from an electrically large target with small features is extended to compute the radiation of a microstrip patch antenna mounted on a complex, three-dimensional body. The technique involves using the finite element method (FEM) to characterize the patch antenna, and then computing the radiation pattern using the reciprocity theorem and the shooting and bouncing ray (SBR) method with edge diffraction. The validity of the calculation is shown by comparison with measured data for a waveguide-fed trihedral. Other calculations show the effects of the external geometry on the radiation pattern of a microstrip patch antenna.

1. Introduction

Recently, a hybrid technique for computation of electromagnetic scattering has been developed at the University of Illinois [1]. By utilizing the both high frequency and low frequency methods, the technique can handle large targets with small cracks and cavities on their surfaces . The high-frequency shooting and bouncing ray (SBR) method is used to evaluate the scattering from the large target with the cracks and cavities filled with perfect conductors, and the low frequency finite-element boundary integral (FE-BI) method is employed to analyze the cracks and cavities. The equivalence principle is used to combine the results of the two methods.

Here, the hybrid method is extended to compute the radiation pattern of a microstrip patch antenna mounted on a complex geometry. First, the FE-BI method is used to analyze the antenna. The result is an equivalent magnetic current on the surface of the antenna. The SBR method is then used to model the surrounding geometry. Because a microstrip patch antenna is a highly resonant structure, it is assumed that the surrounding geometry has minimal effect on the equivalent current. This paper first discusses the theoretical basis of the hybrid FE-BI/SBR method for analyzing the radiation from a microstrip

319

patch antenna. It then presents some numerical results showing the utility and validity of the method.

2. Theoretical Development

Consider a microstrip patch antenna (which is mounted on a complex structure) and a distant, infinitesimal dipole radiating in the same region of space. The FE-BI method is used to numerically evaluate the equivalent current density on the surface of the patch antenna. If the structure containing the patch antenna is in the far-field of the dipole, the field radiated by the dipole produces a plane wave incident upon this structure. Using SBR, the magnetic field due to this incident plane wave is found at points on the surface of the patch antenna.

In using SBR to find the magnetic field on the patch antenna, it is important to consider edge diffraction. Otherwise, the computed magnetic field may contain large errors, particularly at points in the shadow region. To avoid such errors, the first order edge diffraction terms are computed using the Uniform Theory of Diffraction (UTD) and added to the SBR computed magnetic field [2], [3], [4].

Using the reciprocity theorem, we find

$$\int\int\int \mathbf{E}_{\text{MSPA}} \cdot \mathbf{J} dV' = -\int\int \mathbf{H}_{\text{SBR}} \cdot \mathbf{M} ds'$$

where $\mathbf{E}_{\text{MSPA}}$ is the field radiated by the patch antenna, $\mathbf{H}_{\text{SBR}}$ is the field found using SBR and edge diffraction, $\mathbf{M}$ is the equivalent current density on the surface of the patch antenna. and $\mathbf{J}$ is the current density of the dipole. The integral on the left of the equation can be evaluated trivially and is equal to the component of $\mathbf{E}_{\text{MSPA}}$ in the direction of the dipole times the strength of the dipole, Il. Dividing both sides by Il and numerically evaluating the integral on the right gives a result for the component $\mathbf{E}_{\text{MSPA}}$ in the direction of the dipole. Other components of $\mathbf{E}_{\text{MSPA}}$ can be found by changing the orientation of the dipole and repeating the SBR analysis. Similarly, the radiation pattern of the patch antenna can be constructed by varying the dipole location and repeating the SBR analysis.

3. Numerical Results

To illustrate the usefulness of the proposed computational method, numerical

(a) H-plane Geometry   (b) E-plane Geometry

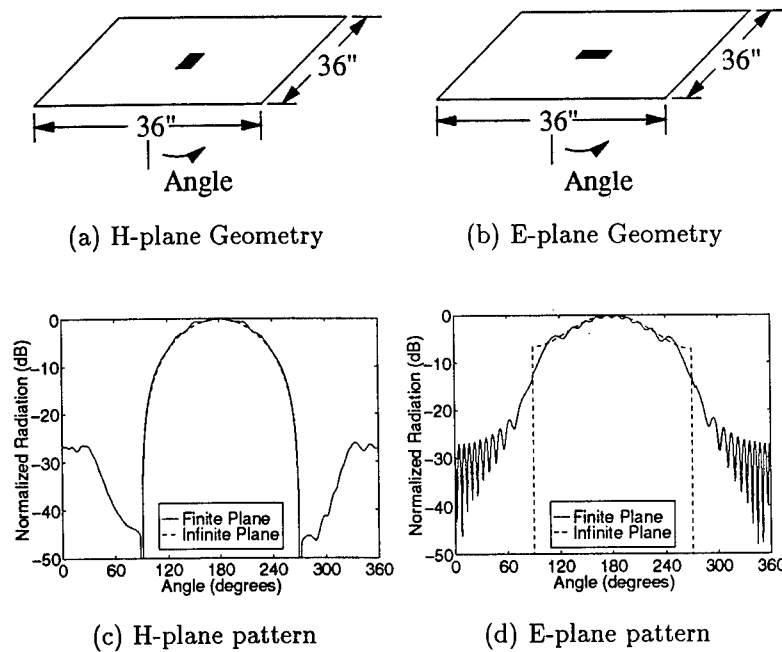(c) H-plane pattern   (d) E-plane pattern

Figure 1: Radiation pattern of a microstrip patch antenna on a finite ground plate.

results for three different geometries are presented. The first two utilize a microstrip patch antenna which is 1.97 inch by 2.36 inch in size. The substrate ($\epsilon_r = 2.17$) is 0.031 inch thick, and the patch is 0.79 inch by 1.18 inch. The feed probe is centered widthwise and 0.15 inch off center lengthwise. The antenna resonates at 3.3 GHz, and it is characterized by an equivalent magnetic current density found using FE-BI.

First, the patch antenna is mounted on a finite ground plate. In Figure 1, resulting computations of the h-plane and e-plane radiation patterns are compared to corresponding patterns generated by the same antenna on an infinite ground plane. Edge diffraction is responsible for the differences between the finite ground plane example and the infinite ground plane case. The asymmetry in the h-plane pattern (Figure 1c) is caused by the asymmetry in the location of the patch antenna feed probe.

Next, the patch antenna is mounted on a stair-step geometry (Figure 2). The computed radiation pattern is again compared to that of the antenna on an infinite ground plane. Edge diffraction and the multiple bounce effect of the

(a) H-plane Geometry   (b) E-plane Geometry

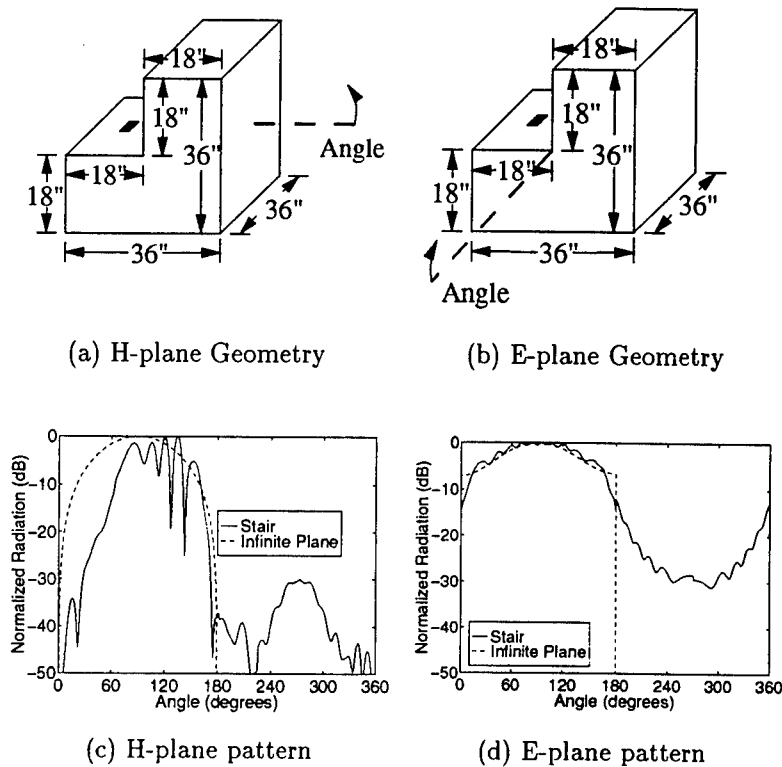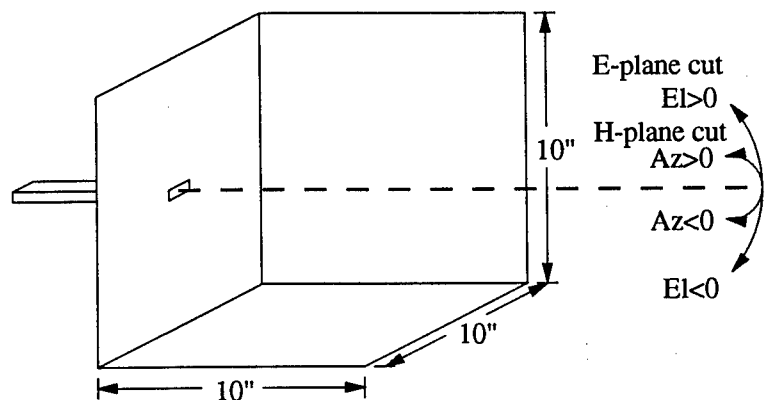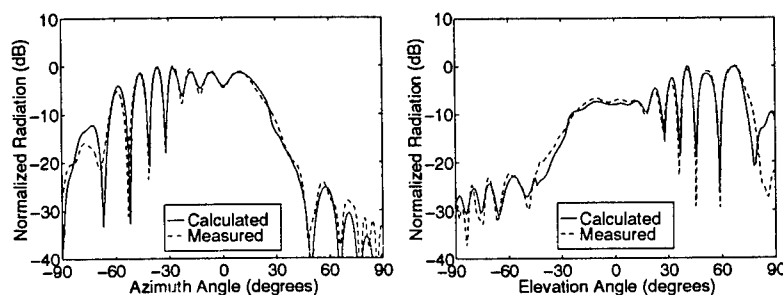(c) H-plane pattern   (d) E-plane pattern

Figure 2: Radiation pattern of a microstrip patch antenna on a stair-step geometry.

SBR algorithm are responsible for the peaks and nulls in the patterns of the stair-step example.

The final numerical example considers a waveguide-fed trihedral (Figure 3a) instead of a patch antenna. This configuration is chosen because of the availability of radiation pattern measurements. The wave guide is 0.9 inch wide by 0.4 tall, and the operating frequency is 9.0 GHz. Assuming an incident TE_{10} wave, the waveguide aperture is characterized by an equivalent magnetic current density, and the radiation pattern is computed using SBR. The calculated results are compared to the measured results in Figures 3b and c, and the calculated results are seen to agree well with the measured results. It should be noted that the waveguide aperture, in contrast to the patch antenna, is not a highly resonant structure. Thus, the current density over the aperture may be altered by the geometry of the problem, resulting in some computational errors.

(a) Geometry

(b) H-plane pattern

(c) E-plane pattern

Figure 3: Comparison of calculated data with measured data for the radiation pattern of a waveguide (0.9 inch by 0.4 inch) fed trihedral at 9.0 GHz.

4. Conclusion

The hybrid method for computing scattering from large objects with small cracks and cavities on their surfaces [1] is extended to compute the radiation pattern of a microstrip patch antenna in a complex geometry. Numerical results (Figures 1 and 2) show the external geometry, including edge diffraction, has a dominant effect on the radiation pattern of the patch antenna. Comparison of the numerical results to measured data (Figure 3) shows good agreement.

References

[1] J.-M. Jin, S. S. Ni, and S.-W. Lee, "Hybridization of SBR and FEM for Scattering by Large Bodies with Cracks and Cavities," *IEEE Transactions on Antennas and Propagation*, vol. 43, pp. 1130–1139, October 1995.

[2] C. A. Balanis, *Advanced Engineering Electromagnetics*, ch. 13, New York: Wiley, 1989.

[3] S. K. Jeng and S.-W. Lee, "Two New Diffraction Coefficients for Physical Theory of Diffraction," Electromagnetics Lab. Tech. Rep. 94-2, Univ. IL., Department of Electrical and Computer Engineering, 1994.

[4] D. A. McNamara, C. W. I. Pistorius, and J. A. G. Malherbe, *Introduction to the Uniform Geometrical Theory of Diffraction*, ch. 7, Boston: Artech House, 1990.

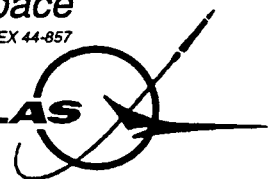# Conformal Antenna System Development Using Method of Moments

Twentieth Annual Antenna
Applications Symposium

September 18-20, 1996
Robert Allerton Park
University of Illinois

Conformal Antenna System Development using Method of Moments

J.L. Bogdanor, M.R. Axe, J.M. Bornholdt, D.D. Car
McDonnell Douglas Aerospace, Mailcode 0642263
P.O. Box 516, St. Louis, MO 63166-0516

Abstract

Modern military fighter aircraft RF antenna systems must be optimized for aerodynamic, volumetric, RCS, and power constraints along with intended RF radiation/receive performance. The subject paper addresses a pod mounted antenna system appropriate for hemispherical, steerable coverage. The McDonnell Douglas MOM radiation code, CARLOS, combined with its geometry configuration code, ZONI3G, are used to configure and evaluate the RF performance of element arrays providing the required RF performance. The resulting radiation is achieved by electrically steering arrays of travelling wave slot elements, each element capable of providing grazing to normal to the surface radiation. Element sizing, array spacing and feeding prescription insight is provided.

Introduction

The development of modern fighter aircraft has reached a high level of sophistication wherein multimission capabilities must be available beyond that of merely fighting. Many diverse capabilities must be integrated not to the detriment of basic speed and maneuverability requirements. Often pod, wing tip or undercarriage, mounted systems can provide extended capabilities for specialized missions.

Here we address one such pod mounted scenario wherein wideband (3:1) steerable, equal amplitude, horizontal and vertical polarization coverage is desired. The general RF performance requirements are illustrated in Figure 1 with the solution approach summarized in Figure 2. The problem is further complicated especially for lower frequencies as typical elements are sized comparable to half wavelength at the lowest frequency of concern thus providing potentially large RCS returns at higher airborne radar frequencies.

Figure 3 provides an example pod typical of that available for a multiple RF system integration. Our focus will be on the integration of low band transceiver antenna capability appropriate to the Figure 1 requirements of hemispherical, H&V polarization of equal amplitude over the 3:1 bandwidth. The challenge presented here is the simultaneous ability of grazing and normal to the surface performance operating over the subject bandwidth. References [1,2] provide insight to the element solution and combining such thought elements via electrically steerable arraying provides the approach taken here. The MDA CARLOS [3]and ZONI3G codes bring the thought solution to the real world.

The Element

Reference [1] addresses narrow slots feed in such a way that an E field propagates or travels down the slot length. The slot width is narrow compared to its length and wavelength, Figure 4. The reality of such a wave launching can be realized via Figure 5, V slot, where the feed is across the intersection of the two slots forming the V shape. Terminating the two, V forming slots in their respective "characteristic" impedances reduces the standing waves to zero, thus allowing the E field, magnetic current, to propagate in only an outward direction, away from the feed. Furthermore, the V shape size can be shown to propagate an electric current between the legs of the V and to naturally launch from a point consistent with dipole sizing of that particular frequency, that is, the highest electric current density exists at a position down the V such that the separation between points on the separate legs is half wavelength at that particular frequency. The result radiation is predominately vertically polarized to the mounting surface. Curving the V legs allows a potential way of compacting the element for arraying purposes, Figure 6.

Where the V maximum separation dimensions are not consistent with the lowest frequency requirements, the element should operate as magnetic current element, as long as the respective slot terminations present the required slot characteristic termination impedance, author's speculation.

Combing the elements into an array consistent with 90 phasing via spacing and 90 degree electrical phasing produces the required grazing to normal incidence steerage, where the two elements are mounted on an infinite ground plane. The reality of such on the actual pod configuration is shown in Figure 7, one array patch, where a shallow cavity backing has been attached with wall lining of a commercially available absorber. The cavity and liner are consistent with equivalencing the slot in the infinite ground plane configuration wherein radiation is equal on both sides of the ground plane.

Figure 7 shows a 2 element array panel and the currents resulting from the forward element only excitation.

The Pod

Figure 3 illustrates the pod installation of the above arrays potentially providing the required performance. Note therein, the ten patches allocated to the subject RF performance requirements. The four end patches mounted on the pod sides, provide horizontal polarization coverage, only, in the principal cut plane and cross polarization radiation coverage otherwise. The bottom eight patches provide the remaining radiation coverages.

Calculations for an undercarriage pod configuration typical of Figure 3 using the Carlos code confirm the satisfactory performance for a single two element array excitation. Figure 8 shows currents and potential mutual coupling between various arrays. Note the bottom mounted eight element performance can be achieved using six elements, the eight being necessitated as the pod configuration was achieved by the use of two planes of symmetry.

The array elements considered in this analysis each contained two V elements which under the 90 degree spatial and 90 electrical phasing are sufficient for single lobe patterns over a 2:1 bandwidth. The addition of a third element within the given pod patch spatial allocation provides the extension of single lobe pattern generation to the 3:1 bandwidth, all elements feed separately utilizing the same cavity backing as illustrated, Figure 9 for a cavity backed infinite ground plane installation.

Summary

MOM and aero configuration codes have been shown to provide a complete performance capability of an installed slot array configuration of traveling wave element arrays installed in a fighter aircraft pod configuration.

Acknowledgements

References:

[1] R.E. Collin & F.J. Zucker, "Antenna Theory Part II" McGraw Hill, 1969
[2] C.H. Walters, "Travelling Wave Antennas" Peninsula Publishing, 1965
[3] J.M. Putnam, L.N. Medgyesi-Mitschang, M.B. Gedera, "CARLOS-3D Three Dimensional Method of Moments Code," McDonnell Douglas Aerospace Technical Report, 1992

Objectives
- Develop Antenna System for a Given Pod Geometry
- Demonstrate Ability for:
  - Horizontal and Vertical Polarizations
  - Hemispherical Coverage
  - 3:1 Bandwidth

Approach
- Numerical Element on Pod Configuration
- "Exact" Numerical Simulation
  - Element and Full Configuration
- Equivalent of Antenna Range Testing   GP64799001.cvs

Figure 1. Project Objectives

- Radiation Requirements (Frequencies, Angles, Polarization, ERP)
- Pod Configuration (Physical Regions for Antenna Locations)
- Required Antenna Radiation Characteristics
- Define Antenna Types
- Element and Array of Element Types (Surface Wave/Traveling Wave/Endfire)

Technology

- Develop Element Model (Numerical Representation)
- Infinite Ground Plane (Single and Multiple Elements)
- Define Spatial and Electrical Phasing
- Validate Numerical Antenna Model vs Empirical Data (Element and Infinite Ground Plane)
- Identify Unique Element and Array Configuration

Integrated Product Team (IPT)

- Define Pod Geometry (Project)
- Define Numerical Representation (Pod)
- Identify Antenna Patch Requirements (Location and Number)
- Verify Pod Geometry Representation (Numerical) With General Antenna Patch
- Add Unique Antenna Representation

GP64799002.cvs
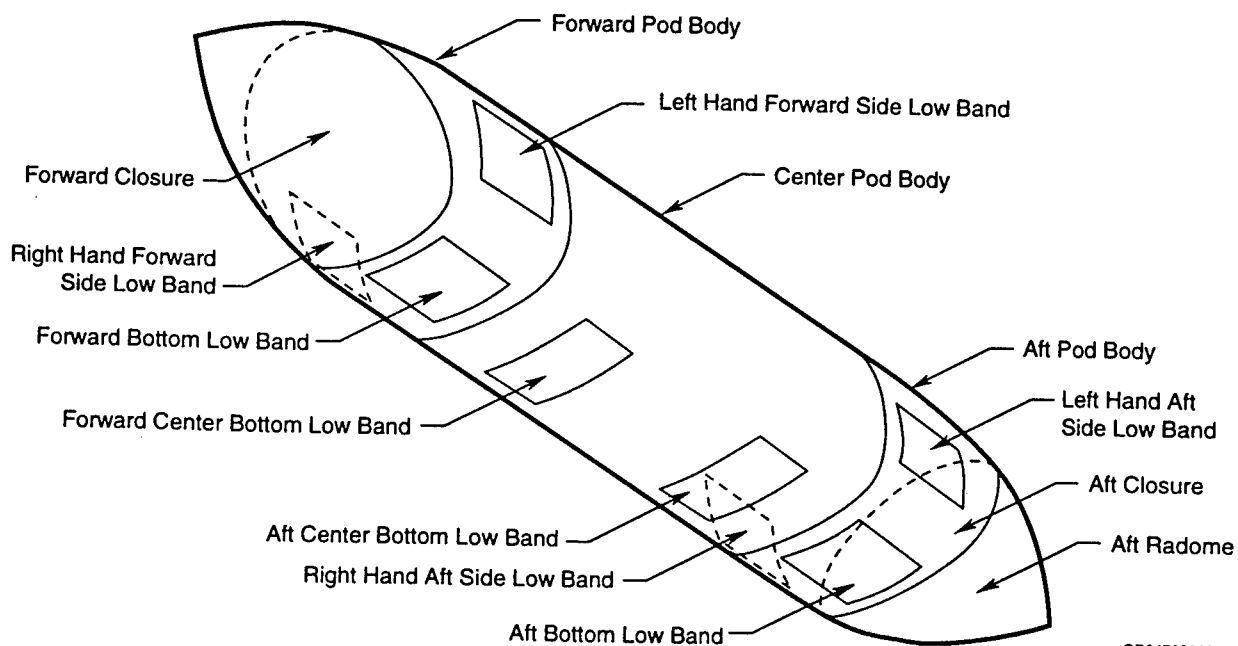
Figure 2. Process

Figure 3. Antenna Analysis Model

GP64799003.cvs

328
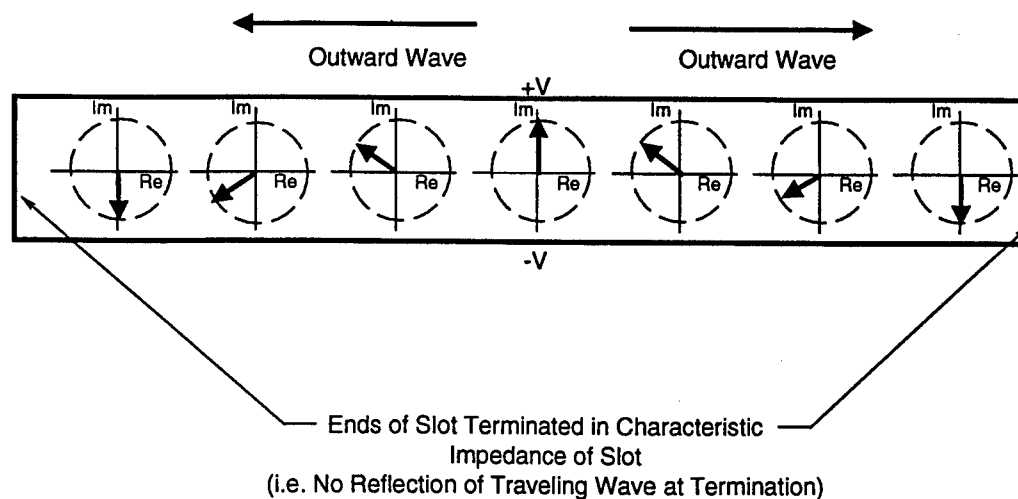
Figure 4. Phase Progression of Aperture Field in a Center Fed Traveling Wave Slot Antenna
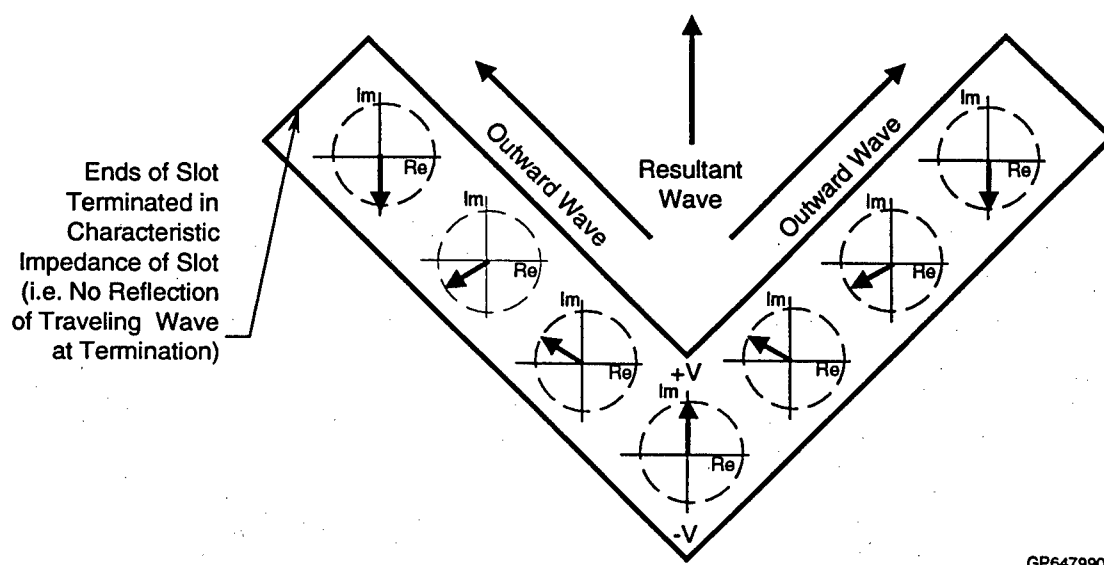
Figure 5. Phase Progression of Aperture Field in a Center Fed Traveling Wave V Slot Antenna
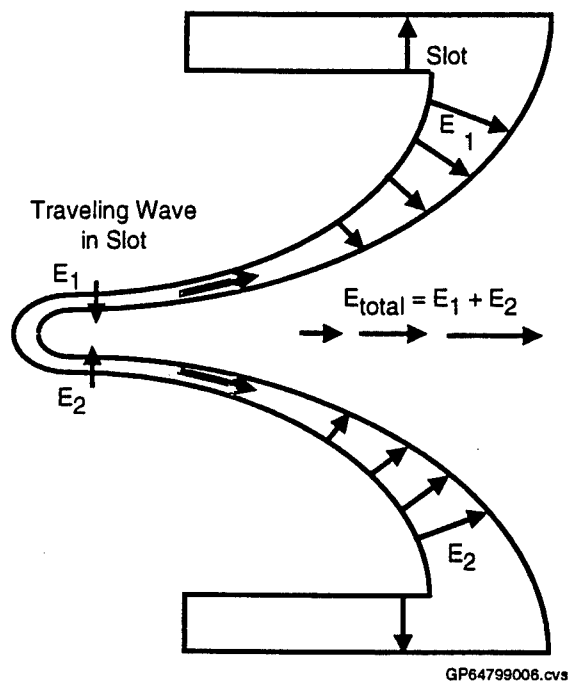
Figure 6. "Slot Notch" Antenna Concept
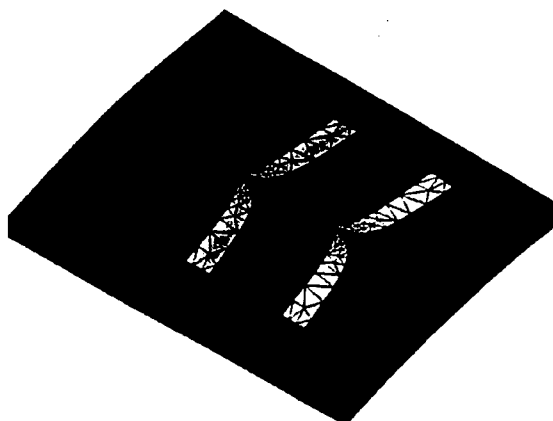
Geometry Definition

Magnetic Field Magnitude

GP64799008.cvs

Figure 7. Low Band Antenna Analysis Model
Forward bottom low band panel.

Geometry Definition

Magnetic Field Magnitude

GP64799007.cvs
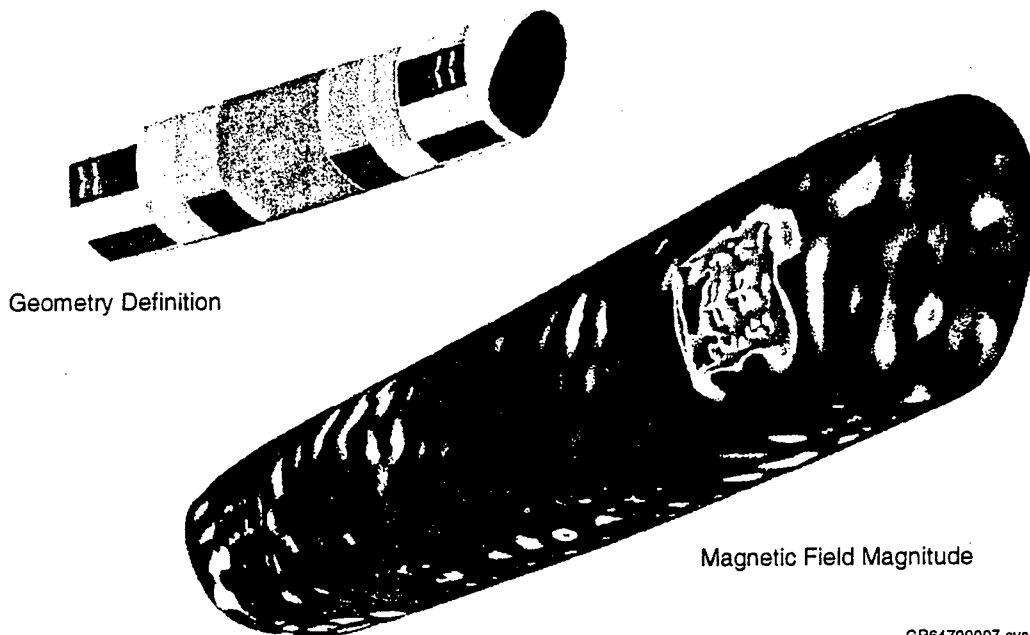
Figure 8. Antenna Analysis Model
Forward right hand side low band panel excited.

V Pol Low End Frequency

Gain (dB)

3 Elements
2 Elements

Theta

Side View

θ

V Pol

Slots in Infinite
Ground Plane

Top Views
Three Element Array

d:
V: 0°   −60°   −90°

Two Element Array

d:
V: 0°   −60°

GP64799009.cvs

Figure 9. Triple Element Array

V. ANTENNA TECHNOLOGY AND MEASUREMENT

NEAR AND FAR FIELD OF MF AND HF ANTENNAS

Valentin Trainotti

LU1 ACM, Senior Member IEEE

Bernardo de Irigoyen 650 2° 10

1072 Buenos Aires, Argentina

NEAR AND FAR FIELD OF MF AND HF ANTENNAS

Valentin Trainotti

ABSTRACT.

Monopole and vertical dipole behaviors are analized in order to show the near field difference and the importance on the radiation efficiency. The big difference between the monopole and dipole field intensity variations as a function of distance from the antenna base and of course the power density give us a clear view of the vertical dipole superiority as a high efficiency radiation element without the necessity of a high conductivity artificial gro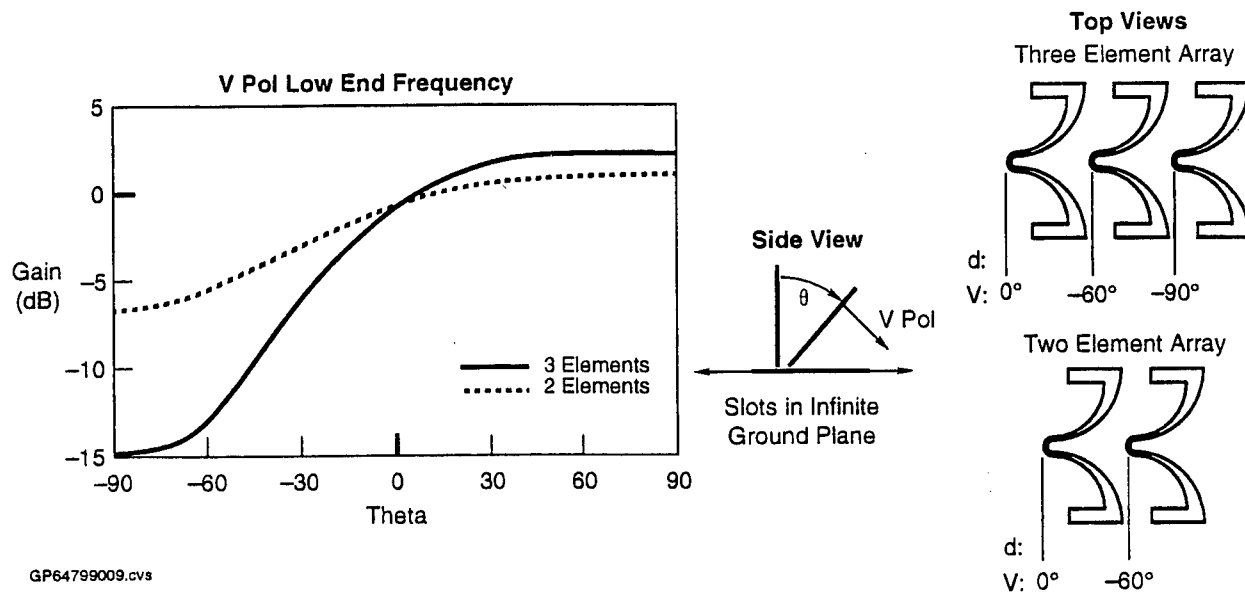und plane like in the monopole case. Measurement near monopole and dipole antenna models in HF frecuencies indicate good correlation between theoretical and measured electric and magnetic field intensities. Theoretical near fields are calculated by means of AWAS software. These results permit good confidence to design MF AM asymmetric vertical dipole antennas for high power stations without the classical 120 wire buried artificial ground plane and with high radiation efficiencies like the classical standard monopoles. Measurements on one of these radiating structures comfirm the theoretical predictions, permitting in the near future the installation of these efficient vertical antennas in MF band in rough places like jungle or mountains and for emergency or military purposes without flattering and digging the place for an artificial ground plane.

1. INTRODUCTION

A century of radiocommunication has been past since the first spark communication Guglielmo Marconi achieved in 1895. All his experiments were based on Heinrich Hertz electromagnetic waves discovery.

Marconi wanted to get a true radiocommunication equipment for practical use, and maximum range was first priority. At that time he saw that maximum range means maximum antenna height for both polarization, vertical or horizontal. Maximum range was achieved too, lowering the operating frequency, but as the antenna was at the same time the wave generator, lower frequencies mean bigger antenna size. So he starts working empirically because science could not give him some advice. Nobody was working in this field before him. He found a practical method to get the spark equipment "at hands", using a monopole, sometime called a Marconi Antenna.

This invention permitted him to get a lower generated frequency and at the same time vertical polarization with a smaller antenna (half the size of the Hertz dipole). This arrangement gives him an improvement in range and the 19 century last years saw a continuing work toward lower and lower frequencies to achieve maximum range. Of course as technique was improved too, more and more power was injected into the antenna systems.

Figure 1 shows historical antennas used by Hertz and Marconi.

1901 is the opening of tansatlantic radiocommunications due to the historical link made possible by Marconi-Fleming team on December 12th, between Poldhu, England and Saint John, Newfoundland.

Monopole antennas was used during the last century in almost every electronic application but especially for the lower radiofrequency spectrum. It was a standard antenna for MF AM stations for omnidirectional or directional applications using high efficiency artificial ground planes. Maximum surface wave is necessary in order to get an optimum link between the transmitting and the receiving sets. Even in the lower part of HF surface wave offer a good possibility for communications or surveillance especially over the sea or ocean and for this application monopoles were used satisfactorily.

Dipole are not so popular in low and medium frequency applications to generate surface waves along the earth surface. This is generally because of its bigger size, for its more complicated physical structure and because its feeding point is not close to ground. Nevertheless in this work vertical dipoles are proposed as an efficient radiating structure without the classical buried artificial ground plane for MF and HF applications.

2. MONOPOLES.

Marconi invented the monopole antenna making a ground connection at one of his antenna ends. How this antenna and how wave propagation worked, was kind of mistery at that time. Nevertheless as more and more scientific and technical people were involved in the radiocommunication field, lot of questions were answered. In 1909 Sommerfeld [1] wrote a paper on electromagnetic wave propagation by a vertical dipole showing the existence of a space as a surface wave. In 1924 Stuart Ballantine [2] wrote a paper in the Proceeding of the I.R.E., founding the bases of an optimum monopole antenna for medium frequencies A.M. broadcast stations. At the same time, optimum antenna height does not mean maximum efficiency, because monopole antenna works with the ground plane as a fundamental part. Supposing perfectly conducting ground, the optimum monopole height is around 0.625 wavelength. This height gives the maximum field strength along the earth, maximum surface wave or maximum gain compared to an isotropic source. Nevertheless for broadcast use, the secondary lobe radiation was found to be excessive and detrimental during the night. This effect is due to ionospheric "reflexions" that occur in the E and F layers and for this reason an undesirable self interference at close distance from the antenna. Monopole radiation patterns not only depend on the monopole height but on the height-radius relationship. Broadcast

optimum antenna height depends on several parameter, frequency, physical height, equivalent stucture radius and on the physical ground characteristics, conductivity and dielectric constant of the earth, in order to get maximum surface wave radiation or maximum diurnal and nocturnal service area or distortionless area. Nocturnal service area is defined as the distance from the transmitting antenna to a point on the earth surface where the relationship between the surface wave and the ionospheric wave is 10 dB. Beyond this point interference between both waves can produce severe information distortion and fast signal fading.

Figure 2 shows monopole radiation patterns as a function of height-radius relationship. Increase in high angle radiation can be seen for low height radius relationship for monopole higher than .45 wavelength. (Table 1)

Dr. George Brown wrote an historical paper [3] on the artificial buried ground plane for broadcast use and at the present 120 buried radials are used as a standard. This kind of monopoles are called high efficiency transmitting monopole antennas because efficiency is very close to 100%, typically 96 to 99 %.

Near electric and magnetic field calculations show that both fields have a maximum in the monopole driving point regardless the monopole height, or it means, that power density of the radiated wave is a maximum on the monopole base.

Figure 3 shows a monopole near electric field representation or dispacement current in the surrounding space as Maxwell called it.

Conducting current is flowing on the metallic monopole structure. In order to close the antenna circuit all the lines of force representing the near electric field intercept the ground plane at a right angle, producing radial conducting current on it, flowing toward the driving point. These radial conducting currents need a low impedance medium to flow, in order not to lose energy. For this reason high conductivity surface or metallic radials are needed. Radial length must be at least quarter wavelength. Nevertheless conducting currents at greater distance doesn't return to the driving point and doesn't increase very much the antenna efficiency. Figure 4 shows near electric and magnetic field strengths as a function of distance for different monopole heights on a perfect ground plane and at the same time maximum power density can be seen at the antenna base for any monopole height.

One important thing to remember is: "Monopole ground plane would be of infinite conductivity or as better as possible because it's the antenna itself". Any departure of this concept gives lower and lower radiation efficiency due to the low conductivity of the earth compared to metal conductivities. As an example:

(Copper conductivity 5.8E7 S/m, Sea Water conductivity 5 S/m, Average ground .01 S/m and Poor Soil .001 S/m. aproximately.)

For this reason monopoles installed over real
ground need an artificial ground plane in order to
lower the soil impedance and to improve the antenna
efficiency. When an artificial ground plane is used
the soil impedance is modified having a value as a
result of the wire structure impedance in parallel
with the soil impedance. Separation between wires
increases as distance from the antenna base
increases and at some point the wire effect is
almost insignificant even for a lot of wires.
Figure 5 shows the impedance of the soil and the
artificial ground plane for different radial
numbers where clearly the impedance increase is
shown as a function of distance. For few radials
the impedance soil level is reached even before to
arrive at the ground plane radius.
In order to calculate the antenna efficiency it's
important to know the power dissipated into the
ground from the antenna base to the artificial
ground plane radius. Power dissipated beyond this
point is considered into the ground attenuation
factor and it's a surface wave propagation problem.
This last factor actuates on any antenna radiated
wave regardless the antenna type. Over perfect
ground, electric field intensity has only one
vertical component, i.e. Ez considering the
standard rectangular coordinates, magnetic field
intensity is Hy if propagation is in x direction
and power density is Px. Over real ground electric
field intensity has two component Ez and Ex,
magnetic field intensity is Hy and power density
has two components Px, the electromagnetic

propagation along the surface of the earth and Pz, the electromagnetic propagation into the ground which is lost into the ground losses. The Ex magnitude and of course Pz depend on the soil impedance. For very low impedance soil Ex and Pz are negligible like in a very good artificial ground plane but as distance is increased from the antenna base, impedance increases and power dissipated into the soil starts to be important. In this work power dissipated is calculated within the artificial ground plane limits, generally quarter wave in radius for standard monopoles and the same limit for the vertical dipole efficiency calculation in order to compare both antennas.

Generally monopole and dipole radiation patterns and antenna gain are calculated in the far field and for high frequency operation. In these cases the surface wave effect is insignificant and for this reason radiation pattern and antenna gain are only for space wave i.e. direct and reflected wave. At the same time most cases are for horizontal polarization where surface wave propagation is almost nonexistent even at short distance from the transmitting antenna. Nevertheless for vertical polarization is very important to calculate not only the direct and reflected fields but the surface wave field too even if this problem involves a more difficult calculation process and the radiation patterns are function of distance, frequency and soil parameters.

3. DIPOLES.

Dipoles are the oldest antennas and was the first radiating element since the Hertz experiments in 1885-1890. It could be used for vertical or horizontal polarization, depending on its installation respect to ground. This is a quite old concept because earth is the reference and it is considered as an horizontal plane. In a modern concept, for example in free space, a coordinate system must be used. Generally speaking horizontal polarization means electric field vector parallel to the earth or natural ground plane.

Dipoles have been used successfully during the last century because it's a high efficient antenna. Nevertheless most of installations are using horizontal dipoles, inverted "V" dipoles or horizontal dipole arrays.

The near field of a vertical dipole produces lines closing a circuit over the dipole itself and only a few lines are in connection with the image. There are less and less lines between the dipole and his image under the ground plane as the dipole height is increased.

Dipoles can be used in vertical polarization, installing the dipole vertically over the earth. What the difference between a dipole and a monopole is? Figure 6 is a representation of the dipole field lines and a comparison with figure 3 can be made. Figures show a big difference between

341

monopole and dipole field lines. In the monopole
case ground plane is fundamental in closing the
antenna circuit, because every field line
intercepts the ground plane and a displacement
current to conducting current conversion is made.
In the dipole case almost all lines close the
circuit in the free space surrounding the dipole.
Free space is a very low loss medium, almost
perfect. Dipole structure is metal, high
conductivity medium, low loss too. Only few lines
are intercepting the ground plane and here there
are losses if the soil conductivity is poor.

These two representations speak about that by
themselves. Monopole requires very high
conductivity ground plane in order to obtain high
efficiency. In the dipole case this is not so
important and depends on the dipole height over
ground. In the latter, ground radials could be
avoided because of their low contribution to dipole
efficiency.

In order to get a theoretical proof, near field
and near power density of the dipole radiated
electromagnetic wave has been calculated
considering a perfectly conducting earth.
Figure 7 shows the dipole near electric and
magnetic field and power density. Comparison
between monopole and dipole can now be made because
they are in a similar environment. In figure 8
comparison between a quarter and a half wave
monopole and a half wave vertical dipole is made.
In both cases infinite ground plane conductivity

342

has been considered, power input is 1 Kw at 1 MHz. Dipole is half a wavelength in length and its lower end has .001 wavelenths height over the ground plane, the worst case for the vertical dipole. The dipole lower end is very close to ground in order to get a good comparison between two radiating structures of similar heights. Nevertheless the power density comparison in figure 8 shows more than 20 dB increase near the antenna base for the monopoles.

Figure 9 shows the near electric and magnetic field as a function of dipole separation from the ground plane "s/2" between .001 and 1 wavelength in the dipole lower end. This is a good view of the near fields and power density behavior. Even for the lowest separation between the dipole end and the ground plane the power density is around 20 dB lower than the monopole power density and this value is lower and lower as the separation from the ground plane increases. This is consequence of low coupling between the dipole and its image because they are collinear and the mutual coupling is no so important especially for separations greater than half a wavelength. Of course for low and medium frequency operations, dipole end separations would be very low because of the high installation costs. Nevertheless if possible the best option is choosing some lower dipole height in order to lower the base power density and increasing the antenna gain. Only in the dipole case the designer has the possibility to play with this parameter to control the antenna gain and the secondary lobe level.

4. NEAR FIELD MEASUREMENTS.

Theoretical predictions indicate a lower power density near the dipole base compared to the monopole case and this density would be around 20 dB down. Measurements are the only way to demonstrate these predictions and for this reason E and H field measurements has been made using electric and magnetic probes along the earth surface in both HF and MF transmitting monopoles and properly calibrated in order to compute absolute field values. For instance, near electric and magnetic fields has been measured near a quarter wave monopole and these values compared with the theory in a 30 MHz frequency, so to use a simple and cheap model. Figure 10 shows good agreement between theory and measurements. Monopole has four buried quarter wave wires as an artificial ground plane.

At the same time vertical dipole near E and H field measurements has been made. Measurement comparison can now be made between the monopole and a half wavelength vertical dipole but without any buried wires into the ground under the dipole. Figure 11 shows near E and H fields and near power density comparison between the quarter wave monopole and the vertical half wave dipole. In this figure a dipole power density lower than 30 dB with respect to the monopole can be seen. This is a very good confirmation of the theoretical predictions.

Near E and H field measurements were made near a high power MF AM standard broadcast monopole in order to compare the theoretical predictions in these important installations. Figure 12 shows good agreement between theory and measurements. These theoretical and measured results gave the author good confidence in the design of a new MF AM transmitting antenna. For more than sixty years high efficiency buried artificial ground plane standard monopole were used for MF AM stations. 120 wires buried ground plane was considered as an optimum after Dr. Brown remarkable work.

Why after this long time nobody were using something different as MF AM transmitting systems?

In the author knowledge no vertical antennas without buried ground plane have been used in MF AM stations in the past so this kind of measurements were considered very important and even though the decision to bilt one of these vertical dipole is not very easy to be taken especially due to the high installation investment.

Nevertheless the first asymmetric vertical MF AM vertical dipole was installed during the month of May, 1994 for a 50 KW broadcast station near Buenos Aires city downtown. Figure 13 shows a comparison between the theoretical near field predictions and the measured values. Good agreements can be seen even if the software is only for perfect ground calculations.

4. FAR FIELD MEASUREMENTS.

Far field measurements can give a better understanding of the transmitting antenna efficiency and it's a practical view if the the antenna can fulfil exactly the service area. HF measurements were made with standard military equipments as power generators in the 30-75 MHz band. Supplied monopoles were used as references in order to check the dipole theoretical predictions. These monopoles are using the transceiver boxes and the real ground as ground plane so efficiency are not really important. Two monopole antennas are supplied with a model 4600 Philips portable military transciever with length of 1 and 3 meters. At the same time transciever has a 50 ohms output BNC connector so an external antenna can be used. A vertical dipole very close to ground and a Rohde-Schwarz field strength meter were used as receiver in order to compute the far field. This equipment were properly calibrate in order to check the received level linearity and the antenna and coaxial factor so to get the maximum received field strength accuracy. Figure 14 shows the far field results where the dipole produces around 13 dB more signal than the 3 meter monopole and 30 dB over the 1 meter monopole at a frequency of 30 MHz. Received signal is really a surface wave even if the frequency is 30 MHz because all the antennas were very close to ground and the dipole has really very high efficiency because is almost independent

of the ground plane. Depending of the battle conditions this experiment can be an advice of what kind antenna must be used in the second line in order to increase the link efficiency. A very light portable vertical wide band dipole could be a practical solution for surface wave propagation in the 30-75 MHz band when the antennas are very close to ground.

MF AM vertical dipole far field measurements were performed using a calibrated loop antenna and a Singer NM-25T field strength meter. Several radials were checked in order to compare the theoretical surface wave field with the vertical dipole field. Figure 15 shows the measured and calculated E field along one of the radials in the open field so to get a more theoretical environment in the field comparison. The "Pampa" is a really good environment because the region is very flat and with very good and almost constant soil conductivity and with a several hundred kilometers in extension. Theoretical calculations were performed using the Sommerfeld-Norton plane earth equation with the inclusion of a shadow or diffraction factor so to calculate the field along the radial with only one expression [5]. Several MF AM stations were checked in order to acquire good confidence in surface wave measurements before the vertical dipole erection and to determine the expression exponential coefficient. Good agreement can be seen and this indicate a very good radiation efficiency in the vertical dipole. 98% efficiency was determined according to the near E and H field measurements for a radius of 100 meter and far fields are giving a good confirmation of it.

5. CONCLUSIONS

In order to check the monopoles and dipoles behaviors lots of calculations and measurements have been made on models. After that, the first medium frequency A.M. asymmetric vertical dipole has been made in Argentina in May 1994, for a 50 Kw A.M. station. Measurements indicate high radiation efficiency and almost 0.5 dB gain over a 120 buried radial standard monopole of the same physical height. So for the first time the standard 120 buried ground plane radials were put away in a standard broadcast station antenna. After more than two years of operation without problems with this antenna during several seasons in any kind of weather give us a very good confidence in future designs.

Really no problems, because it is entirely grounded so to avoid any kind of static electricity and to avoid problems in stormy weather making the ideal antenna for solid state high power transmitters. This experience could be useful for the design of MF AM vertical dipole antenna in difficult environments like jungle, mountain or even over a building where a buried ground plane is impossible to be made or for military or emergency purposes using quick erectable trasportable transmitting systems. At the same time during the vertical dipole transmitting efficiency research, it was possible to demostate the low monopole efficiency in the supplied military equipments and the necessity to improve them.

REFERENCES and BIBLIOGRAPHY.

[1]. Sommerfeld, A., "Uber die Ausbreitung der Wellen in der Drahtlosen Telegraphie". Ann. Phys. Lpz. (4) 28, 665, (1909) and Ann. Phys. Lpz. 81, 1135, (1926).

[2]. Ballantine, S., "On the optimum transmitting wavelength for a vertical antenna over perfect earth". Proc. I.R.E., Vol. 12. pp 833-839, December 1924.

[3]. Brown, G.H., Lewis,R.F., Epstein,J., "Ground systems as a factor in antenna efficiency". Proc. I.R.E., Vol. 25, pp 753, June 1937.

[4]. Abbott, F. "Design of optimum buried conductor R.F. ground system". Proc. I.R.E., Vol. 40, pp 846, July 1952.

[5]. Trainotti V.,"Simplified Calculation of Coverage Area for MF AM Broadcast Stations" IEEE Antenna & Propagation Magazine, pp 41-44, June 1990.

[6]. Trainotti, V., "Height radius effect on MF AM transmitting monopole antenna". I.E.E.E. Trans. on Broadcasting, Vol. 36, N. 1, pp. 82, March 1990.

[7]. Trainotti, V. "MF AM Transmitting Asymmetric Vertical Dipole" I.E.E.E. Trans. on Broadcasting, Vol. 37, N. 3, pp 106, Sept. 1991

	TABLE 1						
	60 DEGREE ELEVATION MONOPOLE RADIATION (dB)						
	H/λ						
H/a	0.40	0.45	0.50	0.52	0.54	0.56	0.58
5	-11.1	-8.7	-5.0	-3.3	-1.7	-0.9	-1.0
7.5	-12.8	-12.4	-8.9	-7.2	-5.5	-3.8	-2.1
10	-13.0	-14.0	-11.2	-9.4	-7.6	-5.8	-4.0
20	-12.9	-15.8	-15.4	-13.6	-11.5	-9 3	-7.4
50	-12.5	-16.0	-19.0	-17.6	-15.1	-13.8	-10.2
100	-12.3	-15.8	-20.4	-19.9	-17.2	-14.2	-11.6
200	-12.1	-15.6	-21.3	-21.6	-18.8	-15.5	-12.6
500	-12.0	-15.4	-21.9	-23.4	-20.6	-16.8	-13.5
1k	-11.9	-15.8	-22.0	-24.5	-21.8	-17.5	-14.0
∞	-11.5	-14.6	-24.0	-28.3	-35.3	-22.6	-17.1
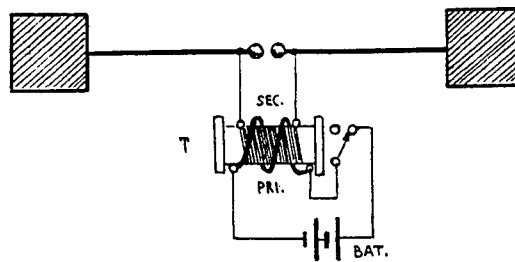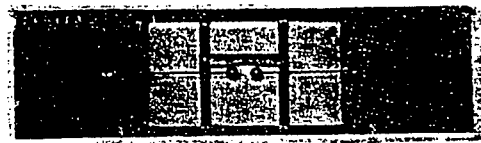
ONE OF HERTZ'S FIRST DIPOLES (1887)
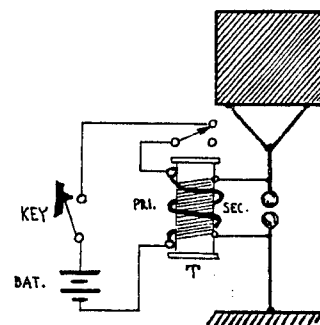
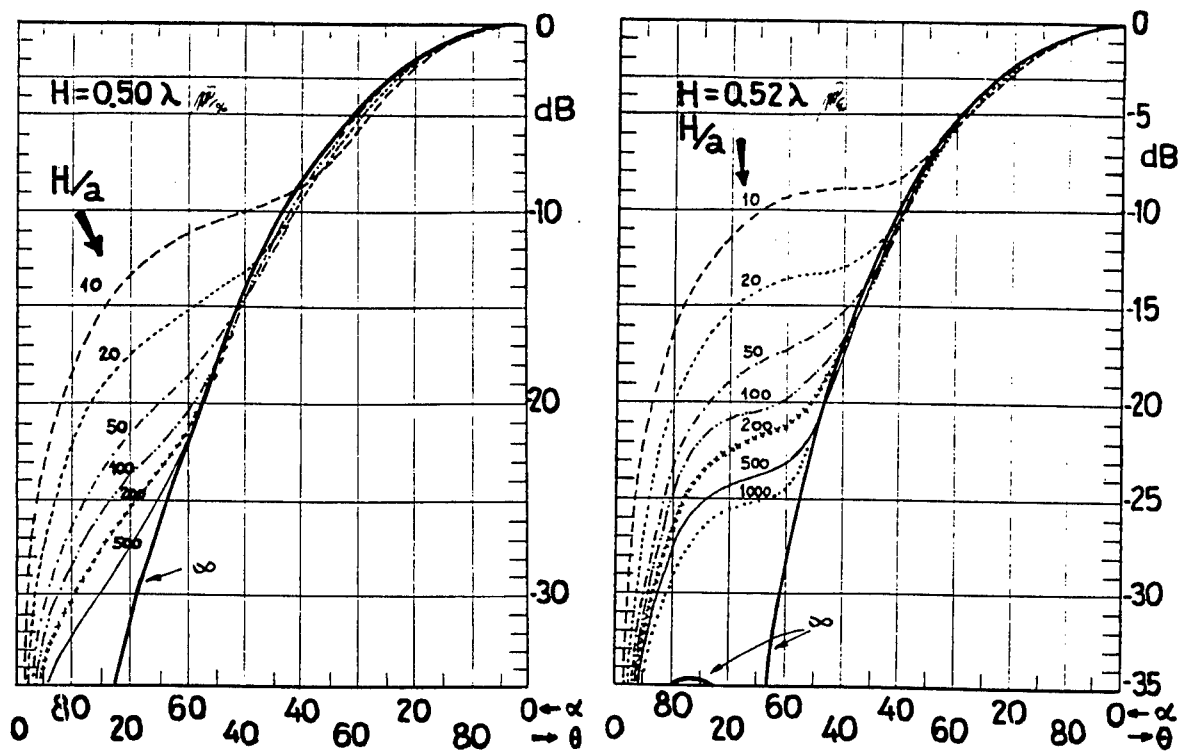MARCONI'S FIRST MONOPOLE (1896)

FIGURE 1. HISTORICAL ANTENNAS.

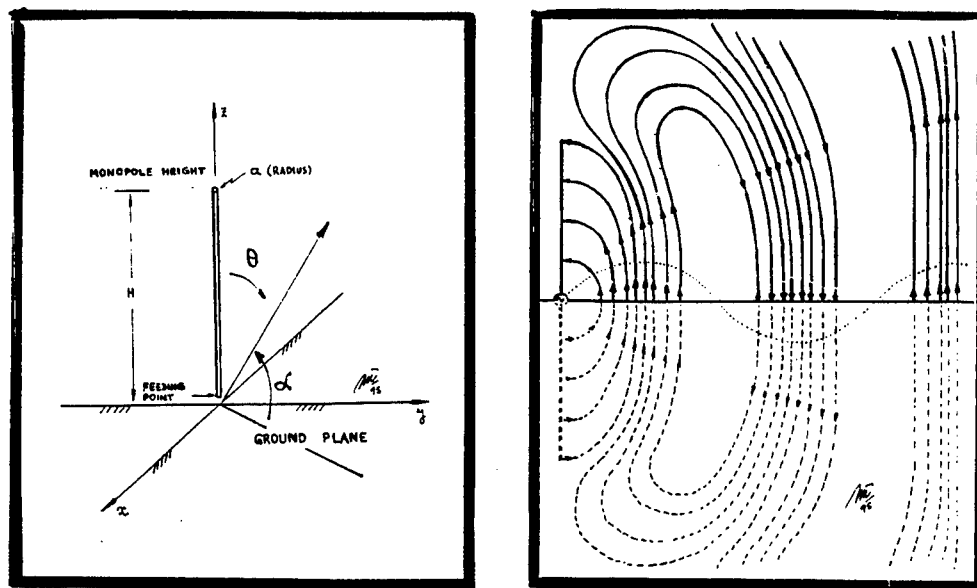FIGURE 2. MONOPOLE RADIATION PATTERNS AS A FUNCTION
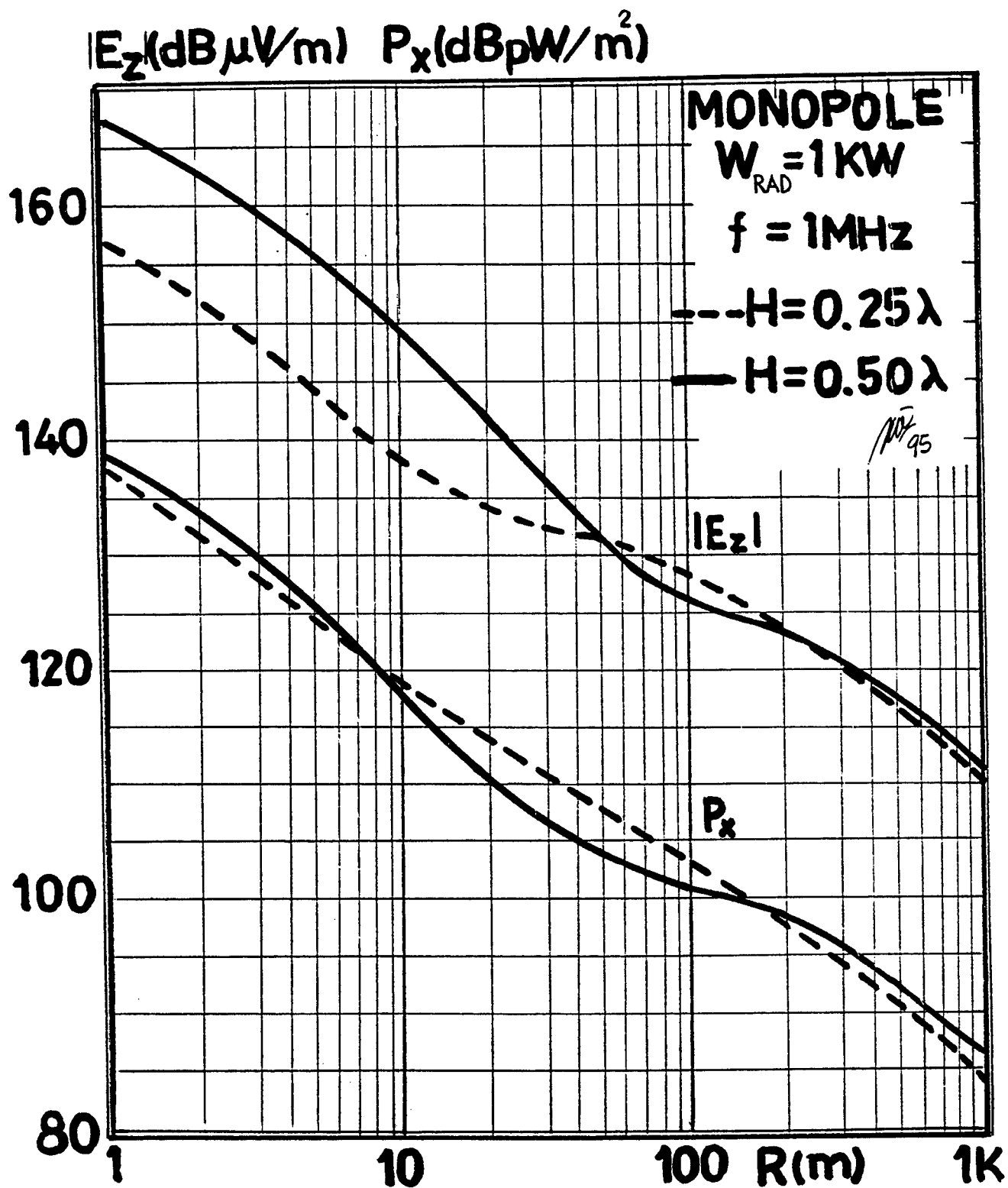OF H/a.

FIGURE 3. MONOPOLE NEAR ELECTRIC FIELD

FIGURE 4a. MONOPOLE THEORETICAL NEAR ELECTRIC FIELD
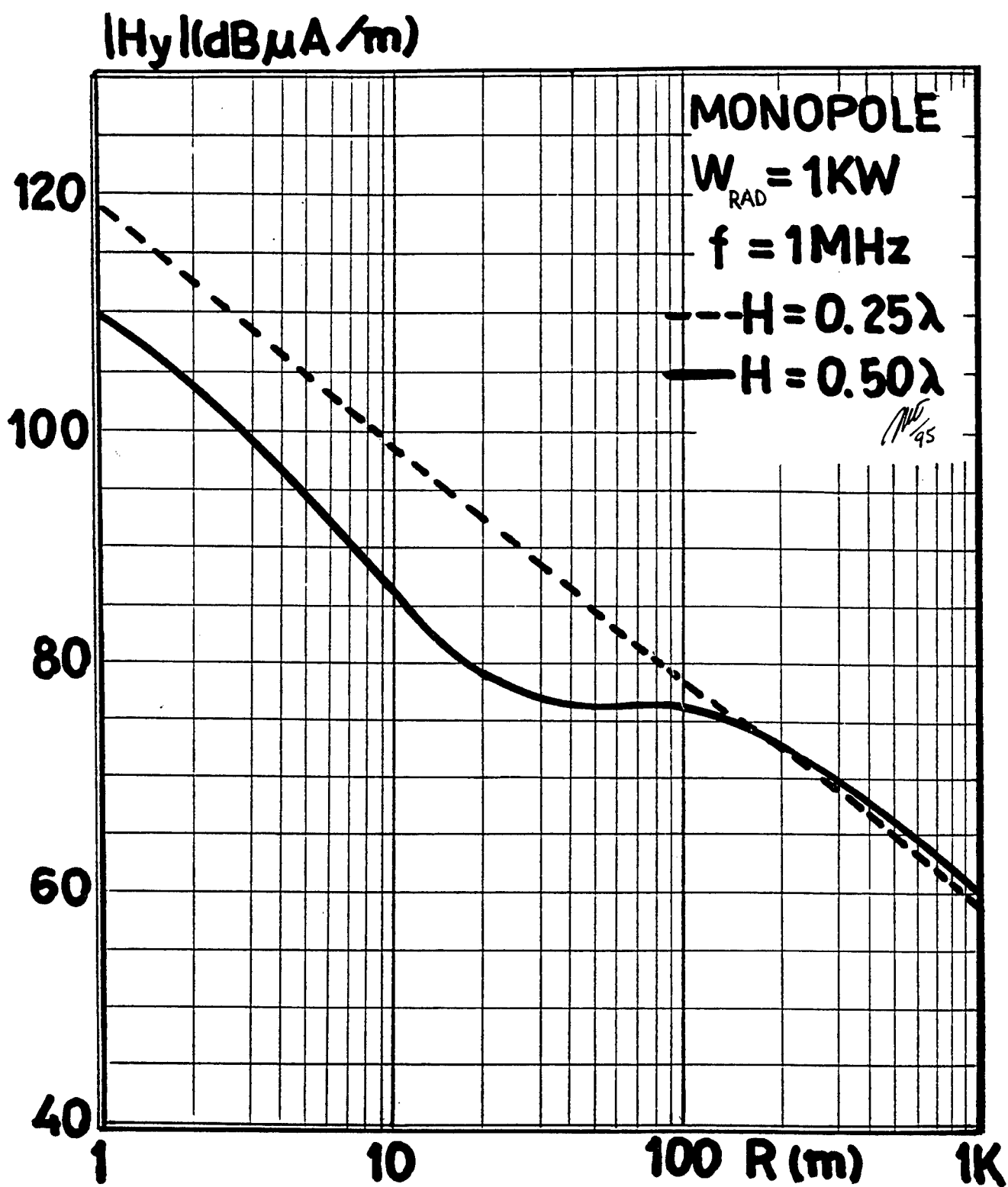AND NEAR POWER DENSITY.

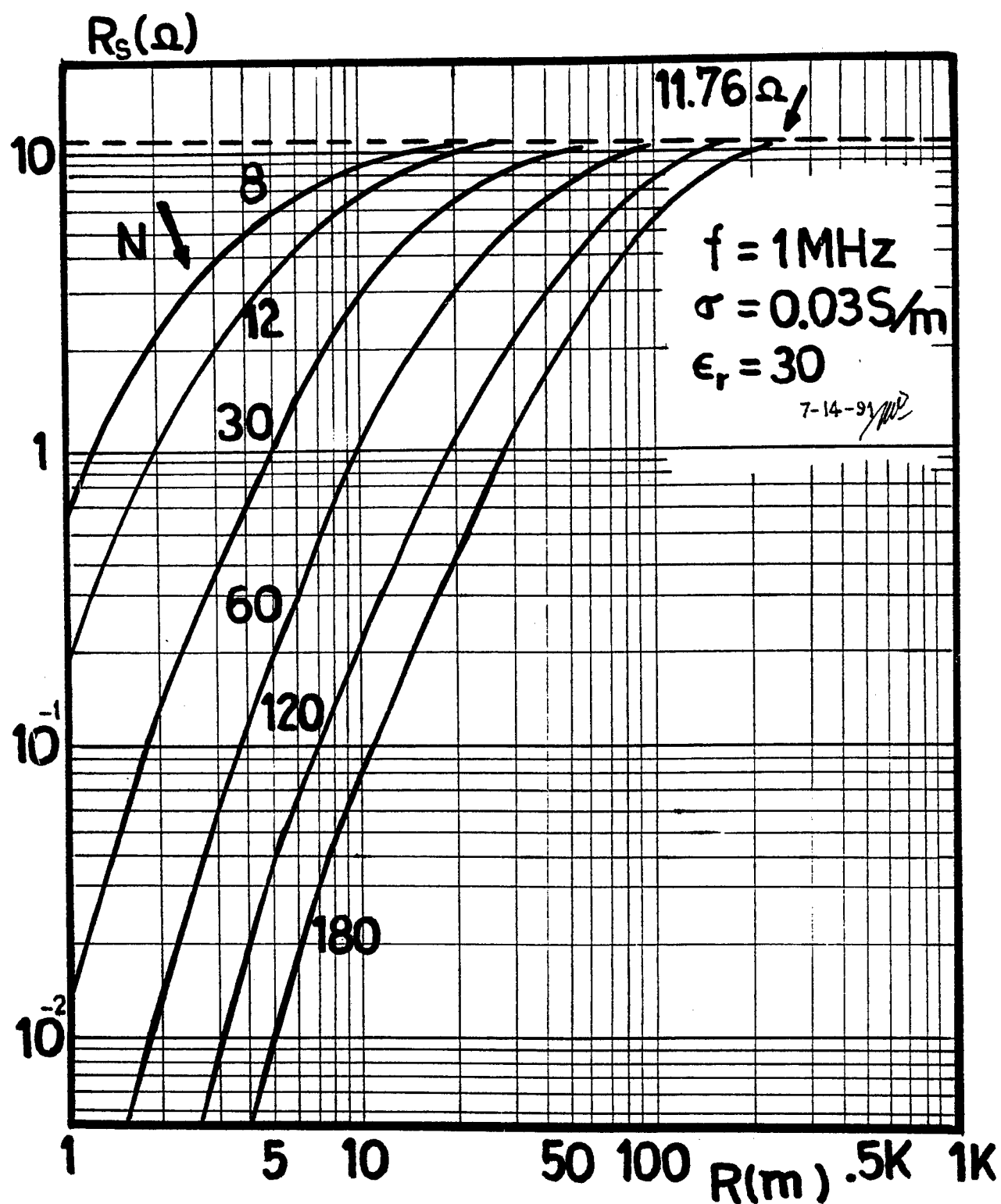FIGURE 4b. MONOPOLE THEORETICAL NEAR MAGNETIC FIELD.

FIGURE 5a. ARTIFICIAL BURIED GROUND PLANE RESISTANCE AS A

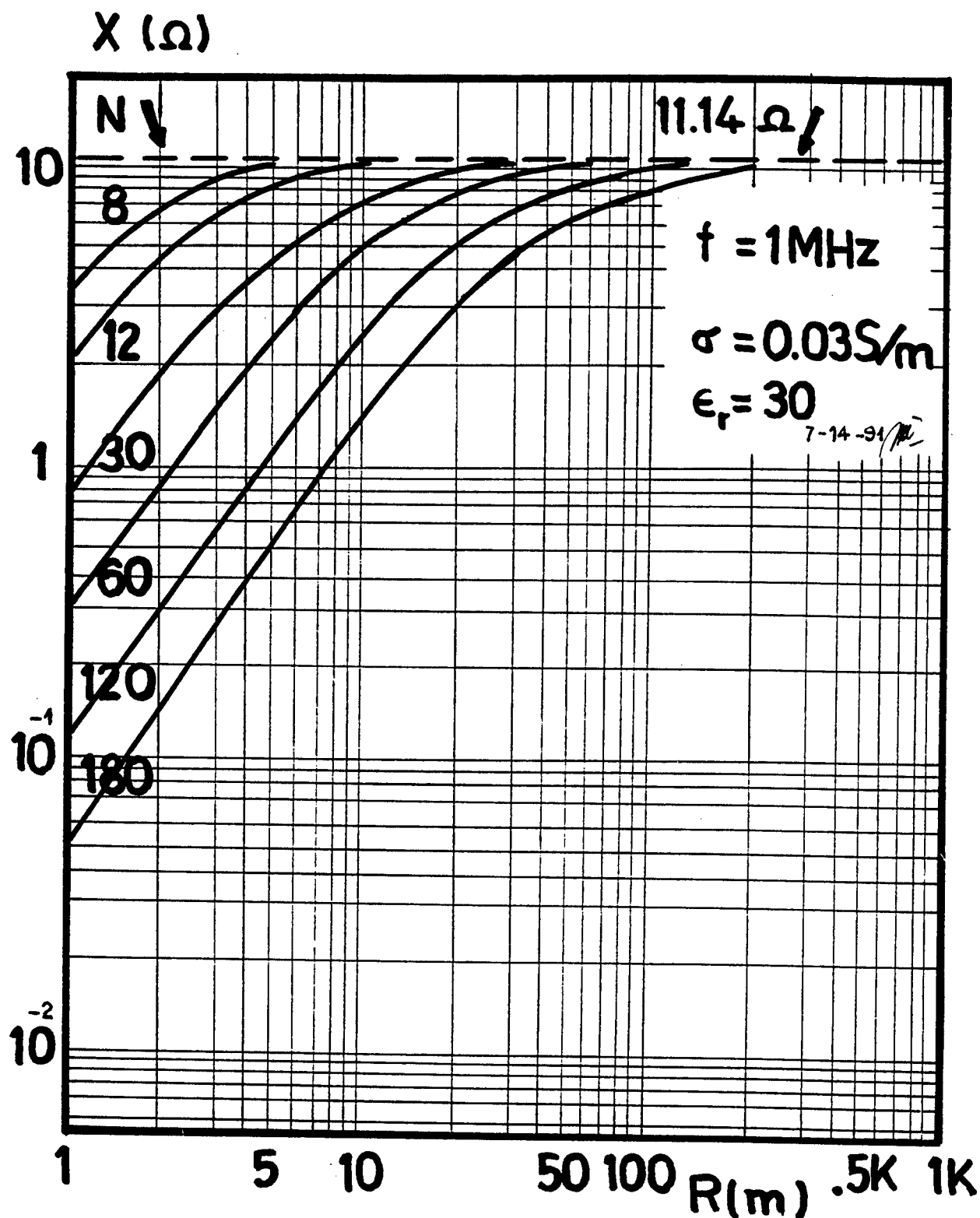FUNCTION OF RADIAL NUMBER (N) and DISTANCE (R)

FIGURE 5b. ARTIFICIAL BURIED GROUND PLANE REACTANCE AS A
FUNCTION OF RADIAL NUMBER (N) AND DISTANCE (R)
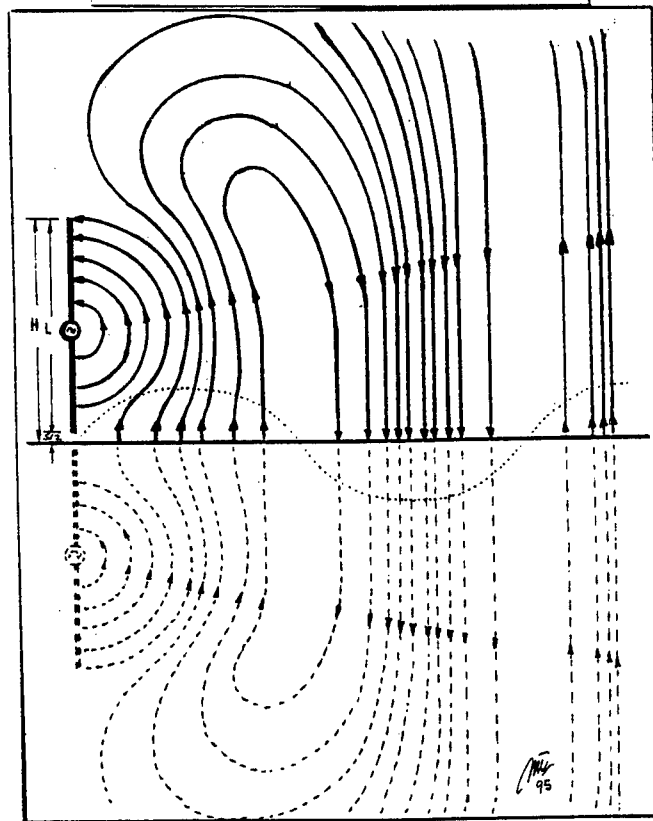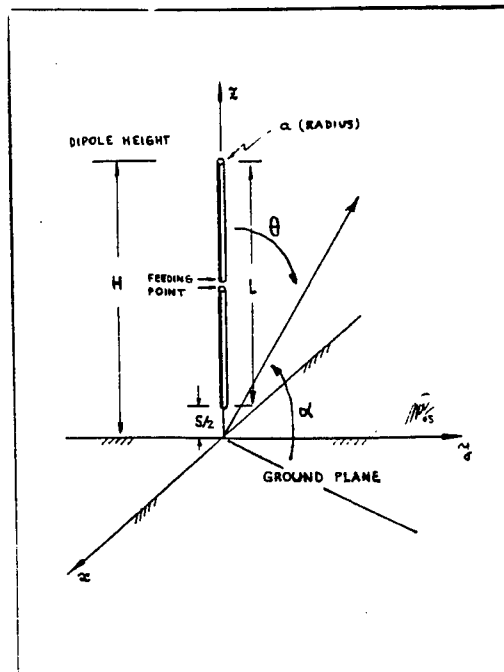
FIGURE 6. DIPOLE NEAR ELECTRIC FIELD.

357
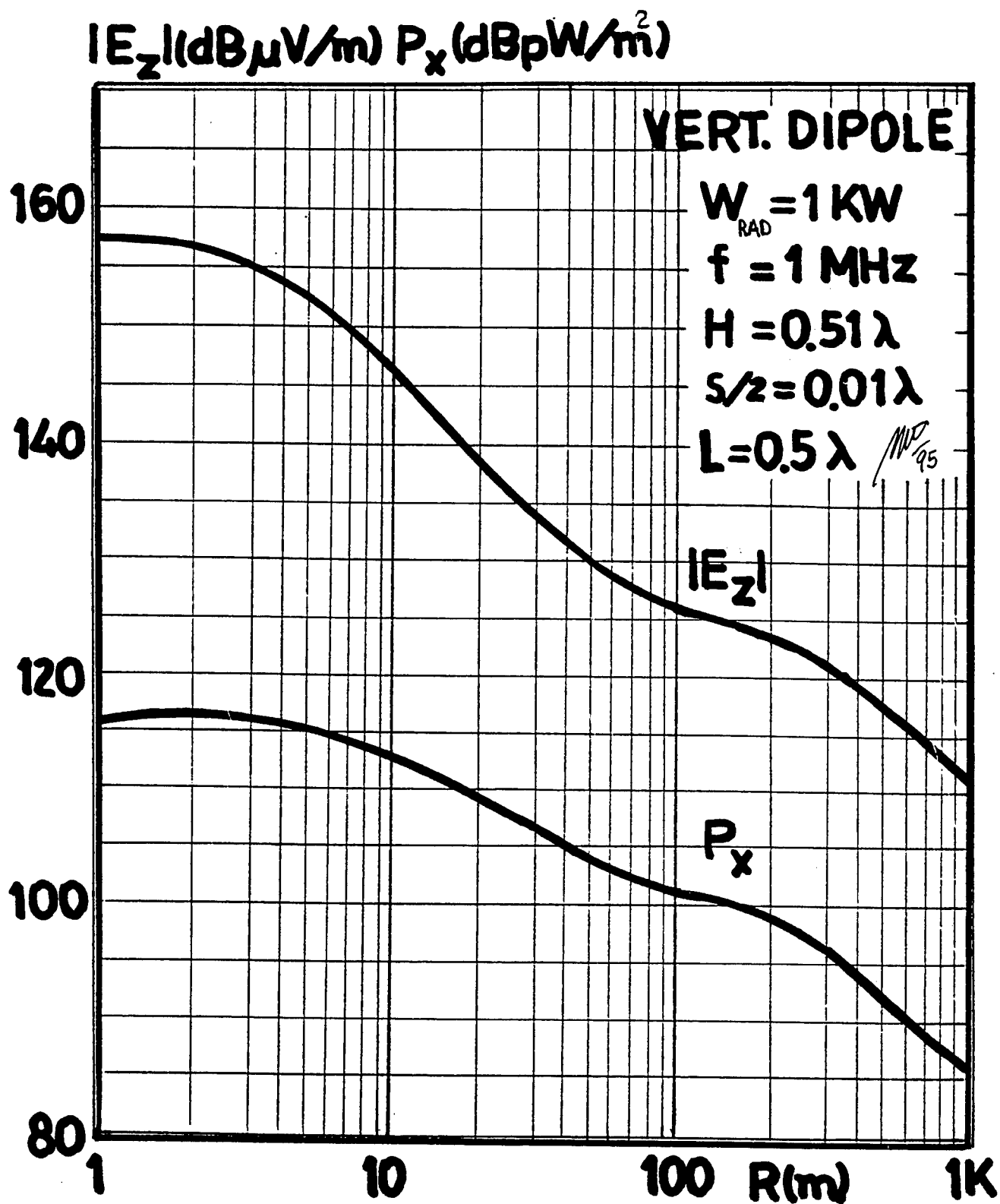
FIGURE 7a. VERTICAL DIPOLE THEORETICAL NEAR ELECTRIC FIELD
AND NEAR POWER DENSITY.
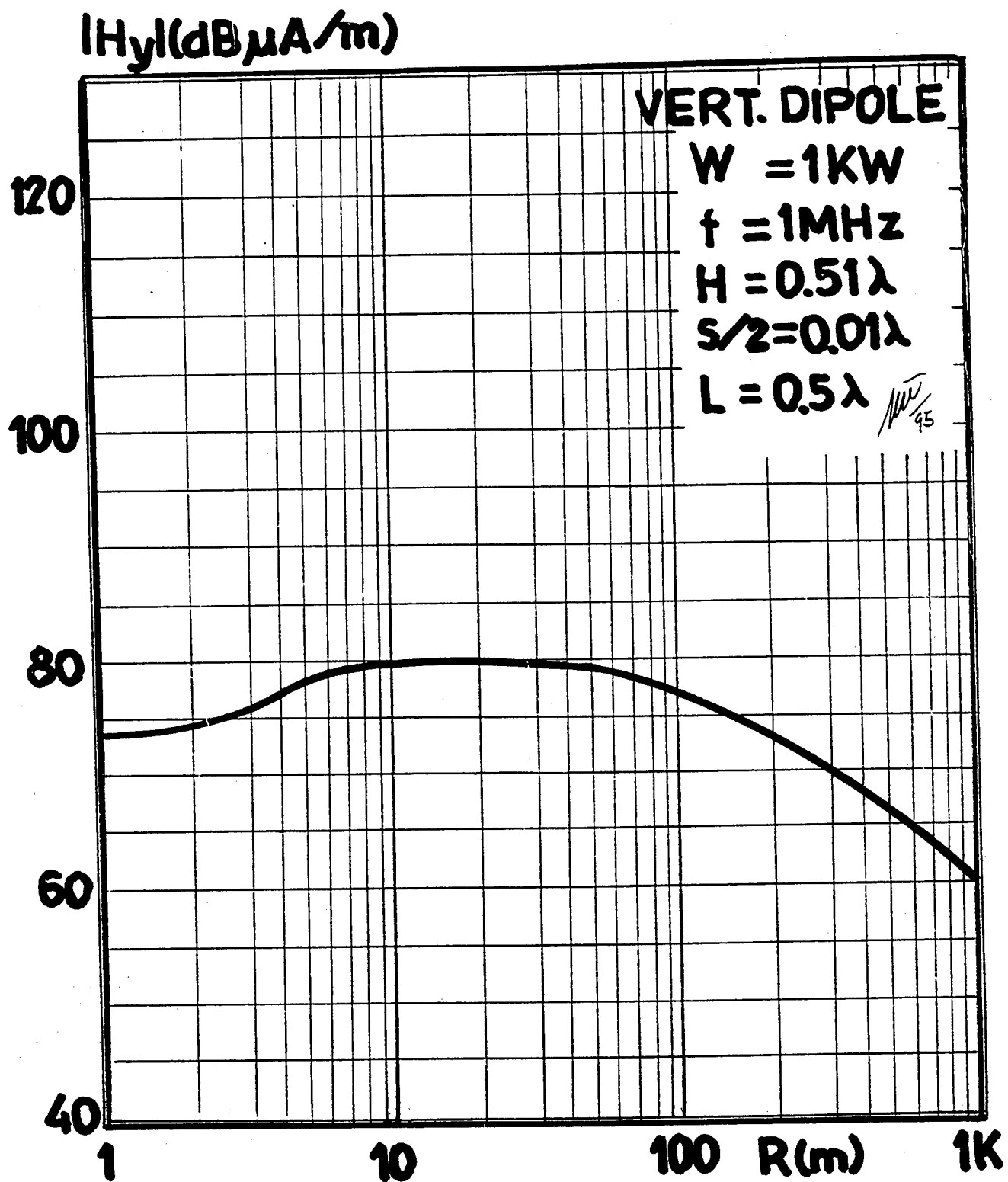
FIGURE 7b. VERTICAL DIPOLE THEORETICAL NEAR MAGNETIC
FIELD.
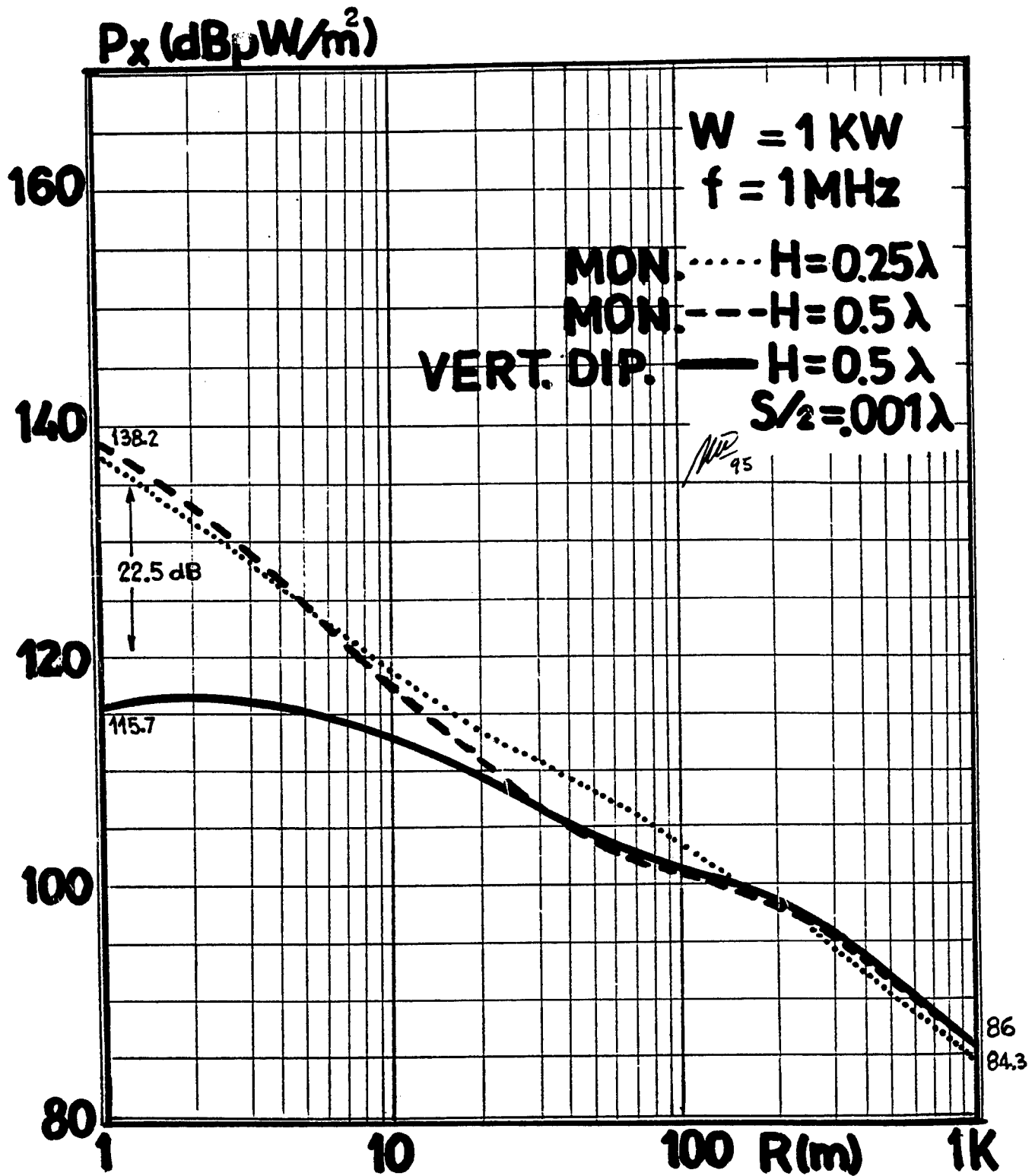
FIGURE 8. MONOPOLE-DIPOLE THEORETICAL NEAR POWER DENSITY
COMPARISON.
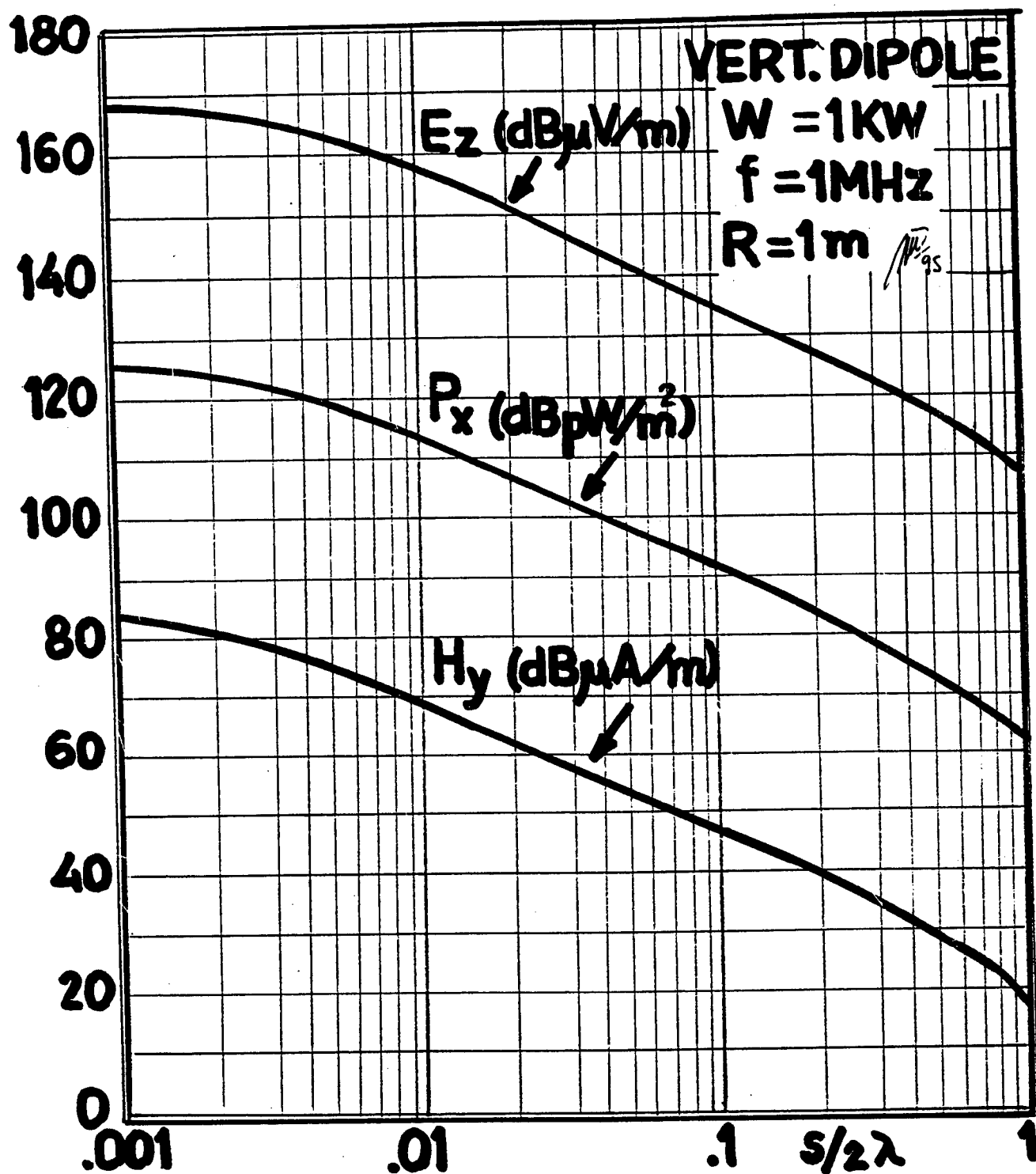
FIGURE 9. VERTICAL DIPOLE BASE ELECTRIC FIELD,
MAGNETIC FIELD AND POWER DENSITY AS A FUNTION OF
SEPARATION FROM THE GROUND PLANE.

361
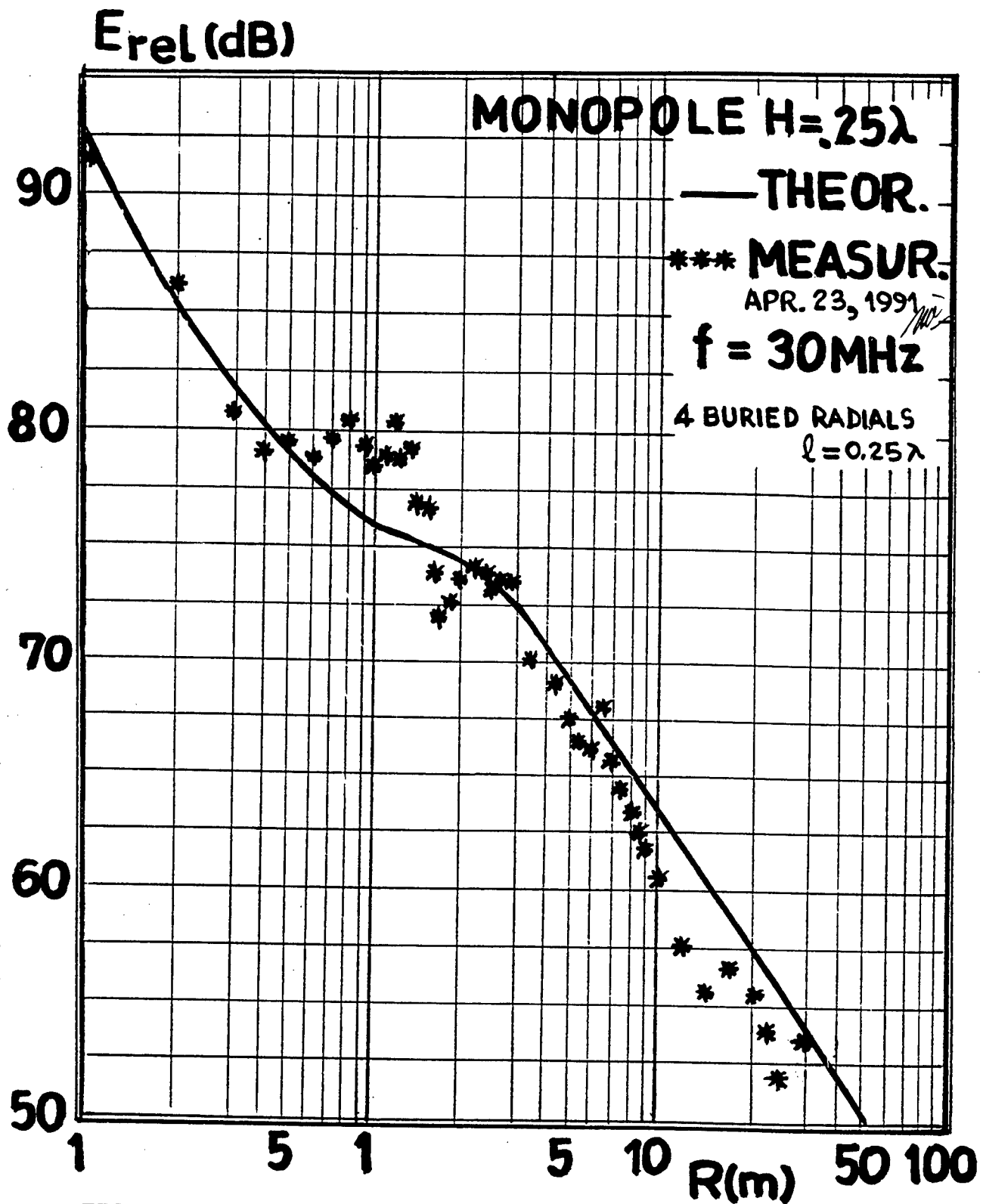
FIGURE 10a. MONOPOLE NEAR ELECTRIC FIELD.
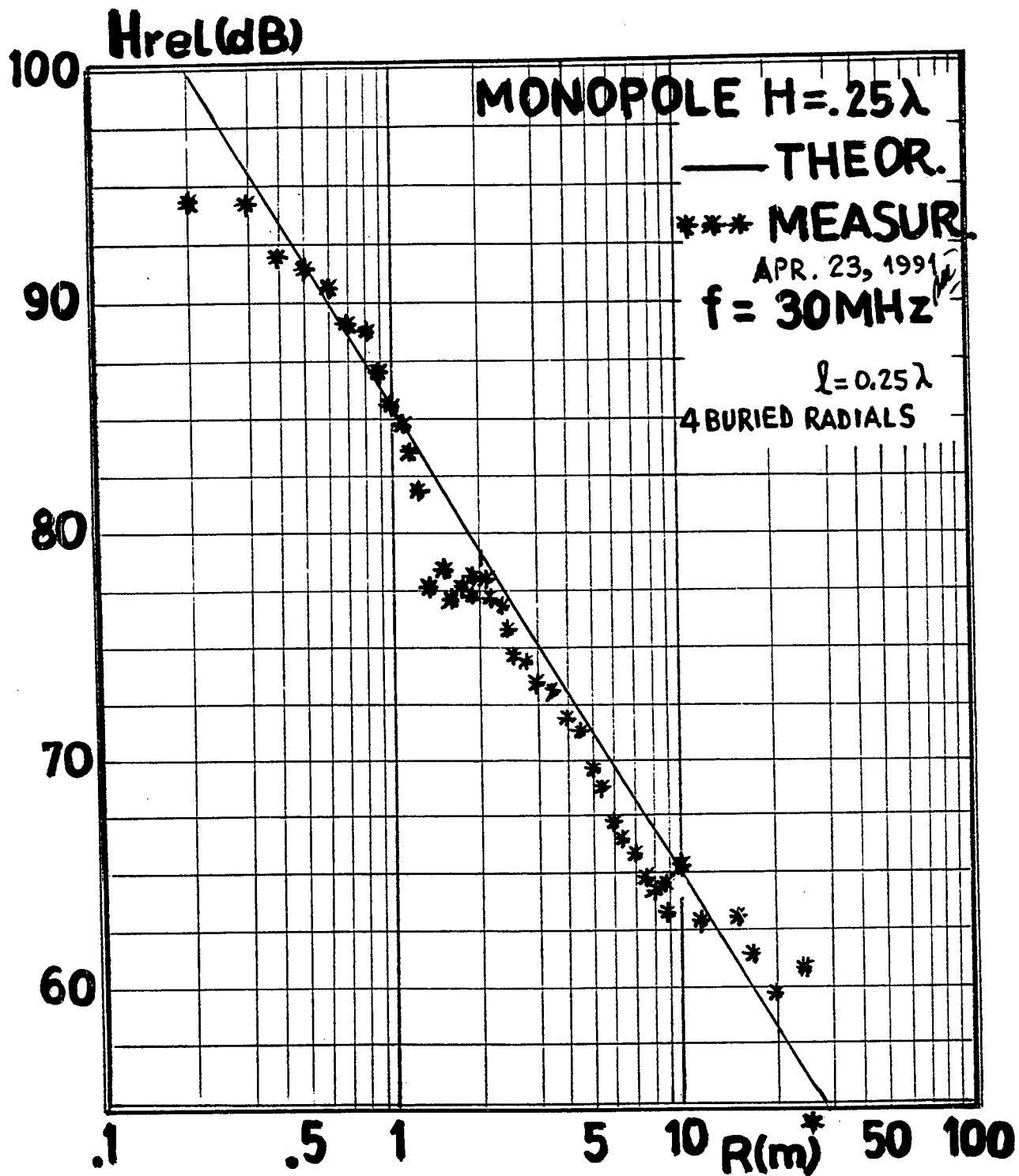
FIGURE 10b. MONOPOLE NEAR MAGNETIC FIELD.
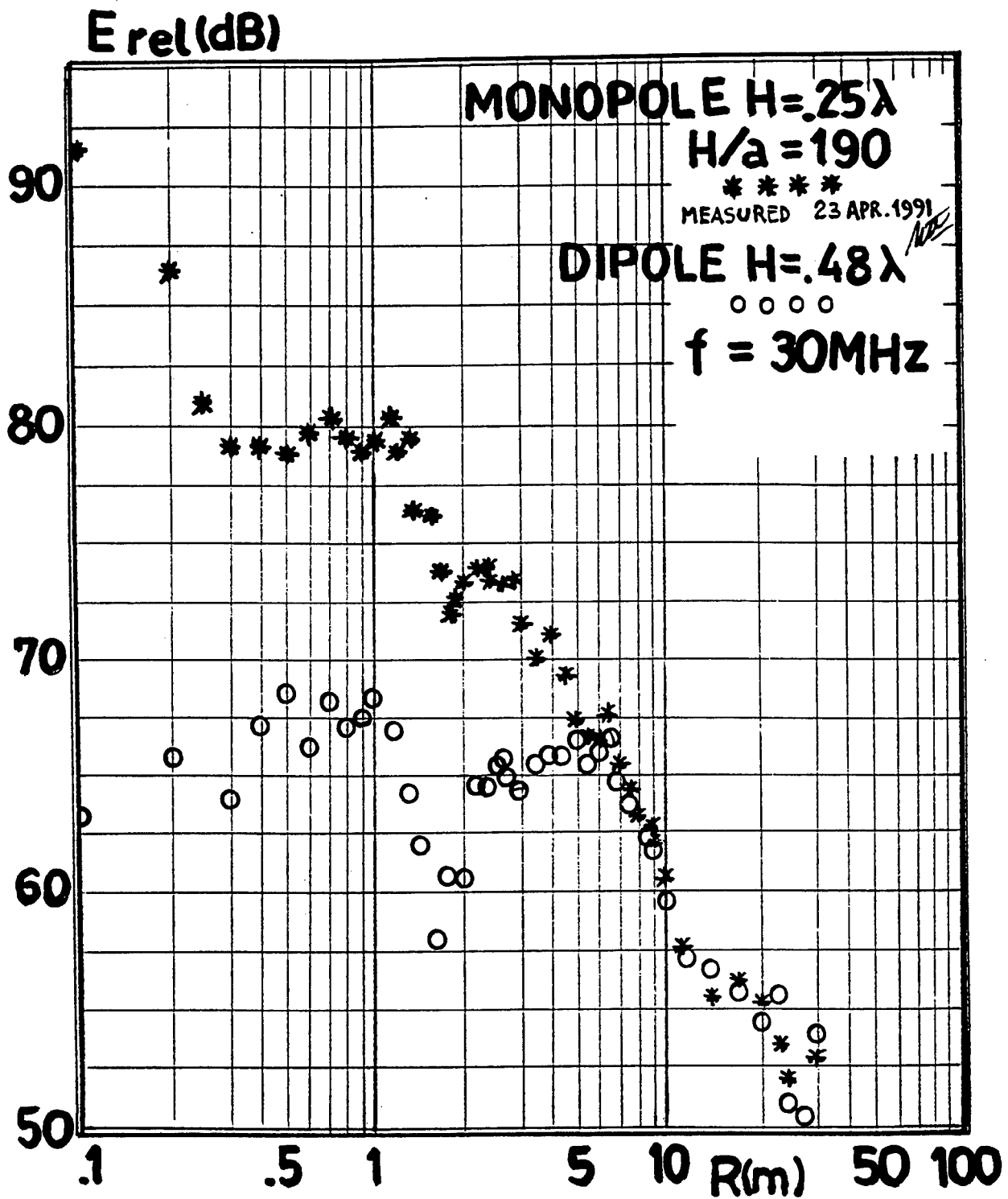
FIGURE 11a. MONOPOLE-DIPOLE MEASURED NEAR ELECTRIC

FIELD COMPARISON.
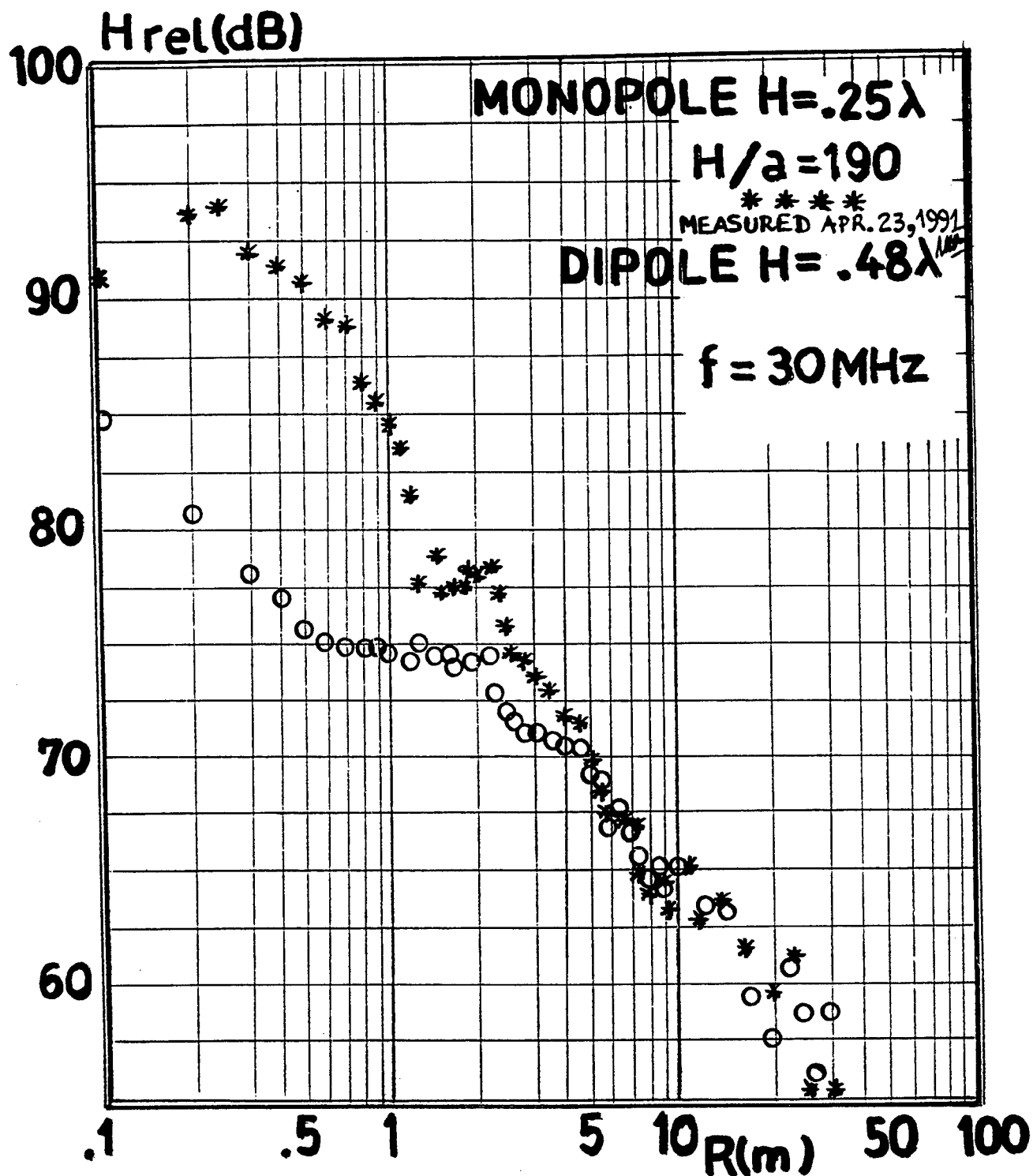
FIGURE 11b. MONOPOLE-DIPOLE MEASURED MAGNETIC

FIELD COMPARISON.
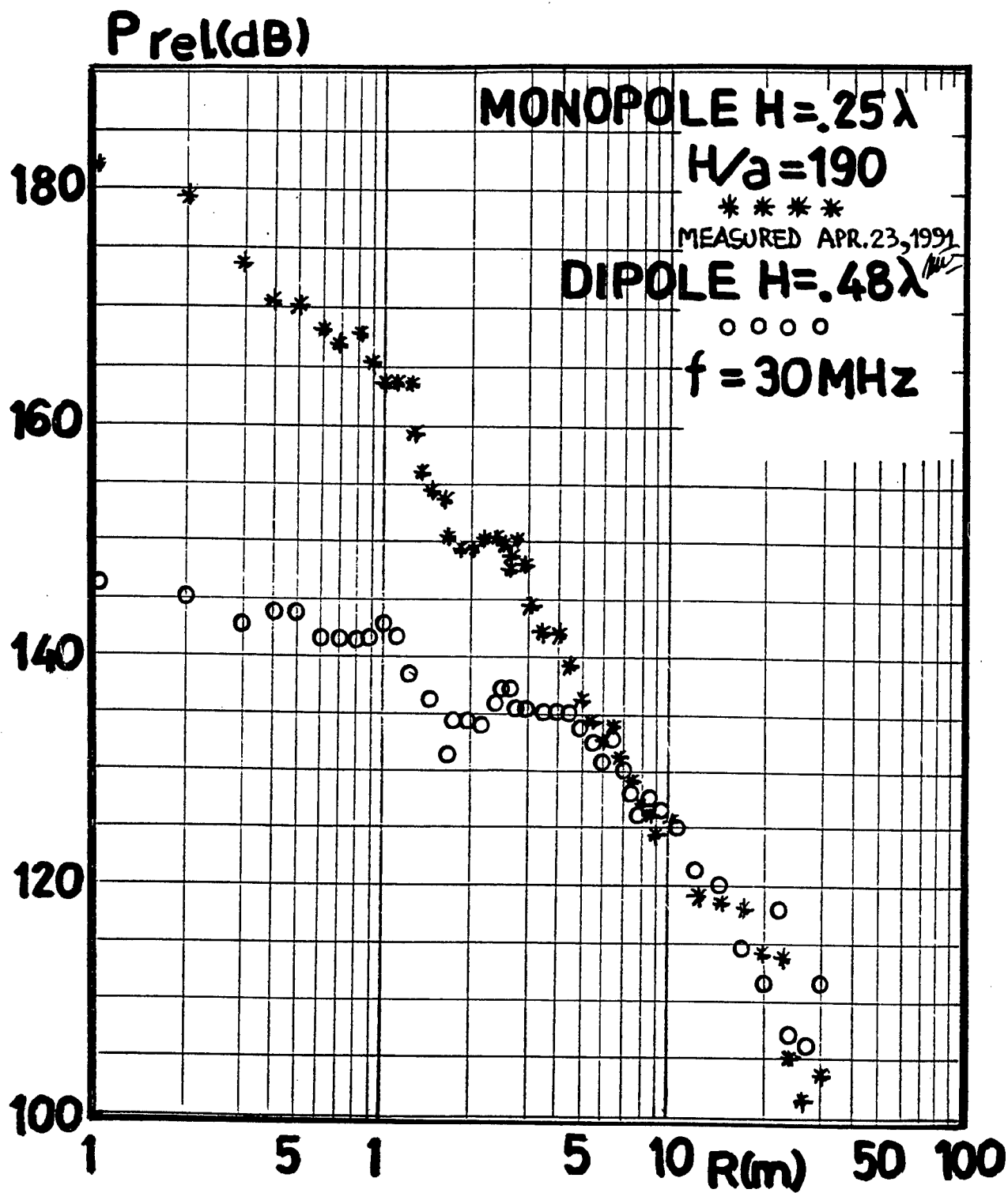
FIGURE 11c. MONOPOLE·DIPOLE MEASURED POWER DENSITY

COMPARISON.
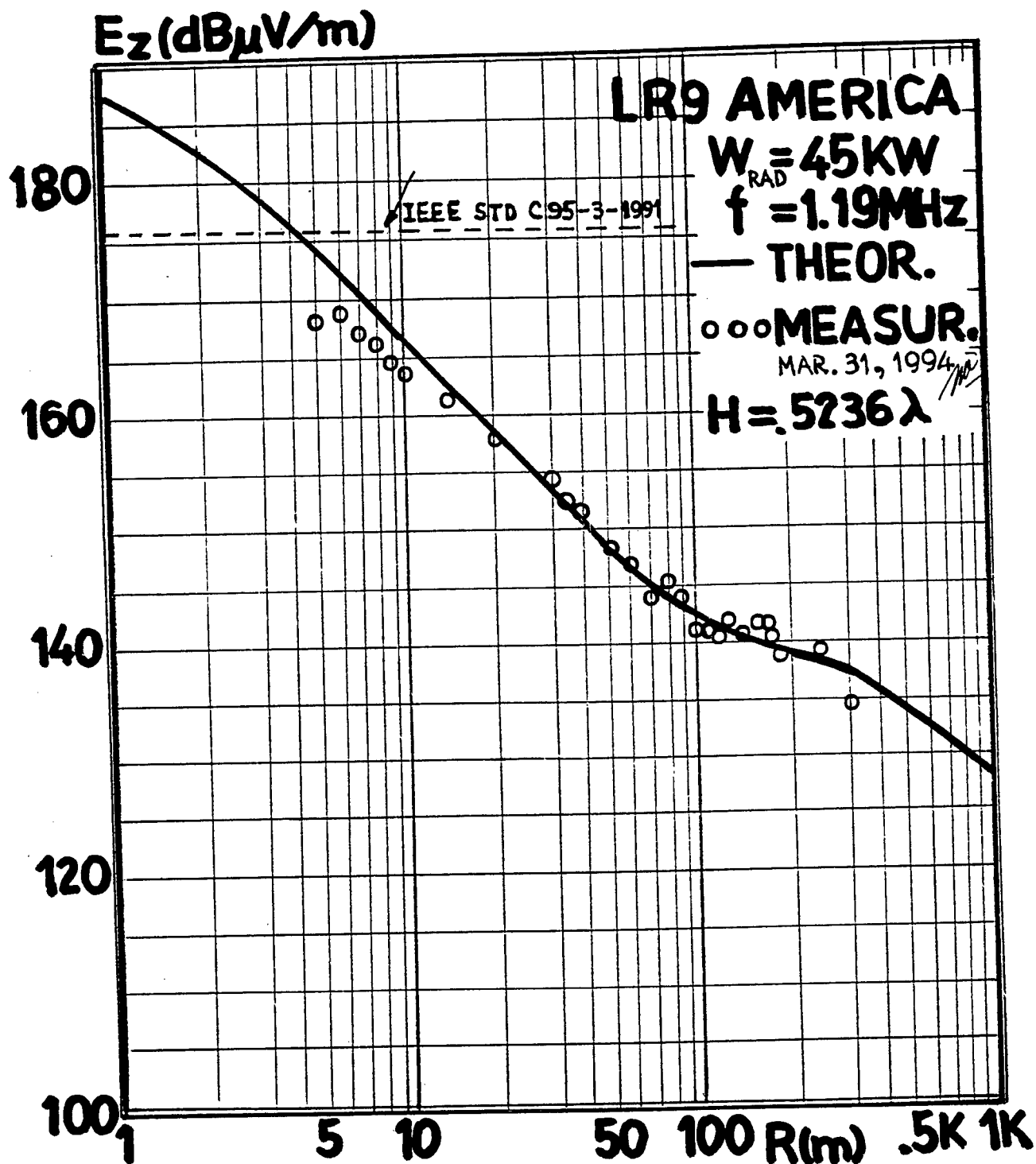
FIGURE 12a. MF AM MONOPOLE NEAR ELECTRIC FIELD

MEASUREMENT.
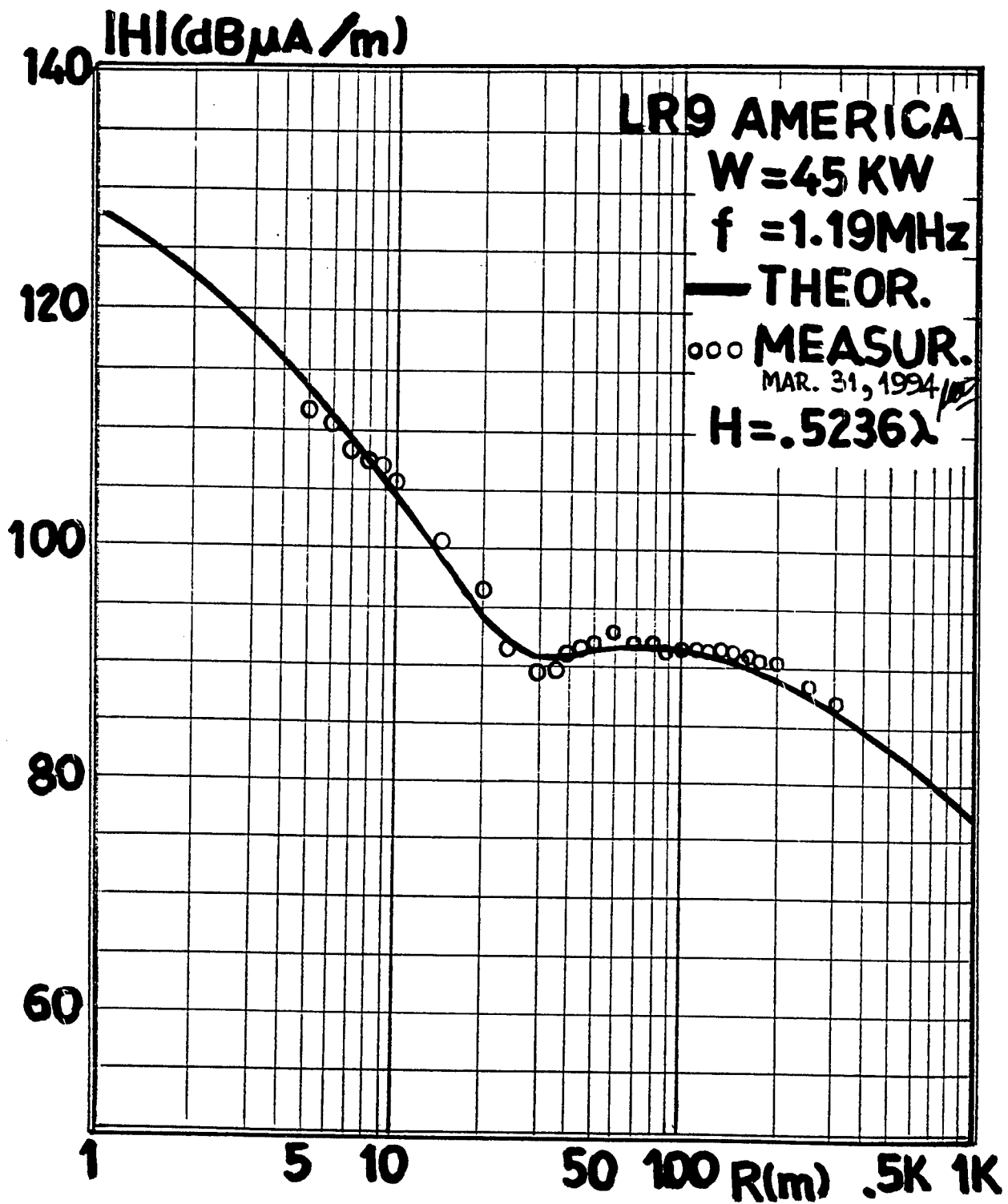
FIGURE 12b. MF AM MONOPOLE NEAR MAGNETIC FIELD

MEASUREMENT.
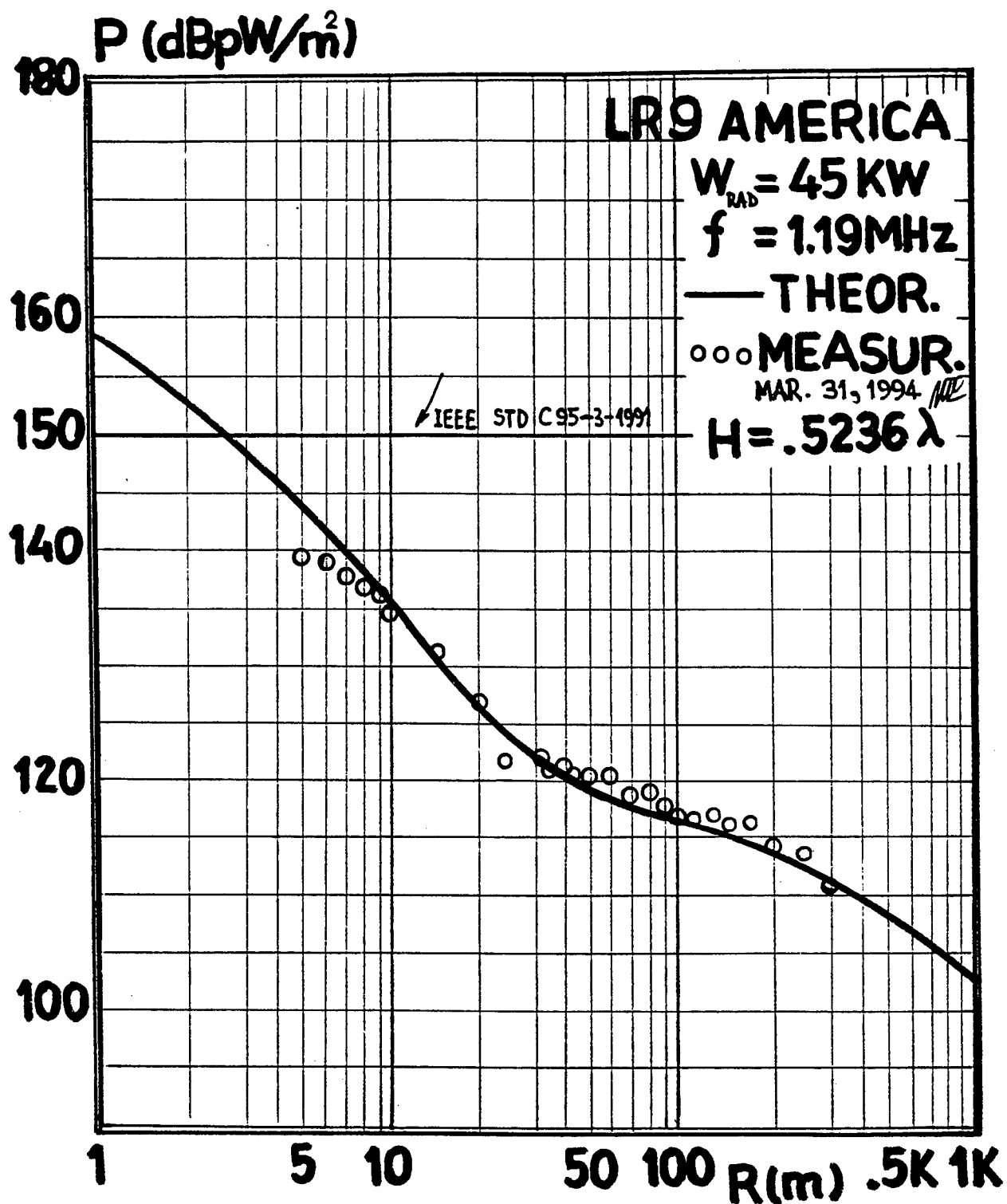
FIGURE 12c. MF AM MONOPOLE NEAR POWER DENSITY.
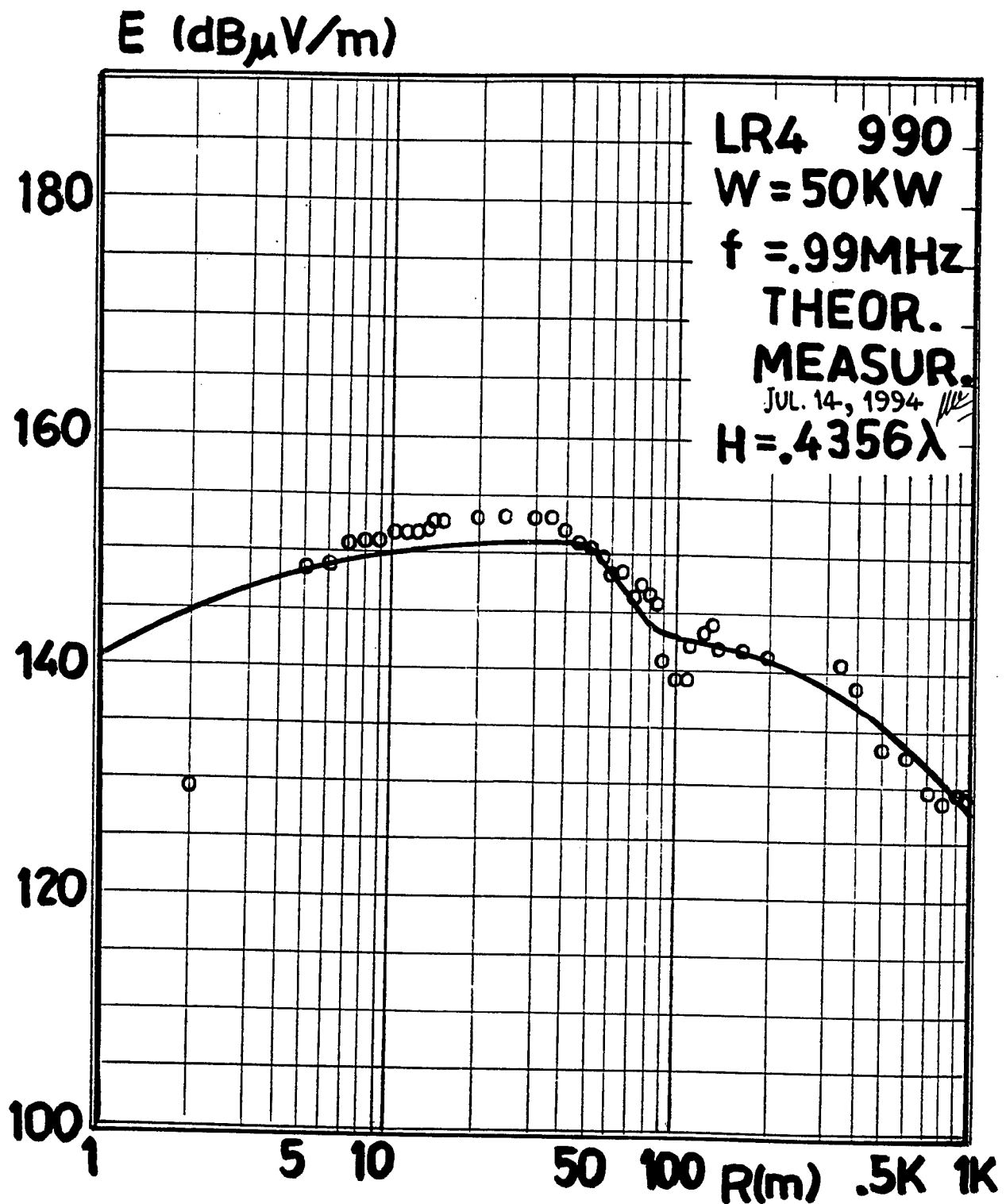
FIGURE 13a. MF AM VERTICAL DIPOLE NEAR ELECTRIC FIELD
COMPARISON.
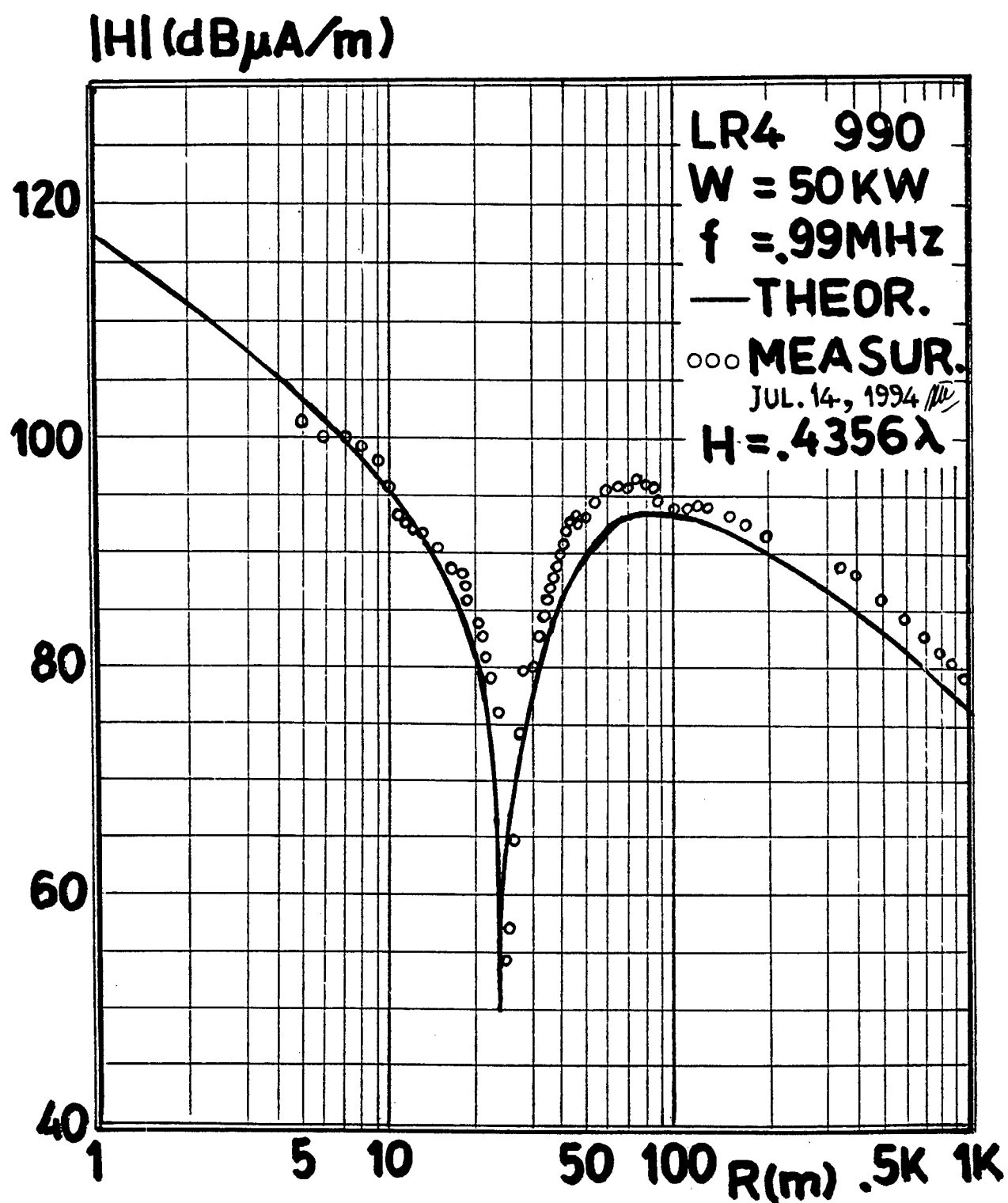
FIGURE 13b. MF AM VERTICAL DIPOLE NEAR MAGNETIC FIELD
COMPARISON.
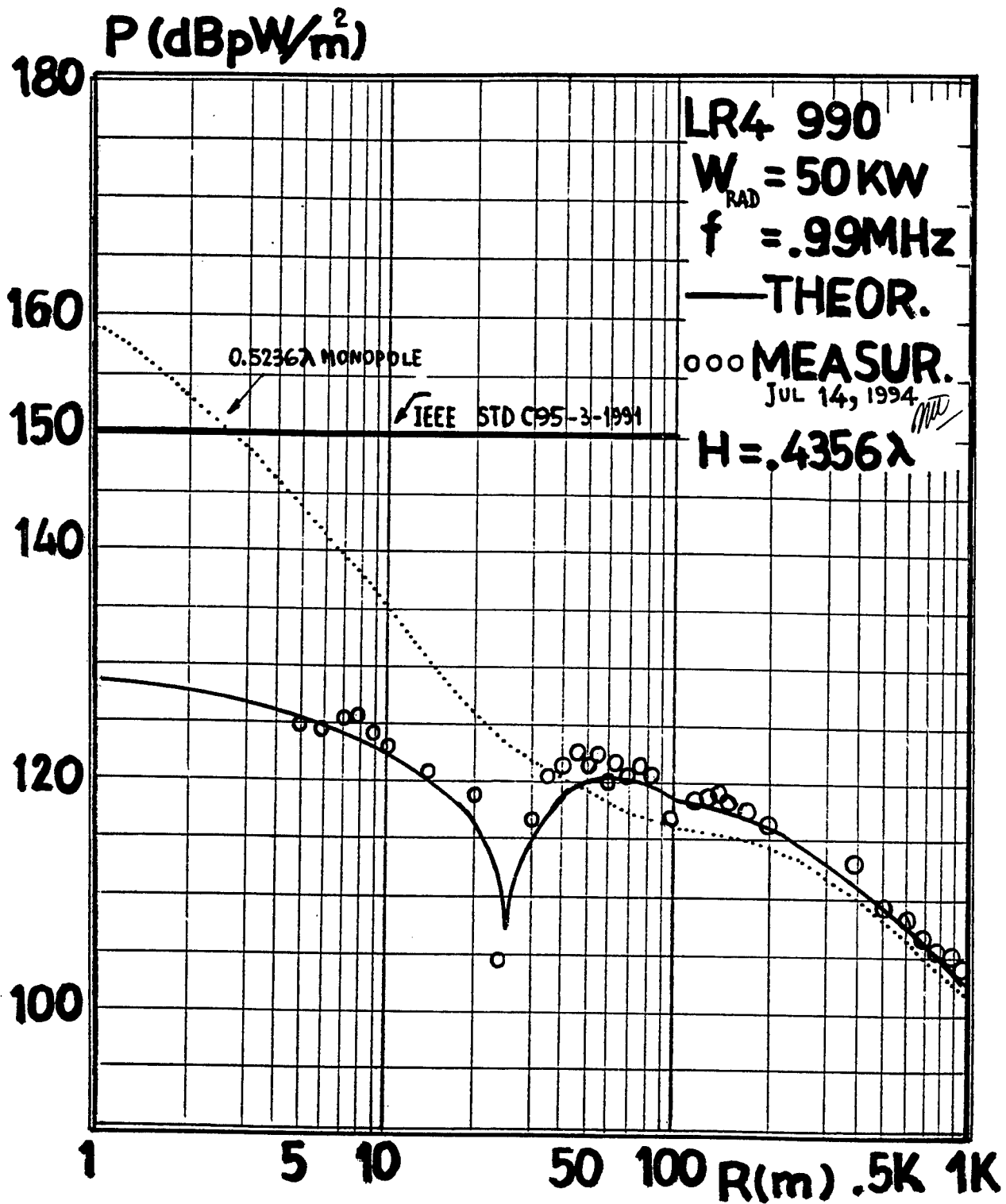
FIGURE 13c. MF AM VERTICAL DIPOLE NEAR POWER DENSITY
COMPARISON.
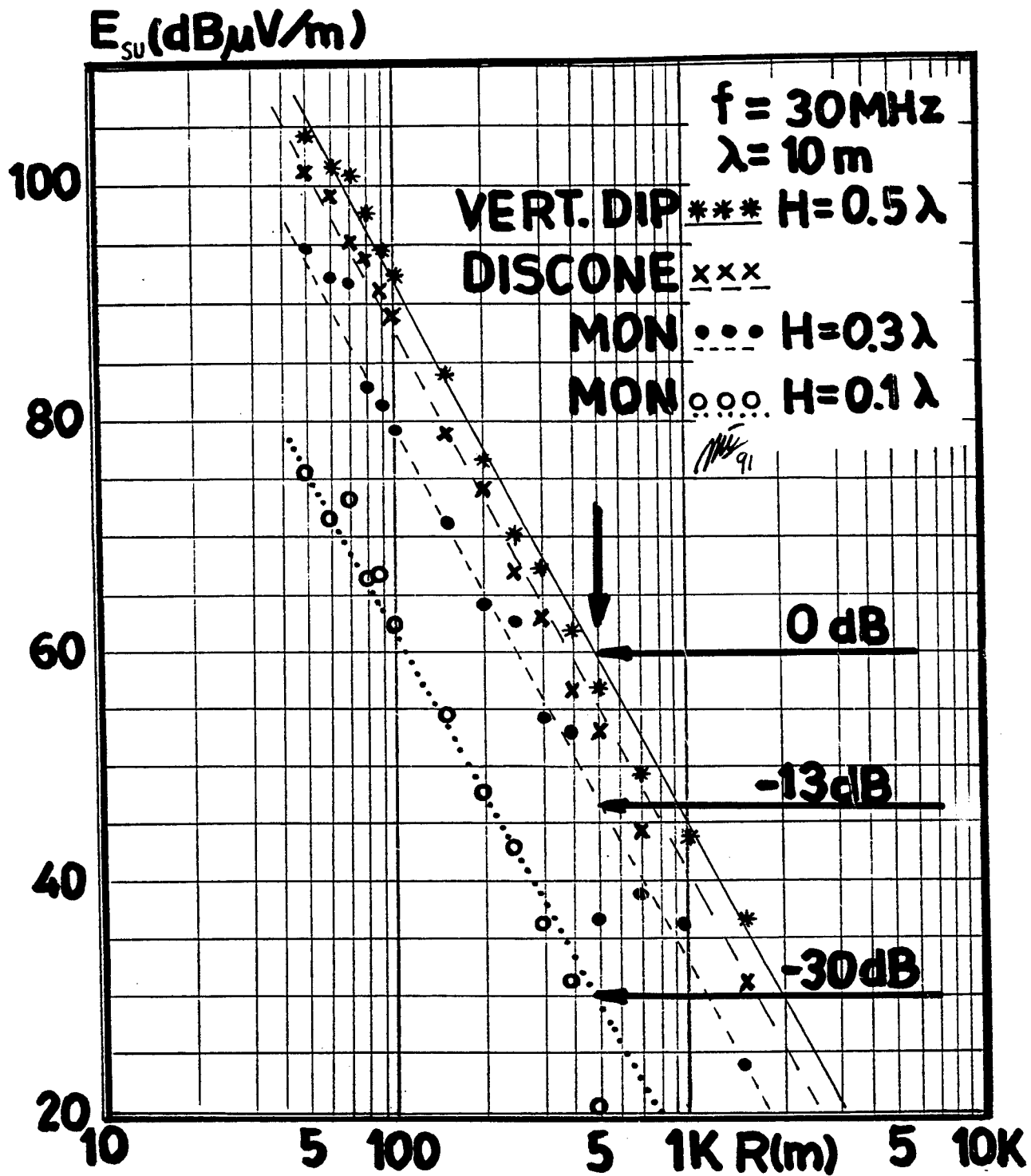
FIGURE 14. MONOPOLE-DIPOLE FAR FIELD SURFACE WAVE
MEASUREMENT COMPARISON.
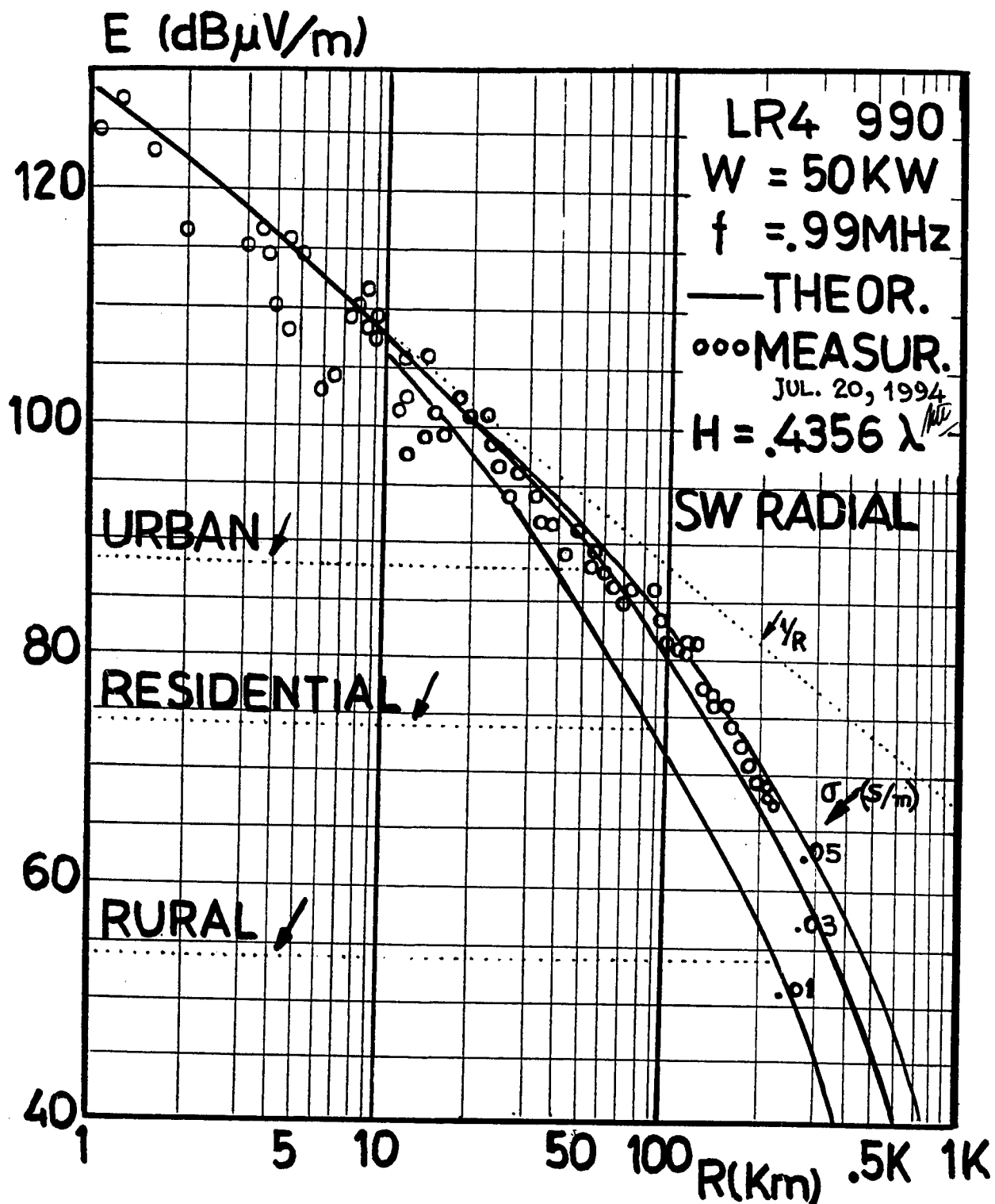
FIGURE 15. MF AM ASYMMETRIC VERTICAL DIPOLE FAR FIELD
MEASUREMENTS.

COST-EFFECTIVE PHASE SHIFTER CALIBRATION

TECHNIQUE FOR LARGE PHASED ARRAY ANTENNAS

Harold Shnitkin
Northrop Grumman Norden Systems
Box 5300
Norwalk, CT 06856

Abstract: Since the cost of a phased array antenna depends to a large extent upon the cost of the individual phase shifter, present-day cost concerns demand a closer look at possible cost reduction. A phase shifter cost break-down reveals that phase shifter calibration cost is a major contributor. This paper describes a technique for phase shifter calibration to be applied **_after_** assembly of the total antenna, which is intended to replace the costly individual phase shifter calibration. A discussion of the measurement errors arising out of the presence of several thousand "non-participating" phase shifters and how to minimize these errors follows. Also included are considerations for overcoming the phase/temperature dependence, test hardware description for injecting transmit and receive test signals, and test techniques supported by a mathematical model with a vector diagram. In addition, a computer program is described and phase shifter costs are estimated.

1. Introduction

Cost is one of the major draw-backs and concerns in the design and fabrication of an electronically scanned phased array antenna. Cost analysis has usually shown that the electronic phase shifter is the major cost contributor. This is especially true if electronic scanning is provided in both azimuth and elevation, where several thousand phase shifters

might be required. Thus a closer look at the major cost contributors is in order to ascertain methods of phase shifter cost reduction.

2. Phase Shifter Cost Problem

The costs of a phase shifter can be divided into those associated with (1) the phase shifting device, (2) the microwave assembly, (3) the driver, and (4) the calibration technique. Each of the above cost items must be attacked individually. By taking advantage of the fact that aperture phase errors generated by phase shifters are uncorrelated, an attempt must be made to generate the widest phase tolerance consistent with antenna pattern and sidelobe requirements. This results in lower cost because of the resulting wider manufacturing and test tolerances. By avoiding individual component-type phase shifters, with one RF connectors at each end, and instead manufacturing phase shifter assemblies, which can be "dropped-into" multi-element microwave feed waveguides, considerable fabrication and assembly cost can be saved. In addition, the use of a monolithic driver configuration can greatly reduce the production cost of arrays with many phase shifters.

assembly. This measurement is best performed by causing a flat RF phase front to impinge normally upon the assembled aperture and attaching a test receiver to the input port of the antenna's corporate feed. Under special circumstances this test can also be performed by injecting an RF signal into a BIT input port, if available. This has the advantage of performing tests in the laboratory instead of on the antenna range, which leads to more accurate control of the antenna's temperature and allows convenient measurements of both simulated transmit and receive conditions.

The test set-up, as illustrated in Figure 1, requires a fixed reference signal path, a signal generator, an RF receiver, and an RF transfer switch to allow either S_{21} or S_{12} measurements. Both, the signal generator and the receiver, may be combined in one network analyzer.

Since the above measurement represents the transfer phase characteristic of the entire array, data processing of the measured data is required to provide "de-embedding" for the purpose of obtaining the phase characteristics of every individual phase shifter. This is described in the next section.

Finally, simplification of the phase calibration technique must be investigated, since this effort usually consumes about 25% of the cost of each phase shifter. Both the time and the cost of testing can be reduced by (1) avoiding time-consuming temperature cycling during calibration by calibrating only at ambient temperature, and (2) avoiding individual phase shifter calibration on the test bench and replacing it by a group-test after partial or final array assembly. The former approach requires reasonable control over the reproducibility of the phase shift generating material, e.g., the ferrite, and the selection of a material whose temperature effects are both, predictable and repeatable from unit to unit. This would allow sufficiently precise prediction of the phase changes for generating an accurate Linearization Table at other than the calibration temperature. After the above mentioned recommendations have been followed, the below described group-phase calibration *after* antenna assembly should be applied to achieve the lowest possible phase shifter testing cost.

3. Phase Shifter Calibration Method

Phase shifter calibration requires a voltage transfer or S_{21} measurement of every phase shifter for every possible command value while "embedded" with all the other phase shifters of the antenna
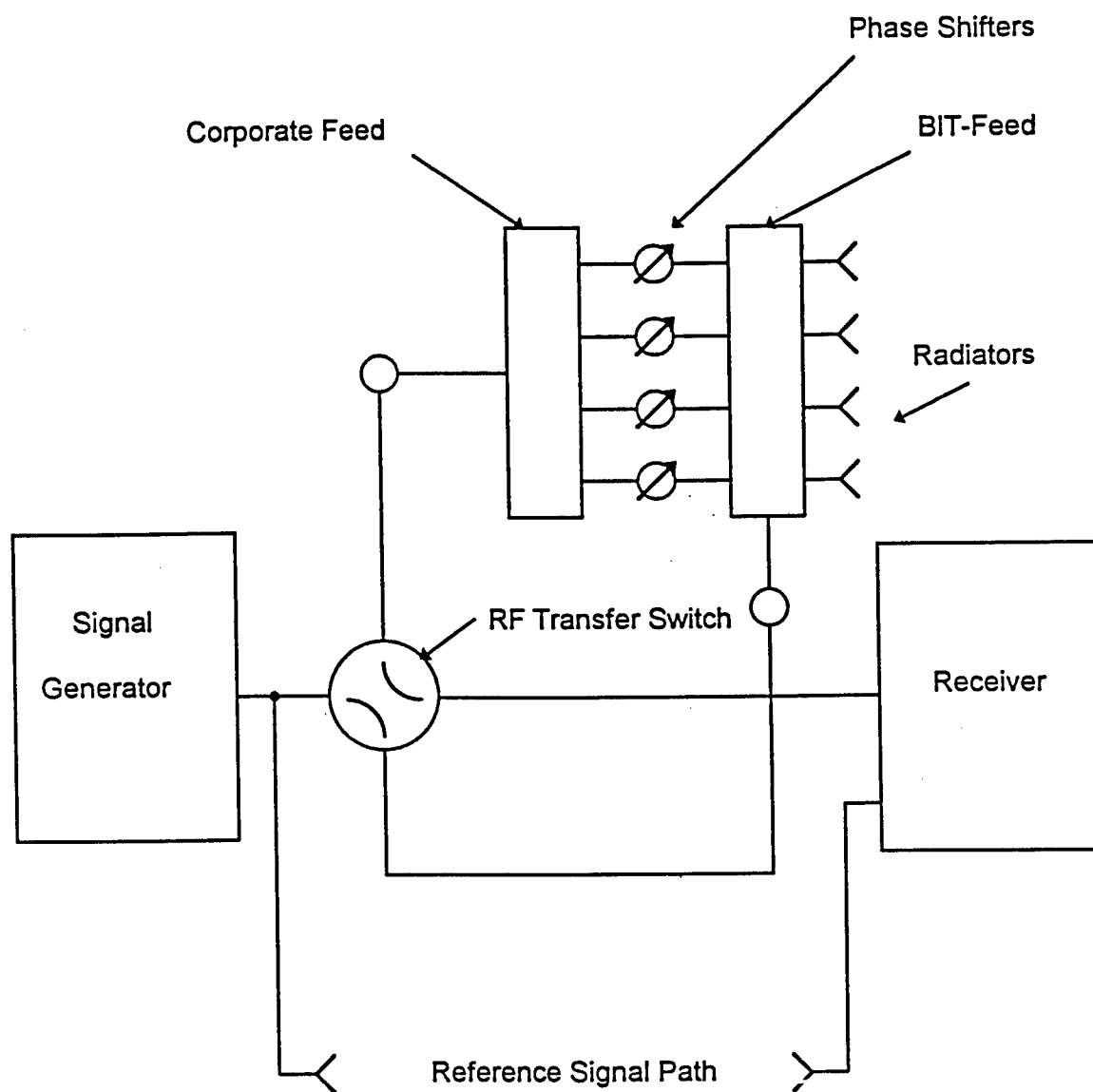
Figure 1. **Measurement Block Diagram**

4. De-embedding Process

For better understanding of the de-embedding process a vector diagram of measured S_{21} is shown in Figure 2. The various vectors are explained below :

CMD	Coord.
0	X_1, Y_1
n-1	X_n, Y_n
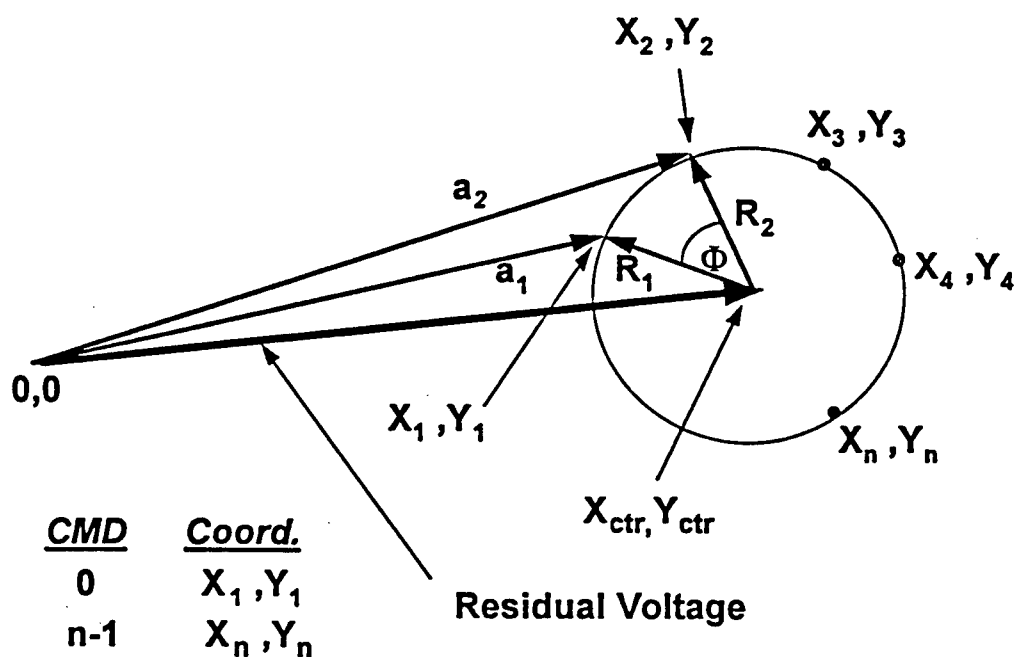
Figure 2. Vector Diagram of Measured S_{21}

a_n = Total measured S_{21} vector

n = Phase shifter command value

R_n = Portion of the total S_{21} contributed by the signal flowing through phase shifter under test

Residual Voltage = Portion of total S_{21} contributed by the signal flowing through all the <u>remaining</u> phase shifters

X_{ctr} = X-coordinate of the center of the circle generated by the <u>rotating</u> , that is phase shifted, vector R_n

Y_{ctr} = Y-coordinate of the center of the circle generated by the <u>rotating</u> , that is phase shifted, vector R_n

Φ = Differential phase shift after de-embedding

The de-embedding process starts with a set of "embedded" phase data, a_n, measured for every possible command value, usually a binary number between 16 and 256. This data is first converted to Cartesian coordinates of X_n and Y_n . Next the phase center coordinates, X_{ctr} and Y_{ctr}, are found by substituting the coordinates of three measured points (X_n and Y_n), displaced by approximately 120 degrees around the rotating vector circle, into the general equation for a circle. The three resulting simultaneous equations are then solved for X_{ctr} and Y_{ctr} This process is first carried out starting with command #1 and is then

repeated for one-third of all available adjacent commands. This entire set of computed X_{ctr} and Y_{ctr} values is subsequently averaged to achieve maximum precision. Finally, insertion phase delay values (IPD_n) for all commands are obtained via equation [1].

$$IPD_n = \arctan [(Y_n - Y_{ctr}) / (X_n - X_{ctr})] \tag{1}$$

5. Creating the Linearization Table

The linearization table is essentially a map of the required digital phase shifter commands for a given number of equally spaced phase settings , m , between zero and 360 degrees. The values of these commands, corresponding to the closest available phase setting compared to each of the required m phase values, are recorded in m addresses.

6. Measurement Errors

In addition to the commonly encountered measurement errors introduced by the test configuration, such as deformation, thermal expansion, VSWR and receiver noise, the effect of the signal contribution

of the residual voltage due to the non-participating phase shifters must be included. Since measurement precision is proportional to total signal level, minimizing this residual voltage will reduce measurement errors. Several techniques for minimizing the total signal level to improve the accuracy of the de-embedding process will be described.

Randomizing the phase shifter commands can help reduce the residual voltage. If this randomization is performed non-coherently a number of times while monitoring the receiver output signal level, a random command set which minimizes the residual voltage can be selected.

The precision of de-embedding can also be improved by measuring phase data K times, with all unwanted phase shifters off-set by 360 x N / K degrees, where N assumes all integral values from 1 to K. These K complex voltage measurements are then added vectorially and subsequently divided by K to obtain a more accurate de-embedded value.

Finally, the preferred technique calls for one set of less accurate phase measurements followed by a second calibration, which uses the

calibration data from the first set to command one-half of all phase shifters to 0° phase and the remaining half to 180°. This will limit the total measured voltage to two times the magnitude of vector R_n.

Confirmation of measurement accuracy is obtained by applying the created Linearization Table to set all phase shifters of the array to 0°, measuring an electronically scanned antenna pattern, and then comparing its sidelobes to those obtained from an antenna pattern computation.

7. Phase / Temperature Dependence

To save the cost of multi-temperature phase calibration all RF calibration tests are performed *only* at ambient temperature. Unfortunately, changes in temperature cause significant phase deviations, due to thermal expansion and material non-linearity (e.g. ferrites). At non-ambient temperatures, the phase calibration tables (also known as "Linearization Tables") must therefore be modified to reflect these deviations. This requires the ability to accurately predict phase/temperature effects. Consequently, the range of suitable phase

1.3 De-embedding Computation

   1.3.1 Finding the center coordinates of the spinning vector

      1.3.1.2 Select three widely separated S_{21} data points (X_n, Y_n)

      1.3.1.3 Find the equation of the circle passing through these

               three points

      1.3.1.4 Find the center coordinates of that circle

      1.3.1.5 Repeat this process for 1/3 the data points

      1.3.1.6 Average all computed center coordinates

   1.3.2 Compute de-embedded S_{21} or *IPD,* using equation [1]

   1.3.3 Assemble the "De-embedded S_{21} vs. Command" table

2.0 Linearization Table Calculation Section

   2.1 For table fineness select the number of table addresses per

        $360°$, *m*   (binary preferred !)

   2.2 Compute the *m* required quantized phase settings

   2.3 Using the table of step 1.3.3, find those command values,

        which most accurately produce the required phase settings

        derived in step 2.2

   2.4 Assemble the " Linearization Table " of *m* commands (from

        step 2.3) in *m* addresses representing *m* quantized phase

        settings (from step 2.2)

shifter materials is limited to those possessing predictable RF phase-vs.-temperature characteristics.

8. Computer Program

The computer program to perform the entire phase shifter calibration process is organized as follows :

1.0   Phase Measurement Section

    1.1   Initializing phase commands by   **either**

        1.1.1   Selecting a random set of commands yielding the

            lowest residual voltage   **or**

        1.1.2   Commanding one-half of the phase shifters to $0°$ and

            the other half to $180°$ by means of a previously

            obtained Linearization Table

    1.2   Spinning of One Phase Shifter

        1.2.1   Sequentially command one phase shifter at a time

            to each possible phase command value

        1.2.2   Perform RF receiver measurements of S_{21} for every

            command value

9. Estimated Phase Shifter Cost

By employing the techniques described, the cost of manufacturing and assembling phase shifters into a corporate feed structure has been considerably reduced. For one phase shifter that cost has been estimated to be $200 for the microwave circuit and $100 for the monolithic digital driver, in production quantities of 20,000. After adding another $50 for each phase shifter to cover calibration testing after assembly, the combined single phase shifter cost becomes $350. This figure compares favorably to the customary cost of several thousand dollars for one individually flanged and calibrated unit.

10. Conclusion

By physically integrating a large set of phase shifters into the antenna's signal distribution feed, by using monolithic drivers, and by calibrating all phase shifters *only* at ambient temperature and *only after* assembly instead of individually, the effective cost of the phase shifters for a large electronically scanned antenna array can be greatly reduced.

ANTIMULTIPATH SYSTEM MEASUREMENT OF
ULTRALOW SIDELOBE LEVEL ANTENNA PATTERNS

Andrew E. Zeger, Burton S. Abrams and Daniel S. Abrams

Zeger-Abrams Incorporated
29 E. Glenside Ave., Ste. #4
Glenside, PA 19038-4669
(215) 576-5566

ABSTRACT

The development of a real time electronic system to accurately measure the pattern of high gain, ultralow sidelobe level antennas in the presence of multipath scatterers is described. Antenna test ranges and anechoic chambers contain objects that scatter the signal from the transmitting antenna into the main beam of a receiving antenna under test (AUT), thereby creating a multipath channel. Large measurement errors of low sidelobes can result. The fabrication of a feasibility demonstration model Antimultipath System (AMPS) is complete. This AMPS uses a 10 MHz wide phase-shift-keyed spread spectrum modulated signal to illuminate the rotating AUT to *tag* each multipath by its delay. The novel receive section of the AMPS sorts out each multipath component by its delay and adaptively synthesizes a composite cancellation waveform (using delay, amplitude, and phase estimates of the scattered components) which is subtracted from the total signal received by the AUT. After subtraction the resultant is the desired direct path signal which produces the free space pattern of the AUT. Laboratory and antenna range test results are presented and show the promise of measuring sidelobe levels 60 dB below the main beam.

1.0 INTRODUCTION

The subject of this paper is a new system for resolving the components of multipath propagation and for suppressing those effects of the multipath that

degrade the accuracy of measurements made on antenna test ranges. This novel system operates in real time to resolve the multipath components on the basis of their different time delays using a spread spectrum test signal and adaptive interference cancellation [1]. Concurrently with resolving the multipath components, the system also develops in real time accurate estimates of the time delay, amplitude, and phase of each multipath component. The antenna gain pattern measurement is provided by the system's estimate of the amplitude of that path with the shortest time delay.

The problems of multipath distortion of patterns taken on outdoor antenna ranges are difficult to solve. Unlike distortion induced by noise and external [2] interference, increasing the transmit power level does not help overcome the degradation of the antenna measurements caused by multipath. Previous solutions include awkwardly pointing the AUT's main beam skyward (free of scatterers) when measuring low sidelobes.

The system described here uses a 10 MHz wide binary phase-shift-keyed, spread spectrum modulated signal [3] to illuminate the AUT in order to tag each multipath by its delay. The novel receive section of the AMPS sorts out each multipath component by its

delay and adaptively synthesizes a composite
cancellation waveform (using delay, amplitude, and
phase estimates of the scattered components) which is
then subtracted from the total signal received by the
AUT [4]. After subtraction the resultant is the
desired direct path signal which produces the free
space pattern of the AUT.

2.0 THE MULTIPATH PROBLEM

Generally, antenna range sidelobe measurements are
concerned with the received amplitude at the AUT of a
transmitted CW test signal as a function of frequency
and of the antenna's orientation. Traditionally these
measurements are made at a single frequency at a time,
or equivalently, using a very slow frequency sweep.
The antenna range is carefully set up with the
objective of ensuring that the propagating test signal
has only one significantly strong propagation path
(direction) to the antenna under test.

In most antenna test ranges and anechoic chambers,
even with the painstaking use of absorbers, there are
multiple undesired signal reflectors at various
locations causing multipath propagation that violates
this objective to some extent. In some cases, the

violation may be severe, usually where the true amplitude is relatively weak. One case of interest is the measurement of the pattern of a highly directional antenna which is expected to have a sidelobe level (SLL) as low as -60 dB (relative to the main beam peak). That measurement may be obscured by multipath propagation when the antenna's main beam happens to be pointed toward multipath reflectors. The measurement accuracy goals are ±1 dB on the SLL.

We present below simulated antenna patterns that would be measured on a range containing multipath (MP) caused by a discrete scatterer to visualize the effect of different strength scatterers upon the patterns and to estimate how much suppression of the MP components is required. In Figure 1 we illustrate the ideal (no MP) pattern of an 18λ long antenna having a $\cos^2$ amplitude taper. The ordinate is the power pattern (in dB) and the abscissa is u = sin θ, where θ = 0 is at broadside. The SLL peaks decrease monotonically as $|\theta|$ increases away from the main beam to a low of -85 dB at the edge of visible space ($|u|$ = 1). Figure 2 illustrates the pattern of the same antenna measured on a simulated range having a MP component incident at θ = 32° with a strength of -40 dB relative to the

direct (desired) component arriving from $\theta = 0^{\circ}$. The small vertical arrow locates the arrival angle of the MP at $u = 0.53 = \sin 32^{\circ}$ where the SLL = -64 dB. The degradation to the pattern due to this multipath can be seen by comparing the SLL at $u = 0.53$ with the unperturbed SLL at $u = -0.53$. If the -40 dB MP component were to be suppressed by 20 dB, this would be equivalent to MP 60 dB below the main beam. Figure 3 illustrates the simulation of the pattern measurement in this situation. The effect of the -60 dB MP on the pattern is clearly less severe (Figure 3) than the -40 dB MP illustrated in Figure 2. If the -40 dB MP component were to be suppressed by 40 dB, then the effective MP strength is reduced to -80 dB relative to the main beam. Figure 4 illustrates the pattern that would be measured with a -80 dB MP component at $\theta = 32^{\circ}$. In this case the distortion (about ±1 dB) to the -64 dB SLL is barely noticeable.

The illustrations in Figures 2 through 4 show the pattern measurement corruption caused by a few particular multipath scenarios. The actual multipath scenario encountered when rotating the receiving antenna to measure its pattern is continually changing as the antenna is rotated. The reason for this

behavior may be visualized from the plan and view and elevation profile of a typical antenna test range, shown in Figures 5a and 5b. Both the Tx antenna and the Rx antenna are directional. The region where there are significant multipath reflectors is the intersecting region of the main beams of the two antennas. As the Rx antenna is rotated, this region moves, so that some multipath reflections shrink while others grow to significance.

We now visualize the effect of the multipath simulated in Figures 1 through 4 on an antenna of the same extent (18λ) but whose SLL falls off less rapidly. With a triangular taper, the SLL peaks roll off monotonically to 70 dB (below the main beam) at $|u| = 1$ ($\pm 90^\circ$). Figure 6 illustrates the pattern in the absence of MP. Figures 7, 8, and 9 show the effect of MP at -40 dB, -60 dB, and -80 dB and correspond to the cases previously illustrated in Figures 2, 3, and 4, respectively. In Figure 9, we note that the -80 dB MP perturbs the local SLL peak (approximately -50 dB) by less than 1 dB.

3.0 THEORY OF OPERATION

Consider a model of a finite discrete multipath medium through which a known binary phase shift keyed (BPSK)-modulated test signal is passed, as shown in Figure 10. BPSK modulation m(t) by a known pseudorandom ±1 sequence of binary code "chips" (a term adopted from spread spectrum communications) is imparted on the transmit test signal. In this model the BPSK-modulated signal S(t) having carrier frequency ω_c and phase ϕ passes through a multiplicity of parallel paths, the iTH of which imparts its own delay τ_i, amplitude A_i, and phase shift ϕ_i to the signal flowing through it. Now consider the multipath emulator shown in Figure 11, in which the BPSK ±1 modulating waveform m(t) progresses through the same number of parallel paths, the iTH of which imparts its own delay λ_i, followed by BPSK modulation onto the carrier at ω_c, and then amplitude scaling by a_i and phase shifting by θ_i . It can be shown that iff for all i = 1, ..., N; $\lambda_i = \tau_i$, $a_i = A_i$, and $\theta_i = \phi + \phi_i - \omega_c \tau_i$ modulo 2π, then the multipath emulator produces at all times exactly the same composite waveform as the actual multipath model. If we adaptively adjust the $3N\{\lambda, a, \theta\}$ parameters of the multipath emulator to cause its

output to be exactly the same as the signal emanating from the multipath propagation medium, then we can read these parameters from the emulator to give an analysis of the multipath propagation parameters.

We generate the sequence m(t) from a shift register with a maximal length feedback configuration [5]. The local timing (i.e., delay) of such a PRN sequence generator can be continuously adjusted by advancing or retarding the oscillator frequency used to clock the shift register. A tracking pseudorandom noise (PRN) sequence generator is made by incorporating in a feedback loop a timing error detector which is then used to adjust the local clock frequency, as is done in spread spectrum communications and GPS navigation receivers [6].

The amplitude and phase adjustment for each path will be accomplished in a complex weight whose inphase (I) and quadrature (Q) components are adjusted in an LMS feedback control loop, as is done in adaptive cancellation and adaptive nulling array systems [7].

4.0 FUNCTIONAL DIAGRAMS

The embodiment of the AMPS is illustrated in the block diagrams of Figures 12 and 13, showing the ZA

Multipath Analyzer-Suppressor as fabricated at the 120 MHz IF. The system (Figure 13) consists of a bank of N parallel Multipath Estimator Modules (MEMs), each of which constructs a waveform estimate $\hat{S}_i$ of one multipath signal component S_i by estimating its unknown amplitude, carrier phase, and PRN sequence timing t_n. The waveform estimates are combined and subtracted from the input, which arrives from the multipath propagation medium, to form a composite error signal

$$\varepsilon(t) = \sum_i (S_i - \hat{S}_i).$$

The Adaptive Control System continuously updates the estimates of t_n, a_n and ϕ_n (for n=1, ..., N) with the goal of minimizing the mean square value of $|\varepsilon|$. All multipath signal components are adaptively canceled in ε to the degree allowed by the accuracy of their waveform estimates.

A top level block diagram of the AMPS is shown in Figure 12. At the transmitter a user supplied stable tunable RF oscillator is tuned to the center frequency of the test signal. The RF oscillator sinusoidal output is BPSK modulated by a pseudorandom noise sequence generator to produce a spread spectrum transmitted test signal with a 10 MHz chip rate.

The receive portion of the AMPS as depicted uses a coherent dual-channel receiver, as do many modern antenna measurement receivers. The antenna under test feeds one channel of that receiver, whose IF output is provided to the ZA Multipath Analyzer-Suppressor, which is the processing unit that suppresses the effects of multipath on the pattern measurement of the AUT. The second receiver channel is fed by a second colocated auxiliary antenna whose orientation is fixed to point at the test transmitting source. The IF downconversion product in the auxiliary antenna channel is used to synchronize two oscillators -- one digital code clock oscillator synchronized by a Tracking PRN Sequence Generator to the incoming PRN sequence. A sinusoidal oscillator is synchronized by a phase locked loop to the IF carrier using the PRN code sequence provided by the tracking PRN Generator. These two oscillator outputs are provided to the ZA Multipath Analyzer-Suppressor.

5.0 AMPS COMPUTER SIMULATION RESULTS

Zeger-Abrams Incorporated (ZA) has developed a FORTRAN computer program to simulate the AMPS operating with a general multipath scenario. We have used that

software on a 80386-based PC to show that the AMPS performs successfully under a wide variety of MP scenarios. Representative results were previously presented [4], for one to four discrete MPs. The simulations generally demonstrated superior MP suppression than a technique [8] that used an equally spaced tapped delay line MP emulator.

6.0 DEMONSTRATION MODEL

A feasibility demonstration model AMPS was developed to cover 0.5 to 18 GHz and is packaged in 19" rack mounted housings.

The dashed lines in Figure 12 denote the three physical units in which the AMPS is housed. The TX Unit is located at the transmit site and contains the BPSK modulator and PRN Sequence Generator. The RF/IF Unit contains the dual RF/IF front ends to convert the received RF signals from the fixed auxiliary antenna and the AUT to IF signals centered at 120 MHz. The IF AMPS Processor receives the AUT signal, the master clock, and the IF carrier from the RF/IF Unit, suppresses the unwanted multipath components, and sends signals to the associated (80X86) PC System for real time calculation of the pattern of the AUT.

A top level block diagram of the feasibility model
of the ZA Multipath Cancellation System that has been
assembled is given in Figure 13. It uses a PRN chip
rate of 10 Mchips/sec, corresponding to a BPSK chip
duration of 100 nanoseconds. The model was designed
with the goal to resolve and suppress MP having delays
as small as 5 nanoseconds. It contains five Multipath
Estimation Modules (MEMs).

A photograph of the receive site portion of the
feasibility demonstration model AMPS is shown in
Figure 14. With reference to the dashed lines in
Figure 12, the RF/IF Unit is 5 1/4" H x 14" D x 19" W.
The IF AMPS Processor housing is 12" H x 21" D x 19" W
and contains the MP estimator and suppression circuits,
presently populated with 5 MEMs. Each MEM is on a
single printed circuit card that is approximately
7" x 16". Prime power is 60 Hz, 110 VAC.

Laboratory and field tests of the AMPS show that
with a high input signal-to-noise ratio, discrete MP
components will be suppressed by 25 to 35 dB.

An operator interfaces with the AMPS through the
keyboard of a personal computer based on an Intel 80386
(or higher) microprocessor chip.

7.0 ANTENNA RANGE TEST RESULTS

Antenna range tests of the AMPS feasibility demonstration model were conducted July 10-12, 1996, at the USAF Rome Laboratory (RL) Irish Hill site near Newport, NY, under the auspices of RL personnel, John S. DeRosa and Carmen Luvera. The AUT was an 8' diameter parabolic dish which was illuminated at a center frequency of 1.5 GHz, λ = 20 cm (D = 12.2λ).

The natural range multipath (MP) was too weak to grossly distort measurement of the sidelobes of the AUT. In order to augment the natural MP, an active RF repeater was placed on the range. The active repeater consisted of a receive antenna (parabolic dish, diameter $\approx$ 3') pointed at the transmit site, an RF transmission line for delay, an RF amplifier (to boost the signal received by the repeater), and a transmit horn antenna pointed toward the AUT.

Elevation patterns of the AUT were recorded (Figure 15-18) with a 1.5 GHz CW test signal using a conventional RL antenna measurement instrument and with a 10 Mbps BPSK modulated test signal centered at 1.5 GHz using the AMPS. Both the conventional system and the AMPS were operated with the active repeater turned on (MP present) and turned off (MP absent). The

following table identifies the solid, dashed, and dotted curves (power patterns in dB vs. elevation angle in degrees) presented in Figures 15-18.

Antenna Pattern Generated With	Active MP Off	Active MP Turned On
Conventional System (CW)	Fig. 15, 16, 18 dotted curves	Fig. 15, 16, 18 solid curves
AMPS (10 Mbps BPSK)	Fig. 17 dotted curves	Fig. 16, 17, 18 dashed curves

The effect of a 60 nanosecond delayed multipath (MP) component on an antenna pattern recorded using a conventional system is illustrated in Figure 15 where the gross distortion is readily evident between -55° and -40°. With the active MP present (solid curve), the pattern sidelobe level (SLL) is increased by as much as 26 dB above the pattern taken without the active MP (dotted curve). The pattern generated by the AMPS with the active MP present is presented as the dashed curve in Figure 16 along with the solid and dotted curves of Figure 15 for comparison. The MP in the region from -55° to -40° has been canceled (by the AMPS) by 16 to 33 dB.

The pattern recorded using the AMPS with the active MP absent is shown as the dotted curve in

Figure 17. For comparison the AMPS pattern with active

MP present (dashed curve) from Figure 16 is reproduced

in Figure 17. It is evident that turning on the active

MP has a very small impact on the patterns recorded

using AMPS. The worst case appears to be a 3 dB

increase in one sidelobe around -43°.

Additional patterns were then taken with the power

in the active repeater reduced by 10 dB and the active

MP delay reduced from ≈ 60 ns to ≈ 40 ns. With the

active repeater MP turned on at the same location on

the antenna range, Figure 18 illustrates the patterns

recorded by the conventional system (solid curve) and

by AMPS (dashed curve). Again the pattern recorded by

the conventional system with the active MP off is

presented (dotted curve) in Figure 18 for comparison as

it was in Figures 15 and 16. The gross distortion (due

to this weaker active MP) on the conventional pattern

is still obvious on the solid curve in the -55° to -40°

region. The pattern generated by the AMPS again shows

its ability to suppress the effects of the active MP.

8.0   SUMMARY

An antimultipath system (AMPS) is described that

suppresses the deleterious effects of MP propagation on

the measurement of low sidelobe levels in patterns of a directional antenna. In particular, ultra-low sidelobe levels (e.g. -60 dB) of future directional antennas could be measured in the presence of test range or anechoic chamber MP whose received strength exceeds the desired component by as much as 30 dB, and whose propagation delay lags the desired component by as little as 20 nanoseconds, using a test waveform with bandwidth of 10 MHz.

Both laboratory and antenna range test results using a feasibility demonstration hardware model AMPS (Figure 14) have confirmed the performance obtained in earlier computer simulations [4]. Antenna range test results are presented that show the measurement of sidelobe levels > 50 dB below the main beam. These test data show that the AMPS suppresses the effects of the MP and produces a pattern of the AUT in the presence of MP that is the same to within a few dB of the conventional pattern of the AUT in the MP absent case.

REFERENCES

[1]   A.E. Zeger and B.S. Abrams, "Multiple Signal Receiver for Direct Sequence, Code Division Multiple Access Spread Spectrum Signals". U.S. Patent No. 5,099,493 dated Mar. 24, 1992. Assignee: Zeger-Abrams Inc.

[2]   R.L. Mitchell, "On the Reduction of Stray Signal Errors in Antenna Pattern Measurements", *IEEE Trans. on A&P*, vol. 43, June 1995, pp. 629-630

[3]   George L. Turin, "Introduction to Spread-Spectrum Antimultipath Techniques and Their Application to Urban Digital Radio," *Proc. IEEE*, March 1980, pp. 328-353.

[4]   A.E. Zeger and B.S. Abrams, "Pattern Measurement of Ultralow Sidelobe Level Antennas", *Proc. AMTA 17th Annual Meeting and Symposium*, Nov. 13-17, 1995, Williamsburg, VA, pp. 43-48.

[5]   W.W. Peterson and E.J. Weldon, *Error Correction Codes*, 2nd Ed., MIT Press, Cambridge, MA 1986.

[6]   P.K. Enge, R.M. Kalafus, and M.F. Ruane, "Differential Operation of the Global Positioning System," *IEEE Communications Magazine*, July 1988, pp. 48-60.

[7]   B. Widrow and S.D. Stearns, *Adaptive Signal Processing*, Prentice Hall,Inc., Englewood Cliffs, NJ 1985.

[8]   B. Himed, P.H. Stockmann, D.R. Miedaner, "Range
      Multipath Cancellation Through Signal Processing,"
      Command, Control, Communications, and Intelligence
      (C^3I) Technology and Applications Conference
      Proceedings, IEEE Mohawk Valley Section,
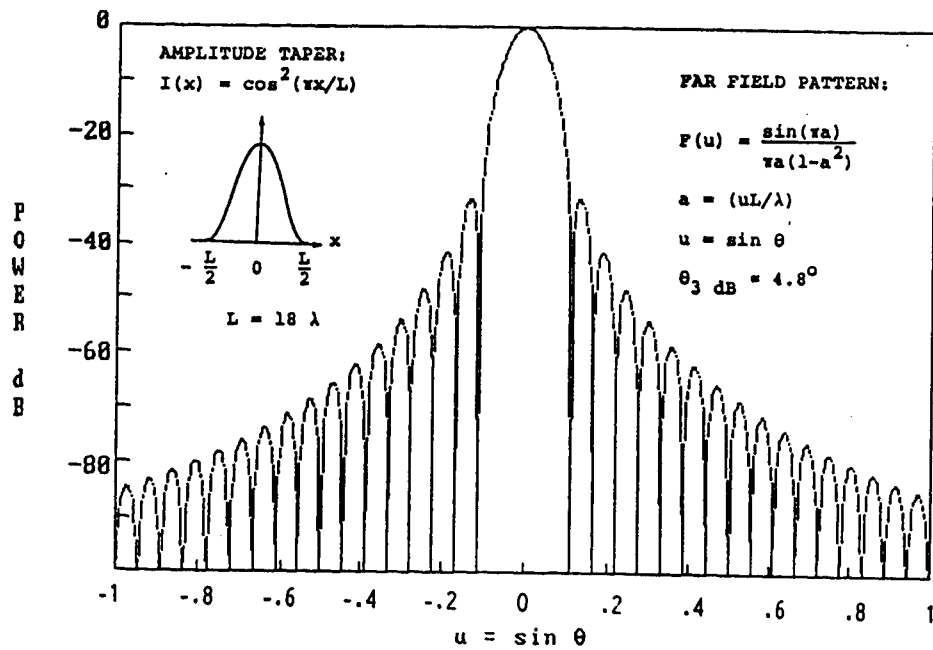   June 1992, pp. 170-174.

MULTIPATH :   NONE (IDEAL SITUATION)

Fig. 1   Simulated Ideal Antenna Pattern

MULTIPATH :   -40 dB   @ θ = 32°   (u = 0.53)
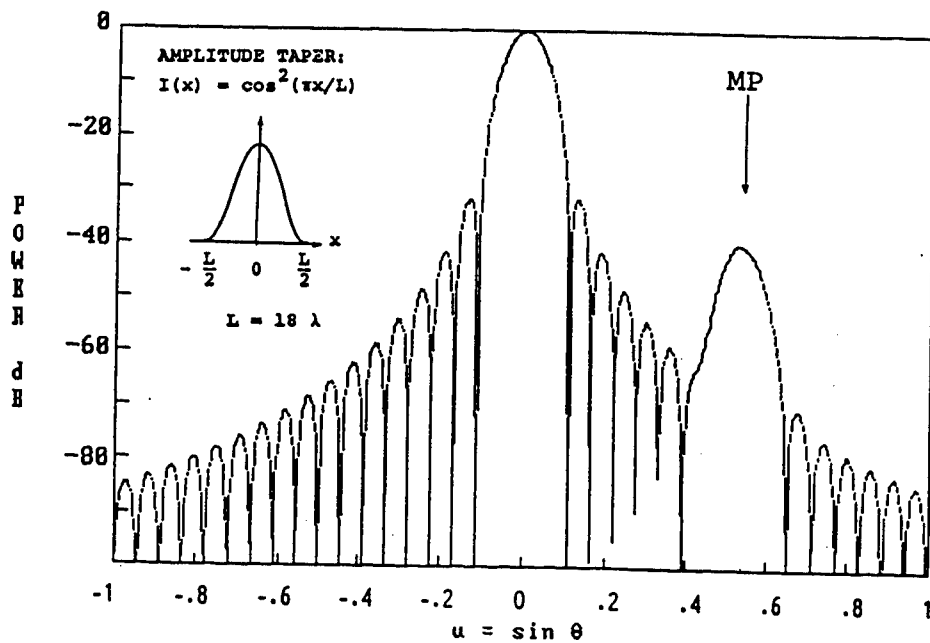

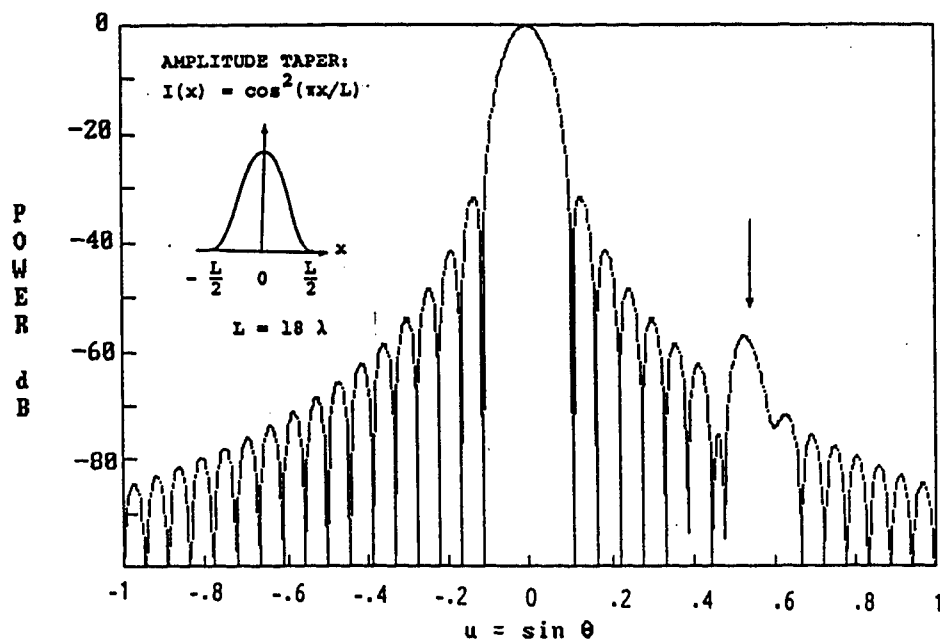**Fig. 2   Simulated Antenna Pattern With Multipath**

Fig. 3   **Simulated Antenna Pattern With Multipath**

MULTIPATH :   -80 dB   @ θ = 32°

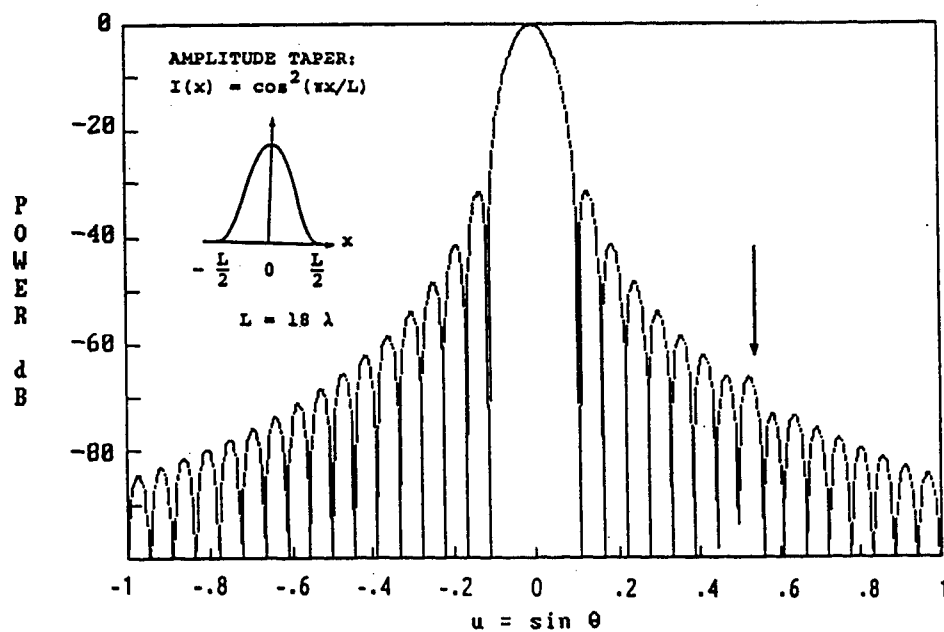Fig. 4   **Simulated Antenna Pattern With Multipath**

Fig. 5a   Illustration of Multipath Corruption Of Measurement Of Low Antenna Sidelobes

PEDESTAL

Rx AUT

45 ft.

e

d

ACTIVE REPEATER
THAT IS OFFSET FROM THE BASE
OF THE PEDESTAL BY d FEET
HORIZONTALLY AND e FEET
VERTICALLY.

MP

MP

DIRECT PATH ≈ 1,400 feet

d ≈ 45', e ≈ 1'

Tx
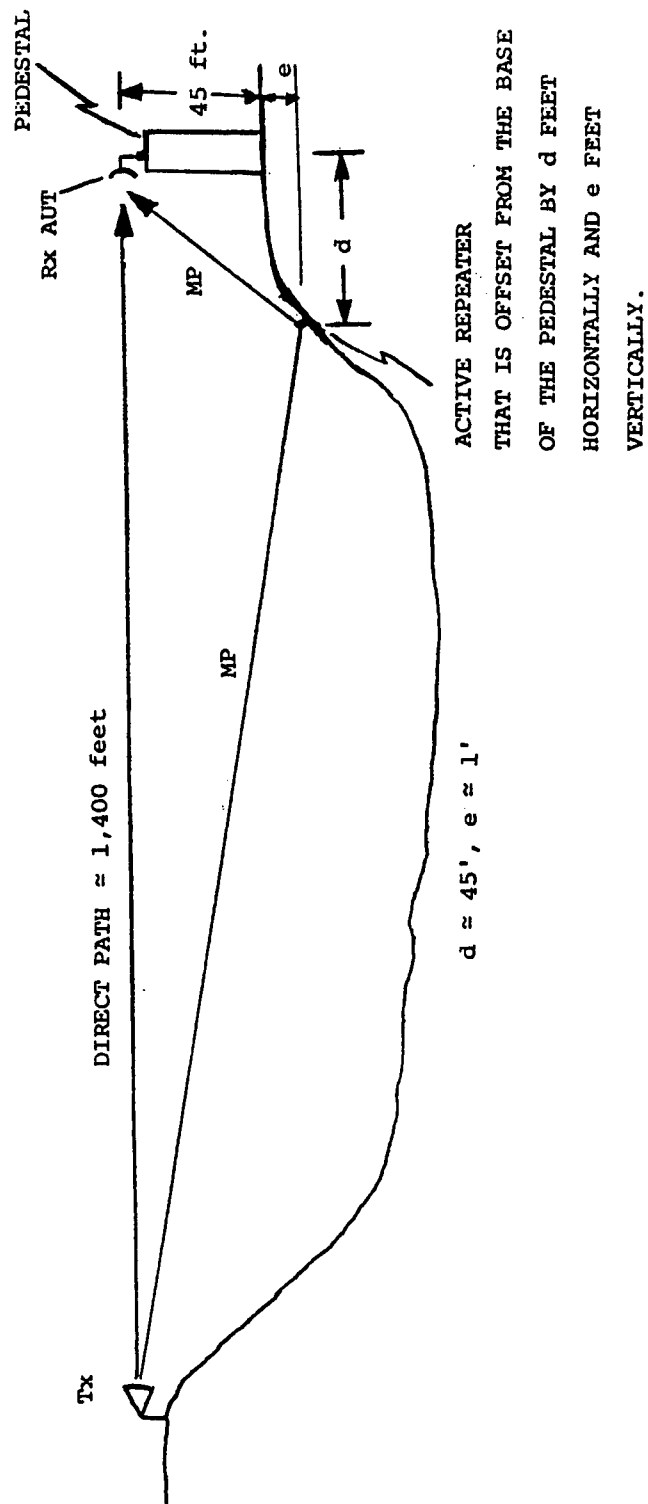
Fig. 5b   Elevation Profile of Newport, NY, RL Antenna Test Range

MULTIPATH :   NONE (IDEAL SITUATION)
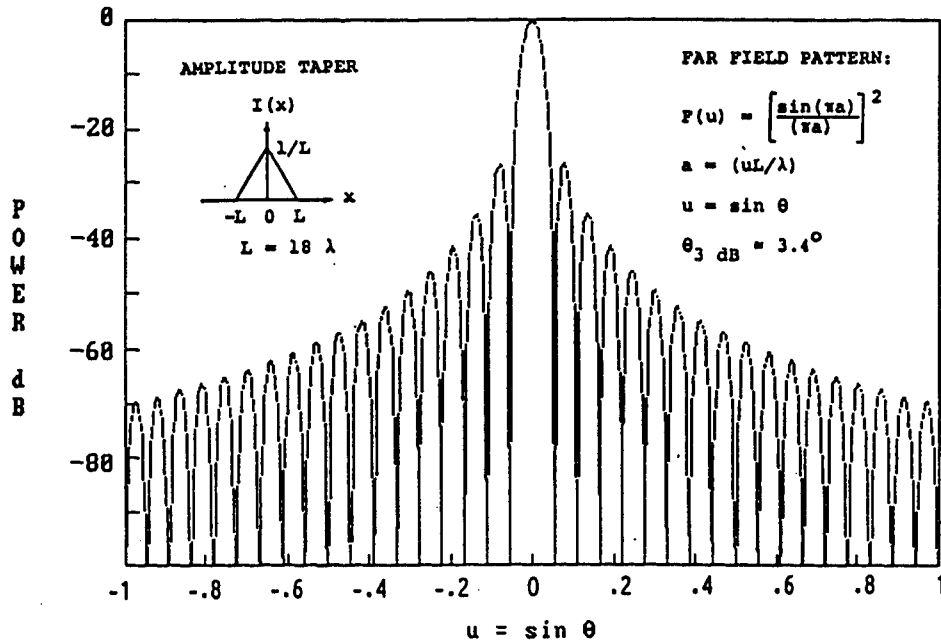
Fig. 6   Simulated Ideal Antenna Pattern

MULTIPATH :   -40 oB   @ θ = 32°   (u = 0.53)
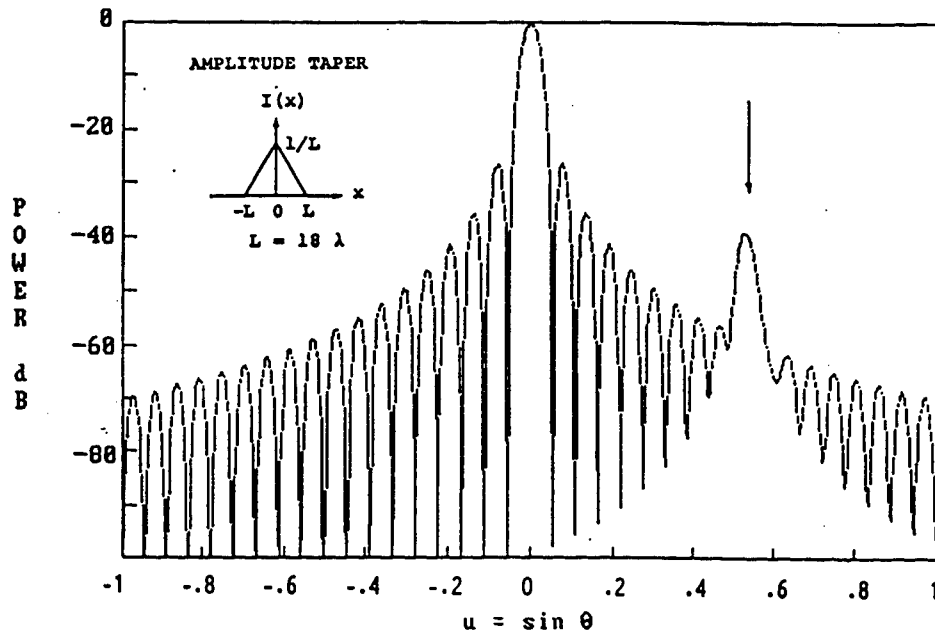
Fig. 7   Simulated Antenna Pattern With Multipath

MULTIPATH :   -60 dB   @ θ - 32°
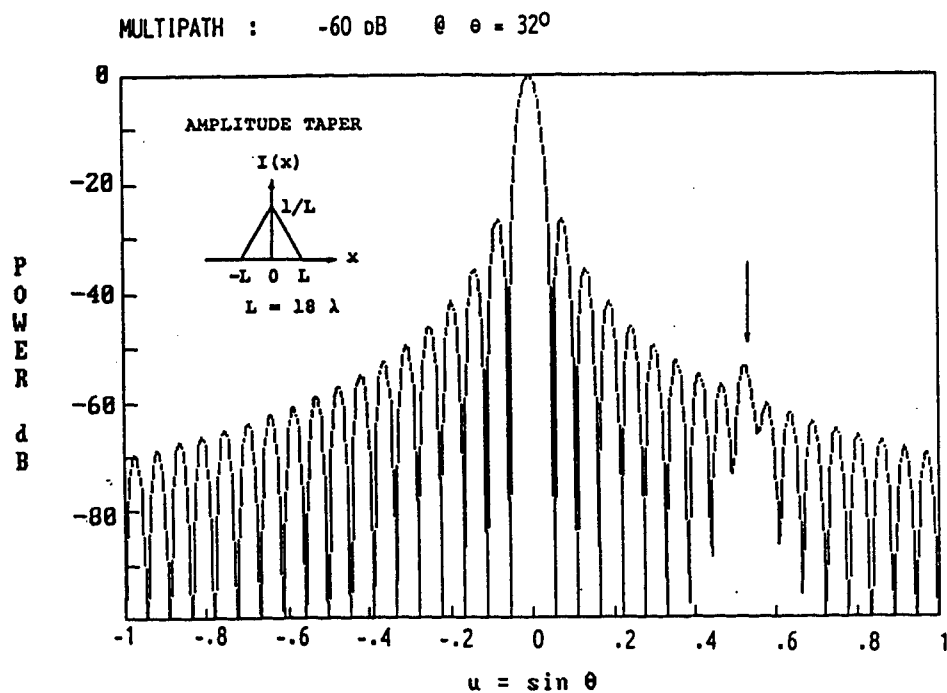
Fig. 8   Simulated Antenna Pattern With Multipath

MULTIPATH :   -80 dB   @ θ - 32°
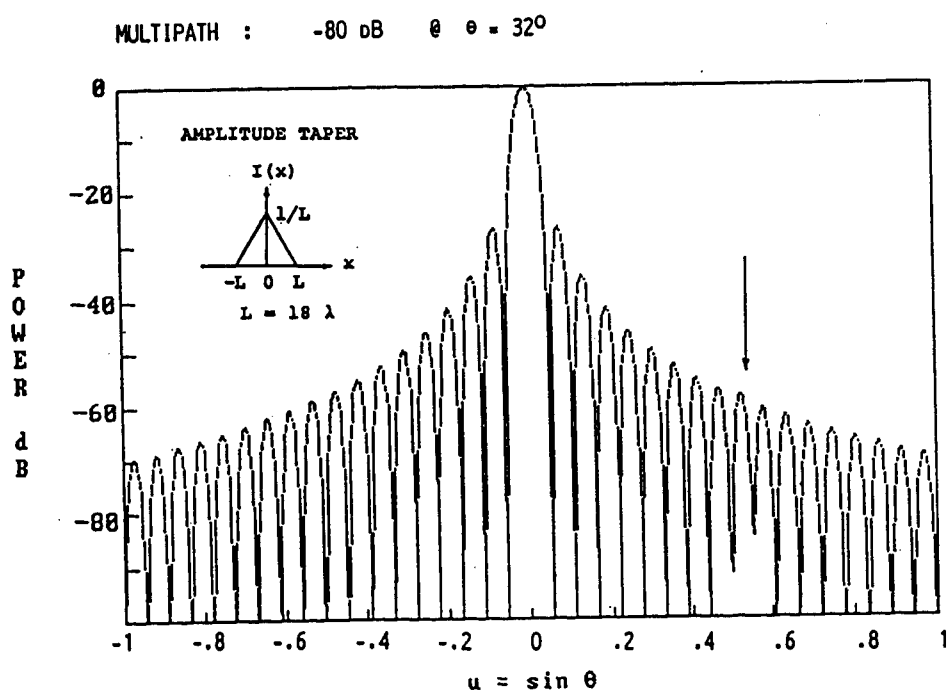
Fig. 9   Simulated Antenna Pattern With Multipath
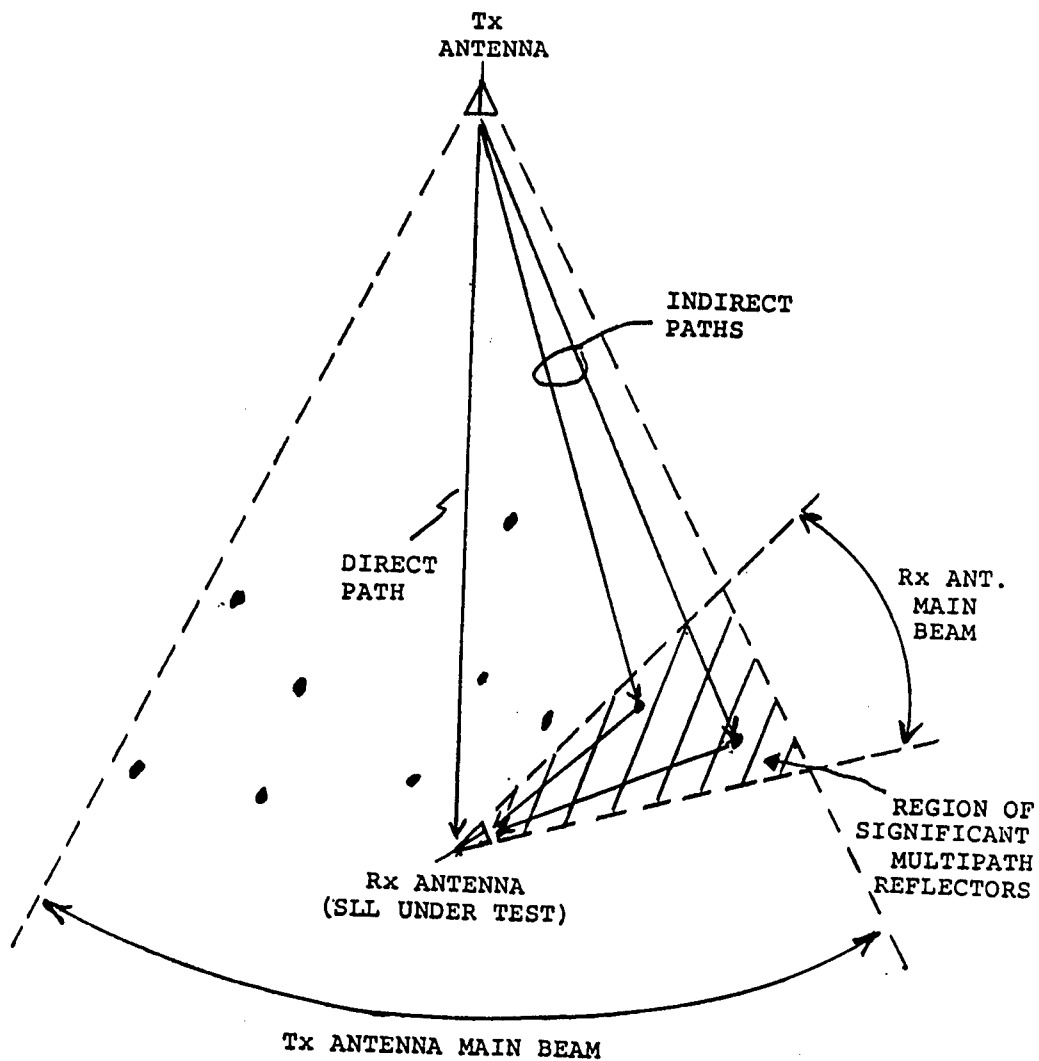
411
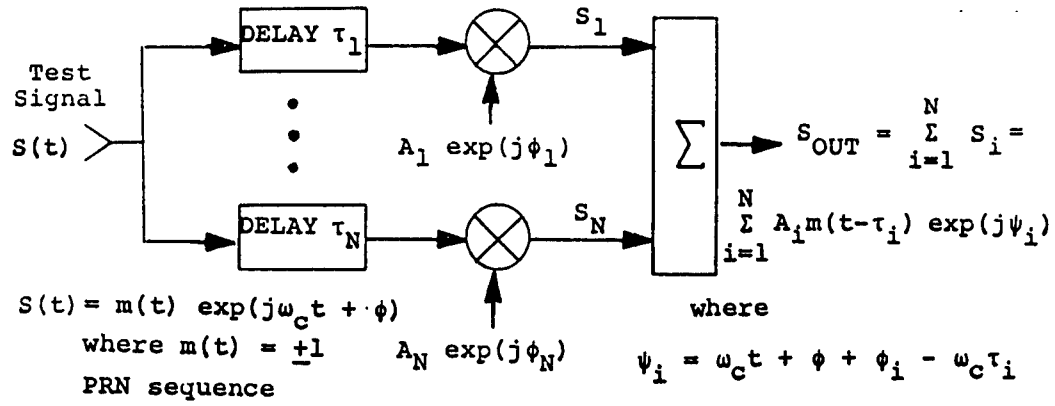
Fig. 10   Multipath Model for BPSK Signal S(t)
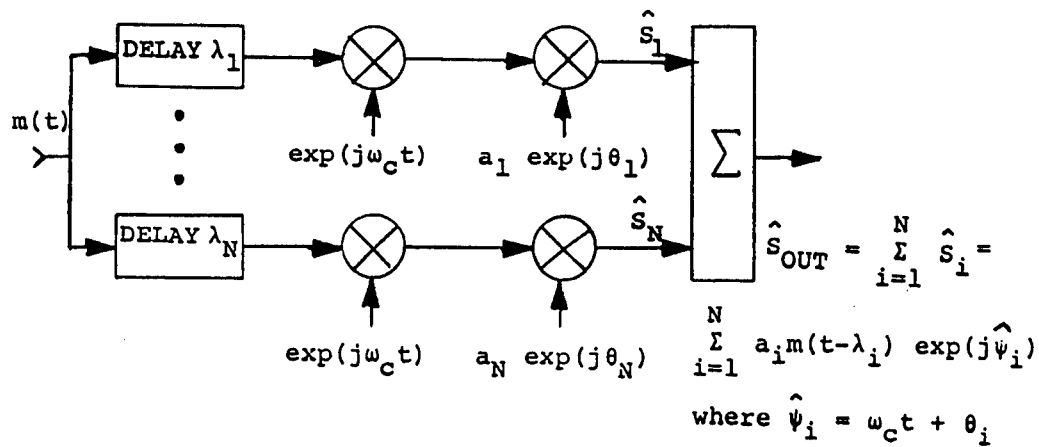
Fig. 11   Multipath Emulator for BPSK Signal S(t)
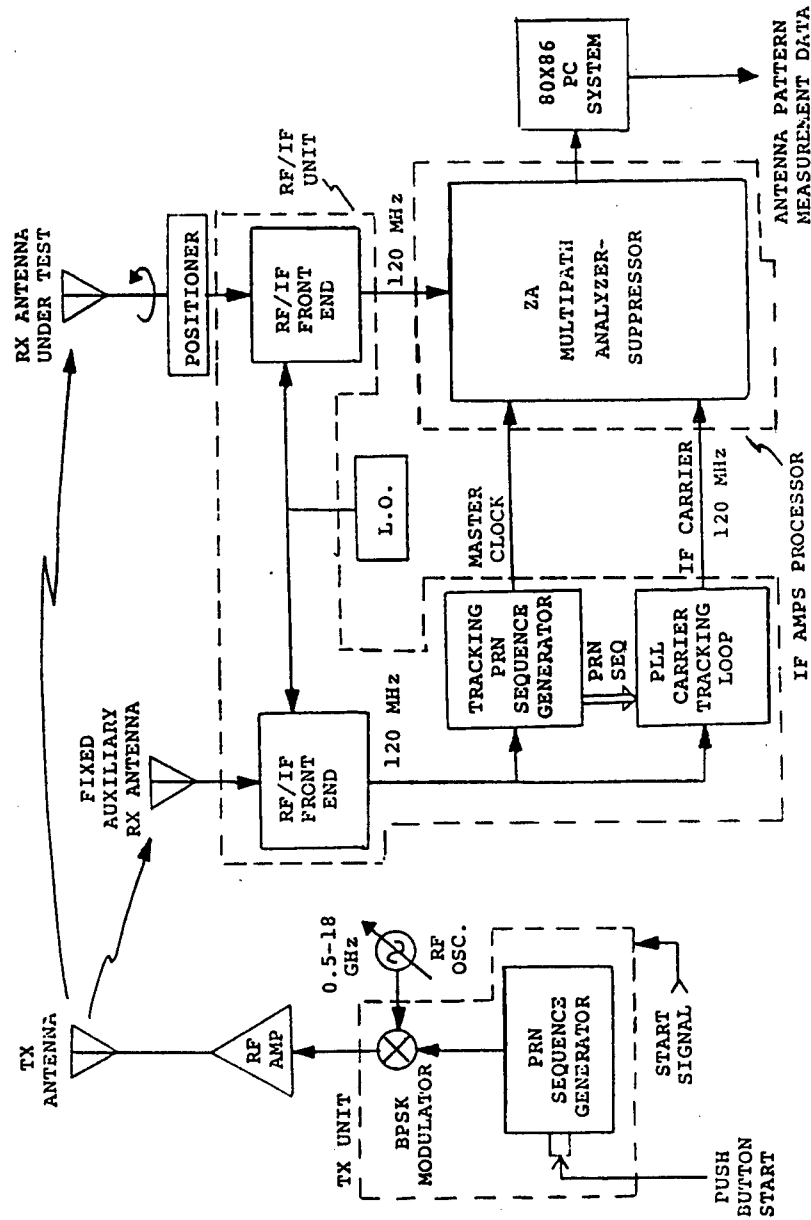
Fig. 12   Antimultipath System (AMPS) Configuration For Antenna Range Measurements

413
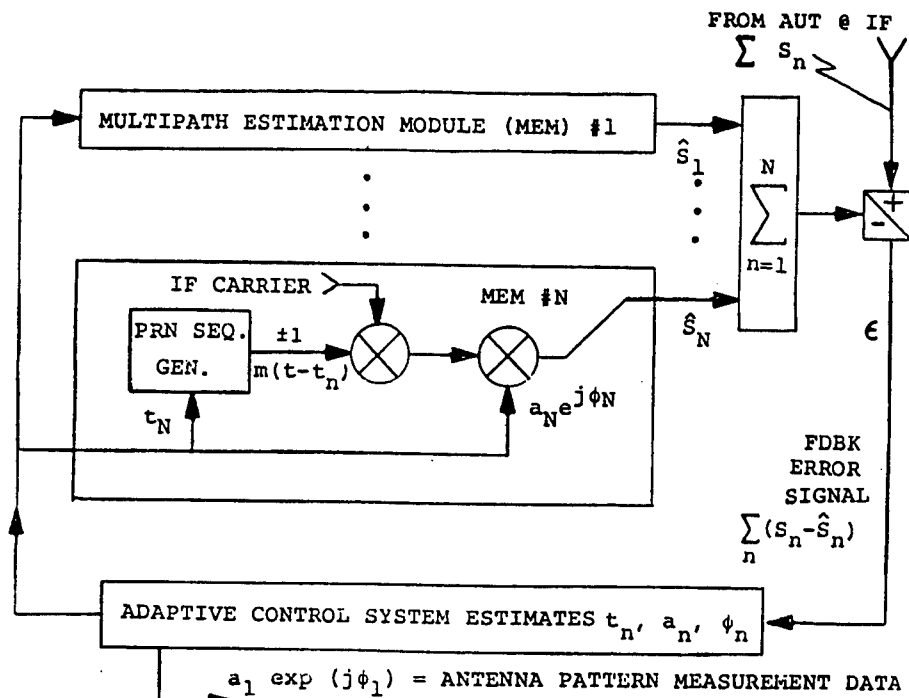
Fig. 13 Multipath Cancellation System Diagram
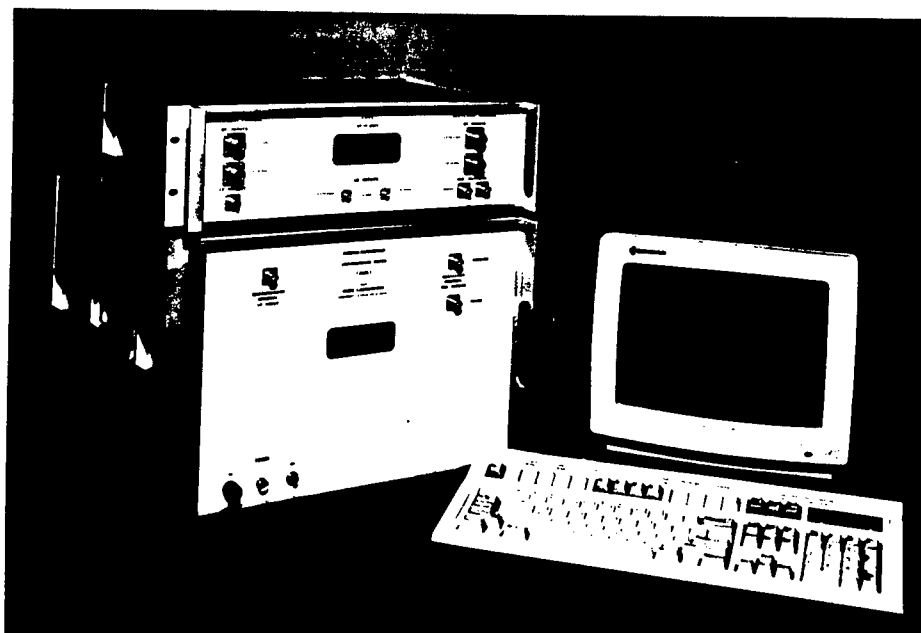
Fig. 14 Photograph of the Receive Site Portion of the Feasibility Demonstration Model AMPS
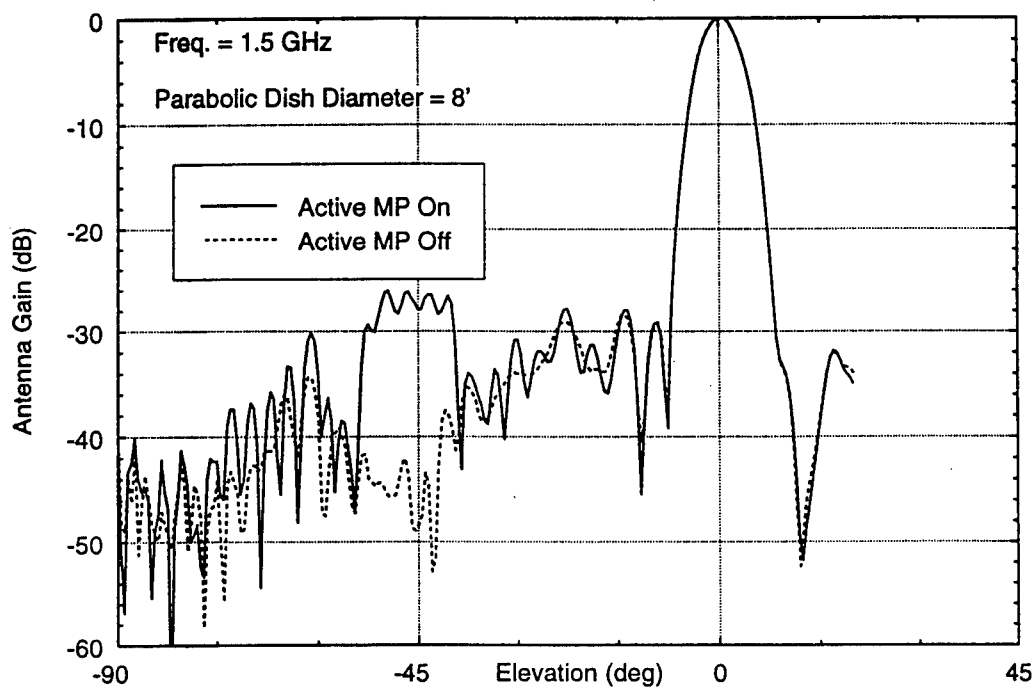
Fig. 15   Antenna Patterns from a Conventional System (CS) With Active Multipath (MP) On and Off
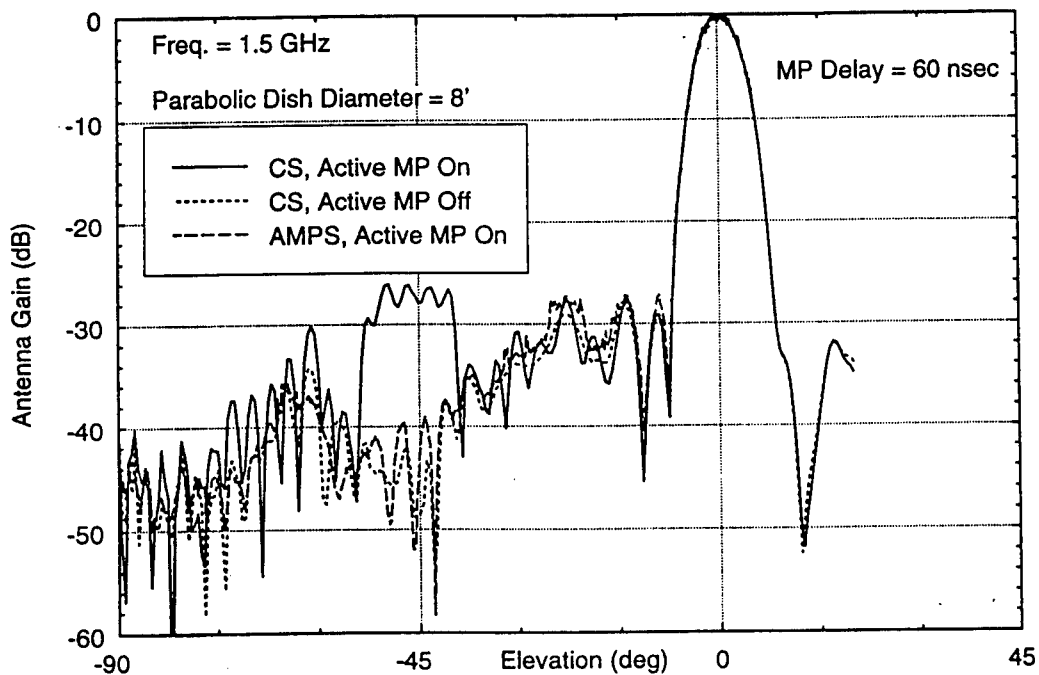
Fig. 16   Antenna Patterns Recorded by a CS With Active MP On and Off and by AMPS With Active MP On

415
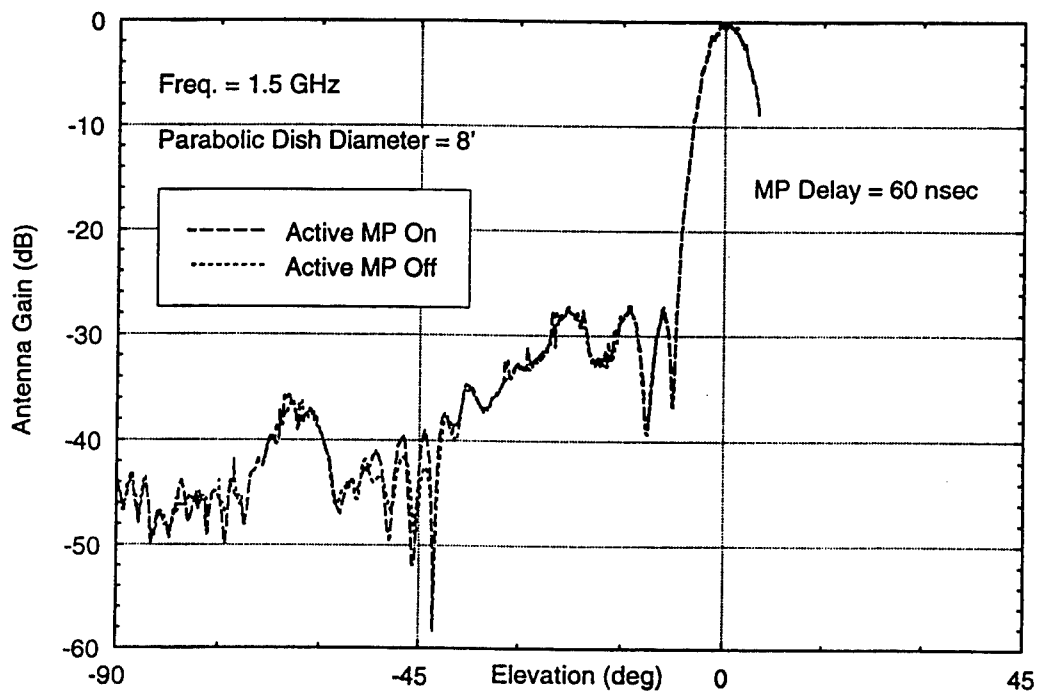
Fig. 17   Antenna Patterns Recorded by AMPS With Active MP On and Off
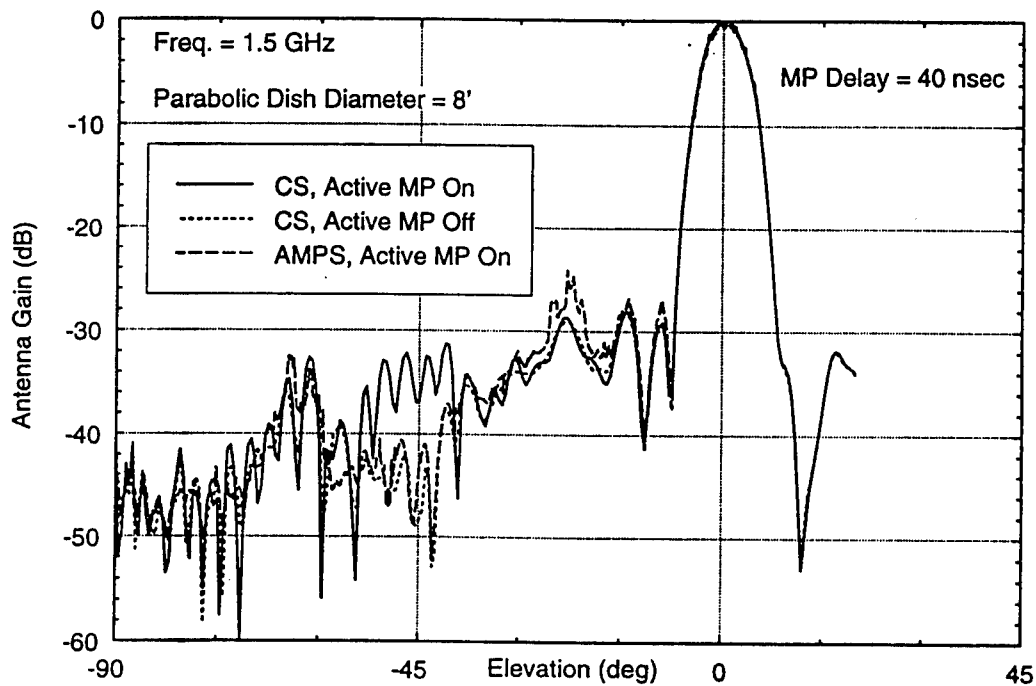
Fig. 18   Antenna Patterns Recorded by a CS With Active MP On and Off and by AMPS with Active MP On

SIMULATION AND EVALUATION
OF AN
ANTENNA POLARIZATION NULLING PROCESSOR

Dr. Leon J. Ricardi
Creative Engineering
865 Manhattan Beach Blvd., Suite 206
Manhattan Beach, California 90266

1. ABSTRACT

Adaptive antenna nulling and spread-spectrum waveforms are two of three methods of reducing interfering signals. Antenna polarization is the third method. It consists of adjusting the receiving antenna's polarization so that it is cross-polarized to the total field produced by all interfering sources, at the receiving antenna. The interfering sources can be co-located with the desired signal source. Variation in the receiving antenna's output signal can be compensated for through conventional signal coding. Because the associated processor's performance is independent of the operating RF, it depends only on the desired signal's data rate.

2. INTRODUCTION

An antenna polarization nulling (APN) processor suppresses interfering signals by adjusting the receiving antenna's polarization such that the antenna rejects jamming signals while still receiving user signals. When a jammer varies the polarization of its radiated signals, the user's signal will vary due to a varying polarization mismatch. In general, the user's signal amplitude will vary less than 10 dB, 90% of the time. Use of a diversity waveform and error correction coding

can eliminate errors due to the fading-like phenomena produced by this variation in the user's signal amplitude. When the user's signal is at least 10 dB greater than its receiver's thermal noise (SNR > 10 dB), APN can reduce the jamming signals more than 30 dB. This occurs even when the user and jammer signal sources are co-located. Since all signals incident on the receiving antenna add to produce a single field, APN can suppress all incident interfering signals simultaneously.

Recall that adaptive nulling antennas use spatial discrimination as a means for suppressing jammer signals while reducing gain to user terminals a tolerable amount. This process requires an electrically large antenna aperture. The required antenna aperture is practical at EHF and barely tolerable at SHF. At UHF, it is virtually impossible to place the required antenna aperture on a spacecraft and still launch the spacecraft.

Spread-spectrum waveforms are also used to suppress jamming signals. However, higher data rate communication systems usually do not have sufficient operating bandwidth to suppress expected jammer threats. Nevertheless, it is wise to always use an AJ waveform if interference is expected. APN can be used in addition to a spread-spectrum waveform and any existing spatial discrimination processors.

Thus, spatial discrimination requires a large antenna aperture, and temporal discrimination requires a large frequency bandwidth — neither of which are available in sufficient quantity at UHF and, possibly, at SHF. APN requires a large SNR ($\approx$ 10 dB) and a robust diversity and error correction processor. Although APN is perhaps must useful at UHF where the other AJ measures are, in effect, not available, it can operate at any RF frequency. It is fundamentally limited to operating at data rates less than 10 Mbps, or to service a large community of users whose total data rate is less than about 10 Mbps.

This paper describes the details of an APN algorithm and a communication simulator designed to demonstrate its performance. It also presents the results of a statistical analysis of the expected bit error performance in the presence of sensor errors. For the impatient reader, an example of the latter study is shown in Figure 1. In this Figure, the probability of an error in the detection of a bit is plotted versus the interfering signal's polarization angle, θ_j. The solid curve is for operation with APN; the dashed curve is for operation without APN. These results are for a jammer occupying the same frequency band as the user and with the jammer's amplitude equal to that of the user. These curves will be discussed in detail later in this paper. Until then, note that for a jammer polarization angle, $\theta_j < 72°$, the probability of a bit error occurring is less with APN than without APN. This improvement in performance increases substantially as the jammer's

polarization approaches that of the user (i.e., $\theta_j = 0$). On the other hand, using APN increases the probability of a bit error when the jammer's polarization angle, θ_j, is greater than 72°. This might be expected as θ_j approaches the user's cross-polarization because the jammer will be completely suppressed when its polarization is orthogonal to the user's polarization. It is indeed fortunate that for $\theta_j > 72°$, the probability of a bit error is less than 0.27 and can be as small as 0.02. Assuming θ_j is uniformly distributed, the probability of a bit error is less than 0.1 with APN versus 0.2 without APN. This reduction in BER usually requires ≈ 10 dB increase in S/N. For those cases where θ_j is not uniformly distributed, it is likely that using APN will result in a much less BER than without APN (e.g., θ_j is constant). Note that the BER with APN is a maximum of 0.32 and it is usually less than 0.1. It is important to note that the curves shown in Figure 1 assume that: (1) the jammer's signal amplitude **equals the user's amplitude** ($S/J = 0$ dB); (2) there is up to a 2 dB error in estimating the user's signal amplitude, A_u, and the jammer's signal amplitude, A_j; and (3) there is up to a $\pi/8$ error in estimating the user's polarization angle, θ_u. If A_j, A_u, and θ_u are known exactly, using APN eliminates all bit errors. The estimate of these signal parameters will be discussed later.

This paper addresses the fundamentals of APN, where it is shown that suppression of interfering signals requires knowledge of the interfering signal's amplitude, user's signal amplitude, and the incident user's signal polarization. Following this, the effect of errors in determining these parameters is analyzed, with respect to producing and determining an error in detecting a QPSK bit. Results obtained with a computer simulation of an APN processor using a QPSK waveform are then presented A summary of this study reviews the results and presents some recommendations for further development of APN.

3. ANTENNA POLARIZATION NULLING

Antenna polarization is often described as vertical linear (VL), horizontal linear (HL), right-hand circular (RHCP), or left-hand circular (LHCP). In general, this is adequate for most communication and radar system designers and specification writers. It is customary to specify the axial ratio of circularly polarized signals and the angular orientation of linearly polarized signals. These polarizations represent a very small subset of the vast number of polarizations that can exist. For example, the instantaneous polarization of signals radiated from the sun vary randomly over all polarizations. It is also true that any polarization has a cross, or orthogonal, polarization. These co- and cross- pairs of polarizations form a set and are usually referred to as a pair of orthogonal polarizations.

The Poincare sphere (see Figure 2) is a common method of representing all possible polarizations. It can be defined such that RHCP and LHCP are located at the poles of the sphere, as shown in Figure 3. In this case, all orientations of linear polarization are located on the Equator of the sphere and all elliptical polarizations are located elsewhere on the sphere. Thus, the sphere represents all possible polarizations of any electromagnetic field. The sphere also has some special characteristics that help in describing APN. Specifically, orthogonal polarization pairs are located diametrically opposite one another, and the coupling between waves with different polarizations is equal to $\cos^2(\beta/2)$, where β is the angle between radial vectors terminating on the two polarization locations on the sphere. For example, with orthogonally polarized fields $\beta = 180°$ and the coupling equals zero, as expected. With a linearly polarized and a circular polarized field, $\beta = 90°$ and the coupling between them equals 0.707, or -3 dB.

In the remainder of this paper, the North and South poles of the Poincare sphere represent VL and Hl, respectively. This does not effect the generality of the analysis — it renders the mathematics somewhat less complicated and improves a physical interpretation of the APN concepts. A standard right-hand spherical coordinate system is used with HL polarization located at $\theta = 0$, and with VL polarization located at $\theta = 180°$.

In its most advanced form, APN will operate with the user's terminal varying the polarization of its radiated signals in a random but known (only to the intended receiver) fashion. This will prevent an interferer from transmitting noise with a polarization identical to that of the user. An APN processor receives signals via a pair of orthogonally polarized co-located antennas. These signals are weighted (their phase and amplitude are modified) and summed to suppress the interfering signals. That is, the processor adjusts the polarization produced by the pair of antennas such that it is orthogonal to the polarization of the total interfering signal, E_j. Note that E_j can be produced by a single interfering source, or several incoherent, or coherent, sources. It is a single field added to the user's incident signal, E_u, to form the total incident signal, E_t. In order to perform this function, an APN processor must know the polarization, P_u, and amplitude, $|E_u|$, of the user's signal and the amplitude of the interfering signals, $|E_j|$. It will be shown that the estimate of P_u and $|E_u|$ can be less accurate than the estimate of $|E_j|$. In the interest of the anxious reader, the data shown in Figure 1 was calculated with the estimate of $|E_u|$ and $|E_j|$ within 2 dB of their actual values and β_u, the angle between the actual user's polarization, P_u, and the estimated value of P_u, less than $\pi/8$.

Note that the user's signal is also reduced as the antenna's polarization is varied to suppress the interfering signals. That is, the amplitude of a received signal power, P_r, can be represented by

$$P_r = A \cos^2(\beta/2) S,$$ (1)

where S is the incident user's signal power flux density and A is the antenna's effective absorption area. Using (1), and assuming the incident interfering signal polarization will be uniformly distributed over all polarizations, the user's received power, P_{ru}, will be suppressed less than a factor α with probability greater than $1-\alpha$. In other words, the user's signals will be reduced less than 10 dB, 90% of the time. For example, if the user's signal–to–thermal-noise ratio (SNR) is greater than 15 dB, an APN processor will suppress the interfering signals and the user's SNR will be greater than 5 dB, 90% of the time. The interfering signals will be suppressed more than 30 dB if the estimate of $|E_j|$ and P_u are sufficiently accurate. A forward error correction algorithm will most likely recover bit errors that occur during those periods when the user's SNR is inadequate to prevent the occurrence of bit errors.

In its simplest form, an APN estimates $|E_j|$ by first measuring the power received with the antenna's polarization set to the user's (or estimated user's)

polarization. Assuming P_u is known, power, P_x, received with the antenna's polarization set to P_{ux}, the user's cross-polarization, will be given by

$$P_X = \left| E_j \right|^2 \cos^2\left(\frac{\theta_{mj}}{2}\right), \tag{2}$$

where θ_{mj} is the angle between the jammer's polarization angle, θ_j, and the user's cross-polarization angle, θ_{ux}. Assuming a value of $|E_j|^2$, θ_{mj} can be calculated using (2). Since we have assumed $\theta_u = 0$, the jammer's cross-polarization angle, θ_{jx}, equals $\pi - \theta_{mj}$. This relationship is shown in Figure 4. Note that finding θ_{jx} defines the circle on the polarization sphere that contains P_{xj}. It remains to determine the value of ϕ_{jx} that uniquely defines the interfering signal's polarization.

Recall that when the antenna's polarization is set to P_{jx}, only the user's signal will be received. For any antenna polarization different from P_{jx}, the total signal received depends on the signal phase, ζ, between the jammer's and user's signals. Diagrams in Figure 4 indicate the variation in the total signal received as the polarization angle, ϕ_{jx}, is varied over its entire range of 0 to 2π radians when $\theta = \theta_{jx}$. When $\zeta = 0$ or $180°$, there is only one point on the circle where the total received signal magnitude equals the estimated user signal amplitude. For all other cases, there are two values of ζ that will give a signal amplitude equal to the

expected user signal amplitude. This is what gives rise to the two solutions for γ in (3), below. The graph in Figure 4 indicates the variation in the signal received at the antenna output as ϕ is varied over its range or as the polarization of the antenna is varied along the circle that contains P_{jx}. It the past, analysts have indicated that it is not possible to pick the correct value of ϕ_{jx}; hence, an APN processor will, on average, fail to implement the desired polarization 50% of the time.

The correct value of ϕ_{jx} can be determined by using both solutions to determine the received information bit. In this case, the bit must be either 0°, 90°, 180°, or 270°. The algorithm selects that bit which yields a minimum value of ξ_e, the phase difference between the phase of the detected bit and the four expected bits. When $|E_u|$, $|E_j|$, and θ_u are without error, $\xi_e = 0$, the correct value of ϕ_{jx} is always selected and the interfering signals are suppressed more than 30 dB.

An estimate of $|E_j|$ can be improved by using ζ_e and the selected received bit to calculate a new value of $|E_j|$ — assuming error-free estimates of $|E_u|$ and θ_u, the user's signal amplitude and polarization angle, respectively. In a next section, the sensitivity of selecting the correct bit will be examined as a function of the error in estimating $|E_j|$, $|E_u|$, and θ_u. Surprisingly large errors in these quantities are tolerable. Future studies of an APN processor can improve the primitive feedback

loop described here so that expected variations in $|E_j|$, the most sensitive parameter, can be predicted or anticipated.

Before discussing the sensitivity of errors in estimating the three uncertain APN processor parameters, it is important to display the simplicity of the algorithm's mathematics, in contrast to the complexity of its derivation and the conceptual discussion given in the foregoing. it can be shown (see Rome Laboratory Final Technical Report RL-TR-170, September 1995, Appendix A, Equation 38) that γ, the phase of the user's received signal, is given by

$$\gamma = a_c \pm \cos^{-1}\left(\frac{a^2 + |t_c|^2 - n_c^2}{2a|t_c|}\right).$$

(3)

With the antenna's polarization set equal to P_u, α_c and $|t_c|$ are the phase and amplitude of the signal received at the antenna's copolarized port, a is the estimated user's amplitude, and n_c is the magnitude of the jammer's signal received at the antenna's copolarized port. Note that n_c is calculated from

$$n_c^2 = |E_j|^2 - n_x^2,$$

(4)

where n_x^2 is the power received at the antenna's cross-polarized port and $|E_j|^2$ is the estimate of the interfering signal's power. The second term on the right side of (3)

introduces the uncertainty in calculating the correct value of γ. Note that when there is not an interfering signal present, $n_c = 0$, $|t_c| = a$, and the second term reduces to zero, as it should.

Note that only two calculations are required; they are indicated by (3) and (4). The resulting values of γ must be compared to γ_e, the expected values of γ. The expected value most nearly equal to γ is selected as the transmitted bit, γ_0. Then, a better estimate of n_c^2 is obtained by substituting γ_0 for γ in (3) and solving for a new value of n_c^2. Using (4), a new value of $|E_j|^2$ can be calculated. The latter is used in calculating γ for the next transmitted bit.

The foregoing algorithm and a simulation of its use as a processor is indicated in Figure 5. In the upper left corner, user and jammer signal generators produce signals that are polarized and then combined as a single signal. In the simulator, described later, the user's signal amplitude and polarization are held constant while the jammer's amplitude and polarization are varied. The combined signal is filtered and down-converted to represent a received signal in the presence of jamming. This signal is sampled and held to convert the incident signals to a digital representation. The APN algorithm uses an estimate of the user's signal amplitude and polarization and the jammer's amplitude to calculate the two values of γ as described in (3). These values are compared with the expected

values — one of which is selected. The selected value is then used to calculate an improved estimate of the jammer's signal amplitude.

Note that the simulator does not have a phase-locked loop (PLL) as would be used by a QPSK signal demodulator. Rather, a sample of the user's signal frequency was used to synchronize the detector to avoid the errors that would be introduced by a less-than-perfect PLL. It was felt that the thrust of the study was to evaluate an APP, as opposed to develop a suitable PLL.

4. Sensitivity to Error in Parameter Estimates

At the risk of saying it too many times, an APN algorithm uses three estimates in calculating the phase of the transmitted bit and adjusts the antenna's polarization to be orthogonal to the incident interfering signal's polarization. These APN estimated parameters are:

1. User signal amplitude;

2. User signal polarization; and

3. Jammer signal amplitude.

Error sensitivity in the above three parameters were investigated by first assuming an error in one parameter with the other parameters error-free, then calculating the probability of an error in the detected phase of a bit. The

calculation assumed a fixed value of θ_j and assumed a uniform distribution of ϕ_j, the jammer's other signal polarization angle, and ξ, its time phase relative to the user's signal time phase. The jammer's and user's signal amplitudes were allowed to vary up to 6 dB above and 6 dB below their error-free values. The user's signal polarization was allowed to vary over the range of $-\pi/4$ to $\pi/4$. The resulting error sensitivities are shown in Figures 6a–6c for a user's signal-to-jammer amplitude ratio (S/J) equal to 0 dB. The data shown in Figures 7a–7c are for $S/J = 3$ dB. A similar set of plots are shown in Figures 8a–8c and 9a–9c for operation without the use of APN.

The decimal annotation (Figures 6a–9c) in each shaded region indicates the fractional number of bit errors that occurred for the range of ϕ_j and ξ used. That is, a total of 324 values of ϕ_j and ξ were used to calculate the detected bit's phase. For each θ_j, $|E_j|^2$, θ_u, and $|E_u|^2 = a^2$, the number of bit errors (BEN) was calculated and divided by 324, the total number of samples. The plots in Figures 6a–9c were prepared by computing the BER for points at the intersection of the grids on each figure. The shaded contours were derived from these points.

These plots indicate that the error in estimating the jammer's amplitude causes the largest increase in producing an error in detecting the phase of a bit. It also shows that using APN reduces the probability of an error in the phase of a bit

from that obtained without the use of APN in those cases when the jammer's power is underestimated and when the user's signal amplitude and polarization are in error. Note that when the jammer's amplitude is known within ≈ 1 dB, use of APN always results in performance superior to that obtained in the absence of APN.

The data shown in Figures 6a–9c are helpful in identifying the accuracy needed in estimating the APN parameters. A more informative calculation of the probability of an error in detecting the phase of the transmitted signal can be obtained by combining the error probability distributions for all three APN parameters and computing the probability of detecting the phase incorrectly. This calculation was carried-out using the probability density functions shown in Figures 10a and 10b. Note that the user's and jammer's signal amplitude estimate errors are assumed to have a Ricean distribution, P_A. That is, it is assumed that signal amplitudes greater than the estimated value is less likely to occur than if they are less than the estimated value. The most likely signal amplitude is equal to the estimated value. The maximum and minimum values are 2 dB more than and 2 dB less than the estimated value. This distribution is shown in Figure 10a.

The user's signal polarization angle, θ_u, was assumed to have a Guassian distribution. P_θ, centered on $\theta_u = 0$, the estimated value of the user's signal

polarization angle. This distribution is shown in Figure 10b. Note that θ_u is

assumed to be between -22.5° and 22.5°.

The probability, $Pe(\theta_j)$, of an error in detecting the phase of a bit error was

computed using

$$Pe(\theta_j) = \sum_m^M A_u P_A \sum_n^N A_j P_A \sum_r^R \theta_u P_\theta \sum_s^S \frac{\phi_s}{S} \sum_t^T \frac{\zeta_t}{T} , \tag{5}$$

where A_u, A_j, and θ_u are the errors in estimating the amplitude of the user's signal,

the amplitude of the jammer's signal, and the user's signal polarization angle,

respectively. The jammer's second polarization angle, ϕ_s, and its time phase, ξ_t,

are assumed to be uniformly distributed over 2π radians; that is,

$$\phi_s = \frac{2\pi s}{S} , \text{ and} \tag{6}$$

$$\zeta_t = \frac{2\pi t}{T} , \tag{7}$$

where S and T are both equal to 18. Thus, ϕ_s and ξ_t have a probability of $1/S$ and

$1/T$, respectively.

$Pe(\theta_j)$ was computed using (5) for $\theta_j = \pi/10, \pi/5, ..., 9\pi/10$, and $S/J = 0$

dB and -3 dB. The computation of (5) was carried-out with and without APN

while assuming the same user's polarization estimate for both cases. It is

important to recognize that APN can change the estimate of the user's polarization

to improve performance in those cases where the jammer's polarization angle, θ_j, is

not randomly distributed. For example, when θ_j is slowly varying or fixed, APN

can anticipate the future values of θ_j and improve its AJ performance. The results

shown in Figure 11a indicate that with APN, the maximum P_e is less than 25%,

whereas without APN, P_e can approach 50%. The results also indicate that, when

$\theta_j > 72°$, P_e is greater with APN than without APN.

The results shown in Figures 11a and 11b are very helpful in indicating the

expected performance of APN. However, these results were obtained using

assumed errors in estimating the three APN parameters. If the error in the

jammer's signal amplitude is reduced to less than 1 dB, using APN will result in a

smaller value of P_e for all values of θ_j, than if APN is not used.

It is important to note that the P_e indicated in Figure 11a is based on

assumed jammer and user characteristics that were selected as a best guess of what

might be worst, or at least, bad estimates of the three APN parameters. For

example, the APN algorithm calculates θ_j, the jammer's polarization angle. A

simple modification of the APN would select the APN-derived transmit bit if

$\theta_j < 72°$ and select the non-APN derived bit for $\theta_j > 72°$. Still further, a historical

record of these parameters could improve the estimate used by APNA. This will

certainly reduce P_e to a value less than ≈ 0.25 for all θ_j. Forward error correcting methods could be used to reduce the BER, as with other communications systems. Consultation with a communications specialist indicates that with practical coding, a BER $< 10^{-5}$ can be readily achieved if the symbol error rate is less than ≈ 0.27.

5. APN SIMULATOR

This section describes a personal computer simulation of an APN, and summarizes the results. A block diagram of the simulator is shown in Figure 12. The transmitter generates a QPSK-modulated RF signal that is passed to a horizontally polarized "radiator." A similar RF signal generator's output was divided and incoherently modulated with random signals. These signals were passed to a horizontally polarized (HL) "radiator" and a vertically polarized (VL) "radiator." In order to keep the simulation free of non-related mechanisms, these signals were not radiated — they were passed directly to the ports of a receiving HL and VL "antenna," respectively. Note that the user's and jammer's HL signals were combined prior to being sent to the "receiver."

Still referring to Figure 12, the "separator" resolves the signal into in-phase (I) and quadrature-phase (Q) signals from the HL and VL signal ports. The "sample-and-hold" function converts these analog signals to a digital

representation and passes them to the APN processor (APNP). The APNP reduces the jammer's amplitude and detects the phase of the received bit. This is compared to the known transmitted bit and any errors are counted. This count is used to measure the bit error rate (BER) of the processor.

The synchronizer adjusts the signal delays introduced by the simulator so that the APNP processes the chips as groups that form a bit. The "power calculator" is used to monitor the recovered power and enable a diagnosis of the performance of the simulator.

This simulator uses MATLAB software and includes a Simulink communications processor manufactured by The MathWorks, Inc. The software was designed to be capable of overall construction by assembling several modules to realize the desired processor. Unfortunately, each module has its own unique, and sometimes unexpected, performance characteristics. The unexpected abnormal behavior of this software caused several problems and diverted attention away from the operation of the simulator.

Test cases were conducted with the user's power set equal to 1 Watt; the jammer's power was set to have a nominal value of 1 Watt and was either: (1) held constant; (2) its amplitude varied sinusoidally up to ≈ 2 dB; or (3) varied randomly up to ≈ 2 dB. At the same time, the jammer's signal polarization angles were

varied randomly over π radians, or held fixed. Therefore, jammers with varying amplitudes and polarizations were studied.

For a typical test, 100 bits were sent and detected. These detected bits were compared with the transmitted bit to accumulate the number of errors. This was done for operation with and without the APNP enabled. The results are given in Table I. The first column in the table lists the amplitude of the randomly varying jammer's signal at the transmitter. The actual jammer's signal power is given in columns 5 and 6. Columns 2 and 3 describe the variation in jammer polarization and column 4 describes the rate over which the variation occurs. The performance of the simulation, both with and without APN, is given in the two rightmost columns. The data rate was 2400 bps.

Referring to Table I, note that with the jammer's amplitude held constant ($A_0 = 0$ V), APN quickly finds the jammer's amplitude and reduces the BER to less than 1%. Time did not permit longer runs to determine a more accurate BER. Suffice it to say, APN substantially reduces the jammer's signal and all but eliminates bit errors. In other words, a relatively constant amplitude jammer can readily be suppressed by an APN processor, even one as primitive as the one developed during this study. This type of jammer is commonly used to jam a band-limited transponder channel. It is common knowledge that the jammer will

transmit a tone within the channel with intent to saturate the transponder's amplifier and increase the channel's noise level through intermodulation distortion and/or small signal suppression. Whether or not this type of jammer varies its polarization or keeps it fixed, an APNP will easily identify the jammer's polarization and suppress its signals, even if the polarization is varied at the communication data rate. Of course, this assumes that an APNP can operate at speeds comparable to the data rate. This will be discussed in the next section.

As the jammer varies its signal amplitude, the bit error rate increases. For example, with a 2 dB peak-to-peak variation in jammer amplitude, use of APN will reduce the BER compared to that obtained without APN. If the jammer's amplitude variation is increased to ≈ 3 dB, then the use of the APN algorithm used in this study does not appear to be justified. However, the algorithm was not designed to use historically generated data, or different methods of sampling the signals. For example, the simulator used five chips per bit in order to use the software as it was designed. The algorithm used only the third chip in a bit instead of several chips. Using the additional chips will improve performance. The magnitude of this performance improvement is not known.

In summary, the simulator verifies the need to estimate the jammer's signal amplitude within a few dB. in agreement with the sensitivity analysis presented in

the previous section. The simulator clearly shows that the current algorithm can readily identify the jammer's amplitude if it varies at a rate slower than about one-half the communications data rate.

Quite aside from the simulator's ability to perform as an APNP, the detector module's performance was checked by determining BER as the signal-to-noise (S/N) ratio was varied from 0 to 8 dB and compared to the theoretical BER for a QPSK modulation. These results are shown in Figure 13.

6. RELATED ISSUES

This study considered only a 2400 bps data rate, QPSK modulation, and continuous, as opposed to pulsed, jammers. These issues will be addressed in this section by applying information gained from the study.

An APN processor requires an analog-to-digital converter (ADC) as it is presented in this study. The speed and accuracy of this device will depend on the data rate and the desired signal suppression. It is expected that a 10-bit ADC operating at twice the data rate will be more than adequate. ADC's that have 12-bit accuracy and operate at several million samples-per-second (Msps) are readily available for less than $200.00. They could be made space-qualified and used in most any COMSAT. It is possible to obtain other ADC's that operate at

50 Msps that are less than ≈ $100,000. It will cost probably a few $100,000 to make them space-qualified. Thus, it is entirely possible that an ADC can be obtained to operate within APNP, handling up to ≈ 25 Mbps.

The APN algorithm used in this study required only 20 lines of computer code that could complete detecting a bit in less than 20 msec. It appears that the equivalent of a 100 MHz Pentium processor can handle up to a 1.5 Mbps data rate. Using buffers and parallel processors, it is likely that at least a 25 Mbps data rate can be handled by an APNP.

The current APN algorithm incorporates a QPSK detector. The logic for this detection could be used to demodulate any digital modulation, such as QPSK, BPSK, DPSK, M-ary FSK, and similar modulation waveforms. It is not designed to detect analog modulations such as FM or AM.

Since the APNP operates on instantaneous signals, it cannot be disrupted by a pulse, partial band, or similar types of jamming waveforms. That is, the APN algorithm samples and processes instantaneous signals. The three APN parameters are estimated using general knowledge and/or historical data. If a jammer chooses to radiate in discontinuous bursts, this information can be incorporated in the process of estimating the three APN parameters.

7. SUMMARY

This study determines the probability of error in detecting QPSK-modulated signals in the presence of a jammer. It was shown in Figure 11a that, for a worst-case jammer signal polarization, estimating the jammer's amplitude within 2 dB may result in a probability of bit error, P_e as large as 0.27. Assuming the jammer's polarization is varied over all possible polarizations, the probability of a bit error is about 0.15. The P_e is dependent on the jammer's polarization distribution — it can be as large as 0.27 or approach zero. The error analysis clearly indicates that using APN will reduce the BER below that obtained if APN is not used, except for those cases when the jammer's signal is nearly cross-polarized with the user's signal. In those cases, P_e with APN is less than ≈ 0.1.

The APN simulator indicates that, with a constant amplitude jammer signal, the APN can immediately determine the received jammer's signal amplitude and lock onto its signal polarization. As a result, there is at most one bit error at the onset of jamming and no errors in all the remaining bits transmitted. Up to 100 bits were transmitted with at least 99 received correctly. The jammer's in-band signal amplitude was equal to the user's signal amplitude. The user was communicating at 2400 bps and the jammer was varying its polarization such that its spectrum was spread over more than 3000 Hz. In other words, the jammer's

polarization angles were varied through 2π radians at up to $2\pi 4000$ radians per second. Similar results were obtained with the jammer's amplitude and polarization varying. These are given in Table I. They indicate that APN does work and can be a useful AJ countermeasure.

The study indicates that the algorithm can be, and should be, improved by using historical data to estimate the jammer's signal amplitude. It further indicates that the simulator can be improved by using more chips (of a transmitted bit) to determine the phase of the received signal. This would enable a larger variation in the jammer's signal amplitude. The study does show that the basic algorithm has significant capability in suppressing jammer signals.

Examination of the principal equation for calculating the detected phase of the transmitted bit (see Equation (3)) shows that, as the jammer's signal amplitude increases above the user's signal amplitude, the accuracy required in estimating the jammer's signal amplitude decreases. The converse is true. Accuracy in estimating the jammer's signal amplitude determines the amount that this signal is suppressed. Thus, APN appears to perform best as better performance is required.

8. RECOMMENDATIONS

This study has accomplished a great deal in demonstrating that APN can be useful as an AJ countermeasure. The next steps in its development should include developing a test bed that will include a QPSK transmitter and a pair of cooperative receivers — one with a horizontally polarized (HL) antenna and one with a vertically polarized (VL) antenna. A second transmitter should be used to radiate noise in the communication band via a pair of HL and VL antennas to simulate a jammer radiating a randomly polarized signal. Appropriately located "hooks" should be included in the receivers so that these signals can be simultaneously processed by an APNP. The comparable BER could be measured and a truly operational APN processor can be evaluated.

It is also advisable to carry-out the design of a COMSAT payload based on APN to accurately determine the cost and viability of such a device. In order to make this as economical as possible, the APN should be designed to operate at 2.4 kbps at either UHF or SHF so that its design would be readily transferable to an existing MILSATCOM satellite.

It may also be of interest to use APN in ground terminals to reduce self-jamming and incidental jamming effects. For example, a UHF terminal normally operates with a circularly polarized antenna. It is subject to accidental

downlink jamming due to the enormous number of UHF communication terminals. In this case, the desired signal polarization and amplitude is very well known and the interfering signals are not designed to defeat the algorithm. Use of APN will permit significant suppression of the interfering signals and improve polarization math to the received downlink signal. It would require that each user's terminal have a dual-polarized antenna. It is likely that the cost of modifying a terminal will justify the improved operational capability.

9. ACKNOWLEDGMENTS

Many people were helpful in contributing to the acceptance of APN as a viable AJ countermeasure. It would be wrong to attempt to mention them all here out of fear that some would be omitted. However, Mr. Robert Cook deserves special mention because he demonstrated a sincere interest in its development and provided the support necessary to carry-out this study. It is also true that the concept of using polarization to suppress jamming signals was first suggested to the principal author of this report by Dr. Walter E. Morrow, Director of the Massachusetts Institute of Technology's Lincoln Laboratory.

Bit Error Probability

Jammer Amplitude Estimate Error: ±2 dB
User Amplitude Estimate Error: ±2dB
User Polarization Error: ±π/8

Reference S/J=0 dB
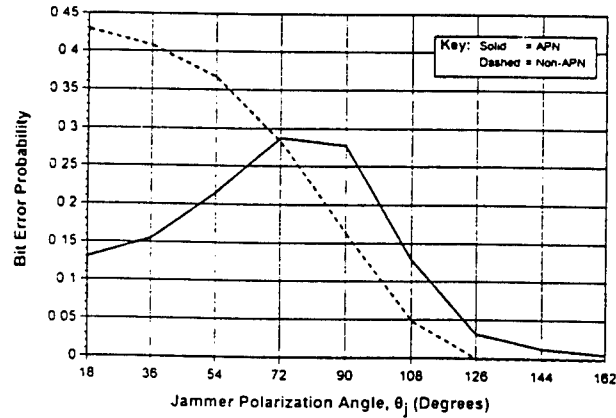
NOTE For each point the second jammer polarization angle, φⱼ, and the relative phase between jammer and user signals, ζ, were varied over 360° in 20° increments
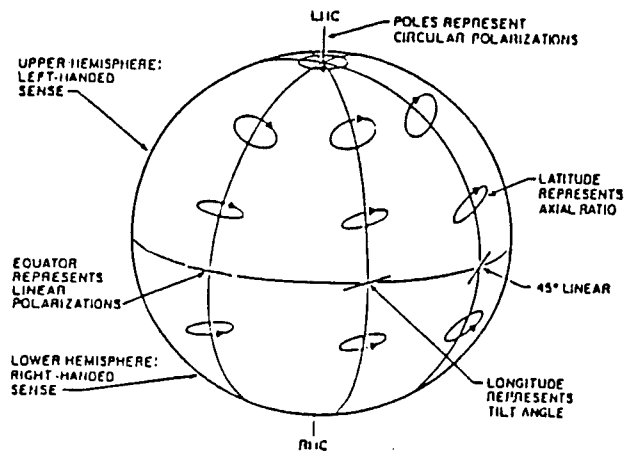
Figure 1

POINCARE POLARIZATION SPHERE

Figure 2

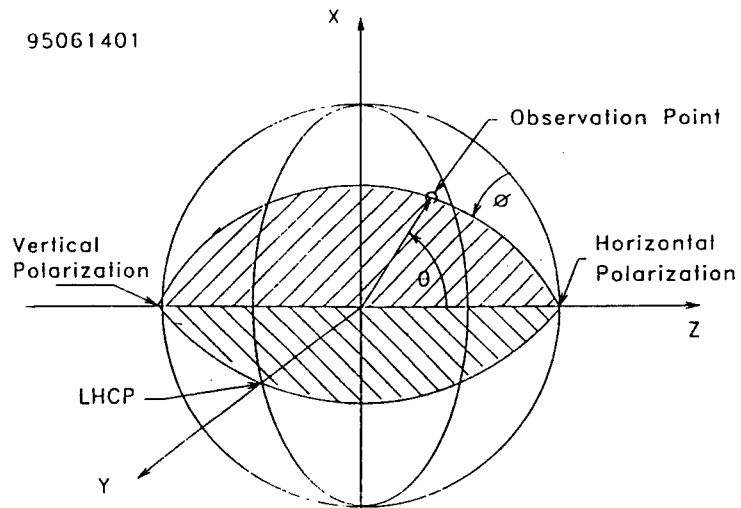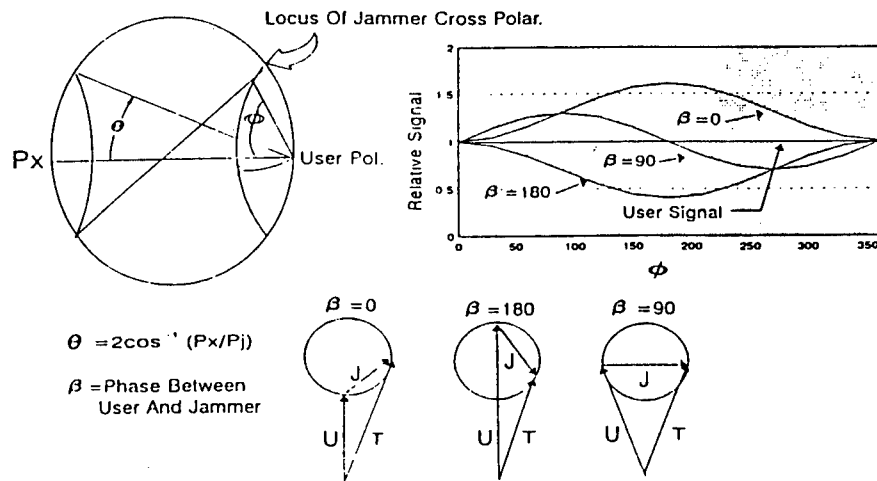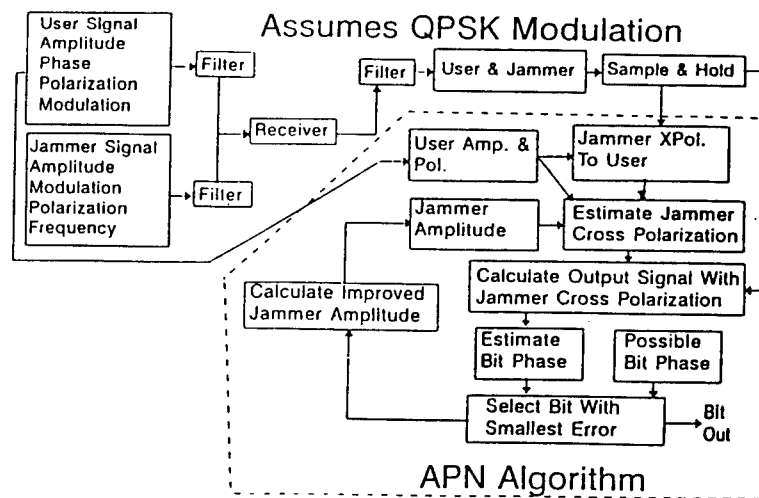# MODIFIED POINCARE POLARIZATION SPHERE
AND COORDINATE SYSTEM

95061401

Figure 3

Locus Of Jammer Cross Polar.

$\theta = 2\cos^{-1}(Px/Pj)$

β = Phase Between
User And Jammer

Figure 4

Assumes QPSK Modulation

Figure 5

Bit Error Sensitivity
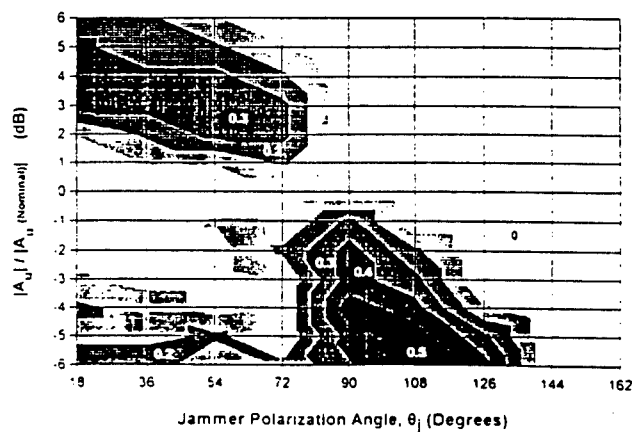
APN Algorithm Enabled

Correct Jammer Amplitude
Reference S/J=0 dB

Jammer Polarization Angle, θ_j (Degrees)

NOTE For each point the second jammer polarization
angle and the relative phase between jammer
and user signals were varied over 360° in 20°
increments

Figure 6a

Bit Error Sensitivity

APN Algorithm Enabled
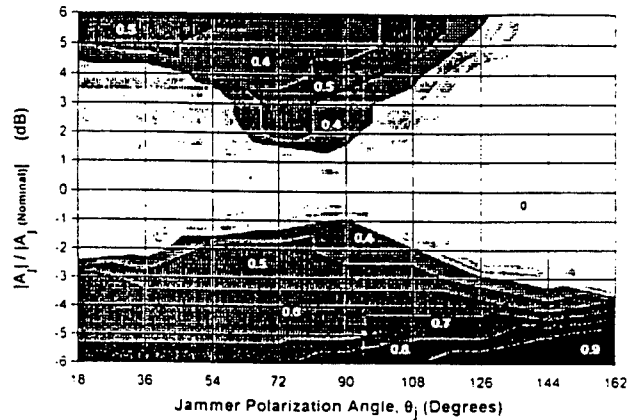
Correct User Amplitude and Polarization
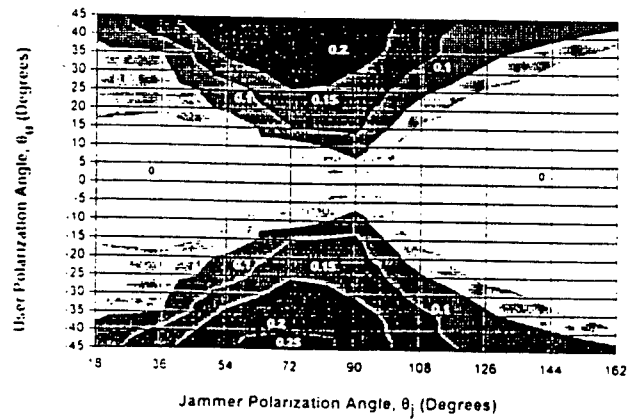Reference S/J=0 dB

Figure 6b

Bit Error Sensitivity

APN Algorithm Enabled

Correct User and Jammer Amplitude
Reference S/J=0 dB

NOTE For each point the second ammer polarization
angle b and the relative phase between ammer
and user signals ζ were varied over 360° in 30°
increments

Figure 6c

Bit Error Sensitivity

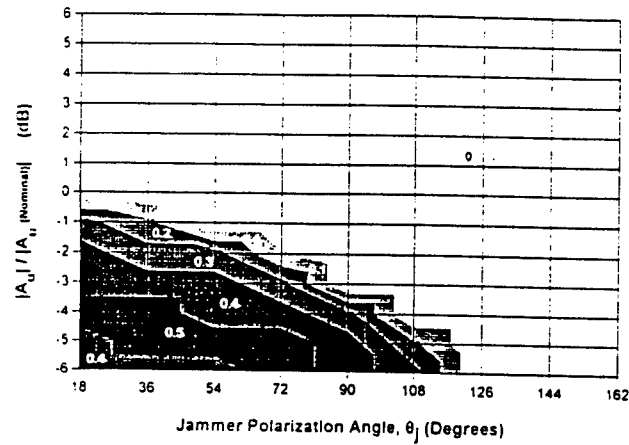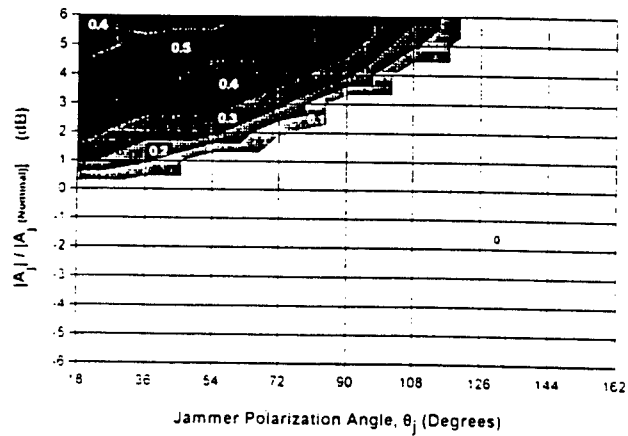## APN Algorithm Enabled

Correct Jammer Amplitude
Reference S/J=3 dB

Jammer Polarization Angle, θ_j (Degrees)

Figure 7a

Bit Error Sensitivity

APN Algorithm Enabled

Correct User Amplitude and Polarization
Reference S/J=3 dB

Jammer Polarization Angle, θ_j (Degrees)

NOTE For each point the second jammer polarization
angle and the relative phase between jammer
and user signals were varied over 360° in 20°
increments

Figure 7b

Bit Error Sensitivity

APN Algorithm Enabled

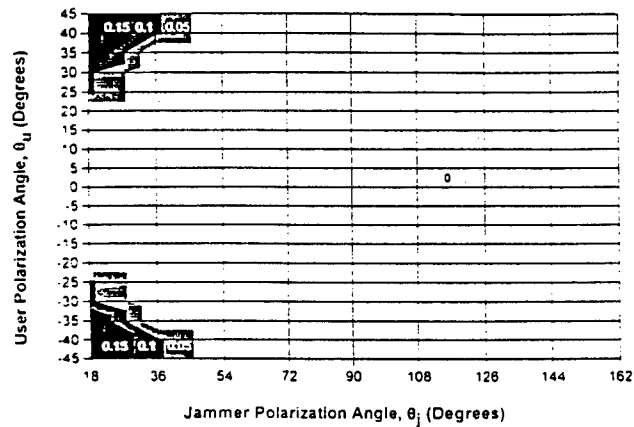Correct User and Jammer Amplitude
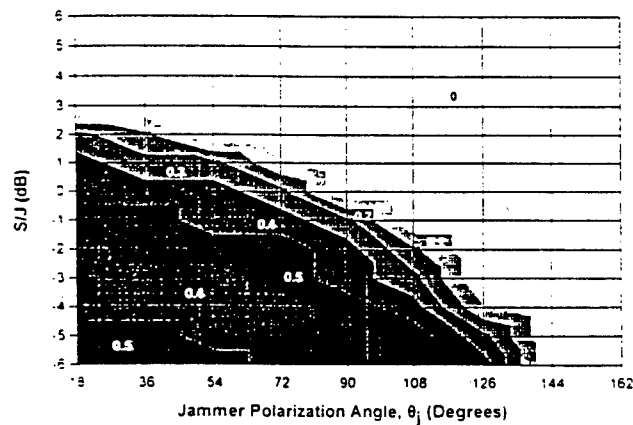Reference S/J=3 dB

Figure 7c

Bit Error Sensitivity

APN Algorithm Disabled

Correct Jammer Amplitude

NOTE For each point the second jammer polarization
angle θ, and the relative phase between jammer
and user signals ζ were varied over 360° in 20°
increments

Figure 8a

Bit Error Sensitivity

APN Algorithm Disabled
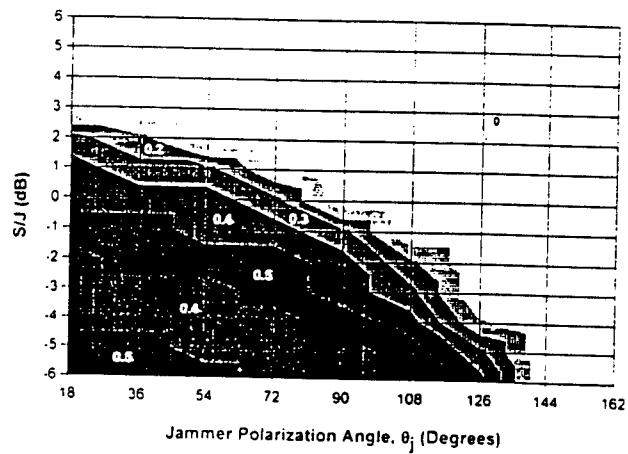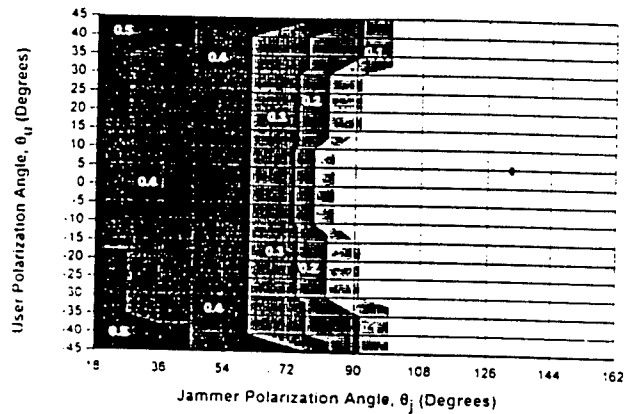
Correct User Amplitude and Polarization

Figure 8b

Bit Error Sensitivity

APN Algorithm Disabled

Correct User and Jammer Amplitude
Reference S/J=0 dB

NOTE: For each point the second jammer polarization angle 0 and the relative phase between jammer and user signals were varied over 360° in 20° increments

Figure 8c

Bit Error Sensitivity

APN Algorithm Disabled

Correct Jammer Amplitude
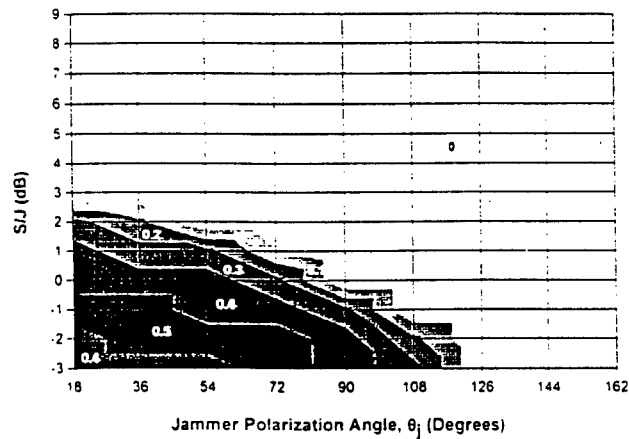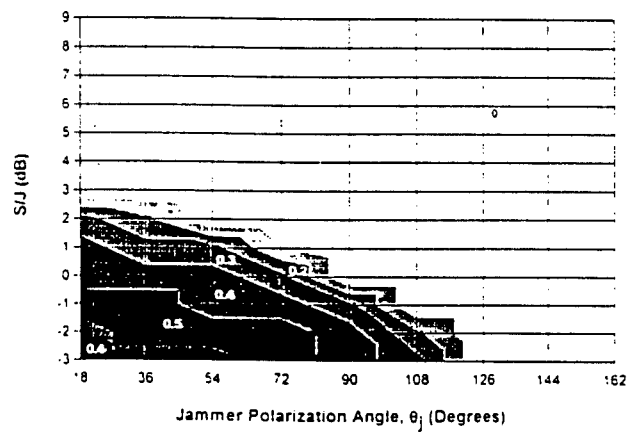

Figure 9a

Bit Error Sensitivity

APN Algorithm Disabled

Correct User Amplitude and Polarization

NOTE: For each point, the second jammer polarization
angle θ, and the relative phase between jammer
and user signals ζ, were varied over 360° in 20°
increments.

Figure 9b

451

Bit Error Sensitivity
APN Algorithm Disabled

Correct User and Jammer Amplitude
Reference S/J=3 dB

NOTE For each point the second jammer polarization
angle, θ_j, and the relative phase between jammer
and user signals, ζ, were varied over 360° in 20°
increments

Figure 9c

Probability Distribution
For Variation In
User's And Jammer's Amplitude, ±2 dB
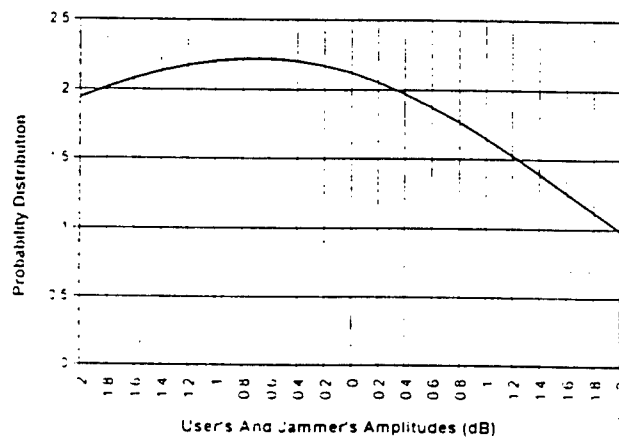
Figure 10a

Probability Distribution

For Variation In
User's Polarization Angle, θ_u, $\pm\pi/8$
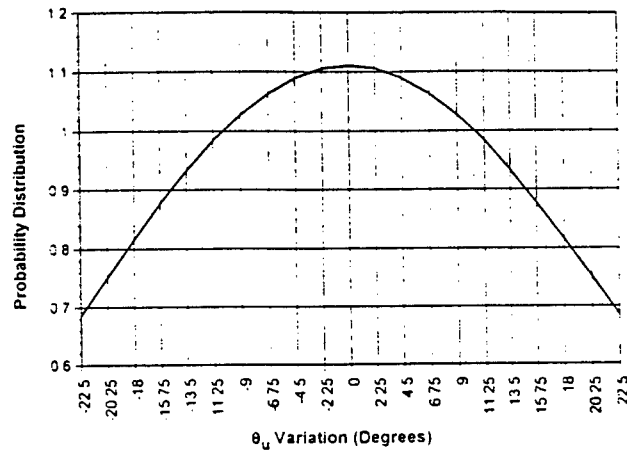
Figure 10b

Bit Error Probability

Jammer Amplitude Estimate Error: ± 2 dB
User Amplitude Estimate Error: ± 2dB
User Polarization Error: $\pm\pi/8$

Reference S/J=0 dB

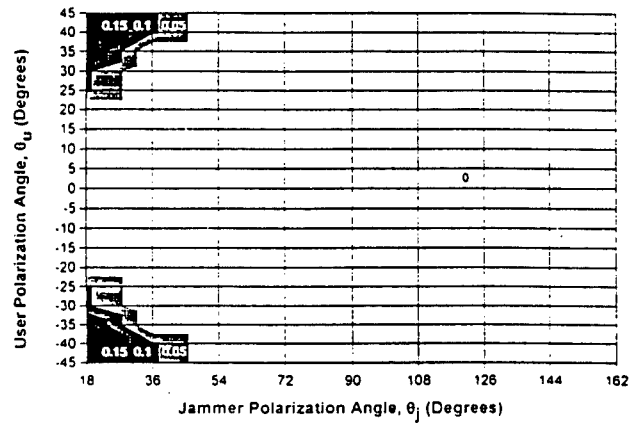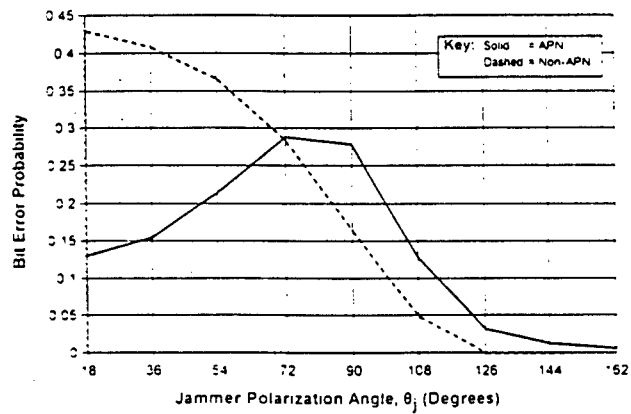NOTE For each point the second jammer polarization
angle θ and the relative phase between jammer
and user signals ζ were varied over 360° in 20°
increments

Figure 11a

Bit Error Probability

User Amplitude Estimate Error: ±2dB
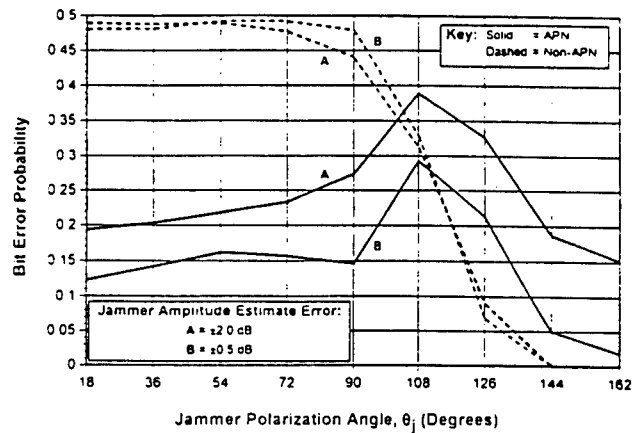User Polarization Error: ±π/8

Reference S/J = -3 dB

NOTE For each point the second jammer polarization
angle θ_j and the relative phase between jammer
and user signals ζ were varied over 360° in 20°
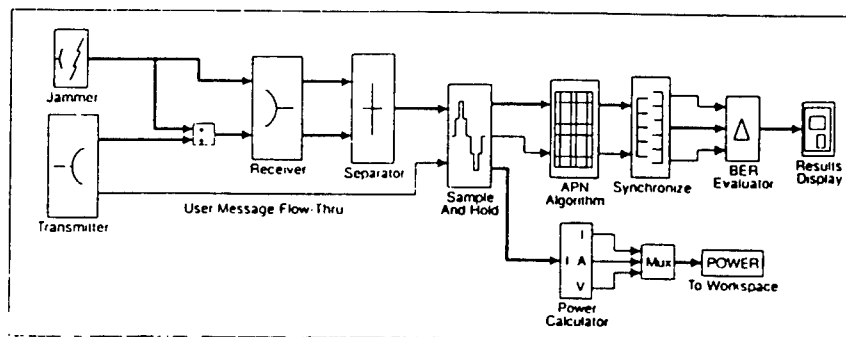increments

Figure 11b

APN Block Diagram

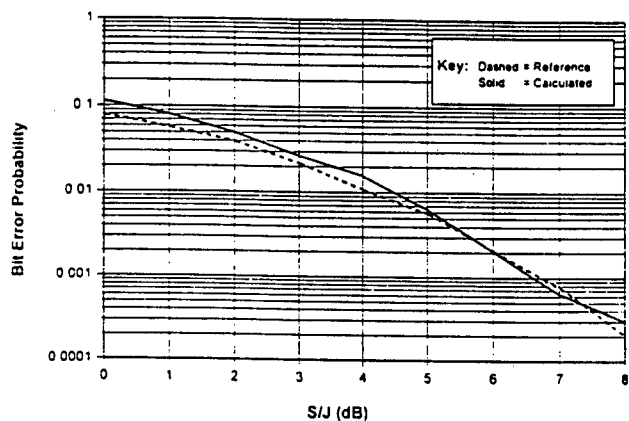Figure 12

Simulator
Bit Error Probability
Comparison

Figure 13

APN Algorithm Performance Improvement
Average User Power: 1.00 W, Variation in User Power: 0.07 W

100 Bits Transmitted Algorithm Non Damped				Jammer Power (Watts)		Bit Error Probability (Percent)	
Ao (Random)	θ Type	Range	F₁ (Hz)	Average	Variation	Non-APN	APN
0 V	Random	0 - π	500	1.00	0.07	25	0
			1000	1.00	0.07	25	0
			2000	1.00	0.07	19	0
			4000	1.00	0.07	18	1
±50 mV	Random	0 - π	500	1.00	0.10	25	5
			1000	0.99	0.11	25	9
			2000	0.99	0.12	19	7
			4000	1.00	0.12	17	10
	Fixed	π/4	500	1.00	0.10	55	8
			1000	0.99	0.11	51	7
			2000	0.99	0.12	51	20
			4000	1.00	0.12	52	40
±100 mV	Random	0 - π	500	1.01	0.16	21	10
			1000	0.99	0.19	17	14
			2000	1.00	0.20	15	14
			4000	1.01	0.21	14	30
	Fixed	π/4	500	1.01	0.16	50	22
			1000	0.99	0.19	43	23
			2000	1.00	0.20	43	39
			4000	1.01	0.21	38	58
±200 mV	Random	0 - π	500	1.04	0.30	24	26
			1000	0.99	0.35	16	52
			2000	1.02	0.38	15	53
			4000	1.04	0.39	15	53
	Fixed	π/4	500	1.04	0.30	46	33
			1000	0.99	0.35	33	46
			2000	1.02	0.38	38	56
			4000	1.04	0.39	15	17

Table 1

Neural Beamforming in the Presence of Near Field Scatterers

Hugh Southall and Peter Franchi

USAF Rome Laboratory

Electromagnetics and Reliability Directorate

RL/ERAA, 31 Grenier Street

Hanscom AFB, MA 01731-3010

Abstract

A radial basis function (RBF), three-layer, feed-forward, artificial neural network was used to calculate phase shifter settings for a C-band, phased-array antenna with the intention of accurately pointing the array main beam (on receive) regardless of the disturbing influence of a near field scatterer. This was demonstrated experimentally for two scenarios: a single scatterer fixed relative to the rotating array and located between the array and the transmitting horn; and, a single scatterer rotating synchronously with the array. The network was trained using phase fronts which were distorted by the near field scatterer. The network showed improved beam-pointing accuracy for both scenarios. The improvements were small since the effect of a single near field scatterer on the main beam pointing direction was not large. Therefore, we also used simulated data to more clearly illustrate the network's capability to accurately point the beam in the presence of near field scattering.

1 Introduction

Previously, we described RBF neural beamformers for single source direction finding (DF) [1, 2, 3, 4, 5], detection [6] and beam-steering [7]. Current research is focused on the control of the radiation pattern of a phased-array antenna using neural network techniques. Here, we describe a neural network which computes element phases to steer the array main beam to any angle in the antenna field of view (typically $-60° \leq \theta \leq +60°$).

We are primarily interested in operation with degraded or failed elements, conformal geometries and non-ideal environments with near field scattering. Previous research has addressed network performance where array elements were not operating properly [6]. This paper shows theoretically and experimentally that steering vectors calculated using an artificial neural network. trained using measured wavefronts (element phases) distorted by a near
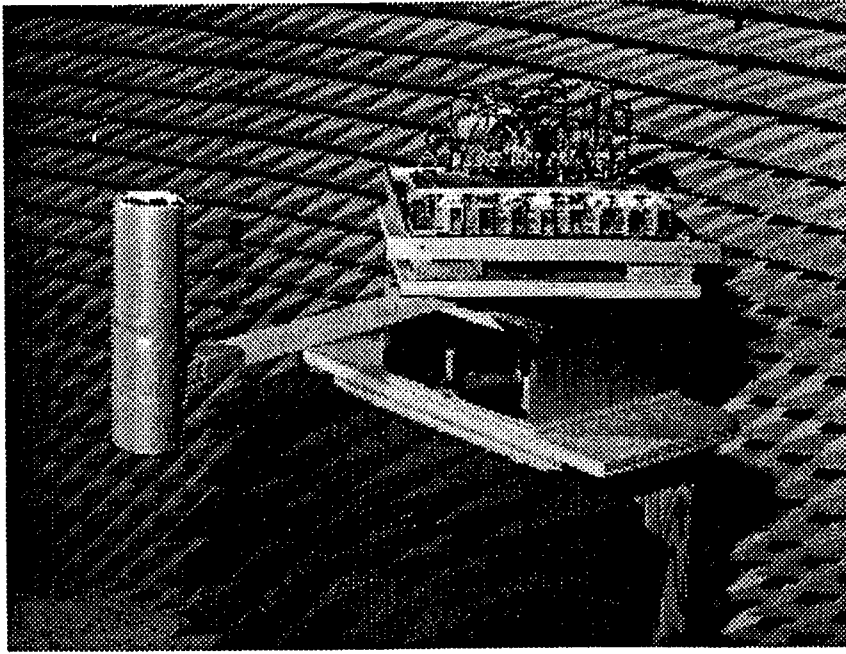
Figure 1: Rotating scatterer experiment. The scatterer is located to the left of the array and the source horn is located out of the picture to the left.

field scatterer, can more accurately steer the main beam than an array using ideal (uniform plane wave) steering vectors.

The paper begins with a description of the experiments. We then describe the network and training technique, present theoretical predictions and, finally, give experimental results.

2 Description of the Scattering Experiments

The C-band (7.1 GHz) antenna consisted of eight open-ended waveguide elements in a linear array and was described in detail in [7]. A ferrite phase shifter was behind each element. Measurements were taken with the array in an anechoic chamber as shown in Figure 1. The scatterer is located to the left of the array. The scatterer rotated synchronously with the array and was positioned relative to the array as shown in Figure 2. The array rotated in front of a stationary source horn located 12 feet away. We also used a scattering scenario where the scatterer was fixed relative to the rotating antenna. The fixed scatterer is shown in the anechoic chamber in Figure 3 and the geometry is shown in Figure 4.

The antenna patterns used in Section 5 to experimentally determine pointing errors are mechanically scanned patterns, ie. the main beam was electronically scanned to a fixed azimuthal angle (the commanded beam steering angle) by setting the eight phase shifters; the array was then mechanically rotated on the positioner. The mechanically scanned antenna pattern is the measured response at the output of an 8-way power combiner [7].
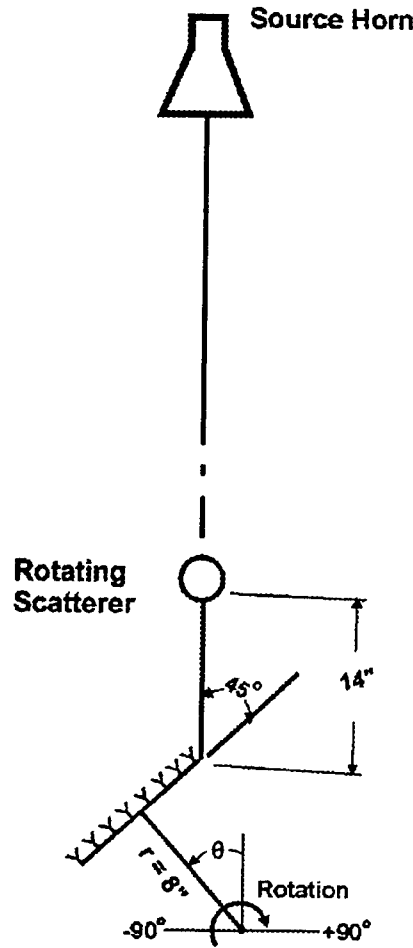
Figure 2: Geometry for the rotating scatterer experiment. The scatterer is attached to the right corner of the array on a 14 inch lever arm.

To train the neural network, the phase at each element (including the cumulative effects of coaxial feed lines and the power combiner) was measured as the array rotated from $\theta = -90°$ to $+90°$. As described in [7], the phase data is pre-processed to obtain the seven phase differences between the eight array elements. These measured phase differences (actually, the negative of the phase differences in order to obtain the conjugate phase gradient) are used as the desired outputs of the network at the selected training angles.

3 Neural Network Beam-Steering

Neural network beam-steering has been described in detail in [7]. The scalar network input is the commanded beam-steering (or scan) angle. The network has a single hidden layer of processing nodes with Gaussian radial basis functions (RBFs) whose outputs depend upon the distance between the scan angle and the node center located in the input space
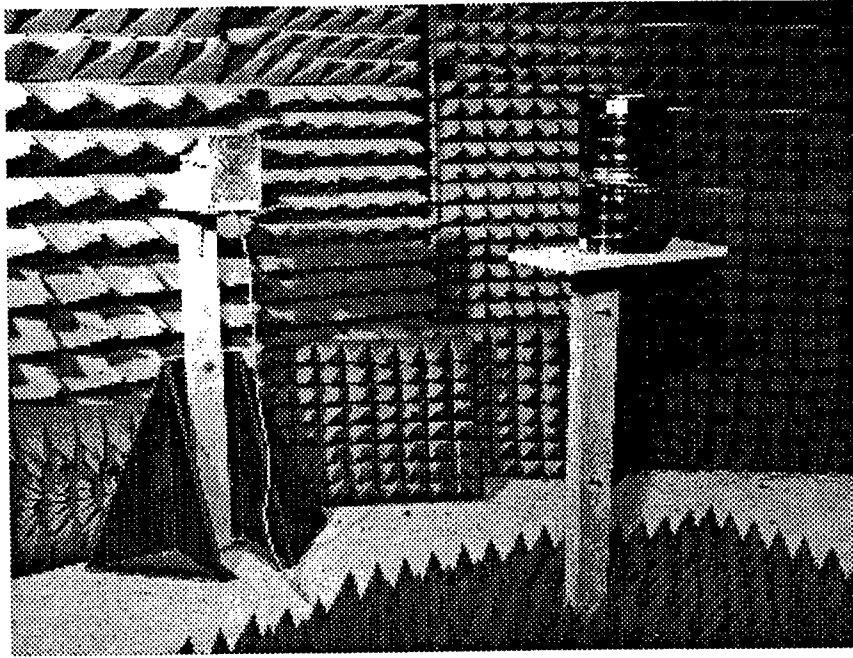
Figure 3: Fixed scatterer experiment. The scatterer is in the foreground with the source horn in the background to the left. The array is located to the right, out of the picture.

of commanded steering angles. The outputs of the RBFs also depend upon the spread parameter, σ. The input space of commanded steering angles is just the antenna field of view ($-60°$ to $+60°$). The output of the ith Gaussian, for steering angle θ, is given by

$$\phi_i(\theta) = e^{-\frac{(\theta-\theta_i)^2}{2\sigma^2}}, \tag{1}$$

for $i = 1, 2, ..., t$. The θ_i are the t Gaussian centers at the t training angles in the input space. We typically used training angles every 5° over the field of view.

Network outputs are the seven phase differences. Postprocessing converts the phase differences to eight digital states (eight bit words) which are sent to phase shifter drivers. The drivers set the eight phase shifters to steer the array main beam.

The role of the network is function approximation [8]. To effectively perform its task, the network is trained using a process called supervised learning described in [7, 9, 10]. In supervised learning, we present the network with teaching examples which consist of beam-steering angles and corresponding "target" or "desired" output vectors. Each target vector consists of the negative of the seven measured phase differences. The network is trained at these angles to output the target vectors. The measured phase differences contain the information in the distorted phase fronts caused by near field scatterers, therefore the network has "learned about" these distortions and uses this information to accurately point the main beam. The trained network generalizes from the training data and can output steering vectors which accurately steer the beam between training angles.
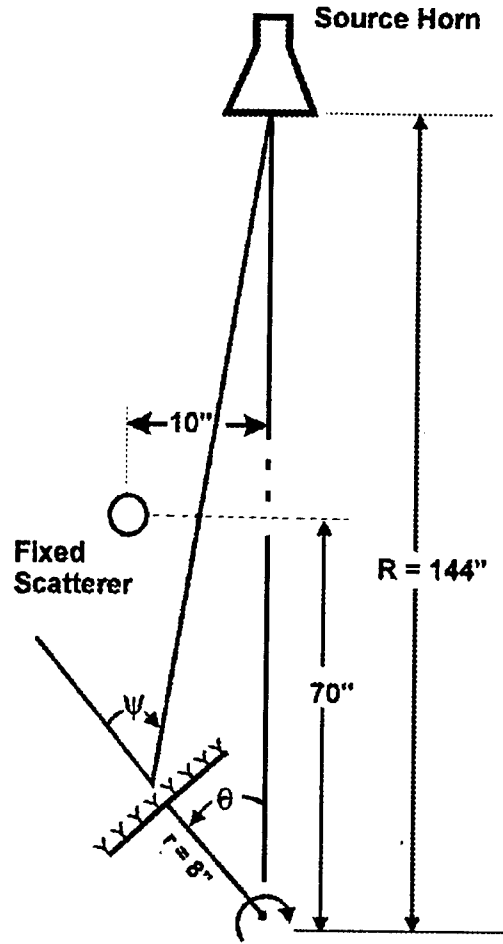
Figure 4: Geometry for the fixed scatterer experiment.

4 Theoretical Predictions (Simulations)

The electric field at each array element can be calculated assuming that the source horn radiates a spherical wave. For free space propagation, the field at the ith element is given by

$$E_i = \frac{e^{jkR_i}}{R_i} , \tag{2}$$

where $k = \frac{2\pi}{\lambda}$ and R_i is the distance from the horn to the phase center of the ith element. (approximately 136 inches). Since $\lambda = 1.66$ inches and the array length is D $= 10.4$ inches, the far field criteria ($\frac{2D^2}{\lambda}$) is about 130 inches. Therefore, there will be a slight curvature to the phase front when it hits the array. However, this effect is very small and the quadratic phase error does not squint the beam when ideal (plane wave) steering vectors are used.

To model the effect of a near field scatterer, we assume that the field incident upon the

scatterer is re-radiated isotropically from the scatterer's center at some fraction of the value of the magnitude of the incident field. We use $\eta = .3$ since this resulted in simulated element phases most similar to measured element phases. At the ith element, the total field is the sum of the direct field from Equation 2 and the field from the scatterer.

$$E_{sum} = \frac{e^{jkR_i}}{R_i} + \eta E_{inc} \frac{e^{jkr_i}}{r_i}$$ (3)

E_{inc} is the electric field incident upon the scatterer from the horn. A fraction, η, is scattered, and travels a distance r_i from the scatterer to the ith element. This can be modeled based on the geometries described in Section 2 for both rotating and fixed scattering scenarios. The geometries determine the R_i and the r_i for any element at any azimuth angle θ (see Figure 2).

The presence of a scatterer in the near field of an antenna distorts the arriving wave front so that it is no longer a uniform plane wave. If it were a uniform plane wave, the phase difference between array elements would be constant and equal to

$$\Delta\phi = \frac{2\pi}{\lambda} d \sin \psi,$$ (4)

where ψ is the angle between the incident wave front and the normal to the array as shown in Figure 4 and d is the distance between elements (about $.78\lambda$).

As described in Section 3, the neural network is trained to output phase differences which are used to calculate the phase commands required to steer the main beam. For a uniform plane wave, all seven phase differences are equal to the negative of Equation 4. The phase differences are not all equal when we place a scatterer in the near field of the antenna. For the fixed scatterer scenario, simulated phase differences, calculated using the element phases predicted by Equation 3, are shown as an * in Figure 5. Note the deviation from the ideal phase difference. We also show measured phase differences in Figure 5 as an o for the same steering angle. The agreement between simulated and measured is not exact since the scatterers are not the ideal point sources assumed in our simplified analysis. We calculated ideal steering vectors and then we calculated steering vectors using the neural network trained on simulated data for the fixed scatterer to obtain the two simulated patterns in Figure 6. Note that the network steering vectors result in a beam pointed in exactly the commanded steering direction of 30°, while ideal vectors result in a squinted beam. We call the difference between observed and commanded steering angles the pointing error.

As a baseline, we calculate the pointing error over the antenna field of view for both neural network and ideal steering vectors for $\eta = 0$, ie. no scatterer. Note that since $\theta \neq \psi$, (see Figure 4) an error will be incurred even with no scatterer, since we calculate phase differences based on $\frac{2\pi}{\lambda} d \sin \theta$. Of course, we could calibrate for this by calculating the correct phase
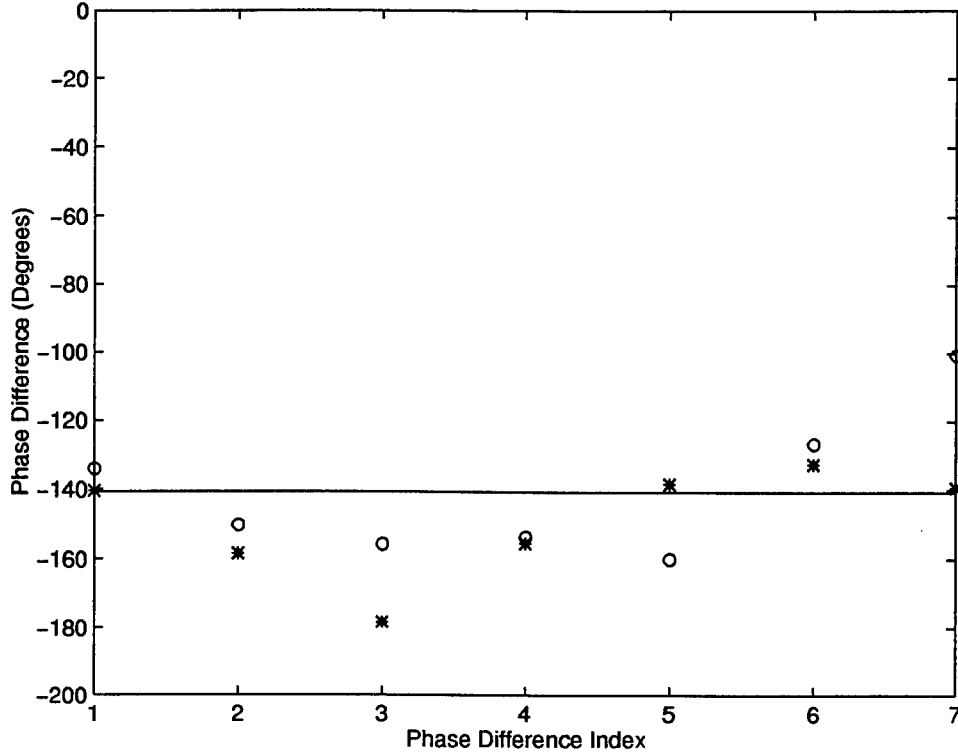
461

Figure 5: Phase differences at a 30° azimuth angle for the fixed scatterer. Solid line is the ideal phase difference. Simulated phase differences calculated from the geometry in Figure 4 are indicated by *. Measured phase differences for the fixed scatterer experiment are indicated by o.

difference, since we can easily find ψ as a function of the azimuthal angle θ; however, that is not the point. We want to show that the network, trained on raw data, can account for effects which ordinarily require careful calibration. The neural network automatically accounts for the fact that $\theta \neq \psi$, since the network has been trained using measured data which, naturally, includes the fact that the array phase center is offset from the center of rotation. The baseline case is shown in Figure 7.

Using simulated data including the presence of the rotating scatterer, with $\eta = 0.3$, we calculated the pointing error as described above. Pointing errors for both ideal and network predicted steering vectors are shown in Figure 8. The simulated pointing error for the fixed scatterer, with $\eta = 0.3$, is shown in Figure 9.

5   Experimental Results

Beam pointing errors were measured experimentally for the two scattering scenarios discussed in Section 2. We set the phase shifters using element phases calculated from ideal steering vectors and from neural network predictions. Phase shifters were set to the closest available
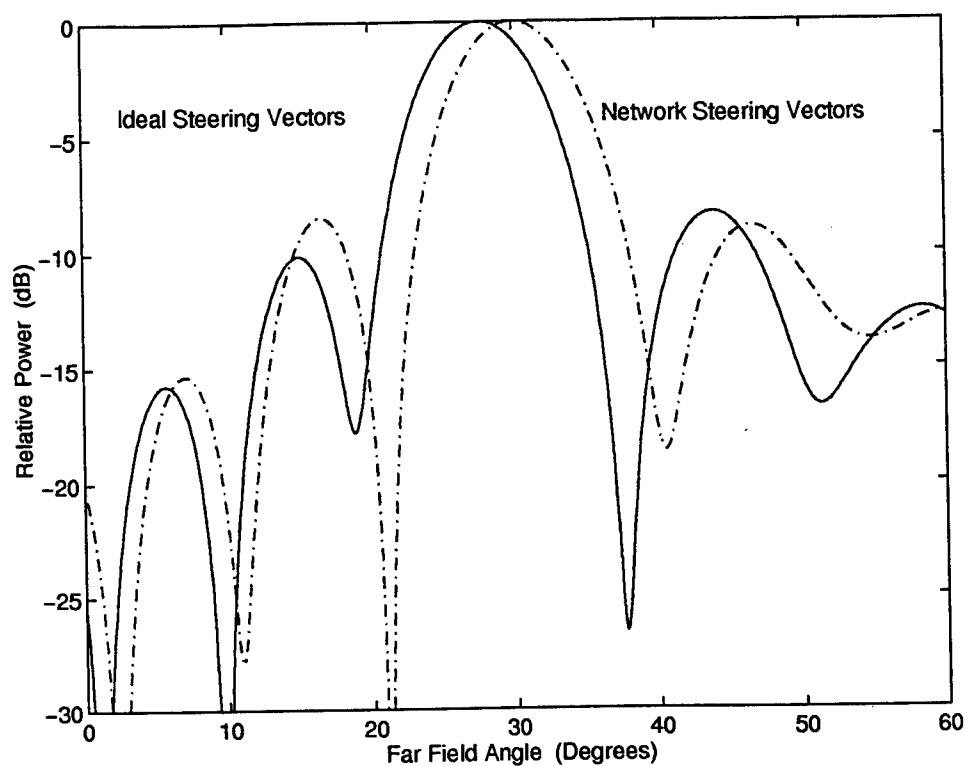
Figure 6: Resulting patterns using the simulated phase differences in Figure 5. Solid line is the array pattern produced by using ideal steering vectors. Dot-dashed line is for network-predicted steering vectors.

insertion phase from a look up table of insertion phase versus state, since the insertion phase versus state was highly non-linear for our Reggia-Spencer phase shifters [7]. There were 256 states for approximately 360° of insertion phase, therefore, the phase shifters could be set with an accuracy of about 1°.

Measured pointing errors for the rotating scatterer and the fixed scatterer are shown in Figure 10 and Figure 11 respectively. For the rotating scatterer, we used commanded steering angles of 25°, 30°, 35°, 40°, 45° and 50° to determine the pointing errors. For the fixed scatterer, we used commanded steering angles of 0°, 5°, 10°, 15°, 20°, 25° and 30°. The experimental beam-pointing angle was determined by taking the average of the measured beam peak angle and the angle corresponding to the mid-point of the measured 3 dB beamwidth.

6 Conclusions

We developed a neural network which computed phase shifter settings to steer the array main beam in the presence of a single near field scatterer. The concept was demonstrated theoretically by showing that the network could correct for distorted phase fronts and accurately
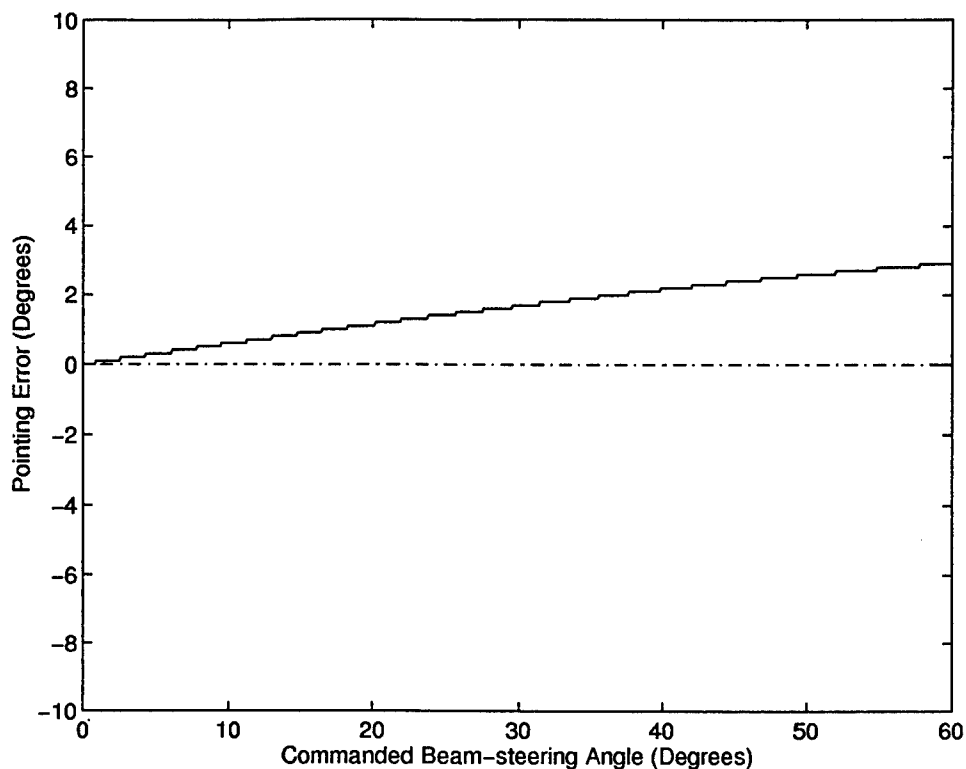
Figure 7: SIMULATED beam-pointing error for the baseline case: no scatterer. Solid line is for ideal steering vectors. Dot-dashed line is for network predicted steering vectors. The error for the ideal vectors is due to the fact that $\psi \neq \theta$, since the phase center of the array is not directly over the center of rotation and the source horn is not infinitely far from the array.

steer the main beam. We also measured phase-steered antenna patterns to experimentally determine pointing errors. Measured pointing errors were reduced by 22% and 24% for rotating and fixed scatterers respectively by using the network generated steering vectors.

7   Acknowledgments

References

[1] H. Southall, J. Simmers, and T. O'Donnell. Direction Finding in Phased Arrays with a Neural Network Beamformer. *IEEE Transactions on Antennas and Propagation.*
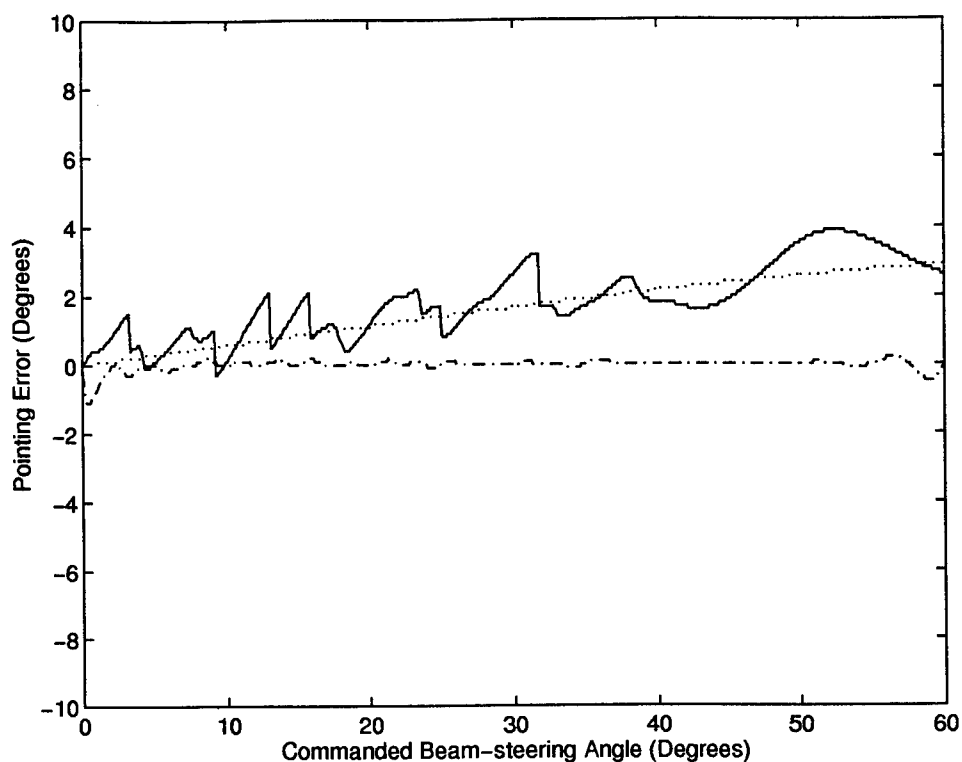
Figure 8: SIMULATED beam-pointing error for the rotating scatterer. Solid line is for ideal steering vectors. Dot-dashed line is for network-predicted steering vectors. Baseline case is shown dotted for comparison.

43(12):1369–1374, December 1995.

[2] J. A. Simmers and T. O'Donnell. Adaptive RBF Neural Beamforming. In *Proceedings of the 1992 IEEE Mohawk Valley Section Command, Control, Communications, and Intelligence (C3I) Technology & Applications Conference*, pages 94–98. IEEE, June, 1992.

[3] T. O'Donnell, J. Simmers, and D. J. Jacavanco. Neural Beamforming for Phased Array Antennas. In *Proceedings of the 1992 Antenna Applications Symposium (Robert Allerton Park)*, Griffiss AFB, NY, September, 1992. USAF Rome Laboratory.

[4] J. Simmers, H. L. Southall, and T. O'Donnell. Advances in Neural Beamforming. In *Proceedings of the 1993 Antenna Applications Symposium (Robert Allerton Park), University of Illinois*, Griffiss AFB, NY, September, 1993. USAF Rome Laboratory.

[5] H. L. Southall, J. A. Simmers, and T. O'Donnell. Phased Array Antennas with Neural Network Signal Processing. In *Proceedings of the 1994 Antenna Applications Symposium (Robert Allerton Park), University of Illinois*, Griffiss AFB, NY, September. 1994. USAF Rome Laboratory.
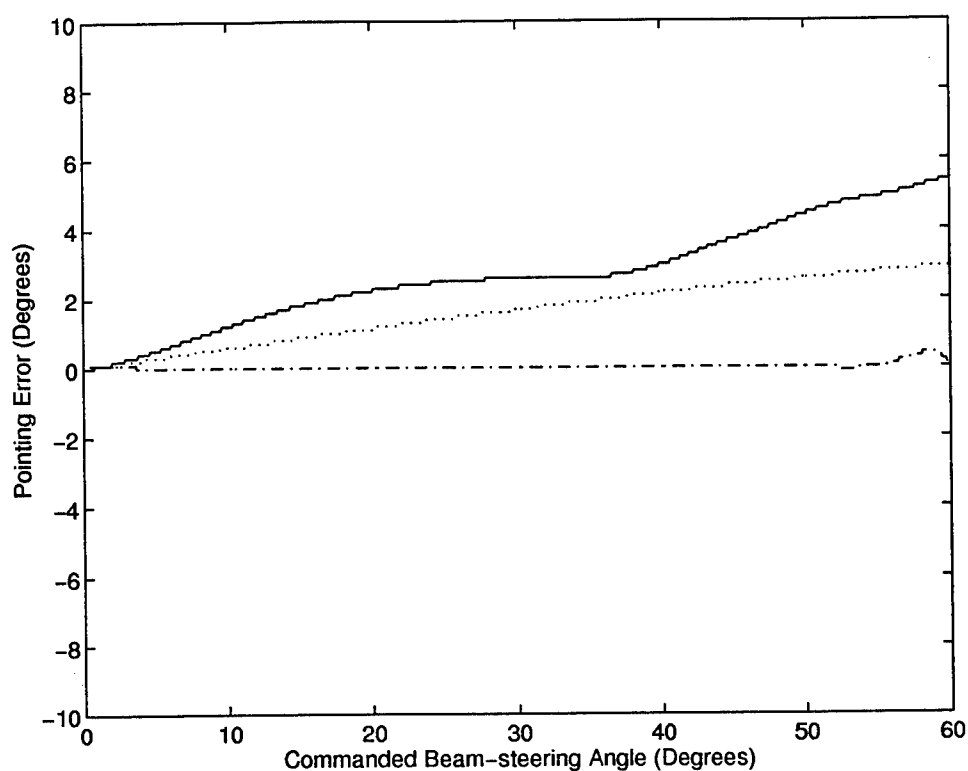
Figure 9: SIMULATED beam-pointing error for the fixed scatterer. Solid line is for ideal steering vectors. Dot-dashed line is for network-predicted steering vectors. Baseline case is shown dotted for comparison.

[6] T. O'Donnell, J. Simmers, H. Southall, and T. Klemas. Neural Network Antenna Processing for Detection and Direction Finding. In *The Record of the IEEE 1995 International Radar Conference*, pages 213–218. IEEE, May 1995.

[7] H. Southall, S. Santarelli, E. Martin, and T. O'Donnell. Neural Network Beam-Steering for Phased-Array Antennas. In *Proceedings of the 1995 Antenna Applications Symposium (Robert Allerton Park), University of Illinois*, Griffiss AFB, NY, September 1995. USAF Rome Laboratory.

[8] T. Poggio and F. Girosi. Networks for Approximation and Learning. *Proceedings of the IEEE*, 78(9):1481–1496, September 1990.

[9] A. C. Tsoi. Multilayer Perceptron Trained Using Radial Basis Functions. *Electronics Letters*, 25(19):1296–1297. September 14 1989.

[10] S. Lee. Supervised Learning with Gaussian Potentials. In B. Kosko, editor, *Neural Networks for Signal Processing*, pages 189–227. Prentice Hall, Englewood Cliffs, NJ, 1992.

Figure 10: MEASURED pointing error for the rotating scatterer. Solid line is for ideal steering vectors (RMS error = 2.36 degrees). Dot-dashed line is for network-predicted steering vectors (RMS error = 1.85 degrees).
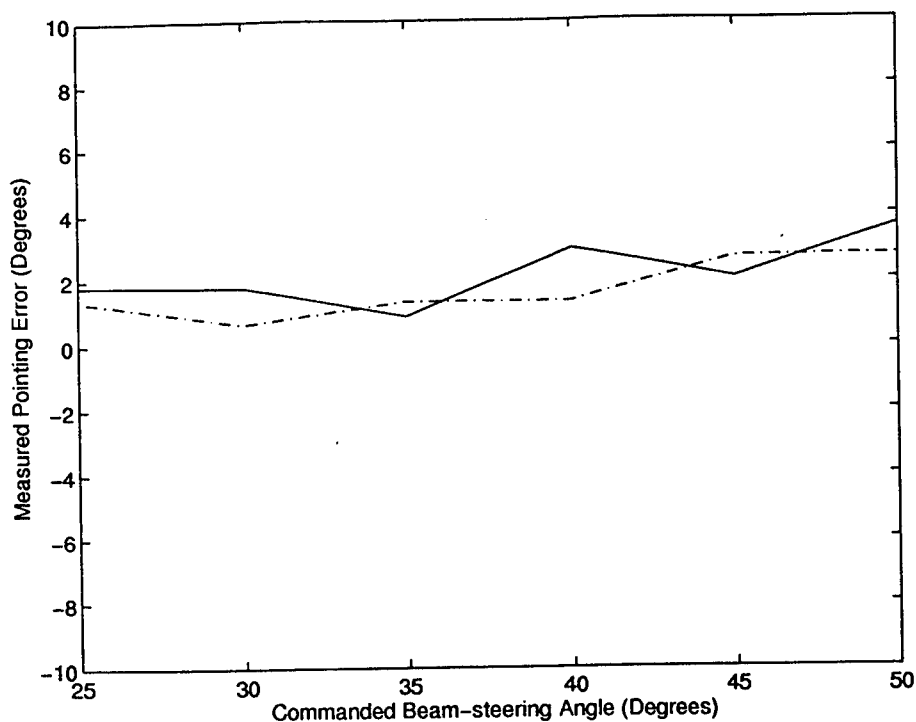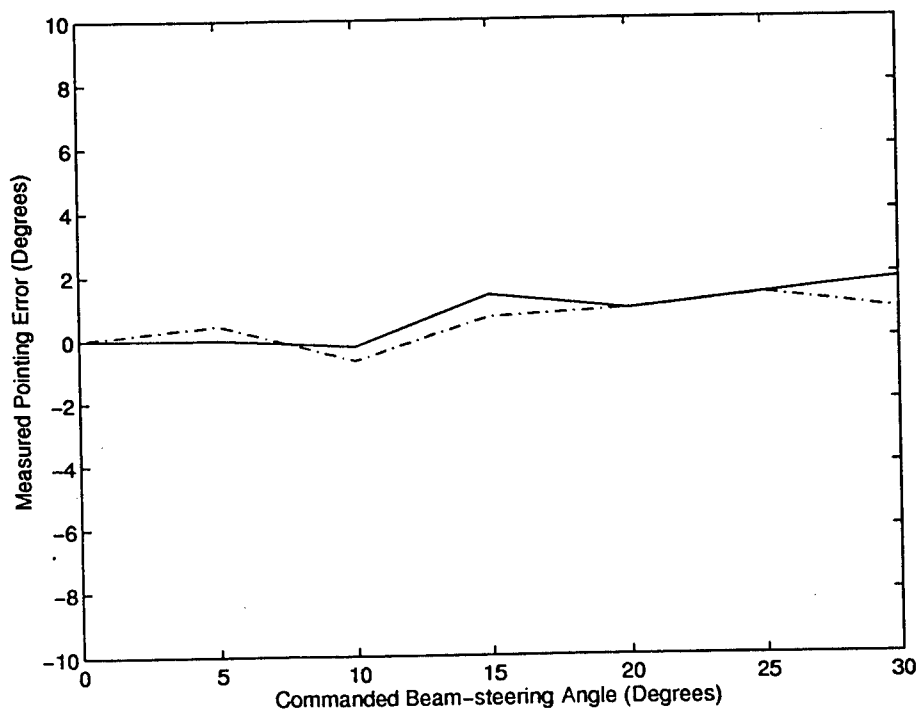

Figure 11: MEASURED pointing error for the fixed scatterer. Solid line is for ideal steering vectors (RMS error = 1.064 degrees). Dot-dashed line is for network-predicted steering vectors (RMS error = .809 degrees).

467

MULTIOBJECTIVE OPTIMIZATION OF ELECTROMAGNETIC DEVICES USING PARETO GENETIC ALGORITHMS

D. S. Weile and E. Michielssen

Center for Computational Electromagnetics
Department of Electrical and Computer Engineering
University of Illinois at Urbana-Champaign
Urbana, Illinois 61801
Tel : (217) 333-3803   Fax : (217) 333-8986
e-mail: michiels@decwa.ece.uiuc.edu

Abstract

Pareto genetic algorithms are applied to the study of choice tradeoffs between reflectivity and thickness in the design of multilayer microwave absorbers, and low beamwidth and sidelobe level in antenna array design. Specifically the design of arrays which are thinned or use digital phase shifters are studied as are absorbers composed of a given number of layers of absorbing materials selected from a predefined database of available materials. Three types of Pareto genetic algorithms for absorber synthesis are introduced and compared to each other, as well as to methods operating with the weighted Tchebycheff method for Pareto optimization.

1. Introduction

Mathematical search procedures have been used in electromagnetics either as stand alone design methods or as part of more interactive design techniques. Very often, however, these methods only optimize one aspect of a design; for instance, they minimize the reflectivity of an absorber or lower the sidelobes of an antenna. In many engineering applications, it is not sufficient to perform such a single minded optimization as several goals may need to be balanced such as low cost and high performance. Because of the inherent conflict between goals in engineering optimization problems, an engineer is often forced to carry out prolonged experiments to determine the best tradeoffs feasible within given design constraints. Designs which represent such optimal tradeoffs are known in the optimization literature as *Pareto optimal* as they are optimal in the sense that there exists no design in the search space which is better with regard to all objectives considered [1-3].

The set of all such designs forms a manifold known as the *Pareto front.* Knowledge of the Pareto front in a particular problem implies of all of the worthwhile tradeoffs inherent to a problem.

This study uses Genetic Algorithms (GAs) to find the Pareto front representing tradeoffs in two separate design problems: finding optimal combinations of narrow beamwidth and low sidelobe levels in several different types of antenna arrays, and finding optimal combinations of thinness and absorbtivity in broadband microwave absorber problems. GAs are nonlinear, stochastic algorithms based loosely upon the Darwinian theory of descent with modification by natural selection [4, 5]. Though absolute convergence of the algorithm is not guaranteed, the stochastic nature of GAs makes them less susceptible to convergence to weak local optima [4]. Another useful property of GAs comes from the fact that they typically operate on a binary encoding of the search variables. For the absorber design problem, they may draw from a database of available materials with arbitrary characteristics, ensuring that the design found by the algorithm can be realized. Additionally, the use of a population of designs makes GAs a natural candidate for Pareto optimization since in a single run they can find an entire front of designs.

This study is organized as follows: Section 2 describes several GAs for Pareto optimization. Section 3 demonstrates the technique with applications to antenna arrays and broad band microwave absorbers. Section 4 presents the conclusions of the study.

2. Pareto Genetic Algorithms

This section describes the actual optimization techniques used in this paper. Section 2.1 describes the simple, one objective GA as an introduction. Section 2.2 then mathematically defines Pareto optimization and describes in general how the simple GA must be modified to accomplish Pareto optimization. Section 2.3 then describes three specific Pareto GA implementations.

469

2.1 Single objective genetic algorithms

As discussed in the introduction, this study uses GAs to find a discrete approximation of the Pareto front. GAs themselves are a class of algorithms which can be applied to reliably find strong local or global optima of a function over a given domain of interest. Loosely based on the principle of survival of the fittest, GAs are complicated like Nature herself: They are nonlinear, stochastic and highly parallel in structure [4, 5].

Unlike more standard classical optimization algorithms, GAs do not operate on single design candidates, but simultaneously act on a whole population of N_p designs. The designs are represented in the population by encoding salient design parameters into bit strings of length N_b called *chromosomes*, after which an initial population of N_p candidate designs is created at random. The GA operates by repeated application of genetic operators to entire populations resulting in a succession of populations of improved designs. Though the GA literature abounds with examples of different operators to improve the GA's ability to search this prodigious expanse of design possibilities, all GAs include three basic operators: *selection, crossover* and *mutation* [4, 5].

The selection operator implements the principle of survival of the fittest, and by so doing is the primary operator responsible for convergence of the algorithm [4, 5]. All designs in the population are evaluated according to an *objective function f* which measures the quality of a solution to a given problem, and represents the quantity optimized by the GA. Selection creates a new generation of N_p designs by allotting more positions in the new population to those designs with favorable objective function values, and eliminating those with poor values. Though there exist several schemes in the literature for accomplishing this, this study uses only the two most common: *tournament selection* in which the better of two randomly chosen designs in placed into the new population until the population is full, and *roulette-wheel selection* which fills each spot in the new population with designs in the old population with probability proportional to their fitness.

470

Once selection has produced a new population of size N_p, the crossover operator constructs another new population of size N_p by combining information from successful designs. Chromosome pairs are picked at random from the population and are crossed over with some predetermined probability p_c usually between 0.8 and 1. For each pair that is to be crossed over, a random crossover site is picked between the kth and $k+1^{th}$ bits of the pair. The selected chromosomes then exchange their $k+1^{th}$ through $N_b{}^{th}$ bits yielding children chromosomes. Chromosome pairs not chosen for crossover are copied unmodified into the next generation [4, 5].

Finally, the mutation operator is applied to prevent premature convergence of the GA, by performing a logical NOT on a few bits in the population randomly selected with probability $0.0005 < p_m < 0.01$. Mutation is not the primary search instrument of the GA but is included mainly to prevent the loss of information initially contained in chromosomes that die off prematurely, but which contain information which may prove useful to the GA in later generations [4, 5].

Selection, crossover and mutation are repeatedly applied to successive populations until some termination criterion is satisfied. Usually, the GA is stopped either when it meets some preset design goal, when a predetermined number or generations has passed, or when no substantial improvement in the objective function value is observed.

2.2 Pareto optimization and genetic algorithms

Though the problems described in this study only involve the minimization of two parameters, the concept of Pareto optimality (and by implication, Pareto GAs) can be applied to design problems of any number of criteria. Imagine a design problem with a vector $\mathbf{f} = (f^1, \cdots, f^G)$ of G objectives, each of which we wish to minimize, and two candidate designs with objective function vectors $\mathbf{f}_1$ and $\mathbf{f}_2$ respectively. Design 1 is said to dominate design 2 (or $\mathbf{f}_2$ is said to be inferior to $\mathbf{f}_1$) if for all $i \in \{1, 2, \ldots, G\}$ $f_1^i \le f_2^i$, and

there exists at least one i such that $f_1^i < f_2^i$. A design is said to be *nondominated* if there exists no feasible design in the entire solution space which dominates it. The Pareto front is the set of all such nondominated designs [1-4, 6].

Several advanced operators have to be added to the single objective GA if the Pareto front is to be located in only one run. These operators assist the GA in pushing the population to the edge of the feasible region, and to ensure the designs spread evenly and densely on the front. Since a Pareto GA must return a curve dense enough to accurately represent the Pareto front and diverse enough to present the full range of possible designs, these operators are essential to the proper behavior of the GA.

A design evaluated according to multiple objectives is considered Pareto optimal if it is nondominated—that is, if there exists no feasible design which is simultaneously superior with respect to all objectives. The definition of Pareto optimality therefore imposes two separate (but intimately related) challenges to the traditional GA: Pareto GAs must (i) select designs on the basis of their relative Pareto dominance standing in the population, and (ii) force the population to converge to a diverse Pareto front, not a single design. If diversity is not actively encouraged in the GA, chromosomes in the population tend to unevenly distribute themselves along the Pareto front resulting in instability known as *genetic drift*. Since the GA is more likely to promulgate traits of the most prevalent designs in a given population, these designs garner more representatives in the population which may result in the loss of diversity. Any successful Pareto GA must both capably evaluate the dominance relations in the population, as well as maintain diversity for the length of the GA run.

Besides Schaeffer's initial attempts at Pareto optimization[7, 8], all other Pareto GA implementations proposed in the literature [6, 9, 10] are variations based on a suggestion from Goldberg [4] that the twin problems of Pareto GAs be handled separately. For the problem of selection according to Pareto dominance, Goldberg suggested the use of

nondomination ranking. Specifically, Goldberg delineates a scheme where all nondominated population members are assigned a rank of one and removed from the population. The nondominated members in the remaining part of the population are then assigned a rank of two, and so on until the entire population is ranked. Each design then receives a fitness based on its nondomination ranking.

To prevent the effects of genetic drift, Goldberg suggests the use of *niching* methods, which were originally developed so that GAs could converge to more than one peak in multimodal problems, but since have been applied to general GA search and Pareto GAs as well [4, 11]. The oldest niching method, called *crowding*, was introduced in DeJong's thesis [11]. Crowding preserves niches by preferentially eliminating over-represented designs so that when new designs are placed in the population novel designs in the current generation have a higher probability of survival than hackneyed ones [4, 11]. An explanation of the crowding algorithm may be found in [4].

Another method for maintaining diversity in the population is *fitness sharing* [4, 12]. Fitness sharing is based on Malthusian competition between organisms for limited resources in relation to the preservation of species under natural selection. In a fitness sharing GA, besides calculating the objective function value f_i for each chromosome i, the GA calculates a *niche count* m_i which measures the density of the population surrounding that chromosome. The niche count is calculated according to the formula

$$m_i = \sum_{j=1}^{N_p} Sh(d_{i,j})$$ (1)

where *Sh(d)* is a monotonically decreasing function of x such that $Sh(0) = 1$ and $d_{i,j}$ is a distance measure between designs i and j. In this study, we use the *triangular sharing function*

$$Sh(d) = \begin{cases} 1 - \dfrac{d}{\sigma_{share}} & d < \sigma_{share} \\ 0 & d \geq \sigma_{share} \end{cases} \tag{2}$$

where σ_{share} is a designer chosen *niche radius*. This study uses *phenotypic sharing*, or, in other words, $d_{i,j}$ measures some distance between designs themselves. This leads to an ambiguity in the definition of phenotype, as this means that phenotypic sharing may be performed on either (i) the design parameters as *decoded* from the chromosome, or (ii) the chromosomes objective function vector. In Pareto GAs, type (ii) phenotypic sharing is usually preferred because we seek a large variety of different optimal tradeoffs in *objective function* space, but we care little whether or not different points on the Pareto front represent large differences in the design of the absorber itself [6, 10]. To ensure that the metric does not weigh objectives inequitably, we normalize it so that all objectives are effectively scaled to range between 0 and 1 [6, 9, 10].

Once the m_i have been calculated, chromosomes are reproduced assuming an objective function value of $f_{shared,i} = \dfrac{f_i}{m_i}$ instead of f_i so that the GA will not allow all chromosomes to converge to one solution, but will try to achieve a steady state where any two chromosomes i and j in the population will satisfy [4, 12]

$$f_{shared,i} = \frac{f_i}{m_i} = \frac{f_j}{m_j} = f_{shared,j} \tag{3}$$

In Pareto GAs, this is used to get a better representation of the front since at equilibrium, all nondominated designs will need to spread out or die off. Lastly, we note that the entire population need not be used to calculate the niche counts m_i; simply sampling some percentage of the population to estimate the niche count usually suffices.

2.3 Three Pareto genetic algorithms

This section details three specific implementations of the Pareto GA. The first implementation just uses the nondomination ranking scheme described in section 2.3 with crowding and tournament selection. We refer to this as the Crowded Tournament Pareto GA (CTPGA).

The second Pareto GA used is known as the Niched Pareto GA (NPGA) [10]. Instead of explicitly using nondomination ranking, the NPGA uses *Pareto domination tournaments* which work by comparing two randomly chosen designs to a randomly chosen comparison set of t_{dom} designs to determine their relative optimality. If no determination can be reached, the winner is chosen to be the design with less similarity to the designs already chosen for the next generation. A full description of the algorithms used can be found in [10] and [13].

Lastly, we implement a third Pareto GA based on Nondominated Sorting GA (NSGA) [9] which executes Goldberg's suggestions most faithfully. In the NSGA, designs are ranked using the nondomination ranking of section 2.3. The designs ranked one are given a nominal fitness value f_{R1} and then their niche counts m_i are calculated. Their shared fitness is then calculated in the usual way $f_{shared,i} = \dfrac{f_{R1}}{m_i}$. The designs ranked two are then assigned a nominal fitness value f_{R2} less than the lowest shared objective function value of those ranked one, and then undergo sharing themselves. This process is continued until all members of the population are assigned a fitness value, and then roulette wheel selection is used to create the next population. In our implementation of the NSGA, the nominal fitness value of groups ranked less than one was actually chosen to be equal to the lowest shared fitness value of the previous group. This choice of nominal fitness value assignment tempers the quick selective action of the NSGA a bit and helps allow the GA to maintain diversity in the population. Additionally, Srinivas and Deb use type (i)

phenotypic sharing in the NSGA; we, however, use type (ii) because as mentioned in Section 2.3 we desire great variety in design response, but not necessarily in the physical construction of the device.

3. Numerical Results

In this section we present the results of applying the techniques applied in the last section to different devices. Section 3.1 describes the using the NSGA to design antenna arrays for low sidelobes and a narrow beam, and Section 3.2 explains the use of Pareto GAs for the optimization of microwave absorbers.

3.1 Antenna array design

Arrays have been extensively studied as a means of increasing the directivity of single antenna elements. To facilitate the inexpensive design of arrays, engineers often have to cope with restrictions on design freedom imposed by economic considerations. For instance, many arrays today are fed using only the phase of the different elements to fashion the characteristics of the antenna array [14]. Such "phase-only" designs are quite often further restricted by the use of inexpensive digital phase shifters in the design [15, 16]. Another such constrained design technique involves the thinning (or selective turning off) of array elements to build an inexpensive array [17, 18]. Within any of these design constraints, a successful communications antenna often must have a narrow beam and low sidelobe level to aid in the exclusion of noise. Because these two goals conflict, this is an ideal problem for the application of Pareto GAs.

First, the NSGA was applied to the problem of thinning a symmetric 40 element array of isotropic antennas spaced one half wavelength apart. Because of the low number of parameters involved in this problem, the space could easily be searched exhaustively to find the true Pareto front. As can be seen in Figure 1, the GA does an admirable job in

solving the problem, using less than one tenth of the function evaluations needed for the exhaustive search.

This problem was then extended to show what could be gained by going to arrays with more elements. Figure 2 shows a plethora of Pareto curves obtained by running the problem for different numbers of elements.

Lastly, the Pareto GA is applied to the design of a 16 by 16 element array of isotropic radiators with three bit phase shifters again spaced one half wavelength apart. The Pareto curve, as well as the maximum reduced sidelobe level design are shown in Figure 3.

3.2 Microwave absorber design

Multilayer microwave absorptive coatings are often used in concert with other devices for reducing the radar cross section of a wide diversity of objects, and they find use in variegated applications ranging from stealth to anechoic chambers. In general, such coatings must not only suppress reflection over a wide band of frequencies, but also need to be thin to be practical and economical. These two goals—thinness and low reflectivity—very often conflict, and designers are forced to rely upon experience or prolonged experiments to determine what tradeoffs are feasible within prescribed design constraints. In cases where thinness and absorption do conflict, the "optimal" design with respect to high absorption may be too thick or expensive to be practical. An engineer is therefore often interested in the thinnest absorber he can build with a given level of reflection suppression. This is therefore another good example of a Pareto optimization problem. Specifically, we wish to design absorbers where given:

- A fixed number of layers,
- A database of available materials with any arbitrary frequency dependence [19],
- A number of incident angles where reflection is to be suppressed, and
- Frequencies across a band over which the absorber is to operate,

the GA will find Pareto optimal tradeoffs between absorber thickness and maximum reflection over the frequency band and incident angles.

First, all three algorithms described in section 2.3 are applied to the design of absorbers in the lower frequency band of 0.2-2 GHz. Pareto fronts are shown in Fig. 4 which shows that the CTPGA was able to keep much diversity over the curve, as well as relatively dense front. The NPGA, however, was unable to maintain such a compromise as shown in Figure 4. Figure 4 also shows that the best front was provided by the NSGA.

The NSGA outperforms the CTPGA and NPGA, but also is the most computationally expensive algorithm we describe, followed by the CTPGA and finally the NPGA. This is quite evident from the algorithms themselves. Both the NSGA and CTPGA involve the ranking of the entire population, the NPGA does not. Additionally, sharing is more expensive than crowding making the NSGA the most expensive algorithm of all. For the above design problem CPU time on a DEC Alpha workstation for the NSGA, the CTPGA and the NPGA were about 1 hour, 50 minutes and 45 minutes, respectively. The differences in time are not very drastic, however, because most of the computational expense comes in calculating the objective function and all three algorithms calculated it exactly the same number of times.

In addition to comparing the various Pareto GAs to each other, we present a comparison of the Pareto front obtained by the NSGA to those produced by iterated runs of Simulated Annealing (SA) and the standard GA optimizing the classical Tchebycheff formula [1]. Like a GA, SA is a stochastic algorithm which has been applied to electromagnetic problems [20, 21], but it is based on the minimization of energy states in a Boltzmann distribution rather than the theory of evolution [22, 23]. A full description of the algorithm may be found in [23]. The results of this experiment, shown in Figure 5 show clearly that for this problem, the NSGA is superior to classical techniques.

We next turned to the 2-8 GHz band and found that all three Pareto GAs behaved[*] much like in the previous example (Fig. 6). Figure 7 gives the frequency response for two particular designs on the curve. Note once again that the Pareto GA returns a whole profusion of designs in only one run. All of these designs may be stored in a database where they could easily be retrieve for future design problems with different criteria.

As a final test of the NSGA, we applied it to a problem which included multiple incidence angles as well as frequencies. The reflectivity objective function was redefined to be the highest reflection over that entire 9-11 GHz band and at incidence angles ranging from 0 to 30 degrees for both TE and TM polarizations. The Pareto curve obtained by the three algorithms is shown in Figure 8.

4. Conclusions

This study has presented three techniques for finding Pareto optimal designs of microwave absorbers and antenna arrays using genetic algorithms. The methods employ niching techniques in combination with nondomination ranking or tournaments to present the designer of absorptive coatings or array antenna with all of the best tradeoffs possible in only one run of the algorithm. Upon executing a Pareto GA, the designer has an abundance of optimal designs available to her/him which may be applied to vastly different types of design problems. A comparison of the several Pareto GA techniques for the problem of designing absorbers was given, and results indicate that the NSGA is the best algorithm most suited to this problem. The NSGA also compared favorably with both GA and SA Pareto optimization schemes based on the Tchebycheff weighing method. For all considered design problems, the NSGA was found to be a powerful tool for confidently designing antireflective coatings as economically as possible.

5. Acknowledgments

References

[1] J. L. Cohon, *Multiobjective Programming and Planning*. New York: Academic Press, 1978.

[2] J. L. Cohon and D. H. Marks, "A review and evaluation of multiobjective programming techniques," *Water Resources Research*, vol. 11, no. 2, pp. 208-219, 1975.

[3] R. E. Steuer, *Multiple Criteria Optimization: Theory, Computation, and Application*. Malabar, FL: Krieger, 1989.

[4] D. E. Goldberg, *Genetic Algorithms in Search, Optimization and Machine Learning*. Reading, MA: Addison-Wesley, 1989.

[5] J. H. Holland, *Adaptation in Natural and Artificial Systems*. Ann Arbor, MI: University of Michigan, 1975.

[6] C. M. Fonseca and P. J. Fleming. "Multiobjective genetic algorithms," *Proceedings of the IEE Conference on Genetic Algorithms for Control Engineering*, London, May 1993, pp. 6/1-5.

[7] J. D. Shaffer, "Some experiments in machine learning using vector evaluated genetic algorithms," Ph.D. dissertation, Vanderbilt University, 1984.

[8] J. D. Shaffer. "Multiple objective function optimization with vector evaluated genetic algorithms," *Proceedings of the First International Conference on Genetic Algorithms*, 1985, pp. 93-100.

[9] N. Srinivas and K. Deb, "Multiobjective Optimization Using Nondominated Sorting in Genetic Algortihms," *Evolutionary Computation*, vol. 2, no. 3, pp. 221-248, 1995.

[10] J. Horn, N. Nafpliotis and D. E. Goldberg. "A niched Pareto genetic algorithm for multiobjective optimization," *Proceedings of the First IEEE Conference on Evolutionary Computation, IEEE World Congress on Computational Intelligence*, Jun. 1994, pp. 82-87.

[11] K. A. DeJong, "An analysis of the behavior of a class of genetic adaptive systems," Ph.D. dissertation, University of Michigan, 1975.

[12] D. E. Goldberg and J. J. Richardson. "Genetic algorithms with sharing for multimodal function optimization," *Genetic Algorithms and Their Applications: Proceedings of the Second International Conference on Genetic Algorithms*, 1987, pp. 41-49.

[13] C. K. Oei, D. E. Goldberg and S. J. Chang, "Tournament selection, niching, and the preservation of diversity," University of Illinois at Urbana-Champaign, 1991.

[14] J. F. DeFord and O. P. Gandhi, "Phase only synthesis of minimum peak sidelobe patterns for linear and planar arrays," *IEEE Transactions on Antennas and Propagation*, vol. 36, no. 2, pp. 191-201, 1988.

[15] R. L. Haupt, "Optimum quantised low sidelobe phase tapers for arrays," *Electronics Letters*, vol. 31, no. 14, pp. 1117-1118, 1995.

[16] M. Shimizu. "Determining the excitation coefficients of an array using genetic algorithms," *Proceedings of the IEEE Antennas and Propagation Society International Symposium*, Seattle, WA, Jun. 1994, pp. 530-533.

[17] R. L. Haupt, J. J. Menozzi and C. J. McCormack. "Thinned arrays using genetic algorithms," *Proceedings of the IEEE Antennas and Propagation Society International Symposium*, Ann Arbor, MI, Jun. 1993, pp. 712-715.

[18] D. J. O'Neill. "Element placement in thinned arrays using genetic algorithms," *Proceedings of OCEANS '94*, Brest, France, Sept. 1994, pp. II/301-306.

[19] E. Michielssen, J.-M. Sajer, S. Ranjithan and R. Mittra, "Design of lightweight, broad-band microwave absorbers using genetic algorithms," *IEEE Transactions on Microwave Theory and Techniques*, vol. 41, no. 6/7, pp. 1024-1031, 1993.

[20] J. Pesque, D. Bouche and R. Mittra, "Optimization of multilayered anti reflection coatings using an optimal control method," *IEEE Transactions on Microwave Theory and Techniques*, vol. 40, no. 9, pp. 1789-1796, 1992.

[21] J. Simkin and C. W. Trobridge, "Optimizing electromagnetic devices combining direct search methods with simulated annealing," *IEEE Transactions on Magnetics*, vol. 28, no. pp. 1343-1348, 1992.

[22] S. Kirkpatrick, J. C. D. Gelatt and M. P. Vechi, "Optimization by simulated annealing," *Science*, vol. 220, no. pp. 671-680, 1983.

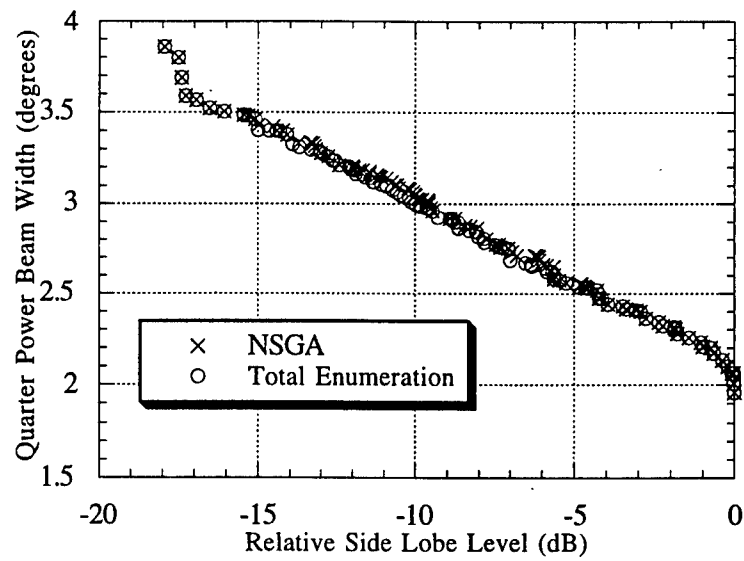[23] L. Davis, *Genetic Algorithms and Simulated Annealing*. London: Pittman, 1987.

Figure 1. A comparison of the NSGA to a complete enumeration of the search space.
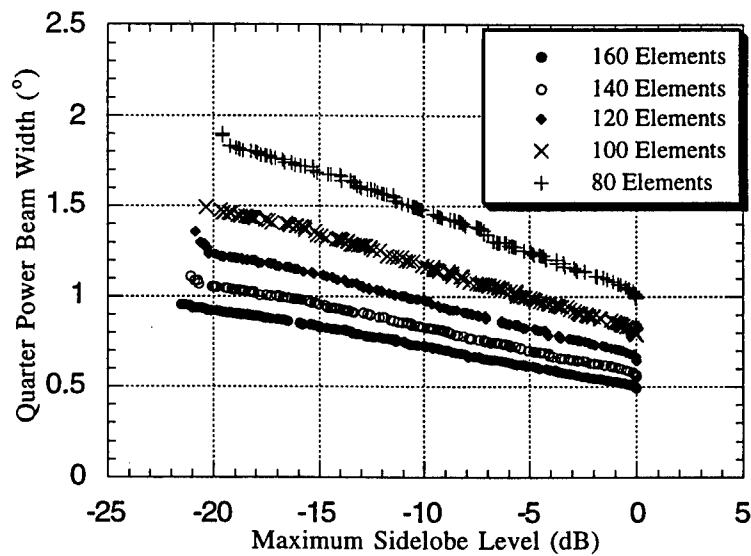

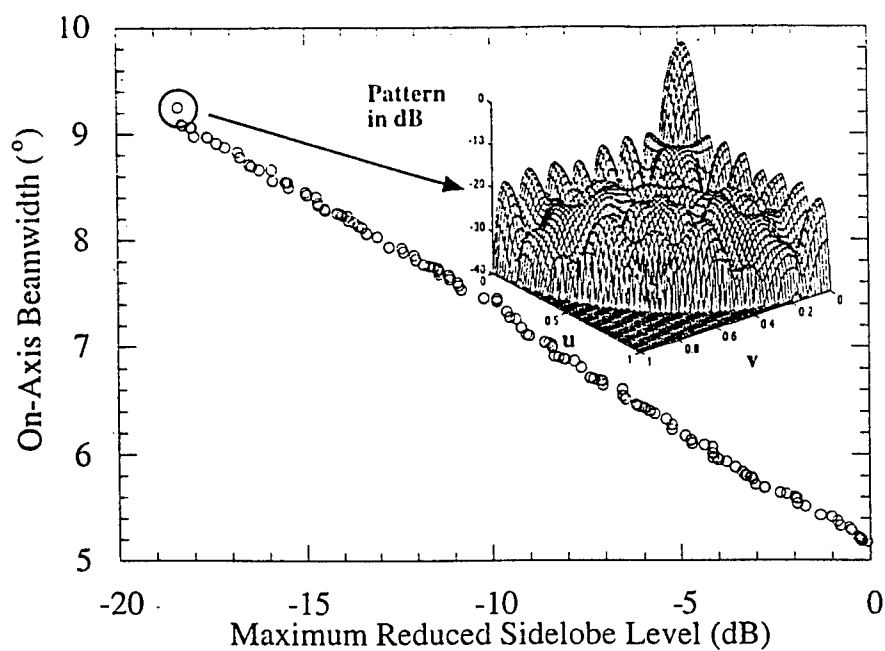Figure 2. Pareto fronts obtained by the NSGA for thinning arrays of varying numbers of elements.

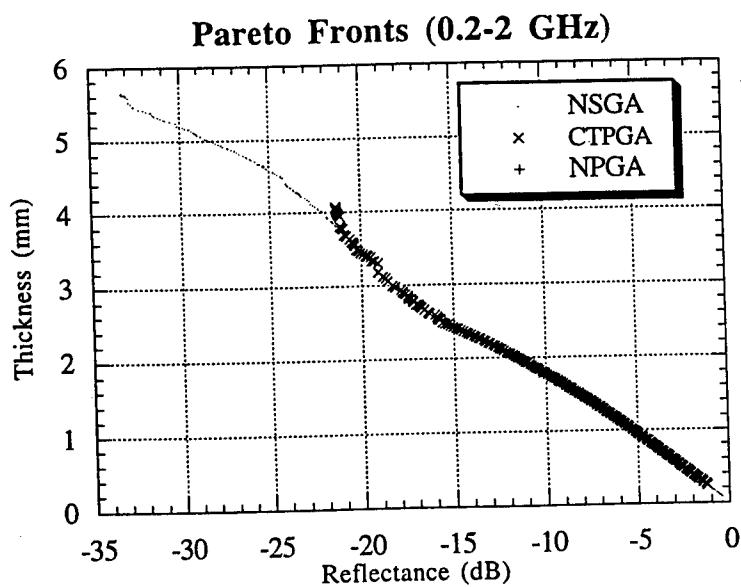Figure 3. Results of applying the NSGA to a 16X16 array problem with digital phase shifters.

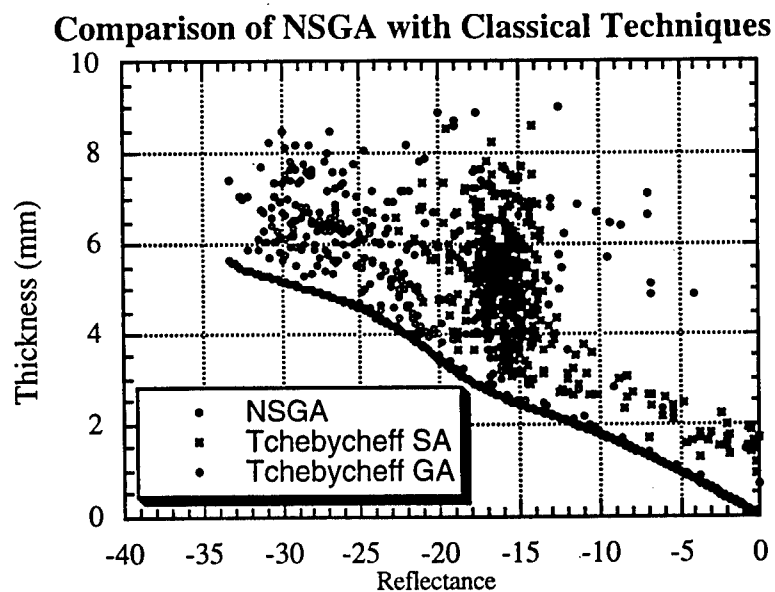Figure 4. The three algorithms applied to an absorber problem.
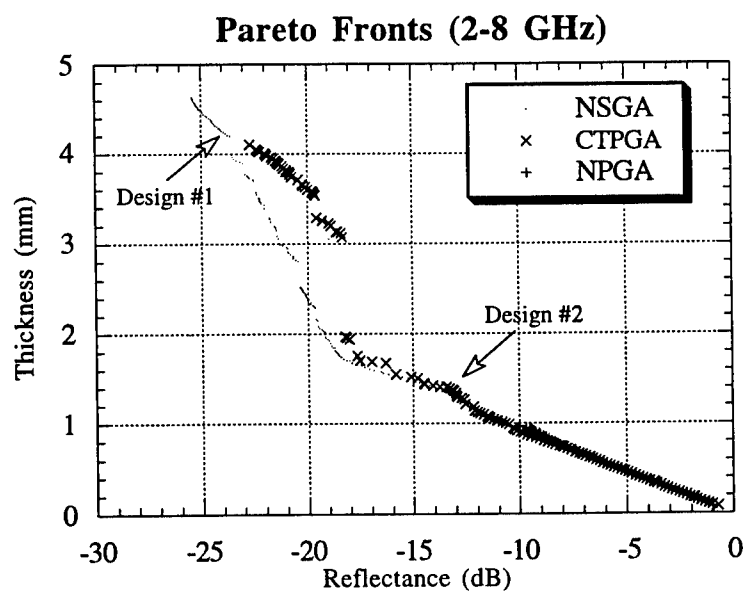
Comparison of NSGA with Classical Techniques

Figure 5. A comparison with classical techniques.

Pareto Fronts (2-8 GHz)

Figure 6. Response of the algorithm in two different bands.

Frequency Response of Pareto Optimal Designs
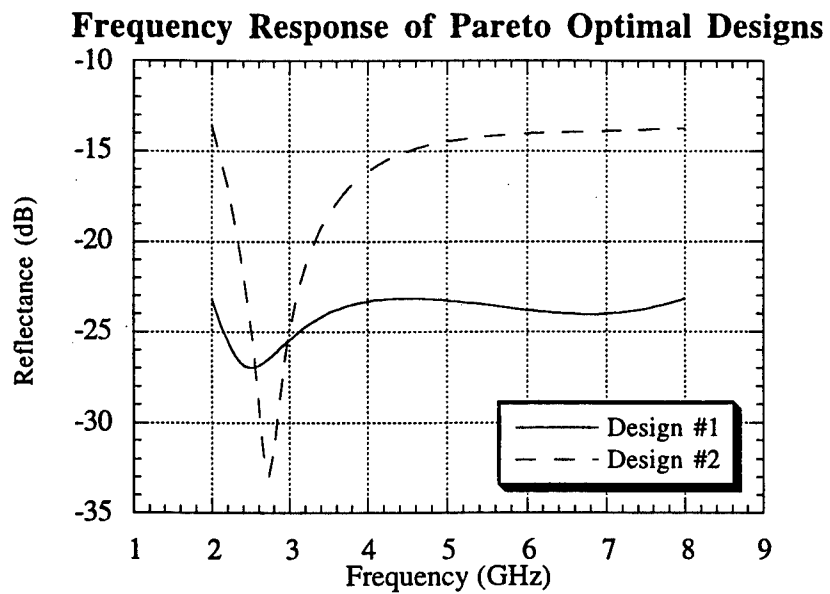
Figure 7. Frequency response of two Pareto optimal designs.
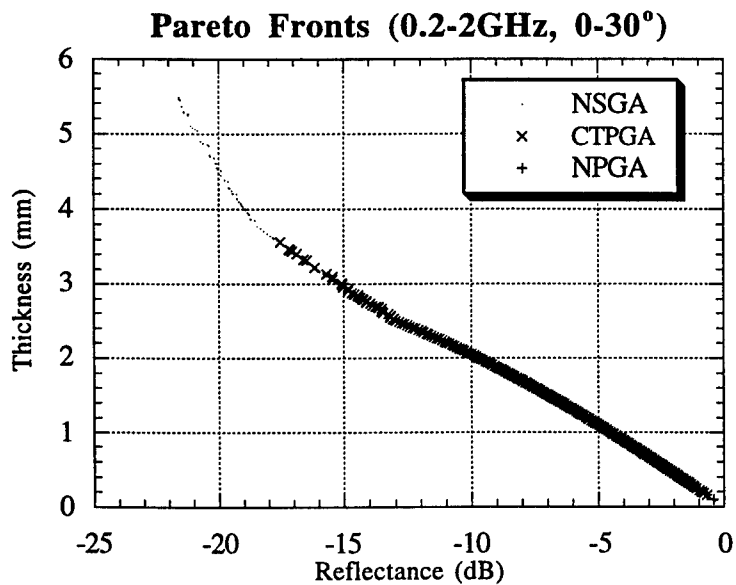
Pareto Fronts (0.2-2GHz, 0-30°)

Figure 8. The Pareto curve for the 0.2-2 GHz band at several angles of incidence.

MISSION
OF
ROME LABORATORY

Mission. The mission of Rome Laboratory is to advance the science and technologies of command, control, communications and intelligence and to transition them into systems to meet customer needs. To achieve this, Rome Lab:

  a. Conducts vigorous research, development and test programs in all applicable technologies;

  b. Transitions technology to current and future systems to improve operational capability, readiness, and supportability;

  c. Provides a full range of technical support to Air Force Material Command product centers and other Air Force organizations;

  d. Promotes transfer of technology to the private sector;

  e. Maintains leading edge technological expertise in the areas of surveillance, communications, command and control, intelligence, reliability science, electro-magnetic technology, photonics, signal processing, and computational science.

The thrust areas of technical competence include: Surveillance, Communications, Command and Control, Intelligence, Signal Processing, Computer Science and Technology, Electromagnetic Technology, Photonics and Reliability Sciences.